Imperial College London
Department of Materials

The Effect of Chemical and Mechanical Lattice Strain on the Transport Properties of Thin Film and Bulk $PrCoO_{3-\delta}$

Mabel Lew

Submitted in part fulfilment of the requirements for the degree of
Doctor of Philosophy in Materials of Imperial College London
and the Diploma of Imperial College, September 2016

Declaration

I hereby declare that this thesis and the work therein was my original research. Where external contributions have been employed, every effort has been taken to reference and acknowledge them appropriately.

Mabel Lew (2016)

The copyright of this thesis rests with the author and is made available under a Creative Commons Attribution Non-Commercial No Derivatives licence. Researchers are free to copy, distribute or transmit the thesis on the condition that they attribute it, that they do not use it for commercial purposes and that they do not alter, transform or build upon it. For any reuse or redistribution, researchers must make clear to others the licence terms of this work

Abstract

The aim of this work is to investigate: enhancement of the oxygen reduction reaction at the $PrCO_{3-\delta}/Pr_2NiO_{4\pm\delta}$ (PCO113/PNO214), inteface; and the mechano-chemical effect in mechanically strained lattice mismatched PCO113 films on $Ce_{0.9}Gd_{0.1}O_2$/8-mol% YSZ(002) fabricated using pulsed laser deposition, PLD, and chemically strained A-site deficient PCO113 ($Pr_{1-x}CO_{3-\delta}$) samples.

PCO113 films on Si(004) and $Ce_{0.9}Gd_{0.1}O_2$(200)/8-mol%YSZ(002) single crystal substrates were deposited by PLD. Out-of-plane compressive PCO113 lattice strains, calculated from the PCO113(002) reflection, between -0.39% to -0.99% were measured. Single phase PNO214 films could not be deposited for the PLD conditions tested in this work. Isothermal measurements of PNO214 at 800°C in air showed the gradual formation of Pr_6O_{11} and $Pr_4Ni_3O_{10}$, suggesting that this process is kinetically limited. Subsequently, investigation of the mechano-chemical effect was limited to the mechanically and chemically strained PCO113 systems.

The chemical expansion on introducing Pr-deficiency, x, in PCO113 was attributed to the formation of Pr vacancies, which effect was large enough to offset the decrease in ionic radii as the oxidation state of Co^{3+} increased to Co^{4+}. High temperature XRD indicated a thermo-chemical expansion though further work is required to identify the exact mechanism(s) behind it. A comparison of the thermo-chemical expansion between the Pr-deficient PCO113 samples confirmed an increase in oxygen vacancy concentration with Pr-deficiency.

^{18}O diffusion profiles of the Pr-deficient PCO113 samples were fitted using Crank's solution for diffusion in a semi-infinite plane. D and k^* values varied between 1.36-2.26$\times10^{-16}$ cm^2/s and 4.48-10.1$\times10^{-10}$ cm/s. D and electrical conductivity was found to increase with Pr-deficiency. Visual analysis of ^{18}O diffusions profiles of the strained PCO113 films suggested that the mechano-chemical effect was present and the introduction of a compressive out-of-plane strain inhibited oxide ion diffusion.

Acknowledgements

I would like to express my deepest gratitude to Prof. Stephen Skinner for the opportunity he has provided me in offering me this post-graduate position at Imperial College and for his unflagging guidance and support throughout, particularly during my write-up. Thank you for your time and efforts these past four years.

Similarly this thesis would not have been possible but for the assistance of the Fuel Cell Group at Imperial College: Prof. John Kilner for his insightful pointers; Stevin Pramana, for the many many hours he spent teaching me various XRD techniques and discussing my results- thank you so much; Florent Tonus, my charming desk neighbor who taught me Le Bail and Rietveld refinement; Andrea Cavallaro and Matthew Niania, for all their training and help with the exchange rig and SIMS; Samuel Cooper, for repeatedly showing me how to fit my diffusion profiles; Celeste van den Bosch, the little voice of calm who leapt to my rescue with the Zygo measurements; and Kuan-Ting, for showing me sample synthesis and advice regarding the deposition of Ruddlesden-Popper phases. The list is extensive. George Harrington, Ryan Bayliss, Cheng Li, Zonghao Shen, Chi Wong, Na Ni, Ji Wu, Rowena Brugges and Duke Shih, you have all played a part in a thousand little ways, progressing my work and keeping the crazies at bay.

In addition, many thanks are due to Mr. Richard Sweeney and Dr. Victoria Bemmer of the AFM, TA and XRD facility, Dr. Sarah Fearn and Dr. Richard Chater of the SIMS (and Zygo) lab, Dr. Mahmoud Ardakani and Mrs. Cati Ware of the SEM suite, Dr. Ignacio Villar-Garcia for his XPS work, and Dr. Peter Petrov and his entire Thin Film Group, for all their aid with the various equipments employed in this work.

Also, I am grateful to KAUST for the financial support they have provided, and the collaborative experience that ensued. My thanks and regards to Prof. Udo Schwingenschlögl, Prof. Enrico Traversa, Dr. Samir Boulfrad and the entire KAUST team, also to Prof. Mary Ryan and Dr. Andrew Horsfield of Imperial College for their work in this project.

I have received invaluable support outside of Imperial College, through my friends, church and family- you all have been so good to me, I am indebted to you all and hope to be as kind and caring as you have all been to me. Of particular mention are my fellowship group, bible study group and the entire student ministry, and my little prayer group of fellow strugglers that cheered me on with daily motivations. And to my family, my dearest family, thank you that you have supported me all through this time; thank you that, as you have always been all my life, once more you have been, overwhelmingly, a steadfast pillar of love and encouragement. To my beloved husband, Christopher Dancel, you have walked this path before me and you walked it again with me, my patient and indefatigable companion weathering the worst of my lows and gently pointing me ahead. I thank you.

Finally, I thank and praise God for the numerous blessings I have enjoyed, and for being my provider and sustainer. What a marvelous creation I have had the privilege to study.

Contents

Declaration i

Abstract ii

Acknowledgements iii

1 An Introduction to Solid Oxide Fuel Cells 1

1.1 Fuel Cells and SOFCs 1

1.2 SOFC Operation 3

1.3 SOFC Design 4

1.4 SOFC Performance 5

1.4.1 Cell Potential and Performance Curve 5

1.4.2 Activation Polarization Losses 6

1.4.3 Ohmic Polarization Losses 7

1.4.4 Concentration Polarization Losses 9

1.5 SOFC Component Requirements and Materials 10

1.5.1 Electrolyte 10

1.5.2 Anode 12

1.5.3 Cathode 12

1.5.4 Interconnect 13

1.5.5 Seals 14

2 General Properties of Perovskites and Ruddlesden-Popper Oxides 15

2.1 Defect Chemistry 15

2.2 Crystal Structure 17

2.2.1 Perovskite Oxides 17

2.2.2 Ruddlesden-Popper Oxides 19

2.3 Ionic Conductivity 20

2.3.1 Diffusion Mechanism of Ionic Conductivity 20

2.3.2 Perovskite Oxides 22

2.3.3 Ruddlesden-Popper Oxides 23

2.4 Electronic Conductivity 25

2.4.1 Electronic Conductivity of Metal Oxides 25

2.4.2 Perovskite and Ruddlesden-Popper Oxides 27

2.5 Chemical Expansion 28

2.5.1 Introduction to Chemical Expansion 28

2.5.2 Modelling Chemical Expansion in Fluorites 29

3 Oxygen Reduction Reaction at the SOFC Cathode 31

3.1 Triple Phase Boundary 32

3.2 The ORR in Cathodes Diffusion and Adsorption Co-limited 32

3.3 The ORR in Mixed Ionic-Electronic Conducting Cathodes 33

3.4 Enhancement of the ORR at the Perovskite/Ruddlesden-Popper Interface . 35

3.5 Enhancement of the ORR due to the Mechano-Chemical Effect 39

4 Thesis Objectives 41

5 Experimental Techniques 43

5.1 Material Synthesis 43

5.2 Pulsed Laser Deposition 44

5.3 Atomic Force Microscopy 47

5.4 Thermal Analysis 48
5.5 Scanning Electron Microscopy and Energy Dispersive X-ray Spectroscopy . 49
5.6 X-ray Photoelectron Spectroscopy 50
5.7 X-ray Diffraction 52
5.7.1 Powder X-ray Diffraction 52
5.7.2 Structural Refinement of Powder X-ray Diffraction Data 54
5.7.3 Thin Film X-ray Diffraction 54
5.7.4 Rocking Curves 55
5.7.5 Phi Scans and Pole Figures 55
5.7.6 Reciprocal Space Maps 56
5.8 X-ray Reflectivity 58
5.9 Vertical Scanning White Light Interferometry 59
5.10 Electrical Conductivity Measurements 59
5.11 Isotope Exchange Depth Profiling 61
5.11.1 Tracer Exchange 62
5.11.2 Secondary Ion Mass Spectrometry 62
5.11.3 Fitting ^{18}O Diffusion Profile 65

6 Synthesis and Characterisation of PLD Targets and Film Substrates 67

6.1 Literature Review 67
6.1.1 Synthesis of $PrCoO_{3-\delta}$ and $Pr_2NiO_{4\pm\delta}$ PLD Targets 68
6.1.2 PLD of $Ce_{0.9}Gd_{0.1}O_{2-\delta}$ Thin Films on YSZ-8mol%(001) 70
6.1.3 $Ce_{0.9}Gd_{0.1}O_{2-\delta}$ Target Stoichiometry During PLD Ablation 73
6.2 Experimental Method 74
6.3 Results and Discussion 75
6.3.1 $PrCoO_{3-\delta}$ Target 75
6.3.2 $Pr_2NiO_{4\pm\delta}$ Target 80
6.3.3 $Ce_{0.9}Gd_{0.1}O_{2-\delta}$ Target and Substrates 83

6.3.4 Si(004) Substrate 86
6.3.5 YSZ-8mol%(002) Substrate 87
6.3.6 Deposited $Ce_{0.9}Gd_{0.1}O_{2-\delta}$ Buffer Layers on YSZ-8mol%(002) 88
6.4 Conclusion and Further Work 90

7 The Effect of Oxygen Partial Pressure and Substrate Temperature on the Deposition of $PrCoO_{3-\delta}$ Films 92

7.1 Literature Review 92
7.1.1 PLD of $PrCoO_{3-\delta}$ 93
7.1.2 PLD of $LaCoO_{3-\delta}$ and $La_{1-x}Sr_xCoO_{3-\delta}$ 93
7.2 Experimental Method 95
7.3 Results and Discussion 96
7.3.1 $PrCoO_{3-\delta}$/Si(004) Films of Varying Thicknesses 96
7.3.2 $PrCoO_{3-\delta}$/Si(004) Films Deposited Using Oxygen Partial Pressures Between 10 mTorr and 500 mTorr 101
7.3.3 $PrCoO_{3-\delta}$/Si(004) Films Deposited Using Substrate Temperatures Between 680°C and 780°C 105
7.3.4 $PrCoO_{3-\delta}$/$Ce_{0.9}Gd_{0.1}O_{2-\delta}$(polycrystalline) Film 110
7.3.5 Repeatability of the PLD of $PrCoO_{3-\delta}$/Si(004) Films 111
7.4 Conclusion and Further Work 114

8 PLD of $Pr_2NiO_{4\pm\delta}$ and the Isothermal Study of $Pr_2NiO_{4\pm\delta}$ 116

8.1 Literature Review 116
8.1.1 $Pr_2(Ni,Cu,Ga)O_{4+\delta}$ 117
8.1.2 PLD of $Pr_2(Ni,Cu,Ga)O_{4+\delta}$ 118
8.1.3 High Temperature Stability of $Pr_2NiO_{4\pm\delta}$ 120
8.2 Experimental Method 123
8.3 Results and Discussion 124
8.3.1 PLD of $Pr_2NiO_{4\pm\delta}$ 124
8.3.2 Isothermal Study of $Pr_2NiO_{4\pm\delta}$ at 800°C in Air 135

8.4 Conclusion and Further Work 139

9 Characterisation of Strained $PrCoO_{3-\delta}/Ce_{0.9}Gd_{0.1}O_{2-\delta}$/YSZ8-mol% Films, Fabricated by PLD 141

9.1 Literature Review 142

9.1.1 The Effect of Lattice Mismatch: Lattice Strain, Strain Relaxation and Film Morphology 142

9.1.2 Strained $Ce_{0.9}Gd_{0.1}O_{2-\delta}$ Films 146

9.1.3 Strained Sr-Doped $LaCoO_3$ Films 149

9.2 Experimental Method 150

9.3 Results and Discussion 154

9.3.1 Morphological and Structural Characterization of Strained $Ce_{0.9}Gd_{0.1}O_{2-\delta}$ Films 154

9.3.2 Morphological and Structural Characterization of Strained $PrCoO_{3-\delta}/Ce_{0.9}Gd_{0.1}O_{2-\delta}$/YSZ8-mol% Films 168

9.4 Conclusion and Further Work 185

10 The Effect of Cation Non-stoichiometry on the Structure and Chemo-mechanical Expansion of $Pr_{1-x}CoO_{3-\delta}$ 187

10.1 Literature Review 188

10.1.1 Chemical Expansion of Perovskites 188

10.1.2 Thermo-Chemical Expansion of Perovskites 189

10.1.3 Current Literature on Cation Non-stoichiometric Perovskites 192

10.1.4 Defect Chemistry of $Pr_{1-x}CoO_{3-\delta}$ 195

10.2 Experimental Method 197

10.3 Results and Discussion 200

10.3.1 Room Temperature Characterization of $Pr_{1-x}CoO_{3-\delta}$ 200

10.3.2 High Temperature Characterization of $Pr_{1-x}CoO_{3-\delta}$ 211

10.4 Conclusion and Further Work 219

11 The Effects of Chemical and Mechanical Strain on the Oxygen Tracer and Electrical Transport Measurements of $PrCoO_{3-\delta}$ 221

11.1 Literature Review . . . 222

11.1.1 Mechano-chemical Coupling in Perovskites . . . 222

11.2 Experimental Methods . . . 225

11.3 Results and Discussion . . . 229

11.3.1 Time-of-Flight SIMS Depth Profiles . . . 229

11.3.2 Oxygen Tracer Transport Measurements . . . 239

11.3.3 Electrical Transport Measurements . . . 251

11.4 Conclusion and Further Work . . . 256

12 Conclusions 258

A 262

A.1 Pseudo-Voigt Fit of the Out-of-plane $PrCoO_3$ Reflections at $\sim 33.5^\circ$ 2θ . . . 262

A.2 XRD Measurements and Rietveld Refinement of Pr_2NiO_4 following Isothermal Treatment . . . 264

A.3 Thermal Analysis Data of $Pr_{1-x}CoO_{3-\delta}$ . . . 266

A.4 XRD Measurements and Rietveld Refinement of $Pr_{1-x}CoO_{3-\delta}$ . . . 267

A.5 ZYGO Crater Depth Measurements of $Pr_{1-x}CoO_{3-\delta}$ . . . 272

A.6 ToF SIMS Profiles of $Pr_{1-x}CoO_{3-\delta}$ Bulk and Film Samples . . . 273

Bibliography 273

List of Tables

1.1 Comparison of fuel cells [1]. 2

6.1 Sol-gel synthesis conditions of Pr cobaltate and nickleate oxide perovskites and R-Ps, as reported in literature. 69

6.2 Table of crystal structure and spacegroup. 70

6.3 Table of the three SZM zones as a function of deposition temperature, and the resulting dominant growth process and ensuing film morphology [2]. . . 71

6.4 AFM images of the CGO(200)/YSZ(002) films deposited using substrate temperatures of 680°C and 780°C, and oxygen partial pressures of 10 mTorr and 30 mTorr. All films were of a low roughness; the CGO(200) film deposited using a substrate temperature of 680°C and oxygen partial pressure of 10 mTorr appeared to be of the best quality, having the lowest roughness and no large deposits on its surface. 90

7.1 Table of the Bragg reflections of $PrCoO_{3-\delta}$, Pr_2CoO_4, $Pr_4Co_3O_{10}$ and Pr_6O_{11} that may correspond to the unidentified peaks at ∼33.0° 2θ and ∼32.5° 2θ. 104

7.2 Table of the Bragg reflections of CoO and Co_3O_4 that may correspond to the unidentified peak at ∼37.1° 2θ. 106

7.3 AFM and SE images of the PCO113 films deposited under nominally identical conditions, in the order of A, B, then C. As PCO113 target damaged increased, the grains of the deposited PCO113 film decreased in average size and size distribution. Also, the occurrence of microcracks in the deposited PCO113 film was reduced. SE scale bar = 100 nm. 113

8.1 Table of the different deposition conditions used in literature for the PLD of PNCG and LNO214, where a KrF excimer laser (λ = 248 nm) was employed. 119

8.2 Table of crystal structures and spacegroups of potential phases deposited in the ablation of PNO214. The lattice parameter of the Si wafer was been included, the mismatch in lattice parameters between Si and Pr_6O_{11}, PCO113, PNO214 or PNO4310 (the a- and b- parameters) is small. 129

8.3 Miller indices and peak positions between 20 and 60° 2θ for: (a) NiO; (b) Pr_6O_{11}; (c) $PrNiO_3$; (d) Pr_2NiO_4; and (e)$Pr_4Ni_3O_{9.85}$. Only reflections with an intensity ≥5% were shown. 131

8.4 Table of refined cell parameters of the phases present as a function of PNO214 anneal time (at 800°C in air). Included are reference cell parameters for PNO214 [3], Pr_6O_{11} [4], and PNO4310 [5]. 139

9.1 Number of laser pulses used in the deposition of CGO and PCO films for all three sample sets. All depositions were performed at 680°C and an oxygen partial pressure of 300 mTorr. 151

9.2 Spacegroup assignments of PCO, CGO and YSZ. Cell parameters of PCO and CGO obtained from Le Bail refinement of targets. YSZ c-cell parameter calculated from YSZ(002) reflection in the out-of-plane XRD measurement of the YSZ single crystal substrate. YSZ a- and b- cell parameters calculated assuming a $1/\sqrt{2}$ relation between the a- (and b-) and c-cell parameters. . . 154

9.3 Rocking curves of the CGO(200) reflection of CGO films deposited using 500 to 2500 pulses, of sample sets 1 and 2. For sample set 1, two different Pseudo-Voigt fits were useds due to the shape of the rocking curve. In the first fit, only one Pseudo-Voigt profile was usee. In the second fit, two Pseudo-Voigt prfiles were used, as if there were to CGO(200) contrbutions- one with low mosaicity, and one with a high mosaicity. Pseudo-Voigt fits are indicated in red. Where more than one Pseudo-Voight fit was used, the first fit is in red, the second in green, and the overall fit in blue. FWHM values have been measured and provided (for the multiple Pseudo-Voigt fit of sample set 1, the first FWHM value corresponds to the first Pseudo-Voigt profile in red, and the second FHWM values corresponds to the second Pseudo-Voigt profile in green. Increasing CGO film thickness decreased CGO film mosaicity. 163

9.4 Surface strain of the CGO film of sample set 1, calculated using (9.3) where ϵ_0 and α are -0.56 nm^{-1} and 0.16 nm^{-1} respectively. 166

9.5 Surface strain of the CGO film of sample set 2, calculated using (9.3) where ϵ_0 = -0.56 nm^{-1} and α = 0.16 nm^{-1} respectively. CGO film thicknesses have been estimated using the relation found of the CGO films of sample set 1, where a values of 6.55 CGO(200) normalized peak area corresponds to a CGO film thickness of 1 nm. 167

9.6 Peak intensities of the (020), (220), and (040) reflections of PCO, relative to the PCO(002) reflection. Two reference PCO patterns were used: from literature and from this work. The reflections at ∼41.2° 2θ was assigned to the PCO(220) reflection. Despite the similar position of the PCO(220) and PCO(022) reflections, the 2θ position of PCO(220) was found to correspond best to that observed of the out-of-plane patterns. In any case, the peak intensities of the PCO(022) and PCO(220) reflections differ by no more than 7.0% of each other, using the PCO reference pattern [6] (or 8.6% using the PCO target diffraction pattern). 177

9.7 FWHM of PCO rocking curves from sample sets 1 and 2, fitted using a Pseudo-Voigt profile. 178

9.8 ϵ_0 and α obtained from fitting the measured out-of-plane strain in (002) and (0k0) oriented PCO films, and (020) oriented LSC films reported in literature [7, 8] to (9.4). 184

10.1 The ionic radii for Pr and Co at different oxidations states and coordination number, as appropriate for the persovskite structure. It was not possible to obtain the ionic radii for Pr^{4+}. Nevertheless, it is expected to be smaller than Pr^{3+}, due to its more positive charge and thus less electrons. This can be seen in the 8-fold coordinated Pr^{3+} and Pr^{4+}, which have an ionic radii of 1.126 Åand 0.96 Årespectively [9]. 196

10.2 SE images of the bar sample surface of PCO with a range of non-stoichiometry, pre- and post-heat treatment at 1200°C in air for 6 h. A greater extent of sintering may be seen in the non-stoichiometric bar samples post-heat treatment. 201

10.3 Measured densities of the non-stoichiometric PCO samples, $Pr_{1-x}CoO_{3-\delta}$, using the Archimedes method. On their own, these density measurements suggests a higher density was obtained in the non-stoichiometric PCO samples pre-heat treatment at 1200°C in air for 12 h. However, coupled with with the SE images of Table 10.2, the density of the non-stoichiometric PCO samples post-heat treatment was confirmed to be higher. 202

10.4 XPS spectra of the non-stoichiometric PCO bar samples, $Pr_{1-x}CoO_{3-\delta}$, at the Pr 3d and Co 2p edges. Background and the Pr $3d_{5/2}$, Pr $3d_{3/2}$, Co $2p_{3/2}$ and Co $2p_{1/2}$ binding energies were obtained Dr. I. Villar-Garcia of Imperial College using the Thermo Advantage software. 203

10.5 Reported binding energies of Pr $3d_{5/2}$ and Co $2p_{3/2}$ spectral lines in literature. 204

11.1 The effective exchange times and temperatures, calculated using two different activations energies: E_A of 0.61 eV and 0.78 eV, for all PCO samples (films and non-stoichiometric bar samples) using the method as proposed by Killoran [10, 11]. 228

11.2 Measured out-of-plane lattice strain in the PCO films of sample set 2 and 3. 238

11.3 Table of the diffusion and exchange coefficients, D^* and k^*, obtained from the fits of the ^{18}O diffusion profiles in non-stoichiometric PCO at an effective exchange temperature of ∼389°C, and the R^2 value of each fit. 242

A.1 Refined parameters and reliability factors in Rietveld analysis of powder XRD sample held at 800°C in air for varying duration. 265

A.2 Refined parameters and reliability factors in Rietveld analysis of non-stoichiometric $Pr_{1-x}CoO_{3-\delta}$ samples, where x denotes A-site deficiency, using the *Pnma* spacegroup assignment. Oxygen positions were not refined but set to (0.5060, 0.25, 0.5675) and (0.2176, 0.0359, 0.2820) for O1 and O2, taken from [6]. . . 268

A.3 ZYGO crater depth measurement of non-stoichiometric $Pr_{1-x}CoO_{3-\delta}$ samples, where x denotes A-site deficiency. 272

List of Figures

1.1 Operation of a solid oxide fuel cell. 3

1.2 Schematic of a cathode-supported tubular SOFC stack and an anode-supported planar SOFC stack [12]. 4

1.3 Typical performance curve depicting polarization losses as a function of current density [13]. Activation, ohmic and concentration polarization losses dominates in regions I, II and III respectively. 6

1.4 Tafel plot of log(current) against overpotential, diagram from [14]. 7

1.5 Concentration loss due to Nernstian effects, $/eta_{conc,Nernst}$ causes a drop in the ideal voltage output of a cell from E to E'. Activation losses, η_{act} causes a further drop in the theoretical EMF to A'[15]. 10

1.6 Specific ionic conductivity of SOFC electrolytes as a function of reciprocal temperature. The operational ranges of different interconnect materials are also included [16]. 11

2.1 Ideal perovskite structure with A^{3+} and B^{3+} at the origin on the left and right respectively [17]. 17

2.2 The effect of ionic size of A- and B-site cations on the observed distortions of the $A^{3+}B^{3+}O_3$ perovksite structure [18]. 18

2.3 Unequally occupied orbitals resulting in the high or low spin states, and a correlation between the octahedral tilt angle with the number of electrons in the transition metal antibonding t_{2g} shell [19]. 19

2.4 Ruddlesden-Popper structure of general formula $A_{n+1}B_nO_{3n+1}$ [20]). 20

2.5 The saddle point, described by the critical radius of the two A-site cations and one B-site cation Ruddlesden [17, 21]. 23

2.6 Arrhenius plot of (a) the oxygen tracer diffusion, D^*, and (b) the surface exchange coefficient, k^*, obtained for different R-P structures [20]. 25

2.7 Example of covalent(left) and strongly ionic (right) bonding. 27

3.1 Proposed mechanisms governing ORR in SOFC cathodes, where phases α β, and γ refer to the electronic, gas, and ionic phase, respectively: (a)incorporation of oxygen into the bulk of the electronic phse (if MIEC); (b) adsorption and/or partial reduction of oxygen on the surface of the electronic phase; (c) bulk or (d) surface transport of O^{2-} or O^{n-}, respectively, to the α/γ interface, (e) electrochemical charge transfer of O^{2-} or (f) combinations of O^{2-} and e^{-}, respectively, across the α/γ interface, and (g) rates of one or more of these mechanisms wherein the electrolyte itself is active for generation and transport of electroactive oxygen species [22]. 32

3.2 Possible pathways for the ORR in a MIEC: the electrode surface path across the "open" triple phase boundary between cathode and electrolyte; or the electrode bulk path across the "closed" two phase boundary . The adsorbed oxygen species, $O_{x(ad)}$, may be any one of: $O_{2,ad}$, O_{ad}, $O^{-}{}_{ad}$ or $O^{2-}{}_{ad}$. The adsorbed oxygen may travel by surface diffusion to the TPB where it is full reduced; or it may incorporated directly into the MIEC as $O^{2-}{}_{ad}$, where it diffuses to the electrode/electrolyte interface [23, 24, 25]. 34

3.3 Schematic of $La_{2-x}CoO_4/La_{0.6}Sr_{0.4}CoO_3$/CGO layers; SIMS of layered PLD layers of $La_{2-x}CoO_4/La_{0.6}Sr_{0.4}CoO_3$/CGO after $^{16}O/^{18}O$ exchange at 0.2 bar, 773 K fo 180s (plane 1, 4, 18 corresponds to a sputtering depth of 70 nm, 2280 nm, 1.26 μm); and top down and cross-sectional SIMS images of PLD layers of $La_{2-x}CoO_4/La_{0.6}Sr_{0.4}CoO_3$/CGO after $^{16}O/^{18}O$ exchange at 0.2 bar, 773 K fo 180s [26]. 36

3.4 Electrochemical impedance spectroscopy (EIS) results of epitaxial microelectrodes ($\sim$200 μm) for the LSC113 reference and the LSC113 films with varying surface coverage of LSC214 at 550°C [27]. A comparison has been made to bulk properties as measured by Souza et al. [28]. 37

3.5 Electrochemical impedance spectroscopy (EIS) results of different epitaxial LSC113 based microelectrodes: LSC113 bulk- yellow [28](extrapolated to 510°C); base film in this study [29] (black hatched, 510°C, 140 nm thick base); base film [30] (grey, 520°C, 130 nm thick base); Sr-decorated film [29] (red hatched, 510°C, 140 nm thick base), heterostructured LSC113/LC214 film [27](green, 550°C, 85 nm thick base) [8]. 38

3.6 Surface-exchange coefficient k^* of MOD-derived LSC113 with nanoporous and dense microstructures in comparison with literature values for bulk LSC materials [31]. References for literature values may be found here [32, 33, 34, 35, 36, 37, 38, 39]. 39

4.1 Schematic of the $PrCoO_{3-\delta}$ samples by which lattice strain has been introduced using three different methods: the deposition of a $Pr_2NiO_{4\pm\delta}$ film on top of the $PrCoO_{3-\delta}$ film; variation in the $Ce_{0.9}Gd0.1O_{2-\delta}$ buffer layer thickness or $PrCoO_{3-\delta}$ film thickness; variation in $PrCoO_{3-\delta}$ metal cation stoichiometry. 42

5.1 Schematic of a typical PLD vacuum chamber, adapted from [40] 44

5.2 Schematic representation of three major film growth processes, from [41]. . 46

5.3 Basic principle of AFM, where a probe is mounted on a cantilever and cantilever deflections, arising atomic forces between the probe tip and sample surface, are monitored, from [42]. 47

5.4 Line profile across the masked edge of a PCO113 film (deposited using 5000 pulses). 48

5.5 Illustrating the requirements for a Bragg reflection, when the extra distance, $dsin\theta$ is equal to $n\lambda$ and $\mathbf{s}$ is parallel to [hkl], adapted from [43]. 53

5.6 XRD setup and scan parameters. 53

5.7 Slight tilts of the [400] diffracting planes resulting in a broad peak (blue) with a large FWHM, compared to a sharp peak (red) if the diffraction plane had been completely flat, from [43]. 56

5.8 Representation of an omega scan (left) and gonio/coupled scan (right) on a Ewalds sphere from [43]. 57

5.9 An asymmetric scan is necessary to differentiate between a compositional change shifting the Bragg peaks, or if the film is strained, adapted from [43]. 57

5.10 The different sources of peak broadening, adapted from [43]. 58

5.11 Schematic of bar and thin film configurations used for measurements of electrical conductivity. 60

5.12 Thin film sample with contacts attached with Ag paint. 61

5.13 Schematic illustrating the two operational modes, from [44]. 64

5.14 A burst-mode mass spectrum of negative secondary ions showing a significant decrease in $^{16}O^-$ counts after the first burst due to the instrument deadtime, from [44]. 64

6.1 Schematic of the minimum lattice mismatch between films and substrate with and without the use of a CGO buffer layer. 70

6.2 The effect of pressure and temperature PLD deposition conditions on the microstructure of the thin film in Zone 1 of the SZM. Regions A and B correspond to the transition zone. At low pressures and temperature (A), the films consist of disordered by coherent grains, which become strongly ordered at higher temperatures (B). At high pressures and low temperatures (D), a loose structure of clusters and pores form, which undergoes dissolution of the clusters into columnar grains at higher temperatures (though the pores persist)[2]. 72

6.3 Microstructural pressure-temperature map for CGO thin film deposition by PLD, where the reduced temperature was calculated from a melting temperature of 2500°C [2]. 72

6.4 Powder XRD pattern of PCO113 precursors following decomposition at 300°C and 600°C for 6 h in air, and following an additional calcination for 6 h at 600°C, 700°C, 800°C, 900°C, 1000°C. Reflections corresponding to unidentified secondary phase(s) when the PCO113 precursor is not calcined/calcined at 700°C have been marked. 76

6.5 Powder XRD pattern of PCO113 target, upon which a Le Bail refinement had been performed. Peak reflections have been indicated in green, diffraction data in red, modeled pattern in red, and the difference between measured and modeled pattern in blue. Main reflections have been labeled. . . 76

6.6 SE images of the PCO113 target surface after grinding with 400 grit paper showing still-distinct particles following sintering. 77

6.7 SE images of the damaged PCO113 target surface post-PLD deposition. (a) is a section of the ring of damage (scale bar = 2 mm); (b)-(f) depict the different target morphologies taken radially across the ring of damage (scale bar = 40 μm), where (b) is the undamaged center of PCO113 target. 78

6.8 XRD pattern of the PCO113 target pre- and post-laser ablation during PLD showing the same Bragg reflections and no apparent degradation of the target. There were no detectable second phases following laser ablation; there was relative confidence that there were no compositional changes arising from the deposition process. 79

6.9 Powder XRD pattern of PNO214 precursors following decomposition at 300°C and 600°C for 6 h in air, and following an additional calcination for 6 h at 900°C, 1000°C, 1100°C, 1200°C, 1300°C. Reflections corresponding to Pr_6O_{11} and NiO have been marked. 81

6.10 Powder XRD pattern of PNO214 target, upon which a Le Bail refinement had been performed. Peak reflections have been indicated in green, diffraction data in red, modeled pattern in red, and the difference between measured and modeled pattern in blue.Main reflections have been labeled. . . . 81

6.11 SE images of the PNO214 target surface (a) and (b) pre-PLD deposition and, (c) and (d) post-PLD deposition. (c) was obtained at the centre of the PNO214 target, indicating no changes in target morphology due to the deposition conditions. (d) was obtained at the ring of damage. Scale bar = 400 μm) for (a) and 40 μm for (b) - (d). 82

6.12 XRD pattern of the PNO214 target pre- and post-laser ablation during PLD. Main PNO214 peaks have been labeled. 83

6.13 Powder XRD pattern of CGO target, upon which a Le Bail refinement had been performed. Peak reflections have been indicated in green, diffraction data in red, modeled pattern in red, and the difference between measured and modeled pattern in blue. CGO reflections have been labeled. 84

6.14 SE images of the damaged CGO target surface post-PLD deposition. (a)-(f) depict the different target morphologies taken radially across the ring of damage, where (a) and (f) are the undamaged centre end edge of the CGO target, respectively. Scale bar = 9 μm for all. 85

6.15 SE image of the CGO target post-ablation indicating the locations at which EDX spectra were obtained. Scale bar = 2 mm. 86

6.16 AFM images of the polished CGO substrate surface of low roughness, that is fully sintered and of a high density, though pores are present. Some artifacts of the polishing process- the scores across it- were observed. 86

6.17 Out-of-plane XRD pattern of the single crystal Si(004) substrate. 87

6.18 AFM images of the single crystal Si(004) substrate surface showing them to be smooth and flat, of a low roughness. 87

6.19 Out-of-plane XRD pattern of the single crystal YSZ(002) substrate. 88

6.20 AFM images of the single crystal YSZ(002) substrate surface showing them to be smooth and flat, of a low roughness. 88

6.21 Out-of-plane XRD patterns of the CGO buffer layer deposited on a YSZ(002) substrate under various PLD conditions. A single CGO reflection was observed for all the CGO buffer layers. 89

7.1 Out-of-plane XRD patterns of the PCO113 films deposited using 1000 to 6000 pulses. PCO113 reflections have been labeled. The reflections between 32-34° 2θ have been enlarged. A slight peak shift may be observed in the PCO113 reflection at ~33.5 ° 2θ. 96

7.2 Film thickness measurements of the PCO113 films deposited using 1000 to 5000 pulses, performed using the Dektak surface profilometer. The deposition rate was 38 nm/1000 pulses. 98

7.3 Integrated peak intensity at ∼33.5° 2θ of the out-of-plane PCO113 reflection, fitted using a pseudo-Voigt profile. The PCO113 films were deposited using a range of pulses. The PCO113 film deposited using 2000 pulses was deemed anomalous. The volume of PCO113 deposited increased with the number of deposition pulses. Some error bays have been obscured by the data marker. 99

7.4 AFM and SE images of the PCO113 films deposited using 1000 to 6000 pulses. As film thicknesses increased, average grain size and the grain size distribution increased. Microcracks may be seen on the surface of the thicker PCO113 films. SE scale bar = 100 nm. 100

7.5 Out-of-plane XRD patterns of the PCO113 films deposited using an oxygen partial pressure between 10 mTorr and 500 mTorr. PCO113 reflections have been labeled. The reflections between 32-34° 2θ have been enlarged. There were three unidentified peaks at 32.5° 2θ, 33.0° 2θ and 44.3° 2θ. Possible phases they may belong to include Pr_6O_{11} and Co_3O_4. 101

7.6 AFM and SE images of the PCO113 films deposited using an oxygen partial pressure between 10 mTorr and 500 mTorr. Besides the (anomalous) PCO113 film deposited using an oxygen partial pressure of 200 mTorr, all PCO13 films deposited from oxygen partial pressures of 100 mTorr have similar morphologies consisting of regular shaped grains and a small grain size distribution. It was not clear if there was an enlargement of grain size as oxygen partial pressure increased. The PCO113 film deposited using an oxygen partial pressure of 10 mTorr had a very different morphology of irregularly shaped grains of a large distribution of sizes. SE scale bar = 100 nm. 103

7.7 Film thickness measurements of the PCO113 films deposited using an oxygen partial pressure between 10 to 500 mTorr, performed using the Dektak surface profilometer. Exempting the PCO113 films deposited using 10 mTorr and 200 mTorr, there was an increase in film thickness as oxygen partial pressure increased. 105

7.8 Out-of-plane XRD patterns of the PCO113 films deposited using a substrate temperature between 680°C and 780°C. PCO113 reflections have been labeled. The reflections between 32-34° 2θ have been enlarged. There were two unidentified peaks at 33.0° 2θ and 37.1° 2θ. 106

7.9 Film thickness measurements of the PCO113 films deposited using a substrate temperature between 680°C and 780°C, performed using the Dektak surface profilometer. Beside the exceptionally thick PCO113 film obtained at a substrate temperature of 700°C, an increase in PCO113 film thickness was found with increasing substrate temperature. 107

7.10 AFM and SE images of the PCO113 films deposited using a substrate temperature between 680°C and 780°C. As substrate temperature increased, average grain sizes increased as did the grain size distribution as the initially regularly shaped grains grew increasingly irregular. At the highest substrate temperature of 780°C, PCO113 film morphology changes significantly: large grains were found interspersed in a background of much smaller and regularly shaped grains. The AFM image showed that these large grains were highly irregular in shape, whereas the SE image showed that these large grains were more regular in shape. SE scale bar = 100 nm. 109

7.11 AFM images of the PCO113 films deposited using a substrate temperature of 740°C and 760°C depicting a very different morphology to that in Table 7.10a where the grains were smaller and of a smaller size distribution. The shape of the grain size distribution in these areas of the PCO113 films was very different, with an increased proportion of extremely large grains. . . . 109

7.12 XRD patterns of the PCO113 target, CGO polycrystalline substrate, and the PCO113 film deposited upon the CGO polycrystalline substrate using 10000 pulses. Reflections belong to either PCO113 and CGO have been labeled. The XRD pattern showed only the presence of a single PCO113 phase, that may be textured (preference to the (002),(121), or (200) orientations). 111

7.13 A comparison of the out-of-plane XRD patterns of the PCO113 films deposited under nominally identical conditions. PCO113 reflections have been labeled. Film A was the first to be deposited, then film B, and lastly film C. The reflections between 32-34° 2θ have been enlarged. There was one unidentified peak at 33.0° 2θ, the intensity of which increased with PCO113 target damage. 112

7.14 Film thickness measurements performed using the Dektak surface profilometer of PCO113 films (A, B, and C, of the same label as in Table 7.3) deposited under nominally identical conditions, as a function of PCO113 target usage (the number of pulses its surface had been ablated with, prior to the deposition of the PCO113 film). As PCo113 target damage increased, the thickness of the depocited PCO113 films decreased. As the intensities of the XRD patterns of Fig 7.13 remained constant despite PCO113 target damage, the decrease in film thickness was likely to be associated with an increase in deposited PCO113 film density with PCo113 target damage. . . 114

8.1 Nuclear density analysis from neutron diffraction data measured in situ at 1015.6°C indicated the two-dimensional network of curves O2-O3-O2 oxide-ion diffusion paths on the (Pr,La)-O layer in PLNCG [45]. 117

8.2 SE image of the PNCG/SDC laminated film with 100 nm thickness for each layer [46]. 120

8.3 Oxygen stoichiometry versus temperature in PN214, and the XRD pattern of single phase PNO214 prior to heat treatment, and a PNO214 sample quenched from 1030°C under oxygen flow which had decomposed into PNO4310 and PrO_y [47]. 121

8.4 XRD patterns of (from left to right): a reference PNO214 sample; PNO214 quenched after annealing in air at 800°C for 50 h; and PNO214 quenched after annealing in air at 1000°C for 24 h [48]. 122

8.5 $In-situ$ measurements of the resistivity versus temperature of PNO214 under the same conditions as in Fig 8.3 by Odier et al [47] 122

8.6 Dilatometric curve of PNO214 on heating in air [48]. 123

8.7 AFM images and the measured R_{rms} of PNO214 films deposited using a range of oxygen partial pressures, at a substrate temperature of 780°C and 3000 laser pulses. 125

8.8 AFM images and the measured R_{rms} of PNO214 films deposited using a range of substrate temperatures, at an oxygen partial pressure of 300 mTorr and 3000 laser pulses. 126

8.9 AFM images and the measured R_{rms} of PNO214 films deposited using a range of laser pulses, at a substrate temperature of 780°C and an oxygen partial pressure of 300 mTorr. 127

8.10 Film thickness measurements as functions of: (a) oxygen partial pressure; (b) substrate temperature; (c) number of laser pulses. Excluding the deposition parameter being varied, PLD was performed at an oxygen partial pressure of 300 mTorr, substrate temperature of 780°C, and using 3000 laser pulses. A deposition rate of ∼45.6 nm/1000 pulses was measured (at an oxygen partial pressure of 300 mTorr and substrate temperature of 780°C). Increasing oxygen partial pressure appeared to increase the deposition rate. There was no clear trend between the deposited film thickness and the substrate temperature. 128

8.11 Out-of-plane XRD patterns of the films deposited at an oxygen partial pressure between 10 and 500 mTorr. Where possible, reflections have been labeled. The film contains Pr_6O_{11}, the proportion of which increases with oxygen partial pressure. A second phase was present. Due to the few reflections, it was unclear if it was PNO113, PNO214 or PNO4310. There was one unidentified reflection at ∼44.3° 2θ that could not be matched to Pr_6O_{11}, PNO113, PNO214 or PNO4310. 129

8.12 Out-of-plane XRD patterns of the films deposited using a substrate temperature between 700 and 780°C. Where possible, reflections have been labeled. The film contains Pr_6O_{11}, the proportion of which increases with substrate temperature. A second phase was present. Due to the few reflections, it was unclear if it was PNO113, PNO214 or PNO4310. There was one unidentified reflection at ∼44.3° 2θ that could not be matched to Pr_6O_{11}, PNO113, PNO214 or PNO4310. 132

8.13 Out-of-plane XRD patterns of the films deposited using 1000 to 6000 pulses. Where possible, reflections have been labeled. The film contains Pr_6O_{11}, the proportion of which increases with substrate temperature. A second phase was present. The thickest film showed three additional peaks not found of the thinner film: at ∼24.4° 2θ, ∼32.5° 2θ and ∼33.2° 2θ It was still not possible to identify the phase(s) present as PNO113, PNO214 and PNO4310 all have reflections around those 2θ values. The peak at ∼24.4° 2θ could not be matched. 133

8.14 Film thickness measurements by the Dektak surface profilometer of films deposited on a polycrystalline CGO substrate using 10000 pulses, an oxygen partial pressure of 300 mTorr and a substrate temperature between 680°C and 780°C. It was unclear if there was a trend between deposition rate (nm) or substrate temperature. Comparisons with the films deposited under identical conditions but using 3000 pulses suggests there was not. 135

8.15 AFM images and measured R_{rms} of PNO214 films deposited on a polycrystalline CGO substrate using 10000 pulses, an oxygen partial pressure of 300 mTorr and a substrate temperature between 680°C and 780°C. A similar porous morphology was found of all the films, no secondary phases could be distinguished. 136

8.16 Out-of-plane XRD patterns of the films deposited on a polycrystalline CGO substrate using 10000 pulses, an oxygen partial pressure of 300 mTorr and a substrate temperature between 680°C and 780°C. Regardless of substrate temperature, the deposited film comprised of two phases: Pr_6O_{11} and NiO. Increasing the substrate temperature appeared to increase the amount of film deposited, as seen through the increase in the film peak intensities and also the film thickness measurements, and also the relative intensities of the Pr_6O_{11} reflections. 137

8.17 XRD patterns of PNO214 powder following different anneal times at 800°C in air. As the heat treatment progressed, increasing amounts of Pr_6O_{11} and PNO4310 was detected, similar to the oxidative decomposition of PNO214 reported in literature [47, 48]. 138

8.18 Fraction of Pr_6O_{11}, PNO214 and PNO4310 present in the heat treated PNO214 (at 800°C in air) as a function of anneal time. 138

9.1 Out-of-plane XRD scan show that the as-grown CGO20 film are c-axis oriented on MgO(002) suggesting a lattice misfit greater than 28%. The inset shows the rocking curve scan of the CGO20(004) reflection with a FWHM of 3.7° [49]. 147

9.2 Out-of-plane XRD scan of the PCO film deposited using 1000 pulses on a CGO buffer layer deposited using 1000 pulses. The PCO peaks around ∼33.5° 2θ were of an irregular shape. Also an additional unidentified peak was detected ∼33.9° 2θ, which was not seen in any other PCO film deposited. Subsequently, this film was deemed anomalous; no further structural characterization was performed on it. 153

9.3 AFM images of some of the deposited CGO-only films, deposited using a range of laser pulses, of sample set 1. Increasing CGO film thickness increased R_{rms} roughness, which nevertheless remained of a comparable value to that of the single crystal Si(004) and YSZ(002) substrates imaged in Chapter 6. 155

9.4 XRR measurements of the CGO-only films. Film thickness values have been calculated from the XRR pattern by Dr. A. Cavellero of Imperial College. The refraction fringes of the CGO film deposited usin 500 pulses could not be fitted to obtain a film thickness value. 156

9.5 Film thicknesses of CGO-only film deposited on YSZ(002), as measured using XRR. Deposition rate was 9.6 nm/1000 laser pulses. Approximate error in the XRRmeasurements: ±1 nm. 157

9.6 Out-of-plane XRD measurements of CGO films, deposited using 500 to 2500 laser pulses, in sample sets 1 (CGO-only films) and sample set 2 (PCO/CGO/YSZ films) between 30 to 38° 2θ. The CGO(200) reflections have been labeled, the intensity of which can be seen to increase with increased deposition pulses. As CGO film thickness increased, a shift in the 2θ position CGO(200) reflection to larger 2θ values can be seen, indicating a decrease in out-of-plane lattice parameters corresponding to the (200) reflection, whereas consideration of the lattice mismatch between CGO and YSZ would suggest an increase in out-of-plane lattice parameters. 158

9.7 Out-of-plane strain in CGO films of sample sets 1 and 2, as a function of measured CGO film thickness (by a Dektak 150 surface profilometer), and the integrated intensity of the CGO(200) reflection at ∼33.0° 2θ, both thought to be reliable indicators of the actual CGO film thickness. The value of the 'measured' CGO film thickness of the thinnest (4.8 nm thick) CGO film deposited using 500 pulses was calculated based on an average CGO deposition rate of 9.6 nm/1000 pulses. Error bars have been included but are mostly obscured by the data points. 159

9.8 CGO(200) peak fits for ∼4.8 nm thick CGO films of sample sets 1 and 2 deposited using 500 laser pulses. For sample set 1, it was possible to separate the CGO(200) and YSZ(002) reflections (the CGO(200) reflection shown here is the case with the largest peak overlap between CGO(200) and YSZ(002)), and Pseudo-Voigt fits were obtained from of a masked region corresponding to the CGO(200) peak position; the fit is indicated in red. For sample set 2, due to the overlap of the CGO(200), PCO(002) and YSZ(002) reflections, Pseudo-Voigt fits had to be made for each of these reflections, indicated in green, blue, and cyan respectively. The combined fit is indicated in yellow. These CGO films were the thinnest and had the lowest CGO(200) intensities, and thus had the largest error associated with their fit. 160

9.9 Out-of-plane lattice strain in the CGO films of sample set 1 (CGO/YSZ) and 2 (PCO/CGO/YSZ) as a function of the integrated intensity of the CGO(200) reflection, which was felt to be the most indicative measure of actual CGO film thickness. The measured out-of-plane lattice strains of the CGO films of sample set 1 were consistently larger than sample set 2 when a PCO film was deposited on top of the CGO. 161

9.10 Schematic of the different potential effects of the PCO film on the lattice strain of the CGO film, depending on the CGO film thickness. If the CGO film is thin enough that it is unable to relax back to a lattice parameter larger than the PCO lattice parameter, the PCO film would introduce an in-plane tensile strain in the CGO film. If the CGO film is thick enough that it is able to relax back to a lattice parameter larger than the PCO lattice parameter, the PCO film would introduce an in-plane compressive strain in the CGO film. 162

9.11 Comparison of the actual measured CGO film thickness using XRR and the integrated CGO(200) intensity of sample set 1. The integrated area of the CGO(200) reflection of the CGO film deposited using 2500 pulses appears anomalous (in red). 164

9.12 RSM of the CGO(200) reflection of CGO(200)/YSZ(002) deposited using 500 pulses, of sample set 1. CGO film intensities were too low to detect a peak in the asymmetric 115 scan, nevertheless it appears that the CGO film is epitaxial albeit with a high mosaicity. 165

9.13 RSM of the CGO(200) reflection of CGO(200)/YSZ(002) deposited using 2500 pulses, of sample set 1. The CGO reflection may be seen in both asymmetric (113) and (115) scans, suggesting that the thicker CGO films are also epitaxial. 166

9.14 (a)CGO films of both sample set 1 and 2 can be seen to share the same relationship between the the integrated area of the normalized CGO(200) reflection and the number of laser pulses used for the deposition of the film. The integrated area of the CGO(200) reflection appeared to be most indicative of CGO film thickness. Thus in (b), the integrated area of the normalized CGO(200) reflections of sample set 1 have been correlated with the measured thickness of the CGO films of sample set 1 to obtain a relationship from which the CGO film thicknesses of sample set 2 may be calculated given its (200) peak area: a values of 6.55 CGO(200) normalized peak area corresponds to a CGO film thickness of 1 nm. 167

9.15 Film thicknesses of PCO films deposited in sample set 2 and 3, as measured using a Dektak 150 surface profilometer. For sample set 2, CGO film thicknesses was calculated assuming a CGO deposition rate of 4.8 nm/1000 pulses. For sample set 3, an average CGO film thickness of 4.8 nm was assumed. PCO films of sample set 2 have been deposited using 3000 pulses. PCO films of sample set 3 have been deposited using a range of laser pulses, between 1000 to 6000 pulses. 169

9.16 Summed integrated intensities of PCO reflections of PCO films in sample sets 1 and 2, as a function of (a) the number of laser pulses used for PCO deposition and (b) the average measured PCO thickness using the Dektak 150 surface profilometer. PCO film thicknesses of sample set 2 were confirmed to have significant variation. 170

9.17 AFM images and measured R_{rms} of the PCO films of sample set 2, where a different number of laser pulses were used in the deposition of the CGO buffer layer (as specified for each image). Increasing CGO buffer layer thickness and thus the lattice mismatch between CGO and PCO had no clear effect on the PCO film roughness, but an increase in PCO grain size was observed though this may have been due to the decrease in PCO thickness (with CGO thickness) despite PCO deposition conditionals being nominally identical. 171

9.18 AFM images and measured R_{rms} of the PCO films of sample set 3, where a different number of laser pulses were used in the deposition of the PCO film (as specified for each image). Increasing PCO film thickness and thus decreasing the lattice strain in the PCO film, increased both PCO film R_{rms} roughness and grain size. 172

9.19 Out-of-plane lattice strain in the CGO films of sample set 1 (CGO/YSZ) and 2 (PCO/CGO/YSZ) as a function of the integrated intensity of the CGO(200) reflection, which was felt to be the most indicative measure of actual CGO film thickness. The measured out-of-plane lattice strains of the CGO films of sample set 1 were consistently larger than sample set 2 when a PCO film was deposited on top of the CGO. 173

9.20 SE images of the PCO films of sample set 2, where a different number of laser pulses were used in the deposition of the CGO buffer layer (as specified for each image). PCO grain size can be seen to increase substantially with the increase in CGO buffer layer thickness and subsequently also the PCO/CGO lattice mismatch, and film morphology can also be seen to evolve into less regularly shaped grains with a larger grain size distribution. 174

9.21 SE images of the PCO films of sample set 3, where a different number of laser pulses were used in the deposition of the PCO film (as specified for each image). Increasing PCO film thickness and thus decreasing the lattice strain in the PCO film, increased the average PCO film grain size. 175

9.22 Out-of-plane XRD patterns of the PCO films of: (a) sample set 2, for which 1000 pulses were used for the deposition of the PCO film, but a range of pulses used for the deposition of the CGO buffer layer (as specified in the figure); and (b) sample set 3, for which a range of pulses were used for the depositin of the PCO film (as specified in the figure). PCO films of both sample sets appears highly textured. Only one family of diffraction planes was found of the PCO films of sample set 2. An additional orientation was found for the PCO films of sample set 3, corresponding to either the (220) or (022) diffraction planes. 176

9.23 An example PCO(002) rocking curve of a PCO film of sample set 3, deposited using 5000 pulses with a Pseudo-Voigt fit (in red). 178

9.24 RSM of the PCO(002) reflection of PCO/CGO(200)/YSZ(002) deposited using 3000 pulses, of sample set 3. An in-plane relationship between PCO, the CGO buffer layer and YSZ substrate may be seen in the asymmetric 113 scan. The PCO film is highly strained, the PCO reflection is just within the boundaries of the scan. While the CGO(200) reflection may be seen in the asymmetric 115 scan, the PCO reflection was beyond the boundary of the scan, and likely to have been of too low an intensity to be detected. . . 179

9.25 Out-of-plane XRD patterns of the PCO films of: (a) sample set 2, for which 1000 pulses were used for the deposition of the PCO film, but a range of pulses used for the deposition of the CGO buffer layer (as specified in the figure); and (b) sample set 3, for which a range of pulses were used for the depositin of the PCO film (as specified in the figure). In sample set 2, as CGO film thickness increases and CGO/PCO lattice mismatch increases, the PCO(002) reflections can be seen to shift to larger 2θ values, while in sample set 3, as PCO film thickness increases and the PCO film relaxes, the PCO(002) reflection can be seen to shift to smaller 2θ values. 180

9.26 Out-of-plane strain in sample set 2, calculated from the CGO(200), PCO(020), PCO(040) and PCO(002) reflections. The differently oriented PCO grains all showed a similar trend. As CGO buffer layer thickness increased, the out-of-plane compressive strain in the PCO film also increased. The lattice strain of the (002) oriented grains of the PCO film appeared to be more highly strained than the (0k0) oriented PCO grains. 182

9.27 Out-of-plane strain in the PCO films of sample set 2 as a function of the out-of-plane strain in the CGO buffer layer. The strain in the PCO film on top of a CGO buffer layer with a CGO(200) out-of-plane strain of ∼-4.2% appears anomalous. 182

9.28 Out-of-plane strain in the PCO films of sample set 3 as a function of average PCO film thickness as measured using a Dektak 150 surface profilometer. The PCO lattice strain in the two differently oriented films can both be seen to relax as PCO film thickness increases. Reported out-of-plane lattice strain of LSC on a CGO buffer layer of similar thickness (∼5 nm), by La'O et al. and Crumlin et al. [7, 8] have also been included in the figure. 184

10.1 Dependence of the change in species concentration, $\Delta[i]$, of lattice (trivalent) B-site cations, ${B_B}^X$, oxidized (quadrivalent) B-site cations, ${B_B}^{\cdot}$, lattice neutral oxygen anions, ${O_O}^X$ and oxygen vacancies, ${V_O}^{\cdot\cdot}$, determined using defect equilibria calculations from [50]. Room temperature was taken as a reference for zero change in concentration. At high temperatures, above ∼600°C, chemical expansion is dominated by the formation of ${B_B}^X$ from ${B_B}^{\cdot}$. 190

10.2 The predicted thermo-chemical expansion coefficient fitted to experimentally determined data in air. The concentration of oxygen vacancies, δ is also shown for comparison with the effective chemical expansion coefficient [51]. 191

10.3 Linear thermal expansion coefficient at 700°C for (a)$La_{0.6-z}Sr_{0.4}Co_{0.2}Fe_{0.8}O_{3-\delta}$, (b)$La_{0.6}Sr_{0.4-z}Co_{0.2}Fe_{0.8}O_{3-\delta}$ and (c)$(La_{0.6}Sr_{0.4})_{1-z}Co_{0.2}Fe_{0.8}O_{3-\delta}$ as a function of A-site deficiency, z [52]. 192

10.4 Pr:Co ratio as calculated from various EDX maps (at two magnifications: 200× and 500×) of the non-stoichiometric PCO samples pre- and post-heat treatment at 1200°C in air for 12 h. 202

10.5 Pr:Co ratio as calculated from XPS measurements of the non-stoichiometric PCO samples, $Pr_{1-x}CoO_{3-\delta}$, showing a correlation with the nominal composition of the non-stoichiometric PCO samples, unlike the EDX compositional measurements in Fig 10.4. 205

10.6 Atomic% C, as measured using XPS, as a function of the PCO nominal composition, $Pr_{1-x}CoO_{3-\delta}$. 206

10.7 XRD powder diffraction pattern of non-stoichiometric PCO samples, $Pr_{1-x}CoO_{3-\delta}$, obtained using two D2 Phaser diffractometers. Inset shows the slight difference in peak shape between the non-stoichiometric PCO samples resulting from the use of the two diffractometers. 206

10.8 Lattice parameters of non-stoichiometric PCO samples, $Pr_{1-x}CoO_{3-\delta}$, calculated from Rietveld refinement of room-temperature powder XRD patterns obtained using a D2 Phaser diffractometer. Error bars have been included but are concealed by the data markers. A reference lattice parameter of stoichiometric PCO (traingle marker) has been included [6]. The lattice parameters of the stoichiometric PCO sample ($x = 0.000$) of this work was anomalous. 208

10.9 Chemical strain in each cell-parameter, as a result of the non-stoichiometry of the PCO samples, $Pr_{1-x}CoO_{3-\delta}$. 210

10.10Co-O1 and Co-O2 bondlengths as a function of the volumetric chemical strain of non-stoichiometric PCO samples, $Pr_{1-x}CoO_{3-\delta}$. 210

10.11XRD powder diffraction pattern of non-stoichiometric PCO samples, $Pr_{1-x}CoO_{3-\delta}$, obtained using the Panalytical X'pert MPD. Trace reflections of the Pt sample holder were detected, the intensity of which depended on PCO sample coverage over the Pt film. 211

10.12XRD powder diffraction pattern of non-stoichiometric PCO, $Pr_{1-x}CoO_{3-\delta}$, where $x = 0.025$, obtained using the Panalytical X'pert MPD. Trace reflections of the Pt sample holder were detected. Inset, the diffraction patterns at ∼22° 2θ and ∼34° 2θ superimposed on top of each other: as temperature increased the PCO reflection at ∼22° 2θ shifted to smaller 2θ values, whereas the PCO reflections at ∼34° 2θ shifted to smaller 2θ values, decreased in FWHM and increased in maximum peak intensity. A phase transformation may be observed between 308°C and 464°C. 213

10.13XRD powder diffraction pattern of non-stoichiometric PCO, $Pr_{1-x}CoO_{3-\delta}$, where $x = 0.100$, obtained using the Panalytical X'pert MPD. Trace reflections of the Pt sample holder were detected. Inset, the diffraction patterns at ∼22° 2θ and ∼34° 2θ superimposed on top of each other. At temperatures above 308°C, FWHM of all reflections broadened, accompanied by a decrease in peak intensity. 214

10.14XRD powder diffraction pattern of non-stoichiometric PCO, $Pr_{1-x}CoO_{3-\delta}$, where $x = 0.025$, pre- and post- heating obtained using the Panalytical X'pert MPD. Trace reflections of the Pt sample holder were detected and labeled. The two diffraction patterns are virtually identical. 215

10.15Volumetric strain (%) in the non-stoichiometric PCO, $Pr_{1-x}CoO_{3-\delta}$ as a function of temperature. Increasing A-site deficiency, x, increases the rate of lattice expansion with temperature. Error bars have been partially concealed by the data markers. 216

10.16% change in a- b- and c-cell parameters of non-stoichiometric PCO samples, $Pr_{1-x}CoO_{3-\delta}$, as a function of temperature. Error bars have been partially concealed by the data markers. A phase transition may be observed in all the PCO samples, where the gradient of the % change in cell parameters, the thermal expansion coefficeint, TEC, changes. 217

10.17Thermal expansion coefficient as calculated from a-, b-, and c-cell parameters of non-stoichiometric PCO samples, $Pr_{1-x}CoO_{3-\delta}$, as a function of A-site deficiency, x. 218

11.1 SE images of a trial (Si) surface encapsulated with Au films of various thicknesses that have been annealed at 400°C. 227

11.2 Example ZYGO crater depth measurement of non-stoichiometric PCO (x = 0.025). In (a), the sample surface reference has been selected, and also the crater area. The profile taken across the plot is shown in (b). 229

11.3 Example of the sensitivity of the calculated effective exchange time and temperature to the activation energy. Even if the activation energy of PCO were half that of LCO ($E_A = 0.61$ eV), the exchange time only decreased by ∼2.5 min, given the temperature profile of the PCO sample measured in (a). 230

11.4 Example depth profile into (a) a non-stochiometric PCO bar sample and (b) a PCO film. The Pr:Co ratio was also calculated as a function of sputter depth to examine for variations in Pr^{O}:CoO^{-} cation ratio across the samples. Intensities of the measured species have been normalized. The GdO^{-} count was low and not included in the depth profile into the PCO film. 231

11.5 SE image of the surface of non-stoichiometric PCO ($x = 0.000$) bar sample post-exchange. Precipitates can clearly be observed where previously the sample surface was clean. 232

11.6 EDX measurements of the surface of non-stoichiometric PCO ($x = 0.00$) post-exchange. EDX spectra were obtained of the precipitates and PCO surface. The precipitates had a higher Pr:Co ratio, suggesting the formation of a Pr oxide. 233

11.7 Normalized intensities of CoO^- and PrO^- as a function of sputter depth of the non-stoichiometric PCO bar samples. 234

11.8 Average PrO^-:CoO^- ratios obtained across the depth of the non-stoichiometric PCO samples. The data point in red is thought to be anomalous. 234

11.9 Normalized intensities of (a) CoO^-, (b) PrO^- and (c) CoO^-, also (d) PrO^-:CoO^- ratios, as a function of sputter depth of the PCO films of sample set 2 (where the CGO buffer layer thickness was varied). 235

11.10Average PrO^-:CoO^- ratios obtained across the depth of the PCO films of sample set 2, as a function of the number of laser pulses used in the deposition of the CGO buffer layer. There may be a trend of increasing PrO^-:CoO^- ratio with increasing CGO buffer layer thickness and subsequently with increasing PCO lattice strain. 236

11.11Normalized intensities of (a) CoO^-, (b) PrO^- and (c) CoO^-, also (d) PrO^-:CoO^- ratios, as a function of sputter depth of the PCO films of sample set 3 (where the PCO film thickness was varied). 237

11.12Average PrO^-:CoO^- ratios obtained across the depth of the PCO films of sample set 3, as a function of the number of laser pulses used in the deposition of the CGO buffer layer. There may be a trend of increasing PrO^-:CoO^- ratio withith increasing PCO film thickness and subsequently with decreasing PCO lattice strain (contrary to what was found of the PCO films of sample set 2). 239

11.13Corrected ^{18}O tracer profile, obtained at an effective exchange time and temperature of ∼15 min and ∼ 389°C, for the non-stoichiometric PCO bar samples. Inset, the diffusion profile at within the first 50 nm of the sample surface is expanded. 240

11.14^{18}O diffusion profiles in the non-stoichiometric PCO bar samples, $Pr_{1-x}CoO_{3-\delta}$, fitted to Crank's solution for diffusion in a semi-infinite medium. Inset, the near-surface profile: 0 to 50 nm. R^2 values of the fit vary between 0.9704 and 0.9966. 241

11.15Arrhenius plot of measured oxygen tracer diffusivity for different oxides cathodes: $La_{0.8}Sr_{0.2}MnO_{3-\delta}$ [53], $La_{0.5}Sr_{0.5}CoO_{3-\delta}$ [53], $La_{0.8}Sr_{0.2}CoO_{3-\delta}$ [53], $GaBaCo_2O_{5+\delta}$ [54] and $La_2NiO_{4+\delta}$ [55], taken from [56]. 242

11.16Diffusion coeffitients, D^*, obtained from ^{18}O diffusion profiles in the non-stoichiometric PCO bar samples at an effective exchange temperature of ∼389°C as a function a A-site deficiency, x, and PrO^-:CoO^- ratio. There appeared to be a trend between D^* and PrO^-:CoO^- ratio, which was not present with x. 243

11.17Exchange coefficient, k^*, obtained from ^{18}O diffusion profiles in the non-stoichiometric PCO bar samples as a function a A-site deficiency, x, and PrO^-:CoO^- ratio. No trends were apparent 244

11.18Corrected ^{18}O tracer profile, obtained at an effective exchange time and temperature of ∼15 min and ∼ 389°C, for strained PCO films of sample set 2 on a CGO buffer layer deposited using 500 to 2500 pulses. Inset, the diffusion profile at within the first 50 nm of the sample surface is expanded. The PCO/CGO interface was at a sputter depth of ∼77.4 nm. 245

11.19Corrected ^{18}O tracer profile, obtained at an effective exchange time and temperature of ∼15 min and ∼ 389°C, for strained PCO films of sample set 2 on a CGO buffer layer deposited using 500 to 2500 pulses. The profile at the PCO/CGO interface, a sputter depth of ∼77.4 nm, may be seen. 246

11.20^{18}O diffusion profiles in the strained PCO film (1000 pulses) on a CGO buffer layer (2000 pulses) of sample set 2, fitted to Crank's solution for diffusion in a semi-infinite medium. Inset, the near-surface profile: 0 to 50 nm. D^* and k^* values are 5.83×10^{-16} cm^2/s and 1.693×10^{-11} cm/s respectively were obtained, however the fit was poor with an R^2 value of 0.7447. 247

11.21Corrected ^{18}O tracer profile, obtained at an effective exchange time and temperature of ∼16 min and ∼ 389°C, for strained PCO films of sample set 3, deposited using 1000 to 6000 pulses, on a CGO buffer layer of a constant thickness. Inset, the diffusion profile at within the first 50 nm of the sample surface is expanded. 248

11.22 ^{18}O diffusion profiles in two differently strained PCO films (∼77.4 nm and ∼129 nm thick) on a CGO buffer layer (deposited using 1000 pulses) of sample set 3, fitted to Crank's solution for diffusion in a semi-infinite medium. Inset, the near-surface profile: 0 to 50 nm. D^* and k^* values for the ∼77.4 nm thick PCO film are 4.95×10^{-16} cm^2/s and 1.57×10^{-11} cm/s respectively.D^* and k^* values for the ∼129 nm thick PCO film are 5.24×10^{-14} cm^2/s and 1.30×10^{-10} cm/s respectively. However, the fit was poor with R^2 value of 0.6649 and 0.7857 for the ∼77.4 nm and ∼129 nm thick PCO films respectively. 249

11.23 Schematic composition diffusion profile. The near-surface steep profile (curve CA) is due mainly to direct lattice diffusion from the surface along the X direction, while the shallow tail (curve AE) is due mainly to fast paths. The contribution of these fast paths to the composite diffusion profile may be described by the curve OFAE. Taken from [57]. 250

11.24 Composite diffusion profiles, fitted to Crank's solution for diffusion in a semi-infinite medium. In (A), there is a departure from Crank's solution due to fast transport paths but which does not result in a clear break and 'tail' section making identification difficult. In (b) and (c), different extents of a tailing function may be seen, similar to the profiles obtained of the PCO films in this work, resulting from the varying contributions of the fast transport paths to the profiles. Taken from [58]. 250

11.25 (a) Measured ^{18}O diffusion profiles in the strained PCO films on a CGO buffer layer (deposited using 1000 pulses) of sample set 2, plotted on a $ln(C')$ against $x^{6/5}$ axis to test for the presence of a tailing function and identify the break in the slope (point A in Fig 11.23). The transition arising from lattice diffusion contributions and fast diffusion paths contributions was less clear than in (b)- an example ^{18}O diffusion profile fit on the same axis by Zhang et al. [57], where the lattice and fast transport path contributions may clearly be fitted in the profile. 251

11.26 Conductivity measurements of non-stoichiometric PCO bar samples ($Pr_{1-x}CoO_{3-\delta}$ where x denotes A-site deficiency. Increasing x resulted in a decrease in electrical conductivity. 252

11.27 Conductivity measurements of strained PCO films of sample set 2 (where the CGO buffer layer was deposited using 500 to 2500 pulses, and the PCO film deposited using 3000 pulses) and sample set 3 (where the CGO buffer layer was deposited using 1000 pulses, and the PCO film was deposited using 1000 to 6000 pulses). The conductivity measurements of the two thickest PCO films of sample set 3 at 400°C in (c) have been omitted. . . . 253

11.28 Conductivity values at 400°C in the strained PCO films of sample sets 2 and 3. 254

11.29Conductivity measurements of (a)CGO and (b)YSZ films on various substrates by [59, 60]- refer to these works for references in the the figures. . . 256

A.1 Pseudo-Voigt fit of the out-of-plane XRD highest intensity $PrCoO_3$ reflection at ∼33.5° 2θ for $PrCoO_3$ films deposited on Si(004) single crystal substrates using a range of laser pulses between 1000 to 6000 pulses. The measured diffraction pattern is in black, and the pseudo-Voigt profile in red. The purple arrows indicate the range of data selected for the fit. 263

A.2 XRD powder patterns of quenched Pr_2NiO_4 samples following an anneal at 800°C in air for up to 12 h. The measured data is in red, the Rietveld fit in black, and the difference between them in blue. The Bragg reflections of Pr_2NiO_4, Pr_6O_{11} and $Pr_4Ni_3O_{10}$ are marked in blue, red and green, respectively. 264

A.3 (a) DSC measurements of non-stoichiometric $Pr_{1-x}CoO_{3-\delta}$ samples, where x denotes A-site deficiency. (b) Example of a TGA measurement of an A-site deficient PCO where $x = 0.050$. An increase in mass can be seen past ∼400°C as oxygen is taken into the lattice. 266

A.4 XRD powder patterns of non-stoichiometric $Pr_{1-x}CoO_{3-\delta}$ samples, where x denotes A-site deficiency. The measured data is in red, the Rietveld fit in black, and the difference between them in blue. The Bragg reflections of $PrCoO_3$ is marked in blue. 267

A.5 In-situ HT-XRD powder patterns of non-stoichiometric $Pr_{1-x}CoO_{3-\delta}$ samples, where x denotes A-site deficiency, in air. 271

A.6 SIMS depth profiles of non-stoichiometric $Pr_{1-x}CoO_{3-\delta}$ samples, where x denotes A-site deficiency. Normalized intensities detected are plotted against sputter depth. 273

A.7 SIMS depth profiles of PCO/CGO/YSZ films of sample set 2, where a range of pulses were used to deposit the $Ce_{0.8}Gd_0.2$ buffer layer. 3000 pulses used to deposit the $PrCoO_3$ film). Normalized intensities detected are plotted against sputter depth. 274

A.8 SIMS depth profiles of PCO/CGO/YSZ films of sample set 3, where a range of pulses were used to deposit the $PrCoO_3$ film. 1000 pulses were used for the deposition of the $Ce_{0.8}Gd_0.2$ buffer layer. Normalized intensities detected are plotted against sputter depth. 275

Chapter 1

An Introduction to Solid Oxide Fuel Cells

In this chapter the context of this work is provided and solid oxide fuel cells, SOFCs, introduced as a potential solution to generating electrical energy without greenhouse emissions. The operation and design of SOFCs are covered as well as their performance and specifically the areas associated with polarization losses, which lower cell efficiency. The impetus of this work is to minimize these polarization losses. Subsequently material selection of the SOFC components is crucial.

1.1 Fuel Cells and SOFCs

Fuel cells are devices that convert chemical energy directly to electrical energy through externally stored reactants (hydrogen and water). They have the potential to achieve higher efficiency conversion than the combustion process. Additionally: operation is silent; it does not produce pollutants; and it can be configured not to produce greenhouse gases (namely water vapour). There is thus a clear motivation in progressing their development

All fuel cells comprise of three active components: the anode, cathode, and electrolyte, wherein two different half-cell reactions and charge transport occur respectively and typically involves the production of water through the overall reaction: $2H_2 + O_2 \rightarrow 2H_2O$. A fuel cell is characterized by the electrolyte employed as it is key in forcing electronic current flow through an external load bearing circuit and determines the half-cell reactions in accordance to the charge carrying species through it. The type of hydrogen fuel cell of interest to this project is the solid oxide fuel cell, SOFC. Due to the solid oxide electrolyte in SOFCs, the mobile ionic species is O^{2-}. Similarly, molten carbonate fuel cells, MCFCs, have a carbonate conducting electrolyte and it is the negative carbonate ions that partake in the reaction, while in proton exchange membrane fuel cells, PEMFCs, the electrolyte is a polymer membrane that conducts protons.

Fuel Cell Type	Operating Temperature	Typical Stack Size	Efficiency	Advantages	Disadvantages
Polymer Electrolyte Membrane (PEM)	50-100°C 122-212° typically 80°C	< 1kW–100kW	60% transportation 35% stationary	• Solid electrolyte reduces corrosion & electrolyte management problems • Low temperature • Quick start-up	• Expensive catalysts • Sensitive to fuel impurities • Low temperature waste heat
Alkaline (AFC)	90-100°C 194-212°F	10–100 kW	60%	• Cathode reaction faster in alkaline electrolyte, leads to high performance • Low cost components	• Sensitive to CO_2 in fuel and air • Electrolyte management
Phosphoric Acid (PAFC)	150-200°C 302-392°F	400 kW 100 kW module	40%	• Higher temperature enables CHP • Increased tolerance to fuel impurities	• Pt catalyst • Long start up time • Low current and power
Molten Carbonate (MCFC)	600-700°C 1112-1292°F	300 kW-3 MW 300 kW module	45-50%	• High efficiency • Fuel flexibility • Can use a variety of catalysts • Suitable for CHP	• High temperature corrosion and breakdown of cell components • Long start up time • Low power density
Solid Oxide (SOFC)	700-1000°C 1202-1832°F	1 kW–2 MW	60%	• High efficiency • Fuel flexibility • Can use a variety of catalysts • Solid electrolyte • Suitable for CHP & CHHP • Hybrid/GT cycle	• High temperature corrosion and breakdown of cell components • High temperature operation requires long start up time and limits

Table 1.1: Comparison of fuel cells [1].

SOFCs have the advantage over other types of fuel cells such as alkali or phosphoric acid fuel cells, PEMFCs and MCFCs, in its flexibility with regards to fuel- being able to use hydrocarbons as opposed to pure hydrogen. SOFCs are the most sulfur resistance fuel cell type, and unlike other fuel cells, SOFCs may use unreformed fossil fuels though if necessary, the high quality waste heat it produces may be harnessed to drive an internal reformer (or for co-generative practices). It is also less susceptible to poisoning by carbon monoxide or dioxide. The solid state of the device allows it mechanical stability and furthermore freedom in its design - for example, the tubular design of SOFCs would not be possible with alkali or phosphoric acid fuel cells with their liquid electrolyte. Moreover, as a result of its oxide electrolyte, there is no risk of a leakage of a highly corrosive electrolyte, or a need for replenishment of ionic species, as in the case of MCFCs where CO_2 may have to be injected, due to the prevalence of oxygen in the atmosphere. The oxide electrolyte of SOFCs is also relatively low in cost in comparison to other fuel cell types. A brief comparison of different fuel cell types can be seen in Table 1.1.

Possibly the most important advantage of SOFCs is its high efficiency, see Table 1.1. However, this performance is only seen at high operating temperatures around 1000°C. These high temperatures also impose stringent material requirements. Thermal and chemical stability under these reducing and/or oxidizing conditions is a requisite and limits material options, often to costlier alternatives, such as Cr or Ni-alloys for the interconnects. Also, degradation of SOFC performance often results from segregation of dopants, such as Sr, and inter-diffusion between components over its lifetime reducing cell performance.

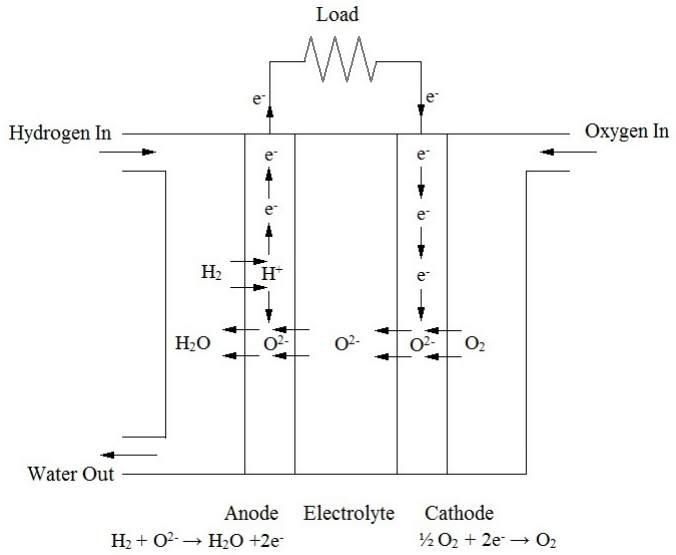


Figure 1.1: Operation of a solid oxide fuel cell.

Besides this, the high temperatures restrict the use of SOFCs to stationary applications.

As a result of this, in recent years, there has been a drive towards lowering the operating temperatures of SOFC to an intermediate range of 500-750°C. This would allow a wider range of materials to be used that better fulfill the material requirements and at lower cost. It would also extend the range of applications for SOFCs. However, at these low temperatures electrolyte conductivity is reduced. Furthermore, and this is the limiting factor of intermediate temperature SOFCs, polarization losses are substantial at these temperatures. It is the improvement in IT-SOFC performance in particular that is the motivation of this work.

1.2 SOFC Operation

The operation of a SOFC is depicted in Fig 1.1. At the cathode, oxygen from air obtains extra electrons and is reduced to O^{2-} that is incorporated into the oxide ion conducting electrolyte. The electrolytic oxide ions migrate through the solid oxide electrolyte to the anode. At the anode, hydrogen loses electrons, and is oxidized to H^{+}. The free electrons travel through an external circuit to the cathode while the hydrogen ions react with the incoming oxygen ions to produce the waste water. Each half cell reaction is dependent on the other half cell reaction occurring concurrently for charge conservation.

Other components of fuel cells include interconnects and seals. Individual fuel cells may be stacked, and their current collected through the interconnect. The interconnect connects multiple fuel cells together to create a stack from which charge may be collected. Lastly, seals serve to prevent fuel leakage or mixing.

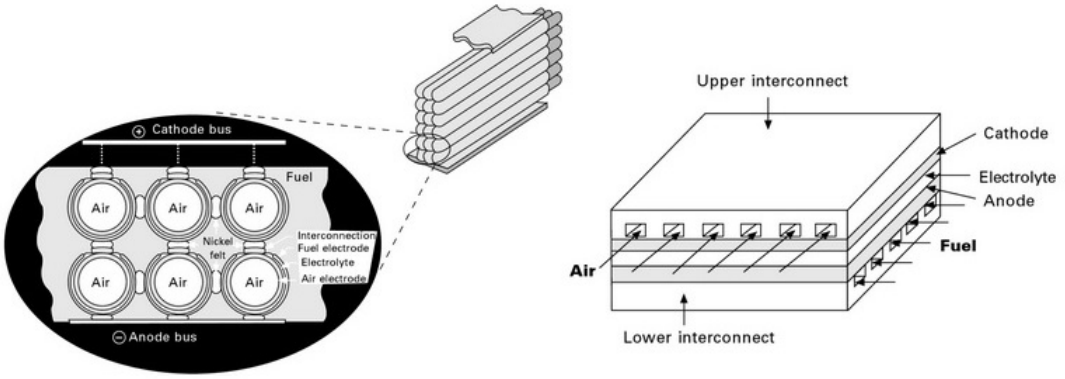


Figure 1.2: Schematic of a cathode-supported tubular SOFC stack and an anode-supported planar SOFC stack [12].

1.3 SOFC Design

There are two predominant designs for the SOFC stack: planar or tubular. The tubular design typically has an array of extruded cathode tubes as the support (air-electrode-support AES). The remaining fuel cell components are deposited over the tube, which is sealed at one end, and open at the other. The biggest advantage of this design is that it eliminates the need for gas-tight seals. Instead, the air flow is separated to the inside of the cathode tube, while the fuel flow is kept to the outside of the tube where the anode coating is. Furthermore, any unused fuel at the anode will combust at the exit of the cell where it mixes with the air supply, removing then as well as preheating the air flow. The design of the tubular stack may also be altered to internally reform the fuel at the anode too. However, the tubular cell design is expensive to fabricate, and the extrusion of the cathode tubes limits their diameter to the millimeter scale. Also, because of the large electronic conduction path, the power density of the tubular design is low. A schematic of the tubular and planar SOFC is provided in Fig 1.2.

The planar design has a stack arrangement that shortens the electronic and ionic current path and thus has a higher power density than the tubular design. It is usually anode and electrolyte supported, and the gas may be delivered along channels in the interconnect layer at the electrode/interconnect interface, see Fig 1.2. However, it requires gas-tight sealing at its edges. These seals are expensive and present material challenges. In addition to the seals, the material requirements of the planar design are more stringent than with the tubular design as the high aspect ratio makes the stack susceptible to thermal cracking (especially at stress concentrations such as at the seals and interconnects) that is aggravated by the brittleness of the stack. The poor mechanical strength of the layered structure and fabrication techniques of thin films also limits the extent by which the size of the SOFC may be scaled up. Thus, the planar design has largely been abandoned for the tubular design in industry.

1.4 SOFC Performance

One of the main advantages of SOFCs and all fuel cells is that they can attain higher conversion efficiencies than with a combustion process. Nevertheless, there still remains a large scope for minimizing cell inefficiencies, also called polarization losses or overpotentials, which has driven much research. Thus, it is important to understand firstly the SOFC output potential, and also the sources of polarization losses.

1.4.1 Cell Potential and Performance Curve

The two half-cell reactions are the source of the electrical energy output of an electrochemical cell: the cell potential, E, measured in volts, also referred to as the electromotive force, emf, which drives an external electric current. From this, the change in Gibbs free energy, ΔG, of that electrochemical system may be calculated:

$$\Delta G = -nFE \tag{1.1}$$

where n is the number of moles of electrons involved in the reaction and thus contributing to the external current generated, and F is Faraday's constant (96,485 C/mol).

Drawing on this relation, and the change in Gibbs free energy associated with an electrochemical reaction, the Nernst equation was derived allowing the Nernst potential, E_{Nerst}, to be calculated for the given reaction conditions:

$$E_{Nernst} = E^o + \frac{RT}{nF} ln \left(\frac{p_{H_2} p_{O_2}^{\frac{1}{2}}}{p_{H_2O}} \right) \tag{1.2}$$

E^o is the electrochemical cell potential at standard temperature (25°C) and pressure (atmospheric) and can be calculated from the change in Gibbs free energy at standard state, ΔG^o, R is the gas constant (8.314 J/Kmol), and p_x is the partial pressure of the gaseous species x. The Nernst potential, E_{Nernst} is the highest possible potential generated by the cell. It is the cell potential at zero current and is also called the open circuit voltage, OCV, theoretical emf, or ideal voltage. This is because the Nernst equation is based on an idealized equilibrium system.

The difference between such an ideal system and a real world device can result in a significant discrepancy between the Nernst potential and the cell potential, as can be seen in the fuel cell performance curve of cell potential against current density depicted in Fig 1.3. These losses may be referred to as overpotentials or polarizations losses. In an electrochemical cell, there are three overpotentials, or polarization losses: activation, ohmic, and concentration. These different sources of inefficiencies all affect cell performance over the

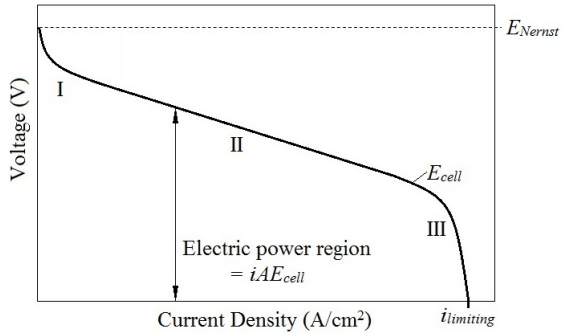


Figure 1.3: Typical performance curve depicting polarization losses as a function of current density [13]. Activation, ohmic and concentration polarization losses dominates in regions I, II and III respectively.

entire range current densities, but to varying degrees. The features of the performance curve are the result of the dominating overpotential at that particular current density range. At low current densities, activation polarization has the greatest contribution to inefficiency, in the intermediate range it is ohmic polarization, and at high current densities it is concentration polarization.

Besides these three main overpotentials mentioned, there are other sources of losses such as crossover losses or mixed conductivity losses in the electrolyte.

1.4.2 Activation Polarization Losses

Activation polarization, η_{Act}, arises from slow reaction kinetics at both electrodes. Previously the Nernst equation was considered. However, it only considers the thermodynamics of the reaction; it does not consider the kinetics or any energy losses thereof. Thus, the general Butler-Volmer equation, below, may be used to give kinetic information by relating the half-cell activation polarization, η ($\eta = E - E^o$, where E^o is the standard potential of the reaction and E is the applied potential) to the transport of charged species it drives (representative of the rate of the reaction).

$$i_{cell} = i_o \left[exp\left(\frac{(1-\alpha)ne}{k_B T}\eta\right) - exp\left(\frac{-\alpha ne}{k_B T}\eta\right)\right] \tag{1.3}$$

The net current density of the cell, i_{cell} is the sum of the catholic and anodic current densities forward and backwards respectively, and given in the equation below. However, it is the exchange current density, i_o, that is the parameter of interest and an indication of the reaction rate at the electrode at equilibrium (it reflects "the effectiveness of the electrode in promoting the electrochemical reaction [13]". Therefore, unlike i_{cell} that must be conserved between the two electrodes, i_o for the cathodic and anodic reaction may differ. α is the charge transfer coefficient, which is a measure of the bias of the system.

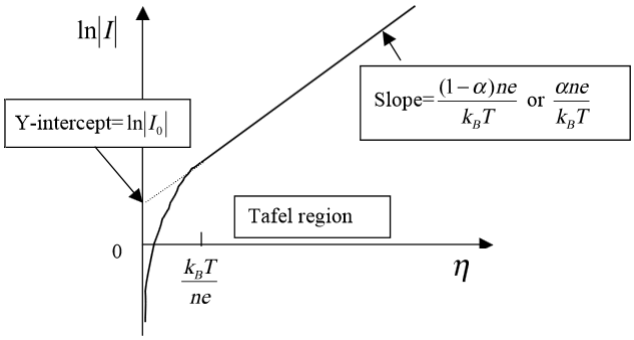


Figure 1.4: Tafel plot of log(current) against overpotential, diagram from [14].

There are two limiting cases to the Butler-Volmer equation. At low overpotentials, when ($\mid \eta \mid << \frac{k_B T}{ne}$), the equation can be linearized (this is called the linearized kinetics region) to:

$$i_{cell} \sim i_o \frac{ne\eta}{k_B T} \tag{1.4}$$

At high overpotentials (in the Tafel Kinetics region), when ($\mid \eta \mid >> \frac{k_B T}{ne}$), the equation simplifies to the Tafel equation. When:

$$\begin{aligned} i_\eta &>> \frac{k_B T}{ne}, \\ i_{cell} &= i_o \left[exp\left(\frac{(1-\alpha)ne}{k_B T} \eta \right) \right] \end{aligned} \tag{1.5}$$

$$\begin{aligned} i_\eta &<< \frac{k_B T}{ne}, \\ i_{cell} &= i_o \left[exp\left(\frac{(1-\alpha)ne}{k_B T} \eta \right) \right] \end{aligned} \tag{1.6}$$

The two different responses of the Butler-Volmer equation can be seen in the Tafel plot below, in Fig 1.4, of ln(current) against overpotential, η. Beyond the Tafel region, mass transfer effects begin to take place (concentration polarization) and the slope breaks off. As can be seen from the equations, the extent of the limiting cases also depends on temperature.

The activation polarization depends on the reactions that occur at the electrodes. For the case for mixed ionic-electronic cathodes in a SOFC, the main contributions to polarization losses arise from the kinetics of the oxygen reduction reaction, ORR, involving: surface exchange reactions and bulk diffusion of oxygen. Recent developments in the understanding of the ORR will be reviewed in Chapter 3.

1.4.3 Ohmic Polarization Losses

Ohmic polarization dominates in the intermediate current density range. It is the sum of losses due to the resistance of cell components to the movement of charged species.

The electronic contribution to Ohmic losses is typically small. On the other hand, ionic resistance in the electrolyte dictates Ohmic polarization in a cell. Besides material resistivity, contact resistance at component interfaces also contributes to Ohmic polarization and may be significant, depending on the SOFC design. For example, Ohmic losses in planar SOFCs tend to have a small contribution from electrolyte resistance but large contact resistance while the opposite is true of tubular SOFCs.

The resistance of a device is a function of its geometry. Thus, in discussing SOFCs, the area specific resistance is a better indication of performance. By considering the potential loss, ΔV, over a length, L, due to the flow of charged species k, I_k, through a cross-section, A, the of species k may be written as in the equation below. However, caution must be exercised in which dimensions of a cell constitutes A, the plane perpendicular to current flow, and l, the length parallel to current flow. The ASR is $A \times R = l/\sigma$

$$R_k = \frac{1}{\sigma_k}\frac{l}{A} \tag{1.7}$$

The equation above may also be written in terms of a materials resistivity, ρ. Resistivity as an intrinsic property and is by definition the inverse of conductivity. Thus:

$$\rho_k = R_k\frac{A}{l} \tag{1.8}$$

From the equation above, it can be seen that there are two ways of decreasing Ohmic polarization: by material selection, or engineering a cell with an electrolyte that has a high area to length ratio. However, the best electrolytes only have ionic conductivities around 0.10 S/cm [15]. Reducing the thickness of the electrolytes also has its limitations. If the electrolyte is too thin, the presence of slight irregularities may result in pinholes, the electrolyte may not have sufficient mechanical integrity to survive operation (such as the stresses involved in thermal cycling), hydrogen crossover or electrical shorting may occur. The physical boundary on electrolyte thickness is the length of the dielectric breakdown field. This material property is usually in the range of several nanometers. However, before this, the practical constraints restricts the electrolyte thickness to about 10-100 μ m [15].

Another design related method of reducing Ohmic polarization is to reduce contact resistance between cell components. The contact resistance is increased if the contacts develop an oxide area over service. To reduce this, they are often made of non-oxidizing materials, or coated with an oxide resistant material. Uniform compression of the fuel cell is also employed to improve current flow, although there is a danger in concentrating current in an area in a locally high state of compression, or that the cell is damaged.

1.4.4 Concentration Polarization Losses

Unlike Ohmic polarization that arose from potential losses related to charge transport, concentration polarization is the sum of losses that result from mass transport. For, in order for any steady-state electrochemical reaction to occur, there must be a ready supply to reactants to the electrodes, as well as removal of the products. At low current densities, the change in partial pressure of reactant or product is sufficient to replenish or remove them respectively at a similar rate. But, at high current densities when the rate of these reactions is high and this is no longer the case. Thus concentration gradients are formed that incur a potential loss and hence the dominance of concentration polarization at high current densities. Another possible cause for concentration polarization is the interference of inert species. For example, nitrogen present in the fuel will build up at the cathode as the fuel is consumed. Eventually it will form a boundary that impedes the transport of fuel to the cathode. Similarly, the electrode or catalyst may be covered by a layer of adsorped contaminants, such as CO in low temperature fuel, to the same effect.

The mass-limiting current density is defined to be the point at which "the rate of mass transport to the reactant surface is insufficient to promote the rate of consumption required for reaction" [13]. It may be calculated by setting the local concentration of to zero and is denoted by i_l. This is the mass transport limit: the highest current density obtainable in the device. It depends on the design of the fuel cell, diffusivity of the materials making the cell components, and any other factors affecting transport to the reactions sites. The mass-limiting current density is of importance, not just as an indication of cell performance, but also because it may be used to calculate the concentration polarization. The concentration affects fuel performance in two ways: its theromodynamics- the Nernst potential generated-and its kinetics- the reaction rate- as both are functions of reactant and product concentrations. The concentration polarization from these two factors may be calculated from the equations below.

Concentration loss due to Nernstian effects:

$$\eta_{conc} = \frac{RT}{nF} ln \frac{j_L}{j_L - j} \tag{1.9}$$

Concentration loss due to kinetic effects:

$$\eta_{conc} = \frac{RT}{\alpha nF} ln \frac{j_L}{j_L - j} \tag{1.10}$$

Thus the total concentration polarization is given in the general equation below, where c is a constant. It can be visualized on the fuel cell performance curve in Fig 1.5.

$$\eta_{conc} = cln \frac{j_L}{j_L - j} \tag{1.11}$$

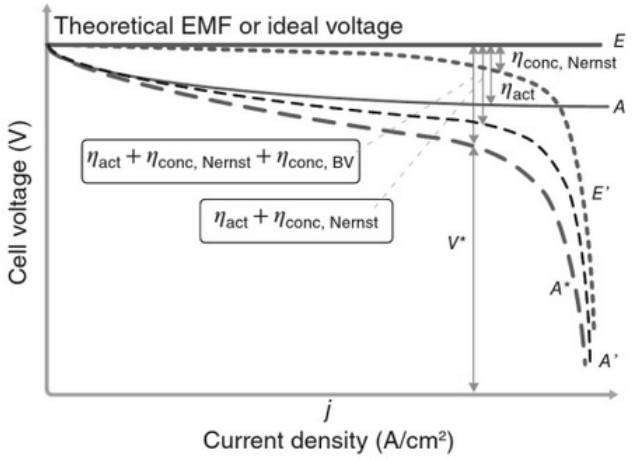


Figure 1.5: Concentration loss due to Nernstian effects, $/eta_{conc,Nernst}$ causes a drop in the ideal voltage output of a cell from E to E'. Activation losses, η_{act} causes a further drop in the theoretical EMF to A'[15].

The concentration overpotential, η_{conc}, calculated is generally lower than that experienced practically, see Fig 1.5. It is usually multiplied by an empirically determined correction factor. Alternative means of calculating the concentration polarization is by a purely empirical method of fitting experimental values m and n to polarization curves models or through consideration of the flow stoichiometry.

1.5 SOFC Component Requirements and Materials

In light of the objective of each SOFC component and also polarization losses with operation, the following section covers the material and design requirements for SOFCs. All components of the SOFC require matching thermal expansion coefficient (TEC) within operating conditions, and chemical and thermal stability. Interdiffusion between cell components should be minimized and all components must be chemically compatible with each other. Ideally, all components should be low cost and easily manufactured. Besides this, the SOFC components should also have the function-specific properties covered below.

1.5.1 Electrolyte

In order to minimize Ohmic polarization, the electrolyte should have good oxide ion conductivity, above 1×10^{-3} Scm^{-1}. It should have low electronic conductivity to reduce mixed conductivity losses as electrons short-circuit across the electrolyte. To reduce crossover losses, it should be fully dense with low hydrogen diffusivity. Ideally, an SOFC electrolyte should have as low an ASR as possible, ideally around 0.1 Ωcm^2. Thus it is also desirable to have an electrolyte that may easily be formed into a homogeneous thin and dense layer. The ionic conductivities of several SOFC electrolytes is given in Fig 1.6.

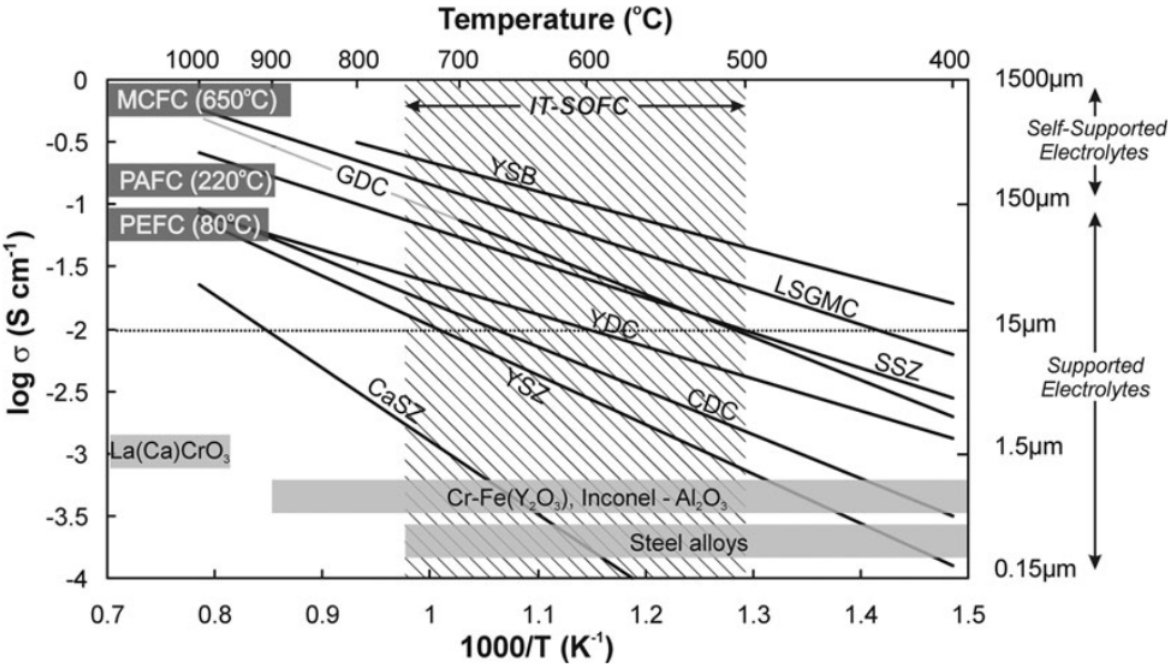


Figure 1.6: Specific ionic conductivity of SOFC electrolytes as a function of reciprocal temperature. The operational ranges of different interconnect materials are also included [16].

Structure types that have the potential to exhibit oxide ion conductivity are fluorites and perovskites, although recently apatite based $Ln_{10}(XO_4)_6O_2$ [61], and $La_2Mo_2O_9$ [62] have been shown to do so too. The most widely used HT-SOFC electrolyte is yttrium-doped zirconium oxide, YSZ. The yttrium dopants stabilize the cubic structure of zirconia at high temperatures and also improve ionic conductivity as it creates oxygen vacancies. However, it has low ionic conductivity in the intermediate temperature range making it less suitable for IT-SOFCs. Efforts have been made to address this by doping zirconia with a range of 3+ ions. The highest ionic conductivity was obtained when doping with scandium. However, while improving ionic conductivity, the presence of scandium affects its long term stability and thus performance.

Alternative electrolytes that have higher ionic conductivities at this temperature mark include bismuth based oxides or cerium based oxides. However, in both cases stability is a problem. Bismuth oxides exhibit many polymorphs and it is challenging to retain the high ionically conductive fluorite $Bi_2O_{3-\delta}$ at lower operating temperatures, while ceria undergoes partial reduction at the anode due to the low oxygen partial pressures pressure when temperatures exceed 600°C. This results in electronic conductivity and volume change, nevertheless gadolinium doped ceria remains one of the more promising IT-SOFC electrolyte materials available.

1.5.2 Anode

Oxidation of hydrogen occurs at the anode. The anode needs to be resistant to reducing conditions and ideally facilitate the hydrogen oxidation reaction, HOR, by catalyzing it. It needs to ensure a good supply of reactants to the active sites for the reaction and so it is usually porous with good gas flow through it. Further increases to the HOR can be achieved by increasing the triple phase boundary, TPB, between the gas phase, anode and electrolyte, as this will increase the number of active sites for the HOR. It must also have adequate electronic conductivity to collect the free electrons that result from the HOR.

Given the reducing conditions at the anode and the requirement for catalytic activity for fuel oxidation, nickel is a prime choice. Furthermore, it has sufficient methane oxidation catalytic activity to internally reform methane (though steam needs to be present to prevent the carbon poisoning the anode), allowing it to operate on fuels containing a mixture of water and methane. However, though this is less of a problem for IT-SOFCs, the mismatch in TEC between Ni ($13.3 \times 10^{-6} ^{\circ}C^{-1}$) and the solid oxide electrolyte is very large. Also, at the high operating temperatures, a porous nickel anode would coarsen and sinter preventing fuel transport to active sites.

In order to increase the TPB, cermets are used: ceramic and metal composites. The most common cermet employed as an anode material, given the reasons above, is Ni-YSZ. The use of the YSZ maintains the anode's open structure by preventing the Ni from coarsening. It increases the TPB and lowers the TEC of the anode that it may better match the rest of the cell components and it may allow better adhesion between anode and electrolyte. Alternative cermats have been researched, such as where Cu is employed instead of Ni, or ceria for YSZ. Single phase mixed ionic and electronic conducting, MIEC, anodes have also been investigated, as have ceramic anodes, such as La-$SrTiO_3$, due to their tolerance to sulfur impurities and matching TEC.

A common method of manufacturing anodes employs the use of pore formers that are later burnt out. However, it often results in a closed and highly tortuous pore structure with insufficient mechanical strength. Also, there are environmental concerns with the burning of the pore formers. Thus, in addition to material constraints, difficulty also lies in the manufacture of the anodes. Recently, freeze-drying has been investigated as a potential route [63].

1.5.3 Cathode

Reduction of oxygen occurs at the cathode. The cathodes need to be resistant to oxidizing conditions and, similarly to the anode, facilitate the oxygen reduction reaction, ORR, by ensuring a good supply of oxygen to the active sites and high electrocatalytic activity. It must also have adequate electronic conductivity to supply electrons to the active sites. The required electronic conductivity depends on the fuel cell design; a tubular, or cathode supported cell would require a higher electronic conductivity for efficient current collection.

Thus cathode materials are selected with the target ASR in mind, though acceptable levels of electronic conductivity would be greater than 100 Scm^{-1} [64].

The highly oxidizing conditions rule out the possibility of using metals other than noble metals for the cathode. Even then, the high operating temperatures mean that only Pt is suitable, which is too expensive. Noble metal cermets have been considered, but again, the cost implications were too great. Thus, oxide materials with high electronic conductivity provide an attractive option.

The two most common cathode materials used are strontium doped lanthanum manganite, (La,Sr)MnO_3, or cobaltate perovskite, (La,Sr)CoO_3, LSM and LSC respectively. LSM is a p-type semiconductor and thus displays fairly high conductivity 200-300 Scm^{-1} at 900°C that is almost purely electronic (ionic conductivity is only on the order of 10^{-7} Scm^{-1} [65, 66]. However, it has fairly low electrocatalytic activity making it unsuitable for use in IT-SOFC due to the retarded oxygen reduction reaction, ORR, kinetics at these lower temperatures. Therefore, one approach to improve its performance, as used with anode materials, is to use it in a composite with a good ionic conductor.

Another method of increasing cathode performance at intermediate temperatures is to use a mixed ionic and electronic conductor, MIEC, to increase the active region of the ORR (see Section 3). In light of that, a cathode material that shows promise for intermediate temperature applications is LSC. LSC has good ionic conductivity and excellent electronic conductivity (up to 0.22 Scm^{-1} and 1600 Scm^{-1} respectively at 800°C [67, 68]. However, there are problems with TEC mismatch and chemical compatibility. LSC forms deleterious phases when paired with a YSZ electrolyte, although it exhibits enhanced performance with a CGO electrolyte. Another MIEC of interest is strontium doped lanthanum ferrate, LSF. It was found that the presence of Fe improves ORR kinetics [69] and b-site doping of Fe in LSC has resulted in one of the best performing cathode materials: (La,Sr)(Co,Fe)O_3, LSCF. A huge amount of research has since been expanded on investigating the effect of the dopant contents on the properties of LSCF and its compatibility with electrolytes [70, 71, 52, 72, 73, 74].

1.5.4 Interconnect

The interconnect connects individual cells together and collects their charge. It needs to have good electronic conductivity and low contact resistance to reduce Ohmic losses. In the stack layout, the interconnects also separates the fuel from air, channeling them to their respective electrodes. Thus, further requirements are that the interconnects have low permeability and that it distributes the reactants homogeneously across the electrodes. The interconnect experiences the severest conditions of the SOFC being subject to both oxidizing and reducing conditions in which it must be stable and corrosion resistant. Lastly, the interconnect should have good thermal conductivity in order to remove waste heat from the device that it may be of a uniform temperature.

HT-SOFC interconnects may be a ceramic or metal. Most commonly used high temperature interconnects are $LaCrO_3$, Cr-rich alloys such as Inconel600 [75] or Ducrolloy. Using the perovsite $LaCrO_3$, often doped to increase electronic conductivity, has the advantage that it has a similar TEC and good adhesion to the electrolyte. The advantage of metallic interconnects is that they have better thermal shock properties and so may be used even at rapid start-up or shut-down. However, these interconnects are the most expensive component of the SOFC by weight. Also, the very chromium that provides the alloys their resistance to oxidation and corrosion, through the formation of a protective chromia, Cr_2O_3, containing scale, also forms deleterious phases at the electrodes and so decreases performance. A method of resolving this is to coat the interconnects to reduce chromium volatility

However, and this forms a motivation for their development, IT-SOFC operating at temperatures below 800°C would allow the use of ferritic steel interconnects, and below 700°C, stainless steel interconnects [76], creating a substantial cost saving.

1.5.5 Seals

Seals prevent reactant leakage or mixing either by being chemically bonded to the cell, or by being held in place by compressive loads during operation. The seals sustain the highest stresses during SOFC start-up and shut-down. To reduce these thermal stresses, it is especially important that they have compatible TEC with the rest of the cell.

Bonded seals are usually glass based. Thus, they may only be used at temperatures above their glass transition temperature: above about 625°C. They are brittle, and the TEC compatibility between cell components must be high to prevent cracking. On the other hand, compressive seals allow for greater TEC mismatch and have better durability. However they are more expensive.

Thus, the basic operation of an SOFC has been covered and also its polarization losses during operation. While these inefficiencies have been minimized through careful cell design, further improvements lie in rigorous material selection and engineering of the SOFC components. With regards to that, two structure types of potential IT-SOFC cathodes have been addressed in the next chapter.

Chapter 2

General Properties of Perovskites and Ruddlesden-Popper Oxides

In the previous chapter, SOFC operation was described and the need to reduce activation polarization losses at the cathode identified. Much effort has been directed toward this; this work having that same objective. Improved cell performance may be attained to some extent through SOFC design, but it is materials engineering that holds the greater scope for improvement. In the materials selection of IT-SOFC cathodes, perovskite oxides have been heavily investigated. Similarly, MIEC oxides of the Ruddlesden-Popper, R-P, structure are rapidly gaining interest. Subsequently, these are the two material classes that are the focus of this work. In this chapter, four key concepts related to the performance of cathode materials are introduced, and the general properties of perovskite and RP oxides are discussed.

2.1 Defect Chemistry

Within any stoichiometric metal oxide, a range of intrinsic processes may occur producing structural point defects as they increase the entropy of the system, lowering the overall free energy of the system. These are primarily Schottky, Frenkel, and Antifrenkel disorder (as well as electronic disorder forming intrinsic electron-hole pairs) [77, 78]. Schottky disorder involves the creation of an oxygen and a metal vacancy on their respective sites. Frenkel disorder involves the creation of a metal vacancy as a metal moves from a metal site to an interstitial site, while in Antifrenkel disorder it is the movement of oxygen to an interstitial site that creates an oxygen vacancy. Thus Schottky disorder is accompanied by a decrease in density, whereas the density remains the same when Frenkel and Antifrenkel disorder dominates. One of these processes will dominate. The dominating process is intrinsic to the material and is determined by the structure of the compounds and the coordination number of its constituent atoms (thus it is dependent on the relative cation to anion radii) as this dictates the formation energy of the defect species. Schottky defects typically occur

in similarly sized ions with a high coordination number, while Frenkel defects typically occur where the ionic radii of the anion far exceeds the cation and the coordination number is low.

$$\text{Schottky disorder: “O”} \iff \mathrm{V}_O^{\cdot\cdot} + \mathrm{V}_M^{\prime\prime}$$
$$\text{Frenkel disorder: } \mathrm{M}_M{}^X \iff \mathrm{V}_M^{\prime\prime} + \mathrm{M}_i^{\cdot\cdot}$$
$$\text{Antifrenkel disorder: } \mathrm{O}_O{}^X \iff \mathrm{V}_O^{\cdot\cdot} + \mathrm{O}_i^{\prime\prime}$$

These intrinsic disorder processes are described above using Kröger Vink notation [79] where the first letter denotes the species (e.g. O for oxygen, M for metal, V for vacancy), the subscript denotes the site of the species, and the superscript denotes the charge of the species, where $^{\prime}$ is a singular negative charge, $^{\cdot}$ is a singular positive charge, and ^{X} indicates it is charge neutral.

By tailoring of the defect chemistry of cathode materials, the properties of cathode materials may be optimized. In order to increase ionic or electronic conductivity extrinsic defects may be introduced: perovskite oxides are often doped with acceptors (ions of a lower oxidation state), creating an excess negative charge. In order to maintain charge neutrality, this is compensated by the creation of an oxygen vacancy (or a hole, depending on the oxide), which would facilitate ion diffusioin through the lattice and thus improve ionic conductivity. An example of this is the prolific use of Sr-dopants in $LaCoO_3$ and $LaCo_yFe_{1-y}O_3$ which are well documented for their ability to accommodate a range of oxygen non-stoichiometry [80, 81, 82, 83, 70, 84, 85, 86, 87, 18].

The formation of intrinsic point defects, whether through Schottky or Frenkel disorder, is thermally activated and follows the Arrhenius relationship. As temperature increases, the concentration of intrinsic defects increase. Conductivity, σ is related to the concentration of charge carriers, $[n]$, through their mobility, μ and charge, c ($\sigma = [n]\mu c$). Therefore, at low temperature, extrinsic defects are the main contributors to ionic conductivity but at high temperatures, the intrinsic contribution dominates (a change in the gradient of $ln\sigma$ against T^{-1} may be observed). The mobility of ionic defects through the lattice may also be described by an Arrhenius equation, so at high temperatures, the mobility of these defects increase and subsequently also its ionic conductivity.

In addition to temperature, the defect system is also a function of oxygen partial pressure. The oxide lattice may undergo oxidation or reduction in order to maintain equilibrium with the surrounding oxygen activity, which is directly related to the oxygen partial pressure. At high oxygen partial pressures, lattice oxidation occurs and oxygen is incorporated into the lattice, creating either a metal vacancy or an oxygen interstitial. Only one of these two oxidation processes will dominate depending on the defect species present in the oxide, and therefore its intrinsic disorder. Both processes are accompanied by creation of holes. Similarly, at low oxygen partial pressures, lattice reduction occurs and oxygen is removed from the lattice, either through the creation of an oxygen vacancy or a metal interstitial. As before, only one of these two reduction processes will dominate, and both processes

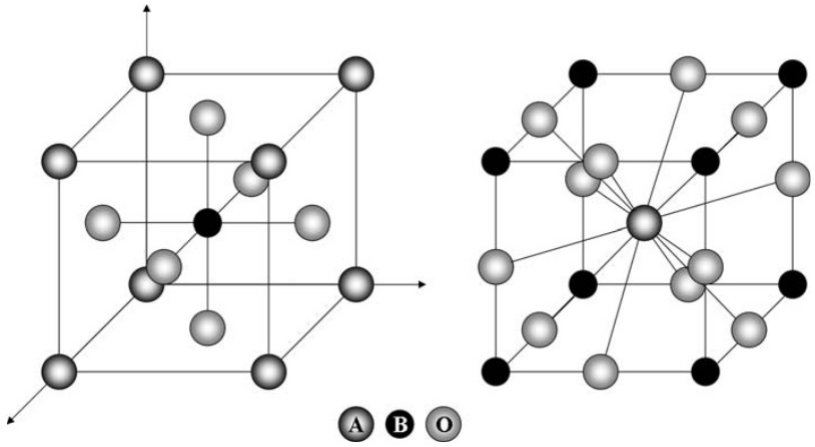


Figure 2.1: Ideal perovskite structure with A^{3+} and B^{3+} at the origin on the left and right respectively [17].

are accompanied by the creation of electrons. The equations of these redox processes are provided below . Therefore, the intrinsic disorder within an oxide and its resulting defect species determines the redox processes it undergoes as oxygen partial pressure is varied.

Lattice oxidation:

$$\frac{1}{2}(O_2)_g \iff {O_O}^X + {V_M}'' + 2\dot{h}$$
$$\text{or}$$
$$\frac{1}{2}(O_2)_g \iff {O_i}'' + 2\dot{h}$$

Lattice reduction:

$${O_O}^X \iff \ddot{V_O} + 2e' + \frac{1}{2}(O_2)_g$$
$$\text{or}$$
$${M_M}^X + {O_O}^X \iff \frac{1}{2}(O_2)_g + \ddot{M_i} + 2e'$$

2.2 Crystal Structure

2.2.1 Perovskite Oxides

Perovskites have the general chemical formula of ABX_3, with X= O for a perovskite oxide. An ideal cubic perovskite may be described by an A-site cation centered between 8 corner sharing BO_6 octahedra. Thus the A-site cation has 12-fold coordination, while the B-site cation has 6-fold coordination. An ideal perovskite, such as $SrTiO_3$, may be described by the cubic $Pm\bar{3}m$ spacegroup [88, 89]: the A atoms are located at $\frac{1}{2}$, $\frac{1}{2}$, $\frac{1}{2}$ (Wyckoff position 1b), the B atoms at 0, 0, 0 (Wyckoff position 1a), and the X atoms are at $\frac{1}{2}$, 0, 0; 0, $\frac{1}{2}$, 0; and 0, 0, $\frac{1}{2}$ (Wyckoff position 3d), see Fig 2.1.

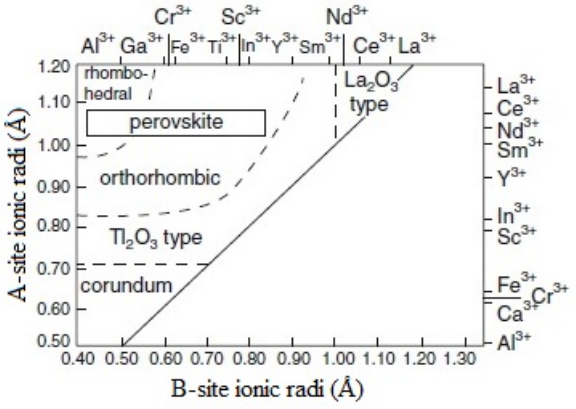


Figure 2.2: The effect of ionic size of A- and B-site cations on the observed distortions of the $A^{3+}B^{3+}O_3$ perovksite structure [18].

Due to the flexibility of the perovskite structure, a wide range of anions (usually O^{2-}, as in this work, but can also be the larger F^- and Cl^- ions) and cations may be accommodated in it. As a result, the pervoskite structure is often distorted from its ideal cubic structure and its BO_6 octahedra tilted. There are three main causes of these distortions: size effects of its constituent ionic radii, its chemical composition, and the Jahn-Teller effect.

Regarding them as purely ionic crystals, the cell parameter, a, of an ideal cubic perovksite based on the ionic radii of its constituent ions may be described as $a = \sqrt{2}(r_A + r_O) = 2(r_B + r_O)$. Also the distortion of the pervoskite structure can be described through the ratio these two expressions for the cell length, which is known as the Goldschmidt tolerance factor, t:

$$t = \frac{r_A + r_O}{(R_B + r_O)\sqrt{2}} \tag{2.1}$$

where r_x is the ionic radii of species x. This tolerance factor is based on the ionic radii of the A- and B-site cations relative to oxygen. For a given A- and B-cation valency, it is possible to predict the lattice structure of the perovskite by calculating t. When $t = 1$, the perovskite has an ideal perovskite structure. In the case of $A^{3+}B^{3+}O_3$ perovskites $t > 1$ results in stable hexagonal structures [88], when $t < 1$ the perovskite becomes rhombohedral, and at even lower values of t becomes orthorhombic [90]. The effect of ionic size on the distortions of the ideal cubic perovskite structure is presented in Fig 2.2.

The tolerance factor is also a useful indicator of the stability of a perovskite and has been shown to have a linear relationship with the standard free energy of formation, t [91, 92]. Besides the tolerance factor, the octahedral factor, $\frac{r_B}{r_O}$ is equally important for perovskite stability [93]. However, pervoskites are not truly ionic compounds, and thus this tolerance factor is only a guide. The occurrence of a perovskite structure also depends on the nature of the bonding of the A and B atoms- whether more ionic or covalent- and the subsequent effect on their coordination number [18].

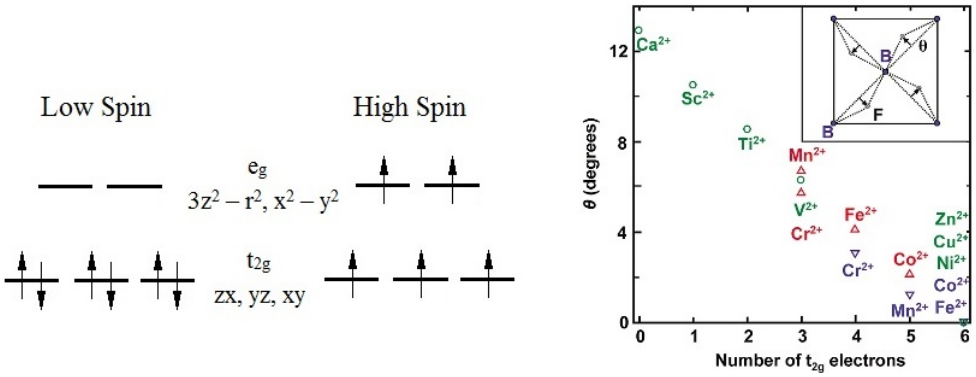


Figure 2.3: Unequally occupied orbitals resulting in the high or low spin states, and a correlation between the octahedral tilt angle with the number of electrons in the transition metal antibonding t_{2g} shell [19].

Defects also may distort the ideal perovskite structure, such as through the creation and ordering of oxygen vacancies. A change in the oxidation state of the cation, may be induced by heating and/or exposure to a reducing or oxidizing atmosphere, which will subsequently be charge compensated by a change in the oxygen stoichiometry. The perovskite composition may be described as $A_nB_nO_{3n-\delta}$. In certain compounds, such as $SrFeO_{2.875}$, vacancy ordering occurs, distorting the lattice.

Lastly, the Jahn-Teller effect [94] is a geometric distortion that occurs when degenerate molecular orbitals (orbitals having the same energy), which are unequally occupied are present, such as in the BO_6 octahedral complexes of certain pervoskites (while the bonds between the A-site cation to the 12 oxygen closest neightbours is of an ionic nature, the B-O bonds of the BO_6 octrahedra are strongly covalent) [95, 96, 97]. In these octahedral complexes, it may occur in degenerate e_g bonding orbitals or t_{2g} antibonding orbitals, but is more pronounced in the e_g bonding orbitals as these are of a higher energy, see Fig 2.3. A Jahn-Teller distortion in this case would result in change in the strength of the B-O bond and an increase in its length. For example, manganite oxide perovskites experience significant distortion due to the Jahn Teller effect, due to the hybridization of the Mn3d e_g and O2p orbitals [95, 98].This distortion is driven by the reduction of symmetry and free energy of the system, and results in an elongation or compression of the octahedral and thus an octahedral tilt [19].

2.2.2 Ruddlesden-Popper Oxides

Ruddelesden-Popper, R-P, structures are made out of the alternating rock salt (or halite), AO, and pervoskite, ABO_3, layers, see Fig 2.4 of the K_2NiF_4 structure, where the A- and B-site cations are trivalent and divalent respectively. The rock salt structure, AO, is made up of a face centered cubic lattice of oxygen ions interspersed with another face centered cubic lattice of A-cations translated by $(\frac{1}{2}, 0, 0)$. Thus the crystal structure of RP is given by $(AO)(ABO_3)_n$, where n is the order of the perovskite and describes the

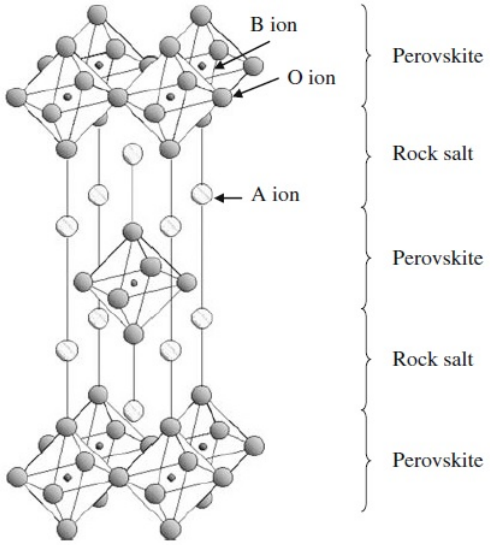


Figure 2.4: Ruddlesden-Popper structure of general formula $A_{n+1}B_nO_{3n+1}$ [20]).

number of repeating units of perovskite between rock salt layers. For a first order R-P, $n = 1$, would be made of interlayers of 1 unit cell perovskite between two rock salt layers; a second order R-P, $n = 2$ would have two unit cells of perovskite separated by rock salt layers. Thus the chemical formula for perfect RP is $A_{n+1}B_nO_{3n+1}$. R-Ps have a number of polymorphs depending on the temperature, oxygen nonstoichiometry, and the radius of the rare earth ion [99, 100, 101]. Within the operating temperature of IT-SOFCs, R-Ps usually have a tetragonal I4/mmm structure. However, oxygen interstitials in the lattice results in tilting or rotation of its BO_6 octahedra, the angle and axis of which determines the orthorhombic distortion that follows [102, 5].

2.3 Ionic Conductivity

2.3.1 Diffusion Mechanism of Ionic Conductivity

Ionic conductivity in materials arises from the movement of oxide ions through the lattice. Therefore, a key indicator of ionic conductivity, σ_{ionic} is the diffusivity of the ions through the lattice, described by the oxide ion diffusion coefficient D, and the two may be related using Nernst-Einstein relationship:

$$\sigma_{ionic} = \frac{z_i^2 e^2 cD}{kT} \tag{2.2}$$

where z_i is te valence of the ion, e is the charge on an electron, c is the total concentration of the mobile oxide ion, k is the Boltzmann constant and T is the temperature.

Diffusion in oxide materials may occur by three different mechanisms: vacancy, interstitial and interstitialcy mechanism. The vacancy mechanism involves the movement of an

ion from its lattice site to a vacancy on an adjacent equivalent site and the interstitial mechanism involves the movement of an interstitial ion to a neighbouring interstitial site. However, the interstitialcy mechanism involves the displacement of a lattice atom by an interstitial atom to a lattice site, the displaced lattice atom then taking up an interstitial site. All three mechanisms are reliant on the presence of point defects within the system and the diffusivity of oxygen may be related to the diffusivity of the corresponding defect (the forward flux of one is equivalent to the backward flux of the other). From Molecular Dynamic modelling, oxygen diffusion has not been found to be present in $LaMnO_3$ and $LaCoO_3$ that have not been acceptor doped [21]. Thus, the presence of an appropriate defect species is crucial.

Oxygen transport, being a diffusion process, is therefore also a thermally activated process that may be described using an Arrhenius relationship. Not only does it require a vacancy in the lattice to hop to, but is also associated with an energy barrier for oxygen ion hopping: the oxide ion migration energy, E_m (or the oxygen vacancy migration energy, depending on the diffusion mechanism) that depends on geometric factors affecting its physical path of migration. There are three main factors that determine the size of the migration barrier and subsequently the ease of oxygen ion transport: the cations around the oxygen migration path, particularly at the 'saddlepoint' of the hop; the distribution of and interaction between the defect species involved with the diffusion (for example, oxygen vacancies) at the beginning and end of the hop (two); and the same of dopant cations

The diffusion of a species may be described using Fick's second law of diffusion [103], where the diffusion coefficient may be derived from a diffusion profile, which is a function of time, t, and depth, x.

$$\frac{\delta c}{\delta t} = \frac{\delta}{\delta x}\left[D\frac{\delta c}{\delta x}\right] \tag{2.3}$$

This law is based on a random walk model, wherein it is assumed that the defect population is small and non-interacting. It should be noted that a good fit was still found with this model in a doped perovksite, despite high oxygen vacancy concentrations being present [104], thus justifying the continued application of it in the MIEC perovskite system where interactions between the oxygen vacancies appears to be weak.

If the rate of isotope exchange across the gas/solid interface is directly proportional to the difference in isotope concentration between the solid and gas during the isotope anneal, then the following boundary condition may be assumed:

$$-D^*\frac{\partial C}{\partial x}\Big|_{x=0} = k^*(C_s - C_g) \tag{2.4}$$

Using this boundary condition, Crank obtained the solution for diffusion in a semi-infinite medium [105] against which the measured ^{18}O profile may be fitted:

$$C'(x,t) = \frac{C(x,t) - C_{bg}}{C_g - C_{bg}} = erfc\left[\frac{x}{2\sqrt{D^*t}}\right] - \left[exp\left(\frac{x}{D^*} + \frac{k^{*2}t}{D^*}\right) \times erfc\left(\frac{x}{\sqrt{D^*t}} + k^*\sqrt{\frac{t}{D^*}}\right)\right] \quad (2.5)$$

where $C(x,t)$ is the measured ^{18}O tracer isotope fraction at position, x, and time, t. Prior to fitting to a diffusion profile, $C(x,t)$ must be corrected for the background ^{18}O isotope fraction, C_{bg}, and the ^{18}O isotope fraction of the exchange gas, C_g, to obtain $C'(x,t)$. D^* is the ^{18}O tracer diffusion coefficient and k^* is the ^{18}O tracer surface exchange coefficient. Thus, the two parameters determining the rate of oxygen transport are D^* and k^*. While D^* describes the diffusion of the oxide ion through the bulk, k^* describes the ability of oxygen to adsorb onto the surface and pass into the lattice and is determined by the oxygen reduction reaction. The exact mechanism of this reaction, as will be covered in Chapter 3, remains unclear. Nevertheless, both surface adsorption and bulk diffusion are required for successful oxide ion transport, and there is further suggestion that these measures are correlated [106, 107].

2.3.2 Perovskite Oxides

As fluorites and perovskite oxides typically exhibit oxygen hypo-stoichiometry, oxygen vacancies are the dominant defect species present. Oxide ion diffusion in these fluorites and perovskites occur by a vacancy migration mechanism [108] and is facilitated by the presence of oxygen vacancies (both the diffusion coefficient and exchange coefficient) [109, 110, 111, 112, 113, 28, 114, 115, 104, 116, 117, 68, 118]. Molecular Dynamic modeling suggests that this vacancy hopping occurs independently along the BO_6 octahedron edge in a curved path, with significant outward relaxation of the cations at a saddlepoint between a triangle of two A-site and one B-site cations [21]. The migration energy for the movement of the vacancy decreased with decreasing A-site cation radius, and increasing B-site cation radius. Thus a linear dependence could be seen between the perovskite tolerance factor and the vacancy migration energy; decreasing the tolerance factor and distorting the BO_6 octahedra resulted in a decrease in the migration energy [119]. On the other hand, lattices that are cubic (or pseudo-cubic) see no tilting of the BO_6 octahedral and have better ionic conductivities.

Similarly, lattices that have a large critical radius at the "saddle point," see Fig 2.5, of that ion hopping pathway also have higher ionic conductivity. A method of increasing oxide ion conductivity is to increase the specific free volume of the lattice [120, 121]. The critical radius is the maximum radius of an ion that should be able to pass through the saddle point. However, consideration of ionic radii alone underestimates conductivity as it does not account for any changes in coordination number in the presence of the mobile oxide ions [21], nor for the effect of lattice (thermal) vibrations [122] or interactions between defect

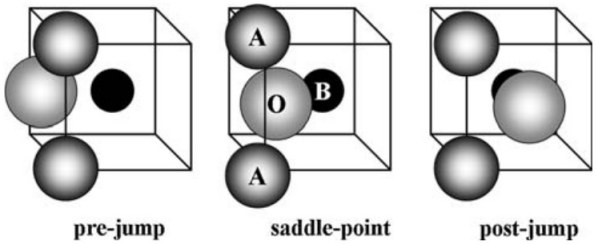


Figure 2.5: The saddle point, described by the critical radius of the two A-site cations and one B-site cation Ruddlesden [17, 21].

species, and between dopant species [123]. The diffusion of metal cations and anions in an oxide material is limited to its own sublattice [124, 125, 126], however it can be seen that the diffusion of the oxygen anions are affected by the cation sublattice.

Given its dependence on the vacancy diffusion mechanism, it is not surprising that D^* has been shown to be proportional to oxygen vacancy concentration in perovskite oxides [127, 84]. However, good correlations have been found between k^* and D^* values from oxygen isotope exchange measurements of various MIEC perovskites (also fluorites) despite a variation in composition [106]. This close relationship regardless of composition points to a strong dependence in both k^* and D^* values on a common factor: the oxygen vacancy concentration. The presence of oxygen vacancies dominates both surface exchange and diffusion through the bulk [106]. Additionally, the relationship between k^* and D^* was found to be dependent on the ratio of ionic to electronic conductivity [106]- electronic conductivity is necessary for good exchange kinetics.

Not only does a high concentration of oxygen vacancies affect both the exchange and diffusion of oxide ions in perovskites, the presence of adsorped oxygen was also found to contribute to surface catalysis. There was a correlation between the surface exchange of a material, and its catalytic activity [128, 129]. Improvements to the oxygen reduction reaction could be obtained by increasing the presence and transport of oxygen vacancies at the surface [130]. Thus A-site dopants with a lower valence cation, such as Sr^{2+}, are frequently used to increase the concentration of of oxygen vacancies. However, a high vacancy content may lead to superstructure ordering of the vacancy sites, producing a distortion (loss of symmetry) in the lattice [131] and a decrease in ionic conductivity [132].

2.3.3 Ruddlesden-Popper Oxides

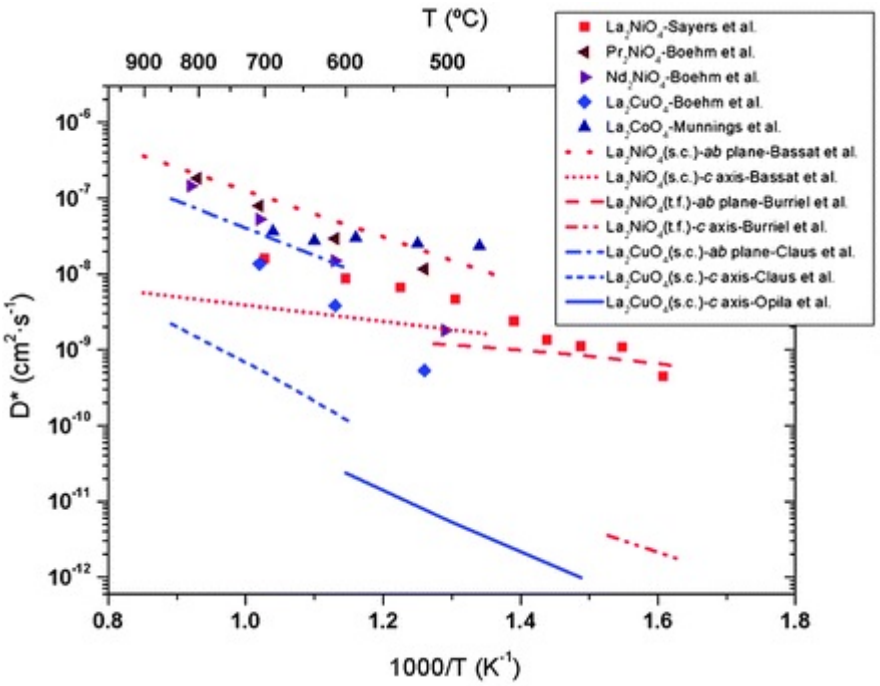
The first order R-P oxides (A_2BO_4) are typically oxygen hyper-stoichiometric. Unlike perovskites, R-P structures may accommodate a large amount of oxygen non-stoichiometry in their structure without the need for a stabilizing dopant such as Sr and Cr, which are known to form deleterious phases at the electrolyte interface. Nevertheless, doping may be used to further extend the range of oxygen nonstoichiometry and even take it from oxygen excess to deficiency. The resultant oxygen diffusion through the lattice is

the sum of contributions to oxygen transport by the two defect species that result from oxygen hypo- and hyper-stoichiometry. However, at the operating temperatures of SOFCs, these defects often recombine so that only the dominant defect species remains. Between hyper- and hypo-stoichiometry in the same R-P system, experimental results show that oxygen excess in the lattice results in higher oxygen diffusion than oxygen deficiency [133]. Subsequently, doping is typically performed with the interest of increasing oxygen interstitial concentration.

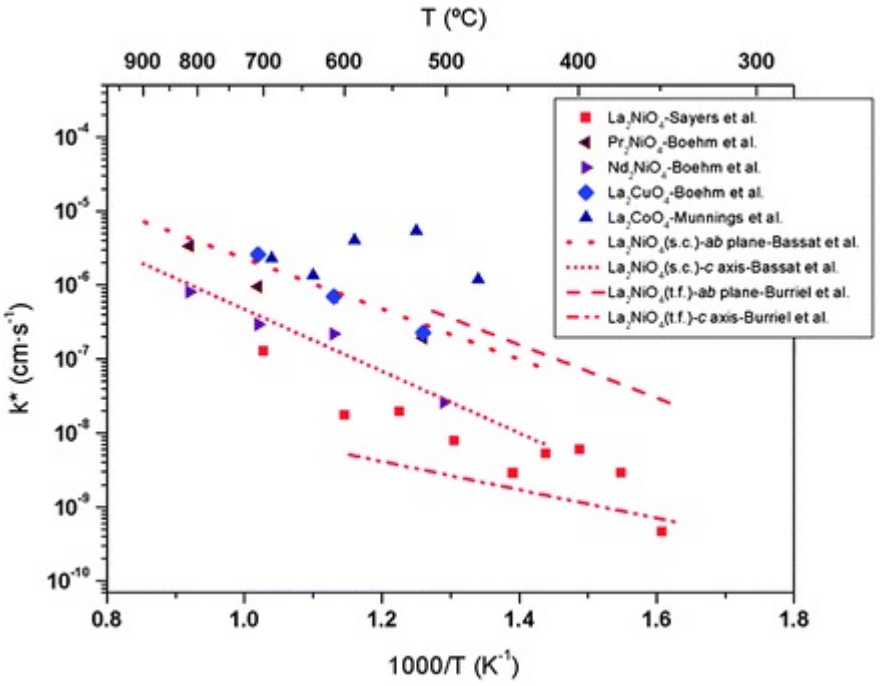
In the case of oxygen hyperstoichiometry, $A_2BO_{4+\delta}$, the oxygen excess takes the form of oxygen interstitials in the lattice, O_i''. Models of hyperstoichiometric tetragonal RP lattices suggests that the most energetically favorable location of oxygen interstitials in the lattice would be at the AO rock salt interlayer [134, 135, 136, 137], surrounded by a tetrahedron of A-site cations [138] suggesting that diffusion would be greatest along this a-b plane [139, 137, 136, 135]. This has been supported experimentally in studies of epitaxial thin films [139, 140, 141, 142, 45]. The presence of these oxygen interstitials has also been shown to alleviate lattice stress in the AO interlayer [143, 144].

In the case of oxygen hypostoichiometry, $A_2BO_{4-\delta}$, the oxygen deficiency results in oxygen vacancies in the lattice. An early model of hypostoichiometric tetragonal RP by Allan et al. predicted a lower energy of formation of oxygen vacancies at equatorial sites[145]. Thus it also predicts anisotropic oxygen transport, occurring faster in the a-b equatorial plane than along the c-axis. This has been confirmed by further models [135, 136, 146, 147] and supported by experimental work [133].

In both cases, predicted activation energy for diffusion has not always been supported by experimental values [135, 148, 149, 142] and the diffusion mechanism uncertain. It was initially proposed that unlike with the case of perovskites, where oxygen diffusion is sensitive to oxygen nonstoichiometry, and hence B-site doping, oxygen diffusion in hyperstoichiometric RP is not sensitive to oxygen nonstoichiometry or the B-site cation [20, 142, 56]. This was thought to be because the diffusion predominantly occurs along the AO rock salt interlayer, and thus it would be the ionic radii of the A-site cation that has most on oxygen diffusion as it would determine the free space at the rock salt interlayer. On the other hand, there is also suggestion that the diffusion coefficient is strongly dependent on nonstoichiometry [150] as it affects the tilting of the BO_6 octahedron that effectively increases or decreases the barrier to oxygen transport [56, 151]. Further experimental support is required in this area. Fig 2.6 depicts the oxygen diffusion coefficient of various polycrystalline R-P systems.



(a) Oxygen tracer diffusion, D^*,



(b) Surface exchange coefficient, k^*

Figure 2.6: Arrhenius plot of (a) the oxygen tracer diffusion, D^*, and (b) the surface exchange coefficient, k^*, obtained for different R-P structures [20].

2.4 Electronic Conductivity

2.4.1 Electronic Conductivity of Metal Oxides

Like oxide ion conductivity, electronic conductivity may be described by the Nernst-Einstein relation, with the substitution of an electron charge carrier species and charge

instead of ionic species. Thus, electronic conductivity is the transport of mobile electrons across the lattice of a material. The ability of a material to conduct electronically depends on the concentration and mobility of the electronic charge carriers. The electronic behavior of a material may be classified as an insulator, semiconductor, conductor or superconductor, depending on its electronic responses to temperature. Increasing temperature would result in a decrease in the conductivity of metals as the delocalized electrons interact with the lattice, but would increase the conductivity of insulators and semiconductors as electrons are excited into the lowest unoccupied molecular orbital and the concentration of mobile charge carriers increases. In superconductors, a large increase in conductivity is experienced upon cooling. In metallic materials, charge is transported through a sea of delocalized electrons. However, in semiconductors and insulators, electronic charge is localized. The electronic properties of a material are, foremost, a result of the electronic structure of its constituent atoms- its atomic orbitals, which describe the possible locations of electrons about an atom- and the resulting electronic charge distribution.

The electrons of each atom are distributed into orbital subshells, each with their own specific energy, angular momentum and spin. The unique properties of each electron are described by its quantum number, comprising its principal quantum number ($n = 1, 2, 3..$), its orbital angular momentum quantum number ($l = n$-1 where $l = 0, 1, 2, 3$ corresponds to the s, p, d, ad f subshell), and its magnetic quantum number, (m_l = - l to +l). Thus, there is one s orbital, three p orbitals, five d orbitals and seven f orbitals within the s, p, d, and f subshells. As electrons may exist as spin up or down ($m_s = +\frac{1}{2}$ or -$\frac{1}{2}$ respectively), each orbital may contain two electrons. Electrons fill the orbitals starting with the lowest energy level orbital, starting with 1s, then 2s, 2p, etc. Lastly, according to Hund's rule, electrons will fill each orbital and a subshell, before the opposite spin electron would pair up within the same orbital.

To describe the electronic distribution in metal oxides, the molecular orbital theory, developed by Hund and Mulliken, may be used [152, 153, 154, 155]. With atomic orbitals, electrons are localized about the atom. However, these atomic orbitals may interact with each other to form bonding orbitals. Atomic orbitals that do not interact with each other are called non-bonding orbitals and do not affect the bonding within the molecule. There are two types of bonding orbitals: bonding and anti-bonding, depending on whether the atomic orbitals interact positively or negatively, respectively, with each other and the resulting distribution of electron density. A bonding orbital concentrates the electron density between the two nuclei creating a strong bond, whereas an anti-bonding orbital concentrates the electron density behind the nuclei so that these two regions are furthest from each other thus weakening the bond between the two atoms. The energies between the bonding and anti-bonding orbitals are determined by the electronegativity (or acidity) of the constituent atoms, which reflects the energy of the atomic orbital see Fig 2.7. This dictates the tendency of an atom to share or withdraw an electron from its bonding neighbor. When the electronegativities of two atoms are identical, the bonding electrons are shared equally. Thus the bonding and anti-bonding orbitals have equal contributions from both atoms and a purely covalent bond is formed. When the electronegativites of

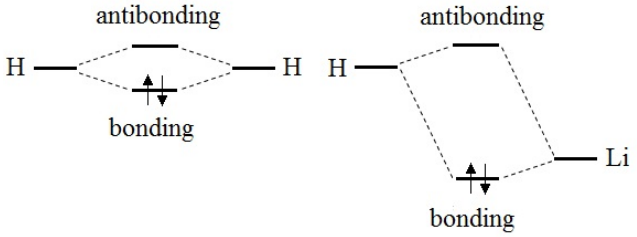


Figure 2.7: Example of covalent(left) and strongly ionic (right) bonding.

two atoms are highly dissimilar, the bonding electrons are effectively acquired by the more electronegative (more acidic) atom, resulting in an unequal contribution to bonding and anti-bonding orbitals and an almost purely ionic bond. As described in MO theory, delocalized valence electrons may move across these bonding and anti-bonding orbitals, which provide a conduction path across the lattice giving rise to electronic conductivity.

2.4.2 Perovskite and Ruddlesden-Popper Oxides

Electronic conductivity in oxide perovskites and Ruddlesden-Popper oxides arises from the octahedral symmetry about the transition metal, TM. The overlapping orbitals of the oxygen and transition metal gives rise to metallic or semi-conducting behavior at high temperatures resulting from delocalised electrons/holes along the BO_6 network [156]. The exact nature of a perovskite's electronic properties depends upon the covalency of the TM-O-TM bonds. As such, it is sensitive to the degree of polarization of the bond, as determined by the B-site cation's polarizing power [157, 158]. Decreasing the covalency of the TM-O-TM bond serves to localize electrons, reducing electron mobility and thus also electronic conductivity [159, 160].

It is also affected by structural distortions that may alter the TM3d and O2p orbital overlap, such as an increase in the TM-O-TM bond length or angle [161, 158]. Structural distortions arise as a result of the different ionic radii of the constituent atoms within the perovskite phase. As covered earlier, an ideal cubic perovskite structure is one where in the Goldschmidt tolerance factor of the A- and B-site ionic radii ratio varies between 0.89 $\leq t < 1$. A decrease in the ionic radii of the A-site cation, decreasing the tolerance factor, would decrease the B-O-B bond angle from 180° in an ideal perovskite, distorting the cell structure and decreasing the orbital overlap between the B3d and O2p orbitals, thus also decreasing electronic conductivity [162, 163, 131].

There are two means by which the ideal cubic perovskite structure may be distorted: cooperative rotations of the TMO_6 octahedra resulting in tilted octahedra, or individual displacements of A or B metal cations from their lattice sites, resulting in distorted octahedra [131, 164, 165, 166]. Both would result in a loss of symmetry and an expansion of the lattice, and subsequently also electronic conductivity, though there is evidence to suggest that a change in A-site cation radii and its effect on electronic conductivity is the result of the octahedral tilting [131]. The Goldschmidt tolerance factor is often used as a

measure of octahedral tilt where: as the tolerance factor deviates from 1(the ideal Fm3m structure), the octahedral are increasingly tilted.

Electronic conductivity additionally depends on the presence of any A-site dopant and whether the cations have single or mixed valencies [167]. Therefore, similar to the case for ionic conductivity, dopants of a difference valence are introduced, again, such as Sr^{2+}. The electronic compensation and the creation of free electrons/holes facilitates electronic transport.

2.5 Chemical Expansion

The term chemical expansion or chemical expansivity was first introduced to the field of SOFC materials by Adler in 2004 [168] from his work on LSCF. Chemical expansion is the change in unit cell dimensions of a material as a result of changes in its chemical composition due to changes in the environment (such as temperature or oxygen partial pressure). Thus the occurrence of chemical expansion is an indicator of the material chemistry, which subsequently impacts its unit cell dimensions. It is typically undesirable as it can result in mechanical instability and failure of devices. However, such changes in bond lengths and the crystal structure of the material, resulting in lattice strain also affect other material properties [169, 170, 171]. By tailoring the chemical expansion of a material, it may be possible to optimize its performance. In view of $PrCoO_{3-\delta}$ as a cathode material for fuel cell applications, interest lies in the effect of chemical expansion on its electrical and oxide ion transport abilities, and whether this effect is similarly found if the source of the changes in unit cell dimensions is different- through mechanical strain arising from lattice mismatch instead.

2.5.1 Introduction to Chemical Expansion

There are two forms of chemical expansion: stoichiometric expansion and phase change expansion. Stoichiometric expansion is characterized by gradual changes in crystal structure with gradual changes in stoichiometry. It is associated with the formation of point defects about the crystal lattice. Similar to thermal expansion, a stoichiometric expansion coefficient, α_c, can be used to relate the chemically induced strain, ϵ, to the molar concentration of the defect causing the expansion, i [172, 173].

$$\epsilon = \alpha_C[i] \tag{2.6}$$

A combination of defect species is often responsible for the change in cell parameters in SOFC cathode materials, such as a change in the ionic radii of cations and simultaneously the creation of oxygen vacancies. Stoichiometric expansion coefficients (as a function of oxygen partial pressure) range between 0.1 and 0.15 for ceria and Gd-doped ceria, whereas

α_c is much lower in perovskites than fluorites, between 0.022 and 0.04 in doped lanthanum cobaltites [173].

However, if the concentration of defect species is large enough, it eventually becomes energetically favourable to form a second phase of a different composition and thus different cell parameters. This abrupt change in lattice parameter due to the formation of a second phase is phase change expansion. The second phase may be of a related crystal structure, separated from the first phase by the miscibility gap that results from their different compositions, or it may be of an entirely different crystal structure. Stoichiometric expansion is associated with lower concentrations of defect species, while phase change expansion occurs at higher concentrations of defect species.

In the context of this work, all later mention of chemical expansion refers to stoichiometric expansion only. References to sample non-stoichiometry relate to changes in the A:B metal cation ratio, unless specifically identified as oxygen non-stoichiometry, which relates to deviation in the oxygen content from stoichiometric integer ratios resulting in oxygen defects.

2.5.2 Modelling Chemical Expansion in Fluorites

While much effort has been made to describe chemical expansion as a function of dopant concentration and type, the first comprehensive study was by Kim et al. in 1989 for five fluorite structures [174]. Fluorites typically have a stable cubic structure and can accommodate a large compositional range and concentration of trivalent cation dopants while remaining a solid solution. Thus they are an excellent system on which to develop the simple empirical models presented by Kim et al. who related the fluorite lattice parameter to the sum, for a given dopant concentration, of the differences in ionic radii and valence of the dopant cation compared to the host ion.

Such empirical fits were used to calculate the constant describing the extent by which changes in the ionic radii and valence affected the lattice parameter. By setting the first derivative of that equation to 0, it was possible to calculate the critical radius, r_c, of a dopant, which would not effect a change in lattice parameter when used. It was found that r_c values were larger than the radius of the host ion, r_h; in order for the dopant atom not to affect the lattice parameter, it had to be larger than the original host atom. The insertion of a dopant atom also resulted in the formation of an oxygen vacancy. Thus, the difference in ionic radii between dopant and host must be what offsets the effect of the formation of an oxygen vacancy in the lattice. It appeared that the creation of oxygen vacancies caused a contraction in the lattice.

Another approach to empirical modelling of chemical expansion in fluorites was introduced by Hong and Vikar in 1995 with the novel concept of treating an oxygen vacancy as another ionic species assuming a hard sphere structural model [175]. Therefore, the fluorite lattice parameter can be derived from the radii of its constituent atoms. The radius of the oxygen

vacancy and described the effective effect of the oxygen vacancy on the lattice and which could be calculated empirically. It was found to be smaller than that of an oxide ion, in accord with the empirical model by Kim [174].

While both models describe the effect of dopants on fluorite lattice parameter, neither provide insights as to how this is realized, except that the presence of oxygen vacancies appears to cause a contraction in the lattice. This was, however, revealed through atomistic modelling by Marrocchelli et al using MD and DFT models of ceria [176, 177, 178]. There are two effects to consider upon doping with a trivalent cation: the change in oxidation state of Ce^{4+} (ionic radius of 0.97 Å) for Ce^{3+} (ionic radius of 1.143 Å), and the creation of an oxygen vacancy where once was an oxide ion. In order to isolate the effect of replacing an oxide ion with an oxygen vacancy from the reduction of Ce^{4+}, a situation is considered where ceria is doped with Ce^{4+}. Thus it was seen that the removal of an oxide ion resulted in two effects, depending on the charge of the surrounding atoms. The nearest cations are no longer screened from the coloumbic repulsion of each other and are repelled away from the vacancy by ∼0.1 Å, while the nearest oxide ions moved towards a vacancy by ∼0.16 Å. The overall effect was a contraction of the unit cell, explaining the effects reported by Kim, and Hong and Vikar [174, 175].

However, this is only true for low levels of dopant concentrations, as required by Vegard's law upon which both Kim's and Hong and Vikar's empirical models are based [174, 175]. At high dopant concentrations, defect interactions may occur and have been experimentally observed to form short-range groups termed defect complexes and associates that cause a contraction in the lattice [51, 179, 180]. Therefore, increasing oxygen vacancy concentration decreases the rate of lattice expansion [51, 181, 179]. This is not unexpected as the modeling by Marrocchelli et al. showed that the lattice relaxation on creation of an oxygen vacancy occurs over several unit cells.

There is also a further complication in extending this work to the perovskite system as it uses the concept of an ionic radius as described by Shannon, which assumes localized electrons [182, 183, 184, 185]. However, many perovksites exhibit metal-like conductivity behavior, suggesting that there has been electron delocalization (for which there is also experimental evidence that it affects chemical expansion). It may not be appropriate to use the Shannon ionic radii for perovskites. A review of the chemical expansion of pervoskites is covered in Chapter 10. Nevertheless, this work on SOFC electrolytes clearly indicated the importance of the effect of defect concentration not just on transport properties, but also on mechanical properties that contribute to the materials selection criteria of SOFC cathode materials.

Chapter 3

Oxygen Reduction Reaction at the SOFC Cathode

Previously, it was seen that interest in IT-SOFC lies in its lower cost material selection, improved durability, and extended range of applications. However, one of the consequences of operating in the 500-750°C range of an IT-SOFC is that there are significant cathodic activation polarization losses during the oxidation reduction reaction, ORR. This is the limiting factor to IT-SOFC operation. An understanding of the factors affecting the ORR is important for material selection and engineering of cathode materials to minimize this loss and increase the efficiency of IT-SOFCs.

ORR reactions at gas diffusion electrodes, GDEs, such as the cathode of an SOFC, can be shown to conform to Tafel kinetics [186]. Thus, until recently it was inferred that the ORR at GDEs are limited by charge transfer at the cathode surface in accordance to traditional electrochemical-kinetics involving the creation of an electrical double layer [187, 188, 189]. However, this does not prove that the ORR in GDEs is activation limited, just that it behaves as though it were. In actuality, results from electrochemical impedance spectroscopy, EIS, measurements suggest that the ORR is not charge limited and that traditional electrochemical kinetics may not be applied to GDEs.

In this chapter, the concept of triple phase boundaries, TPB, is introduced and the rate-limiting steps of the ORR in cathodes discussed. It is the generally accepted view that the ORR is co-limited by oxygen diffusion and adsorption (chemical) steps, as opposed to charge transfer. In order to improve cathode performance there has been a move to mixed ionic-electronic conductors, MIEC. Also, the report of ORR enhancement at perovskite-RP oxide heterojunction and the mechano-chemical effects are investigated as additional means of improving cathode performance.

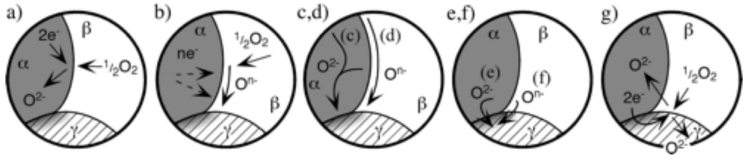


Figure 3.1: Proposed mechanisms governing ORR in SOFC cathodes, where phases α β, and γ refer to the electronic, gas, and ionic phase, respectively: (a)incorporation of oxygen into the bulk of the electronic phse (if MIEC); (b) adsorption and/or partial reduction of oxygen on the surface of the electronic phase; (c) bulk or (d) surface transport of O^{2-} or O^{n-}, respectively, to the α/γ interface, (e) electrochemical charge transfer of O^{2-} or (f) combinations of O^{2-} and e^{-}, respectively, across the α/γ interface, and (g) rates of one or more of these mechanisms wherein the electrolyte itself is active for generation and transport of electroactive oxygen species [22].

3.1 Triple Phase Boundary

The TPB is the active site where the electronic, ionic, and gaseous species, and their corresponding phases come into contact with each other that the ORR may occurs. Each phase has the following roles: the gas phase supplies oxygen to the interface between cathode and electrolyte; the cathode must provide an electronic conduction path from the interconnect to the interface in order to provide a supply of electronic charge; and the electrolyte must provide an ionic conduction path from the interface to the electrolyte in order to remove the oxide ions produced.

The TPB is a phenomenological concept- it may be described by Tafel kinetics. It is thought to involve at adsorption of the oxygen molecule, partial reduction into an electroactive species before incorporation into the electrolyte as an oxide ion. However, it is uncertain where these reactions occur, the transport of the various intermediate species about the TPB, or which steps are rate limiting. Fig 3.1 describes some mechanisms thought to occur in the ORR. Despite that, the TPB concept has been applied to great success in improving SOFC performance.

3.2 The ORR in Cathodes Diffusion and Adsorption Co-limited

The first indication of diffusion being the rate limiting step was when EIS was performed on a Pt GDE. The impedance values, when modeled against and equivalent circuit, indicated an unusually high capacitance value that could not be accounted for solely on the basis of the electrical double layer [190]. It was thus suggested that there were additional diffusive effects [191]. Later work by a separate party also suggested that electrode kinetics were limited by diffusion, and furthermore, that it was also limited by oxygen adsorption [192]. These surface exchange processes have been labeled to be chemical steps in the ORR [22].

More evidence supporting a diffusion and adsorption limited electrode kinetics was provided by Verkerk and Burgraff whose results indicated the occurrence of diffusion processes during the ORR and that this was at the electrode surface [193]. Their work was taken a step further by Mizusaki et al. [194]. Mizusaki showed that electrochemical kinetics at the TPB were definitively not the rate limiting step of the ORR. Instead it was limited to either the adsorption of oxygen molecules on the electrode surface or the diffusion (transport) of the adsorped species to the TPB. While there has been some contention as to the location of the rate limiting diffusion step, this has since been resolved to occur on the electrode surface in contact with the gas phase [195, 192]. It is now accepted that for these purely electronically conducting systems co-limitation of diffusion and adsorption during surface exchange is the rate limiting step for the ORR in SOFC cathodes, not charge transfer processes as would be predicted by electrochemical kinetics.

The co-limitation model provides the best explanation of ORR measurements to date. Still, much research remains to be carried out. For examples, for surface paths, the region over which diffusion and adsorption occurs has yet to be quantified (though early predictions suggest it scales with the TPB [196, 197]. Also, this work only involves the production of oxide ions. There is little understanding of how the oxide ion is incorporated into the electrolyte as electrolytic oxide ions, a process that is thought to contribute as much as 50% to the cathode overpotential [198]. Investigations regarding the influence of the electrolyte on the ORR are also limited, though there is evidence to suggest it too contributes a catalyzing effect [199].

3.3 The ORR in Mixed Ionic-Electronic Conducting Cathodes

In the case of purely electronically conducting GPEs, the active region of the ORR kinetics is confined to the interface at the TPB. The drive to extend the TPB and increase the active area, has resulted in the transition from single phase electronically conducting cathodes to composite cathodes comprising of an ionic and electronic phase, and finally to MEICs. The use of a MIEC, would increase the transport of electroactive species, allowing oxygen reduction to occur at the electrode/electrolyte even when not at the TPB and subsequently increasing electrode performance.

Previously, it was seen that during the ORR at TPB in a purely electronically conducting GDEs, the adsorption and diffusion of electroactive species occurred at the gas/electrode interface followed by charge transfer at the electrode/electrolyte interface. In the case of a dense MIEC, the chemical steps may now also involve absorption and diffusion into the bulk of the electrode, then charge transfer at the electrode/electrolyte interface, see Fig 3.2. Thus, as was first suggested by Tekada et al. based on his work on LSC electrodes [200, 23], the ORR kinetics in MIECs may be affected by the electrodes bulk properties (though a slight different situation would arise for the case of porous MIECs [201, 202, 203]).

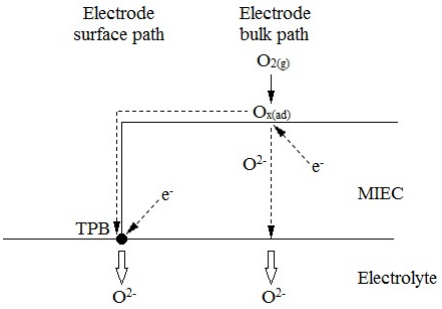


Figure 3.2: Possible pathways for the ORR in a MIEC: the electrode surface path across the "open" triple phase boundary between cathode and electrolyte; or the electrode bulk path across the "closed" two phase boundary . The adsorbed oxygen species, $O_{x(ad)}$, may be any one of: $O_{2,ad}$, O_{ad}, ${O^-}_{ad}$ or ${O^{2-}}_{ad}$. The adsorbed oxygen may travel by surface diffusion to the TPB where it is full reduced; or it may incorporated directly into the MIEC as ${O^{2-}}_{ad}$, where it diffuses to the electrode/electrolyte interface [23, 24, 25].

In order to investigate the effect of bulk material properties on the ORR, it is necessary to minimize surface effects such as contributions from the surface path b-d-f of Fig 3.1. To that objective, ORR kinetics were studied in dense thin-film MIECs perovskites, thus limiting ORR steps to the bulk path a-c-e of Fig 3.1. It was found that thin film perovskites with high ionic conductivity had little resistance to bulk transport of absorbed oxygen species. Therefore, the dominant transport path of the chemical step was now through the bulk, not surface [204, 205, 206, 34, 207, 208, 209, 22, 210, 211]. Whereas in cathodes with low ionic conductivities, such as lanthanide manganite oxide perovskites, $LaMnO_{3-\delta}$, the dominant transport path was the surface pathway to the TPB [212, 213, 214].

The Adler-Lane-Steele, ALS, model is a notable model that has been proposed to describe the ORR in MIECs [203]. In MIECs, the electrode reactions are no longer confined to the TPB. Thus in the ALS model, the overall reaction is assumed to occur as three separate reaction steps over three interfacial regions: charge transfer of oxygen ion vacancies and electrons across the MIEC/electrolyte and current-collector/MIEC interface respectively; and chemical exchange of oxygen across the gas/MIEC interface. A key result of this model was that the electrode performance was found to be directly linked to the bulk diffusion, D, and surface exchange, k of the MIEC- properties that may be measured quantitatively. This has been experimentally validated (though only with Fe- and Co- containing perovskites), and found to be consistent with MIEC with high ionic conductivities where ionic transport is the key mechanism by which the reduction reaction is extended beyond the TPB. Thus, it is an appropriate model for this work wherein the material of interest is a colbaltite perovskite with a high ionic conductivity. Additionally, it also defined a penetration depth, δ, describing the active region of the MIEC that actually participates in the reduction reaction. Typically, this is no more than a few microns from the electrolyte interface; modifying the cathode beyond this active region would not affect the ORR. Subsequently, much work on cathode materials have been directed at optimizing D and k. Similarly this work culminates in the measurement of D^* and k^*, to assess if an improvement in cathode performance has been attained.

3.4 Enhancement of the ORR at the Perovskite/Ruddlesden-Popper Interface

The ORR mechanism in rare earth perovskites and R-P materials are rate limited by the (mass-transfer) chemical steps of oxygen exchange (oxide ion incorporation at the surface) and diffusion of the oxide ion into the electrolyte[215, 216, 217, 107, 218, 219, 220, 221]. Thus, to minimize cathodic overpotential losses, the cathode material should have a high oxygen diffusion coefficient, D, in addition to a high surface exchange coefficient, k. However, there have been reports of ORR enhancement as a result of coupling Sr-doped lanthanum colbatite perovskite oxide with the R-P oxide [32, 26, 222, 27, 29, 31]. This phenomenon formed the basis of this work investigating the means of improving the ORR and thus cathode performance. In the following is a review of this research, initiated by Sase et al. [32, 26, 223]. For the remainder of this section, Sr-doped lanthanum colbaltate perovskite and R-P oxides have been denoted as LSC113 and LSC214 respectively.

Originally, it was the enhancement of oxygen surface exchange at the grain boundaries of rhombohedral LSC113 ($x = 0.4$), based on earlier work [223], that was the point of investigation. However, the long annealing times necessary for grain growth also resulted in the known decomposition of the perovskite [224, 225] into approximately 4 μm to 5 μm tetragonal LSC214 precipitates where the Sr content, x, is thought to be larger than 0.5 or 0.6 [32]. Isotope oxygen exchange was carried out on polished and unpolished samples, followed by secondary ion mass spectrometry, SIMS, analysis. In both cases, ^{18}O concentration was found to be enhanced at the LSC113/LSC214 interface but at about the same level within the LSC214 as in the LSC113. Values of the diffusion coefficient, D^*, and surface exchange coefficient, k^*, for the perovskite phase was found to be $(4.8 \pm 0.3) \times 10^{-9}$ cm^2s^{-1} and $(2.10 \pm 0.05) \times 10^{-8}$ cms^{-1} respectively, in the same range as reported results [224, 28]. However, at the interface, this was 3.5×10^{-9} cm^2s^{-1} and 8×10^{-6} cms^{-1} (3 orders larger than than the LSC113 matrix) respectively. Thus, ORR is enhanced at the LSC113/214 interface. For the perovskite matrix, these values were calculated by fitting the oxygen profile to the solution, by Crank [226], for Fick's second law for a semi-infinite medium. For the modeling of the interface, it was thought that inhomogeneous oxygen exchange best represented the situation. The precipitate was assumed to be spherical, and that the isotope concentration is uniform at the interface. These assumptions that isotope concentration and exchange at the interface were homogenous may even underestimate k^* and D^*.

Subsequently, to confirm ORR enhancement, Sase deposited $La_{0.6}Sr_{0.4}CoO_3$ and $La_{2-x}S_xCoO_4$ (x = 0.5, 1.0) thin films, of approximately 1.5 μm and 0.5 μm thick respectively, onto a $Ce_{0.9}Gd_{0.1}O_2$, CGO, substrate using pulsed laser deposition [26]. SIMS analysis of ^{18}O isotope exchange reveals a pathway of enhanced isotope concentration at the LSC113/214/gas interface, down through the LSC113, and into the CGO substrate, see Fig 3.3. The perovskite layer was found to be a crucial component of the diffusion path; SIMS images do not show the same degree of oxygen exchange into the CGO at the LSC214/CGO inter-

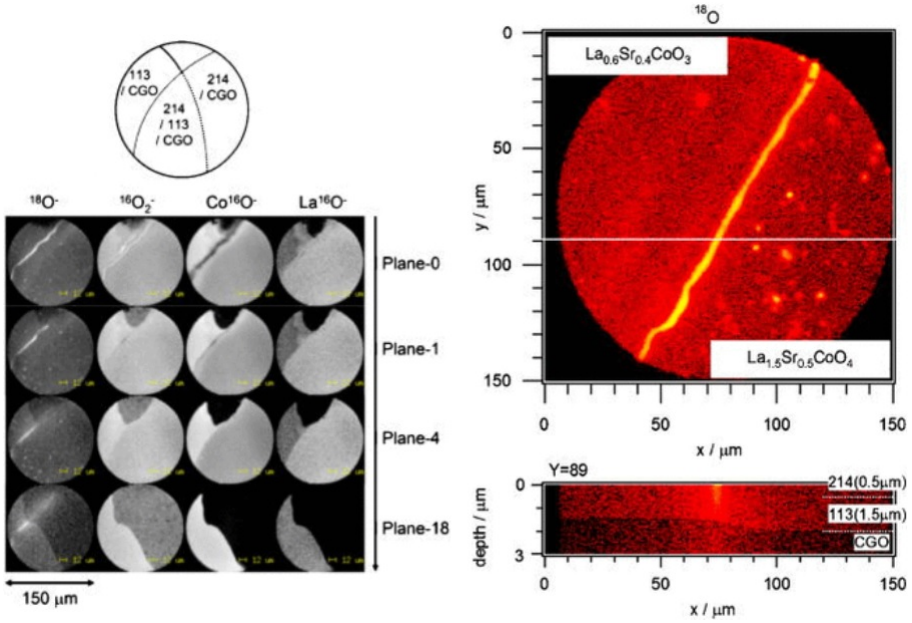


Figure 3.3: Schematic of $La_{2-x}CoO_4/La_{0.6}Sr_{0.4}CoO_3$/CGO layers; SIMS of layered PLD layers of $La_{2-x}CoO_4/La_{0.6}Sr_{0.4}CoO_3$/CGO after $^{16}O/^{18}O$ exchange at 0.2 bar, 773 K fo 180s (plane 1, 4, 18 corresponds to a sputtering depth of 70 nm, 2280 nm, 1.26 μm); and top down and cross-sectional SIMS images of PLD layers of $La_{2-x}CoO_4/La_{0.6}Sr_{0.4}CoO_3$/CGO after $^{16}O/^{18}O$ exchange at 0.2 bar, 773 K fo 180s [26].

face, despite high isotope concentration at the LSC214/CGO/gas interface. Thus, these results support Sase's earlier work (though no D^* or k^* values were calculated) suggesting enhanced ORR at the LSC113/LSC214 heterointerface and additionally the importance of the pervoskite layer as a necessary oxygen diffusion path into the CGO.

To further investigate the effects of the LSC113/214 interface, Yashiro et al. [222] used EIS to examine the electrochemical performance of single phase screen printed $La_{0.6}Sr_{0.4}CoO_3$ and $(La,Sr)_2CoO_4$ cathodes against a composite LSC113 on LSC214 cathode, all on approximately 3 mm thick $Ce_{0.9}Gd_{0.1}O_2$ substrates. These results support the earlier SIMS analysis indicating the enhanced oxygen exchange may not be attributed to just the LSC214 layer, but is a consequence of the LSC113/214 interface. Interfacial conductivity values as a function of partial O_2 pressure showed consistently higher values for the composite cathode. A point of interest is the similar dependence on O_2 partial pressure between the LSC113 and LSC113/214 cathodes suggesting similar reaction mechanisms between the two cathodes.

Enhancement in ORR has also been demonstrated in the use of $La_{1-x}Sr_xCoO_3$ epitaxial films [30]. Thus, in the hopes of compounding both occasions of ORR enhancement Ethan et al. [27] fabricated heterojunctioned epitaxial films of $La_{0.8}Sr_{0.2}CoO_3$ (approximately 85 nm thick) and $LaSrCoO_4$ (varying coverage of approximately 0.1, 0.8, 5, 15 nm) on a (001) oriented single crystal yttria-stabilized zirconia, YSZ(001), substrate. Prior to the pulsed laser deposition of the colbaltate oxides, a $Ce_{0.8}Gd_{0.2}O_2$ (approximately 5 nm thick) buffer layer was first deposited over the YSZ substrate to accommodate for

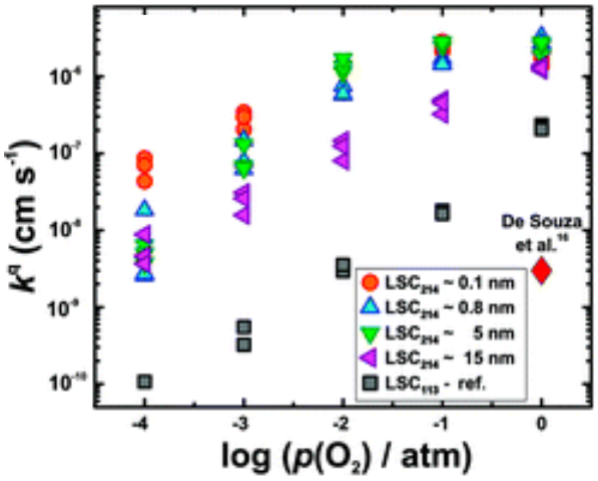


Figure 3.4: Electrochemical impedance spectroscopy (EIS) results of epitaxial microelectrodes (∼200 μm) for the LSC113 reference and the LSC113 films with varying surface coverage of LSC214 at 550°C [27]. A comparison has been made to bulk properties as measured by Souza et al. [28].

lattice mismatch and also to prevent deleterious Co phases forming at the interface. The electrical surface exchange coefficient, k^q, was calculated from EIS measurements of the ASR, see Fig 3.4. Thus it can be seen that k^q is enhanced for the case of epitaxial films over bulk (comparing it to the k^q value of bulk LSC113 [28], and that the presence of the LSC113/LSC214 heterointeface through the surface decoration of LSC214 further increased k^q. Moreover, k^q obtained in this case of the epitaxial heterointerface can be up to a magnitude larger than that of k^* in porous LSC113/LSC214 layers screen printed by Yashiro et al. So, on both accounts, does the use of heterojunctioned epitaxial films result in improved ORR, suggesting a progression of IT-SOFC cathodes to epitaxial films, although in subsequent work [227], Crumlin found that epitaxial LSC113 (x = 0.2 instead of 0.4) had comparable activity to its bulk equivalent.

Another important outcome of Crumlin's work is the insight it gives to surface oxygen exchange kinetics. Crumlin also determined the oxygen nonstoichiometry, δ, for the different degrees of LSC214 surface decoration and found δ did not change as the LSC113/LSC214 heterointerfacial area increased. Therefore, the enhanced ORR kinetics can not be due to an increase in oxygen vacancies. After further investigation in the LSC113 reference film, similarly to Sase and Yashiro, Crumlin also concluded that it is the interface of the perovskite and RP films that is the cause for the ORR enhancement. Lastly, also with regards to ORR mechanisms, in Fig 3.4, it can be seen that increasing the degree of surface decoration of LSC214 on the perovskite lowers k^q, and also that the graph of k^q flattens out as the partial pressure of O_2 increases. Crumlin proposed that this was due to a reduction in the triple phase boundary of the LSC113/LSC214/gas, and that at higher oxygen partial pressures bulk diffusion in the thin films starts to become rate limiting (as opposed to oxygen exchange).

Other occasions where the presence of a LSC113/LSC214 heterojunction has been at-

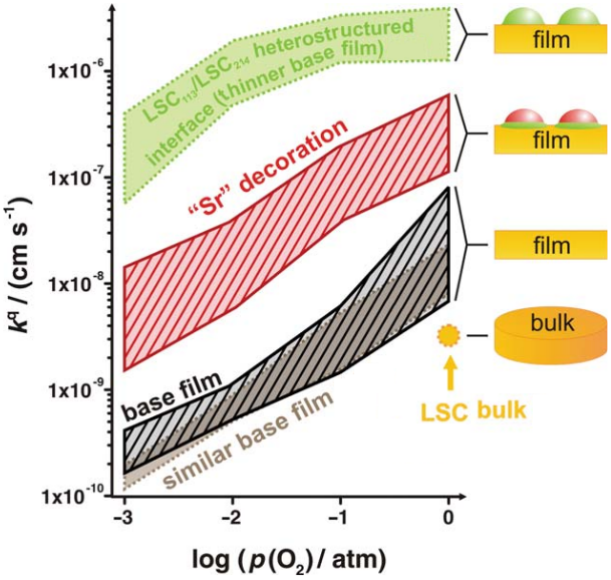


Figure 3.5: Electrochemical impedance spectroscopy (EIS) results of different epitaxial LSC113 based microelectrodes: LSC113 bulk- yellow [28](extrapolated to 510°C); base film in this study [29] (black hatched, 510°C, 140 nm thick base); base film [30] (grey, 520°C, 130 nm thick base); Sr-decorated film [29] (red hatched, 510°C, 140 nm thick base), heterostructured LSC113/LC214 film [27](green, 550°C, 85 nm thick base) [8].

tributed to enhanced ORR are the work by Mutoro et al. [8] and Hayd et al. [31]. Mutoro adopted an identical setup to Crumlin, but surface decorated epitaxial (001) $La_{0.2}Sr_{0.2}CoO_3$ film (∼140 nm thick,) with Sr, La and Co. Calculating the electrical surface exchange coefficient, k^q, from EIS measurements (like Crumlin) revealed that only in the case of Sr decoration was there an improvement in ORR kinetics. Taking into account the slow diffusion of Sr, this enhancement was postulated to be due to the formation of LSC214 phases at the interface between the Sr decoration and the LSC113 film. Comparison against k^q values obtained for surface decoration of LSC214 showed that Sr decoration resulted in a lower enhancement. This was thought to be due to the Sr also forming ORR inhibiting oxides, see Fig 3.5.

On another occasion, the creation of LSC113/LSC214 heterojunctions by Hayd was achieved through the deposition of $La_{0.6}Sr_{0.4}CoO_3$ films using metal organic deposition, MOD [31]. This fabrication method consistently produced films with a higher surface exchange coefficient, k^*, than elsewhere in literature, see Fig 3.6. Hayd suggested that though the MOD films may be nominally stoichiometric, chemical inhomogeneities may exist in the form of LSC214 phases, which interface with the perovskite would cause the ORR enhancement. This is supported by transmission electron microscopy, TEM, analysis revealing Co_3O_4 crystallites that inferred the presence of a finely dispersed LSC214

Therefore, there has been a compelling collection of results that suggest the enhancement of the ORR as a result of the coupling at the LSC113/214 heterojunction though the mechanism by which this was effected has not been definitively identified. However, it has been proposed to be due to mechano-chemical effect [228].

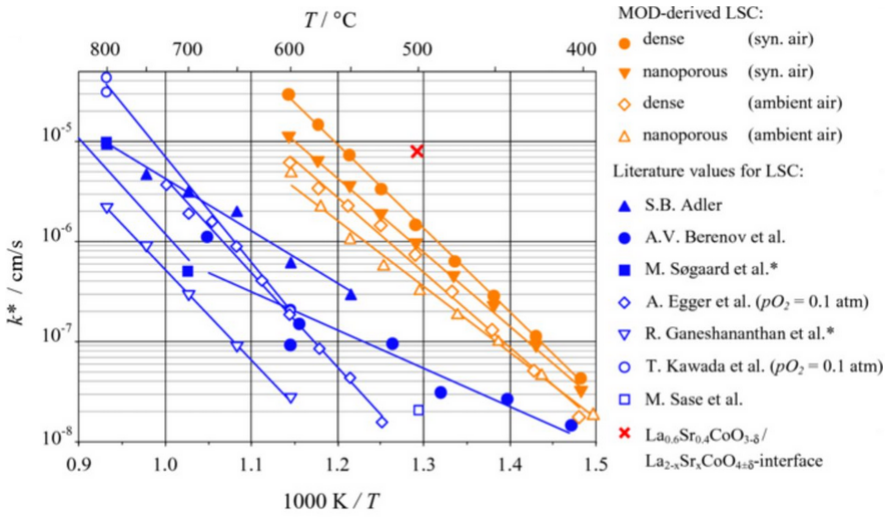


Figure 3.6: Surface-exchange coefficient k^* of MOD-derived LSC113 with nanoporous and dense microstructures in comparison with literature values for bulk LSC materials [31]. References for literature values may be found here [32, 33, 34, 35, 36, 37, 38, 39].

3.5 Enhancement of the ORR due to the Mechano-Chemical Effect

Mechano-chemical coupling was first observed in metals, when oxygen was shown to preferentially adsorb on tensile strained regions [229]. This was investigated through density functional theory, DFT, modelling, which revealed large variation of CO and O chemisorption energies, and CO dissociation energy barrier, with lattice strain. DFT models showed that the application of lattice strain to Ru(0001) affected its electronic structure, and hence its interaction with the adsorbed species, by increasing energy of the metal d-states and shifting the energy of the d-states up [230, 231]. The hybridization of Ru d states with the adsorbates states can be significantly altered using strain, and with it the reaction energies [232]. Later experimental work with other metal catalysts also demonstrated the mechano-chemical coupling effect [231, 233, 234, 235, 236, 237]. Additionally, the shift in metal d-state as predicted by early DFT calculations, on application of a compressive strain was experimentally observed [238].

Mechano-chemical coupling has been found in other material systems [239, 240]. Due to the large stresses that can be accommodated in thin oxide films, lattice strain has also been proposed to affect the surface reactivity and oxygen transport of fluorite and perovskite oxides [241, 56, 151]. However, unlike with metals in which electronic structure and reactivity may be described using the d-band model [232], the electronic structure of metal oxides and how it relates to reaction kinetics is less well understood. The interaction of states between the metal and oxygen components of perovskite oxides are more complex and they exhibit electronic and magnetic state transitions that also affect bonding [242, 243, 244, 245]. Their exact surface chemistry is still under investigation and is not static, being extremely sensitive to temperature and oxygen [171, 246, 247]. Much effort remains

to understand the reactivity of metal oxides. Nevertheless, mechano-chemical coupling has recently been shown to affect the reactivity and conductivity of strained fluorites (where an eight magnitude increase in oxide ion conductivity has been reported reported [248]) [248, 215, 107, 249, 250, 251], and also perovskites [151, 252, 253, 254, 255]. It is a phenomenon that warrants further investigation for its application in improving oxygen transport, and subsequently performance, in IT-SOFC cathode materials.

Chapter 4

Thesis Objectives

The barrier to the practical application of IT-SOFCs lies in its low efficiencies due to high activation polarization and thus its inability to reach acceptable power densities at these lower temperatures (though microtubular SOFCs developed by NGK Insulators and collaborators have been able to achieve power densities exceeding 2 W/cm^2 at 550°C [256]. The Ohmic losses at intermediate temperatures are also significant, but to a lesser degree and can be resolved through the use of recent ceria carbonate composite electrolytes that have sufficient ionic conductivity to temperatures as low as 300°C so as not to inhibit SOFC operation [257, 258, 259, 260, 261, 262, 263]. Thus, a significant contributor to polarization losses during IT-SOFC operation is the retarded ORR kinetics in this 500-750°C temperature range. This work is a part of the ongoing research to address this issue through the enhancement of the ORR via mechano-chemical coupling.

The objective of this thesis was to investigate and compare the effect of various types of strain on the oxide ion and electrical transport of praseodymium colbate perovskite, $PrCoO_{3-\delta}$. While Sr-doping is typically used to improve the transport properties of cathode materials, it was deliberately avoided in this work due to its tendency to forming surface segregates [264, 265] (though lattice strain has been proposed to suppress Sr surface segregation [169]). The application of a lattice strain was to be achieved using three different methods:

1. The deposition of a praseodymium nickleate R-P, $Pr_2NiO_{4\pm\delta}$, thin film on top of the $PrCoO_{3-\delta}$ thin film to create a perovskite/R-P interface analogous to that investigated by Sase et al. [32, 26].

2. The introduction of a mechanical strain arising from the lattice mismatch between the $PrCoO_{3-\delta}$ thin film and substrate, and the strain relaxation effect.

3. The introduction of a chemical strain arising from the chemical expansion as the $PrCoO_{3-\delta}$ metal cation ratio is varied.

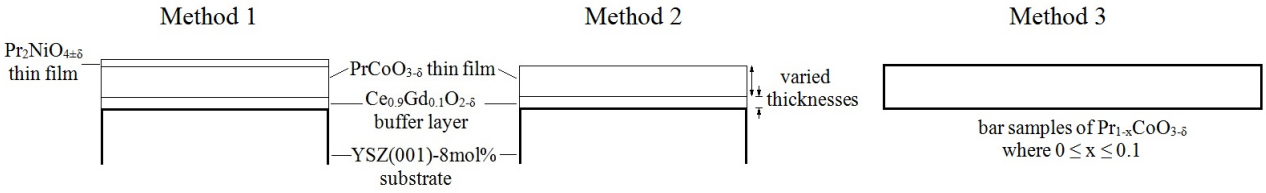


Figure 4.1: Schematic of the $PrCoO_{3-\delta}$ samples by which lattice strain has been introduced using three different methods: the deposition of a $Pr_2NiO_{4\pm\delta}$ film on top of the $PrCoO_{3-\delta}$ film; variation in the $Ce_{0.9}Gd0.1O_{2-\delta}$ buffer layer thickness or $PrCoO_{3-\delta}$ film thickness; variation in $PrCoO_{3-\delta}$ metal cation stoichiometry.

Methods 1 and 2 involved the use of pulsed laser deposition as the thin film fabrication technique. A $Ce_{0.9}Gd_{0.1}O_{2-\delta}$ buffer layer was deposited upon a YSZ(001)-8mol% substrate, and the $PrCoO_{3-\delta}$ thin films on top of that. In Method 1, a $Pr_2NiO_{4\pm\delta}$ thin film was additionally to be deposited on top of the $PrCoO_{3-\delta}$ layer. In Method 2, two sample sets were be used. In the first, the $Ce_{0.9}Gd_{0.1}O_{2-\delta}$ buffer layer thickness was varied to obtain a range of lattice mismatch between PCO and $Ce_{0.9}Gd_{0.1}O_{2-\delta}$ as the $Ce_{0.9}Gd_{0.1}O_{2-\delta}$ buffer layer relaxed. In the second sample set the ce$PrCoO_{3-\delta}$ film thickness was varied and a range of lattice strains obtained as the $PrCoO_{3-\delta}$ film relaxed. Lastly in Method 3, powder $Pr_{1-x}CoO_{3-\delta}$ where $(0 \leq x \leq 1)$ were synthesized and sintered into bar samples. A schematic of the $PrCoO_{3-\delta}$ samples are illustrated in Fig 4.1. Electrical measurements were performed using 4-point DC and Van der Pauw setups for the bar $Pr_{1-x}CoO_{3-\delta}$ and thin film $PrCoO_{3-\delta}$ samples respectively. Oxide ion conductivity measurements were performed using ^{18}O isotope exchange depth profiling.

For the remainder of this work, $PrCoO_{3-\delta}$ and $Pr_2NiO_{4\pm\delta}$ have been referred to as PCO113 and PNO214, and $Ce_{0.9}Gd0.1O_{2-\delta}$ has been referred to as CGO. Similarly, the oriented single crystal silicon and 8-mol% yttria-stabilized zirconia substrates have been referred to as Si(001) and YSZ(001). Unless specifically stated to be oxygen non-stoichiometric, all mention of the non-stoichiometry of PCO113 refers to metal cation non-stoichiometry.

Chapter 5

Experimental Techniques

5.1 Material Synthesis

Three synthesis routes were considered for the production of PCO113 and PNO214: solid-state, sol-gel (Pechini method) [266] and combustion (glycine-nitrate process, GNP) [267]. For the solid-state process, oxide precursors are milled together and heated until the end product is formed. Mixing is on the microscopic scale, thus control of the precursor particle size is necessary. The powder may require several cycles of milling and heat treatment before all the precursors have been reacted.

Both the Pechini and GNP processes are solution methods. Mixing is achieved on the molecular level as the precursors are dissolved in a nitrate solution, thus achieving a much higher homogeneity than in the solid state process. In both processes a complexing agent, such as citric acid or glycine for the Pechini and GNP respectively, is used. This ensures that the molecular scale mixing is maintained even upon evaporation.

To furthermore prevent the selective precipitation of the metal atoms upon evaporation, a gelling complexant such as polyethylene glycol, PEG, is used in the Pechini method. Thus the metal atoms are bonded in a cross-linked network to form a homogeneous suspension. Another advantage of mixing on the molecular scale is that, following decomposition, the calcination temperature required to produce the final powder is lowered.

For the GNP process, as well as being a complexant for the metal cations, glycine also serves as the fuel for the combustion reaction. The solution is heated and when it is fully dried the glycine self-combusts in the presence of the nitrate, which is the oxidizer. The final product is in the form of a very fine ash. The oxides synthesized using the combustion process may have an amorphous structure, unlike the solid-state and sol-gel processes that utilizes long heat treatments and subsequently produces a crystalline structure. Further heat treatment may be necessary for a crystalline powder.

While the solid-state process is relatively straight forward, the milling step may be lengthy

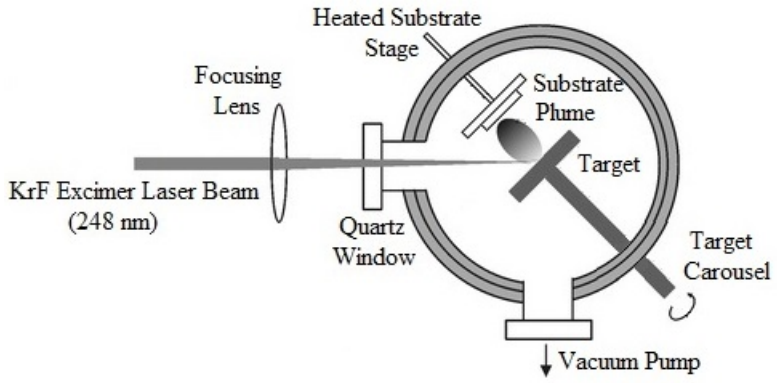


Figure 5.1: Schematic of a typical PLD vacuum chamber, adapted from [40]

and may introduce contaminants within the powder. There is also the possibility of precursor material remaining within the particle core, which would not be the case with the solution routes. The Pechini process is lengthy with its decomposition and calcination steps. However, due to its relatively low calcination temperatures, sintering during the heat treatment is minimized and a relatively small particle size may be achieved, which is desirable for obtaining high densities through sintering. The GNP method produces the smallest particle size that requires little extra processing. However, the collection of this ash often introduces contaminants. The combustion conditions are also extremely sensitive to the fuel to oxide ratio. Therefore, as good cation homogeneity can be achieved with high purity, the Pechini method was used for the synthesis of all oxide materials used in this work.

5.2 Pulsed Laser Deposition

During pulsed laser deposition, a pulsed laser is used to ablate material from a target, which is ejected from the target, creating a forward-directed plasma plume. This then impinges upon a substrate, positioned parallel to the target, resulting in the nucleation and growth of a film. A schematic of a PLD system is depicted in Fig 5.1

The ablated plume may comprise a range of species from atomic particles to macro-molecules. The plume may also contain large macroscopic particulates, several microns in diameter (from hydrodynamic sputtering) [268]. For the growth of epitaxial or high quality thin oxide films, it is necessary to have only low mass species in the ablation plume. To achieve this the absorption volume (the volume into which the energy of the laser pulse is transferred) of the target needs to be minimised while the absorption volume of the plume is maximised by optimising the laser energy and pulse duration (or pulse width) respectively. For oxide thin films, the deposition of particulates in the film may be reduced by using smooth and dense targets.

Upon ablation, the plume is very narrow and forward-pointed, in a direction normal to the target surface, and expands away from the point of ablation. The shape of the plume

is determined by the particle density distribution of the plume and is largely determined by the energy of the laser fluence. The particle distribution of the plume as it impinges upon the substrate also depends on the background pressure of the PLD chamber and the distance of the substrate from the target. As the plume is responsible for carrying material flux to the deposition surface, the particle distribution of the plume often results in a film of highly non-uniform thickness, which may have compositional variation.

As the plume impinges onto the substrate, the incident flux initially sputters off the substrate surface. The sputtered flux creates a thermalized region where it collides with incoming flux. This region allows the incoming flux to condense and adsorb on the substrate. Due to the pulsed nature of this deposition technique, the adatoms have time to rearrange on the substrate surface for nucleation and growth before particles from the next plume arrive, resulting in a good film quality [269]. However, if the incident species is very energetic, it can embed into the substrate forming defects, or re-sputter the deposited film thus lowering the deposition rate or affecting the film stoichiometry. The background pressure of the PLD chamber may be used to tailor the energy of the incident species, besides also affecting the oxygen stoichiometry of the deposited species in the case of oxide deposition. Increasing the background pressure decreases the energy of the incident flux.

Nucleation occurs when the decrease in energy in forming a solid from a gaseous phase exceeds the cost associated with surface and interfacial energy. This is the case when the impinging plume creates a high supersaturation in the gas phase at the substrate surface. Thus the nucleation density is dependent on: the plume density, which is a function of laser fluence (and also the background pressure); substrate temperature; and the substrate surface. Compared to other physical deposition techniques, PLD has the highest nucleation density due to the high energy density of the laser. Following nucleation, if the radius of the nuclei exceeds the critical radii, it will be thermodynamically favourable for it to grow. There are three modes of film growth. The mode of film growth depends on the surface and interfacial energies of the substrate, nuclei and vapour.

If the energy associated with the nuclei/vapour and nuclei/substrate interface is much greater than the vapour/substrate interface, then adatom-adatom interactions are more favourable and growth will occur in three dimensional clusters or islands that grow and coarsen as deposition continues. This is Volmer-Weber growth (or island growth). If the opposite is true, adatom interactions with the substrate will be favourable and adatoms will diffuse to step edges in the substrate surface from which 2D growth occurs in fully formed layer. This is Frank van der Merwe growth (or layer-by-layer growth). Lastly, Stranski-Krastanov growth (or layer-plus-island growth) is a combination of 2D layer and 3D island growth [41]. Initially, islands nucleate as in Volmer-Weber growth. However, as they grow and coalesce, there is a transition to Frank van der Merwe growth at a critical layer thickness. The different film growth modes are depicted in Fig 5.2

The main reason PLD was chosen for this work is that PLD allows stoichiometric transfer of target material to the substrate. There is also straightforward control of the film thickness and the ability to deposit multiple materials without the need for breaking the

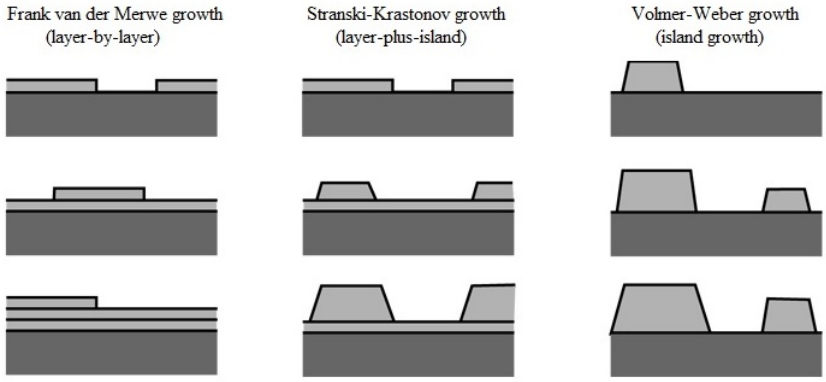


Figure 5.2: Schematic representation of three major film growth processes, from [41].

vacuum. Further advantages of PLD over other film deposition techniques include its high deposition rate, the use of only a small target, and an external heating source (removing the possibility of filament contamination).

However, it should be noted that due to the highly directed nature of the plume, the deposition rate decreases away from the centre of the plume, resulting in only a small film coverage that also varies in thickness. Additionally, there is a large range in the size of the particulates comprising the plume, up to $\sim$10 μm if globules of molten material are present, which if deposited, would lower the quality of the film. While there are means of mitigating these effects, such as: using a line-focus laser to increase coverage; rastering the laser, target, or substrate to deposit a film of uniform thickness; mechanically filtering the plume for large particulates or using an"off axis" geometry [270], these were not available in the PLD system used for this work. The only precaution available to minimise the range of particulate size of the plume, which was undertaken, was to use a dense smooth target.

For the entirety of this work, a 248 nm KrF eximer laser was used. Unless specifically stated, PLD was performed in the following manner. Prior to deposition, all substrates were cleaned by immersing in an ultrasound bath with acetone, isopropanol and deionized and distilled water respectively for at least 5 min in each bath. Substrates were adhered to the sample stage using silver paint. A corner of the substrate was masked off using TiO_2 powder suspended in isopropanol for film thickness measurements. Precaution was taken to ensure the silver paint had fully dried before being subject to vacuum conditions, which may cause the substrate to delaminate, by slowly heating the substrate to 80°C at 5 °C/min and holding at that temperature for 5 min. During the deposition process, the deposition chamber was first pumped down to a vacuum of 0.03 mTorr before being backfilled with and O_2 for burn-off. The chamber was then pumped back down to 0.03 mTorr and backfilled once more with the desired oxygen partial pressure. The substrate was heated to the desired temperature at a rate of 30 °C/min and cooled to 200°C temperature at a rate of 10 °C/min. Deposition was performed using a laser pulse rate of 10 Hz, and a laser fluence of $\sim$80 mJ and $\sim$520 mJ for the $Ce_{0.9}Gd_{0.1}O_2$, and $PrCoO_3$ and Pr_2NiO_4 films, respectively. Prior to each deposition, a pre-ablation run was performed

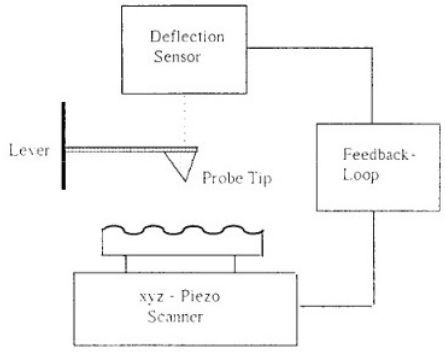


Figure 5.3: Basic principle of AFM, where a probe is mounted on a cantilever and cantilever deflections, arising atomic forces between the probe tip and sample surface, are monitored, from [42].

to clean the surface of the target. During deposition, the target was rotated at 50 °/s.

5.3 Atomic Force Microscopy

Atomic force microscopy, AFM (a type of scanning probe microscopy) is a surface profiling technique [42]. A typical configuration is illustrated in Fig 5.3. The probe is a cantilever, on the end of which is a sharp tip. As it is brought to the sample surface (it may be run in contact mode or non-contact mode), atomic forces cause a deflection in the cantilever, which is measured. The probe is rastered across the sample surface to obtain a map. Thus, the lateral resolution of these maps depends on how sharp the ARM tip is, and can be reduced by prolonged use of the same AFM tip. However, the vertical resolution, depending on the detection method, is much higher and can be up to 0.1 nm. In addition to topographical information, factors that affect this atomic force interaction, such as hardness, may also be measured. Depending on the tip used, other interactions besides atomic forces may be measured.

For the extent of this work, a Bruker DiInnova was used obtain all AFM images, and WsXM to handle the data and calculate all roughness values [271]. Tapping mode was used in all instances. This involves oscillating the probe tip using a piezoelectric element as it rasters across the surface in order to minimise damage to the sample surface. 512 samples were obtained per line at a scan rate of 1 Hz. Sample surfaces analysed were either 10 μm by 10 μm, or 2 μm by 2 μm.

Additionally, a Veeco Dektak150 Surface Profilometer was used to measure thin film thicknesses. Prior to thin film deposition, an area of the substrate would be masked off using a titanium dioxide suspension in isopropanol. The film edge was then profiled at 5 locations per sample. 300 μm scans were performed over 20 s. Using the Dektak software, the profile would first be corrected for any sample tilt, then the thickness of the film calculated from an average surface height from a selected region, which was most representative,

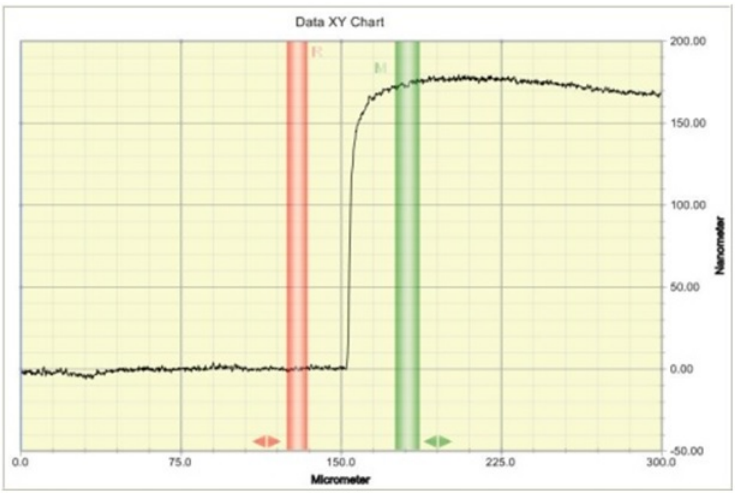


Figure 5.4: Line profile across the masked edge of a PCO113 film (deposited using 5000 pulses).

between the substrate and the film. An example of this process can be seen in Fig 5.4. The vertical resolution according to the equipment specification is up to 1 nm. However, a large amount of noise was present in the profiles obtained for the thinner samples. For such samples, if they are sufficiently thin, X-ray reflectivity was used to obtain thickness values instead

5.4 Thermal Analysis

Thermal analysis involves the measurement of physical or chemical properties of a material as a function of increasing temperature under a constant heating rate, or as a function of time under isothermal conditions. Two different forms of thermal analysis were employed in this work: thermogravimetric analysis, TGA, and differential scanning calorimetry, DSC.

TGA involves the quantitative measurement of mass loss or gain within a heating regime. Thus, it allows for the investigation of any physical or chemical phenomena with an associated weight change. It is typically used to study the thermal stability or degradation of a material, solid-gas reaction (oxidation or reduction), or its organic or inorganic content. The thermogravimetric curve may also be used to identify materials that undergo a characteristic sequence of physiochemical changes which are reflected in their mass change.

DSC involves the quantitative measurement of the difference in heat required to maintain a constant increase in temperature of a sample. Thus the enthalpy associated to any physiochemical processes that occurs during the analysis may be measured. The experimental setup requires the use of a sample and reference against which the rate of heat flow of the sample is compared. For example, in the endothermic phase transition from solid to liquid, a greater heat flow to the sample is required to increase its temperature at the

same rate as the reference.

Besides temperature control and measurement, TGA and DSC require the precise measurement of mass change (scales) and heat flow (calorimetry) respectively. Both measurements may be performed using two different modes: a constant heating rate wherein changes in mass and heat flow are measured, or for the heating to produce a constant mass change or heat flow with time. Typically a prescribed inert (nitrogen) or oxidative (oxygen) gas environment is employed according to the form of physiochemical processes investigated (thermal, oxidative, or both).

TGA and DSC results in this work have been obtained simultaneously using the Netzsch STA 449C thermo-microbalance. This was of a vertical design, with samples top-loaded, and the ultra-microbalance isolated during loading for its maintenance and protection. Temperature measurements are taken directly at the sample crucible.

5.5 Scanning Electron Microscopy and Energy Dispersive X-ray Spectroscopy

The maximum resolution, d of any wave is diffraction limited and described by the Rayleigh criterion: $\delta = \frac{0.61}{sin\beta}$ where d is the smallest distance between two objects that may be individually resolved, n is the refractive index of the lens, and β is the semi-angle subtended by the aperture. As such, it can be reduced by decreasing the wavelength of the imaging medium, such as through the use of an electron beam instead of light and achieving resolutions as low as 10 nm. Scanning electron microscopy is a technique in which a focused electron beam is rastered across the surface of a sample. Typically, it comprises of an electron source from which electrons are produced by thermionic heating of field emission guns and condensed into a narrow beam by lenses into the sample chamber. This focused electron beam is directed by scanning coils across the sample stage where various detectors are located. The interaction between the electron beam and sample results in the emission of several primary signals, including backscattered electrons, BSE, secondary electrons, SE, and X-rays, that are detected.

BSE or Rutherford scattering results from elastic couloumbic interaction between electrons and the nucleus. Consequently these electrons have a high energy, experience large angles of deflection and their yield depends on the atomic number of the scattering atom. An element of a high atomic number would result in a greater yield of BSE; the BSE signal is sensitive to composition. BSE may also interact with the sample and, being of a sufficiently high energy, may produce SE electrons. Secondary electrons arise from the inelastic interaction between the high energy bombarding electrons and the valence electrons of the sample. The sample is ionized as loosely bound valence electrons are emitted. Due to their low energy, only SE emitted close to the sample surface are able to escape and thus the SE signal is extremely sensitive to sample topography [272, 273].

Lastly, X-rays are emitted when an incident electron ionizes an inner orbital electron. Electrons from an outer shell move to replace it, resulting in a cascade effect as electrons decay to a lower energy state and results in the emission of X-rays with a characteristic family of energies. These may be used to obtain compositional information of the sample if their frequency and energy were measured using an energy-dispersive spectrometer. This technique is called energy dispersive X-ray spectroscopy, EDX. However, there is also a background emission of X-rays, Brahmstrallung radiation, from the inelastic collisions in the sample that will also be detected.

Two SEMs were employed in this work to obtain SE images of bulk and thin film sample surfaces: JSM6400 SEM (JEOL Ltd., Tokyo, Japan) and Leo Gemini 1525 FEG-SEM (Carl Zeiss, Oberkochen, Germany), respectively. The JSM 6400 was fitted with an Oxford Instruments INCA energy dispersive analytical system and also used for EDX measurements. This software was used for the quantitative analysis of the EDX data [274]. An accelerating voltage of 20 kV was applied, the working distance was ∼17 mm, the process time was 5 (for high resolution in the EDX spectrum) and the condenser lens current was 9-10 A. All EDX point measurements and maps had a livetime of ∼50 s and ∼500 s, respectively. A Co reference spectrum was obtained prior to each session for accurate quantification of the sample composition. All images obtained using the Leo Gemini was at a lower accelerating voltage of 5 kV, and a working distance between 6-7 cm.

5.6 X-ray Photoelectron Spectroscopy

Much like the EDX, XPS is a chemical analysis technique that involves the excitation of electrons. However, rather than an electron beam, a focused X-ray is used instead. If the energy of the X-ray exceeds the binding energy of the electron, the electron is emitted with a kinetic energy that is the difference between the incident energy from the X-ray and the electron's binding energy, BE. Depending on the location of the emission even within the sample, the freed electron may be reabsorbed by the sample, or may escape the sample surface where it can be detected and its kinetic energy determined. Thus this photoemission process may be considered in three steps: photo absorption and ionisation, the response of the element and the emission of a photoelectron, and lastly the transport of the electron to the surface. The first two are intrinsic steps from which characterisation can be made, while the last is an extrinsic step contributing to the background energy of scattered electrons.

As a monochromatic X-ray source is used of a known energy, it is possible to calculate a spectrum of the binding energies of the electrons detected- the XPS spectrum. The binding energy is characteristic of the element and the electron orbital. Subsequently, the XPS spectra comprises of characteristic peaks that provide information on all of those three aspects and are labeled according to the subshell from which emission occurred. Furthermore, the intensities of the peaks are related to the concentration of the elements present and thus quantitative analysis of the sample composition is possible.

For the outer orbitals, such as the p, d and f core levels, the photoemission is actually split between two peaks. This is due to spin-orbit coupling. The removal of an electron from these outer orbitals (L) result in an unpaired spin(S). The resultant spin of the electron interacts with its orbital angular momenta differently depending whether it is spin parallel or antiparallel relative to its motion. Thus there is a coupling between the two that results in two possible different energies- a multiplicity- hence a split in the binding energy forming a doublet. The area ratio of these two peaks, which reflects this degeneracy, is fixed. A subscript is used, following the subshell notation, to label the two states, according to the L-S coupling. Both the BE peak positions and spin orbital splitting, and their area ratios, are used for the identification of an element.

Lastly, the BE of the electrons also depends on the oxidation state of the ion, and the chemical and physical environment of the measurement. These cause a shift in the BE spectrum called chemical shifts. In order to correct for environmental contributions to chemical shift, the spectra is always aligned against a reference peak such as the C 1s signal.

A clear advantage of the XPS technique is that it is possible to differentiate between the oxidation states of the constituent elements. However, it does require additional precautions in maintaining the conditions of the measurement. Comparison between spectra should be done with caution. Similarly, quantification of XPS measurements are typically only as accurate as $\pm 10\%$ due to the difficulty in separating intrinsic photoelectrons from the extrinsic photoelectrons (the background). This can be improved through the use of standards measured by the same instrument under the same conditions.

XPS is a surface technique, which sampling depth is limited to the ability of emitted electrons to escape the sample surface. According to the Beer-Lambert law describing the attenuation of the emitted electron intensity ($I_s = I_o exp(-d/\lambda)$), 95% of all the photoelectrons would be scattered if created more than 3λ from the surface. Within this region is the sampling depth. For XPS using Al K_α radiation, λ is in the range of 1-3.5 nm, making the sampling depth 3-10 nm. Thus, the signal of surface contaminants will be amplified.

All XPS measurements were performed by Dr I.Villar-Garcia. The XP spectra were recorded using a K-alpha+ XPS spectrometer equipped with a MXR3 Al K_α monochromated X-ray source ($h\upsilon$ = 1486.6 eV). X-ray gun power was set to 72 W (6 mA and 12 kV). At this setting, the intensity of the Ag $3d_{5/2}$ photoemission peak for an atomically clean Ag sample, recorded at 20 eV pass energy (PE), was 5 × 106 counts s^{-1} and the full width at half maximum was 0.58 eV. Binding energy calibration was made using Au $4f_{7/2}$ (84.01 eV), Ag $3d_{5/2}$ (368.20 eV) and Cu $2p_{3/2}$ (932.55 eV). Charge compensation was achieved using the FG03 flood gun using a combination of low energy electrons and the ion flood source. All spectra were acquired using 20 eV pass energy, 0.1 eV step size and 1 second (50 ms × 20 scans = 1000 ms) dwell times. Pellets of the samples were pressed down onto the sample holder using metal pins and analysed at an electron take-off angle normal to the surface with respect to the analyser. Pressure during the measurement of

XP spectra was $\leq 1 \times 10^{-8}$ mbar. Thermo Avantage software was used for data interpretation. Shirley or two point linear background subtractions were employed depending on background shape. Thermo scientific sensitivity factors were used for quantification analysis. All XP spectra were charge corrected by referencing the fitted contribution of C-C graphitic like carbon in the C 1s signal to 285 eV.

5.7 X-ray Diffraction

X-ray diffraction, XRD, is a non-destructive technique for the structural characterization of crystalline materials. The underlying principle for this technique is described by Bragg's law and as such it utilizes the diffraction of X-rays, whose wavelength is in the same order of magnitude as the atomic spacing between crystal lattices, in order to probe the periodicity of the lattice. A diffraction pattern is obtained from which the atomic positions of a unit cell may be calculated and its crystallography characterized. Additionally the pattern serves as a fingerprint of the crystalline material. It is thus possible to identify the sample by referencing it against the International Centre for diffraction Data, ICDD, database through the Xpert HighScore interface [275].

Braggs' law describes the condition for Bragg diffraction peaks to be observed:

$$n\lambda = 2dsin\theta \tag{5.1}$$

Where n is the order of the reflection, λ is the wavelength of the incident X-ray, d is the lattice spacing and θ is the angle of incidence. Additionally, the plane normal [hkl] must be parallel to the diffraction vector **s**, which bisects the angle between the incident and diffracted beam, see Fig 5.5. Thus, incident X-ray beams are diffracted by the atomic planes. However, when integer values of the wavelength of the incident X-ray are the same as the difference in X-ray path length between two atomic planes, $dsin\theta$, and interfere constructively causing a spike in the intensity of the diffracted X-rays. This is often referred to as an XRD or Bragg peak or reflection [276]. From the separation between the planes, it is possible to identify the diffraction planes contributing to a Bragg reflection, and subsequently the orientation of the cell structure, if the crystallographic space group of the material is known.

5.7.1 Powder X-ray Diffraction

For material identification purposes, XRD samples are typically prepared as finely ground powders. These are loaded onto the sample holder such that it forms a flat homogeneous surface at a prescribed height. The grinding of the sample removes texture from the XRD pattern wherein an orientation contributes disproportionately to the intensities detected, such as if a large crystal were present. Similarly a variation in sample height would affect

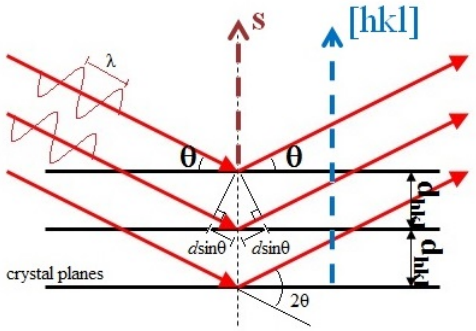
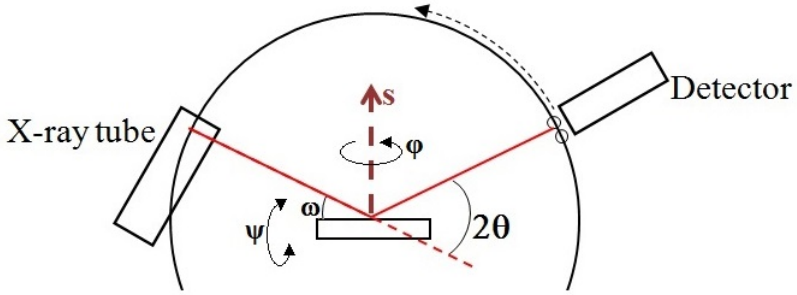


Figure 5.5: Illustrating the requirements for a Bragg reflection, when the extra distance, $dsin\theta$ is equal to $n\lambda$ and **s** is parallel to [hkl], adapted from [43].



(a) Schematic of the various XRD scan parameters, adapted from [43].

Scan Type	Scan Parameters
Gonio Scan	2θ - ω scan
Rocking Curve	ω scan
Pole Figure	360° ϕ scan over a ψ range
Reciprocal Space Map, RSM	2θ - ω scan over an ω range

(b) Typical XRD scan parameters for texture analysis of thin films.

Figure 5.6: XRD setup and scan parameters.

the path length of the incident and diffracted X-ray and should result in a shift in the 2θ values, while surface contours would affect the angle of incidence. The diffraction pattern is obtained by performing a gonio scan (or a coupled scan): where the diffraction intensities across a diffracted angle (2θ) range is detected but for which incident angle (ω) varies according to $\frac{1}{2} * 2\theta$ + offset, as in Fig 5.6a.

Powder XRD has been used extensively in this work in order to ascertain the phases present and cell parameters of synthesized powders of varying composition. Room temperature measurements were performed using a PANalytical Pro Materials Research Diffractometer, MRD . High temperature measurements were performed using a PANalytical X'pert Multi-Purpose Diffractometer, MPD, equipped with a Buehler high temperature stage.

5.7.2 Structural Refinement of Powder X-ray Diffraction Data

Powder XRD patterns may be refined to obtain structural information of the material. Besides the unit cell tensor parameters (a, b, c and α, β, γ), there are other refineable parameters such as the zero point instrumental error, background intensities, peak width and shape variables U, V, W, X and Y (depending on which peak shape function is employed), and peak asymmetry. These are the variables refined in a Le Bail refinement [277]. The more comprehensive Rietveld refinement would also account for structure factors such as atomic positions, site occupancies and thermal factors of the constituent atoms [278].

For the Le Bail refinement, the unit cell parameters and space group must first be predetermined. Then, refineable parameters are fitted using the least squares method to minimise the difference between calculated and observed profile. A key feature of the Le Bail method is that peak intensities are not a parameter to be fitted using least squares (as they would be in the similar Pawley method). Instead, an arbitrary starting peak intensity is used, and after each least squares fit, a new peak intensity calculated and set as the arbitrary starting peak intensity. Having performed a Le Bail fit, a Rietveld refinement may then be performed. The additional structure factors introduced determine peak intensities. Thus for Rietveld refinements, the peak intensities may be calculated from the structure model.

The Fullprof software [279] was used for all Le Bail and Rietveld refinement in this work. A Pseudo-Voigt peak shape function was employed that had an additional function for axial divergence asymmetry. The quality of the fit was assessed visually and through consideration of the goodness of fit, chi-squared, defined as the fraction of weighted profile residual, R_{wp}, over the expected profile residual, R_{exp}, and the Bragg residual, R_B. The Bragg residual is the only figure of merit that depends almost entirely on structural parameters (as opposed to both structural and profile parameters) and as such is the best indication of the accuracy of the model of crystal structure used in a Rietveld refinement [280]. As the fit improves, chi-squared tends to 1, and the Bragg residual to 0.

5.7.3 Thin Film X-ray Diffraction

An epitaxial film is a single crystal layer which is lattice-matched with the substrate it is grown upon; it shares a similar lattice to the substrate and is able to strain in order for the atomic bonding across the film and substrate to be matched. There is a defined geometric relationship between film and substrate. This relationship may be commensurate, coincident on incommensurate, depending on the extent by which the lattice points of the film coincides with that of the substrate. A textured polycrystalline film consists of multiple grains, but with a preferred orientation that may be correlated to the substrate.

By utilizing a number of different scan parameters, see Fig 5.6a, it is possible to use high

resolution XRD to determine if a thin film is epitaxial and to probe the structure and defects of epitaxial thin films. Structural information that may be obtained using XRD include the composition, thickness and superlattice period, while that of defects include mismatch, relaxation, misorientation, dislocation density, mosaic spread, curvature, inhomogeneity and surface damage [43]. Gonio scans of thin films may be used to study factors affecting the position of Bragg reflections and therefore provide information regarding the presence of lattice mismatch of relaxation, and also the film composition. If thickness fringes are observed in the gonio scans, they may also be used to calculate film thickness.

For all thin film gonio measurements in this work, the sample position relative to the beam was first optimised for diffraction intensity. Following that, using the single crystal substrate refection as a reference, the psi and offset values were also adjusted, if necessary, for the plane normal [hkl] to be parallel to the diffraction vector.

There are a number of other scan parameters available, which have been employed in this work to characterise other structural aspects of thin films. These include rocking curves, pole figures, and reciprocal space maps, RSMs, corresponding to omega scans, phi scans, and gonio scans over a range of omega values in order to produce a map, respectively, see Table 5.6b. Additionally, the thin film may be tilted (an offset) in order to measure diffraction peaks from different orientations, instead of just when the plane normal is perpendicular to the sample surface as in a symmetric scan where $\omega = \frac{1}{2} * 2\theta$. Such a scan, where an offset value is introduced, is called an asymmetric scan.

5.7.4 Rocking Curves

Rocking curves were obtained by first locating the Bragg angle of a specific orientation. While the detector is set at that 2theta angle, the sample is tilted by scanning through a range of omega values. If the crystal lattice planes are perfectly parallel, a very sharp peak will be obtained, see Fig 5.7. However, the presence of mosaicity, dislocation and film curvature would broaden the peak. A means of measuring this peak broadening is its peak full width at half maximum (FWHM). Crystallite size may also be calculated from the FWHM using the Scherrer equation, though care should be taken to calibrate for instrumental contributions to peak broadening first.

5.7.5 Phi Scans and Pole Figures

During a phi scan, the sample is rotated about an axis normal to a sample surface. If the sample is tilted (psi) such that a diffracting plane normal [hkl] is parallel to the diffraction vector, it is possible to obtain a number of reflections in the phi scan according to the symmetry of the diffracting plane. For example, if the detector 2θ position is aligned at the (001) reflection of an epitaxial film with a primitive cubic structure, a tilt of psi = 45° would result in the diffraction of the 110 family of planes as phi is rotated between 0 to 360° producing 4 peaks. By repeating these phi scans over a range of tilts (psi value), a

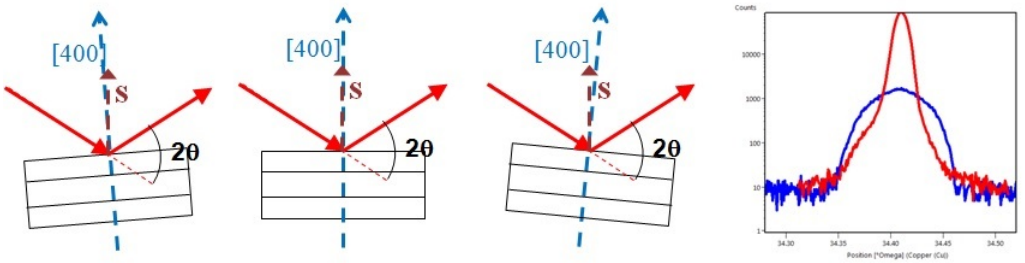


Figure 5.7: Slight tilts of the [400] diffracting planes resulting in a broad peak (blue) with a large FWHM, compared to a sharp peak (red) if the diffraction plane had been completely flat, from [43].

pole figure may be constructed. Rocking curves may also be performed on these peaks to evaluate in-plane mosaicity.

Phi scans and pole figures provide in-plane information of the texture, orientation, and symmetry of the thin film. The absence of a peak would suggest a distortion of the lattice hence the loss in symmetry. It also provides information of the geometric relationship between the thin film and substrate lattice, whether it is commensurate, coincident on incommensurate. A commensurate thin film would share the same peak positions in a phi scan as the substrate. 0 to 360° phi scans and pole figures were not explicitly presented in this work, but performed during the alignment for reciprocal space map measurements, which also provides in-plane information on the relationship between film and substrate lattice orientation.

5.7.6 Reciprocal Space Maps

Reciprocal space comprises of a reciprocal lattice, each point of which is a projection of the reciprocal vector, $\mathbf{d}^*_{hkl}$, where $\mathbf{d}^*_{hkl} = \mathbf{d}_{hkl}$ and $\mathbf{d}_{hkl}$ is the vector from the origin to the normal of the crystallographic plane in the family (hkl). Thus each reciprocal vector represents a set of Bragg planes. The reciprocal lattice may be represented on the Ewald sphere, of radius $\frac{1}{\lambda}$. Therefore lattice points on the surface of the Ewald sphere satisfy the condition for Bragg diffraction. Rocking curves and gonio scans cover an arc centered on the origin, or a straight time from the origin, respectively, of the reciprocal space, see Fig 5.8.

RSMs are an invaluable tool for assessing effects such as strain or compositional variations that would cause a shift in the Bragg diffraction and subsequently reciprocal lattice points as multiple scans may be employed to map that shift. Additionally, the scan range may be extended in order to see reciprocal lattice points of the substrate, providing information of the geometric relationship between film and substrate. In a symmetric scan, $\theta = \omega$. However, as earlier mentioned, a tilt (offset) value may be introduced to perform asymmetric scans. These asymmetric scans are necessary for in-plane structural assessment and may be achieved using either a grazing incidence configuration (as has been employed in this

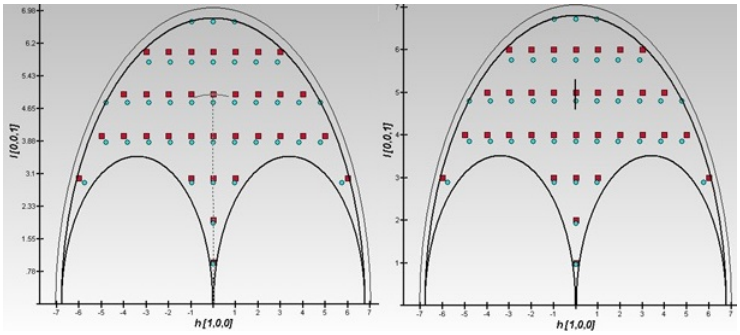


Figure 5.8: Representation of an omega scan (left) and gonio/coupled scan (right) on a Ewalds sphere from [43].

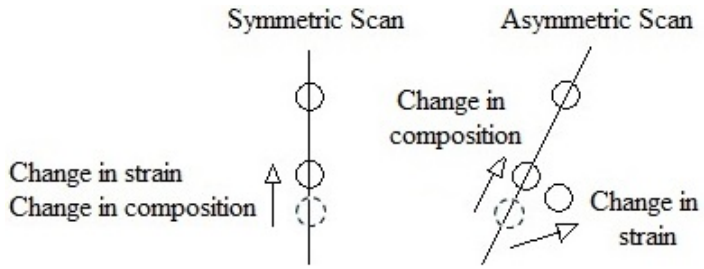


Figure 5.9: An asymmetric scan is necessary to differentiate between a compositional change shifting the Bragg peaks, or if the film is strained, adapted from [43].

work) or a grazing exit, where $\omega = \theta$ - tilt or $\omega = \theta$ + tilt, respectively.

It is necessary to have both symmetric and asymmetric RSM in order to identify if shifts in reciprocal lattice points are due to strain or compositional changes. In a symmetric scan, both would result in a shift along the direction from the reciprocal lattice point to the origin. However, in an asymmetric scan, it can be see that while a compositional change would also result in a shift along the direction from the reciprocal lattice point to the origin, the presence of lattice strain would result in a shift of the reciprocal lattice point off the line between its unstrained position and the origin, see Fig 5.9.

Broadening of the Bragg reflection would result in a spreading of the reciprocal space point, which would be detected in the RSM. The spread of a reciprocal space point (not a shift in its position) may arise from compositional or strain gradients, or the presence of defects. By observing the direction of the reciprocal space point spreading relative to the direction of the reciprocal lattice point to the origin, it is possible to identify the cause of the spreading, see Fig 5.10. Similarly, in the case where defects have caused a broadening of the Bragg reflection, it is possible correlate the extent of the broadening normal and parallel to the reflective plane to mosaic spread or lateral correlation length respectively.

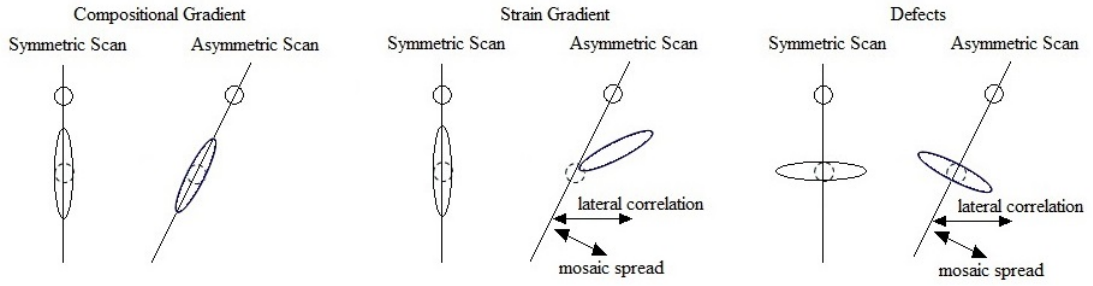


Figure 5.10: The different sources of peak broadening, adapted from [43].

5.8 X-ray Reflectivity

Based on a similar principle to XRD but with reflecting smooth and flat surfaces and interfaces rather than diffracting planes, XRR measurements provide information about thin film layer thicknesses and densities, and the surface or interface roughness of the film(s) [281]. If the X-rays are directed at a sample surface at extremely small grazing angles of incidence, all the X-rays will be reflected by the sample surface. However, as the angle of incidence is increased beyond a critical angle X-rays begin to penetrate the material and there is a large decrease in the detected X-ray intensity. As the angle of incidence increases, the X-rays transmit deeper into the material, and is reflected at the film/substrate interface. These multiple reflected waves have a phase difference between each other and interfere, producing interference fringes which may be related to the film thickness by the modified Bragg equation [282], where D is the thickness of the film layer, n is the integer number of fringes, is the wavelength of the incident X-ray, and a_c and a_i are critical angle and observed angle of the fringes, respectively.

$$2D\sqrt{sin^2(a_i) - sin^2(a_c)} = m\lambda \tag{5.2}$$

Thus the distance between the fringes is inversely proportional to the film thickness. The roughness of the film surface and film-substrate interface affects the reflectivity of the X-rays, causing diffuse scattering. Thus the XRR measurements for a rougher film would have a sharper decay in intensity beyond the critical thickness. The decrease in intensity with incident angle may be used to determine surface roughness. As the critical angle is a function of electron density, changes in the critical angle for the same chemical composition must indicate a change in the sample density. Thus film layer thickness and density, and surface roughness may be determined from XRR measurements. XRR measurements in this work were performed using the PANalytical X'pert Pro MRD. Determination of film thickness values was performed by Dr. A. Cavallaro of Imperial College London.

5.9 Vertical Scanning White Light Interferometry

White light interferometry, or coherence scanning interferometry is a technique based on the superpositioning of (in this case) light waves to create interference fringes from which surface height measurements may be calculated. A vertical scanning white light interferometer setup consists of a white light source from which the light is collimated, sent through an objective lens, then split using a beam splitter to get a reference and test beam. The reference beam is reflected off an internal reference mirror while the test beam is reflected off the sample surface, before the recombined intensity is detected. The interference fringes vary according to the position of the objective lens as the reflection of different sample surface heights cause a variation in phase difference. Thus by varying the position of the objective lens, it is possible to map the topology of a surface. A large number of interference fringes and curvature of the fringes indicate a rough surface and surface curvature respectively.

All crater-depth measurement by white light interferometry was performed by C. Van den Bosch of Imperial College, using the NewView 200 instrument by Zygo Corp. Prior to each measurement, careful positioning of the sample on the z-axis was performed to focus the sample as indicated by fringe contrast (a focused sample would produce a high fringe contrast).

5.10 Electrical Conductivity Measurements

4-point measurements were used for all electrical conductivity measurements. Two electrodes are used to supply the current, while the remaining two measure the voltage loss. Such a setup removes contact resistance contributions to the measurement that would be present if just two terminals were used. For the bar samples, the electrodes were arranged in a linear manner. Though the resistivity measured is directional, the sample is polycrystalline and isotropic. For the sheet conductivity measurements of the textured thin films, the van der Pauw method was used in order to obtain an average conductivity of the sample [283]. Both configurations, for bar and for thin film samples of a square geometry are depicted in Fig 5.11 for measurements of electrical conductivity. The equation for the resistivity of the thin film assumes a flat, homogenous, isotropic sample with point-size contacts along the sample circumference, according to the van der Pauw theorem [283].

However, in practical application, contact placement and a finite contact size result in a deviation from the ideal van der Pauw case condition. Measurement errors arising from contact size or placement can be reduced by employing a square or cloverleaf sample shape, whereas a circular sample shape is associated with larger errors [284]. The effects of contact size and shape (square or triangular) on measurement error have also been investigated in square samples [285]. It was found that a triangular contact at the corners of a square sample provided the best approximation to van der Pauw's infinitesimal contacts.

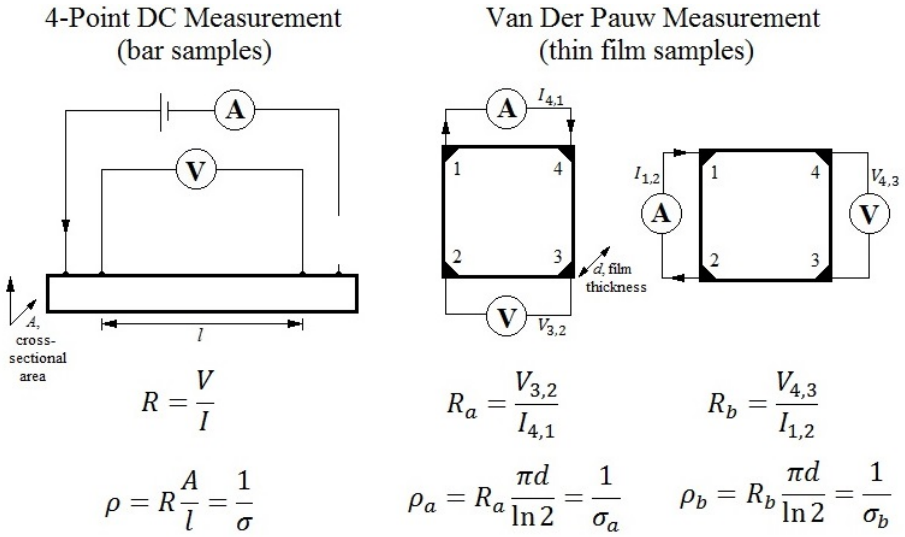


Figure 5.11: Schematic of bar and thin film configurations used for measurements of electrical conductivity.

Decreasing contact size improved the approximation. Nevertheless, though the two short edges of the triangular contact may be as large as $\frac{1}{8}$ of the sample length, the measurement error was a low $\pm 0.25\%$ [285]. Thus, van der Pauw measurements in this work have been performed using square samples and triangular contacts, at the sample corners, which do not exceed $\frac{1}{8}$ of the sample length.

To account for the measurement error associated with the square sample geometry, 4 different measurements may be made for each sample by interchanging the contacts, see Fig 5.11. By symmetry, $\frac{V_{cd}}{I_{ab}}$ should be the same as $\frac{V_{ab}}{I_{cd}}$, and $\frac{V_{cb}}{I_{ad}}$ should be the same as $\frac{V_{ad}}{I_{cb}}$, and as such it is only necessary to measure at the two different configurations where the current directions are perpendicular to each other. From the van der Pauw equation [283]:

$$exp\left(\frac{-\pi d}{\rho}R_a\right) + exp\left(\frac{-\pi d}{\rho}R_b\right) = 1 \tag{5.3}$$

Assuming R_a and R_b values are similar, a correction factor, $f\left(\frac{R_a}{R_b}\right)$, a dimensionless quantity that depends on the $\frac{R_a}{R_b}$ ratio [283, 286, 287] may be introduced. Thus the sample resistivity is given by :

$$\rho = \frac{\pi l}{ln2}\left(\frac{R_a + R_b}{2}\right) f\left(\frac{R_a}{R_b}\right) \tag{5.4}$$

The correction factor, f, has been empirically determined for a range of $\frac{R_a}{R_b}$ ratios, from 1 to 200, where $\frac{R_a}{R_b} = 1$ represents the ideal situation with a perfectly square array, [287]. Depending on $\frac{R_a}{R_b}$ for each sample measurement, the appropriate correction factor was applied.

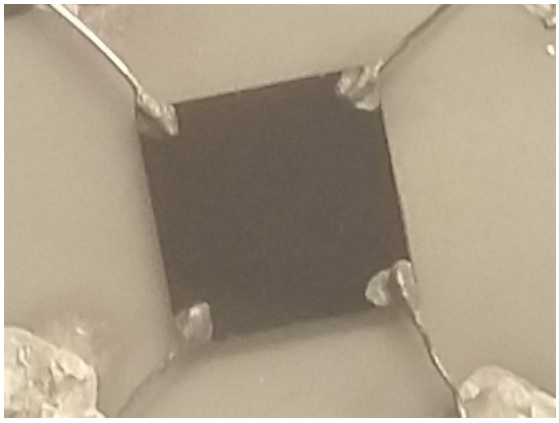


Figure 5.12: Thin film sample with contacts attached with Ag paint.

Electrical contacts with bar samples were made by wrapping an Au wire once around its breadth. Care was taken to ensure a constant distance between contacts along the sample length, and good contact between the wire and the sample. For the van der Pauw measurements, Pt wires were attached to the four corners of the square samples using Au paint, applied in a roughly triangular shape. A good bonding was achieved upon subsequent heating of the sample. A photo of a sample is provided in Fig 5.12. All electrical measurements were performed in static air. The samples were positioned at the centre of a tube furnace, as close as possible to a thermocouple, which would measure near sample temperatures every second. The electrical data were collected using an Agilent 34401A Multimeter at 1 s intervals.

The bar and thin film samples were heated at a rate of 10 °C/min to 700°C. Upon reaching 700°C, the samples were held at that temperature for at least an hour to equilibrate. While equilibrating, trial measurements would be taken to identify an appropriate current, within the Ohmic region, to use. As the operation of the furnace was found to affect measurements, it was turned off and electrical measurements were taken upon cooling from 700°C to room temperature within the furnace.

5.11 Isotope Exchange Depth Profiling

Oxide ion conductivity, as covered in Chapter 5, comprises of a surface exchange event as oxygen is incorporated into the lattice, and bulk diffusion as the oxide ion is transported away. These processes may be described by the surface exchange coefficient, k^*, and self-diffusion coefficient, D, respectively. A technique that enables the measurement of both values is Isotope Exchange Depth Profile, IEDP [116]. There are 3 steps to this technique: the isotope exchange wherein an isotope diffusion profile is introduced into the sample; the depth profiling using secondary ion mass spectrometry, SIMS, wherein the diffusion profile may be mapped; and lastly fitting the profile to obtain k^* and D values.

5.11.1 Tracer Exchange

The ^{18}O isotope was used as the tracer due to its relatively low natural abundance. Prior to exchange, sample preparation included the grinding and polishing of dense pelletized samples in order to create a flat interface at which oxygen exchange may occur (crucial for accurate modeling of the diffusion profile later). This process is the same as described for the preparation of the $Ce_{0.9}Gd_{0.1}O_2$ polycrystaline substrate in Section 6.2. Thin film samples were encapsulated in Au to prevent oxygen exchange through the $Ce_{0.9}Gd_{0.1}O_2$/8mol%-YSZ substrate; exchange could only occur at a section of the film surface that had been masked off before sputtering on the Au. Samples were placed in a quartz holder in the exchange chamber. A thermocouple was located at the base of the holder.

The exchange procedure requires two anneals. The first anneal was performed in pure oxygen: the exchange chamber was pumped down to a vacuum of at least 10^{-7} mbar before research grade oxygen (99.9995%) of a normal isotopic abundance was introduced at a nominal ρO^2 of 1 atm. The sample was then rapidly heated to the temperature of interest and annealed for a duration at least 1 order of magnitude larger than when annealing in ^{18}O. This was to ensure that chemical equilibrium at the anneal temperature and oxygen partial pressure was achieved. This anneal also served to remove any volatile species on the sample surface. Following the anneal, the sample was quenched to room temperature, and the exchange chamber pumped down to a vacuum of at least 10^{-7} mbar, again, prior to the exchange anneal. This time however, oxygen enriched with the ^{18}O tracer was introduced into the exchange chamber at the same nominal ρO^2 of 1 atm. The exchange anneal was then performed and the sample quenched. Following the exchange anneal, a mass spectroscopy of the chamber gases was performed to measure ^{18}O concentrations. The temperature-time profiles, of both anneals, were recorded.

5.11.2 Secondary Ion Mass Spectrometry

Secondary ion mass spectrometry, SIMS, is a technique for the compositional analysis of surfaces. The main advantage of this technique is that it is mass sensitive, and therefore can differentiate between different isotopes of the same element. It requires the use of an ion beam, which is directed at a sample surface. These energetic primary ions collide with surface atoms, transferring energy to them and knocking them off their lattice sites creating a vacancy and a secondary particle. The secondary particle may be a neutral species, or charged, and may an atom, a cluster of atoms or a molecular fragment. The primary ion will continue into the sample lattice, losing energy in a series of collisions as it continues to damage the lattice by knocking deeper lattice atoms off their sites until it has insufficient energy and embeds into the lattice. The secondary particles will also cause a similar damage on the surrounding lattice. This damage inducing process is called ion beam induced mixing, and occurs within the primary ion penetration depth. However, if the secondary particles have sufficient energy to sublime, and are formed within the escape depth at the sample surface, they are ejected from the sample. This sputter yield is the

signal that is detected. The sputtered particles may have a range of energies and charge. A mass spectrometer is used to analyse the composition of the secondary ion yield.

There are two different modes of SIMS operation: dynamic and static SIMS. In dynamic SIMS, a much higher energy primary ion beam is used, producing a larger secondary ion yield. Thus it is often used for bulk analysis of elements and isotopes. Additionally, it allows for accurate concentration depth profiling of the sample as the primary ion beam is able to sputter craters into the sample with monolayer precision. However with a higher primary ion beam energy, the penetration depth and ion beam damage is greater. Depth resolution is determined by primary ion beam mixing. Static SIMS is used for surface atomic monolayer analysis. Ion beam energies are sufficiently low that sputtering does not result in significant removal of the surface monolayer. Additionally a low ion flux ensures that, statistically, secondary ion yield is representative of a fresh original and undamaged surface.

There are four types of mass spectrometry commonly used for their large mass range, sensitivity and resolution: radio frequency, RF; quadrupole; magnetic sector; and time-of-flight, ToF. In the RF uadrupole system, secondary ions are passed between 4 parallels poles, one pair with a constant DC bias while the other pair has an additional oscillating radio frequency. By tuning the radio frequency, ions of the desired $\frac{m}{z}$ ratio retain a stable trajectory and are able to pass through the quadupole, while the other ions spin out. In a magnetic sector spectrometer, the secondary ion beam is directed through a magnetic sector, which deflects the ions. The extent of the deflection depends on ion mass. Thus the ion mass may be determined by calibrating against the angle of deflection. Lastly, in a ToF mass spectrometer, secondary ions are accelerated by an electric field of a known strength. Thus ions of the same charge all acquire the same kinetic energy. As the velocity of the ion is also a function of its mass, heavier ions (of the same charge) would have a lower velocity. ToF mass spectrometry differentiates between ions of different masses by the different lengths of time they take to reach the detector. Further details of the SIMS technique may be found in the work of Vickerman et al. [288].

The objective of the SIMS analysis in this work was to map the ^{18}O tracer diffusion profile into bulk and thin film PCO113 samples. The secondary ion yield may be positive or negative, only one of which may be detected at a time. Oxygen is electronegative and as such has a high negative ionisation yield. Therefore, to optimise yields for the oxygen secondary ions, though at the expense of the electropositive matrix cation yield, it was the negatively charged secondary ion yield that was measured. A summary of the advantages and disadvantages of collect positive or negative secondary ions with respect of ^{18}O tracer diffusion profiling is provided by Kilner et al. [116]. The negative ionisation efficiency for electronegative elements can be improved by using a Cs^+ primary ion beam.

ToF mass spectrometry has the advantage over other mass spectrometry techniques in that it is able to detect the entire spectrum of secondary ions (of the same polarity) in a single measurement. An in depth study has been performed by de Souza et al. on advantages and limitations of ToF SIMS in determining oxygen isotope profiles in oxides [44]. One of the

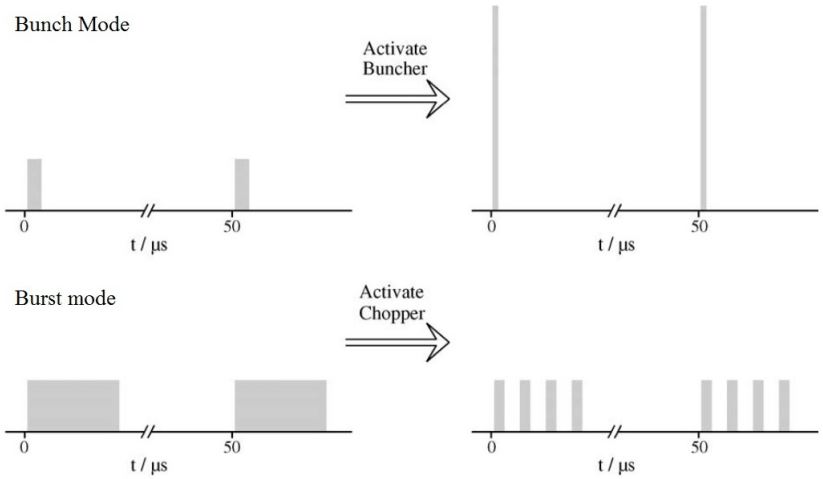


Figure 5.13: Schematic illustrating the two operational modes, from [44].

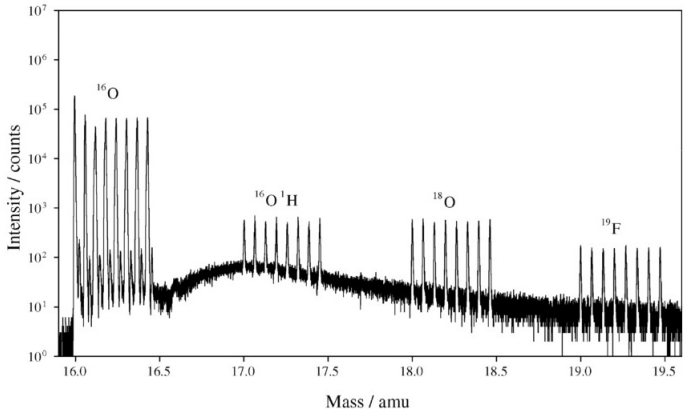


Figure 5.14: A burst-mode mass spectrum of negative secondary ions showing a significant decrease in $^{16}O^-$ counts after the first burst due to the instrument deadtime, from [44].

main difficulties in profiling tracer concentrations is in measuring sufficiently high levels of $^{18}O^-$ without saturating the detector with the $^{16}O^-$ major isotope signal. A solution to this is to operate in 'burst-mode'. The primary ion beam pulses ('bunch mode') are modulated into smaller pulses, which measurement can later be summed. A schematic of the bunch and burst modes are provided in Fig 5.13.

A key observation from experimental results was the large variation in $^{16}O^-$ intensity within the bursts, whereas the intensities of other species remained roughly equal, see Fig 5.14. Even in burst-mode, the detector was saturated from the $^{16}O^-$ signal. The decrease in $^{16}O^-$ signal following the first burst was due to the detectors inability to recover before the onset of the next wave of $^{16}O^-$, and thus was unable to register its full intensity in all subsequent bursts. To obtain the correct $^{16}O^-$ intensity, the intensity peaks must either be corrected using Poisson statistics (non-trivial given the multitude of peaks) and summed, or the intensity of the first Poisson corrected peak to be multiplied by the total number of bursts.

In this work, a TOF-SIMS V instrument (ION-TOF GmbH, Munster, Germany) was used for IEDP measurements, operated in static burst mode. It was equipped with a Bi^+ liquid metal ion gun, LMIG, which served as the primary ion source. This ion beam generated the secondary ion beams analysed. A second ion gun with a Cs^+ thermal ionisation source was also equipped and used to mechanically remove sample surface to allow for depth profiling. Thus the data collection sequence involved an alternation of these two guns to build a depth profile. First the low dose 25 keV Bi^+ primary ion beam would be rastered across the analysis area, ejecting secondary ions that would be mass profiled. Then, the 2keV Cs^+ ion sputter beam would be used to remove the top surface of the sample. Analysis would resume with the Bi^+ ion beam on a fresh, undamaged surface at a greater depth within the sample. The $^{16}O^-$ tracer concentration was summed over each analysis area. An analysis area of 100 μum by 100 μm, and a sputter area of at least 300 μm by 300 μm was used. The large sputter area was to ensure that the analysis area was a sufficient distance from the crater edge that its surface remained flat. Profiling of the craters was performed to verify this. The bombardment of charged particles on an insulating sample may result in surface charging that deflects the primary ion beam. As evidence of surface charging was found on the PCO113 samples in this work, an electron flood gun was used to charge compensate this effect.

5.11.3 Fitting ^{18}O Diffusion Profile

ION-TOF's Surface Lab software (ver. 6.2, Ion-Tof, GmbH, Munster, Germany) included a Poisson correction feature for the burst mode intensities. This was applied to the signal in order to extract accurate $^{16}O^-$ intensities. The $^{18}O^-$ fraction, C^*, was calculated as follows [44]:

$$C^* = \frac{[^{18}O]}{[^{18}O] + [^{16}O]} \tag{5.5}$$

As mentioned in Chapter 2.3.1, it is necessary to normalize the $^{18}O^-$ fraction, C, against the natural abundance of ^{18}O (0.2%), and the abundance of ^{18}O during the exchange anneal. As a mass spectrum of the exchange anneal atmosphere was obtained, it was possible to determine the abundance of ^{18}O during the exchange through consideration of all oxide species. The corrected ^{18}O tracer isotope fraction, C', may then be fitted against Crank's solution for diffusion in a semi-infinite medium [105], see Chapter 2.3.1.

In order to determine sputter rates, crater depth measurements were performed using the Zygo NewView 200 3D optical interferometer and correlated to Cs^+ ion beam sputter time. Exchange anneal times and temperatures were calculated from the measured temperature profile based on the principal of an effective duration of a linear slow-cool as proposed by Killoran [10], which has been validated for use with the IEDP technique [11]. Fitting of the corrected ^{18}O tracer isotope fraction, C', diffusion profile to Cranks solution was

performed via the least squares methods, using the TraceX Software developed by Dr. S. Cooper of Imperial College.

Chapter 6

Synthesis and Characterisation of PLD Targets and Film Substrates

Previously in Chapter 4, the objectives of this thesis were stated. It required the fabrication of $PrCoO_{3-\delta}$, PCO113, and $Pr_2NiO_{4\pm\delta}$, PNO214, thin films, and also $Ce_{0.9}Gd_{0.1}O_{2-\delta}$, CGO, buffer layers. Pulsed laser deposition, PLD was the thin film deposition technique to be employed. In this chapter, the preliminary work in preparing the three PLD targets and characterizing the two different film substrates, Si(004) and 8-mol% yttira stabilized zirconia, YSZ(002), was performed. The Si(004) substrate was to be used for the optimization of the PLD conditions, and the YSZ(002) substrate for the deposition of thin films to be investigated. Prior to its use as a substrate for the PCO113 thin film, a CGO buffer layer had first to be deposited by PLD upon the YSZ(002) substrate. PLD conditions for a CGO buffer layer were also tested in this chapter. Additionally, a polycrystalline CGO substrate was also prepared for the deposition of thick polycrystalline PCO113 and PNO214 thin films.

6.1 Literature Review

PCO113 and PNO214 powders had first to be synthesized before they could be sintered into PLD targets. In the following literature review, synthesis methods employed for similar perovskites were examined from which a range of conditions to be trialled were identified. The deposition of high quality dense and homogeneous thin films requires the use of a dense PLD target, see Section 5.2, which was also a consideration.

CGO was identified to have the lowest lattice mismatch with PCO113. In order to optimize CGO buffer layer quality and microstructure, structural zone models (a concept from the physical deposition of metallic films) of CGO have been used. The deposition conditions of epitaxial CGO films on YSZ(001) reported in literature were also reviewed. Lastly, the preservation of CGO target stoichiometry was considered.

6.1.1 Synthesis of $PrCoO_{3-\delta}$ and $Pr_2NiO_{4\pm\delta}$ PLD Targets

As covered in Section 5.1, the Pechini sol-gel synthesis method offers many advantages and is frequently employed in the synthesis of Pr-based perovskite [289, 6, 290] and R-P materials [291, 292, 293, 294] oxide powders. Where provided, details of these different conditions may be found in Table 6.1. Typically, Pr and Co nitrate precursors were used in conjunction with citric acid. Where an oxide precursor was used, a solution was obtained by dissolving in concentrated HNO_3. Following the preparation of a stoichiometric citrate and nitrate solution, it was agitated and slowly dried into a resin before being decomposed then calcined. On all occasions, powder XRD was used to confirm a single phase product. For this work, the ratios of citric acid and polyethylene glycol used were adopted from work by Zhong et al. [292, 293]. Based on these conditions a range of calcination temperatures, from 600°C to 1300°C have have been tested here.

PCO113 targets for PLD have been sintered by Prakash and Mehta [295, 296, 297]. Prakash used the combustion method to synthesize the powder and the PLD target was obtained by sintering at 1200°C for 12 h. No density measurements were taken of the target, but SEM images of the deposited PCO113 thin films suggested good homogeneity and that it was the substrate used that the film morphology was sensitive to [295, 296]. Mehta used the solid state method to synthesize PCO113 powder, which was cold pressed into a disc (∼16000 psi) and also sintered at 1200°C in air, but for 96 h. Again, no density measurements were made of the PCO113 PLD target, though epitaxial PCO113 films of a high crystallinity (the full width half maxima of the PCO113(002) reflection did not exceed 0.7° even for the thicker films) and lower surface roughness (RMS ∼2.5-5 Å) was successfully deposited on a single crystal (001) oriented $SrTiO_3$ substrate [297].

Preparation of dense PNO214 pellets for the determination of its transport properties has been reported by Boehm et al. [142]. The glycine-nitrate combustion process was used in conjuction with a high temperature calcinations between 950-1077°C, the high temperatures being deemed necessary to obtain a pure and well crystallized compound, to obtain single phase PNO214 powder. To sinter a ceramic with a density exceeding 96% as measured using the sample dimension and the Archimedes method, the powders were first ground at 1200 rpm for 3 h in an ethanol medium, uniaxially pressed (∼100 MPa) into 10 mm diameter discs 3 mm thick, then isotatically pressed (∼180 MPa). The green bodies were sintered at 1200°C for 1 h, with a heating and cooling rate of 5°C/min and 10°C/min respectively. Sintered $Pr_{2-x}Sr_xCoO_{4\pm\delta}$ and PNO214 have also been produced by Zhong et al. and Allancon et al. (sintering conditions of: 1100°C for 10 h and at 1327°C, respectively) [293, 294], however no measurements were taken of the pellet density. In Cu and Gd doped PNO214: $Pr_2Ni_{0.71}Cu_{0.24}Ga_{0.05}O_{4\pm\delta}$, PLD targets were prepared by cold isotatically pressing (300 MPa) and sintering at 1250°C for 6 h. Again, no density values of the target were provided.

Product	Synthesis Conditions	Reference
$PrCoO_{3-\delta}$	Stoichiometric solution dried at 120°C, decomposed at temperatures up to 600°C for 12 h, and treated at 950°C in air for 12 h to obtain a polycrystalline powder.	[289]
$Pr_{(1-x)}Sr_xCoO_{3-\delta}$ (where $0.1 \leq x \leq 0.5$)	Excess citric acid monohydrate at 5-10 times the molar amount of cations used. Stoiciometric solution dried at 180°C overnight and decomposed at 350°C then pressed into pellets and sintered at 900°C in air.	[6]
$Pr_{(1-x)}Sr_xCoO_{3-\delta}$ (where $x > 0.6$)	Nitrate precursors dissolved in dilute nitric acid, citric acid and polyethylene glycol. Dried residues were pelletized and calcined at 1100°C under flowing oxygen for up to 3 days and cooled to room temperature at a rate of 2°C/min, with intermediate re-grinding and re-pelletizing.	[290]
$PrSrCoO_{4+\delta}$	Equal mole ratios of metal precursor and citric acid, and polyglycol 20,000 at 0.03 mol/mol metal cation were mixed, dried, and calcined at 600°C for 4 h. It was then pelletized and calcined at 1100°C for 10 h. The pellet was pulverised to 0.250 - 0.177 mm.	[291]
$Pr_{(2-x)}Sr_xCoO_{4+\delta}$ (where $0.2 \leq x \leq 1.0$)	Stoichiometric ratios of the precursors were dissolved in citric acid and polyglycol 20,000, and dried at 80°C. Dried residues were calcined at 550°C for 4 h, pelletized and calcined again between 750-950°C in air for 10 h.	[292]
$Pr_{(2-x)}Sr_xCoO_{4+\delta}$ (where $0.2 \leq x \leq 1.0$)	As in [292] except the dried residues were calcined at 600°C for 4 h, pelletized and calcined again at 1100°C for 10 h. The sintered pellet was crushed to ∼0.25 - 0.18 mm.	[292]
$Pr_2NiO_{4+\delta}$	Dried residues were decomposed at 700°C and then calcined at 1200°C underair with one intermediate grinding step. Samples were slow cooled in air to room temperature.	[294]

Table 6.1: Sol-gel synthesis conditions of Pr cobaltate and nickleate oxide perovskites and R-Ps, as reported in literature.

Composition	Crystal Structure and Spacegroup	Cell Parameters (Å)	Reference
$PrCoO_{3-\delta}$	Orthorhombic $Pnma$	a = 5.3403(2) b = 7.5744(2) c = 5.3754(2)	[6]
$Pr_2NiO_{4\pm\delta}$	Orthorhombic $Fmmm$	a = 5.45670(9) b = 5.39292(9) c = 12.4464(2)	[299]
$Ce_{0.9}Ge0.1O_{2-\delta}$	Cubic $Fm\bar{3}m$	a = b = c = 5.418	[298]
$(Y_2O_3)_{0.08}(ZrO_2)_{0.92}$	Tetragonal $P4_2/nmc$	a = b = 3.6294(4) c = 5.1433(8)	[300]

Table 6.2: Table of crystal structure and spacegroup.

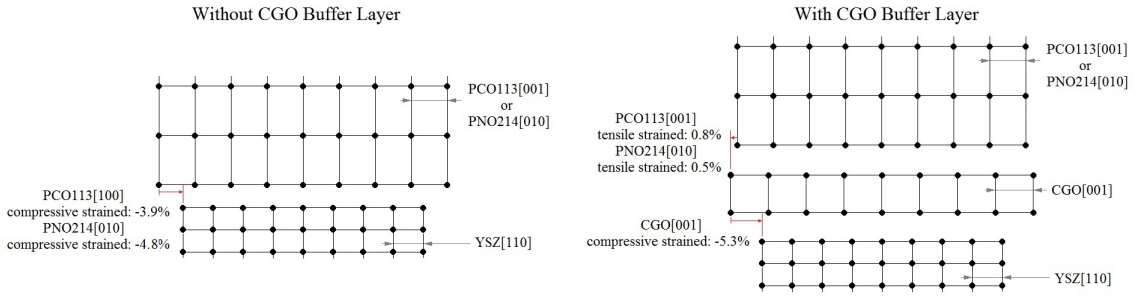


Figure 6.1: Schematic of the minimum lattice mismatch between films and substrate with and without the use of a CGO buffer layer.

6.1.2 PLD of $Ce_{0.9}Gd_{0.1}O_{2-\delta}$ Thin Films on YSZ-8mol%(001)

For this work, the objective of using a CGO buffer layer on the single crystal YSZ substrate is, primarily, to minimize lattice mismatch. This is necessary for the growth of an epitaxial PCO113 or PNO214 film. The smallest lattice mismatch between the PCO113 and CGO system is 0.8%, at the PCO113[001]/CGO[001] edge, based on literature values of cell parameters where the $Pnma$ and $Fm\bar{3}m$ spacegroups have been assigned to PCO113 and CGO respectively [6, 298]. For $Fmmm$ PNO214 [299] on CGO, this is 0.5% at the PNO214[010]/CGO[001] interface. Whereas, if a CGO buffer layer were not employed, and the oxide films deposited directly upon tetragonal $P4_2/nmc$ YSZ [300], the smallest mismatch obtainable is -3.9% at the PCO113[100]/YSZ[110] interface and -4.8% at the PNO214[010]/YSZ[110] interface (given that the YSZ substrate has a (001) out-of-plane orientation). A table of the lattice parameters and an illustration of the different lattice mismatches arising from the introduction of a CGO buffer layer are depicted in Table 6.2 and Fig 6.1. By varying the thickness of the CGO buffer layer the lattice mismatch with the PCO113 film can be controlled, and a range of PCO113 lattice strain obtained. Thus, it was necessary to optimise PLD conditions to grow a dense, epitaxial flat film.

The deposition and microstructure of metallic thin films deposited using a physical vapour deposition process have been extensively studied. Such films typically have a porous colum-

Zone	T_r	Growth Process	Film Morphology
1	$T_r < 0.3$	Shadowing	Porous columnar
2	$0.3 < T_r < 0.5$	Surface diffusion	Dense columnar
3	$T_r > 0.5$	Bulk diffusion	Enhanced crystallization and grain growth

Table 6.3: Table of the three SZM zones as a function of deposition temperature, and the resulting dominant growth process and ensuing film morphology [2].

nar structure due to the nature of the physical deposition process involving the bombardment (or sputtering) of particulates onto the substrate surface. The film microstructure is therefore predominantly determined by the interaction within the bombarding species and also between the bombarding species and the substrate surface, and by the energy of the system (through substrate heating or from the bombarding species) [301]. Thus, early structural zone modes, SZMs, were developed relating the deposited film microstructure to the reduced temperature, T_r , defined as T_s/T_m where T_s is the substrate temperature during deposition and T_m is the melting temperature of the deposited material [302, 303, 304]. Three zones were identified according to their morphology as a result of the process dominating film growth, see Table 6.3

As the energy of the incoming abladed species is also affected by the partial pressure, SZMs have been adapted to account for the effects of deposition pressure. It was found that in Zone 1 (when T_r <0.3), a transition zone was found at low oxygen partial pressures where dense films were deposited having fine fibrous grains without the pores typically associated with this zone in the SZM. Additionally, due to the nature of the PLD process and the formation of nanoclusters at high pressures [305, 306] the nucleation and growth of clusters is enhanced in films deposited at high pressures in Zone 1. A schematic of the resulting microstructure within Zone 1 is depicted in Fig 6.2. Thus deposition temperature primarily determines the crystallization of the deposited species, while deposition pressure determines the film structure [2].

This concept is also applicable to the deposition of crystalline ceramics, and a SZM has been proposed for the CGO system [2], see Fig 6.3. As predicted by SZMs, the morphology of CGO thin films deposited at low partial pressures below 0.05 mbar corresponded to that of the transition zone within zone 1. At higher deposition pressures, crystalline clusters were stable and nucleated on the substrate surface resulting in a loose porous structure with clusters were observed. Increasing deposition temperature increased film density and adhesion to the substrate.

CGO is commonly deposited as a buffer layer between YSZ and lanthanum-based cathodes [30] to prevent chemical reaction between the stabilised zirconia and the cathode, if it contains Co [307, 308], or to reduce interfacial resistances at both anode and cathode [309]. In work investigating oxygen reduction kinetics in the LSC113/LSC214 system, epitaxial CGO buffer layers were also deposited onto a YSZ thin film substrate [27, 29, 227, 310, 311]. These experimental conditions employ substrate temperatures of around 680°C and low oxygen partial pressures of around 10 mTorr to 30 mTorr. Deposition

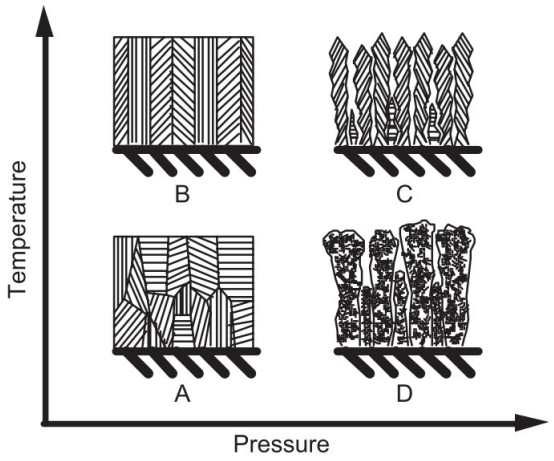


Figure 6.2: The effect of pressure and temperature PLD deposition conditions on the microstructure of the thin film in Zone 1 of the SZM. Regions A and B correspond to the transition zone. At low pressures and temperature (A), the films consist of disordered by coherent grains, which become strongly ordered at higher temperatures (B). At high pressures and low temperatures (D), a loose structure of clusters and pores form, which undergoes dissolution of the clusters into columnar grains at higher temperatures (though the pores persist)[2].

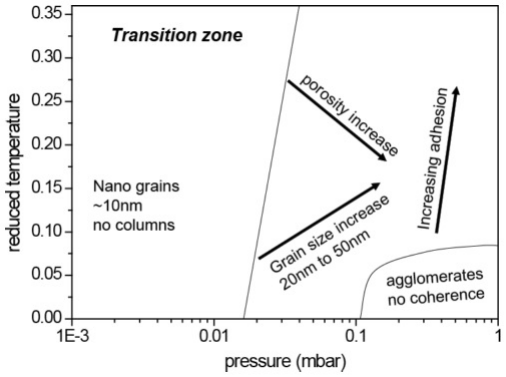


Figure 6.3: Microstructural pressure-temperature map for CGO thin film deposition by PLD, where the reduced temperature was calculated from a melting temperature of 2500°C [2].

of CGO on other substrates such as Pt, sapphire, $NdGaO_3$ and $LaAlO_3$, have also been carried out successfully, over a much larger substrate temperature range between 500°C and 850°C [60, 312, 313].

Therefore, for the PLD of CGO on YSZ, two different substrate temperatures were employed: 680°C ($T_r = 0.272$) and 780°C ($T_r = 0.312$), corresponding to literature values for the successful deposition of PCO113 and doped PNO214 [295, 296, 297, 314, 315], both temperatures having been used for the successful deposition of CGO. Similarly, following on for reported deposition conditions, oxygen partial pressures of 10 mTorr (0.013 mbar) and 30 mTorr (0.040 mbar)were trialled [27, 29, 227, 310, 311]. Based on the SZM by Infortuna et al. [2], these conditions do not lie within the transition zone of CGO, which produces the ideal film morphology. A cluster morphology is expected instead, see Fig 6.3, especially for the deposition at an oxygen partial pressure of 30 mTorr. Due to instrumental limitations, it was not possible to deposit a CGO film at the low oxygen partial pressures of the transition zone. Nevertheless, a dense CGO film with good adhesion to the YSZ substrate was expected. For finer control of film thickness, a low laser pulse energy was used.

6.1.3 $Ce_{0.9}Gd_{0.1}O_{2-\delta}$ Target Stoichiometry During PLD Ablation

One of the greatest advantages of PLD as a fabrication technique is that it is possible to have stoichiometric transfer between target and deposited film. But, this does depend on deposition conditions [316]. Ideally, the laser would ablate many layers off the target material, resulting in an overall stoichiometric removal of material. However, if the target components have a low cohesive energy, too low a laser fluence would lead to preferential evaporation of the most volatile component of the target [317, 318]. The laser fluence also needs to be uniform across the entire beam spot, or a mixture of ablation and evaporation of the target will occur resulting in target segregation. Thus, PCO113 and PNO214 targets, with their volatile Cu and Ni components, may be susceptible. It is worth examining the effects of the laser ablation on the target.

Work on the PLD of CGO on Si(100) has indicated that target stoichiometry is not maintained in the deposited film, which can be Gd rich by up to a factor of 2 [319]. It should be noted that a relatively low laser fluence of 90 mJ was used, which may have contributed to the Gd enrichment. This low fluence is required for this work in order to have fine control of the CGO film thickness and cannot be compromised. However, even if the film stoichiometry changes to $Ce_{0.8}Gd_{0.2}O_{2-\delta}$ (cubic $Fm\bar{3}m$, a = b = c = 5.42573(1) Å[156], the lattice mismatch should still only be 0.9% at the PCO113[001]/CGO[001] edge, and 0.6% at the PNO214[010]/CGO[001] interface. Additionally, if deposition conditions were consistent through all the samples, this Gd enrichment and its effect on the CGO lattice parameters should be constant between samples, thus allowing for comparisons within the CGO films produced in this work.

6.2 Experimental Method

Prior to the synthesis of PCO113 and PNO214 samples, the water of hydration content of $Pr(NO_3)_3.xH_2O$, $Co(NO_3)_2.xH_2O$ and $Ni(NO_3)_2.xH_2O$ were calculated. The hydrous nitrates were weighed, decomposed and re-weighed. XRD patterns were taken of the resulting oxides to identify their composition. Given the molar content of the metal cation, the water of hydration was calculated. This was performed prior to each batch synthesis of PCO113 and PNO214 and a range of hydrations calculated, varying with precursor age and exposure.

For the sol-gel synthesis of PCO113, $Pr(NO_3)_3.xH_2O$, $Co(NO_3)_2.xH_2O$ and citric acid (3 times moles of metal cations) were dissolved, at stoichiometric proportions, in distilled water at a concentration of 0.75 mol metal cation/l. Polyethylene glycol was added to the solution at a concentration of 0.03 mol/mol metal cation. The solution was heated at 120°C on a hot plate and agitated with a magnetic stirrer until a gel formed. The gel was treated in a decomposition oven in air for 3 hours at 300°C and 600°C. This removed most of the organic materials. After each treatment, the obtained precursors were ground with a mortar and pestle. A final calcination was performed between 600°C and 1000°C, for 12 h in air. The same procedure was followed for the synthesis of PNO214, except that $Ni(NO_3)_2.xH_2O$ was used instead of $Co(NO_3)_2.6H_2O$ and the final calcination was performed between 900°C and 1300°C.On all occasions, the heating and cooling rates of the furnace were set to 5 °C/min.

If the samples were to be pelletized, such as for PLD targets, it would be uniaxially pressed into a 30 mm diameter green body prior to the final calcination. The green bodies were then cold isotatically pressed (300 MPa) for 30 s. The remaining organics acted as binders within the green body. The green bodies were then cold isotatically pressed (300 MPa) for 30 s (without the isostatic pressing, the targets would warp and crack during the heat treatment), then the final calcination performed. Thus the final calcination step served also to also sinter that pellets.

CGO9010 powder was supplied by Praxair Surface Technologies. CGO9010 powder specifications include a particle size distribution where $d_{50} < 1$ μm, and $d_{95} < 15$ μm, with an average surface area of 6.4 m^2/g, The YSZ(004) substrates were supplied from MaTeck Gmbh respectively with an orientation accuracy of < 0.5 ° and one epi-polished side upon which deposition was performed.

To make the CGO polycrystalline substrates, CGO green bodies were also formed by uniaxially pressing pellets then isostatically pressing (300 MPa) for 30 s, and sintered for 5 h at 1300°C. A 10 mm diameter die was used to press the substrates and a 30 mm diameter die was used to press the target. Densities of the CGO pellets exceeded 96%, as measured using the Archimedes density method. The substrate surfacess were ground then polished through a sequence of water based diamond suspensions (supplied by Kemet), starting from a grit size of 6 μm, then 3 μm , 1 μm, and lastly 0.25 μm. The CGO target was ground up to a grit size of 1200 (12-18 μm).

PLD deposition of CGO on YSZ was performed using the experimental setup as described in Section 5.2. Two different substrate temperatures, 680°C and 780°C, and two different oxygen partial pressures, 10 mTorr and 30 mTorr were used. It was not possible to maintain a constant chamber pressure of 10 mTorr oxygen partial pressure with the experimental setup: chamber pressure fluctuated between 5 mTorr and 14 mTorr. 1000 pulses were fired for each film, with a laser pulse energy of ∼76 mJ.

6.3 Results and Discussion

6.3.1 $PrCoO_{3-\delta}$ Target

XRD measurements were performed on the PCO113 powder before and after the final calcination, see Fig 6.4. The patterns have been normalized against the integrated peak intensity of the PCO113(121) reflection (with the *Pnma* space group assignment [6]) at ∼33.5° 2θ . Following the second decomposition at 600°C, it can be seen though some PCO113 was present, it was not single phase and multiple unmatched reflections were observed. These reflections decreased upon re-grinding and calcination at 600°C for another 12 h but a single phase PCO113 product was still not achieved. Higher calcinations temperatures of at least 700°C for 12 h were required to obtain a single crystalline PCO113 phase. The diffraction patterns from calcinations temperatures between 700-1000°C were mostly identical, with no apparently changes in PCO113 crystallinity or crystallite size as reflected in the similar full width half maxima of the diffraction patterns.

Based on this result, a stoichiometric PCO113 target was sintered at 900°C for 12 h. The XRD pattern of the PCO113 target, see Fig 6.5, is identical to that synthesized under identical conditions in Fig 6.4 as a powder. There were no preferred orientations within the polycrystalline target. The density of the target was measured using the Archimedes density method and found to be >98% dense. To obtain unit cell parameters, a Le Bail refinement of the target was performed using the *Pnma* space group. Cell parameters were found to be: a = 5.341(1) Å, b = 7.576(2) Å, c = 5.376(1) Å.

A point of discussion is the simulated (011) reflection at 20.2° 2θ, which intensity was not measured in the XRD (nor was it present in the reference pattern by Brinks et al.). Two other space groups, *Pmmm* and *Pbnm*, were used in the Le Bail refinement and both also predicted this missing peak at 20.2° 2θ. The pattern was checked for other mismatches. However, due to the high background noise, it was uncertain if the identified peaks around 39.4° 2θ, 44.7° 2θ and 52.6° 2θ were actually peaks or just background noise. The only suggestion for the extra simulated (011) reflections is that there may be a slightly higher background intensity at that angle, so the Le Bail refinement assumed the presence of a peak. A proper Rietveld refinement would take into account the peak intensities, but would require higher quality data and is potential further work. Nevertheless, the interest of this exercise was to obtain cell parameters of the PCO113 target to calculate the lattice mismatch between the deposited films and the CGO buffer layer, which has been achieved.

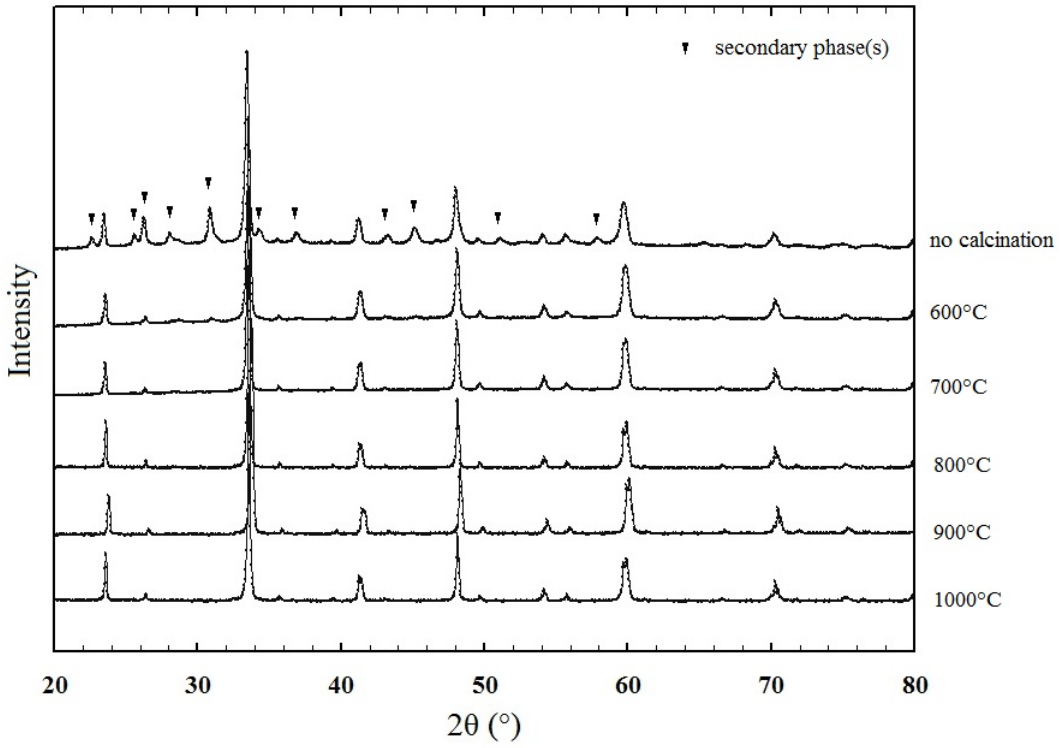


Figure 6.4: Powder XRD pattern of PCO113 precursors following decomposition at 300°C and 600°C for 6 h in air, and following an additional calcination for 6 h at 600°C, 700°C, 800°C, 900°C, 1000°C. Reflections corresponding to unidentified secondary phase(s) when the PCO113 precursor is not calcined/calcined at 700°C have been marked.

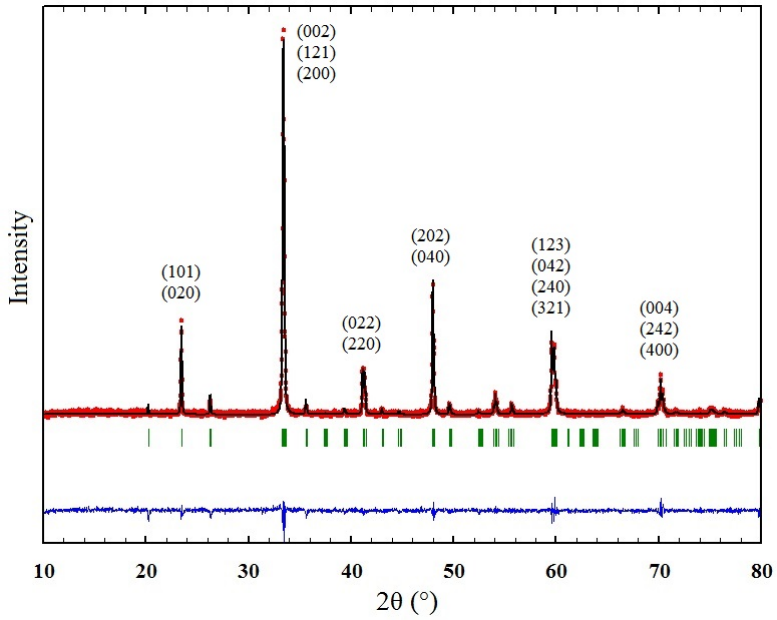
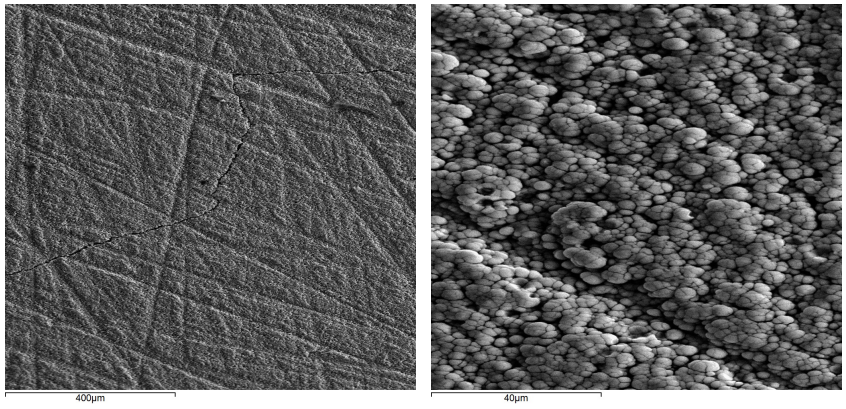


Figure 6.5: Powder XRD pattern of PCO113 target, upon which a Le Bail refinement had been performed. Peak reflections have been indicated in green, diffraction data in red, modeled pattern in red, and the difference between measured and modeled pattern in blue. Main reflections have been labeled.



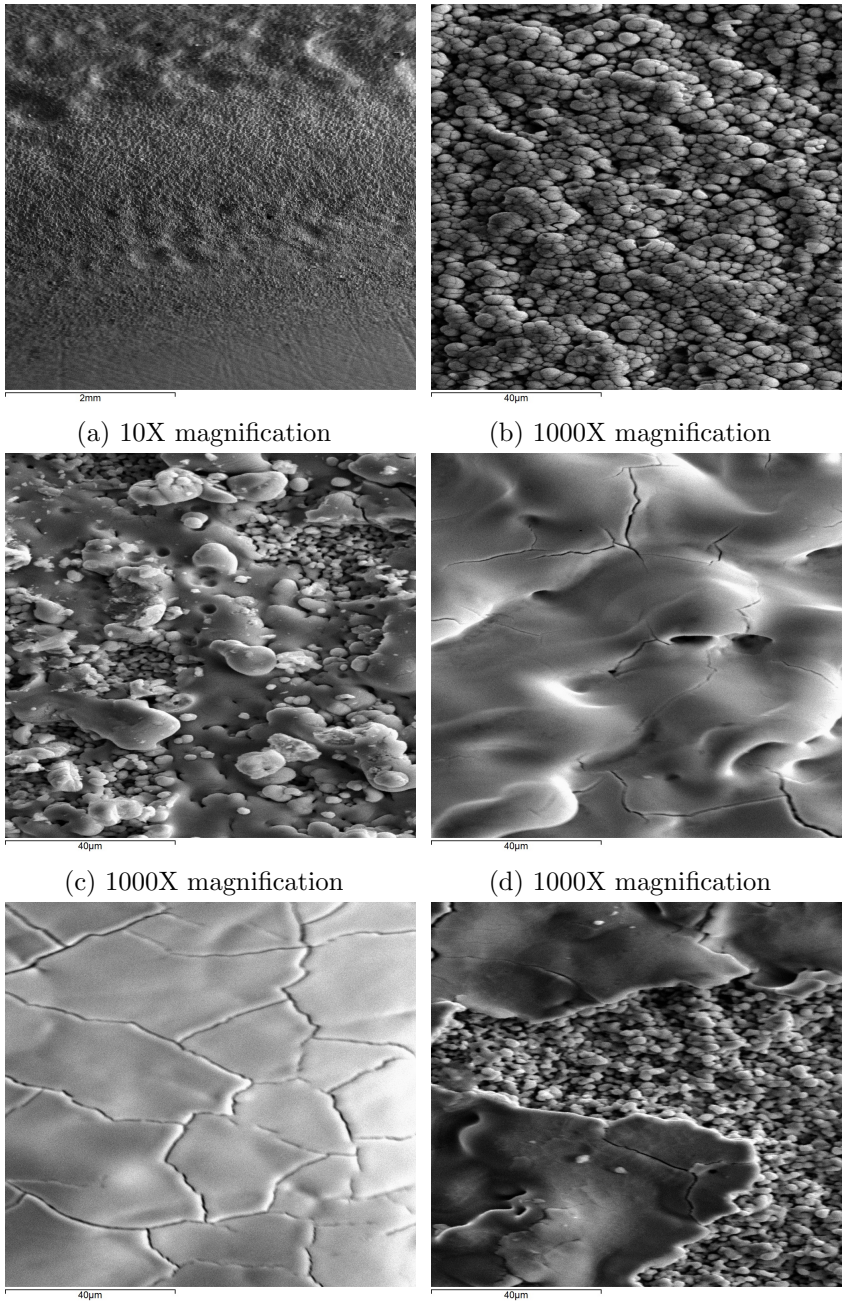
(a) 100X magnification (b) 1000X magnification

Figure 6.6: SE images of the PCO113 target surface after grinding with 400 grit paper showing still-distinct particles following sintering.

Secondary electron, SE, images were taken of the PCO113 target using the JEOL JSM6400, see Fig 6.6. The target was ground with 400 grit paper, which traces can be seen on the target surface. These images suggest that little sintering had occurred with the individual particulates clearly visible, and that the density of the target was lower than the value obtained through the Archimedes density measurement.The Archimedes density measurement may have calculated if the pores were interconnected. However, cross-sectional SE images would be required to confirm if this was the case. Nevertheless, there was confidence that the Archimedes density measurement was the better representation of the sample as it was physical measurement of the entire sample, while the SE image was only of a small section of the sample surface and may not have been representative.

Nevertheless, some trial depositions were performed using the porous target. SE images were taken of the PCO113 target. Any thermomechanical effects arising from the deposition conditions have not resulted in cracking of the target. The region where the laser does not impact appears unchanged. However, in the regions where the laser does impact, there are distinct morphologies that result from the laser ablation, depending on the radial position relative to the laser, see Fig 6.7.

As mentioned in Section 5.2, the target is rotated during the deposition, so the laser sputters off a ringed band. At the centre of the band is the area of most damage, where most of the target material is ablated off. The perimeters of the band corresponds to the edge of the laser. Images were taken moving out radially from the undamaged core of the target, across the band of damage. In the area of most damage, the target surface is completely densified and flat, with cracks running across it. Away from this area, the surface remains dense, however the surface is no longer flat but contoured. The smooth surfaces in these two regions suggest the target may have melted by the laser plume, resulted in the fluid morphology observed. Moving further away from the centre of damage, large pieces of the densified surface have spalled off, exposing the undamaged porous target beneath. In the last region, smaller pieces of the surface have broken off



(a) 10X magnification (b) 1000X magnification

(c) 1000X magnification (d) 1000X magnification

(e) 1000X magnification (f) 1000X magnification

Figure 6.7: SE images of the damaged PCO113 target surface post-PLD deposition. (a) is a section of the ring of damage (scale bar = 2 mm); (b)-(f) depict the different target morphologies taken radially across the ring of damage (scale bar = 40 μm), where (b) is the undamaged center of PCO113 target.

and the area is covered in loose debris.

The laser ablation process is known to cause pitting of the target surface, which is detrimental for the growth of particulate free films. However, the opposite appears to be true in this situation, possibly as the target was not originally of a high density. Instead, it has caused a densification of the target surface, either by melting it or sintering it. Thus, it

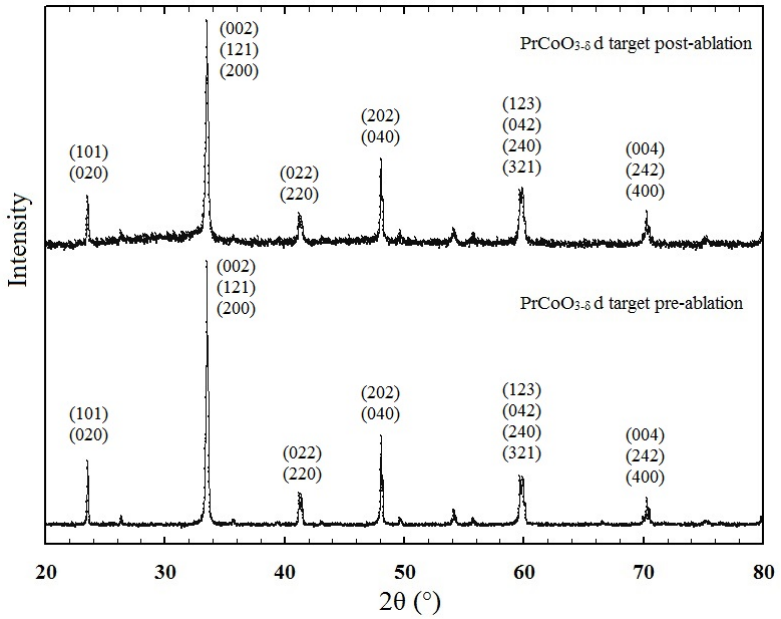


Figure 6.8: XRD pattern of the PCO113 target pre- and post-laser ablation during PLD showing the same Bragg reflections and no apparent degradation of the target. There were no detectable second phases following laser ablation; there was relative confidence that there were no compositional changes arising from the deposition process.

is expected that film quality would actually improve with target ablation. Also, there is no appearance of target segregation. Thus there is no need to remove the damaged target surface between depositions. Inspection of the PCO113 films indicates that good surfaces had been obtained; the film quality has not been affected by the potentially low density of the target (and the laser fluence was sufficiently high and uniform). This target was used for the PLD of PCO113 films.

Finally, XRD patterns were taken of the PCO113 target after all PLD depositions had been performed. A comparison of the pre and post-ablation patterns may be seen in Fig 6.8. It appears that the PCO113 target is stable in the deposition environment, at least for the duration of the deposition. The peak positions have been maintained suggesting no changes in stoichiometry of the target. However, there seems to be a slight preferential loss of crystallinity, as can be seen from the decrease in peak intensity at 33.5° 2θ, which may be matched to the (002), (121) or (200) reflections ,while all other relative peak intensities are maintained, and the amorphous region now present. It should be noted that most of the area of interaction between the laser and the target covers only a fraction of the target, and the laser damage occurs only on the surface of the target. However, the bulk of the XRD signal is from depths greater than 10um below the sample surface. Target segregation may not be detected with this technique.

Thus there was the option of grinding off this dense but slightly amorphous surface between depositions in order to ablate off a crystalline but less dense surface, or preserving it. As a high substrate temperature was used for the deposition of PCO113, which should facilitate the deposition of a crystalline film, this surface damage was not removed between

depositions in order to retain a dense surface at the point of ablation. On consideration of the out-of-plane XRD patterns of deposited PCO113 films in Section 7, it did seem that the substrate temperature was high enough that crystallinity was restored during the deposition and growth of the film.

In order to obtain dense samples (of nonstoichiometric PCO113 for electrical conductivity DC-measurements), the sintering temperature of those bar samples were increased to 1200°C. The crystal structure of the PCO113 was unaffected by the increase in sintering temperature, and samples were over 95% dense, according to the Archmedes density measurement and supported by SEM images. Further details of these samples are provided in Chapter 10.

6.3.2 $Pr_2NiO_{4\pm\delta}$ Target

XRD measurements were performed on the PNO214 powder before and after the final calcination, see Fig 6.9, and normalized to the integrated peak intensity of either the PNO214(112) reflection (using a $Fmmm$ space group [299]), or the Pr_6O_{11}(111) reflection (using a $Fm\bar{3}m$ space group [4]). At a calcination temperature of 900°C, only Pr_6O_{11} [4] and NiO was present [320]. As the calcination temperature increases, PNO214 was formed. A calcination temperature of 1200°C appeared to be the optimal temperature. Higher temperatures resulted in Pr_6O_{11} decomposing out, although the NiO (that must also be present unless Ni is subliming out of the samples) peaks cannot be detected. Its presence may be below the detection limit. Decomposition of PNO214 at high temperatures in air has been reported in literature [47, 48] where $Pr_4Ni_3O_{10}$ and Pr_6O_{11} were the decomposition products and is likely to be what is observed. Further work is required to investigated the instability of PNO214 at high temperatures in air.

A last point of interest is that as the calcination temperatures increased, the symmetry of the PNO214 crystal structure also increased as splitting of the orthorhombic peaks lessened: the peaks around 32° 2θ, 44° 2θ, 56° 2θ, 66° 2θ, 69° 2θ and 78° 2θ can all be seen to shift closer together. This would be expected if the diffraction patterns were obtained at the sintering temperatures. However, these diffraction patterns are obtained at room temperature. It appears that the effect of the calcination temperature on the structure is retained even down at room temperature. No changes in the full width half maxima of the reflections were observed upon varying the final calcination temperatures; the calcination temperature has not affected crystallite size.

Based on this, a stoichiometric PNO214 target was sintered at 1200°C for 12 h. The resulting target was measured to be >90% dense, using the Archimedes method. A Le Bail refinement was performed on the XRD pattern of the PNO214 target using the $Fmmm$ spacegroup [299], see Fig 6.10. The synthesized PNO214 target had cell parameters of: a = 5.456(1) Å, b = 5.389(1) Å, c = 122.449(6) Å. No Pr_6O_{11} was detected; the target appeared to be a single phase.

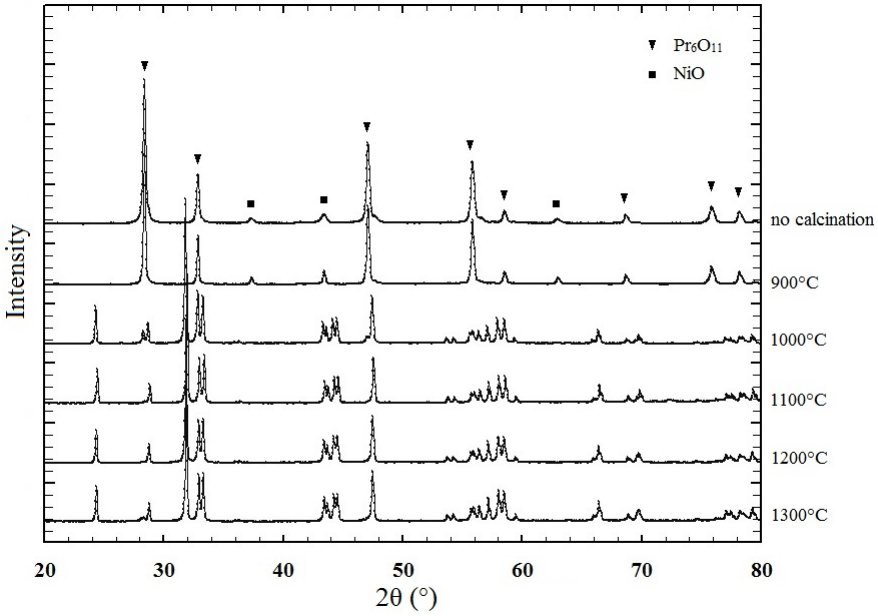


Figure 6.9: Powder XRD pattern of PNO214 precursors following decomposition at 300°C and 600°C for 6 h in air, and following an additional calcination for 6 h at 900°C, 1000°C, 1100°C, 1200°C, 1300°C. Reflections corresponding to Pr_6O_{11} and NiO have been marked.

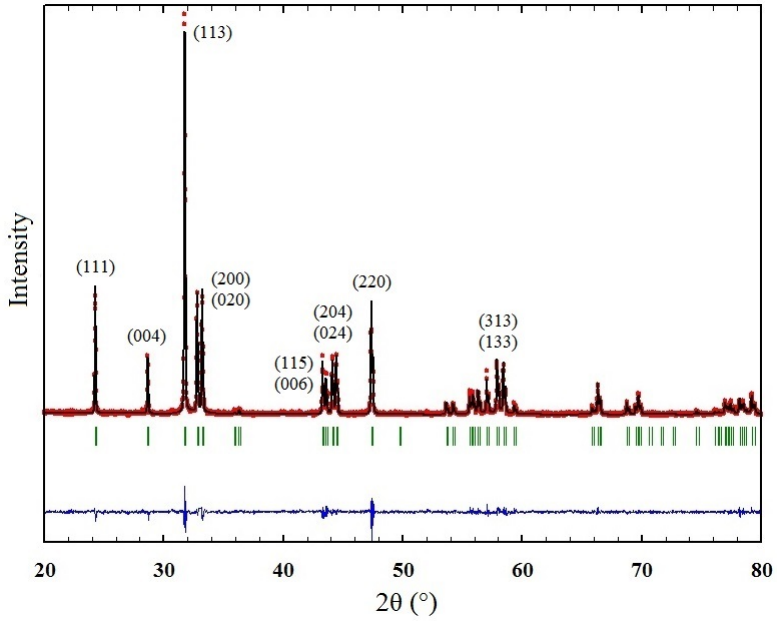
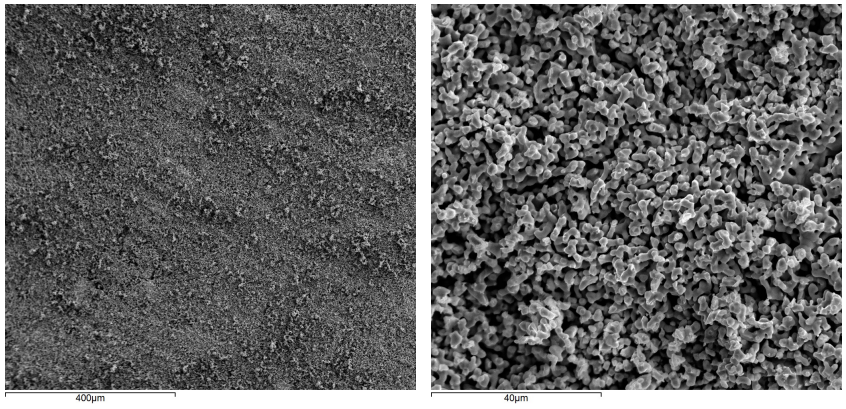
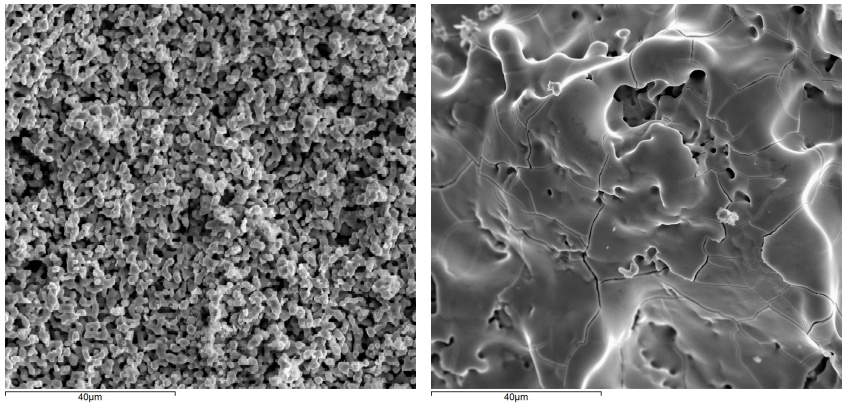


Figure 6.10: Powder XRD pattern of PNO214 target, upon which a Le Bail refinement had been performed. Peak reflections have been indicated in green, diffraction data in red, modeled pattern in red, and the difference between measured and modeled pattern in blue.Main reflections have been labeled.



(a) 10X magnification (b) 1000X magnification



(c) 1000X magnification (d) 1000X magnification

Figure 6.11: SE images of the PNO214 target surface (a) and (b) pre-PLD deposition and, (c) and (d) post-PLD deposition. (c) was obtained at the centre of the PNO214 target, indicating no changes in target morphology due to the deposition conditions. (d) was obtained at the ring of damage. Scale bar = 400 μm) for (a) and 40 μm for (b) - (d).

SE images were taken from the ground surface of a PNO214 reference target and compared against a target that had been ablated, see Fig 6.11. While some sintering (more than seen with the PCO113 target) has occurred, there has been little densification as large pores have formed instead. A greater extent of densification would have been expected given the high densities measured using the Archimedes method. Where the laser had not impacted the target, the morphology remained unchanged suggesting that there was no, or little, decomposition of the target though compositional analysis is required to confirm this. Like the PCO113 target, at the area of laser damage, the surface of the target was much denser and it is likely that the target was melted in these areas. Thus, so long as the damaged surface was not removed, the target was deemed suitable for PLD despite its low bulk density.

An XRD pattern was taken of an ablated PNO214 target and compared to it's pre-ablation pattern, see Fig 6.12. The ablation amorphsized the target significantly and a large broad halo was clearly present. Additional unmatched reflections were also observed. The instability of PNO214 at high temperatures in reducing conditions has previously been

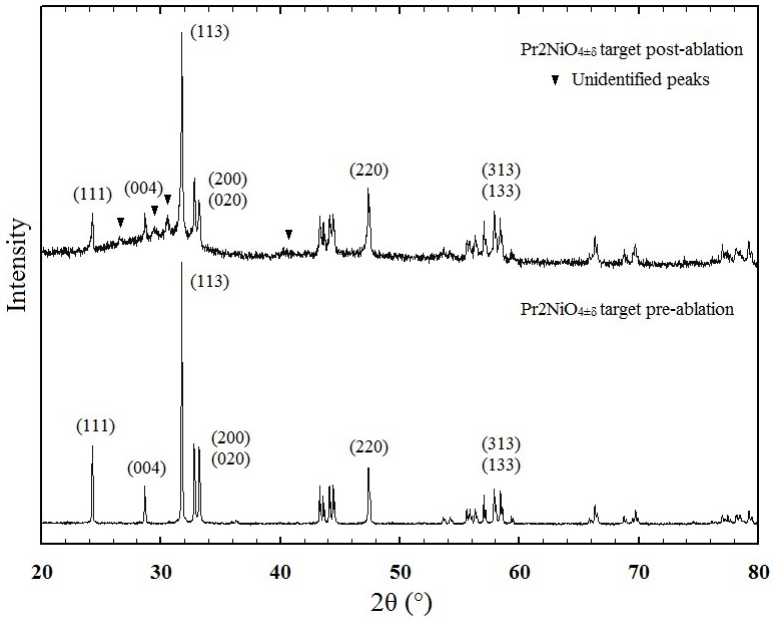


Figure 6.12: XRD pattern of the PNO214 target pre- and post-laser ablation during PLD. Main PNO214 peaks have been labeled.

documented [294, 48, 47]. However, the additional reflections did not correspond that that of $Pr_4Ni_3O_{10}$ and Pr_6O_{11}- the typical decomposition pr oducts reported. Due to the few reflections, it was not possible to identify these secondary phases. It was unclear if these secondary phases were the result of the deposition conditions, or the ablation process, or a combination of the two. However, based on a comparison of the SE images of the PNO214 target pre- and post- PLD deposition, it suggests that the secondary phases were the result of the ablation process. The XRD pattern of the remaining PNO214 phase was comparable to the pre-ablated pattern, except for a decrease in the intensity of the (111) and (020) reflections suggesting that these orientations were particularly susceptible to laser damage (and/or reduction at low oxygen partial pressures).

At the peak intensities measured by XRD, the secondary phases should be visible on the target surface. However, none were detected when looking at the damaged target surface using the SEM (as in the SE images of Fig 6.12d). The morphology depicted was no different to that seen for the (apparent) single phase PCO113 target. This may be due to the small sample area, but care was taken during the microscopy to take representative images of the entire sample. Further chemical analysis is required to identify the damage products on the target surface.

6.3.3 $Ce_{0.9}Gd_{0.1}O_{2-\delta}$ Target and Substrates

XRD patterns of the received CGO powder and the sintered pellets (to be used as a PLD target and as a substrate to deposit upon) were obtained, see Fig 6.13. A Le Bail refinement was performed using the $Fm\bar{3}m$ spacegroup [298] and unit cell parameters

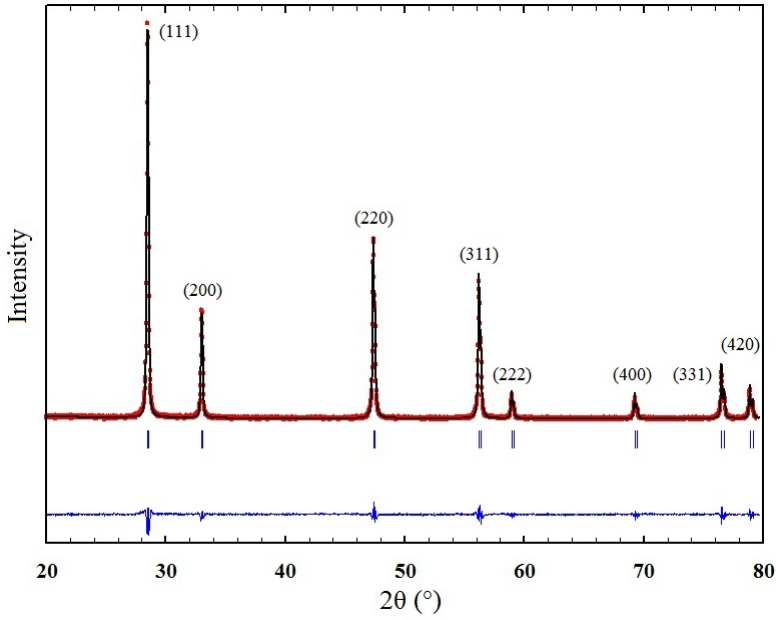
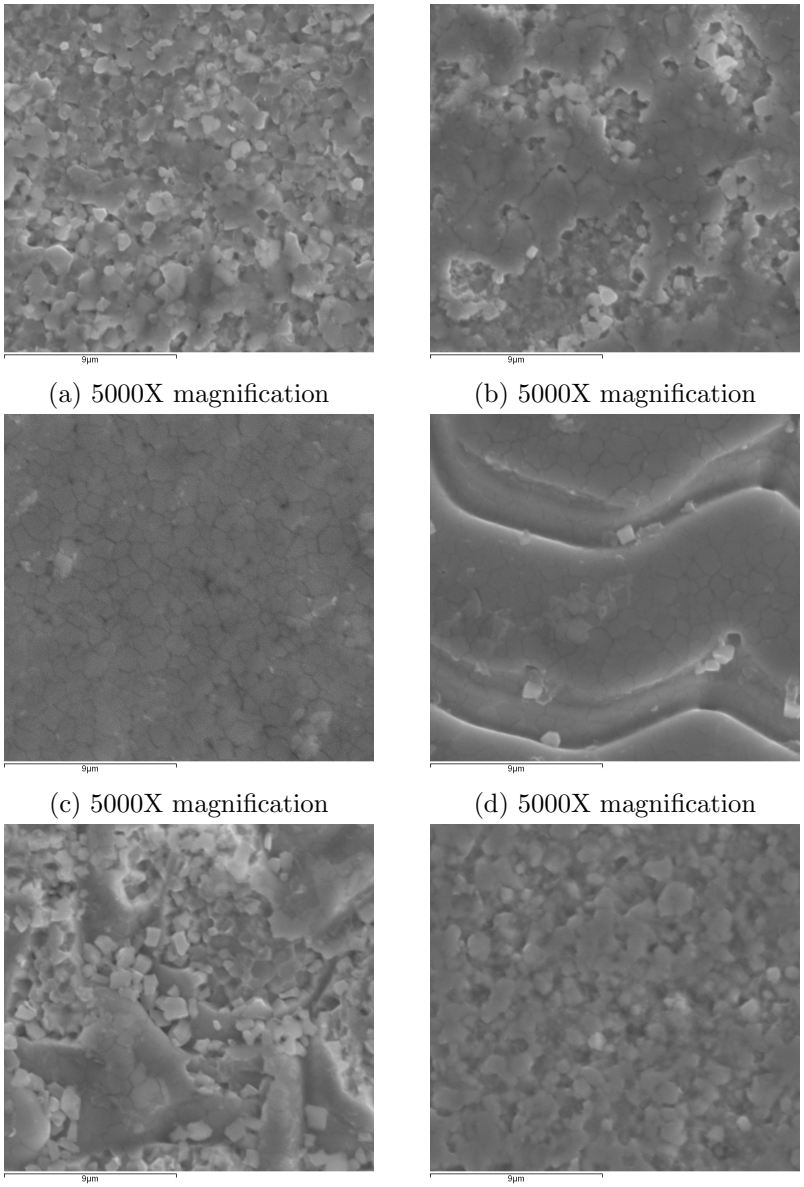


Figure 6.13: Powder XRD pattern of CGO target, upon which a Le Bail refinement had been performed. Peak reflections have been indicated in green, diffraction data in red, modeled pattern in red, and the difference between measured and modeled pattern in blue. CGO reflections have been labeled.

were found to be a = b = c = 5.4223(1) Å. Based on these lattice parameters, the lowest lattice mismatch calculated was 0.9% and 0.5% for the PCO[001])/CGO[001] and PNO[010]/CGO[001] interfaces respectively. In both these cases, a highly textured or epitaxial thin film is expected to be deposited on the CGO buffer layer assuming that this is also epitaxial. The densities of the sintered samples were all determined to be greater than 95% of the theoretical density of CGO.

SE images were taken of the CGO target pre- and post-ablation using the JEOL JSM 6400, see Fig 6.14. The particle size of the received CGO target was much smaller than the synthesized PCO113 and PNO214. A greater extent of sintering may be observed, though the measured density was comparable to that of PCO113 and PNO214. Comparing the post-deposition target surface (where it was not damaged by the laser) with a pre-deposition image suggests that morphologically the CGO target was unaffected by the deposition conditions. As before, the laser ablations densified the CGO target surface. There was a graduation as the morphology moved from being granular to having a densified surface regions to becoming completely dense and flat. There was an additional target morphology, not seen with the PCO113 or PNO214 targets, where a striated dense surface formed, which eventually broke up into a granular form once more.

EDX data were collected across the ring of laser damage to see if there are any variations in stoichiometry, see Fig 6.15. 10 point spectra were acquired over the entire area of damage. A depletion of Gd in the target composition with the mol% of Gd was found to vary between 7-9.1 mol%. This concurs with literature reports of Gd-rich films being



(a) 5000X magnification (b) 5000X magnification

(c) 5000X magnification (d) 5000X magnification

(e) 5000X magnification (f) 5000X magnification

Figure 6.14: SE images of the damaged CGO target surface post-PLD deposition. (a)-(f) depict the different target morphologies taken radially across the ring of damage, where (a) and (f) are the undamaged centre end edge of the CGO target, respectively. Scale bar = 9 μm for all.

deposited by PLD [319]. Due to the error associated with an uneven sample surface, which could not be polished as it would remove the surface of interest, it was not possible to identify trends in CGO metal cation stoichiometry across the damaged area.

The CGO pellets to be used as substrates were ground and polished. In order to characterise the surface, AFM was performed using a Bruker DiInnova on sample areas of 10 μm by 10 μm and 2 μm by 2 μm, see Fig 6.16. The surface RMS roughness was calculated to be 7.6 nm and 1.21 nm respectively. The rough surface seen in the SE images has been

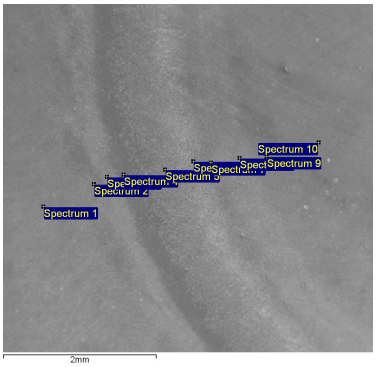
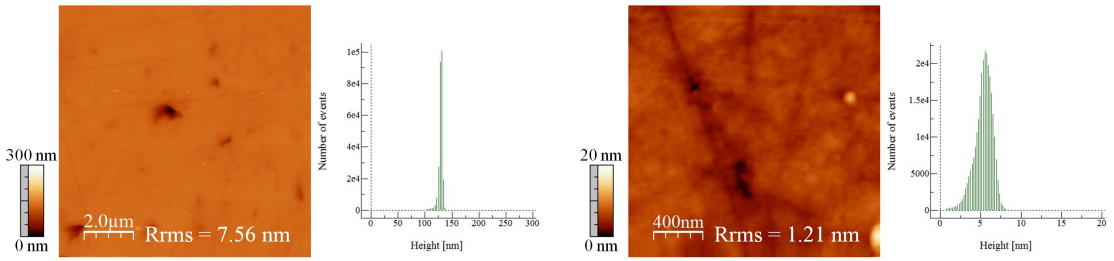


Figure 6.15: SE image of the CGO target post-ablation indicating the locations at which EDX spectra were obtained. Scale bar = 2 mm.



(a) 10 μm by 10 μm sample area.

(b) 2 μm by 2 μm sample area.

Figure 6.16: AFM images of the polished CGO substrate surface of low roughness, that is fully sintered and of a high density, though pores are present. Some artifacts of the polishing process- the scores across it- were observed.

removed with only a few protruding features remaining. While the sample has sintered well, a few pores could be seen. The shapes of the height distribution over both sample areas were similar. Scratches may still be seen on the substrate surface. However, the polycrystalline films that are to be deposited on these substrates are to be in the order of several hundred nm thick. Thus, this surface was sufficiently smooth for its purpose despite the pores, which were its largest features: the peak to peak value for the 10 μm by 10 μm sample area was 163 nm.

6.3.4 Si(004) Substrate

Prior to any depositions, a reference out-of-plane XRD pattern and AFM images were taken of a cleaned Si(004) substrate, see Fig 6.17 and Fig 6.18. As expected, there was only one out-of-plane reflection: the (004) reflection at 69.15° 2θ (but two peaks due to the splitting of the K-α_1 and K-α_2 wavelengths). This was in keeping with literature values with the Si(004) peak of $Fd\bar{3}m$ occurring at 69.12° 2θ [321] and within instrumental error.

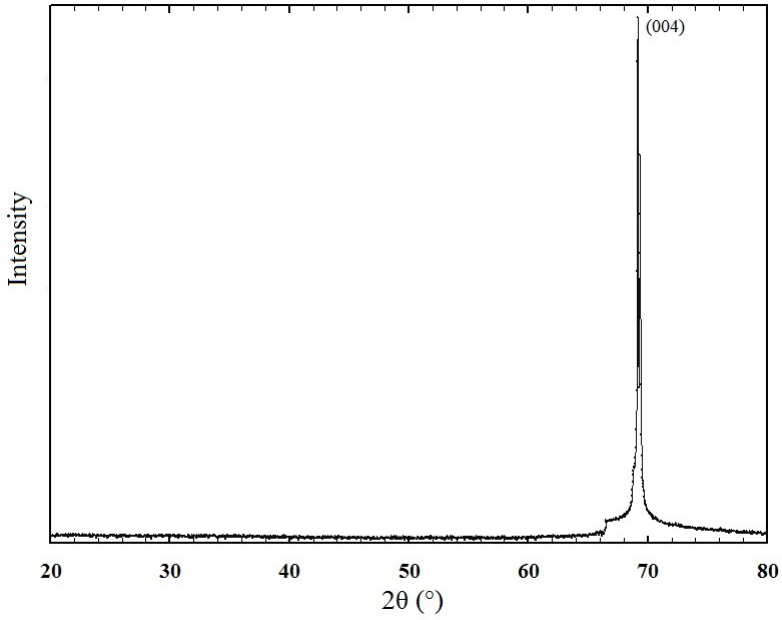
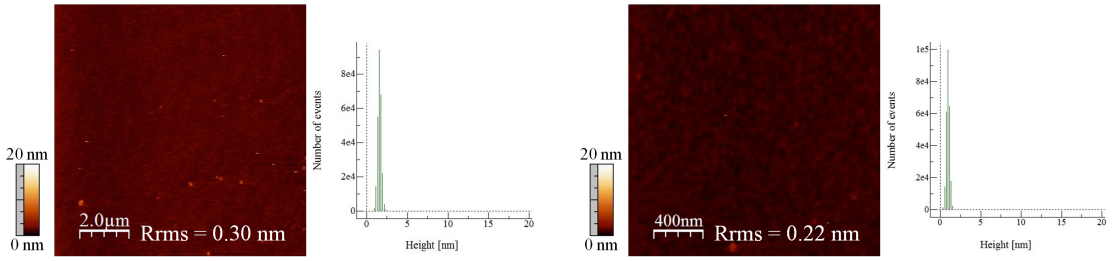


Figure 6.17: Out-of-plane XRD pattern of the single crystal Si(004) substrate.



(a) 10 μm by 10 μm sample area.

(b) 2 μm by 2 μm sample area.

Figure 6.18: AFM images of the single crystal Si(004) substrate surface showing them to be smooth and flat, of a low roughness.

6.3.5 YSZ-8mol%(002) Substrate

Similarly, prior to any deposition, a reference out-of-plane XRD pattern was taken of a cleaned YSZ(002) substrate, see Fig 6.19. As with the Si(004) substrate, there was only one out-of-plane (002) reflection detected at 34.86° 2θ, using the $P4_2/nmc$ spacegroup assignment [300]. This would correspond with a c-cell parameter of 5.148 Å, similar to literature values [300]. The sample position was been aligned prior to the diffraction measurement. This small discrepancy in 2θ values provided confidence in the alignment. AFM images were also obtained using a Bruker DiInnova, see Fig 6.20. The substrates were of a low roughness, with RMS values of 0.36 nm and 0.88 nm for the 10 by 10 μm and 2 by 2μm measured respectively.

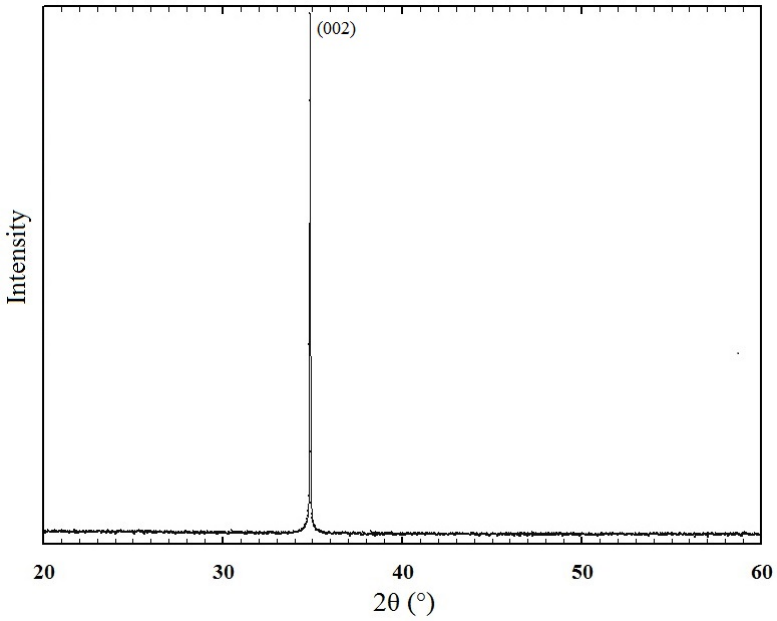
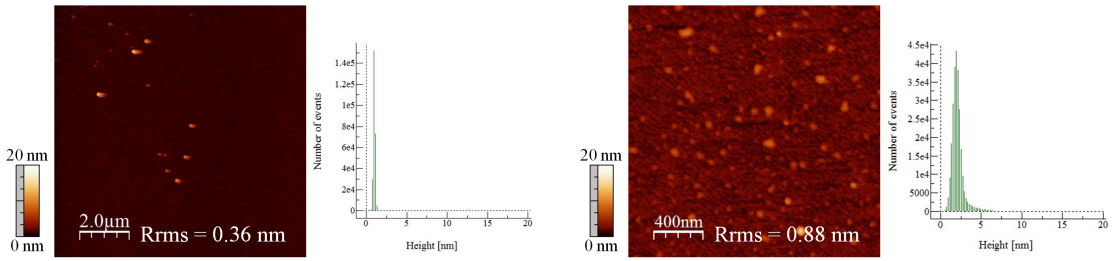


Figure 6.19: Out-of-plane XRD pattern of the single crystal YSZ(002) substrate.



(a) 10 μm by 10 μm sample area.

(b) 2 μm by 2 μm sample area.

Figure 6.20: AFM images of the single crystal YSZ(002) substrate surface showing them to be smooth and flat, of a low roughness.

6.3.6 Deposited $Ce_{0.9}Gd_{0.1}O_{2-\delta}$ Buffer Layers on YSZ-8mol%(002)

As mentioned in the experimental method, two different nominal substrate temperatures, 680°C and 780°C, and two different oxygen partial pressures, 10 mTorr and 30 mTorr, were used for the deposition of CGO buffer layers on YSZ. Based on the cell parameters of YSZ-8mol% (a = b = 3.6294 Å, c = 5.1433 Å[300]) and the Le Bail refinement of the received CGO powder (a = b = c = 5.4223 Å), the lattice mismatch at CGO[001]/YSZ[110] interface was expected to be -5.6%. Despite this mismatch, epitaxial CGO films have been successfully deposited on YSZ(001) [27, 29, 227, 310, 311], and should be obtainable. Out-of-plane XRD measurements were taken of CGO films deposited under the four different conditions, using the PANalytical MDP, see Fig 6.21. All patterns have been normalized to the integrated intensity of the YSZ(002) reflection. For all four deposition conditions, a single CGO(200) out-of-plane reflection was detected, at similar intensities between the samples. There appeared to be no clear effect of oxygen partial pressure on the diffraction pattern of the films. Increasing substrate temperature resulted in a decrease in the full

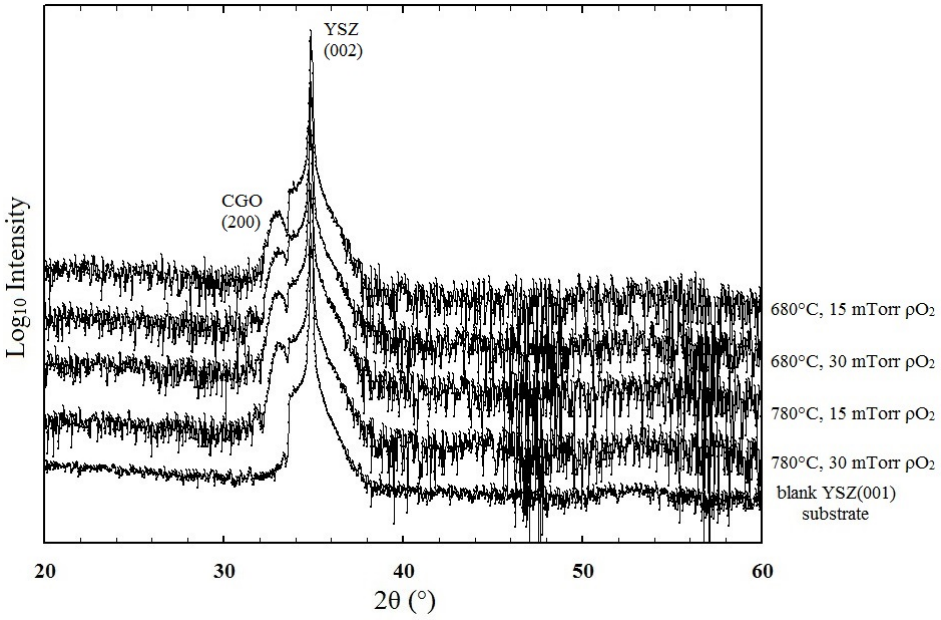


Figure 6.21: Out-of-plane XRD patterns of the CGO buffer layer deposited on a YSZ(002) substrate under various PLD conditions. A single CGO reflection was observed for all the CGO buffer layers.

width half maxima of the CGO(200) reflection, suggesting an increase in film crystallinity.

AFM images of the resulting CGO films, see Fig 6.4 indicated the formation of a columnar structure. According to literature, increasing the substrate temperature should lower the porosity of the film, while increasing oxygen partial pressure should increase the formation of clusters on the substrate surface [302, 303, 304, 2]. From the surface height distribution measured, increasing the oxygen partial pressure or substrate temperature increased the range of height distributions and thus the film R_{rsm} by 0.3 nm and 0.6 nm for the CGO buffer layers deposited at 680°C and 780°C respectively, and also the average height measured. The increase in roughness may be attributed to the increase in cluster formation at high oxygen partial pressures during deposition (though it should be noted that the upward shift in the height distribution of the CGO film deposited at 680°C, with an oxygen partial pressure of 30 mTorr was largely due to the presence of a pore in the film which lowered the baseline value, and the columnar grains were still present, but masked out because of the height graduation key). Based on the AFM images, it seemed that the best film quality was obtained at a substrate temperature of 680°C, with an oxygen partial pressure of 10 mTorr. Thus these were the conditions employed for the deposition of CGO buffer layers by PLD. The R_{rms} roughness for this film was 0.4 nm, which was comparable to the R_{rms} roughness measured for the YSZ(002).

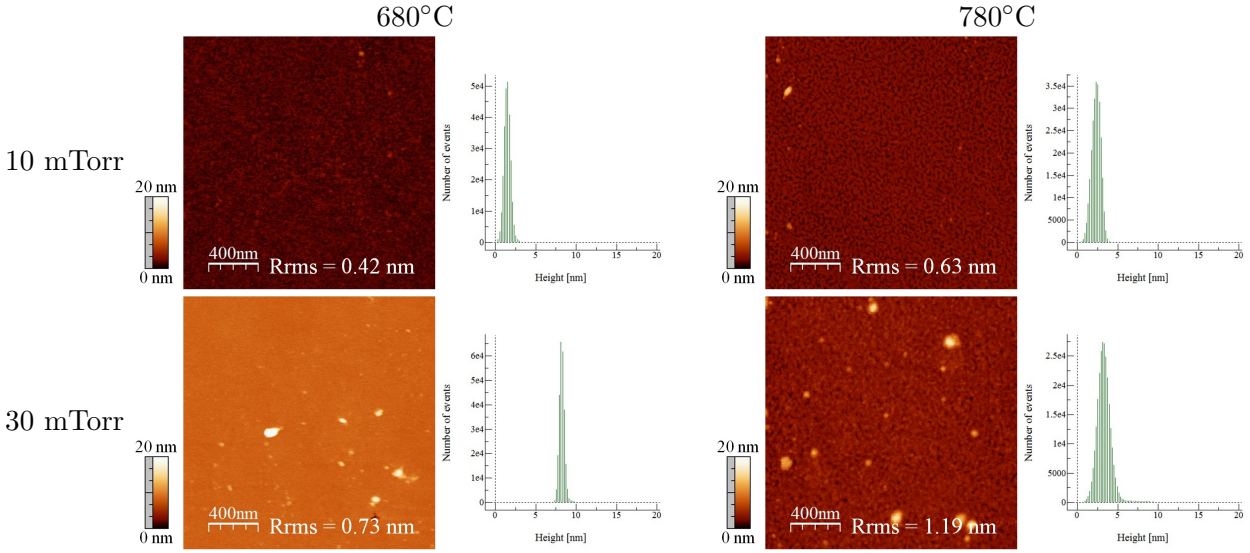


Table 6.4: AFM images of the CGO(200)/YSZ(002) films deposited using substrate temperatures of 680°C and 780°C, and oxygen partial pressures of 10 mTorr and 30 mTorr. All films were of a low roughness; the CGO(200) film deposited using a substrate temperature of 680°C and oxygen partial pressure of 10 mTorr appeared to be of the best quality, having the lowest roughness and no large deposits on its surface.

6.4 Conclusion and Further Work

Stoichiometric PCO113 and PNO214 targets have been synthesized. Both targets undergo amorphisation and are densified by the laser ablation process. While the bulk of the targets have not attained the recommended 90% density required for PLD, the laser-damaged surfaces do; these damaged surfaces were retained between depositions. While the PCO113 target appears stable in deposition conditions, secondary phases were detected in the PNO214 targets post-deposition. The instability of PNO214 at high temperatures has been reported previously. PLD of PNO214 may still be possible, as long as the target stoichiometry is maintained. Dense PCO113 samples were also synthesized, by raising the sintering temperature to 1200°C, also dense CGO substrates and targets. Further work should include an investigation of the stability of both PCO113 and PNO214 at high temperatures. Following laser ablation, rough EDX measurements found the CGO target to be Gd-deficient. Coupled with literature reports of Gd-rich films being fabricated by PLD, it may be that Gd preferentially ablates under these deposition conditions though further work is required to ascertain the cause for the non-stoichiometric transfer.

Si(004), YSZ-8mol%(002) and polished CGO polycrystalline substrates were surface mapped using AFM. All were of a sufficiently good finish for deposition. Using the lattice parameters of PCO113 and PNO214 calculated from Le Bail refinement of powder XRD patterns, and the position of the CGO(200) reflection in an out-of-plane XRD measurement, the lattice mismatch at the PCO113[001]/CGO[001] and PNO214[010]/CGO[001] interfaces were as low as 0.9% and 0.5% respectively. The successful growth of highly textured thin

films is anticipated.

Deposition conditions of CGO on YSZ have been investigated. In agreement with literature, increasing substrate temperature and oxygen partial pressure increases the density and the formation particulates on the film respectively. Textured CGO films have been deposited with a low RMS roughness. These optimized deposition conditions will be replicated exactly for the deposition of thin PCO113 and PNO214 films of varying thickness.

The preliminary work is now complete. Based on this, PLD deposition of PCO113 and PNO214 films on CGO/YSZ may now be investigated. Similarly, stability and transport measurements on dense non-stoichiometric PCO113 samples may now be performed.

Chapter 7

The Effect of Oxygen Partial Pressure and Substrate Temperature on the Deposition of $PrCoO_{3-\delta}$ Films

Previously in Chapter 6, the $PrCoO_{3-\delta}$, PCO113, target and $Ce_{0.9}Gd_{0.1}O_{2-\delta}$, CGO, polycrystalline substrate were fabricated and characterized through the use of XRD, AFM and SE images. The same characterization was performed for single crystal Si(004) substrate. All components necessary for the deposition of PCO113 by PLD have been prepared. Prior to deposition on single crystal YSZ-8mol%(002), YSZ(002), substrates, PCO113 was first deposited on Si(004). A range of deposition temperatures and oxygen partial pressures were used to examine their effect on the deposited PCO113 film. The out of plane texture and surface morphology of the films were characterised by XRD and AFM surface mapping to observe the effect of deposition conditions on the resulting films. Films of varying thicknesses were also deposited on Si(004) to observe how the quality of the film changed with its thickness. Initial deposition conditions were adopted from literature.

7.1 Literature Review

A brief review was made of the deposition of PCO113 by PLD on a range of different substrates. The deposition of colbatite oxide perovskites of the same lanthanide family was also reviewed, as a point of comparison against the deposition of PCO113.

7.1.1 PLD of $PrCoO_{3-\delta}$

Successful deposition of PCO113 by PLD was first published by Prakash et al. in 2010 [295]. A 248 nm KrF excimer laser was used and deposition performed at a substrate temperature of 680°C and oxygen partial pressure of 40 Pa. The PCO113 thin films were initially deposited on $LaAlO_3$(001), LAO(001), and, in later work by Prakash et al., on Si(111) and $SrTiO_3$(001), STO(001) [296]. Out-of-plane XRD was performed on the thin films to ensure a single phase film had been deposited and to determine the grain size using the Debye-Scherrer formula. The PCO113 thin films deposited on STO and LAO were of a single out of plane orientation corresponding to that of the single crystal substrate (001), but on Si(111), a textured film was produced with (110), (200), and (220) out of plane reflections observed. No further structural characterisation of the thin films was performed. SE imaging of the film indicated a highly cracked (depending on the substrate) but flat film surface. EDX confirmed the composition of the film to be close to stoichiometric PCO113.

More recently, in 2013, Mehta et al. deposited epitaxial PCO113 films on STO(001) and Nb-doped STO(001) with the objective of tailoring the spin state of the Co, whether high spin, low spin or intermediate spin, through lattice strain [297]. PCO113 films between 8 to 115 nm thick were fabricated by PLD using a 248 nm KrF excimer laser (∼1 J/cm^2). Deposition was performed at a substrate temperature of 650-700°C and oxygen partial pressure of 320 mTorr. Only the (002) out-of-plane reflection was observed, and asymmetric reciprocal space mapping of the (013) reflection comfirmed an in-plane coherent strain between film and substrate that relaxed as the film thickness increased. PCO113(002) rocking curves indicated good crystallinity with the FWHM below 0.7° even for the thickest films and RMS measurements over a 5 μm length scale fall within 2.5 to 5 Å.

To date, there has not been any published literature on the deposition of PCO113 on Si(004) substrates or on YSZ, nor the effects of substrate temperature and oxygen partial pressure during deposition on the growth of PCO113 thin films in these systems. Due to the large lattice mismatch of PCO113 with Si, it is unlikely that an epitaxial film will grow. Nevertheless, this study is of interest in view of optimizing future deposition of PCO113 films on CGO/YSZ.

7.1.2 PLD of $LaCoO_{3-\delta}$ and $La_{1-x}Sr_xCoO_{3-\delta}$

While literature on the PLD of PCO113 is sparse, more work has been done on the PLD of $LaCoO_3$, LCO113, particularly with respect to its ferromagnetic behavior, and $La_{1-x}Sr_xCoO_3$ (LSC113), in the field of fuel cells. Strained epitaxial LCO113 films have been deposited on a range of single crystal substrates, such as $(LaAlO_3)_{0.3}(Sr_2TaAlO_6)_{0.7}$, LSAT,$SrLaAlO_4$, SLAO, STO, LAO, all of the (001) orientation, with polycrystalline LCO113 deposited on thermally oxidized Si wafers [200, 223, 322, 323, 324, 325, 326, 327].

The epitaxial LCO113 films were seen to accommodate in-plane compressive and tensile strains as large as -1.5% (on SLAO) and 2.5% (on STO), respectively [328]. For the PLD of LCO113, substrate temperatures ranged between 650°C and 750°C and oxygen partial pressures between 300 mTorr to 350 mTorr, which is in line with what was previously reported for the deposition of PCO113.

With respect to fuel cell applications, the fabrication conditions employed for LSC113 films on YSZ substrates have been performed under a different emphasis: to prevent the formation of highly resistive $La_2Zr_2O_7$ or $SrZrO_3$ phases, at the LSC113 and the YSZ interface [200, 223, 322]. Additionally, to combat delamination of the LSC113 film from the YSZ substrate due to TEC mismatch and to improve interconnectivity at the interface, post deposition annealing has been employed to obtain a columnar microstructure with fine vertical pores [323, 324, 325, 326, 327]. For these films, PLD deposition was successfully carried out at room temperature, with an oxygen partial pressure of about 100 mTorr. However, though processing temperatures were kept below 650°C, cell performance was still found to be compromised [329]. An impedance study of the LSC/YSZ system suggested a maximum deposition temperature of 500°C to prevent the formation of those resistive phases [330].

It is known that LCO113 is not stable at high temperatures in reducing atmospheres, as would be encountered during PLD [331]. As temperature increases, the perovskite becomes increasingly oxygen deficient, resulting in an expansion of the lattice. A study of the thermodynamic stability of LCO113 has also been performed by Navrotsky et al. [332] which shows a decreasing ionic Ln^{3+} radii was associated with a higher oxygen non-stoichiometry and greater formation enthalpies of mass loss reaction products (Ln_2O_3, Co and O). Based on this alone, Pr^{3+}, with its smaller ionic radii than La^{3+}, should be less thermodynamically stable and it will not be possible to deposit them at as high temperatures as LCO113. This does not account for the effect of a change in oxidation state of Pr^{3+} to Pr^{4+}.

Work has also been performed on the effect of pulse duration and oxygen partial pressure on ablated LSC113 films which found that for LSC113 thin films produced using an excimer laser, high oxygen partial pressures are required for successful depositions [333]. This is due to the longer pulse duration of the excimer laser, and thus longer period of elevated temperature at the target. At lower oxygen partial pressures, the target surface is likely to decompose.

The deposition conditions to be employed in this work are based on that used in literature. PCO113 films are known to be deposited at 680°C, while LCO113 and LSC113 have been deposited in a similar temperature range. In the interest of further work involving the deposition of a Ruddlesden-Popper $Pr_2NiO_{4\pm\delta}$, PNO214, film upon the existing PCO113 layer, PNO214 deposition conditions were also considered. However, no literature could be found on the deposition of PNO214, although $Pr_2Ni_{0.71}Cu_{0.24}Ga_{0.05}O_4$(PNCG), thin films have been successfully deposited at 780°C [314, 46]. With that in mind, a temperature range between 680°C and 780°C was attempted. While a higher substrate temperature

would result in a more crystalline and dense deposited film, both desirable characteristics, when coupled with low oxygen partial pressures, it may cause the decomposition of the LnCO113 [331, 334, 335]. Similarly, successful PLD of PCO113 has been performed at an oxygen partial pressure of around 300 mTorr. Nevertheless, it would be of interest to see if within the oxygen partial pressure range of 10 mTorr and 500 mTorr, PCO decomposition occurs, or if target anion stoichiometry is maintained at either ends of the spectrum.

7.2 Experimental Method

PCO113 films were deposited on Si(004) at substrate temperatures of between 680°C to 780°C at a constant oxygen partial pressure of 300 mTorr, and at oxygen partial pressures between ∼10 mTorr to 500 mTorr at a constant substrate temperature of 680°C. In both these cases, 3000 pulses were deposited. Finally, using literature conditions of a substrate temperature of 680°C and oxygen partial pressure of 300 mTorr, PCO113 films of varying thicknesses were deposited in order to observe the growth of the film. A final deposition was made using 10000 pulses under literature deposition conditions on a polycrystalline CGO substrate to confirm the deposition of single phase PCO113.

Control of the deposition duration (the number of pulses) was precise, as was ambient pressure during deposition at higher pressures. Using an ambient pressure of 10 mTorr was at the limit of the equipment's capability and there was some difficulty in maintaining a constant pressure: it would fluctuate between 5 mTorr and 14 mTorr. While control of the heating element used under the substrate platform was good, the actual temperature of the substrate remains uncertain. The substrate holder surface was ground after each deposition to ensure there was a clean contact between the platform and the substrate. However, the position of the substrate relative to the heating element would inevitably vary between depositions. Similarly there is the concern of progressively removing the platform surface bringing the substrate closer and closer to the heating element. Lastly, the temperature of the substrate depended on the heat transport of the substrate itself. There were no available means of measuring the actual substrate temperature.

Out of plane XRD patterns were obtained for all of the deposited thin films using the Panalytical Pro MRD diffractometer. The objective of this work was to investigate the effect of deposition conditions on film quality and as such, only a 2θ range between 15 and 65° 2θ was measured. A larger range to include the Si(004) reflection was measured for initial runs and they showed zero-corrections within instrument error ($\pm 0.02°$ 2θ). All patterns have been scaled according to their background intensities. AFM and SE images were also taken of the PCO113 films using the Bruker DiInnova and Leo Gemini 1525 FEG-SEM respectively. SE and AFM images were obtained from several locations on the films to ensure that the images displayed are representative of the samples.

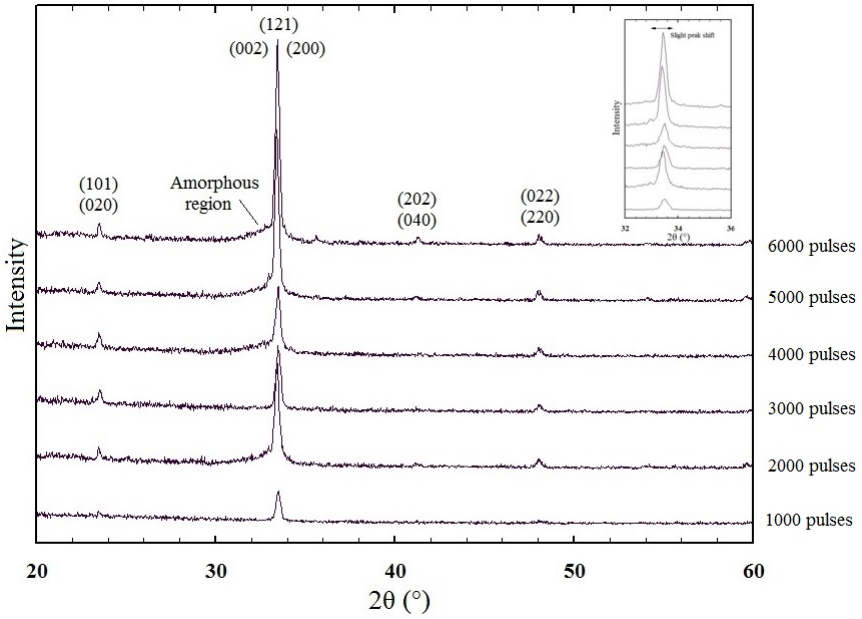


Figure 7.1: Out-of-plane XRD patterns of the PCO113 films deposited using 1000 to 6000 pulses. PCO113 reflections have been labeled. The reflections between 32-34° 2θ have been enlarged. A slight peak shift may be observed in the PCO113 reflection at ∼33.5 ° 2θ.

7.3 Results and Discussion

7.3.1 $PrCoO_{3-\delta}$/Si(004) Films of Varying Thicknesses

PCO113 films of a range of film thicknesses were first deposited using PLD parameters as described by Mehta et al. [297] to test if the deposition of PCO113 may be replicated on Si(004) wafer. A substrate temperature of 680°C and oxygen partial pressure of 300 mTorr was used. Out-of-plane XRD measurements of the PCO113 films are depicted in Fig 7.1. These films correspond to a deposition of between 1000 to 6000 pulses. Though it was not immediately clear with the thinner films, as the thickness of the film increases, it can be seen that a polycrystalline PCO113 film has been deposited. The observed reflections of the thickest film correspond to all the higher intensity reflections in the powder pattern table, which have been labeled. Deposition of a epitaxial PCO113 film was uncertain given the lattice match between PCO113 and Si ($Fd\bar{3}m$, a = b = c = 5.4309 Å[321]), which would be 1.70% or 1.03% for the Si(004) orientation, obtained at the PCO113[100]/Si[100] or PCO113[100]/Si[010] interfaces respectively.

Using the *Pnma* space group assignment of PCO113, from the Le Bail refinement: there were three reflections around ∼33.5° 2θ : the (002), (121), and (200) reflections, corresponding to 33.34° 2θ, 33.45° 2θ, and 33.56° 2θ positions respectively. In the deposited PCO113 film, it can be seen of this highest intensity peak at ∼33.5° 2θ that as the deposition time increases, the peak intensity shifts to lower 2θ values. All other PCO113 peak intensities were too low to ascertain if this shift was also found in the positions of the

other PCO113 reflections. The cause of this shift may be instrumental error. However, careful positioning and alignment was adopted for all thin film samples and comparisons of other thin film measurements suggest instrumental error to be within 0.05° 2θ, which is just smaller than the peak shifts observed. A possible explanation is that increasing the thickness of a texture PCO film allowed the lattice to relax and contract in-plane, and expand out-of-plane, and hence the shift to lower 2θ values in the out-of-plane XRD pattern.

An amorphous region can be seen at the highest intensity reflection for some of the thin films, but was absent in two. This was likely to be because the films deposited using 1000 and 3000 pulses were the first two depositions from the PCO113 target. As such, the target had not yet acquired any damaged amorphized regions (which were detected in the XRD of the target post-ablation). The amorphous regions found in the films could be a reflection of the structure of the now ablation-damaged target, and that the substrate temperature was not sufficiently high to restore crystallinity- this will be further explored when substrate temperatures during deposition were varied in Section 7.3.3. However, this slight amorphous region was not detected in later PCO113 films deposited when further target damage should have accummulated. As such, the cause of this regions remains uncertain.

For the films deposited using 2000 and 5000 pulses, there was an additional reflection at 32.9° 2θ suggesting the presence of a secondary phase. These films were deposited under nominally identical conditions except for the number of laser pulses. It is unclear why this additional phase is present in only these two films. It may be that this second phase was below detectable limits in the other films. However, it should then also have been detected in the film deposited with 6000 pulses, which has the highest peak intensities, where it was not. This will be considered further when examining the other effects of PLD conditions on PCO113 films. Nevertheless, there is confidence that a substrate temperature of 680°C and an oxygen partial pressure of 300 mTorr would result in the successful pulsed laser deposition of PCO113 thin films.

Film thicknesses have been measured using the Dektak surface profilometer. A height profile was obtained across a region that was masked off by TiO_2 during the deposition. Several profiles were obtained for each film and can be seen in Fig 7.2. The average deposition rate was about 38 nm/1000 pulses. However, given that these film thickness measurements were made in close proximity to each other, some of the ranges of thicknesses measured for the films, especially the film deposited using 6000 pulses where a variation in film thickness of 57.9 nm was measured are considerable. These profiles were over a length of 30 μm, and positioned so that half of it comprised of the film surface. Thus, it is unlikely that these variations were due to surface features. This was also supported by AFM and SE images of the film surface showing it to be mostly flat without features of this size, see Table 7.4. The large range in measured film thicknesses undermined confidence in the accuracy of these film thickness measurements. Intensities of the deposited film may be the better indicator of the actual film thickness.

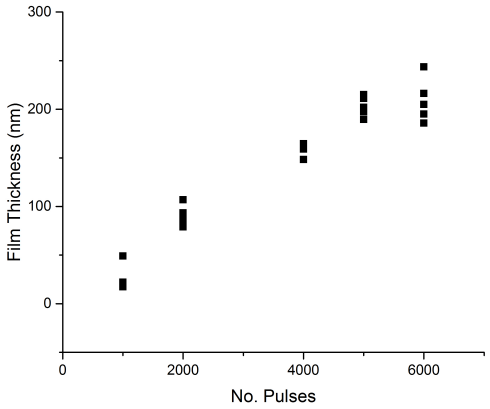


Figure 7.2: Film thickness measurements of the PCO113 films deposited using 1000 to 5000 pulses, performed using the Dektak surface profilometer. The deposition rate was 38 nm/1000 pulses.

The main PCO113 peak of the thin film samples, around 33.5°, were fitted using a pseudo-Voigt profile (Appendix A.1). The amorphous contributions were not accounted for in the fits. R^2 values varied between 0.915 for PCO113 films deposited using 2000 pulses and 4000 pulses, and 0.987 for the PCO113 film deposited using 1000 pulses. The integrated peak intensities of these observed reflections around 33.5° 2θ roughly corresponded with the number of pulses, with the exception of the film deposited using 2000 pulses that was exceptionally thick, see Fig 7.3. It may also be argued that the integrated peak intensities were comparatively low for PCO113 films deposited using 3000 pulses and 4000 pulses. These were also the films of the lowest crystallinity, having the largest full width half maxima, FHWM (the general trend was for a decrease in FWHM as film thickness increased).

AFM images of the PCO113 films are depicted in Table 7.4. The film appeared dense and flat with no cracks. As deposition continues, the columnar PCO113 grains increased in size and the roughness of the films increased. The columnar grains were of a uniform size, except for the 1000 pulse film. For this film, the majority of the grains were small, with large grains evenly distributed across the surface. As it was the first film to be deposited, this may be the result of using a 'fresh' and therefore more porous PCO113 target.

The SE images of the PCO113 films complement those obtained using the AFM. As the film thickness increased, the grain size increased. The variation in grain sizes here correlates with evolution of the peak reflection intensities of the XRD patterns. Additionally, these SE images indicate the presence of microscopic cracks in the thicker PCO113 films. These cracks are likely due to the coupled effects of TEC mismatch between the Si(004) substrate and the PCO113 polycrystalline film, and chemical effects from variations in oxygen nonstoichiometry with temperature, which has been reported of LSC113 thin films: due to the rigidity that came of depositing dense LSC113 thin films 1 μm thick, large cracks and film delamination occurred [325].

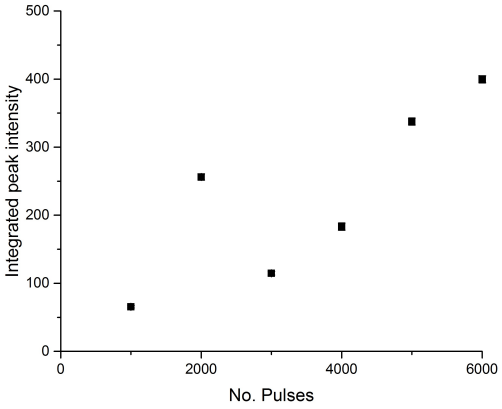
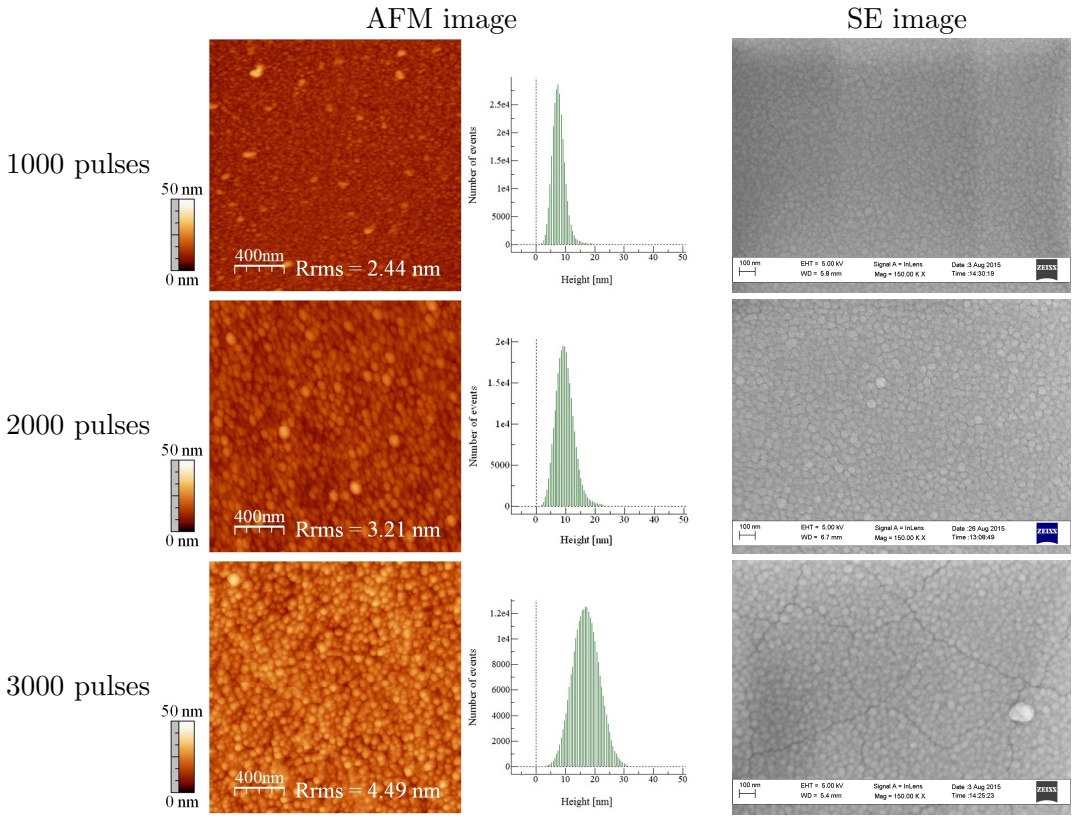
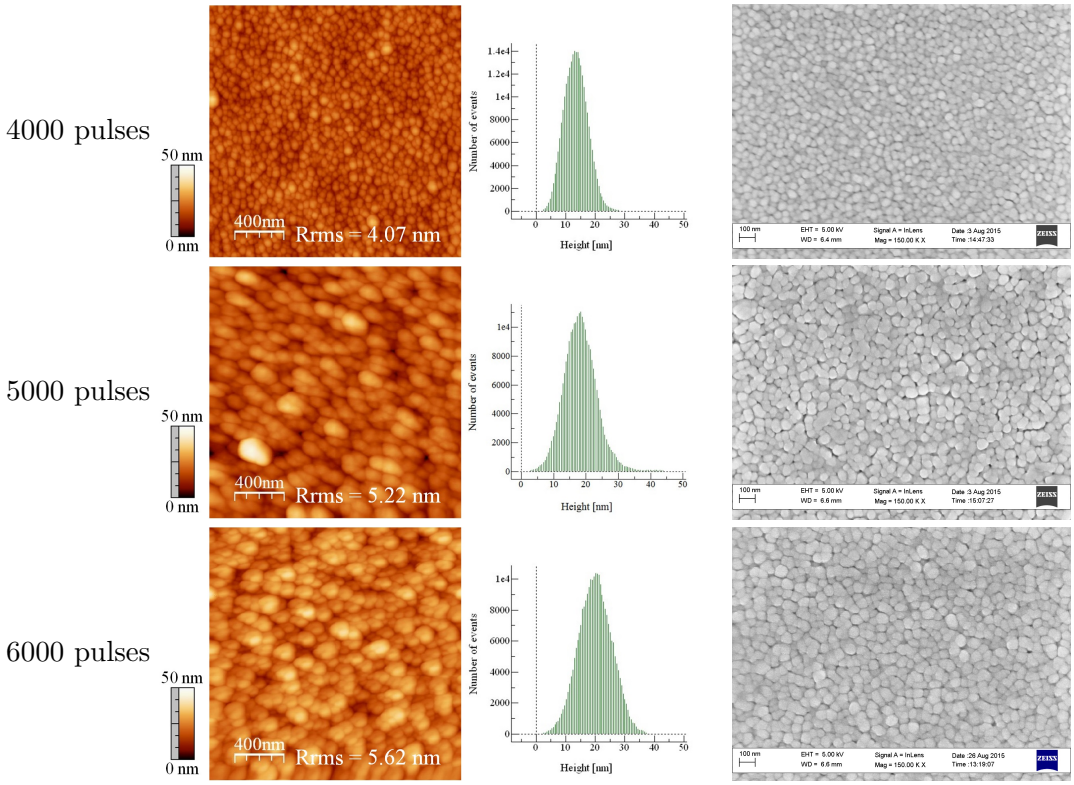
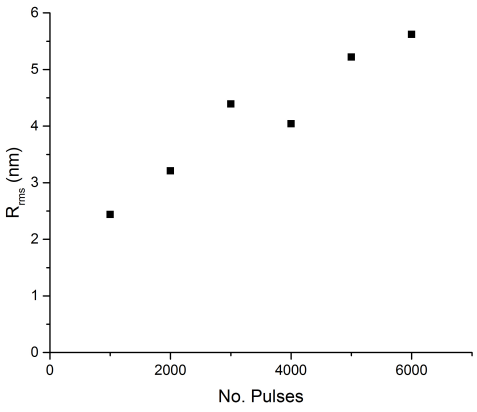


Figure 7.3: Integrated peak intensity at ∼33.5° 2θ of the out-of-plane PCO113 reflection, fitted using a pseudo-Voigt profile. The PCO113 films were deposited using a range of pulses. The PCO113 film deposited using 2000 pulses was deemed anomalous. The volume of PCO113 deposited increased with the number of deposition pulses. Some error bays have been obscured by the data marker.





(a) AFM and SE images



(b) R_{rms} values

Figure 7.4: AFM and SE images of the PCO113 films deposited using 1000 to 6000 pulses. As film thicknesses increased, average grain size and the grain size distribution increased. Microcracks may be seen on the surface of the thicker PCO113 films. SE scale bar = 100 nm.

Thus, single phase polycrystalline PCO113 thin films have been successful deposited using an oxygen partial pressure of 300 mTorr, and a substrate temperature of 680°C. No secondary phases were detected. As film thickness increased, so too did all the PCO113 reflections. The intensities of the PCO113 reflections relative to each other remain fairly

constant as film thickness increased suggesting a polycrystalline film throughout with no preferred orientations as film thickness varied. The effect of oxygen partial pressure (and later substrate temperature) will now be examined with the objective of optimizing film morphology.

7.3.2 $PrCoO_{3-\delta}$/Si(004) Films Deposited Using Oxygen Partial Pressures Between 10 mTorr and 500 mTorr

PCO113 films were deposited on Si(004) wafers, using 3000 pulses and a substrate temperature of 680°C, at oxygen partial pressures between 10 mTorr and 500 mTorr. The out-of-plane XRD patterns, AFM and SE images of these films may be found in Fig 7.5 and Table 7.6, respectively.

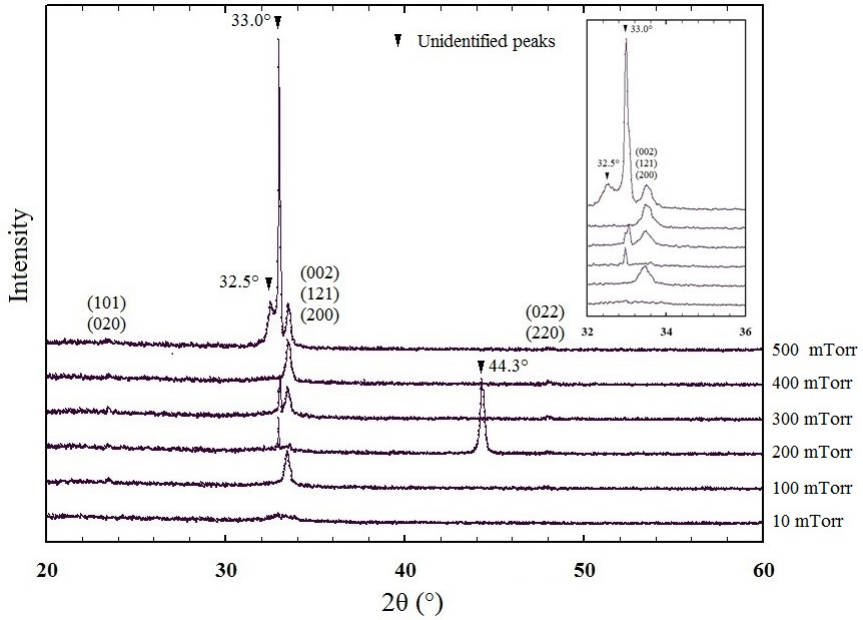
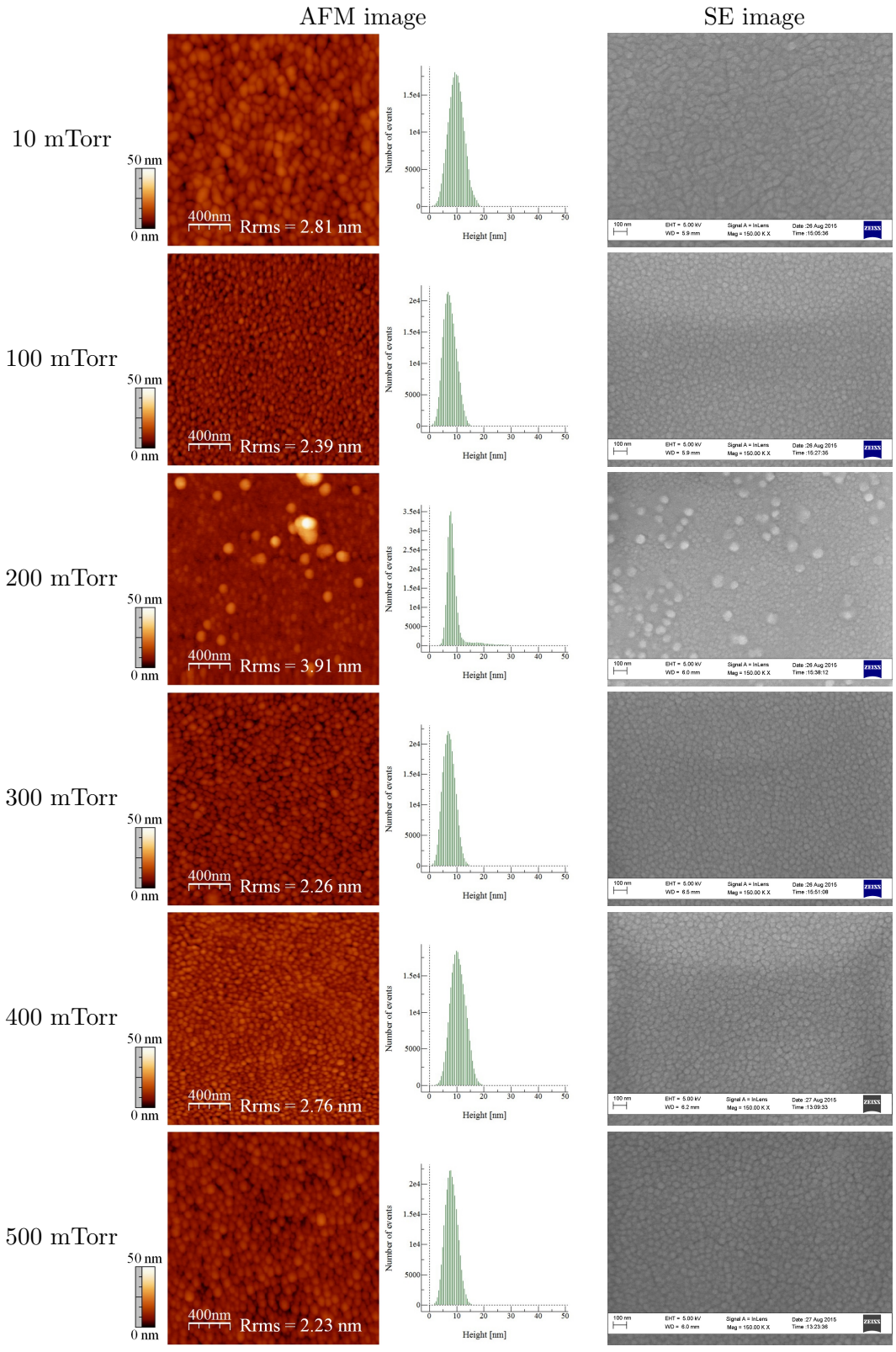
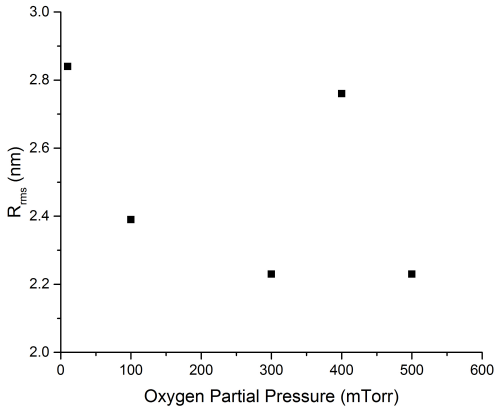


Figure 7.5: Out-of-plane XRD patterns of the PCO113 films deposited using an oxygen partial pressure between 10 mTorr and 500 mTorr. PCO113 reflections have been labeled. The reflections between 32-34° 2θ have been enlarged. There were three unidentified peaks at 32.5° 2θ, 33.0° 2θ and 44.3° 2θ. Possible phases they may belong to include Pr_6O_{11} and Co_3O_4.

In Fig 7.5, the film deposited using an oxygen partial pressure of 10 mTorr has a barely discernable peak in its XRD pattern corresponding to the PCO113(002), (121), or (200) reflection at ∼33.5° 2θ. Such a low intensity suggests a very thin film, whereas the AFM and SE images in Table 7.6 depicted a flat film with large grains and the beginnings of microcracks, which were earlier associated with thicker films. The grains of this film (deposited at an oxygen partial pressure of 10 mTorr) were less regular in shape, have a larger range of grain sizes, which were on average larger than those described in the previous section where the deposition pressure was 300 mTorr.



(a) AFM and SE images



(b) R_{rms} values

Figure 7.6: AFM and SE images of the PCO113 films deposited using an oxygen partial pressure between 10 mTorr and 500 mTorr. Besides the (anomalous) PCO113 film deposited using an oxygen partial pressure of 200 mTorr, all PCO13 films deposited from oxygen partial pressures of 100 mTorr have similar morphologies consisting of regular shaped grains and a small grain size distribution. It was not clear if there was an enlargement of grain size as oxygen partial pressure increased. The PCO113 film deposited using an oxygen partial pressure of 10 mTorr had a very different morphology of irregularly shaped grains of a large distribution of sizes. SE scale bar = 100 nm.

With the exception of the PCO113 film deposited at an oxygen partial pressure of 200 mTorr, increasing the oxygen partial pressure resulted in a marginally higher intensity reflection about ∼33.5° 2θ, and similarly trace peaks corresponding to the other PCO113 reflections. Based on the this reflection, increasing oxygen partial pressure increased PCO113 film thicknesses. At these oxygen partial pressures higher than 10 mTorr, the film consisted of regular grains of a uniform size. No microcracks were observed. This morphology was consistent regardless of oxygen partial pressure. It appeared that there was a threshold oxygen partial pressure ∼100 mTorr, above which oxygen partial pressure had little affect on film morphology.

The film deposited at an oxygen partial pressure of 200 mTorr had a significantly different XRD pattern and film morphology. While some PCO113 had been deposited, as evidenced by a main PCO113(121) reflection and other trace reflections, another single-orientated phase had also been deposited: the reflection at ∼44.3° 2θ that did not clearly correspond to any of the PCO113 reflections nor any cobalt or praseodymium cobaltite R-P oxides, or praseodymium oxides. The closest match of this reflection at ∼44.3° 2θ was to the Co_3O_4(400) reflection, see Table

However, as the oxygen partial pressure increased, an additional reflection was seen at ∼33.0° 2θ and, at 500 mTorr ρO_2, another reflection at ∼32.5° 2θ. The reflection at ∼33.0° 2θ clearly belongs to a secondary phase, having a FHWM less than half that of the reflections at ∼33.0° 2θ and at ∼44.3° 2θ. As only one reflection corresponding to

Composition	h	k	l	2θ	I(%)	Reference
$PrCoO_{3-\delta}$	0	0	2	33.3023	-	This work
	1	2	1	33.42	-	
	2	0	0	33.53	-	
Pr_2CoO_4	0	0	4	28.22	25.0	[336]
	1	0	3	31.55	100.0	
	1	1	0	32.68	75.0	
$Pr_4Co_3O_{10}$	0	0	10	32.74	100.0	[225]
	2	0	0	33.22	73.0	
Pr_6O_{11}	1	1	1	28.25	100.0	[4]
	2	0	0	32.74	28.0	

Table 7.1: Table of the Bragg reflections of $PrCoO_{3-\delta}$, Pr_2CoO_4, $Pr_4Co_3O_{10}$ and Pr_6O_{11} that may correspond to the unidentified peaks at ∼33.0° 2θ and ∼32.5° 2θ.

this phase was seen, it was not possible to identify this second phase with certainty. The reflections at ∼32.5° 2θ was likely to correspond to a third phase, as its FWHM did not match that of the second phase and neither are there any PCO113 reflections at that position. It was not possible to identify this phase either. Table 7.1 provides a list of potential phases this second phase may be, and the positions of their Bragg reflections. There were no exact matches for these two additional reflections. It should be noted that these reflections were not detected in any of the PCO113 thin films of Section 7.3.1 deposited at an oxygen partial pressure of 300 mTorr, yet were present in the PCO113 thin film of this sample also deposited at an oxygen partial pressure of 300 mTorr. This raised concerns over the repeatability of the PLD process.

Film thickness measurements were also taken of the PCO113 films deposited between 10 mTorr and 500 mTorr ρO_2, see Fig 7.7. It can be seen that with the except of the PCO113 film deposited at 10 mTorr ρO_2 and the anomalous film deposited at 200 mTorr, the increase in oxygen pressure resulted in an increase in film thickness corresponding that the increase in peak intensities seen in the out-of-plane XRD patterns. Given that the deposition times have been kept constant, similar intensities in the XRD pattern are expected for all the films. A possible explanation for the increasing XRD intensities is that at lower background pressures, the kinetics of the incoming ablated particles are high enough to re-sputter the deposited film resulting in less material deposited. The large film thickness of ∼80 nm for the PCO113 film deposited of 10 mTorr and the low peak intensity of that film suggests that it may have been of a low density, and amorphous. The microcracks seen in this film may be due to the high thickness of the film, or the extremely low oxygen partial pressures. As no microcracks were found in the ∼90 nm thick PCO113 film deposited at 500 mTorr ρO_2; in the previous section, microcracks were only observed in films from ∼113.7 nm thick; and as porosity is meant to reduce the formation of cracks [325], it was more likely to be due to the latter. The chemical expansion of perovskites is known to occur due to the loss of oxygen from the lattice at low oxygen partial pressures.

Thus, PCO113 films have been successfully deposited at between 10 and 500 mTorr ρO_2.

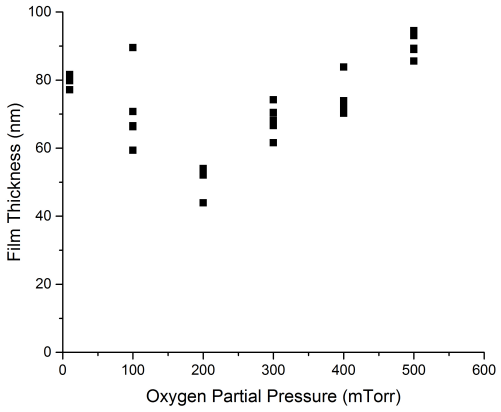


Figure 7.7: Film thickness measurements of the PCO113 films deposited using an oxygen partial pressure between 10 to 500 mTorr, performed using the Dektak surface profilometer. Exempting the PCO113 films deposited using 10 mTorr and 200 mTorr, there was an increase in film thickness as oxygen partial pressure increased.

Increasing oxygen partial pressure had the effect of increasing the amount of PCO113 film deposited. As oxygen partial pressure increased, secondary and tertiary phases were detected, though they could not be identified. A secondary phase was found even for the PCO113 film deposited under identical conditions as in Section 7.3.1, when a single phase PCO113 film was obtained. The cause for this difference was unclear; the reproducibility of the PLD process warrants investigation. The use of an oxygen partial pressure of below 100 mTorr resulted in a porous film with large irregular grains. While this oxygen partial pressure should be used for the deposition of the CGO buffer layer, it was not ideal for the PCO113 film- a higher oxygen partial pressure should be used.

7.3.3 $PrCoO_{3-\delta}$/Si(004) Films Deposited Using Substrate Temperatures Between 680°C and 780°C

PCO113 films were deposited on Si(004) wafers, using 3000 pulses at an oxygen partial pressure of 300 mTorr, at substrate temperatures between 680°C and 780°C. Out-of-plane XRD measurements, AFM and SE images of these films may be found in Fig 7.8. The presence of the PCO113 reflection at ∼33.5° 2θ suggest that PCO113 have been successfully deposited for all six films. Unlike in Section 7.2 when the PCO113 film thicknesses were varied, the other PCO113 reflections (at ∼23.5° 2θ, ∼41.3° 2θ and ∼48.1° 2θ) were of a much lower intensity given the intensity of the PCO113 refelction at ∼33.5° 2θ, suggesting that they may be a preference to either the (002), (121) or (200) orientation. This may have been true of the PCO113 films deposited in Section 7.3.2, though due to the low intensity of the PCO113 reflection at ∼33.5° 2θ, it could not be confirmed. There appeared to be no trend between the crystallinity of the PCO113 film (as indicated by the FHWM of its reflection at ∼33.5° 2θ) and the substrate temperature.

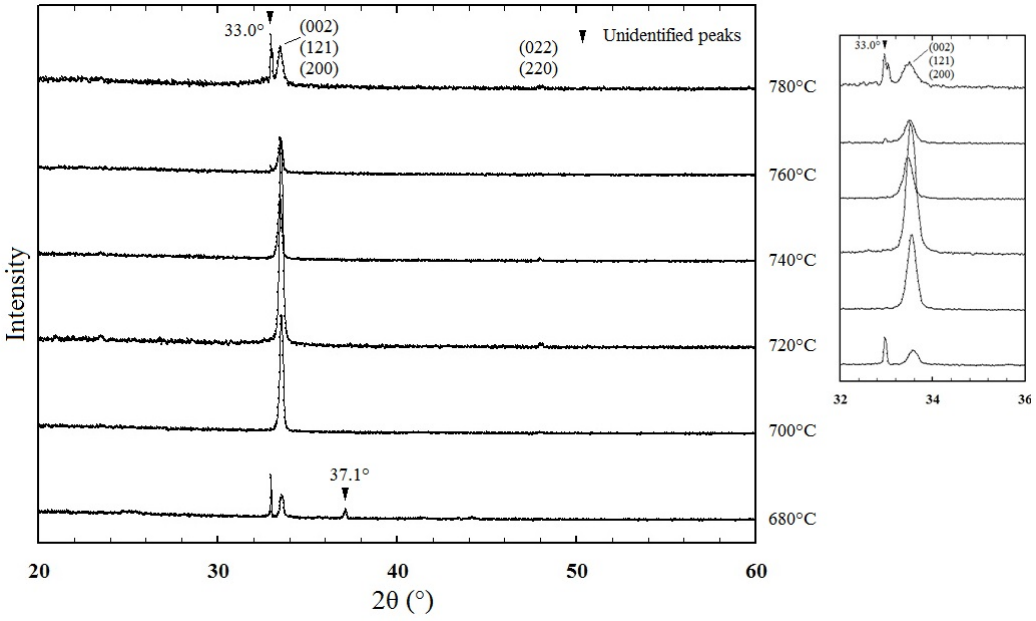


Figure 7.8: Out-of-plane XRD patterns of the PCO113 films deposited using a substrate temperature between 680°C and 780°C. PCO113 reflections have been labeled. The reflections between 32-34° 2θ have been enlarged. There were two unidentified peaks at 33.0° 2θ and 37.1° 2θ.

Composition	h	k	l	2θ	I(%)	Reference
CoO	1	1	1	36.51	72.5	[337]
	2	0	0	42.41	100.0	
Co_3O_4	2	2	0	31.34	32.0	[338]
	3	1	1	36.93	100.0	
	2	2	2	38.64	10.3	
	4	0	0	44.92	16.9	

Table 7.2: Table of the Bragg reflections of CoO and Co_3O_4 that may correspond to the unidentified peak at ∼37.1° 2θ.

Similarly to the PCO113 films of Section 7.3.2 when the oxygen partial pressure was varied, a secondary phase with a reflection at ∼33.0° 2θ was present when substrate temperatures of 680°C and 780°C were used. For the PCO113 film deposited at 780°C, this unidentified peak can be seen to split (though this has provided no further clues as to the identification of this phase). Additionally, for the PCO113 film deposited at 680°C, a third phase was also found corresponding to a reflection at ∼37.1° 2θ. This position did not match any reflections in PCO113 or cobalt oxides, see Table 7.2. As was noted before, none of these additional phases were detected in the PCO113 films of Section 7.2 deposited under identical conditions for a range of PCO113 film thicknesses.

There was quite a large variation in the integrated intensities of the out-of-plane XRD patterns indicating a variation in deposited material, though no clear trend was found. It was unclear if this variation was due to irregularities of the deposition process, of if the de-

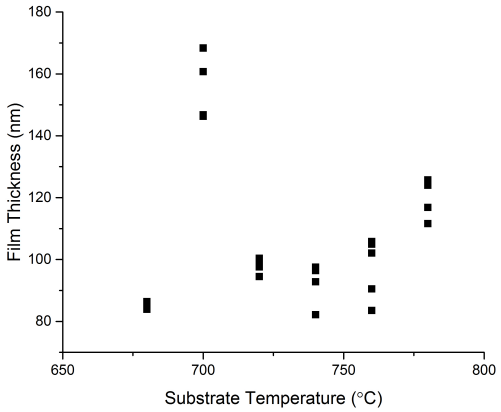
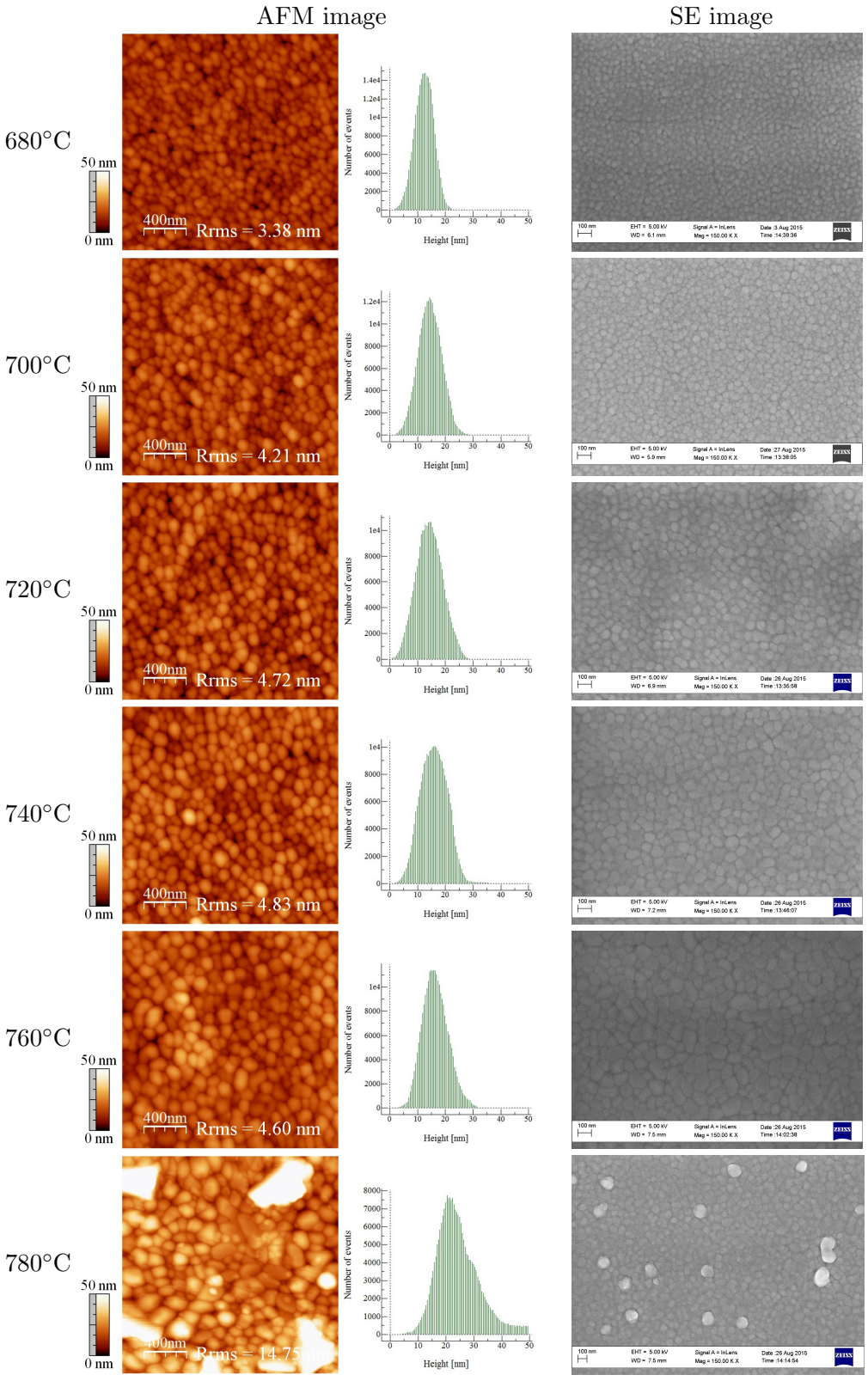


Figure 7.9: Film thickness measurements of the PCO113 films deposited using a substrate temperature between 680°C and 780°C, performed using the Dektak surface profilometer. Beside the exceptionally thick PCO113 film obtained at a substrate temperature of 700°C, an increase in PCO113 film thickness was found with increasing substrate temperature.

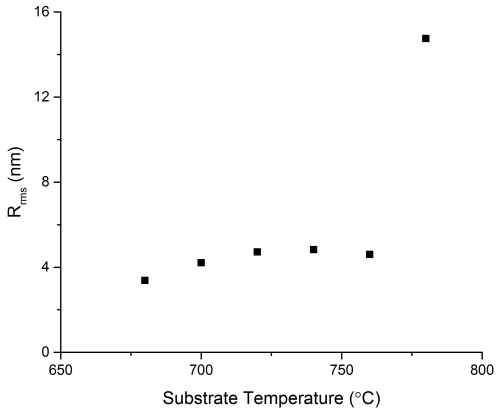
position rate was affected by substrate temperature. Dektak measurements of the PCO113 films, see Fig 7.9 indicated an increase in film thickness with substrate temperature. The film deposited using a substrate temperature of 700°C appeared to be anomalously high.

Both AFM and SE images of the PCO113 films depict a flat surface with uniform grains, see Fig 7.10a. They also indicate that grain size increases with substrate temperature and became less regular. Grain size distribution also increased. No microcracks were observed despite the average PCO113 film thickness of all six films being 98 nm (excluding the film deposited at 700°C). The images of the PCO113 film deposited at 700°C that was measured to be almost twice as thick as all other firms showed no features typical of thicker films (microcracks and large grains) further suggesting that the film thickness measurement of this film was anomalous. However, the SE and AFM images also showed that the PCO113 film deposited at 780°C had a significantly different film morphology from the other films deposited at lower substrate temperatures. Extra large grains are found interspersed, at a lower frequency than that seen previously, among a background of smaller PCO113 grains. There was a discrepancy in the two images in that these large grains appeared regular in shape in the SE image, while the AFM image suggested that these grains were of an irregular shape.

Additionally, contrary to the SE images, several other AFM images taken at different locations on the film surface also indicated the presence of extra large, interspersed, regularly shaped, grains (among a background of smaller PCO113 grains) at substrate temperatures $\geq$740°C, see Fig 7.11. These large grains were not found of the PCO113 films of varying thickness, in Section 7.3.1, but were found of the anomalous PCO113 film deposited using an oxygen partial pressure of 200 mTorr in Section 7.3.2, where it was suggested to be due to a third phase. There were no common factors correlating the presence of these large grains to its deposition conditions or diffraction pattern.

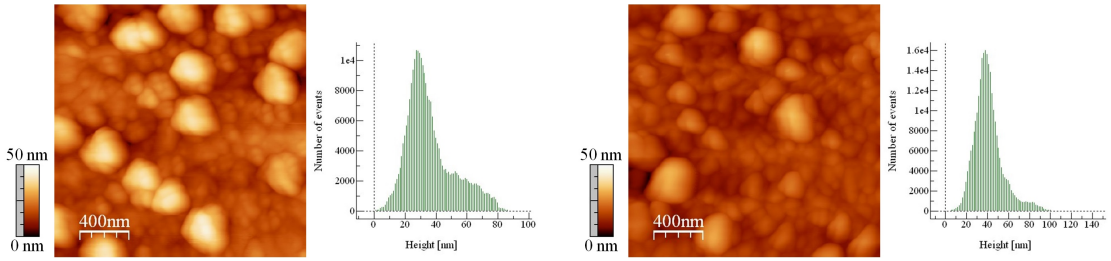


(a) AFM and SE images



(b) R_{rms} values

Figure 7.10: AFM and SE images of the PCO113 films deposited using a substrate temperature between 680°C and 780°C. As substrate temperature increased, average grain sizes increased as did the grain size distribution as the initially regularly shaped grains grew increasingly irregular. At the highest substrate temperature of 780°C, PCO113 film morphology changes significantly: large grains were found interspersed in a background of much smaller and regularly shaped grains. The AFM image showed that these large grains were highly irregular in shape, whereas the SE image showed that these large grains were more regular in shape. SE scale bar = 100 nm.



(a) 740°C (b) 760°C

Figure 7.11: AFM images of the PCO113 films deposited using a substrate temperature of 740°C and 760°C depicting a very different morphology to that in Table 7.10a where the grains were smaller and of a smaller size distribution. The shape of the grain size distribution in these areas of the PCO113 films was very different, with an increased proportion of extremely large grains.

If these large grains were a second phase (corresponding to the reflection at ∼33.0° 2θ, it should not be present in the film deposited at 740°C, as the out-of-plane XRD pattern of this film indicated it to be single phase PCO113. On the other hand, if these large grains were PCO113, it should not be present in the film deposited at 200 mTorr, which XRD pattern suggested that no PCO113 had been deposited. It could be argued that there was actually a trace PCO113 reflection in this film deposited at 200 mTorr. Therefore, it could be suggested that these large grains were the result of PCO113 grain growth. However, they were not detected in any of the PCO113 films where the film thicknesses were varied and much thicker films deposited. The most plausible correlation is that,

if the PCO113 film deposited at 200 mTorr were anomalous, it was the high substrate temperatures used that caused the PCO113 films to take on a different morphology. A higher substrate temperature would facilitate the diffusion of atoms, and thus also the growth of large grains at the expense of the surrounding smaller grains. Based on that, in the interest of depositing a film of uniform grain size and low roughness, high substrate temperatures would not be recommended

Thus, PCO113 films have been successfully deposited at temperatures between 680°C and 780°C. Increasing substrate temperature potentially had the effect of increasing the presence of a secondary phase (the reflection at 33.0° 2θ). AFM images showed a different surface morphology for the PCO113 films deposited at temperatures $\geq$740°C. Extremely large grains were found amidst a background of smaller grains. It was unclear if this change in morphology was the result of the presence of the second phase, or the result of the substrate temperature affecting the grain growth. Regardless, high substrate temperatures should probably be avoided for the deposition of PCO113 thin films. There is still reasonable confidence a deposition at 300 mTorr ρO_2, and substrate temperature of 680°C, as applied by Mehta et al. [297], should result in the successful growth of single phase PCO113 thin films. A final test of this was performed in the following section.

7.3.4 $PrCoO_{3-\delta}/Ce_{0.9}Gd_{0.1}O_{2-\delta}$(polycrystalline) Film

A thick PCO113 film (10000 pulses) was deposited on a polycrystalline CGO substrate. The objective of this deposition was to confirm that single phase PCO113 could be deposited at a substrate temperature of 680°C, and oxygen partial pressure of 300 mTorr. A polycrystalline substrate was used to ensure that the deposited film was without texture so all reflections may be detected to facilitate phase identification. The XRD pattern of this thick PCO113 film on polycrystalline CGO was compared against the XRD pattern of the CGO polycrystalline substrate, and PCO113 target XRD pattern in Fig 7.12.

All reflections of CGO and PCO113 can be seen in the XRD data of the PCO113 film. The PCO113 peak intensities were much lower (some are only just detectable) due to the low PCO113 sample volume, with the exception of the PCO113 reflection at ~33.5° 2θ. The majority intensity comes from the bulk CGO substrate. There appeared to be a slight peak shift of the CGO reflections as compared with the reference pattern of the CGO substrate. This was likely due to a height correction- the CGO substrate was under the PCO113 film. All the PCO113 reflections were present. However, despite being deposited on a polycrystalline substrate that had no preferred orientation, the PCO113 film was highly textured. A disproportionately high intensity was observed at ~33.5° 2θ, compared to the intensities of the other PCO113 reflections. In the XRD pattern of the PCO113 target, the peak at ~23.5° 2θ was a quarter of the maximum intensity of the peak at ~33.5° 2θ. However, for the deposited PCO113 film, only traces of the peak at ~23.5° 2θ may be seen. It was not clear if this was also the case for the peaks at ~41.4° 2θ and ~59.7° 2θ due to their low intensities. Nevertheless, there does appear to have been some

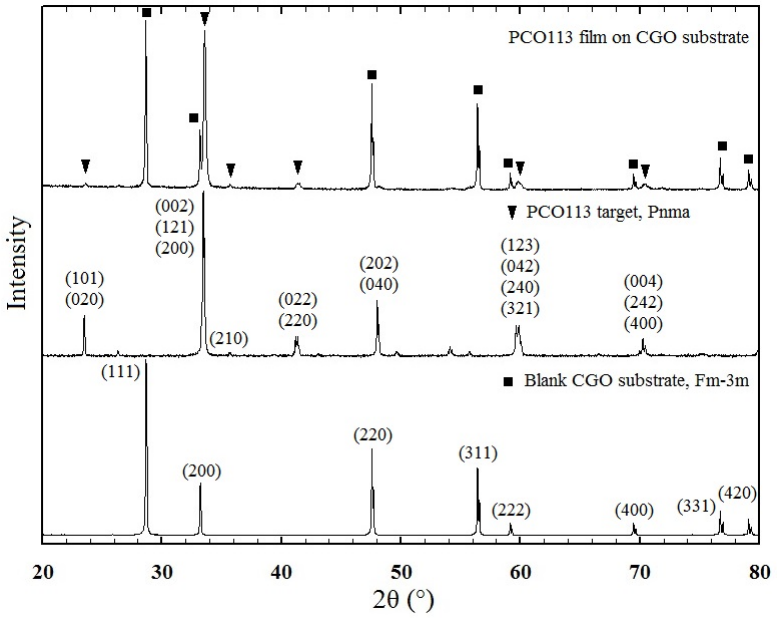


Figure 7.12: XRD patterns of the PCO113 target, CGO polycrystalline substrate, and the PCO113 film deposited upon the CGO polycrystalline substrate using 10000 pulses. Reflections belong to either PCO113 and CGO have been labeled. The XRD pattern showed only the presence of a single PCO113 phase, that may be textured (preference to the (002),(121), or (200) orientations).

texture in the thick PCO113 film deposited with a preference for either the (002), (121) and/or (200) orientations.

Further analysis would be required to confirm any in-plane texture of the thick PCO113 film deposited. However, the objective of this exercise was accomplished: a substrate temperature of 680°C and oxygen partial pressure of 300 mTorr would result in the deposition of single phase PCO113 films.

7.3.5 Repeatability of the PLD of $PrCoO_{3-\delta}$/Si(004) Films

A difficulty in drawing firm conclusions of the effect of oxygen partial pressure, substrate temperature and deposition time on the deposition of PCO113 thin films was the need to assume that all other conditions were kept constant. However, this type of control was not available with PLD. A comparison has been made of three PCO113 films from each data set, deposited under nominally identical conditions: using 3000 pulses, a substrate temperature of 680°C and an oxygen partial pressure of 300 mTorr, in Fig 7.13.

PCO113 has been deposited in all three films. In all cases, images of a flat film with uniform grains and microcracks have been obtained. It appeared that a similar amount of material was deposited between the three films, based on the intensities of the observed reflections. However, while it was absent in the first of the three to be deposited, an unidentified peak was seen in the later PCO13 films at ∼33.0° 2θ coinciding with a decrease in the intensity

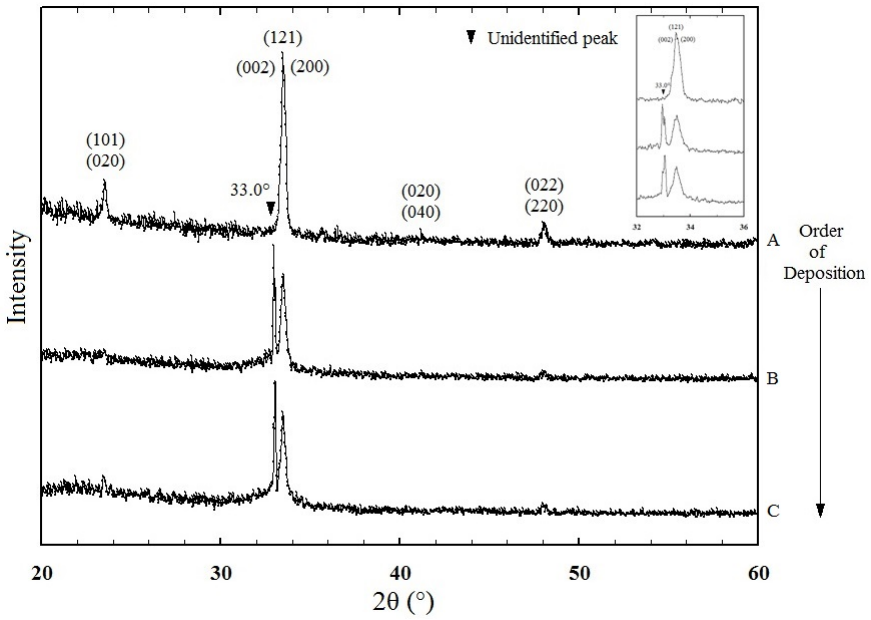


Figure 7.13: A comparison of the out-of-plane XRD patterns of the PCO113 films deposited under nominally identical conditions. PCO113 reflections have been labeled. Film A was the first to be deposited, then film B, and lastly film C. The reflections between 32-34° 2θ have been enlarged. There was one unidentified peak at 33.0° 2θ, the intensity of which increased with PCO113 target damage.

of the PCO113 reflection at ∼33.5° 2θ. The presence of this unidentified phase has been noted as oxygen partial pressure and substrate temperatures were varied. It may be due to the deterioration of the target as it was not detected in initial depositions of varying film thicknesses. The XRD of the PCO113 target post-ablation did show an amorphous region at that 2θ position. Additionally, as the usage of the PCO113 target increased, so too did the intensity of this secondary phase. However, if that were the only explanation, these reflections at ∼33.0° 2θ should be present on all latter films, which it was not.

Other differences between the films are: the degree of the mircrocracks and the grain size, see Table 7.3. In chronological order of deposition, earlier films had larger microcracks and a larger grain size, while later films had smaller microcracks and a smaller grains size. A possible explanation could again be the accumulation of damage of the PCO113 target. For earlier films, when the degree of ablation damage is less, the target surface would have been less amorphised and less dense which would have resulted in a more porous and thicker film for the same amount of material ablated, or a lower deposition rate. This is supported by the reduction in film thickness, under nominally identical deposition conditions, as a function of target usage, see Fig 7.14. Prior to the experiment, an attempt was made to mitigate the effect of accumulating damage by damaging the target first, that any further laser damage would be marginal. This appeared not to have been successful.

Besides the variables within the deposition process itself, PLD is also sensitive to the condition of the target. The composition and morphology of the film was visibly (detectably) affected. Care is required to separate the effect of laser damage on the target

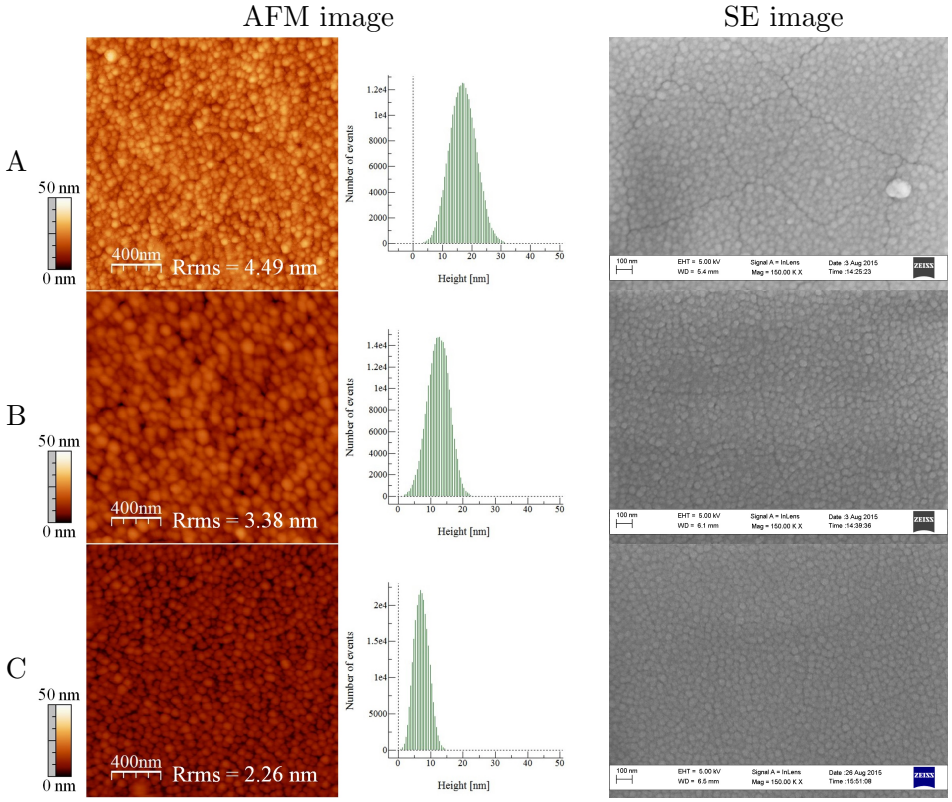


Table 7.3: AFM and SE images of the PCO113 films deposited under nominally identical conditions, in the order of A, B, then C. As PCO113 target damaged increased, the grains of the deposited PCO113 film decreased in average size and size distribution. Also, the occurrence of microcracks in the deposited PCO113 film was reduced. SE scale bar = 100 nm.

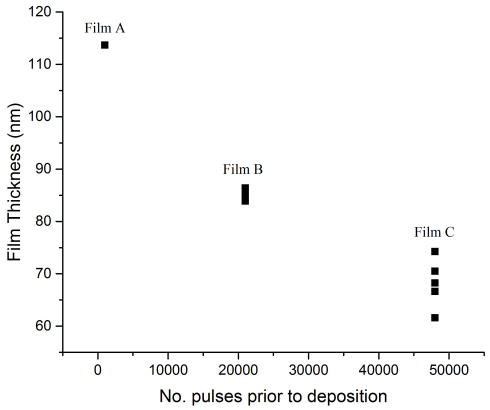


Figure 7.14: Film thickness measurements performed using the Dektak surface profilometer of PCO113 films (A, B, and C, of the same label as in Table 7.3) deposited under nominally identical conditions, as a function of PCO113 target usage (the number of pulses its surface had been ablated with, prior to the deposition of the PCO113 film). As PCo113 target damage increased, the thickness of the depocited PCO113 films decreased. As the intensities of the XRD patterns of Fig 7.13 remained constant despite PCO113 target damage, the decrease in film thickness was likely to be associated with an increase in deposited PCO113 film density with PCo113 target damage.

from the effect of the PLD conditions. Currently, the most feasible conclusion given the inconsistencies in the samples was that the presence of extra reflections about $\sim$33.0° 2θ, potentially an increase in PCO113 film texture, and the decrease in: porosity; grain size; and grain size distribution of the film over time may be ascribed to the accumulation of damage in the PCO113 target. The actual effect of oxygen partial pressure and substrate pressure may only been morphological, rather than compositional. The result of using an oxygen partial pressure below 100 mTorr was the deposition of large, porous and irregularly shaped grains, while the result of using a higher oxygen partial pressure had nominal effects on film morphology. The result of increasing substrate temperature was the enlargement of certain grains at a much faster rate than other and thus a film morphology comprising of a distribution of large grains amidst a background of smaller grains.

7.4 Conclusion and Further Work

Successful deposition of flat films of PCO113 with uniform grains has been performed using a substrate temperature of 680°C and oxygen partial pressure of 300 mTorr. The deposition of a single phase film was confirmed through the deposition of a thick PCO113 film of a polycrystalline CGO substrate using 10000 pulses. Though the CGO substrate had no texture, the resulting PCO113 film was (the cause of this was not identified as the objective of this deposition had been achieved, though it should be investigated in further work).

Film deposition rate was found to be 38 nm/1000 pulses, but decreased with time as ablation damage on the target accumulated. The composition of the PCO113 film appears sensitive to ablation damage, often exhibiting a second unidentified phase with reflections at 32.5° 2θ, 33.0° 2θ and 33.1° 2θ. However, the occurrence of these peaks were intermittent, and not on all latter films. It was unclear why this is the case.

While there has been some inconsistency in the PCO113 films deposited, general trends have been proposed with regards to the effects of oxygen partial pressure and substrate temperature on the morphology of the films. From oxygen partial pressures of 100 mTorr, oxygen partial pressure had little effect on film morphology. However, decreasing oxygen partial pressure below 100 mTorr resulted in porous films with irregularly shaped grains. Increasing substrate temperature increased the presence of large grains against a background of smaller grains (possibly due to the formation of a second phase, or just as the process of PCO113 grain growth).

Difficulty in drawing firm conclusions from these results stemmed from the inability to replicate PLD conditions. A variable that results were highly sensitive to was the condition and history of the PCO113 target. In order to remove this variable and consistently deposit similar PCO113 films, the damaged surface of the target was removed by polishing the target surface until no traces of the ablation damage were visible, prior to each deposition in all later work.

Chapter 8

PLD of $Pr_2NiO_{4\pm\delta}$ and the Isothermal Study of $Pr_2NiO_{4\pm\delta}$

In the previous chapter, polycrystalline $PrCoO_{3-\delta}$, PCO113, films have been successfully deposited on trial single crystal Si(004) substrates using PLD. From XRD patterns, and SE and AFM images, the effect of PCO113 film thickness, oxygen partial pressure and substrate temperature on the structure and morphology of the deposited films were investigated and optimal conditions have been identified. In Chapter 6 (200) oriented $Ce_{0.9}Gd_{0.1}O_{2-\delta}$, CGO(200), buffer layers were deposited on YSZ(001) substrates. Thus, the preliminary work for the deposition of PCO113 on CGO(200)/YSZ(002) has been completed. As one of the objectives of this work is to investigate the ORR at the perovskite/R-P interface, it is also necessary to deposit $Pr_2NiO_{4\pm\delta}$, PNO214, films.

In this chapter, PLD of PNO214 on Si(004) was attempted using a range of substrate temperatures, oxygen partial pressures and film thicknesses. Similar characterisation was performed, as in Chapter 7, using XRD, AFM and SE images. For phase identification purposes, thick polycrystalline films were also deposited on a polycrystalline CGO substrate at different substrate temperatures. Additionally, the stability of PNO14 at 800°C and over long anneal times in atmospheric conditions was investigated instead.

8.1 Literature Review

There are two topics of interest: PLD of PNO214 and the stability of PNO214. To date, there has been no published literature on successful fabrication of pure PNO214 thin films using PLD, whereas Cu and Gd stabilized variants of PNO214, $Pr_2(Ni,Cu,Ga)O_{4+\delta}$ or PNCG have been reported. Thus, the properties of PNCG have been briefly covered and the motivation for the synthesis of PNCG thin films due to the transport path of oxide ion through the R-structure, and then consequently the PLD of PNCG films. High

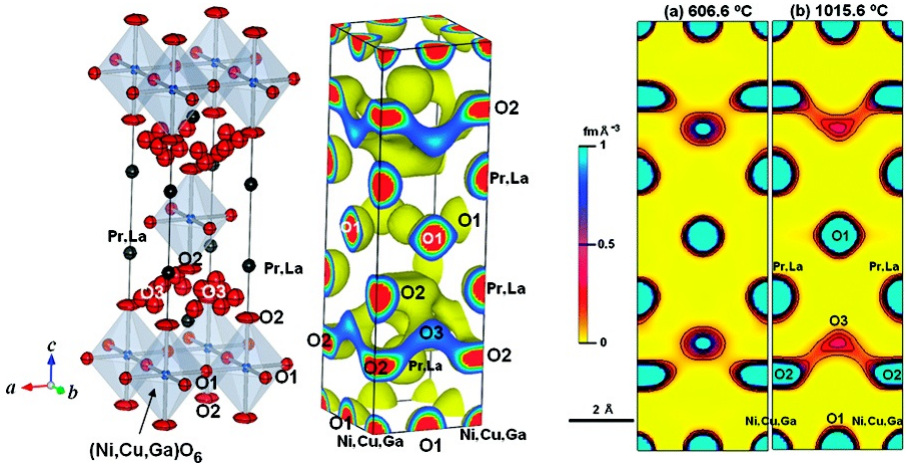


Figure 8.1: Nuclear density analysis from neutron diffraction data measured in situ at 1015.6°C indicated the two-dimensional network of curves O2-O3-O2 oxide-ion diffusion paths on the (Pr,La)-O layer in PLNCG [45].

temperature instability of PNO214 has been observed in two key studies by Odier et al. and Kovalevskty [47, 48]. These works were also reviewed.

8.1.1 $Pr_2(Ni,Cu,Ga)O_{4+\delta}$

Ruddlesden-Popper, R-P, oxides of the K_2NiF_4 structure, such as those based on PNO214, have been found to exhibit high level of oxygen hyper-stoichiometry and have been investigated as potential new MIECs for intermediate temperature applications [142, 148]. Bulk oxide-ion diffusion pathways of these materials have been proposed to be along the rocksalt-type AO layers [218, 136, 139, 142]. In 2008, high temperature neutron diffraction studies were used to characterise the structure of $(Pr_{0.9}La_{0.1})_2(Ni_{0.74}Cu_{0.21}Ga_{0.05})O_{4+d}$, PLNCG. by Yashima et al [45]. In the Rietveld refinement performed, the interstitial excess oxygen (labeled O3) was identified at 16n sites. It also revealed highly anisotropic thermal motion of the apical oxygen atoms (labeled O2) at the 4e site, promoting diffusion between the O2 and interstitial O3 sites and thus confirming the oxygen diffusion path way proposed and the reliance on an interstitial oxygen population for oxygen transport, see Fig 8.1. Consideration of the nuclear density distribution of the O2-O3 diffusion path also suggested the use of larger A-site cation dopants, and higher valence A and B cations to increase the interstitial O3 atoms population and thus improve diffusion, as has indeed been found of the metal cation access doping of Ga [339].

The study in 2008 showed an enlargement of the O2-O3 diffusion path with temperature. Furthering this work, Yashima et al observed a bottle-neck effect along the oxygen diffusion path where nuclear density was at a minimum, which could be correlated with oxygen conductivity [156]. As temperature increased, so too did the nuclear density along the O2-O3 path and oxygen conductivity. A notable outcome was that the activation energy of oxygen diffusion at the bottle neck was calculated from the nuclear density and found

to be very low (12 kJ/mol), suggesting high oxide ion conductivity in single crystals or epitaxial thin films [156]. This prompted the move to thin film deposition.

In a final work on PNCG in 2012, it was shown that oxygen conductivity may be correlated to the oxygen probability density at the bottle neck for diffusion, ρ_N, where ρ_N is a function of the formation energy of oxygen atoms (basically its migration energy) at the bottleneck, E_N, the temperature, and the population of interstitial O3 atoms [340]. As ρ_N was found to be relatively independent of temperature and E_N, it was the change in interstitial O3 concentration that predominantly affected oxygen conductivity; oxygen conductivity was proportional to the concentration of oxygen interstitials. Through consideration of the O2-O3-O2 diffusion pathway, the interstitial diffusion mechanism was identified to be the interstitialcy mechanism [340]. The higher mobility of oxygen on the apical O2 site may be attributed to the longer covalent bond between O2 and its neighbouring cations (Ni, Cu, Ga) as compared to that of the equatorial O1. The higher mobility of oxygen on the interstitial O3 site is due to its lower coordination of 4, instead of 6 for O1 and O2.

The use of La-dopants in all prior work was to stabilize the high temperature PNO214 I4/mmm structure as PNO214 was found to decompose at high temperatures into the higher order RP phase (3rd order $Pr_4Ni_3O_{10}$, PNO4310) and Pr oxide [47, 48], which had the effect of lowering oxygen transport [156]. However, in this latest work, high temperature neutron and synchrotron X-ray diffraction found the PNCG system to be stable up to 1011°C [340] and the successful deposition of PNCG thin films by PLD was reported.

8.1.2 PLD of $Pr_2(Ni,Cu,Ga)O_{4+\delta}$

PLD of polycrystalline PNCG films 100nm to 1000nm thick by PLD was first performed by Ishihara et al [341]. Deposition conditions of all reported films have been tabulated in Table 8.1. Despite the polycrystalline substrate, the PNCG film showed a preference for the (004) out-of-plane orientation. This was likely due to the similarity in dimensions of the c-lattice length of PNCG (12.538 Å) and three of the cubic unit cells of MgO (12.633 Å). This preference decreased as PNCG film thickness increased. A light broadening and shift of the PNO peak suggested the presence of a lattice strain. Chemical analysis using EDX and WDX showed a homogeneous composition across the film that was almost identical to that of the PLD target, regardless of film thickness. From SEM images, the film was found to be uniform and flat, with no cracks or delaminations. However, from the XRD measurements, a single reflection around 46° 2θ was present in the 100 nm thick PNCG film only. This was attributed to Pr_6O_{11}, though a match on the basis of a single reflection is uncertain. Nevertheless, it does raise concerns of the possibility of using PLD for the deposition of very thin PNCG films. No mention of the observation of a second phase using EDX or SEM images was made. It may be that the Pr_6O_{11} formed the immediate layer at the MgO substrate, after which PNCG deposited. It may also be related to the change in oxidation state of Pr (and Ni) seen in the thinnest film.

Film	Substrate	Laser Fluence (mJ/pulse)	Pulse Rate (Hz)	Substrate Temperature (°C)	Oxygen Partial Pressure (mTorr)	Reference
PNCG	MgO	180	10	800	5	[341]
PNCG	MgO	180	10	800	0.7	[46]
LNO214	$SrTiO_3$			780	100	[342]
LNO214	$SrTiO_3$		10	600-800	75	[343]
	SiO_2					
	Si(111)					
	Si(001)					
	Pt(1111)					
LNO214	YDC		10	850	23	[344]
LNO214	$SrTiO_3$(001)		8	700-780	250	[345]
	$NdGaO_3$(001)					
LNO214	MgO(001)			650	7.5	[346]
	$SrTiO_3$(001)					
LNO214	CGO/YSZ(001)	45	10	650	50	[171]

Table 8.1: Table of the different deposition conditions used in literature for the PLD of PNCG and LNO214, where a KrF excimer laser (λ = 248 nm) was employed.

Following this, Hyodo et al published several works on PNCG thin films, all fabricated using the same conditions as detailed in Table 8.1 [46, 347, 348]. Laminated films were deposited made up of alternating layers of Sm-doped {CeO_2, SDC, and PNCG, starting with SDC, on a MgO polycrystalline substrate. The laminated structure was chemically and structurally analyzed using EDX, SIMS, and XRD. Cross-sectional SEM images were also obtained, see Fig 8.2. The results indicated that the PNCG layers were single phase, at least within detection limits, sharing the same composition as the target material and with the same preferential orientation as observed by Ishihara et al [314]. The layers were uniform, flat and dense, with good contacts with between the layers, and little diffusion of cations between the interfaces [46].

Hyodo et al varied the thicknesses of the SDC layers, and the PNCG layers to investigate their effect on electrical conductivity. It was seen that increasing the PNCG layer thicknesses increased electrical conductivity, while increasing SDC layers decreased electrical conductivity, especially at lower temperatures, and increased ρO_2 dependence [46]. Following on from that the Hebb-Wagner ion blocking method was employed to measure the oxide ion conductivity and electronic conductivity of PNCG/SDC laminated films and comparisons made against bulk values [347]. The effect of the lamination was to supress the electronic conductivity of PNCG/SDC due to decreased interstitial oxygen in the rock salt block layer. At low ρO_2, a depletion layer also formed at the PNCG/SDC layer further inhibiting electronic conductivity. On the other hand, a high oxide ion conductivity was measured (even higher than LSGM [349]).

In his latest work, Hyodo et al deposited PNCG film interspersed with Au particles by PLD [348]. The presence of the Au particles imparted a tensile lattice strain to the PNCG

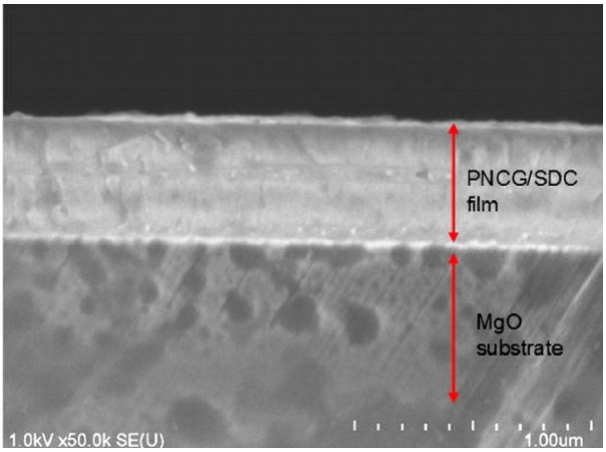


Figure 8.2: SE image of the PNCG/SDC laminated film with 100 nm thickness for each layer [46].

at high temperatures due to the difference in their TEC. This stabilized the oxidized stated of PNCG, increasing hole concentration and thus improving electronic conductivity even though hole mobility was reduced. XRD analysis indicated single phase PNCG was deposited; no traces of Pr_6O_{11} were detected.

On both accounts, deposition of PNCG was performed at a high substrate temperature of 800°C, and an extremely low ρO_2 $\leq$5 mTorr. The in-house PLD equipment does not allow for substrate temperatures to reach 800°C, and has difficulty maintaining a stable oxygen partial pressure of 10 mTorr during deposition. PLD conditions of the closely related LNO214 system were considered, see Table 8.1. The PLD of LNO214 appears less sensitive to deposition conditions, and has been successfully deposited through a large range of substrate temperature (650 to 850°C) and oxygen partial pressures ($\sim$7.5 to 260 mTorr)[341, 46, 342, 343, 344, 345, 346, 171]. Thus, the deposition conditions tested in this chapter are a range of oxygen partial pressures between 5 and 500 mTorr, at a substrate temperature of 780°C, and a range of substrate temperatures between 700°C and 780°C, at an oxygen partial pressure of 300 mTorr. Lastly, due to the results of Ishihara et al wherein decomposition products were only observed in the thinnest PNCG film, a range of PNO214 film thicknesses were also deposited.

8.1.3 High Temperature Stability of $Pr_2NiO_{4\pm\delta}$

TGA has been performed on a powdered PNO214 between the temperature range of 200 to 1200°C (300 °C/h ramp) under oxygen flow (30 l/hr) by Odier et al. [47]. The results, see Fig 8.3, showed that upon heating from 200 to 850°C, the oxygen hyperstoichiometry, δ, decreased at a constant rate. At 850°C, a sharp increase in δ was observed, which plateaued at 1020°C with d more than twice its original value. Further heating to 1150°C resulted in a decrease in δ, at the same rate by which it increased, so that by 1200°C it had returned to its original value if extrapolated from 850°C.

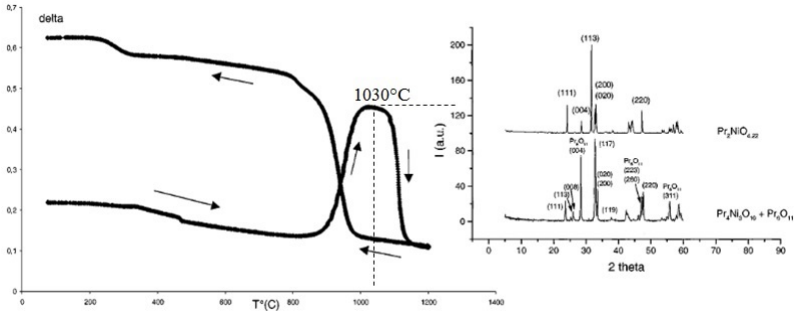


Figure 8.3: Oxygen stoichiometry versus temperature in PN214, and the XRD pattern of single phase PNO214 prior to heat treatment, and a PNO214 sample quenched from 1030°C under oxygen flow which had decomposed into PNO4310 and PrO_y [47].

The increase in oxygen excess is due to the oxidative decomposition of PNO214 into high order R-Ps: $Pr_3Ni_2O_7$, PNO327, or $Pr_4Ni_3O_{10}$, PNO4310. It is known that the reduction of the LNO4310 system results in the progressive removal of apical oxygen and subsequently a transformation from LNO4310 (T, when the apical oxygen is present) to LNO439 (T*) to LNO438 (T′, when the apical oxygen has been removed). Applying this to the current PNO214 system and taking into account the equilibrium composition of PrO_y as described by Hyde et al's work on the PrO system, it is suggested that at 850°C PNO439 and $2PrO_{1.76}$ are formed. Thus, as the temperature increases to approximately 1000°C, $PrO_{1.76}$ oxidises to form the alpha phase, $PrO_{1.8}$ (stable above 900°C), and PNO439 oxidises to PNO439.75 (PNO4310-δ), resulting in the weight gain observed. This is supported by XRD results of PNO214, heated to 1030°C then quenched, which indicated that the oxidative decomposition of PNO214 results in the formation of an oxygen deficient PNO4310 and a Pr oxide, see Fig 8.3.

As the temperature increases further, the PrO1.8 alpha phase reverts to the $PrO_{1.6}$ omega phase. Similarly, the R-P PNO439.75 phase also lost oxygen until it returned to PNO439. In a separate study, Kovalevksy et al. also obtained an XRD of a PNO214 sample at 1200°C, after δ had fallen back down to its original value, see Fig 8.4. It showed that the powder had indeed returned back to single phase PNO214 albeit with traces of Pr_6O_{11}, the removal of which was kinetically limited by the slow cation diffusion [48]. On cooling the sample back down from 1200°C, at temperatures below 1000°C, the oxidative decomposition occurred again forming PNO439.75 and $PrO_{1.8}$. This time, the oxidation was irreversible.

This reasoning is supported by resistivity measurements between 0 to 1200°C [47], see Fig 8.5. PNO4310 has a high electronic conductivity (it has metallic electrical resistivity). As expected, under identical conditions as for the TGA measurement, a drop in the resistivity was seen where the presence of PNO4310 is presumed. This is due to the formation of a percolated PNO4310 network in the compound [47]. Odier et al observed that this oxidative decomposition was highly dependent on the oxygen partial pressure (oxygen flow rate) and that increasing the oxygen partial pressure would not only decrease the onset temperature for the reaction but also increase the extent of oxygen uptake.

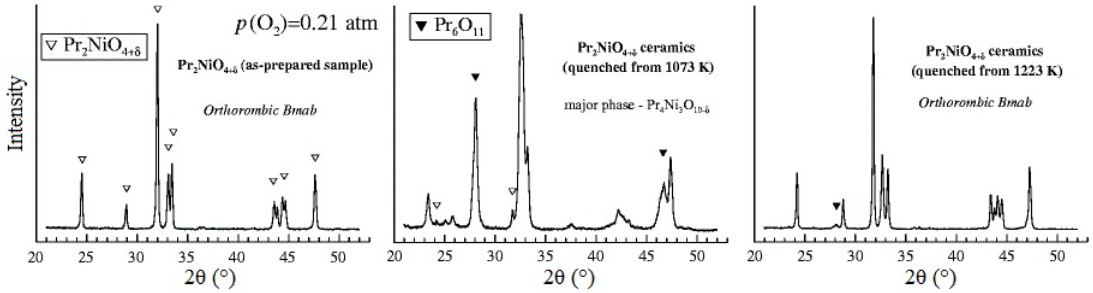


Figure 8.4: XRD patterns of (from left to right): a reference PNO214 sample; PNO214 quenched after annealing in air at 800°C for 50 h; and PNO214 quenched after annealing in air at 1000°C for 24 h [48].

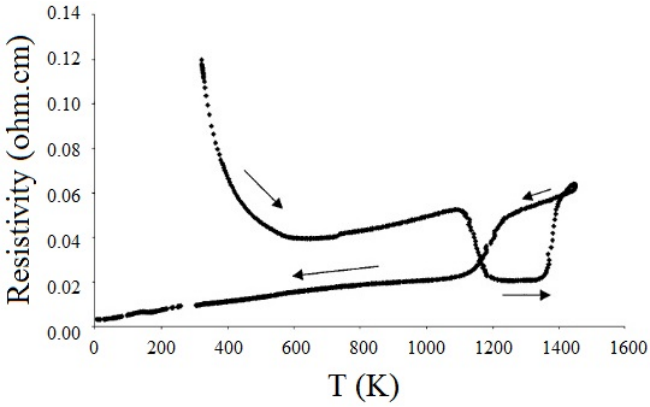


Figure 8.5: $In-situ$ measurements of the resistivity versus temperature of PNO214 under the same conditions as in Fig 8.3 by Odier et al [47]

These TGA results for the heating run are replicated in a separate study by Kovalevsky et al, as well as the conductivity measurements during cooling, both of which support the formation of PNO4310 and PrO_y during the oxidative decomposition [48]. Kovalevsky et al also performed a dilatometric study of PNO214 between 30 to 1400K, at a heating rate of 3 K/min and oxygen partial pressure of 0.21 atm, see Fig 8.6. Up until around 1000 K, PNO214 has a near constant TEC in the range of 13.0-13.6$\times 10^{-6}$ K^{-1}. On the onset of the oxidative decomposition, a volume expansion can be seen (increase in TEC) due to the oxygen uptake and decomposition. As the temperature increased and the process reverses, there was a volume contraction (negative TEC) before it resumed a TEC close to that pre-decomposition, in the range of 12.9-13.3$\times 10^{-6}$ K^{-1}.

It should be noted that, in literature, this phase separation was not observed in as-prepared PNO214, but only when it was subject to further heat treatment. Kovalevsky et al prepared PNO214 powder using the glycine-nitrate process. The resulting ash was further calcined in air at 927 to 1077°C for 2 h to remove any remaining organics, before being sintered in air at 1100 to 1300°C 3 to 5 h, in order to obtain samples of 95-98% density. Both calcination and sintering processes were at sufficiently high temperatures for oxidative decomposition to occur. However, XRD on these samples revealed single phase orthorhombic Bmab PNO214, with unit cell parameters: a=5.3934(1)Å, b=5.4564(1)Å,

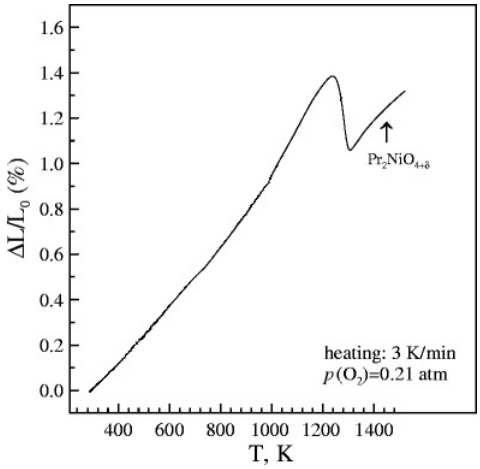


Figure 8.6: Dilatometric curve of PNO214 on heating in air [48].

c=12.4479(2)Å. This would explain why earlier studies [294, 101] on as-prepared PNO214 powders showed no indication of its instability at high temperatures and high oxygen partial pressures. This instability of PNO214 may prevent its deposition as a single phase PNO214 film by PLD.

8.2 Experimental Method

The experimental method of this chapter with regards to the deposition, structural and morphological analysis of the thin films deposited on Si(001) substrate is identical to that of PCO113 thin films examined in Chap 7. The same range of substrate temperatures and oxygen partial pressures were investigated, in line with deposition parameters reported in literature. Films of varying thicknesses were also deposited at an oxygen partial pressure of 300 mTorr, and substrate temperature of 780°C.

As in Chap 7 out-of-plane XRD patterns, between 15 and 60° 2θ, were obtained for all of the deposited thin films on the Si substrate. As zero-corrections were within instrument error, no zero-corrections were made to the 2θ positions. All patterns have been corrected for their background intensities. Film thickness measurements were performed using the Dektak150 and AFM images obtained using the Bruker DiInnova.

In order to obtain more diffraction peaks from which the deposited films may be better identified, thicker films were also deposited on CGO polycrystalline substrates (characterised in Chap 6) using 10000 pulses at an oxygen partial pressure of 300 mTorr. Substrate temperatures between 680 to 780°C were used. XRD patterns of these films were measured using the two in-house Bruker D2 Phaser instruments. It was thus necessary to correct for shifts in the peak positions between the two instruments, and also background intensity. For better comparison, peak intensities were scaled to the intensity of the CGO(111) reflection at ∼28.7° 2θ. AFM images were also taken of the surface of these thick films using the Bruker DiInnova.

To study the stability of PNO214, PNO214 powder samples were annealed at 800°C in air for 3 to 36 h. Following the anneal, the samples were quenched in order to retain their high temperature phases. The decomposition of PNO214 has been shown to be reversible on cooling [48]. XRD patterns were taken of the sample using the two in-house Bruker instruments. All patterns presented have been scaled according to background intensities. Rietveld refinements were performed on the PNO samples annealed between 3hr and 12 hr in air in order to determine phase fractions (%) present. Two phase fits, cubic $Fm\bar{3}m$ Pr_6O_{11} and orthrombic $Fmmm$ PNO214 were used for the samples annealed for 3 h and 6 h. In the sample annealed for 12 h, traces of PNO4310 were detected, and a three phase fit was used that included orthorhombic $Fmmm$ PNO4310. All shape and asymmetry parameters were refined separately.

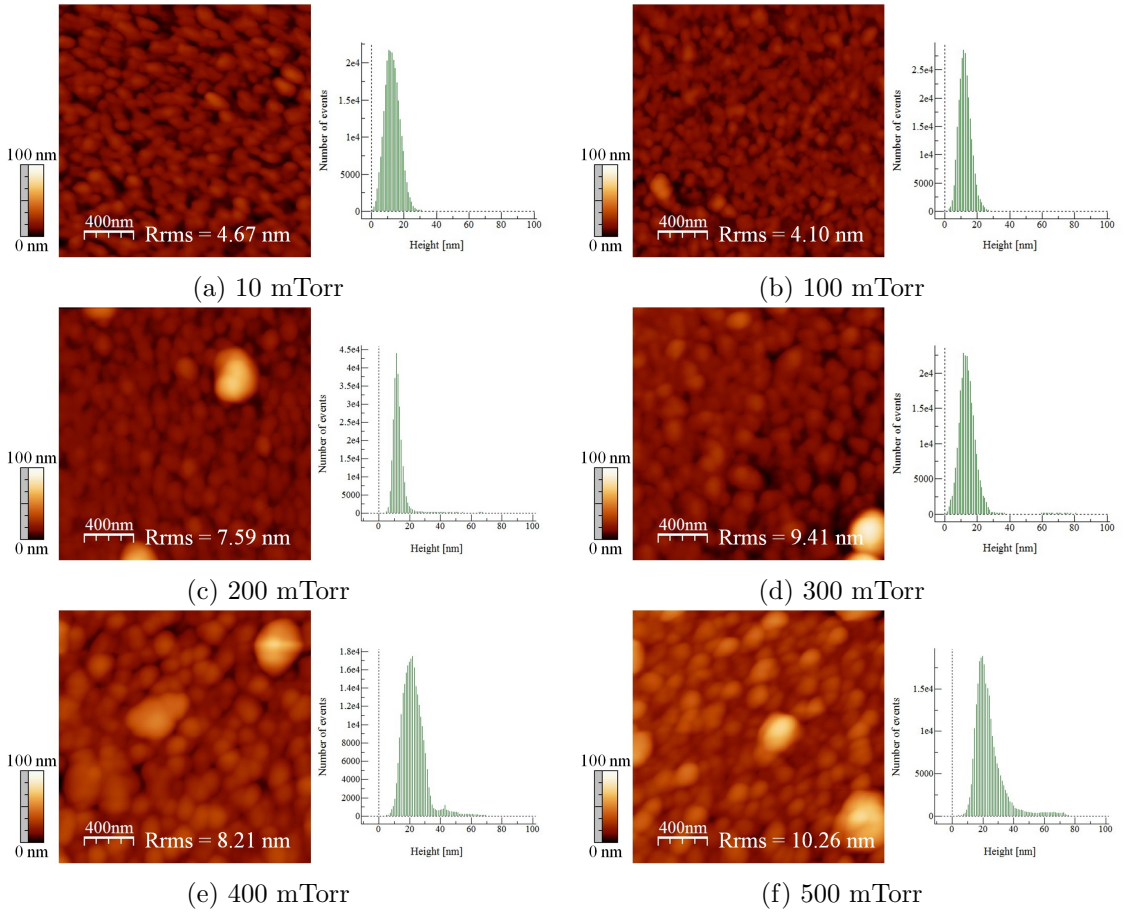
8.3 Results and Discussion

8.3.1 PLD of $Pr_2NiO_{4\pm\delta}$

AFM images of the PNO214 films deposited under varying PLD conditions, and their measured thicknesses, are depicted in Figs 8.7, 8.8, 8.9 and 6.7, respectively. The deposition rate at an oxygen partial pressure of 300 mTorr and substrate temperature of 780°C was ∼45.6 nm/1000 pulses. At low film thicknesses, the film comprised of uniform sized and regularly shaped grains. As film thickness increased, disproportionately large grains were increasingly observed and with it a corresponding increase in RSM roughness of the film. On increasing oxygen partial pressure during PLD, deposition rate increased- for the same number of pulses, film thicknesses were larger when deposited at higher oxygen partial pressure. The increase in film thickness was again associated with the presence of large grains. There appears to be little other effect oxygen partial pressure on the morphology of the deposited films and no secondary phases were observed. Several of the films imaged using AFM had large grains interspersed against a background of smaller grains, similar to the morphology found in PCO113 films deposited at higher substrate temperatures, see Section 7.3.3. However, this appeared to occur at random for the films deposited between a range of oxygen partial pressure and film thicknesses. This morphology was not found of the films deposited over a range of substrate temperatures.

The film morphology obtained when varying the substrate temperature during deposition remained mostly unchanged besides a slight coarsening of the grains. This was reflected in the increase in RMS roughness as substrate temperature increased. There did not appear to be any clear trend between film thicknesses and substrate temperature, and it seemed that these deposited films were sufficiently thin that the formation of large grains on its surface had not yet begun.

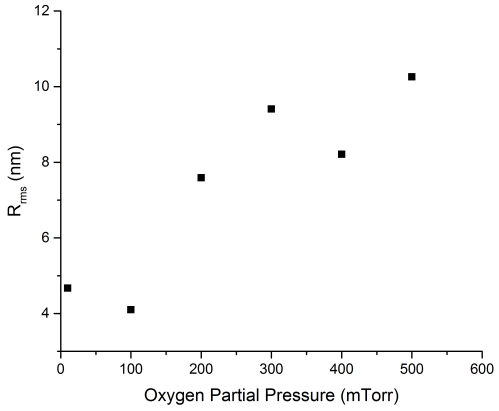
The thin film deposited using 3000 pulses at an oxygen partial pressure of 300 mTorr and substrate temperature of 780°C appears to be irregularly thin, see Fig 8.10. This comparison was true between films deposited using a range of oxygen partial pressures,



(a) 10 mTorr (b) 100 mTorr

(c) 200 mTorr (d) 300 mTorr

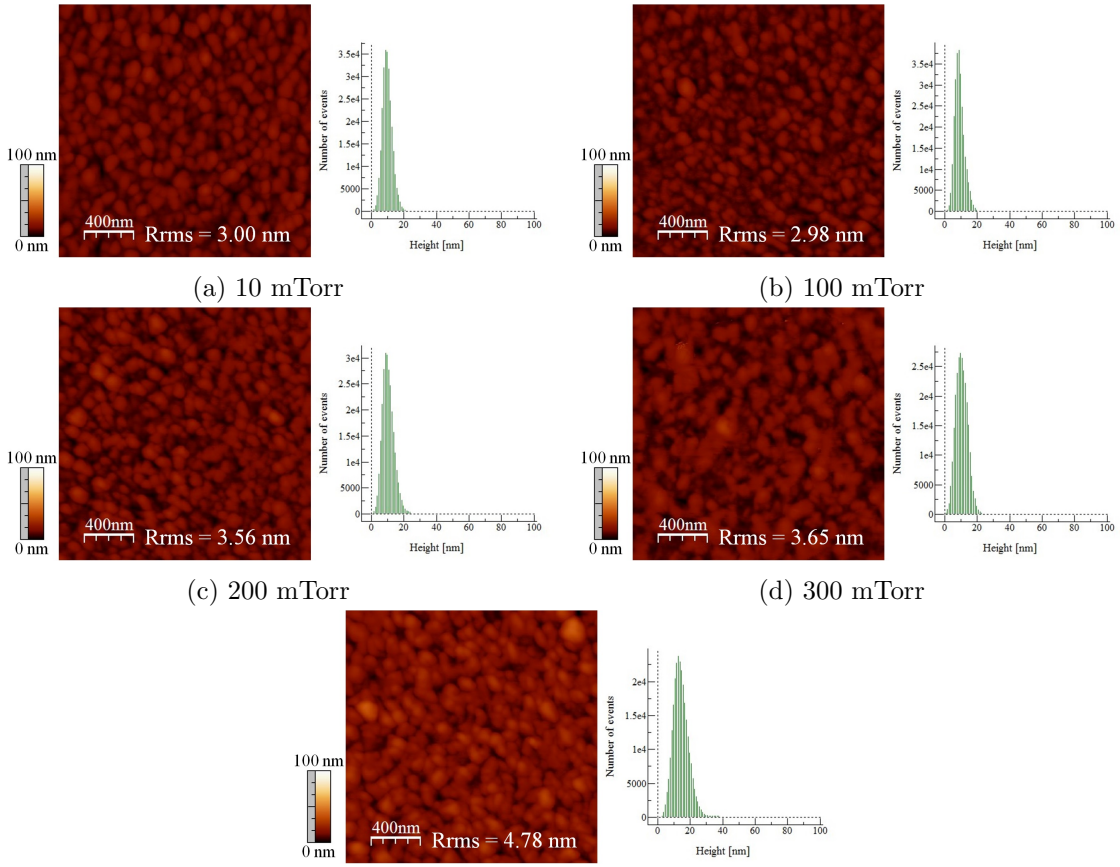
(e) 400 mTorr (f) 500 mTorr



(g) R_{rms}

Figure 8.7: AFM images and the measured R_{rms} of PNO214 films deposited using a range of oxygen partial pressures, at a substrate temperature of 780°C and 3000 laser pulses.

and deposition times. Taking an average of thin films deposited using 3000 pulses at an oxygen partial pressure of 300 mTorr over a range of substrate temperatures, it should be of a thickness ∼128 nm, which is more in keeping with the deposition rate calculated, instead of the 78.7 nm it was measured to be. Nevertheless, the morphology of these films appear promising. No cracks or delaminations were observed that would undermine film



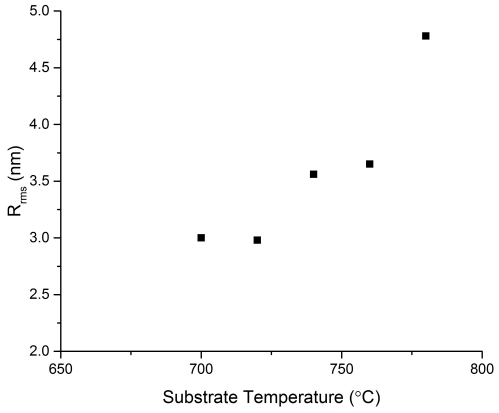
(a) 10 mTorr

(b) 100 mTorr

(c) 200 mTorr

(d) 300 mTorr

(e) 400 mTorr

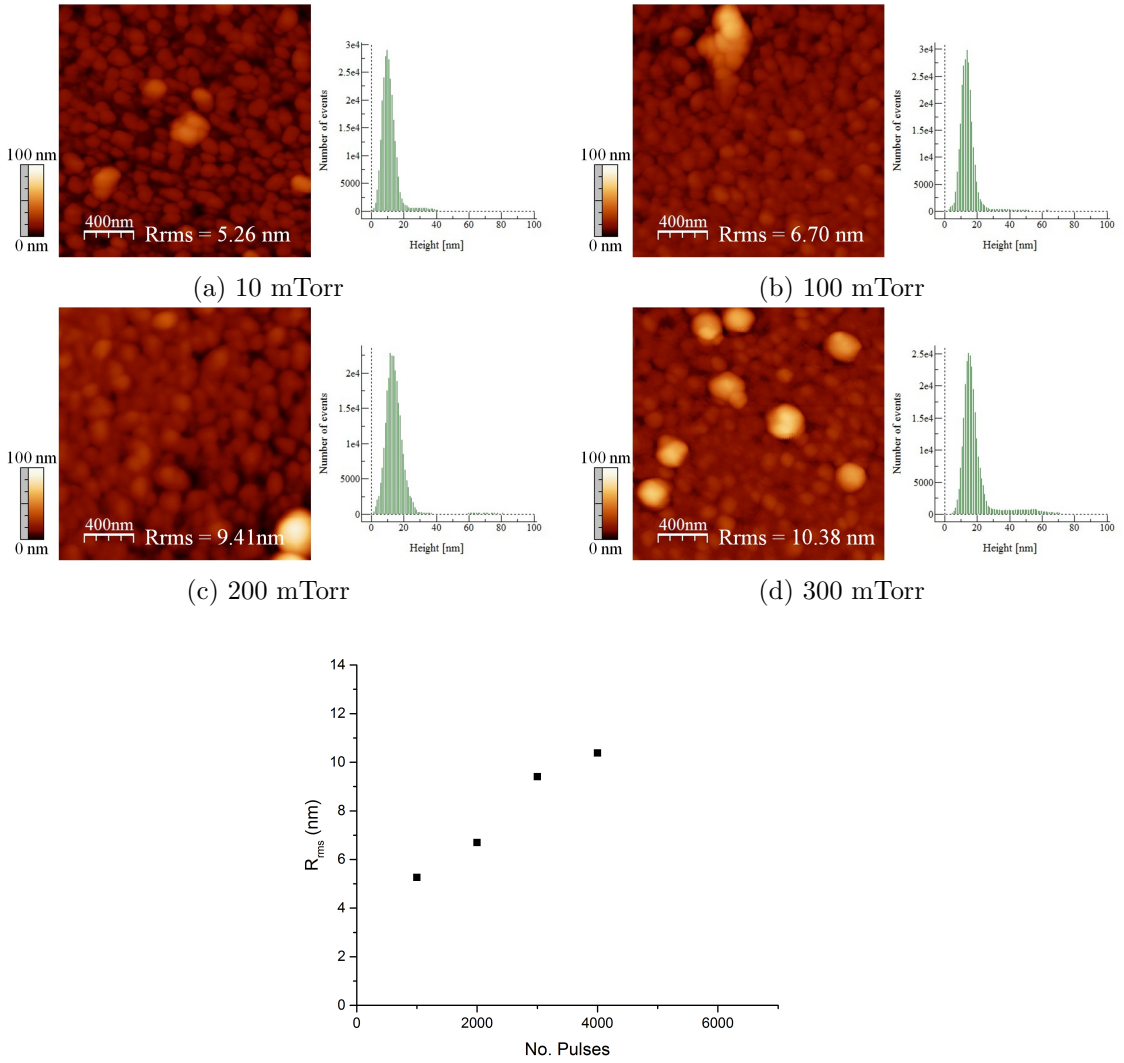


(f) R_{rms}

Figure 8.8: AFM images and the measured R_{rms} of PNO214 films deposited using a range of substrate temperatures, at an oxygen partial pressure of 300 mTorr and 3000 laser pulses.

performance in an SOFC device.

Out-of-plane XRD patterns of the thin films, deposited at oxygen partial pressures between 5 mTorr and 500 mTorr are presented in Fig 8.11. There were very few reflections present.



(a) 10 mTorr

(b) 100 mTorr

(c) 200 mTorr

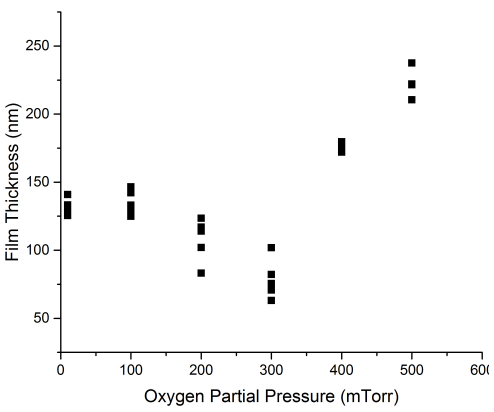
(d) 300 mTorr

(e) R_{rms}

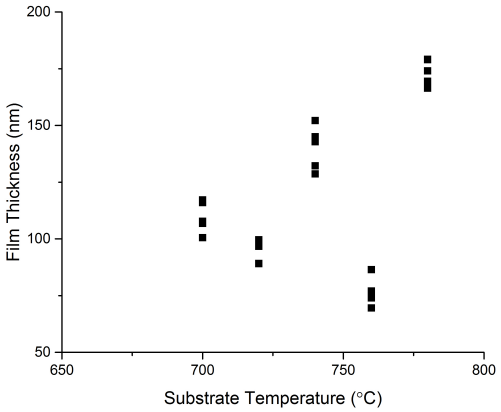
Figure 8.9: AFM images and the measured R_{rms} of PNO214 films deposited using a range of laser pulses, at a substrate temperature of 780°C and an oxygen partial pressure of 300 mTorr.

It was unclear if this was due to low signal for the thin films, or if it was the result of texture in the film due to the use of a single crystal substrate. If the first, then the reflections may be matched using only the highest intensity reflections of a powder diffraction pattern; identification of the deposited film is possible. If it is the latter, identification of the deposited film would not be possible. The unit cell parameters of PNO214 and known decomposition product of PNO214 at high temperatures, Pr_6O_{11} and PNO4310 [48, 47] along with the Si substrate are listed in Table 8.2. The mismatch between the a and b parameters of the Pr oxides and the Si substrate is small. Thus there may be preference to the [001] family of orientations in the Pr oxides.

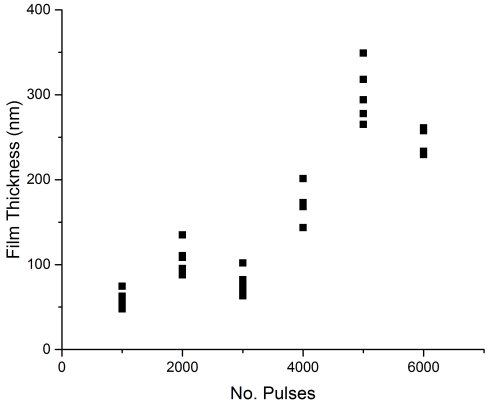
From the out-of-plane diffraction pattern of all the thin films, there are two main reflections at ∼28.3° 2θ and ∼33.0° 2θ, and three other trace reflections at ∼44.3° 2θ, ∼47.4°



(a) Oxygen partial pressure



(b) Substrate temperature



(c) Number of laser pulses

Figure 8.10: Film thickness measurements as functions of: (a) oxygen partial pressure; (b) substrate temperature; (c) number of laser pulses. Excluding the deposition parameter being varied, PLD was performed at an oxygen partial pressure of 300 mTorr, substrate temperature of 780°C, and using 3000 laser pulses. A deposition rate of ∼45.6 nm/1000 pulses was measured (at an oxygen partial pressure of 300 mTorr and substrate temperature of 780°C). Increasing oxygen partial pressure appeared to increase the deposition rate. There was no clear trend between the deposited film thickness and the substrate temperature.

2θ and ∼58.7° 2θ. The reflections of potentially deposited phases- NiO, Pr_6O_{11}, $PrNiO_3$, PCO113, PNO214 and PNO4310 are provided in Table 8.3. The first of the two main reflections at ∼28.3° 2θ has been matched to the 100% intensity (111) reflection of cubic Pr_6O_{11}, and the trace reflections at ∼58.7° 2θ to its second order (222) reflection, though intensities are lower than expected. The second main reflection at ∼33.0° 2θ- the same position as the unidentified peak in Chapter 7 during the PLD of PCO113. For the nickleate series, this peak may be matched to a multitude of reflections belonging to the PNO113, PNO214 or PNO4310 phases: the 99.0% intensity PNO113(110) reflection (32.79° 2θ), the 100.0% intensity PNO113(104) reflection (33.24° 2θ), the 34.9% intensity PNO214(200)

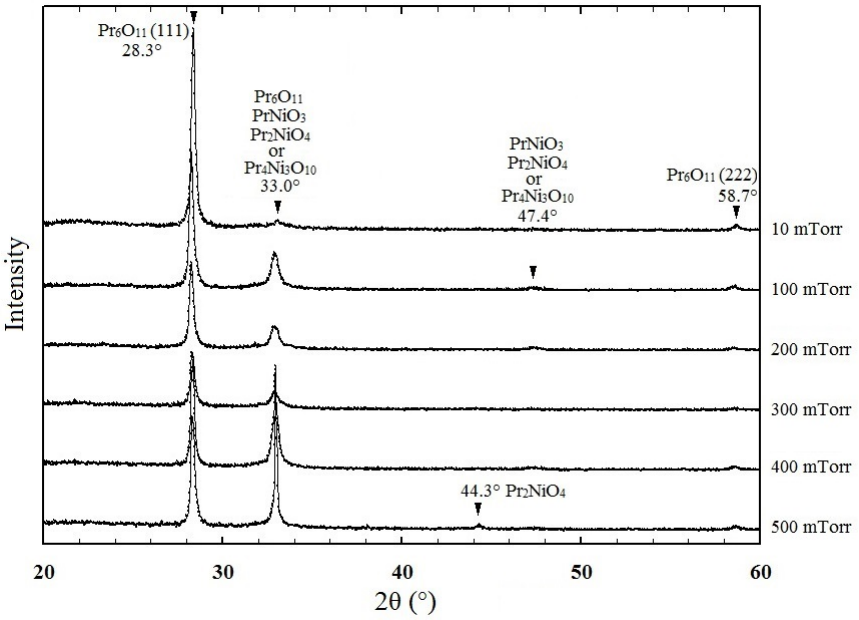


Figure 8.11: Out-of-plane XRD patterns of the films deposited at an oxygen partial pressure between 10 and 500 mTorr. Where possible, reflections have been labeled. The film contains Pr_6O_{11}, the proportion of which increases with oxygen partial pressure. A second phase was present. Due to the few reflections, it was unclear if it was PNO113, PNO214 or PNO4310. There was one unidentified reflection at ∼44.3° 2θ that could not be matched to Pr_6O_{11}, PNO113, PNO214 or PNO4310.

Composition	Crystal Structure and Spacegroup	Cell Parameters	Reference
Si	Cubic $F\bar{4}3m$	a = b = c = 5.3920 Å	[350]
Pr_6O_{11}	Cubic $Fm\bar{3}m$	a = b = c = 5.4678 Å	[4]
$PrNiO_3$	Rhombohedral $R\bar{3}c$	a = b = 5.4582 Å c = 13.1061 Å	[351]
Pr_2NiO_4	Orthorhombic $Fmmm$	a = 5.4568 Å b = 5.3929 Å c = 12.4464 Å	[299]
$Pr_4Ni_3O_{9.85}$	Orthorhombic $Fmmm$	a = 5.3700 Å b = 5.4620 Å c = 27.5280 Å	[5]
NiO	Cubic $Fm3m$	a = b = c = 4.1769 Å	[320]

Table 8.2: Table of crystal structures and spacegroups of potential phases deposited in the ablation of PNO214. The lattice parameter of the Si wafer was been included, the mismatch in lattice parameters between Si and Pr_6O_{11}, PCO113, PNO214 or PNO4310 (the a- and b- parameters) is small.

reflection (32.80° 2θ), the 33.7% intensity PNO214(020) reflection (33.20° 2θ), the 100% intensity PNO4310(117) reflection (32.62° 2θ), or the 48.0% intensity PNO4310(200) reflection (33.36° 2θ). Of the two remaining trace peaks, the peak at ∼44.3° 2θ matches only with the 7.3% intensity PNO214(006) reflection. The intensity of this reflection increased with decreasing oxygen partial pressure, the same as was found for the reflection at ∼33.0° 2θ. It may be that these two reflections belong to the same phase. If this is true, PNO214 must have been deposited as PNO4310 does not have any reflections at ∼44.3° 2θ. Similarly, the peak at ∼47.4° 2θ may equally belong to PNO113(024), PNO214(220), or PNO4310(220). The intensity of this peak was too low to observe any trends in intensity with oxygen partial pressure. Another possibility was that the reflection at ∼33.0° 2θ belongs to the Pr_6O_{11}(200) diffracting planes. In this case, the variation in oxygen partial pressures affects the orientation of the deposited Pr_6O_{11} film. As the oxygen partial pressure does in part determine the energy of the ablated material, and therefore would affect its growth, this would be a plausible occurrence.

Pr_6O_{11} was almost definitively present. That being the case, NiO or Pr- nickelate perovskite or R-P oxide must also be present if target stoichiometry was maintained. Identification of this second phase based on the trace reflections at ∼44.3° 2θ, ∼47.4° 2θ and ∼58.7° 2θ was not clear. On the one hand, PNO214 was the better fit based on peak position and the presence of a trace peak at ∼44.3° 2θ that was only detected when intensity of the main peak at ∼33.0° 2θ was at its highest. However, this presumes a preference for the PNO214(200) orientation while consideration of the PNO214 and Si cell parameters suggests that any preference should be for the long axis to be normal to the film surface- the (001) orientation. On the other hand, based on the intensities of reflections in a powder diffraction pattern, it seems more likely that PNO113 or PNO4310 has been deposited. The PNO113(104) and PNO4310(117) reflections were the highest intensity reflection of the powder diffraction, and thus most likely to be observed. Also the second trace peak at ∼47.4° 2θ may also be matched to another high intensity reflection for PNO113 or PNO4310: the 68.0% intensity PNO113(024) reflection or the 49.0% intensity reflection of PNO4310(220). Whereas this reflection would be much lower for PNO214, at 26.9% intensity for the PNO214(220) reflection. If this peak at ∼44.3° 2θ did correspond to PNO4310, there would be a substantial 0.4° 2θ peak shift at the ∼33.0° 2θ reflection (if this may even be matched to PNO4310) that needs to be accounted for that was not present at ∼47.4° 2θ. Thus, there was a good possibility that the deposited film comprised of two phases: Pr_6O_{11} and PNO113. However, the presence of Pr_6O_{11} suggests that PNO4310 was present, as Pr_6O_{11} and PNO4310 are known decomposition products of PNO214 [47, 48]. From these diffraction patterns alone, it was not possible to ascertain this definitively. Future references to the second phase preset in the film are as belonging to the PNO4310 phase of the R-P phase.

The oxygen partial pressure during deposition appeared to alter the proportion of Pr_6O_{11} and R-P phase present: decreasing oxygen partial pressure increased the intensity of the Pr_6O_{11} reflection while it decreased the intensity of the R-P reflection. If the proportions of these phase were changing, it must imply that the oxygen partial pressure affected the

(a) Pr_6O_{11} [4]

h	k	l	d (Å)	2θ (°)	I (%)
1	1	1	3.15650	28.250	100.0
2	0	0	2.76640	32.740	28.0
2	2	0	1.93200	46.995	30.0
3	1	1	1.64870	55.708	24.0

(b) NiO [320]

h	k	l	d (Å)	2θ (°)	I (%)
1	1	1	2.41000	37.281	91.0
2	0	0	2.76640	43.298	100.0

(c) $PrNiO_3$ [351]

h	k	l	d (Å)	2θ (°)	I (%)
0	1	2	3.8335	23.184	31.0
1	1	0	2.7288	32.793	99.0
1	0	4	2.6928	33.244	100.0
2	0	2	22.2232	40.543	28.0
0	0	6	21.1845	41.295	9.0
0	2	4	1.9168	47.389	68.0
1	2	2	1.7237	53.089	9.0
1	1	6	1.7054	53.704	8.0
3	0	0	1.5756	58.536	26.0
2	1	4	1.5688	58.816	49.0
0	1	8	1.5479	59.688	18.0

(d) Pr_2NiO_4 [299]

h	k	l	d (Å)	2θ (°)	I (%)
1	1	1	3.66560	24.261	30.3
0	0	4	3.1160	28.666	14.8
1	1	3	2.8164	31.745	100.0
2	0	0	2.72835	32.799	34.9
0	2	0	2.69646	33.198	33.7
1	1	5	2.08810	43.296	11.4
0	0	6	2.07440	43.596	9.1
2	0	4	2.05143	44.110	13.7
0	2	4	2.03777	44.421	13.5
2	2	0	1.91786	47.362	26.9
2	2	4	1.63265	56.304	7.0
1	1	7	1.61317	57.045	8.5
3	1	3	1.59163	57.890	13.5
1	3	3	1.57890	58.402	13.0

(e) $Pr_4Ni_3O_{9.85}$ [5]

h	k	l	d (Å)	2θ (°)	I (%)
1	1	1	3.6656	24.261	30.3
0	0	4	3.1116	28.666	14.8
1	1	3	2.8165	31.745	100.0
2	0	0	2.7283	32.799	34.9
0	2	0	2.6965	33.198	33.7
1	1	5	2.0881	43.296	11.4
0	0	6	2.0744	43.596	9.1
2	0	4	2.0514	44.110	13.7
0	2	4	2.0378	443421	13.5
2	2	0	1.9179	47.362	26.9
2	2	4	.16327	56.304	7.0
1	1	7	1.6132	57.045	8.5
3	1	3	1.5789	57.890	13.5
1	3	3	1.5789	58.402	13.0

Table 8.3: Miller indices and peak positions between 20 and 60° 2θ for: (a) NiO; (b) Pr_6O_{11}; (c) $PrNiO_3$; (d) Pr_2NiO_4; and (e)$Pr_4Ni_3O_{9.85}$. Only reflections with an intensity $\geq$5% were shown.

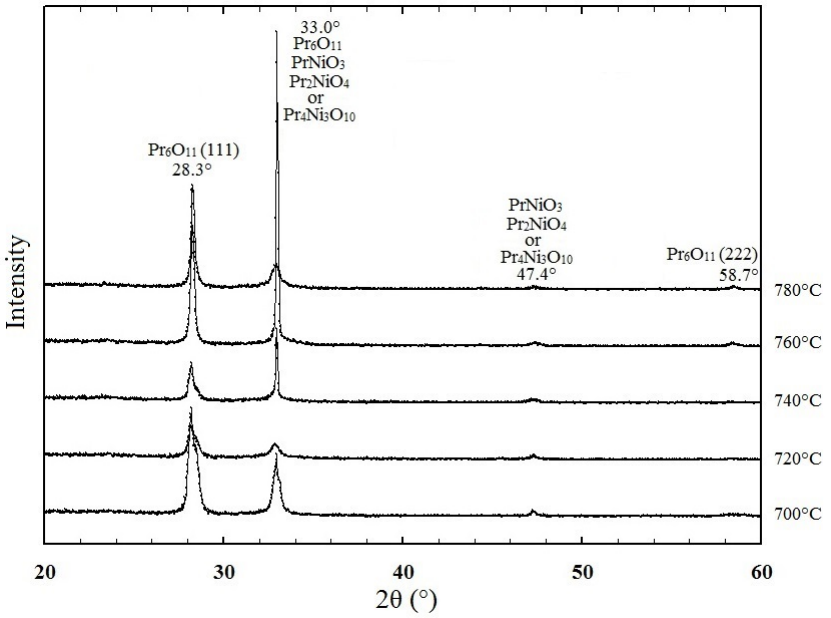


Figure 8.12: Out-of-plane XRD patterns of the films deposited using a substrate temperature between 700 and 780°C. Where possible, reflections have been labeled. The film contains Pr_6O_{11}, the proportion of which increases with substrate temperature. A second phase was present. Due to the few reflections, it was unclear if it was PNO113, PNO214 or PNO4310. There was one unidentified reflection at ∼44.3° 2θ that could not be matched to Pr_6O_{11}, PNO113, PNO214 or PNO4310.

Pr:Ni ratio of the film. A possible explanation is that at the lower oxygen partial pressures, Ni volatilized and the Ni content of the deposited film was reduced. Thus, at the lowest oxygen partial pressure used (10 mTorr), almost all the Ni had volatilized resulting in a film that consisted predominantly of Pr_6O_{11}, hence the absence of the R-P reflection. As oxygen partial pressure increased, eventually the Pr:Ni ratio of the target was reached, and the ratio of Pr_6O_{11} to R-P phase also stabilised.

Out-of-plane XRD patterns of the thin films, deposited at a substrate temperature between 700 and 780°C are presented in Fig 8.12. The same four reflections were observed when substrate temperature was varied, as when oxygen partial pressure was varied. Additionally, the ratio of peak intensity between the Pr_6O_{11} reflection and the R-P reflection varied with substrate temperature. However, unlike with oxygen partial pressure, there was no clear trend in the proportion of Pr_6O_{11} and PNO4310 present. At a substrate temperature of 780°C, 720°C and 700°C, the ratio of peak intensity at ∼28.3° 2θ and ∼33.0° 2θ were roughly constant with the Pr_6O_{11} reflection being of greater intensity. However, at a substrate temperature of 740°C, and especially at 760°C, the area under the PNO4310 reflection was larger than that of the Pr_6O_{11} reflection. Another notable feature was that at a substrate temperature of 700°C, both Pr_6O_{11} and PNO4310 reflections have started to split. The cause for this was unclear and the identity of the second phase remains debatable.

Lastly, the instance where film thickness was increased was investigated, see Fig 8.13. In

the work of Ishihara et al decomposition products (Pr_6O_{11}) were only observed in the thinnest PNCG film (100 nm) deposited via PLD. XRD patterns of thicker PNCG films from 217 nm upwards, showed no traces of the Pr_6O_{11}. It was of interest to see if those results may be replicated with the films deposited in this work. Films of thicknesses between ∼57.7 nm and ∼300.1 nm were deposited. This was within the range of film thicknesses where Pr_6O_{11} was no longer detected by Ishihara et al, [314]. The XRD patterns of the deposited films have the same four reflections as seen when oxygen partial pressure and substrate temperature were varied. Pr_6O_{11} and R-P phases were detected in all films deposited, though at varying ratios to each other. For the films deposited using more than 2000 pulses, there may be a general trend where increasing film thickness decreased the ratio of Pr_6O_{11} present, as was observed by Ishihara et al. Thus, increasing film thickness may further reduce the presence of Pr_6O_{11}.

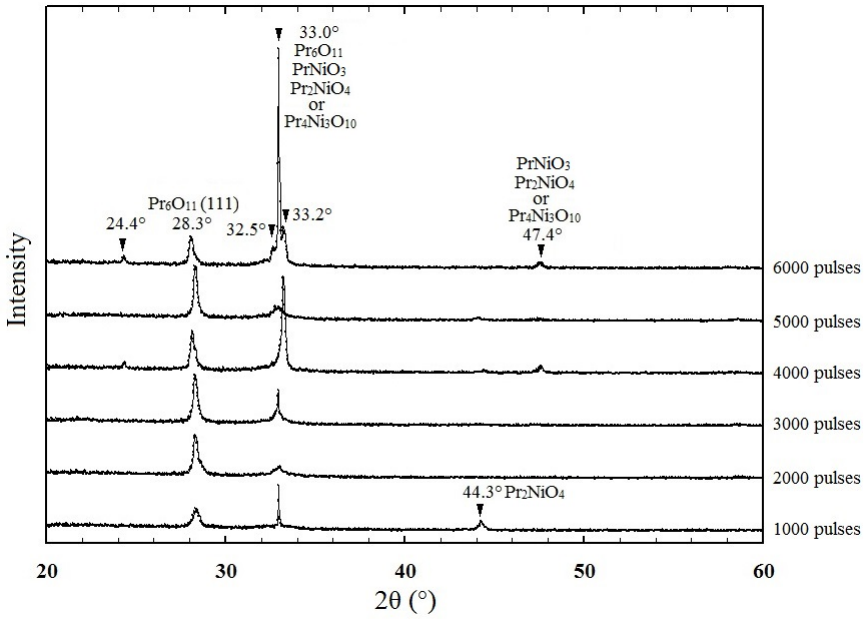


Figure 8.13: Out-of-plane XRD patterns of the films deposited using 1000 to 6000 pulses. Where possible, reflections have been labeled. The film contains Pr_6O_{11}, the proportion of which increases with substrate temperature. A second phase was present. The thickest film showed three additional peaks not found of the thinner film: at ∼24.4° 2θ, ∼32.5° 2θ and ∼33.2° 2θ It was still not possible to identify the phase(s) present as PNO113, PNO214 and PNO4310 all have reflections around those 2θ values. The peak at ∼24.4° 2θ could not be matched.

As film thickness increased, the main Pr_6O_{11} peak shifted to a lower 2θ position to ∼28.1° 2θ from ∼28.3° 2θ. Three additional reflections were detected that had not been seen in any of the films deposited earlier in this chapter. Two of these new reflections were close to the main R-P-reflection at ∼33.0° 2θ: at ∼32.5° 2θ and∼33.2° 2θ. This triple peak around ∼33.0° 2θ was also found of a PCO113 film in Chapter 7, and could not be identified on that occasion. Even with the detection of these peaks, the identity of the second phase or whether a third phase was present remains ambiguous. PNO113 and PNO4310 both have two reflections that may match the additional two reflections found.

For both these phases, the relative peak intensities of the two peaks do not match that of the powder diffraction pattern, but that may be due to texturing. For this case, the peak at ∼33.0° 2θ must belong to either Pr_6O_{11} or PNO214. Alternatively, PNO214 also has three reflections that may match all three reflections found between ∼32.5° 2θ and ∼33.5° 2θ (again the relative intensities of these three detected peaks to not conform to that of the powder diffraction pattern, which may be attributed to texturing). A myriad of different possibilities still exist with regards to the phases present in the deposited film. It could be that just PNO214 and Pr_6O_{11} was deposited, or with any amount of a PNO113 or PNO4310 third phase. The nature of the thin film samples has meant that it has not been possible to identify which, between these structurally similar phases, were the phases deposited using out-of-plane XRD only.

The third additional reflection was at ∼24.4° 2θ. No matches could be found for this reflection. There was also an increase in intensity of the peak at ∼47.6° 2θ for some of the thicker films, compared to earlier depositions of PNO214, when oxygen partial pressure and substrate temperatures were varied. Lastly, for the thinnest film, a distinct reflection was also seen at ∼44.3° 2θ- the same as that for the film deposited at an oxygen partial pressure of 10 mTorr for which the only match would be PNO214. It was possible that traces of PNO214 were deposited, along with Pr_6O_{11} and PNO4310.

From the XRD patterns, there was confidence that Pr_6O_{11} had always been deposited throughout the range of deposition conditions employed in this work and R-P phases are likely to be present, though given the limited diffraction peaks, it has not been possible to determine of which order, or if both first and third order phases are present. No single phase films were deposited. In order to identify the deposited films, much thicker films were subsequently deposited using 10000 pulses, and on a polycrystalline CGO substrate to remove the occurrence of texturing. A range of substrate temperatures was used to clarify the effect of substrate temperature on deposited film. Film thicknesses of these films were measured, see Fig 8.18. It is arguable that there was a trend between film thickness and substrate temperatures. However, a comparison with the film thicknesses obtained at different substrate temperatures for the films deposited using 3000 pulses suggests that there is no trend. AFM images have also been obtained of deposited films, see Fig 8.15, showing the same morphology as the thinner films, except rougher with a larger average grain size and grain size distribution. These thicker films were also more porous, and had crevices in the film surface.

XRD patterns were also obtained of the thick films deposited using 10000 pulses. The reflections corresponding to the film can be seen superimposed on top of the CGO diffraction pattern Fig 8.16. For these thicker films, the full diffraction patterns of Pr_6O_{11} and NiO (at much lower intensities) were present. There appeared to be a slight texture in the deposited film, with the Pr_6O_{11}(111) reflection having a suppressed intensity in some of the samples. There were no indications of the R-P phases detected in the thinner films; while the main peak of the R-P phases may have been concealed by the Pr_6O_{11}(200) reflection as ∼32.7° 2θ, the remainder of the diffraction pattern should be present in this

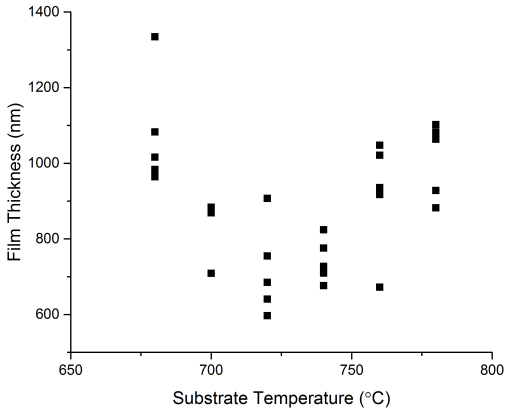


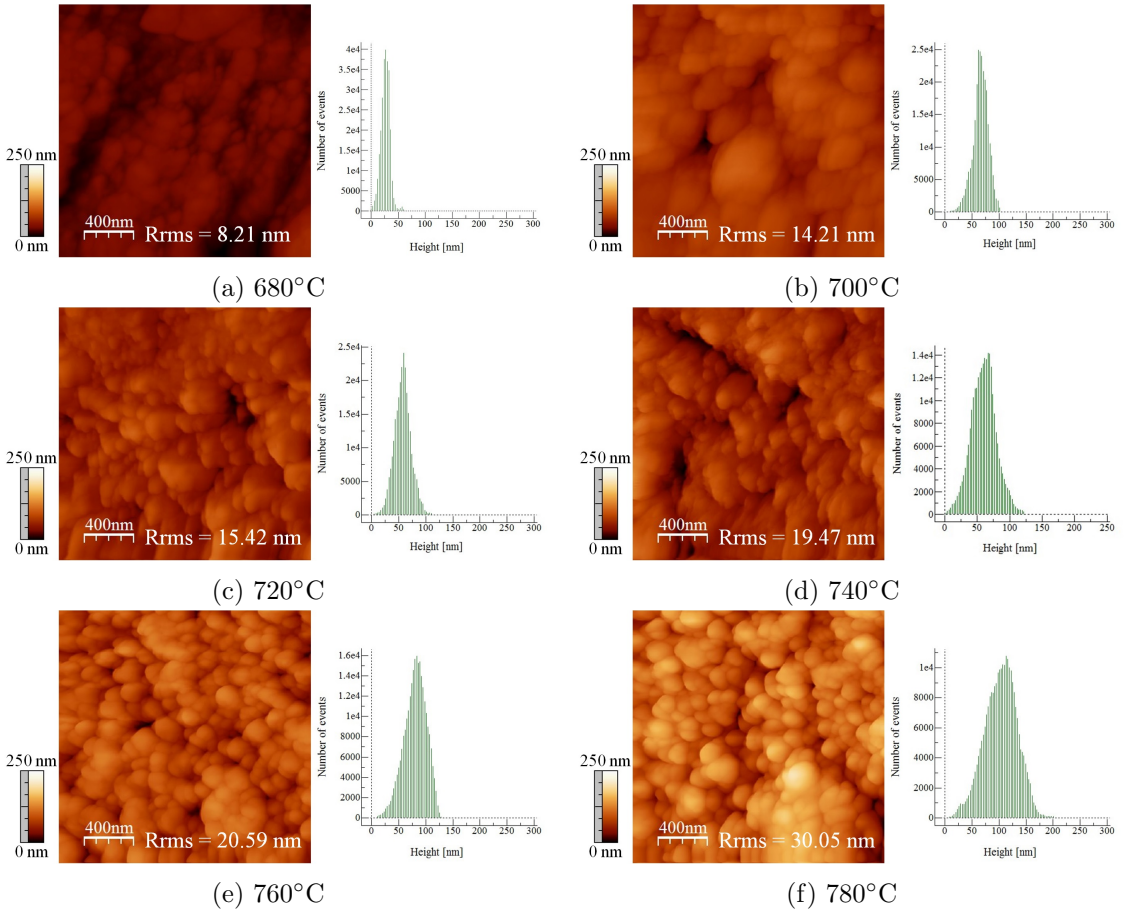
Figure 8.14: Film thickness measurements by the Dektak surface profilometer of films deposited on a polycrystalline CGO substrate using 10000 pulses, an oxygen partial pressure of 300 mTorr and a substrate temperature between 680°C and 780°C. It was unclear if there was a trend between deposition rate (nm) or substrate temperature. Comparisons with the films deposited under identical conditions but using 3000 pulses suggests there was not.

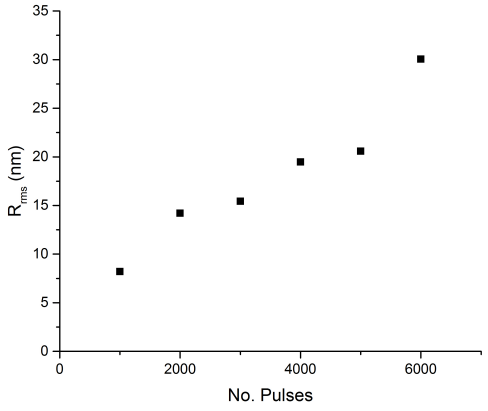
polycrystalline film. Increasing the substrate temperature had the overall effect of increasing film diffraction pattern intensity (the increase in film thickness as measured using the Dektak surface profilometer was not due to an increase in porosity but to the deposition of more material), and affecting the texture of the Pr_6O_{11} component of the film. It was unclear the reason why at substrate temperatures of 760°C, 740°C, and 720°C, the main Pr_6O_{11}(111) reflection is of a lower intensity than the (200) reflection. No evidence was found for the deposition of PNO113, PNO214 or PNO4310.

It has not been possible to fabricate single phase PNO214 films using the deposition conditions trialled in this work, despite reports of the deposition on PNCG using similar conditions in literature. In the thinner films deposited on Si, the PNO214 degraded into Pr_6O_{11} and praseodymium nickelate oxide(s) (it was not possible to identify which, whether perovskite or R-P). In the thicker films deposited on polycrystalline CGO, the deposited film was clearly found to be polycrystalline Pr_6O_{11} and NiO. The introduction of Cu and Ga dopants in PNCG appears to stabilise its high temperature structure, allowing for its successful deposition using PLD. The stability of PNO214 will now be further investigated.

8.3.2 Isothermal Study of $Pr_2NiO_{4\pm\delta}$ at 800°C in Air

The instability of PNO214 has been reported at temperatures above 900°C in air. The unsuccessful PLD of PNO214 suggests that PNO214 is unstable even at 700°C, at low oxygen partial pressures. Subsequently, single phase PNO214 powders have been annealed at 800°C in air, for different durations and quenched to retain the high temperature





(g) R_{rms}

Figure 8.15: AFM images and measured R_{rms} of PNO214 films deposited on a polycrystalline CGO substrate using 10000 pulses, an oxygen partial pressure of 300 mTorr and a substrate temperature between 680°C and 780°C. A similar porous morphology was found of all the films, no secondary phases could be distinguished.

structure of the powder and prevent any possible recombination or decomposition products as it cooled. XRD patterns of these powders are presented in Fig 8.17. A reference pattern is provided of the PNO214 powder that was not annealed- its starting structure. Even

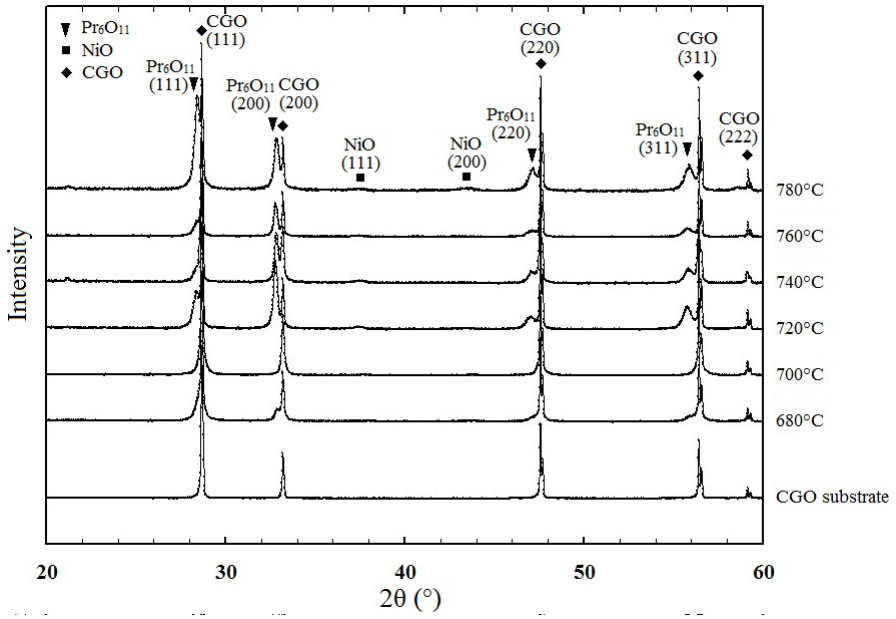


Figure 8.16: Out-of-plane XRD patterns of the films deposited on a polycrystalline CGO substrate using 10000 pulses, an oxygen partial pressure of 300 mTorr and a substrate temperature between 680°C and 780°C. Regardless of substrate temperature, the deposited film comprised of two phases: Pr_6O_{11} and NiO. Increasing the substrate temperature appeared to increase the amount of film deposited, as seen through the increase in the film peak intensities and also the film thickness measurements, and also the relative intensities of the Pr_6O_{11} reflections.

only after annealing for 3 h at 800°C, trace Pr_6O_{11} peaks may be detected. These grow in intensity as the anneal time increases. No traces of other secondary phases are detected for anneal times up to 12 h. However, upon annealing for 24 h, only trace amounts of PNO214 remains; the highest intensity (113) reflection at ∼31.7° 2θ had all but vanished. The powder was predominantly Pr_6O_{11} and PNO4310; the entire pattern of both may be seen. Increasing the anneal time did not have any further effect. To date, this is the first work on the kinetics of the thermal decomposition of PNO214.

A Rietveld refinement was performed on the powder patterns to quantify the proportion of Pr_6O_{11} formed and the rate of decomposition. This is plotted in Fig 8.18. The patterns and the accuracy of the fits may be found in Appendix A.2. Pr_6O_{11} was the first phase to segregate out. At 6 h anneal time, no traces of PNO4310 was detected. The presence of Pr_6O_{11} without PNO4310 could be due to the oxygen hyper-stoichiometric nature of PNO214 and its ability to effectively accommodate excess B-site cations. However, at 12 h anneal time, with the formation of PNO4310, the rate of decomposition appeared to accelerate. It may be that the PNO4310 phase acted as a catalyst for the decomposition. There was a large decrease in the proportion of PNO214 present, mostly offset by a large increase in the fraction of PNO4310. The fraction of Pr_6O_{11} remained small and PNO4310 became the dominant phase. This time dependency suggests that the oxidative decomposition of PNO214 was kinetically restrained and also facilitated by the presence of PNO4310.

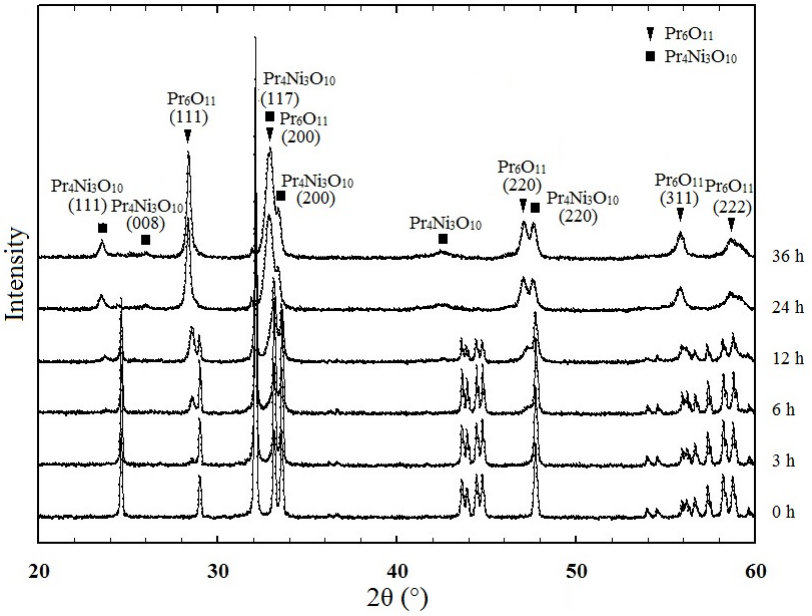


Figure 8.17: XRD patterns of PNO214 powder following different anneal times at 800°C in air. As the heat treatment progressed, increasing amounts of Pr_6O_{11} and PNO4310 was detected, similar to the oxidative decomposition of PNO214 reported in literature [47, 48].

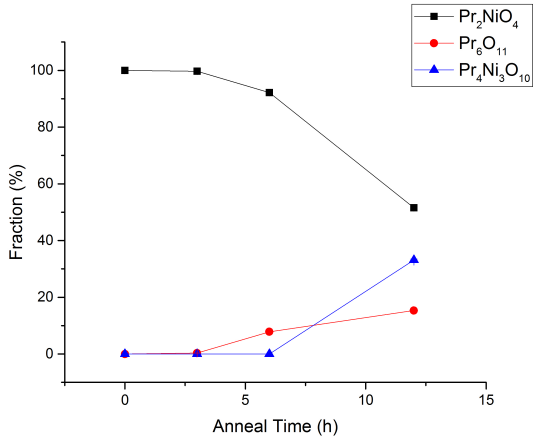


Figure 8.18: Fraction of Pr_6O_{11}, PNO214 and PNO4310 present in the heat treated PNO214 (at 800°C in air) as a function of anneal time.

To better understand the evolution of the structure as Pr_6O_{11} forms, the lattice parameters of the phases have been collated in Table 8.4. Atomic positions and occupancies (besides Pr) could not be refined and have been defined according to standardized crystal structure data from ICSD. Any bond-lengths or bond-angles calculated from the refinement, especially of the low intensity patterns for the minority phases, have been considered unreliable and have not been presented.

Throughout the anneal, Pr_6O_{11} maintained a constant lattice parameter ~5.473 Å, suggesting that its oxygen hypo-stoichiometry remained constant. This lattice parameter was

Anneal Time (h)	Pr_2NiO_4, $Fmmm$			Pr_6O_{11}, $Fm\bar{3}m$	$Pr_4Ni_3O_{10}$, $Fmmm$		
	a	b	c	a = b = c	a	b	c
0	5.461(1)	5.396(1)	12.462(3)				
3	5.458(1)	5.391(1)	12.455(2)	5.474(8)			
6	5.454(1)	5.390(1)	12.458(2)	5.472(5)			
12	5.4560(1)	5.390(1)	12.462(3)	5.473(2)	5.393(1)	5.44(12)	27.35(50)
Reference	5.393	5.455	12.446	5.468	5.415	5.465	27.959

Table 8.4: Table of refined cell parameters of the phases present as a function of PNO214 anneal time (at 800°C in air). Included are reference cell parameters for PNO214 [3], Pr_6O_{11} [4], and PNO4310 [5].

substantially larger than the reference Pr_6O_{11} lattice parameter, suggesting a different oxygen hypo-stoichiometry. Oxygen vacancies have also been shown in fluorite oxides (as is Pr_6O_{11}) to result in an overall expansion of the lattice, see Chapter 3. On the other hand, the lattice parameters of PNO214 can be seen to vary with anneal time. After 3 hrs of annealing, as the Pr_6O_{11} content increased, the PNO214 lattice contracted as the PNO214 became Ni-rich. However, as PNO4310 formed, while the b-cell parameter remains fairly constant, both a- and c-cell parameters expanded once more resulting in an overall expansion of the unit cell. The reduction in the concentration of B-site cations allowed the lattice to expand back to its original parameters. That the b-cell parameter remained contracted suggested that the PNO214 had a slightly higher concentration of B-site cations than originally at the start of the anneal, and that these excess cations occupied preferential positions, the lowest energy of which affected the b-cell parameter.

8.4 Conclusion and Further Work

A range of PLD conditions were used to attempt the synthesis of PNO214 thin films: substrate temperatures between 700°C and 780°C, and oxygen partial pressures between 10 mTorr and 500 mTorr. AFM images showed the films to be flat and of uniformly sized and regular grains. However as film thickness increased, large island grains were also seen. The deposition rate at an oxygen partial pressure of 300 mTorr and substrate temperature of 780°C was ∼45.6 nm/1000 pulses. The presence of PNO214 in the deposited film could not be confirmed. Pr_6O_{11} was always detected, along with one or two other phases. It was not possible to identify the other phase(s) with certainty, which could equally have been PNO113, PNO214 or PNO4310. The deposition of Pr_6O_{11} was favored at lower oxygen partial pressures.

The stability of PNO214 was subsequently investigated. Powder XRD patterns were obtained for PNO214 samples annealed for various durations at 800°C in air. The decomposition of PNO214 into Pr_6O_{11} and PNO4310 was observed, even at this low temperature, and was kinetically limited and within 24 h, only trace amounts of PNO214 remained.

Increasing the anneal time further had no effect on the diffraction pattern; Pr_6O_{11} and PNO4310 were the thermodynamically stable phases.

Rietveld refinement showed that oxidative decomposition of PNO214 initially began with the formation of Pr_6O_{11}, expanding the PNO214 lattice as it became Ni rich. Subsequently, at sufficiently high Ni concentrations, PNO4310 formed, and the PNO214 lattice contracted. The Pr_6O_{11} lattice parameters remained constant throughout. The presence of PNO4310 appeared to facilitate the decomposition of PNO214, and within 24 h at 800°C in air, only trace amounts of PNO214 remained. Further work would involve the analysis of in-situ synchrotron diffraction patterns of PNO214 obtained at Diamond Light Source in order to better trace the evolution of the PNO214 structure as it undergoes oxidative decomposition.

The inherent instability of PNO214 suggests that other techniques besides PLD should be used to deposit thin films of PNO214, which do not involve low oxygen partial pressures. However, the use of these other techniques lies beyond the scope of this work. Alternatively, stabilizing dopants, such as Cu and Gd need to be employed if PLD is to be used as the fabrication technique of PNO214 thin films. However, the use of PNCG films also lies outside the scope of this work. Due to the inability to produce PCO113/PNO214 films, the ORR enhancement proposed to be due to interfacial effects was not examined. Attention was focused instead on the effect of chemical and mechanical strain on the properties of thin film and bulk PCO113.

Chapter 9

Characterisation of Strained $PrCoO_{3-\delta}/Ce_{0.9}Gd_{0.1}O_{2-\delta}$/YSZ8-mol% Films, Fabricated by PLD

One of the main objectives of this work was to investigated the effects of mechanical strain, introduced through the lattice mismatch between the PCO113 film and its substrate, on the transport properties of $PrCoO_{3-\delta}$, PCO113. For this, a single orientation substrate with a small lattice mismatch with PCO113 is required. In Chapter 6, (200) oriented single crystal $Ce_{0.9}Gd_{0.1}O_{2-\delta}$, CGO, was found to be an ideal substrate with a PCO113[001]/CGO[100] and PCO[010]/CGO[100] lattice mismatch of 0.8% and 0.6% respectively.

In Chapter 6, the deposition conditions for a textured CGO film on YSZ(002) with only the CGO(200) out-of-plane reflection detected was identified, and similarly in Chapter 7 for the deposition of PCO113 films on (004) oriented Si substrates. These PLD conditions may now be employed for the deposition of strained PCO113 films on a CGO buffer, on top of a YSZ substrate: PCO113/CGO(200)/YSZ(002). The minimum lattice mismatch between PCO113 and CGO (0.9%), would be at the PCO113[001]/CGO[100] interface. Due to the lattice mismatch between CGO and YSZ, the deposition of a CGO(200) oriented film on the YSZ(002) should result in a compressive in-plane strain. Thus, the in-plane lattice compression of the CGO buffer layer should decrease the lattice mismatch between PCO113 and CGO. The deposition of highly textured (and strained) PCO113 films was anticipated.

In this chapter, strained PCO113 films were prepared. Two methods were used to induce a range of strains in the PCO113 films. Firstly, the thickness of the PCO film was varied while the thickness of the CGO film was kept constant so that the average strain over the

entire film decreased as the film thickness increased and the film relaxed. Secondly, the thickness of the CGO buffer layers was varied while the thickness of the PCO113 film was kept constant so that it was the relaxation of the CGO buffer layer that provided a range of lattice mismatch and subsequently strain.

The resulting films were structurally and morphologically characterized using XRD, XRR, AFM and SEM. In-plane structural analysis was performed through the use of reciprocal space maps, phi-scans and omega-scans. The strains in these films were calculated. As R-P phases were no longer considered in the remainder of this work, the 113 and 214 notations differentiating between perovskite and R-P phases were not required. All future references to PCO113 have been shortened to PCO.

9.1 Literature Review

In this chapter, strain was introduced into PCO films through lattice mismatch between the PCO film and the CGO buffer layer (the CGO buffer layer itself was also lattice strained due to mismatch between itself and the YSZ(002) substrate). This induced strain, or lattice strain, and its effect on the deposited film is of interest. Additionally, strain relaxation, a phenomenon that arises from lattice strain, was employed in the CGO buffer layer to produce a range of lattice strain in the deposited PCO113 film. Therefore, in the following review, a brief introduction to lattice strain was covered, before the specific cases of lattice strain in CGO and $LaCoO_3$, LCO or LSC if Sr-doped, films were examined. Within this section, the extent of Gd- or Sr-doping in CeO_2 and LCO is indicated by the values after the CGO and LSC acronym: thus CGO10 refers to $Ce_{0.9}Gd_{0.1}O_2$, and LSC10 refers to $La_{0.9}Sr_{0.1}O_3$. Beyond this section, the CGO10 films deposited in this work are referred to as CGO.

9.1.1 The Effect of Lattice Mismatch: Lattice Strain, Strain Relaxation and Film Morphology

Lattice strain has long been investigated in the semiconductor devices due to its effect on bandgap energies. Though initial work concentrated on minimizing lattice strain [352], it was later utilized [353, 354, 355], to improve device performance. Much of the literature here is of general principles based on research in semiconductor systems. More recently, such as in the work of Mehta et al. [297] mentioned in Chapter 7, it has also been used to tailor spin properties, and also the electronic properties of perovskite materials by distorting the 3d-orbital overlap.

Lattice strain, or misfit strain, can be produced in a thin film if a lattice mismatch exists between the film and the substrate. For thin films, the film adopts the substrate in-plane lattice parameters, creating a homogenous strain. This strain energy and the interfacial

energy (determined by the character of the interfacial bonding) governs the orientation of the deposited film, which will orient in a way to minimize strain and interfacial energy.

The elastic energy per unit area, E_H^{epi} resulting from this homogeneous strain in a perfectly epitaxial film is [356, 357]:

$$E_H^{epi} = Bhf_m^2 \tag{9.1}$$

where h is the thickness of the layer, f_m is the misfit parameter, which varies as a function of material composition and lattice mismatch, and the elastic constant, B, is:

$$B = 2\mu\frac{1+\nu}{1-\nu} \tag{9.2}$$

where μ is the shear modulus of elasticity and ν is Poisson's ratio.

It was seen in the TiN/Si(001) and TiN/GaAs(001) systems that for very thin films, when they are still in their early stages of growth, within 10 Åthick, that the interfacial energy matters most and determined film orientation [358]. It was only as the film thickness increased that the strain energy became significant and the orientation to minimize lattice mismatch was adopted.

As the thickness of the film increased, it was observed that the elastic energy within it increased linearly. Eventually, a critical thickness was reached whereupon dislocations were introduced into the lattice to relieve the strain and lower free energy, forming domains. The film was no longer coherent as periodicity between the film and substrate was no longer identical. Nevertheless, epitaxial growth may resume as domain epitaxial growth. Thus, as the film thickness increased beyond the critical thickness, the film relaxed. A highly lattice strained film will result in many small domains, while decreasing the lattice strain would increase the domain size. The total energy of the strained film now has three contributions: the energy associated with the strain arising from lattice mismatch, the energy associated with the strain arising from the presence of dislocations and the energy associated with the interactions of these two strains.

The critical thickness may be calculated using the principle of minimizing free energy, as developed by Ball and Van der Merwe [359, 360, 361]. The critical thickness is the point at which the change in energy of the film is zero when a dislocation is introduced. Below the critical thickness, introducing the dislocation would increase the free energy of the film, while above the critical thickness, introducing the dislocation would decrease the free energy of the film making it the thermodynamically favorable outcome.

The critical thickness of the film may also be calculated using Matthews and Blakeslee [362, 363, 364] method of balancing forces. Two forms of dislocations are identified: misfit dislocations, the presence of which relieves lattice strain, and threading dislocations, the movement of which produces misfit dislocations. The net force acting on the threading

dislocation determines if it moves or not. The driving force for motion is the reduction of strain(+ve), while the line tension of the threading dislocation opposes motion(-ve). At the critical thickness, these two forces are balanced. Above the critical thickness, the net force is positive and a misfit dislocation is formed.

Both theories predict the same critical thickness which has been validated experimentally [365, 366, 356, 367, 368, 369, 370, 371]. The equation for critical thickness may be written with respect to the forces on the threading dislocation, or the energy of the system.

Besides the necessary condition of the film critical thickness being exceeded, the strain relaxation of the film is also dependent on the ease of the (misfit) dislocations processes such as its nucleation and propagation (or impingement) [362, 363, 372, 373, 374, 375]. Nucleation of a dislocation requires the activation energy to be overcome and a critical dislocation loop radius achieved. The presence of defects within the film can lower the activation energy, and thus serve as heterogeneous nucleation sites. The effect of a strain field on the activation energy for dislocation is unclear. Similarly, existing (misfit) dislocations may interact with threading dislocations, potentially blocking their movement. For the threading dislocation to continue through the lattice would depend on the nature of the dislocation and the slip systems present, and would require an energy barrier to be overcome.

There is evidence that multiplication of dislocations also plays a significant role in strain relaxation of the thin film [376, 377]. Rather than the nucleation of new dislocations, it appeared that existing dislocations multiplied [376, 377, 378]. Due to strain relaxation, often it is only the region at the film/substrate interface that experiences lattice strain. This region tends to be small, and the strain profile within it can be described by the following equation, regardless of the relaxation mechanism present [312, 379, 380, 381]:

$$\epsilon(x) = \epsilon_0 exp(-\alpha x) \tag{9.3}$$

Where ϵ_0 and α are material constants, and s is the distance from the film/substrate interface.

Therefore the film comprises of a lattice strained region with a strain profile and, if the film is thick enough and the film is able to relax completely, an unstrained region. Thus, the average strain of the film, funny $\tilde{\epsilon}$ (the strain measured experimentally using XRD), is a function of the volume fraction of the film that experiences a lattice strain within the entire film thickness, and may be written as:

$$\tilde{\epsilon}(t) = \frac{\int_0^t \epsilon_0 e^{-\alpha x} dx}{t} = \epsilon_0 \frac{1 - e^{-\alpha t}}{\alpha t} \tag{9.4}$$

In the characterization of the strained CGO10 and PCO films reported in this chapter, the effect of lattice strain on film morphology should also be noted. As well as governing

the orientation of the deposited thin film, lattice mismatch, in conjunction with interfacial energy, is also a key determinant in the growth mode of the thin film and thus its subsequent morphology. As covered in 3, three modes of film growth have been identified: planar growth, island growth (Volmer-Webber growth) and planar then island growth (Stranski-Krastonov growth) [382]. In order to obtain planar growth, a low lattice mismatch and interfacial energy is required, while at higher interfacial energies, island growth results.

Besides the growth modes, lattice mismatch may also modify the film surface structure. A large lattice mismatch often results in mosaicity, when subgrains of the film exhibits slight tilts with respect to each other and the orientation of the substrate. Similarly, the presence of misfit dislocations, as a result of strain relaxation, also affect the surface structure such as through the creation of large scale ripples or"crosshatch" surface pattern [383, 384, 385, 386, 387, 388].

It is clear from the work on semiconductor devices and metallic films that the thermal history of the film is crucial to the strain relaxation of its lattice. The same principles are expected to hold for the PCO/CGO10 system in this work. All thin film samples in this section were produced under nominally identical conditions- they underwent the same heat treatment during deposition. However, two different methods have been used to produce films of different lattice strains: varying the CGO10/PCO lattice mismatch (by varying the strain relaxation of the CGO10 film by varying its thickness) or varying the strain relaxation of the PCO film (by varying the thickness of the PCO film). The objective of this chapter is to produce a range of lattice strains. The extent of strain relaxation in the CGO10 and PCO films, while it was the means by which the range of lattice strains in the PCO was produced, is of less importance than the actual strain measured, which is the objective of this chapter. However, it is an important consideration in Chapter 11 in understanding the electronic and ionic transport through the films prepared.

The affect of lattice mismatch on film morphology is also of consequence in this work because the deposition of all PCO films was performed upon a lattice mismatched CGO10 buffer layer, yet an atomically smooth surface is that which was modeled by van der Merwe [361] and may be necessary for coherent epitaxial growth on a lattice mismatched substrate [389]. Furthermore, while in one of the sample sets, the PCO films should all be deposited on nominally identical CGO10 buffer layers, in the other sample set, a range of thicknesses of the CGO10 buffer layer is used in order to obtain a range of substrate lattice parameters. For this sample set, differences in the CGO10 buffer layer morphology would be expected that may subsequently affect PCO film growth and strain relaxation. Hence the importance of imaging the surface of CGO10 films (only), of varying thicknesses, to determine if CGO film morphology changes and to evaluate the consequences of this for the PCO films.

9.1.2 Strained $Ce_{0.9}Gd_{0.1}O_{2-\delta}$ Films

Previously in Chapter 6, the PLD of CGO10 thin films was examined in view of the effect of deposition conditions on film structure and morphology [2, 390]. Interest now lies in the strain of the CGO films reported.

Strain effects on charge transport properties first came under investigation over 40 years ago when hydrostatic pressures were applied to bulk materials [391, 392, 393]. This same effect can be reproduced at the strained interface of epitaxial thin films deposited on a substrate of mismatching lattice parameters. In the case of CeO_2, molecular dynamic simulations suggest that the effect of lattice strain on the oxide ion transport properties is linked to the interaction between the defect species that arise when doping ceria with Gd [394, 395, 396, 397, 398, 399, 400, 401]. If Gd^{3+} dopants and oxygen vacancies exist at a sufficient concentration, they segregate to eventually form "nano-domains" [402, 403, 404, 405], which lower oxide ion conductivity. The formation of these defect segregations expand or contract the lattice, depending on the extent of their formation [405]. Thus by imposing a lattice strain, the extent of defect segregation may be controlled. Indeed, from simulations and supported by experimental work, a uniaxial lattice strain was found to reduce the activation energy for oxygen migration in CGO [400, 401, 312, 406], possibly by reducing the binding energies of oxygen vacancy clusters [400, 401].

The intents of this chapter lies with the structural characterization of strained CGO10 films. Therefore, literature examples of oriented CGO films deposited on various substrates, such as MgO(001) [49], $SrTiO_3$ (001) [406], $LaAlO_3$(100) [407], Pt(111) and sapphire(001) [60, 312], have been examined to understand the different lattice structure and strains produced, and how strain may potentially affect the deposition of PCO films atop the CGO10. While several thin film fabrication techniques have been used for the deposition of Gd-doped ceria films, such as spray pyrolysis [65] and magnetron sputtering [408, 409] only CGO10 and CGO20 thin films fabricated using PLD were considered, being the same deposition process and material (given a slight variation of Gd-doping) used in this work.

Chen et al. deposited CGO20 on MgO(001) substrates [49]. Cross-sectional high-resolution tunneling electron microscopy, TEM, image showed the CGO20 films to be single phase, with no precipitates in or on the film interface, and to have a columnar structure. The expected orientation to minimize lattice mismatch would be a CGO20[110]//MgO[100] relationship, which would result in a 9% tensile strain of the CGO20 in-plane lattice. However, the CGO20(002) reflection was observed instead, and an inplane relationship of CGO[001]//MgO[001] and CGO20[100]//MgO was observed from TEM studies: the CGO20 film was epitaxial with cube-on-cube growth and a lattice misfit greater than 28%, see Fig 9.1. It was concluded that for this system, the determining factor for CGO20 film orientation was the formation of the lowest energy CGO20 surface, rather than lattice mismatch. Nevertheless, for the deposition of CGO10 on YSZ, it has been found that the preferential orientation was also one where lattice mismatch was minimized

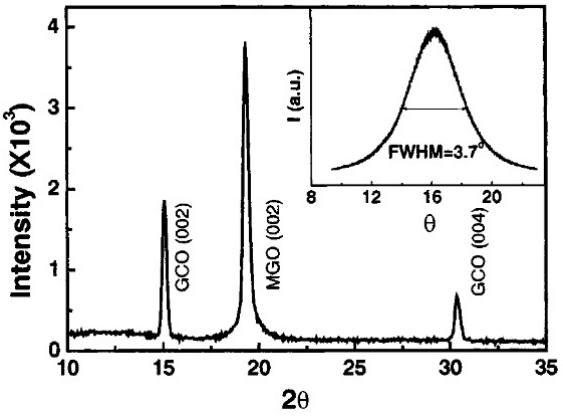


Figure 9.1: Out-of-plane XRD scan show that the as-grown CGO20 film are c-axis oriented on MgO(002) suggesting a lattice misfit greater than 28%. The inset shows the rocking curve scan of the CGO20(004) reflection with a FWHM of 3.7° [49].

[27, 7, 29, 227, 8]. Lattice defects and a large mosaic spread, strain relieving features, were observed in the film.

Further to this, Kant et al. deposited CGO10 on MgO(001) with $SrTiO_3$(001) buffer layers, as the lattice mismatch between CGO10 and $SrTiO_3$ was a lower 9.1% [406]. A range of $SrTiO_3$(001) buffer layers were used, to induce different extents of strain in the CGO10 film, as was done in this work, to investigate if the presence of the $SrTiO_3$(001) buffer layer improved lattice matching. From in-plane and out-of-plane XRD measurements, it could be seen that as $SrTiO_3$ buffer thickness increased, out-of-plane compressive strains and in-plane tensile strains in the CGO10 film decreased, as was hypothesized, and a magnitude reduction in the FHWM of the CGO10(002) reflection was found, as compared to CGO20 films deposited directly upon MgO(001) by Chen et al. [49]. The CGO10 film was epitaxial. The strain in the CGO10 film enhanced its in-plane ionic conductivity.

Huang et al. performed an indepth structural characterization of CGO10 deposited upon $LaAlO_3$(001) [407]. Here, the effects of lattice strain on the microstructure were investigated. The main phase of the film was found to be $Gd_{0.2}Ce_{0.8}O_{1.0}$, though parallel lines of Gd-rich precipitates ($Gd_{0.3}Ce_{0.7}O_{2-\delta}$) at 8° angles to the film surface normal were observed throughout the film cross-section. These precipitates served to relax lattice strain, either by generating an opposite strain field, or through the generation of interfacial dislocations at the precipitate//bulk interfaces. This was thought to mitigate large lattice distortions, especially for thicker films, as it allowed for a uniform strain relaxation and consequently a high film crystallinity. Thus the film was found to have a sharp interface with the substrate, with no traces of interfacial reactions, a low mosaicity with the FWHM of the CGO10(002) rocking curve reflection measured to be 0.56° , and an epitaxial relationship with the substrate of $LaAlO_3$[100]//CGO10[110], $LaAlO_3$[001]//CGO10[001], and $LaAlO_3$[010]//CGO10[0110]. Nevertheless, areas of lattice distortion were still observed where tilting away from the on-axis[100] direction occurred. This was not seen at lattice-distortion-free regions.

Joo et al. also deposited CGO20 on sapphire(001) and Pt(111) [60]. A highly textured (111) out-of-plane oriented CGO20 film was obtained for the sapphire(001) substrate. However, despite a smaller lattice mismatch with Pt(111) than MgO(001), a polycrystalline CGO20 film exhibiting the (111) and (200) orientations was deposited on the Pt(111). Lattice strain was not measured and it is unclear from the out-of-plane XRD pattern if it was present in the polycrystalline CGO20 film. SEM micrographs of the surface and cross-section of the two films showed that both films comprised of columnar grains. This columnar microstructure was more apparently in the polycrystalline CGO20 on Pt(111). The column diameter was ∼90 nm for the polycrystalline CGO20 film on Pt(111), and ∼40 nm for the oriented CGO20 film on sapphire(0001).

Further work was done with the epitaxial CGO10(111)/sapphire(001) system by Lee [312]. Here, the thickness of the CGO10 film was varied between 52 to 403 nm to create a range of lattice strains. The subsequent decrease in activation energy for oxygen migration with increasing film thickness was attributed to the out-of-plane lattice dilation and any subsequent lattice distortion arising from that (as grain boundary and space charge layer effects should not be present). Based on a clear correlation between lattice strain and the measured activation energy, and ab-initio calculations of the oxygen migration activation energy as a function of strain along the <111> axis for different oxygen diffusion paths, it was proposed that the application of a tensile strain altered the oxygen migration path and subsequently also the activation energy for oxygen migration. The strain relaxation of the films was also calculated, with the film becoming almost completely relaxed after a thickness of 26 nm. Out-of-plane (tensile) strains of up to 0.23% were achieved.

In the work of Cho et al., CGO10 was deposited on YSZ(001) and its electrical properties were investigated with respect to its crystallinity and grain size, which was tailored by varying deposition temperatures between RT at 700°C [410]. At higher deposition temperatures, the CGO10 films became more crystalline, with larger grain sizes, and the electrical conductivity of the films was found to increase, while their activation energy decreased. Kim et al. also investigated the effect of grain size of epitaxial CGO10 on YSZ by post annealing the films (the higher the post anneal temperature, the larger the grain size), and saw that reducing grain size, and thus increasing grain boundary density reduced the cathodic interface resistance [411]. Cho et al. found that only films deposited above 500°C exhibited epitaxy with the YSZ(001) substrate, with a cube-on-cube relation despite the 5% lattice mismatch between CGO10 and YSZ. This relation is commonly reported [27, 7, 29, 227]. Based on the CGO(002) and CGO(004) peak positions, Cho et al. suggested a domain matching epitaxy of 20 (004)YSZ lattices to 19 (004)CGO10 lattices, resulting in a residual lattice mismatch of 0.05%.

Thus, epitaxial Gd-doped ceria films have been deposited by PLD on a range of substrates of varying lattice mismatch, including YSZ(002) - the substrate of interest in this work. The Gd-doped ceria films were able to accommodate a large amount of strain, such as when paired with a MgO(001) substrate; h,owever this was also found to be highly dependent upon the interfacial energy between the film and substrate. The ability of the Gd-doped

ceria films to accommodate large strains while maintaining epitaxy was facilitated by additional strain relieving mechanisms due to the presence of the Gd dopant. This reduces the occurrence of lattice distortions and allows for a flatter surface morphology.

For the purposes of this work, the uses of CGO10 is twofold: as a buffer layer, and to induce a range of strains. It is important that the film surface morphology is flat and exhibits a low mosaicity, in order to deposit a strained PCO film on top of it that has epitaxial growth [389]. The actual strain relaxation mechanisms present that allows for this are of less interest. Key structural analysis would include the average lattice strain from XRD patterns, FWHM of rocking curves, and AFM imaging for roughness measurements.

A last important consideration is that the CGO10 film was calculated to be fully relaxed at a thickness of 26 nm from the CGO10(111)/sapphire(0001) interface [312]. Beyond this thickness, the film would have reverted back to its unstrained lattice parameters (the lattice strain measurements only provide an average strain across the film). Therefore, it is necessary that the CGO10 buffer layers deposited in this work had a range of thicknesses below this threshold in order to obtain a range of CGO10 lattice parameters at the CGO10/PCO113 interface.

9.1.3 Strained Sr-Doped $LaCoO_3$ Films

Similar to the literature view on strained CGO10 films, the objective of this review is the morphological and structural characterization of $LaCoO_3$, LCO, thin films deposited on CGO/YSZ. A review on the effect of lattice strain on the electronic and oxide ion transport of LCO thin films is in Chapter 11.

To date, there has been no published literature on PCO films by PLD besides that by Prakash et al. and Mehta et al. On the other hand, much has been done on the related lanthanide system: LCO and its Sr-doped variants. As with PCO, most work in updoped strained LCO films lies in its ferromagnetic ordering and LCO films have been deposited by PLD on a range of substrates, such as $SrTiO_3$(001), $LaAlO_3$(001), $Pb(Mg_{1/3}Nb_{2/3})_{0.72}Ti_{0.28}O_3$(001) [412, 413, 414, 244]. For Sr-doped LCO, due to its application an SOFC cathode material, it is its oxygen reduction activity and its electronic and oxide ion transport properties that is investigated. LSC has been deposited by PLD onto $LaAlO_3$(001) and $SrTiO_3$(001) or even directly onto YSZ(001), YSZ(110) and YSZ(111) [255, 415, 246, 416, 402, 417, 418]. However, it is the characterization of the LSC/CGO/YSZ system that is currently being reviewed.

An exception to the work on strained LCO films that is applicable in the SOFC field is the study by Hong et al., investigating the effects of spin states in LCO thin films on the ORR [419]. LCO films between 45 to 110 nm were deposited on 10 nm CGO buffer layers on YSZ(002) substrates. Using a pseudo-cubic assignment for LCO, and cubic assignments for CGO and YSZ, out-of-plane XRD patterns and pole figures indicated epitaxial cube on cube growth of CGO(100) on YSZ(001), and epitaxial growth of

LSC$(001)_{pc}$ that is rotated by 45° , about the plane normal. Thus the in-plane relationship is LCO$_{pc}$[100]//CGO$_{cubic}$[110]//YSZ$_{cubic}$[110]. This is as expected given $a(CGO) \sim \sqrt{2}a(LSC_{pc})$. As, this is also true for the PCO/CGO/YSZ system, this orientation relation is expected in this work. Additionally, at room temperature, Hong et al. measured a 1.6% volumetric tensile strain in the LCO film as compared to the bulk. AFM images revealed mostly uniformly sized grains and a low surface roughness of measured in all films from AFM images, $R_{rms} < 0.8$ nm.

Crumlin et al. has worked extensively with the LSC20/CGO20(∼5 nm)/YSZ system prepared using PLD [7, 8, 227, 27, 29]. In 2010, a range of LSC20 film thicknesses were grown, between 20 to 130 nm. Surface roughness measurements using AFM was performed on the 45 nm thick LSC10 film, which was found to have a R_{rms} of 3 to 6 nm. The columnar grains were of a uniform size, although some appeared to be growing at the expense of others [7]. In later work, AFM images were obtained of LSC40 film 25 nm and 77 nm thick, which both had surface roughness R_{rms} values of 0.8 nm. The films were of a uniform grain size [227].

Also using a pseudo-cubic assignment for LSC20 (where a_{pc} ∼3.837 Å), Crumlin et al. saw the same LSC20 orientations as described by Hong et al. [7, 8, 227, 27]. A tensile in-plane and compressive out-of-plane strains between 0.30% and 1.40%, and -0.20% and 0.93% respectively, using a poission ratio, ν, of 0.25 [420] was found in LSC20 films between 20 to 130 nm thick [7]. In a separate work, the stability of these films have also been investigated and revealed that a high crystallinity of ∼85 nm thick LSC20 films could be achieved and maintained, to 500°C, with FWHM values of ∼0.25° for the LSC20$_{pc}$(200) and LSC20$_{pc}$(101) reflections [8]. A variation in in-plane and out-of-plane strain with temperature has also been measured, which is associated with the TEC mismatch between film and substrate [8].It has been noted that the relaxed unit cell volume of the deposited LSC20(001) film was larger than that of LSC20 powder [8]. This has been attributed to a larger oxygen deficiency in the thin films [7]. Whereas, in his work in a similar system, but with LSC40 films between 24 and 157 nm thick, smaller relaxed lattice parameters of the thin film compared to bulk values were reported, suggesting a lower oxygen deficiency in the thin film [227].

Besides the published literature by Crumlin et al., no other reports of the LSC/CGO/YSZ system were found. Nevertheless, there is a reasonable good expectation of the structure and morphology of PCO films to be prepared by PLD. For the remainder of this work, the $Ce_{0.9}Gd_{0.1}O_2$ films deposited have been referred to as CGO.

9.2 Experimental Method

PLD of PCO and CGO was performed at 300 mTorr and 10 mTorr oxygen partial pressure respectively. As mentioned earlier, there was difficulty in maintaining a constant oxygen partial pressure of 10 mTorr- it would fluctuate between 5 mTorr and 14 mTorr. A nominal

Sample Set	$Ce_{0.9}Gd_{0.1}O_3$ Film	$PrCoO_3$ Film
1	500 pulses	
	1000 pulses	
	1500 pulses	
	2000 pulses	
	2500 pulses	
2	500 pulses	3000 pulses
	1500 pulses	3000 pulses
	2000 pulses	3000 pulses
	2500 pulses	3000 pulses
3	1000 pulses	500 pulses
	1000 pulses	1000 pulses
	1000 pulses	2000 pulses
	1000 pulses	3000 pulses
	1000 pulses	4000 pulses
	1000 pulses	5000 pulses

Table 9.1: Number of laser pulses used in the deposition of CGO and PCO films for all three sample sets. All depositions were performed at 680°C and an oxygen partial pressure of 300 mTorr.

substrate temperature of 680°C was used for both materials.

For the CGO-only on YSZ films, 500 to 2500 pulses were used, at 500 pulse increments. For the sample set of varying PCO film thickness, 1000 to 6000 pulses were used for the deposition of the PCO films, at 1000 pulse increments, while 1000 pulses was used for the deposition of the CGO buffer layer. For the sample set of varying CGO buffer layer thickness, 500 to 2500 pulses were used for the deposition of the CGO buffer layer, at 500 pulse increments (excluding 1000 pulses already deposited in the previous sample set), while 3000 pulses were used for the deposition of the PCO film. A table of number of laser pulses used for the depositions is depicted in Table 9.1.

XRR was used for the CGO only films, being the most appropriate technique for reliable film thickness measurement for films of this scale. The Dektak 150 surface profilometer was used for all other PCO113/CGO films. SE data were obtained for all films, with the exception of the CGO only films, due to charging effects. The use of Cr- or Au-coatings to negate surface charging was found to mask surface features. Out-of-plane XRD measurements were performed on all deposited films: CGO only and PCO113/CGO. For the PCO113/CGO/YSZ films, additional in-plane measurements were made. All XRR and thin film XRD measurements were performed using the PANalytical X'pert Pro MRD. AFM images were obtained of all the films using the Bruker DiInnova.

As with all thin film XRD measurements, the samples were aligned prior to the measurement. Scans were taken to ensure that the sample was centered in the X-ray beam. Using the substrate YSZ(002) reflection, sample tilts (ω and ψ) were corrected for. Thus, any zero-corrections due to sample height should be minimal, as can be seen from the

data where deviations in the YSZ(002) peak position is within instrumental error (also in Chapter 6). X-ray intensities have also been optimized. Out-of-plane gonio ($2\theta - \omega$) scans were taken of all thin film samples.

For in-plane measurements, having aligned the sample, these values were set to the 'zero' position. Asymmetric grazing incidence scans were used to obtain reciprocal space maps, RSMs, of the 113 and 115 reflection of 7 samples. First, the angles between the YSZ [001] lattice vector and the [113] and [115] plane normals were calculated. For this, a cubic YSZ unit cell with lattice parameters determined from the YSZ(002) peak position was assumed. Second, symmetric scans were performed at the (113) and (115) reflections (at 59.27° 2θ and 101.88° 2θ respectively), at the appropriate psi angle, to ensure the peaks were present. The alignment was adjusted to optimize peak intensities. Finally, the asymmetric setup was used. Further alignment scans were again performed as the psi step size was much larger than omega. After this last alignment, the RSM scan was carried out, within the range of omega values accessible.

For comparison between samples, background intensities from the out-of-plane XRD were subtracted. All patterns were normalized to the integrated YSZ(002) peak area. Rather than fitting the peak to calculate the area (it would not have been possible to fit the YSZ(002) peak for a reliable peak intensity as it comprised of only 6 or 7 data points), a rougher value was taken by summing the intensities within the peak. To define the data points comprising the peak, an arbitrary threshold of 2.5% of the peak intensity was used. The best fit of the CGO(200) and PCO113 reflections at ∼23.5° 2θ, ∼33.5° 2θ, and ∼48.0° 2θ could only be obtained using the Pseudo-Voigt peak shape model. This model was also used to obtain FWHM values from rocking curves. The obtained fits are presented later in this chapter.

In fitting the CGO(200) peak of the CGO-only thin films, a range of data encompassing just the CGO(200) reflection was selected and this range fitted. Thus the CGO(200) peak was fitted individually, without account for the YSZ(002) reflection as it was not possible to fit both CGO(200) and YSZ(200) reflections together- the model would not converge, not even for the peak position of the CGO(200) reflection due to the high intensity of the YSZ(002) reflection. However, as it was only for the thinnest CGO film where there was a peak overlap between the CGO(200) and YSZ(002) reflections, any contributions from the YSZ(002) reflection to the range of data selected should be minimal for all but that thinnest CGO film. For all other PCO/CGO/YSZ films, the entire XRD pattern was fitted. A constant background value was used. The intention was to obtain as good a fit of the PCO and, where possible, the CGO peaks as possible. The YSZ(002) reflection would never have a good fit due to the small number of data points. The priority when fitting the YSZ(002) reflection was to isolate its contribution to the PCO and CGO reflections.

There were two additional complications when fitting the films of varying PCO film thickness (sample set 2). Firstly, the CGO(200) peak was almost completely obscured by the PCO reflection. Therefore, peak parameters (position, FWHM and Lorentz fraction) were taken from the fit of the CGO-only film, deposited under nominally identical conditions.

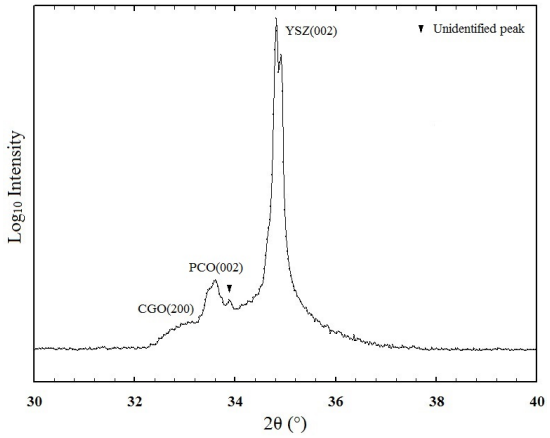


Figure 9.2: Out-of-plane XRD scan of the PCO film deposited using 1000 pulses on a CGO buffer layer deposited using 1000 pulses. The PCO peaks around ∼33.5° 2θ were of an irregular shape. Also an additional unidentified peak was detected ∼33.9° 2θ, which was not seen in any other PCO film deposited. Subsequently, this film was deemed anomalous; no further structural characterization was performed on it.

The area under the CGO(200) peak was the only parameter that was refined. Secondly, an additional PCO peak was detected at 33.9° 2θ. Due to the low intensity of this reflection, none of the peak parameters converged during the fit. Instead, values had to be arbitrarily selected to minimize the residual plot. As with the YSZ(002) peak fit, the objective of fitting this peak is not to obtain any information from it but to obtain a better fit for the surrounding reflections.

It was not possible to fit the peaks between 32 and 36° 2θ for the out-of-plane XRD pattern of the sample: PCO(1000 pulses)/CGO(1000 pulses)/YSZ due to the irregular shape of the PCO peaks, see Fig 9.2. Furthermore, an additional PCO(121) peak was detected, which was not present in all other PCO films deposited. The irregularly shaped PCO peaks and the presence of this additional orientation within the PCO film suggests the structure of this PCO film was significantly different to the other PCO films deposited. Thus, this one sample deposited using 1000 pulses was deemed anomalous and excluded from the analysis.

For the entirety of this work, PCO, CGO and YSZ have been defined using the $Pnma$, $Fm\bar{3}m$ and $P4_2/nmc$ space groups respectively [6, 298, 300], see Chapter 6. To calculate lattice strain values, the PCO peaks at ∼23.4° 2θ and ∼48.0° 2θ have been assigned to the (020) and (040) reflections. The PCO peak at ∼33.5° 2θ, in keeping with the same family of planes, could be assigned to either the (002) reflection, or the (200) reflection. The assignment of this peak was based on the strain values calculated in sample set 2. A (200) assignment would result in a tensile out-of-plane strain, while the (002) assignments results in a compressive out-of-plane strain, which would be expected due to the in-plane tension from the PCO[010]/CGO[110] mismatch.

The strain in the film has been calculated using the position of the XRD reflections against

Composition	Spacegroup	Lattice parameter		
		a (Å)	b (Å)	c (Å)
$PrCoO_3$	$Pnma$	5.3414(1)	7.5756(2)	5.3766(1)
$Ce_{0.9}Gd_{0.1}O_2$	$Fm\bar{3}m$	5.4223(1)	5.4223(1)	5.4223(1)
YSZ-8mol%	$P4_2/nmc$	3.640	3.640	5.148

Table 9.2: Spacegroup assignments of PCO, CGO and YSZ. Cell parameters of PCO and CGO obtained from Le Bail refinement of targets. YSZ c-cell parameter calculated from YSZ(002) reflection in the out-of-plane XRD measurement of the YSZ single crystal substrate. YSZ a- and b- cell parameters calculated assuming a $1/\sqrt{2}$ relation between the a- (and b-) and c-cell parameters.

the lattice parameters obtained from the LeBail refinements of the CGO and PCO PLD targets, and the YSZ substrate (002) peak position at 33.01° 2θ in Chapter 6, see Table 9.2

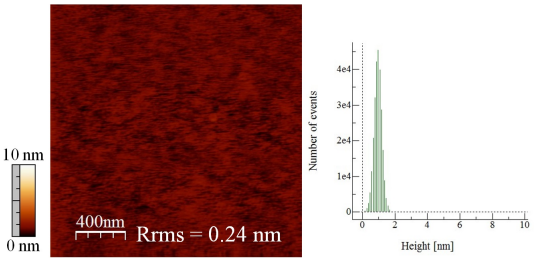
9.3 Results and Discussion

9.3.1 Morphological and Structural Characterization of Strained $Ce_{0.9}Gd_{0.1}O_{2-\delta}$ Films

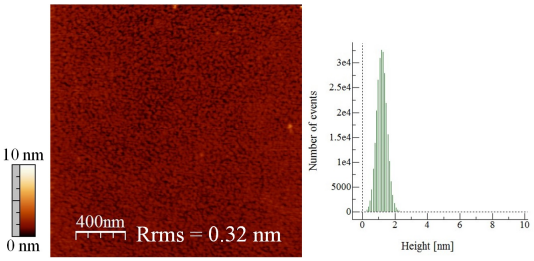
CGO buffer layers of a range of thicknesses were deposited on YSZ(001). Sample set 1 consisted of CGO/YSZ films, while in sample set 2 a further PCO film was deposited on top of the CGO/YSZ. Nominally identical deposition conditions have been used for the deposition of CGO in both sample sets 1 and 2.

AFM images were recorded from the CGO film surface of sample set 1, see Fig 9.3. As they have been deposited using identical conditions as the CGO buffer layers in sample set 2, they were expected to be representative of the CGO buffer layers in sample set 2. As found in the CGO trial films discussed in Chapter 6, grains of uniform size were obtained. In line with literature reports, the images suggest columnar grain growth , with a columnar grain diameter of ∼40 nm for the thickest CGO film, similar to that of oriented CGO(111) deposited on sapphire(0001) [60].

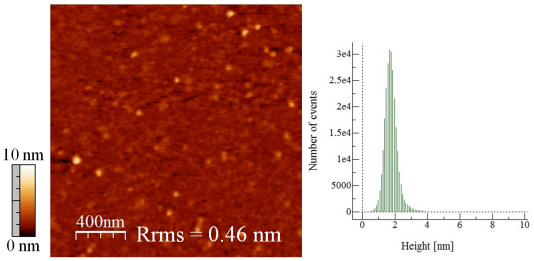
It can be seen that as the CGO deposition duration increased from 500 pulses to 2500 pulses, the film R_{rms} roughness values increased from 0.24 to 0.46 nm, respectively as would be expected as film thickness increases. Even for the thickest CGO buffer layer, R_{rms} roughness values are comparable to those of blank Si(004) and YSZ(002) substrates. So, regardless of the thickness range here, any surface roughness of the CGO buffer layer should affect the PCO film deposited upon it no more than a clean substrate would, which is the most atomically flat option available- the pre-requisite for coherently strained epitaxial growth. The limiting condition for epitaxial growth of PCO would not be the surface roughness of the CGO buffer layer. Therefore, the expectation was that: as it



(a) 500 pulses



(b) 1500 pulses



(c) 2000 pulses

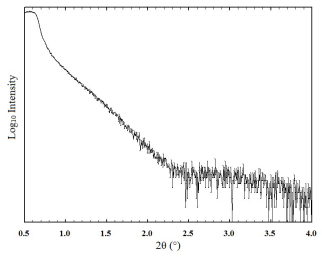
Figure 9.3: AFM images of some of the deposited CGO-only films, deposited using a range of laser pulses, of sample set 1. Increasing CGO film thickness increased R_{rms} roughness, which nevertheless remained of a comparable value to that of the single crystal Si(004) and YSZ(002) substrates imaged in Chapter 6.

was found possible to deposit PCO on the single crystal Si(001) substrate in Chapter 7, it should be equally possible to deposit it when there is a CGO buffer layer no matter the thickness, and subsequently roughness, of the CGO buffer layer within the range of CGO buffer layer thicknesses investigated. Nevertheless, there is an upward trend of surface roughness with CGO buffer layer thickness present, and this should be kept in mind when discussing sample set 2. The effect would be small, if present, and would be within error of the YSZ(001) substrate quality.

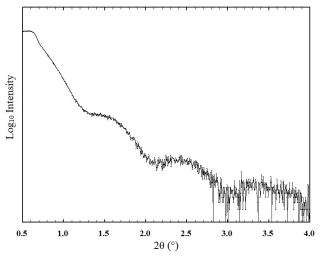
A low film roughness is not the only requirement for the successful deposition of coherently strained epitaxial films. It is also necessary that the mosaicity of the YSZ substrate is maintained in the CGO buffer layer. This shall be investigated in the structural analysis using XRD of the CGO films later in this section.

From the literature review, it was found that for the case of an epitaxial CGO(111) film deposited on sapphire(0001), that the relaxation length was 26 nm [312]. In order to obtain a range of lattice parameters at the CGO/PCO interface, the thicknesses of the CGO buffer layer had to be within that relaxation length. XRR measurements using a

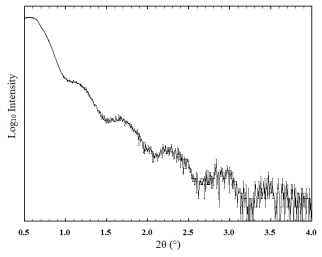
grazing incidence were performed on the CGO thin films of sample set 1 to measure their thicknesses, see Fig 9.4.



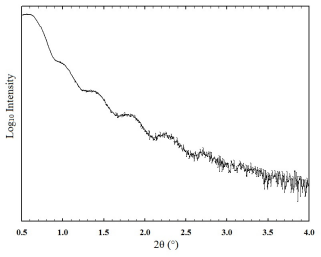
(a) 500 pulses



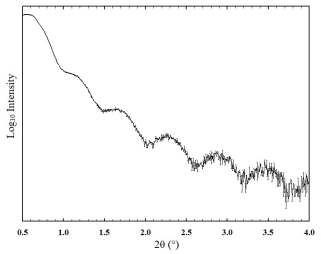
(b) 1000 pulses, thickness: 9.5 nm



(c) 1500 pulses, thickness: 15.6 nm



(d) 2000 pulses, thickness: 18.5 nm



(e) 2500 pulses, thickness: 24.0 nm

Figure 9.4: XRR measurements of the CGO-only films. Film thickness values have been calculated from the XRR pattern by Dr. A. Cavellero of Imperial College. The refraction fringes of the CGO film deposited usin 500 pulses could not be fitted to obtain a film thickness value.

Film thickness values as a function of deposition conditions are presented in Fig 9.5. Even for the thickest CGO film, deposited using 2500 pulses, a film thickness of 26 nm was not exceeded. Based on this reported system, it is expected that for the range of CGO buffer layer thicknesses used in this work, it should see a range of CGO lattice parameters at the CGO/PCO interface. To support this work, the strain relaxation length of the deposited CGO buffer layers was calculated from the film lattice strain. Deposition rate was 9.6 nm/1000 laser pulses.

Out-of-plane XRD patterns were taken for sample set 1 (CGO films of varying thickness on YSZ(001)), and sample set 2 (PCO films of constant thicknesses on CGO films of vary-

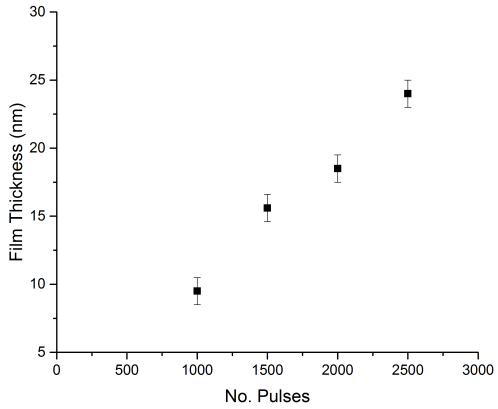
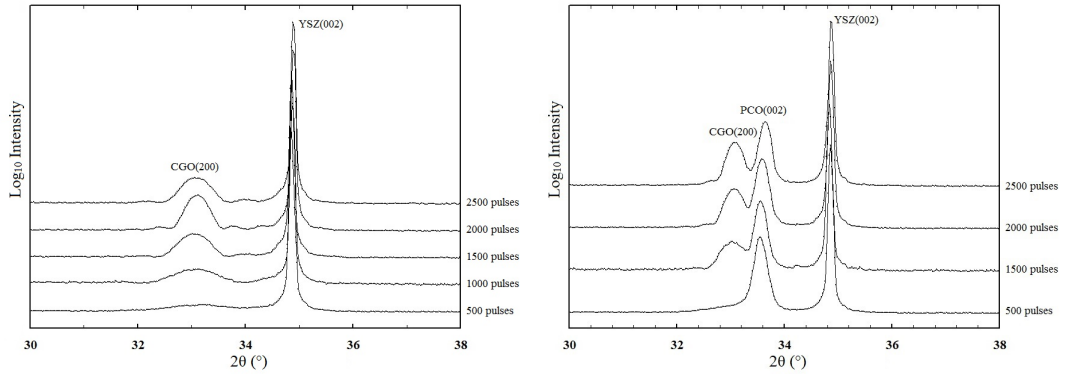


Figure 9.5: Film thicknesses of CGO-only film deposited on YSZ(002), as measured using XRR. Deposition rate was 9.6 nm/1000 laser pulses. Approximate error in the XRRmeasurements: ±1 nm.

ing thickness on YSZ(001)), see Fig 9.6. For sample set 1, only the CGO(200) reflection around ∼33.0° 2θ and the YSZ(002) reflection around 34.8° 2θ were detected. Therefore, based on the lattice parameters of CGO and YSZ and also observed in literature of similar configurations, the cubic CGO lattice stacks directly upon the tetragonal $P4_2/nmc$ assigned YSZ lattice but with a 45° rotation of the cubic CGO lattice about the axis normal to the film surface. This should result in a lattice mismatch at the CGO[100]/YSZ[110] interface of -5.29% (CGO film with in-plane lattice compression). The in-plane compression of the CGO film should be compensated by an out-of-plane tension that should be observed in the XRD patterns. The same is true of sample set 2, although the PCO reflection masks the CGO(200) reflection of thinner CGO films.

In the out-of-plane XRD patterns of both sample sets, faint Keissig fringes can be seen in the CGO(200) reflection suggesting a smooth interface. It was not possible to fit these reflectometry patterns to obtain film thickness values. A peak shift to a lower d-spacing can be observed in the out-of-plane XRD patterns as CGO buffer layer thickness increased. The CGO(200) reflections at ∼33.0° 2θa were fitted using the Pseudo-Voigt model, as described in the Experimental Methods section and the out-of-plane strain was calculated for both sample sets of CGO films of varying thicknesses. This is depicted in Fig 9.7. Average out-of-plane strain values have been plotted against the XRR measured CGO film thickness as well as against the area under the CGO(200) reflection that was though to be more indicative of the true CGO film thickness than the number of pulses used for the deposition.

If the CGO lattice stacks directly upon the YSZ lattice with a 45° rotation about the axis normal to the film surface, the CGO film should experience an in-plane compression of -5.29% at the CGO/YSZ interface. An average out-of-plane tension should be observed. Instead, a compressive out-of-plane strain was measured in all CGO films.



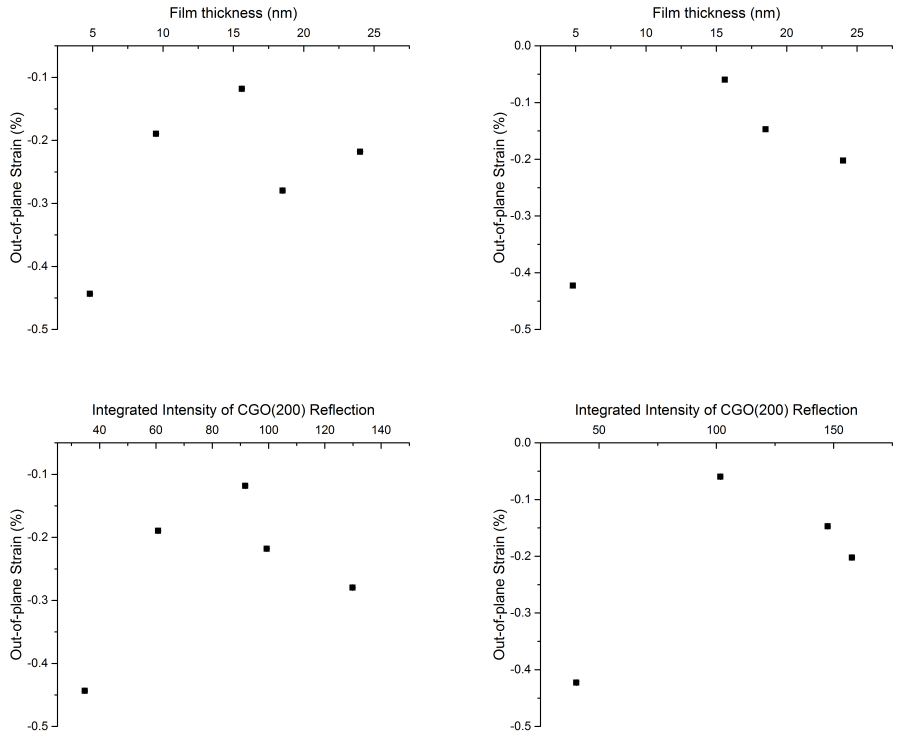
(a) Sample set 1 (CGO/YSZ) (b) Sample set 2 (PCO/CGO/YSZ)

Figure 9.6: Out-of-plane XRD measurements of CGO films, deposited using 500 to 2500 laser pulses, in sample sets 1 (CGO-only films) and sample set 2 (PCO/CGO/YSZ films) between 30 to 38° 2θ. The CGO(200) reflections have been labeled, the intensity of which can be seen to increase with increased deposition pulses. As CGO film thickness increased, a shift in the 2θ position CGO(200) reflection to larger 2θ values can be seen, indicating a decrease in out-of-plane lattice parameters corresponding to the (200) reflection, whereas consideration of the lattice mismatch between CGO and YSZ would suggest an increase in out-of-plane lattice parameters.

While CGO buffer films are commonly paired with a YSZ substrate, no explicit mention of the CGO lattice strain could be found in literature. Instead, the CGO films were established to be epitaxial, of the (200) orientation, and with a cube on cube alignment with the YSZ lattice [27]. The PLD conditions used in this work were the same as in that report. So, though no asymmetric pole figures were obtained in this work and the in-plane relation between film and substrate was not ascertained, a similarly oriented CGO should have been produced. It is unlikely that a different in-plane relation was obtained in this work that resulted in the compressive out-of-plane CGO lattice strain observed. Therefore, there may be other factors, besides lattice mismatch, that are contributing to lattice strain.

One such possibility is the effect of chemical strain. CGO can accommodate a range of oxygen deficiencies, which would necessitate a reduction of ceria from Ce^{+4} to Ce^{+3} and subsequently an expansion in the lattice parameters. However, it was a reduction in out-of-plane lattice parameters that was observed here, and if this were true, the CGO target from which bulk lattice parameters were calculated has to have a higher concentration of oxygen vacancies than in the film. However, no chemical analysis of the CGO films or target was performed to further investigate this possibility as it was not the main purpose of this work.

Similarly, the change of lattice parameter may also be attributed to chemical strain arising from variations in the dopant concentration. This has been reported to be sensitive to PLD conditions, and has been mentioned in to result in non-stoichiometric transfer from target to film. While no chemical analysis has been performed, all films were deposited under nominally identical conditions. Any chemical contributions to the lattice strain



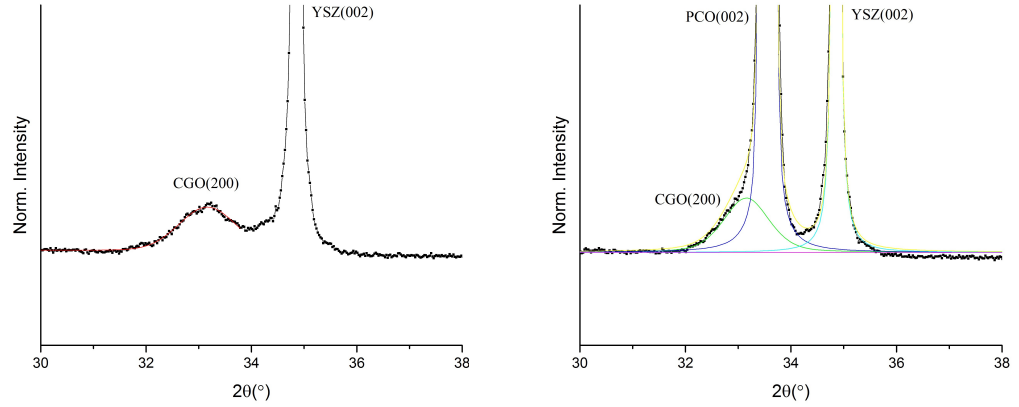
(a) Sample set 1 (CGO/YSZ) (b) Sample set 2 (PCO/CGO/YSZ)

Figure 9.7: Out-of-plane strain in CGO films of sample sets 1 and 2, as a function of measured CGO film thickness (by a Dektak 150 surface profilometer), and the integrated intensity of the CGO(200) reflection at ∼33.0° 2θ, both thought to be reliable indicators of the actual CGO film thickness. The value of the 'measured' CGO film thickness of the thinnest (4.8 nm thick) CGO film deposited using 500 pulses was calculated based on an average CGO deposition rate of 9.6 nm/1000 pulses. Error bars have been included but are mostly obscured by the data points.

observed should be uniform across all the films.

Another potential contribution to lattice strain particular to the PLD process is plume-induced stress. This has been reported for CeO_2 and CGO films deposited at low oxygen partial pressures [390, 421]. The energetic irradiated target species impinge upon the substrate, building imperfect and strained crystallographic lattices. However, in both cases, plume-induced stress has resulted in a lattice expansion, rather than a compression. No definitive explanation can be given for the out-of-plane compressive strains observed.

As the CGO film thickness increases, the CGO film should relax and the measured strain decrease as film thicknesses increase. Due to the significant scatter in the results, coupled with the small number of samples, there is a large degree of uncertainty in the actual trend between average lattice strain and film thickness observed despite error margins being small, see Fig 9.7. It may be that the strain values for the thinnest, 4.8 nm thick, CGO film in both sample sets are anomalous. The X-ray signal from these CGO film was very small. For the CGO-only film, the broad nature of the CGO(200) reflection meant



(a) Sample set 1

(b) Sample set 2

Figure 9.8: CGO(200) peak fits for ∼4.8 nm thick CGO films of sample sets 1 and 2 deposited using 500 laser pulses. For sample set 1, it was possible to separate the CGO(200) and YSZ(002) reflections (the CGO(200) reflection shown here is the case with the largest peak overlap between CGO(200) and YSZ(002)), and Pseudo-Voigt fits were obtained from of a masked region corresponding to the CGO(200) peak position; the fit is indicated in red. For sample set 2, due to the overlap of the CGO(200), PCO(002) and YSZ(002) reflections, Pseudo-Voigt fits had to be made for each of these reflections, indicated in green, blue, and cyan respectively. The combined fit is indicated in yellow. These CGO films were the thinnest and had the lowest CGO(200) intensities, and thus had the largest error associated with their fit.

that it overlapped with the YSZ(002) reflection. In order to fit this peak, only a section of the peak was selected and fitted. This is also true for the PCO/CGO samples, but instead it was the PCO reflection at ∼33.5° 2θ that obscured the CGO(200) peak, and although all three peaks were fitted, it was not possible to get the fit to converge for the CGO(200) reflection. The fits of the CGO(200) for both CGO film of 4.8 nm nominal thickness (deposited using 500 pulses) in sample sets 1 and 2 are shown in Fig 9.8.

If this is the case, then a trend can be seen in both films wherein lattice strain increases with film thickness. This is contrary to the expectation that as film thickness increases, lattice parameters relax to the bulk value and thus lattice strain decrease to zero. No explanation can yet be suggested as to why this would occur. However, if these two data points are reliable, it could then be argued that the strain in the CGO films do relax as film thickness increases. Or, it could be that this is only true once when CGO film thicknesses exceed 15 nm, below which there is a different CGO/YSZ lattice mismatch relationship. Either of these may be said of the CGO films in both sample sets. Due to the few samples available, it is not yet possible to draw any firm conclusions. In any case, the interest of these films lies in obtaining a variation of their lattice parameters through strain, and less so its strain relaxation behavior though this should be investigated in further work.

Another point to note from the 'compressive' out of plane strains found in the CGO films of the PCO/CGO samples were lower than that found in the CGO films of the CGO/YSZ

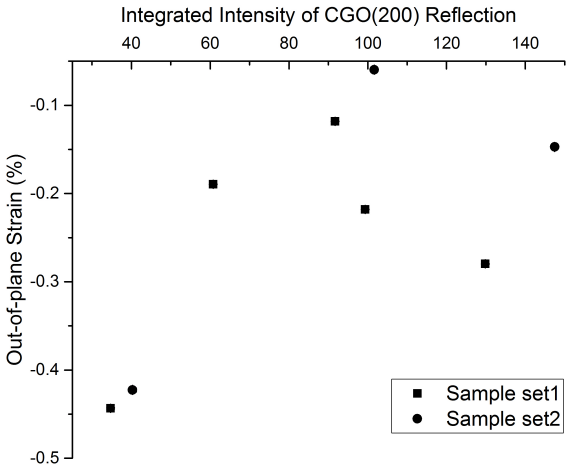


Figure 9.9: Out-of-plane lattice strain in the CGO films of sample set 1 (CGO/YSZ) and 2 (PCO/CGO/YSZ) as a function of the integrated intensity of the CGO(200) reflection, which was felt to be the most indicative measure of actual CGO film thickness. The measured out-of-plane lattice strains of the CGO films of sample set 1 were consistently larger than sample set 2 when a PCO film was deposited on top of the CGO.

samples, of a similar CGO film thickness, see Fig 9.9 where the strains in the CGO films of both sample set 2 are compared against each other as a function of the integrated intensity of the CGO(200) reflection. This may be due to the presence of the PCO film, introducing another constraint on the CGO buffer layer in sample set 2. If the CGO buffer layer relaxes as its thickness increases, then depending on how thick the CGO layer is and therefore what its lattice parameters are relative to that of PCO, the PCO film may additionally compress or stretch the in-plane lattice parameters. This should be reflected in an increase or decrease in the out-of-plane lattice parameters respectively. These two outcomes are illustrated in Fig 9.10.

As seen in Fig 9.10, the presence of the PCO film reduced the compressive out-of-plane strain in the CGO buffer layered (compared to the compressive lattice strains in the CGO-only film). Therefore, all things being constant, the PCO film must contribute an in-plane compressive strain, reducing the out-of-plane lattice compression). The CGO film must have relaxed sufficiently that the lattice parameters at the CGO/PCO interface are larger than that of the matching PCO parameters. Calculations for the actual CGO lattice parameter at the CGO/PCO interface will be performed later in this section.

Alternatively, the peak shift of the CGO(200) reflection for the PCO/CGO films may be the result of zero error rather than any real changes to the CGO strain state. With the PCO/CGO films, the CGO signal comes from below the sample surface. However, the average PCO layer thickness for these films was only about 78 nm. It was unclear if such a small offset would result in such a discrepancy in the calculated CGO out-of-plane strain values.

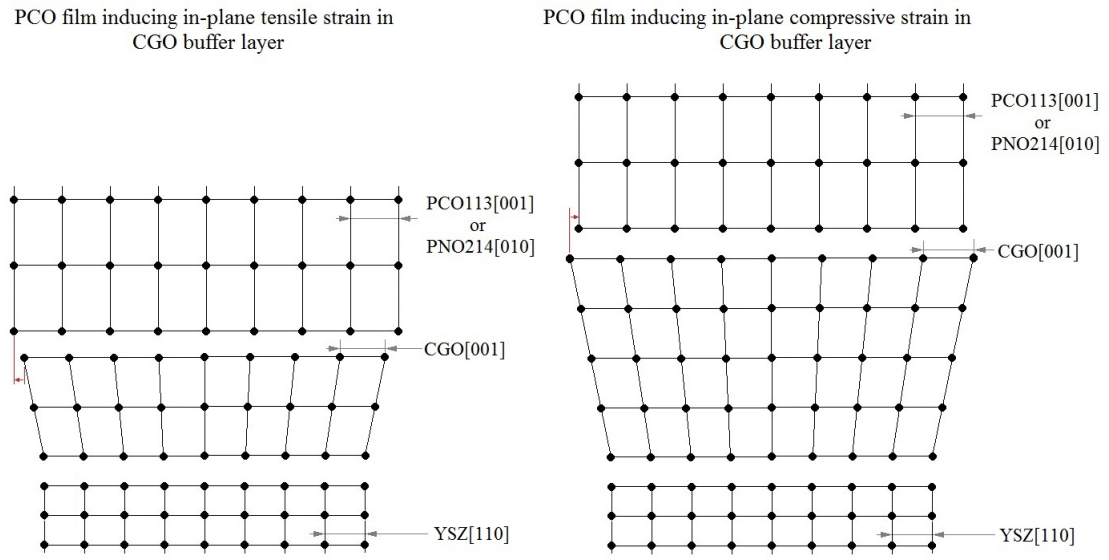


Figure 9.10: Schematic of the different potential effects of the PCO film on the lattice strain of the CGO film, depending on the CGO film thickness. If the CGO film is thin enough that it is unable to relax back to a lattice parameter larger than the PCO lattice parameter, the PCO film would introduce an in-plane tensile strain in the CGO film. If the CGO film is thick enough that it is able to relax back to a lattice parameter larger than the PCO lattice parameter, the PCO film would introduce an in-plane compressive strain in the CGO film.

Rocking curves of the CGO(200) reflections for various film thicknesses of sample sets 1 and 2 are presented in Table 9.3. FHWM values were calculated by using a Pseudo-Voigt fit. The CGO films of the CGO/YSZ samples were of a much lower mosaicity, 0.32° to 0.46°, compared to those of the PCO/CGO/YSZ samples, which had FWHM values between 1.09° and 1.18°. It appears that increasing CGO film thickness reduces the mosaicity of the film, perhaps as a result of strain relaxation. This is present in both sample sets (see discussion later), however it is not possible to say with any certainty due to the small number of samples.

The shapes of the CGO(200) rocking curves between the CGO/YSZ and PCO/CGO/YSZ samples are very different. For the PCO/CGO/YSZ samples, there appears to be a uniform distribution of lattice tilts resulting in a more typical peak that is easily fitted. However, from the CGO(200) rocking curves for the CGO/YSZ samples, the CGO film appears to have a split distribution of tilts, with tilt angles being either very small, or very large. Therefore, each rocking curve was fitted using two curves, centered at the same position were but with different FWHM. Using this fit, it can be seen that the CGO films of the CGO/YSZ samples exhibit very low mosaicity in parts with an FWHM between 0.19° and 0.30°, and in other parts, exhibit a mosaicity that is comparable to that found in the CGO films of the PCO/CGO/YSZ samples.

As CGO film thickness increases, it appears the proportion of large off-plane-normal tilts increases. This broad base is not seen at all for the thinnest CGO film, but becomes

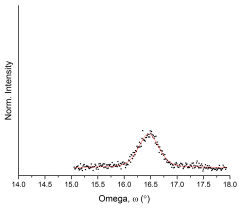
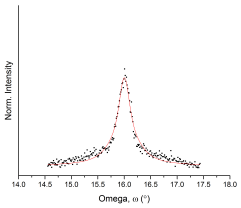
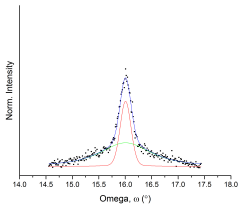
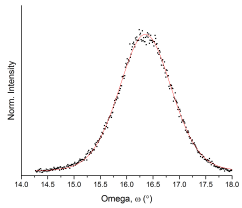
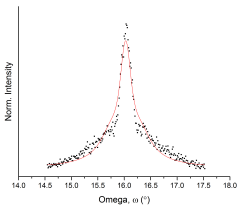
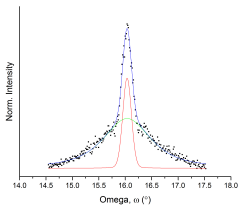
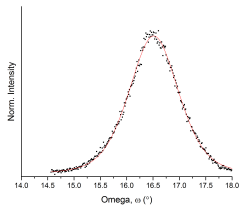
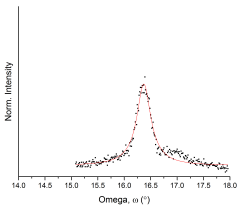
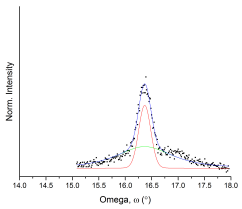
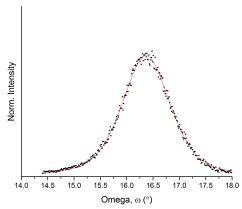
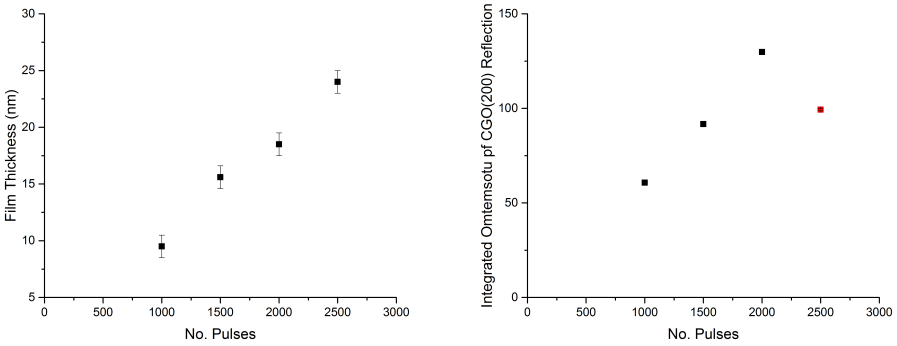
	Sample set 1		Sample set 2
1000 pulses			
	FHWM = 0.46°		
1500 pulses			
	FHWM = 0.32°	FHWM = 0.24° , 1.14°	FWHM = 1.18°
2000 pulses			
	FHWM = 0.35°	FHWM = 0.19°, 1.08°	FWHM = 1.13°
2500 pulses			
	FHWM = 0.32°	FHWM = 0.30°, 1.24°	FWHM = 1.09

Table 9.3: Rocking curves of the CGO(200) reflection of CGO films deposited using 500 to 2500 pulses, of sample sets 1 and 2. For sample set 1, two different Pseudo-Voigt fits were useds due to the shape of the rocking curve. In the first fit, only one Pseudo-Voigt profile was usee. In the second fit, two Pseudo-Voigt prfiles were used, as if there were to CGO(200) contrbutions- one with low mosaicity, and one with a high mosaicity. Pseudo-Voigt fits are indicated in red. Where more than one Pseudo-Voight fit was used, the first fit is in red, the second in green, and the overall fit in blue. FWHM values have been measured and provided (for the multiple Pseudo-Voigt fit of sample set 1, the first FWHM value corresponds to the first Pseudo-Voigt profile in red, and the second FHWM values corresponds to the second Pseudo-Voigt profile in green. Increasing CGO film thickness decreased CGO film mosaicity.



(a) XRR calculated film thickness (b) Integrated CGO(200) intensity

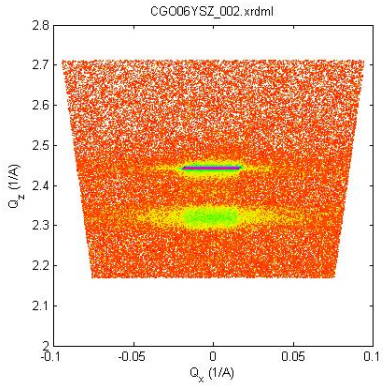
Figure 9.11: Comparison of the actual measured CGO film thickness using XRR and the integrated CGO(200) intensity of sample set 1. The integrated area of the CGO(200) reflection of the CGO film deposited using 2500 pulses appears anomalous (in red).

more apparent as film thickness increases. The exception is the CGO film deposited using 2500 pulses, which had almost identical proportions of large and small off-plane-normal tilts as the CGO film deposited using 1500 pulses. However, the actual peak areas of the CGO(200) reflections in the sample set suggests that the 2500 pulse film is actually of a comparable thickness to the 1500 pulse film, and therefore a smaller proportion of large off-plane-normal tilts would be expected, as is seen.

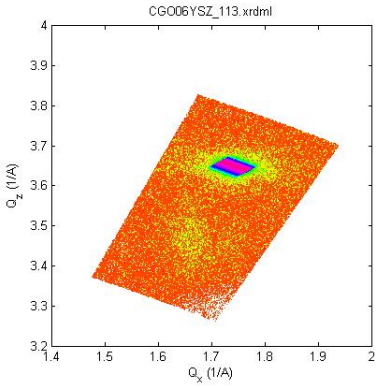
However, this now raises a discrepancy in the thicknesses measured of the CGO thin films of sample set 1. XRR measurements of the 2500 pulse CGO film thickness provide a thickness value of 24 nm. However, CGO(200) peak area calculations suggest that the 2500 pulse film is only as thick as the 1500 pulse film, 15.6 nm, Fig 9.11. This discrepancy is not within the error of the measurements. The only suggestion that can be offered lies in the preparation of multiple samples within the same PLD run. These samples should be identical. However, due to the different positions of the samples relative to the laser plume, there maybe differences in, for example, film thicknesses. Thus it may be that different samples were used between XRR measurement and the out-of-plane XRD measurement, hence the discrepancy, despite both samples being deposited in the same PLD run. The CGO deposition rate of 9.6 nm/1000pulses is valid, however, it should be noted for the CGO(200) reflection, peak area was a better indicator of CGO film thickness, for the strain measurements.

All things being constant, the different mosaicity between CGO films of the CGO/YSZ samples and the PCO/CGO/YSZ samples can only be attributed to the presence of the PCO layer. The PCO layer appears to even out the mosaic spread of the CGO layer beneath it. A possible explanation for this is, if the PCO film is sufficiently thick, a different strain relaxation mechanism occurs as dislocation dipoles are created instead [365]. This may be reflected in the mosaicity of the CGO films.

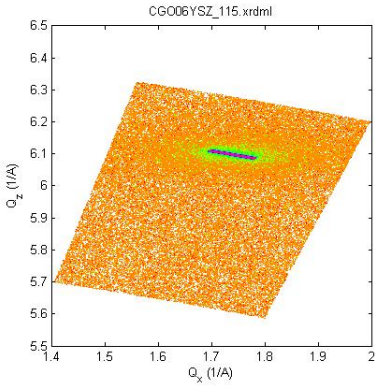
To further investigate the structure of the CGO film and its inplane orientations, RSM



(a) Symmetric (002) scan



(b) Asymmetric (113) scan

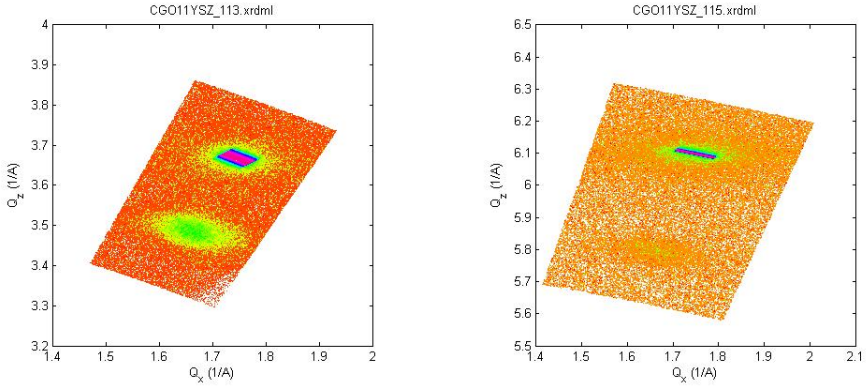


(c) Asymmetric (115) scan

Figure 9.12: RSM of the CGO(200) reflection of CGO(200)/YSZ(002) deposited using 500 pulses, of sample set 1. CGO film intensities were too low to detect a peak in the asymmetric 115 scan, nevertheless it appears that the CGO film is epitaxial albeit with a high mosaicity.

were obtained of the CGO(200) reflection for the thinnest CGO film (deposited using 500 pulses) and the thickest 24.0 nm thick CGO film, see Fig 9.12 and Fig 9.13 respectively. In the symmetric scan of the thinnest CGO film, both YSZ(002) and CGO(200) reflections could clearly be seen. However, in the asymmetric scan of the (113) pole, the CGO(200) reflection was much more diffuse, and could not be detected at all for the (115) pole. For the asymmetric scans of the thickest CGO film, the (113) and (115) poles of CGO can more clearly be seen, confirming epitaxy of the CGO film. The shape and shift of the CGO poles confirm in-plane strain, and also mosaic spread.

The strain profile of the film is independent of the strain relaxation mechanism present. However, only the results from sample set 1 (CGO/YSZ films) may be fitted to calculated the constants, ϵ_0 and α for the CGO film, as in sample set 2, there is the additional strain inducing effect of the PCO film at the CGO/PCO interface. Using Eqn. (9.4), ϵ_0 and α have been found to be -0.56 and 0.16 nm^{-1} respectively, compared to values of ϵ_0 and α of 0.023 and 0.17 nm^{-1}, respectively, by Lee et al. [312]. The rates of relaxation, indicated by α are very similar. The negative value for ϵ_0 is due to the out-of-plane strain being compressive and should reflect the strain in the CGO/YSZ interface. However, based on only



(a) Asymmetric (113) scan (b) Asymmetric (115) scan

Figure 9.13: RSM of the CGO(200) reflection of CGO(200)/YSZ(002) deposited using 2500 pulses, of sample set 1. The CGO reflection may be seen in both asymmetric (113) and (115) scans, suggesting that the thicker CGO films are also epitaxial.

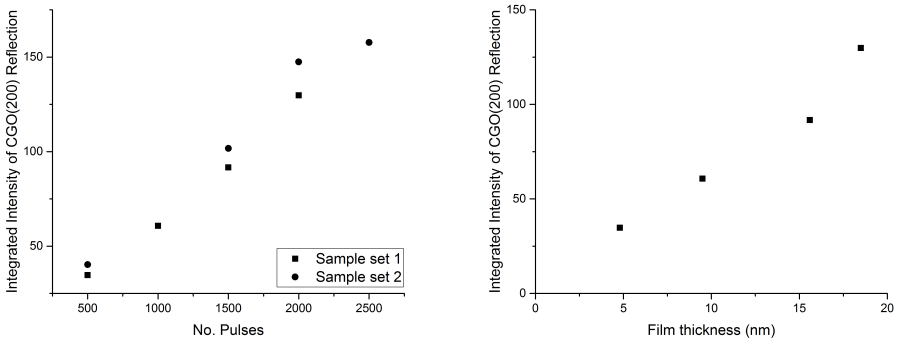
Number of pulses	CGO film thickness (nm)	Measured average lattice strain (%)	Lattice strain at CGO surface (%)
500	4.8	-0.44	-0.26
1000	9.5	-0.19	-0.12
1500	15.6	-0.12	-0.05
2000	18.5	-0.28	-0.03
2500	24	-0.22	-0.01

Table 9.4: Surface strain of the CGO film of sample set 1, calculated using (9.3) where ϵ_0 and α are -0.56 nm^{-1} and 0.16 nm^{-1} respectively.

the CGO(200) out-of-plane reflection being detected, and a suspected CGO[100]/YSZ[110] relation as has been reported in literature, the -5.29% in-plane compression of the CGO lattice should be compensated by an out-of-plane tension around 1.59% at the CGO/YSZ interface, based on a Poisson ratio, ν of 0.3 for CeO_2 [422]. This was not what has been obtained, reasons for which have been suggested earlier.

It should be noted that there is a significant error in this fit due to the small sample set and the large variance. Nevertheless, it does provide an indicator of the strain profile within the film. The film thickness required for the CGO lattice to relax to 99.99% of its bulk value is 54.12 nm (more than double the relaxation length of (111) oriented CGO films on sapphire(0001) [312]). All CGO films deposited were within that thickness. The predicted out-of-plane lattice mismatches in the CGO film surface, calculated using (9.3), are shown in Table 9.5.

The CGO buffer layers of sample set 2 following the same correlation between CGO(200) peak area with deposition time, as the CGO films of sample set 1, excluding the CGO film deposited using 2500 pulses in sample set 1. This relation justifies the use of the correlation in CGO(200) peak area with XRR thickness measurements of sample set 1, see Fig 9.14. Based on this, the CGO buffer layer thicknesses of sample set 2 have been



(a) (b)

Figure 9.14: (a)CGO films of both sample set 1 and 2 can be seen to share the same relationship between the the integrated area of the normalized CGO(200) reflection and the number of laser pulses used for the deposition of the film. The integrated area of the CGO(200) reflection appeared to be most indicative of CGO film thickness. Thus in (b), the integrated area of the normalized CGO(200) reflections of sample set 1 have been correlated with the measured thickness of the CGO films of sample set 1 to obtain a relationship from which the CGO film thicknesses of sample set 2 may be calculated given its (200) peak area: a values of 6.55 CGO(200) normalized peak area corresponds to a CGO film thickness of 1 nm.

estimated from its CGO(200) peak area, and subsequently also the out-of-plane lattice strains at the CGO/PCO interface of these samples have been calculated using ϵ_0 and α values calculated from sample set 1, see Table 9.5.

Therefore, the morphology of the CGO films have been found to be flat, with uniformly sized columnar grains. Surface roughness values were comparable to those of blank substrates. The CGO films were highly textured, exhibiting the (200) out-of-plane orientation. Mosaicity of the films was found to decrease as the CGO film thickness increased. The CGO films of sample set 1 did not have a normal distribution of surface tilts, but had a broad background of large surface tilts, the proportion of which increased with film thickness. It remains to be seen if this surface is of a sufficient quality for successful deposition

Number of pulses	Normalized CGO(200) peak area (arb. Intensity)	Estimated CGO film thickness (nm)	Lattice strain at CGO surface (%)
500	40.26	6.15	-0.21
1500	101.68	15.53	-0.05
2000	147.46	22.52	-0.02
2500	157.78	24.10	-0.01

Table 9.5: Surface strain of the CGO film of sample set 2, calculated using (9.3) where ϵ_0 = -0.56 nm^{-1} and α = 0.16 nm^{-1} respectively. CGO film thicknesses have been estimated using the relation found of the CGO films of sample set 1, where a values of 6.55 CGO(200) normalized peak area corresponds to a CGO film thickness of 1 nm.

of strained PCO films.

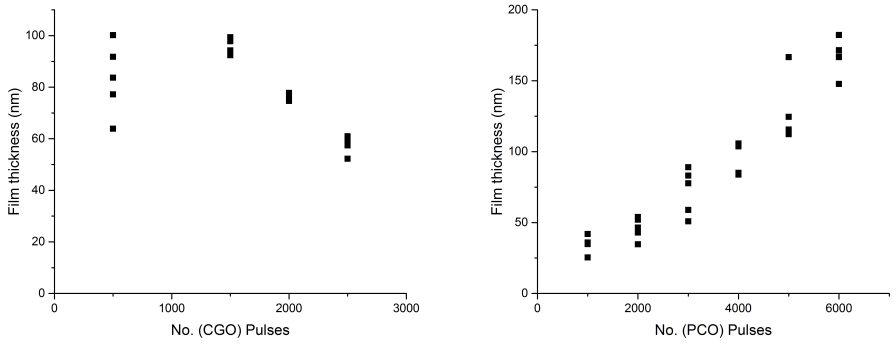
Contrary to the expectation of an out-of plane tensile strain in the CGO films, based on lattice mismatch with the YSZ substrate, a range of out-of-plane lattice compression was measured in CGO films of both sample sets. If oxygen stoichiometry is maintained between CGO target and deposited film, and the trend exists wherein the strain in the CGO film relaxes as its thickness increases, ϵ_0 and α were found to be 0.023 and 0.17 nm^{-1} respectively. Based on this, all CGO film thicknesses were within the CGO strain relaxation length (calculated to be 54.12 nm for 99.99% for the lattice strain to have relaxed back to bulk parameters), and a range of lattice strains at the CGO surface and at the CGO/PCO interface have been calculated: between -0.012% and -0.211%. A range of lattice strains is expected in the PCO films deposited on top of the CGO buffer layers of varying thicknesses.

9.3.2 Morphological and Structural Characterization of Strained $PrCoO_{3-\delta}/Ce_{0.9}Gd_{0.1}O_{2-\delta}$/YSZ8-mol% Films

Previously, the CGO films of sample set 1 and 2 were examined. In this section, the PCO films of sample set 2 and sample set 3 will be inspected. The PCO films of sample set 2 are of nominally identical thicknesses (deposited using 1000 pulses) on CGO buffer layers of varying thicknesses. These CGO buffer layers have a compressive out-of-plane lattice strain at the CGO/PCO interface from -0.211%, decreasing to -0.012%, as the CGO buffer layer thickness increases, and the lattice relaxes. The PCO film experienced various degrees of lattice mismatch. The PCO films of sample set 3 are deposited upon a ∼4.8 nm thick CGO buffer layer using 1000 to 6000 pulses.

Film thickness measurements of the PCO/CGO films of both sample sets were made using the Dektak 150 surface profiler. These results were adjusted for the thickness of the CGO buffer layer, see Fig 9.15. For sample set 2, CGO buffer layer thickness was found through the relation between the area under the CGO(200) peak in the previous section, see Fig 9.14. However, for sample set 3, where CGO buffer layers were deposited using 1000 pulses, the CGO(200) reflection could not be fitted nor its area obtained. Thus, a constant CGO deposition rate of 4.8 nm/1000 pulses was assumed for these films.

In sample set 2, a variation in PCO film thicknesses, between 57.9 and 89.5 nm was measured, despite deposition conditions of the PCO films being nominally identical. The average PCO film thickness measured was 72 nm. It is unclear why this has occurred but must be attributed to slight variations in the deposition conditions and the nature of the PLD process involving the ablation of a range of particle sizes. This does raise concern as to the repeatability of the PLD process and should be noted in the discussion of the average strain of these films. In addition to the effect of different lattice mismatch at the CGO/PCO interface, there also exists different extents of strain relaxation arising from the different film thicknesses. In sample set 3, a linear increase in film thickness with



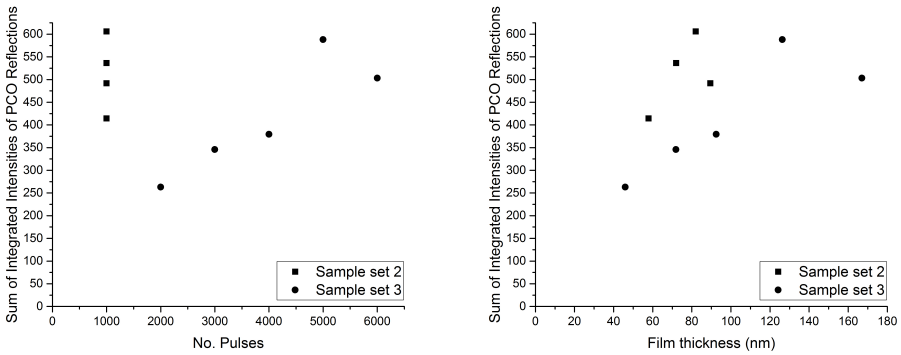
(a) Sample set 2 (b) Sample set 3

Figure 9.15: Film thicknesses of PCO films deposited in sample set 2 and 3, as measured using a Dektak 150 surface profilometer. For sample set 2, CGO film thicknesses was calculated assuming a CGO deposition rate of 4.8 nm/1000 pulses. For sample set 3, an average CGO film thickness of 4.8 nm was assumed. PCO films of sample set 2 have been deposited using 3000 pulses. PCO films of sample set 3 have been deposited using a range of laser pulses, between 1000 to 6000 pulses.

deposition conditions was measured. The PCO deposition rate on CGO(200) was found to be ∼25.8 nm/1000 pulses.

In order to check the reliability of these film thickness measurements, a comparison was made against the area under PCO reflections from out-of-plane XRD patterns, see Fig 9.16. The area under the PCO reflections are indicative of the PCO film thickness, a similar correlation with measured thicknesses and the number of pulses during deposition should be seen in PCO films of sample sets 2 and 3, as was found of the CGO films from sample set 1 and 2. However, while a correlation may be seen between PCO peak area and the measured PCO thicknesses for both sample sets, there was a large range of measured PCO thicknesses in sample set 2 for which 1000 laser pulses were used during the deposition of those films. Thus, especially for the PCO films of sample set 2, the number of laser pulses employed during deposition may not be the best indicator of actually PCO film thickness- there was significant variation in PCO film thickness despite the identical deposition conditions. Additionally, the relationship between PCO peak area and the measured thickness of the film was not the same between sample set 2 and 3 (as it was with the CGO films), despite deposition conditions of the PCO films being nominally identical. Therefore, there is some certainty in the PCO deposition rate obtained, but there are significant differences in the thicknesses in the PCO films of sample set 2.

AFM images were taken from sample set 2 and 3 and are depicted in Fig 9.17 and Fig 9.18, respectively. These PCO films were significantly rougher than the CGO buffer layers, with PCO film R_{rms} values as much as a magnitude larger than the R_{rms} values of the CGO buffer layers measured earlier in Section 9.3.1. The increase in film roughness was not unexpected given the thickness of the deposited PCO films. On all occasions, uniform distributions of grain sizes were seen in the PCO films.



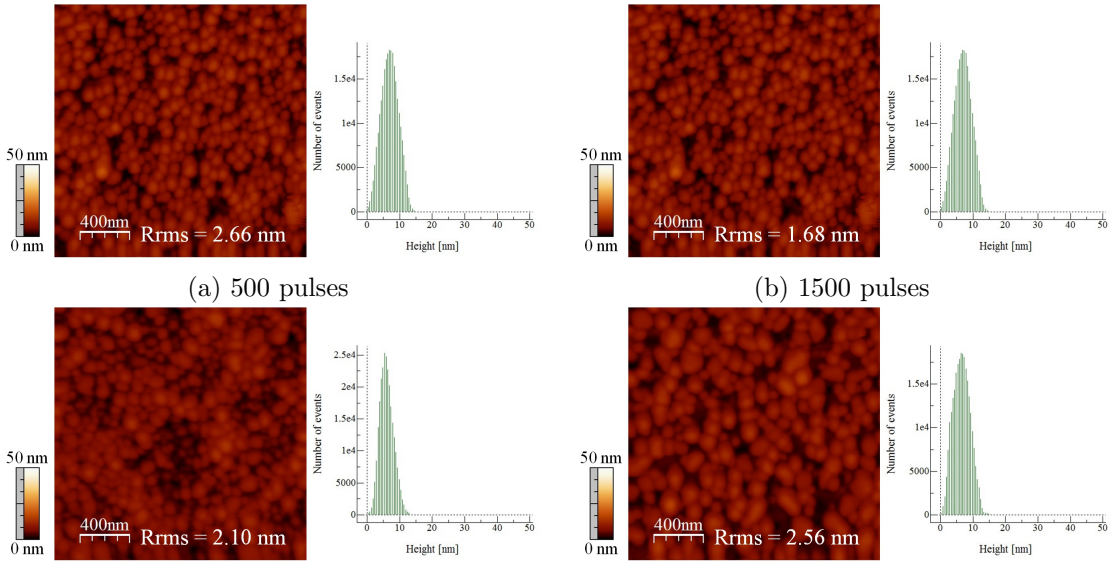
(a) (b)

Figure 9.16: Summed integrated intensities of PCO reflections of PCO films in sample sets 1 and 2, as a function of (a) the number of laser pulses used for PCO deposition and (b) the average measured PCO thickness using the Dektak 150 surface profilometer. PCO film thicknesses of sample set 2 were confirmed to have significant variation.

In sample set 2, the effect of increasing the buffer layer thickness was a slight increase in the diameter of the columnar PCO grains deposited. The change in PCO grain size may be attributed to the variation in the strain state of the CGO buffer layer as its thickness increases and it relaxes, or to the variation in CGO buffer layer roughness. The surface roughness values of the PCO films of sample set 2 are comparable, with R_{rms} values between 1.68 nm and 2.66 nm. It appears from the AFM images that PCO films experiencing a greater lattice mismatch have columnar grains of a larger diameter. In sample set 3, R_{rms} surface roughness increased 1.21 nm to 4.63 nm as the number of pulses used to deposit the PCO film increased from 1000 to 6000. R_{rms} roughness was plotted against PCO XRD peak area (the better indication of actual film thickness) in Fig 9.19. Thus, film roughness can be seen to deteriorate by an R_{rms} value of 0.57 nm/10 nm increase in PCO film thickness. Increasing PCO film thickness also increased the grain size of the film.

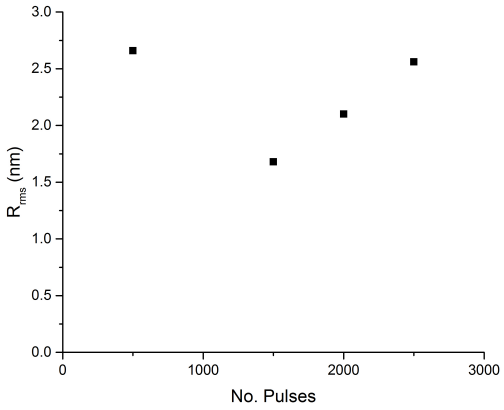
Besides the LSC thin films produced by O'La et al. [7], these PCO films have a significantly rougher surface when compared to LCO and LSC films of similar thicknesses reported in literature (where $R_{rms} \leq$0.8 nm) [419, 8, 227, 29].There also appears to be a slight increase in grain size with PCO film thickness, which was also not reported in previous literature [419, 7, 227]. It should be noted that the increase in grain size with film thickness was more marked in polycrystalline PCO films deposited on Si(004) in Chapter 7. The diameter of the columnar grains of the PCO films appears sensitive to a number of factors related to its strain state. Also different strain relaxation mechanisms can give rise to the same trend in surface morphology.

SE images were taken of these two sample sets, see Fig 9.20 and Fig 9.21, and are in relative agreement with the AFM images: PCO film grain sizes are mostly uniform and an increased grain size can be seen as the thickness of the CGO buffer layer or PCO film increased. The grain size of the PCO films of sample set 2 was found to increase at a



(a) 500 pulses (b) 1500 pulses

(c) 2000 pulses (d) 1500 pulses



(e) R_{rms}

Figure 9.17: AFM images and measured R_{rms} of the PCO films of sample set 2, where a different number of laser pulses were used in the deposition of the CGO buffer layer (as specified for each image). Increasing CGO buffer layer thickness and thus the lattice mismatch between CGO and PCO had no clear effect on the PCO film roughness, but an increase in PCO grain size was observed though this may have been due to the decrease in PCO thickness (with CGO thickness) despite PCO deposition conditionals being nominally identical.

greater rate than samples set 3. However, from the SE images, the increase in grain size of the PCO films of samples set 2 was much more distinct than suggested in the AFM images. There are two other differences, observed in the SE images but not the AFM, discussed below. The reason for these discrepancies is unknown.

For sample set 2, SE images revealed full coverage of the PCO film over the CGO buffer layer. For the PCO films deposited on the thicker CGO buffer layers (notable for the thickest ∼24.1 nm thick CGO buffer layer deposited using 2500 pulses, see Fig 9.20d), the

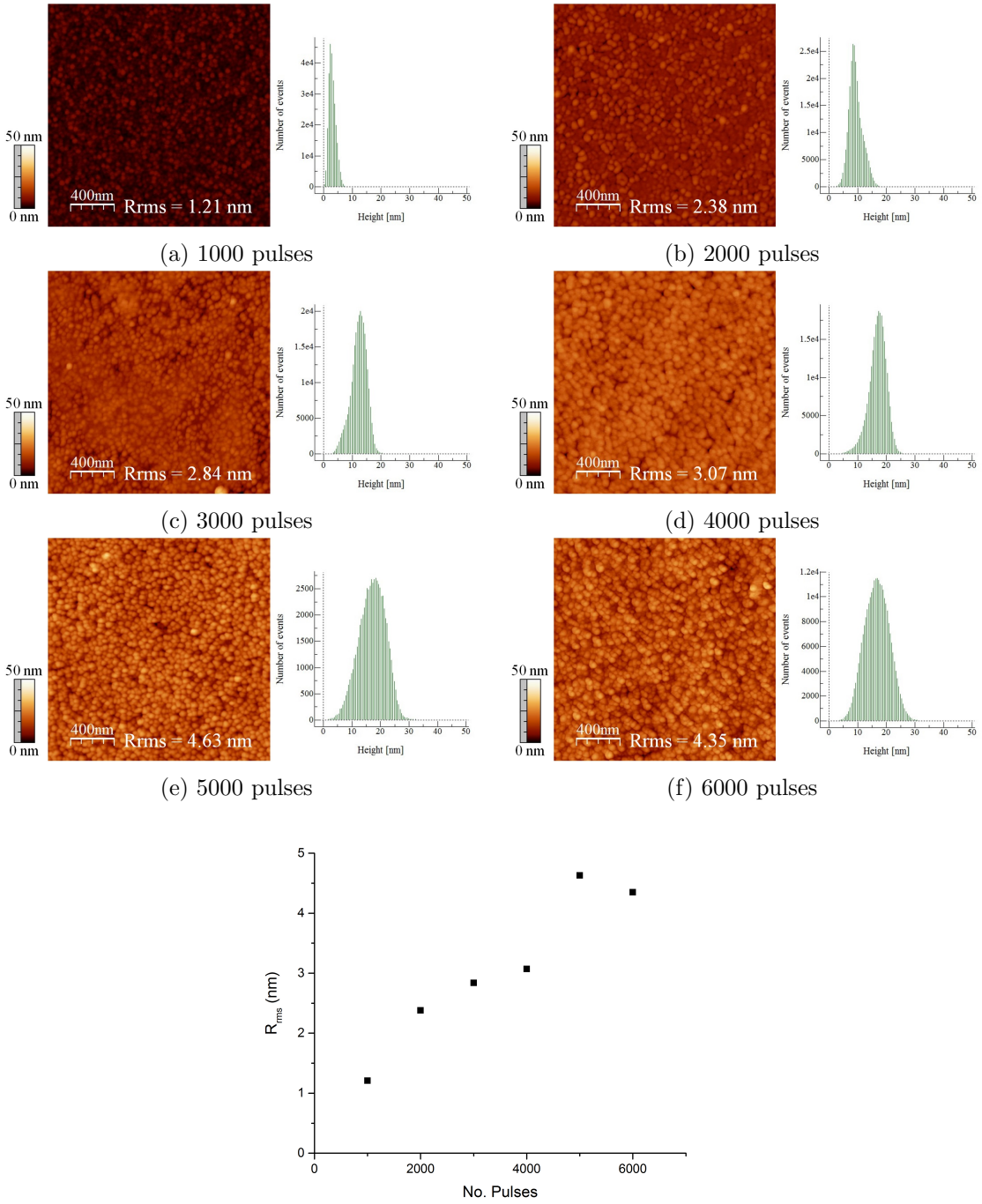


Figure 9.18: AFM images and measured R_{rms} of the PCO films of sample set 3, where a different number of laser pulses were used in the deposition of the PCO film (as specified for each image). Increasing PCO film thickness and thus decreasing the lattice strain in the PCO film, increased both PCO film R_{rms} roughness and grain size.

PCO grains were much less regular in shape, with a range of sizes, and it appears that some grains were growing at the expense of others. While this has been seen previously in LSC films, it was not to this extent. For the thickest CGO buffer layer, the PCO film

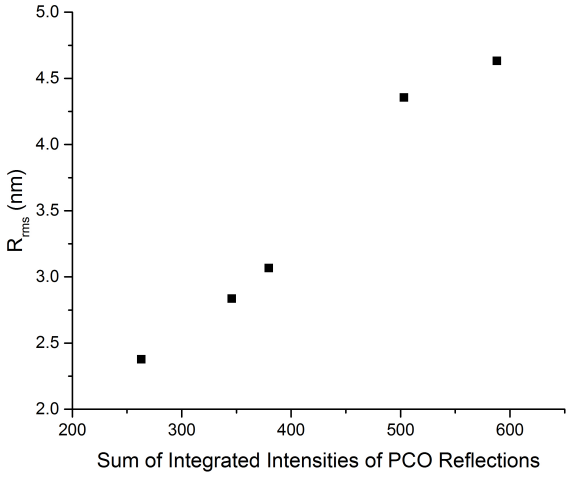
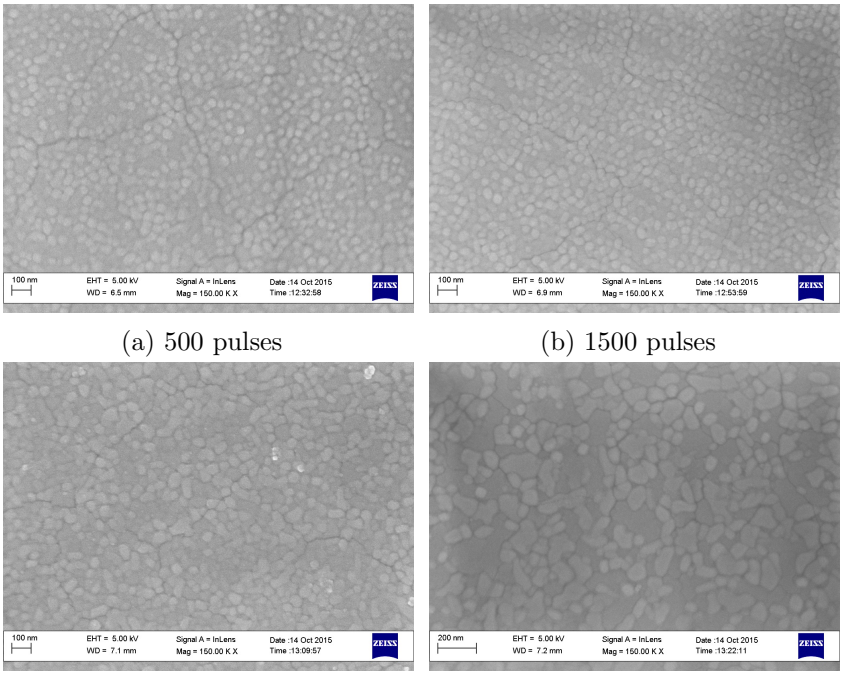


Figure 9.19: Out-of-plane lattice strain in the CGO films of sample set 1 (CGO/YSZ) and 2 (PCO/CGO/YSZ) as a function of the integrated intensity of the CGO(200) reflection, which was felt to be the most indicative measure of actual CGO film thickness. The measured out-of-plane lattice strains of the CGO films of sample set 1 were consistently larger than sample set 2 when a PCO film was deposited on top of the CGO.

thickness was measured to be ∼57.9 nm. It was considerably thinner than the other PCO films deposited also using 3000 pulses. The different film morphology may be the cause of this decrease in PCO film thickness if it results in a PCO film of a higher density. It is unclear if this PCO film was an outlier which was thinner and had a different morphology, or if it was related to the thickness of the CGO buffer layer and the subsequent lattice strain induced. As a gradual change in PCO film morphology of sample set 2 may be observed, and it may also be argued that there was a trend in PCO film thickness with CGO buffer layer thickness (Fig 9.15a), a more likely conclusion was that increasing the CGO buffer layer thickness and thus changing the lattice mismatch between CGO and PCO caused this shift in film morphology and increase in film density.

Also, for the PCO films of sample set 3, as the PCO film thickness increased, though grain size also increased, the grains remained regular shaped and of a uniform size ∼50 nm, except for one film. The thickest PCO film (∼167.0 nm) has a distinctly different surface morphology. The grains are now highly irregular in shape, and it is unclear if a columnar grain structure still exists. All things being constant, this change in surface morphology can only be attributed to the increased thickness of the PCO film. This morphology has not been previously identified in the literature. However, reported film thicknesses do not exceed 140 nm [29].

The out-of-plane XRD patterns of sample sets 2 and 3 are depicted in Fig 9.22 with peak assignments for the PCO reflections found at ∼23.4° 2θ, ∼33.5° 2θ, ∼41.2° 2θ and ∼48.0° 2θ. These assignments were based on the presence of a recurring family of planes, as seen in oriented thin films. Unlike what was found for LSC films deposited on CGO/YSZ



(a) 500 pulses (b) 1500 pulses

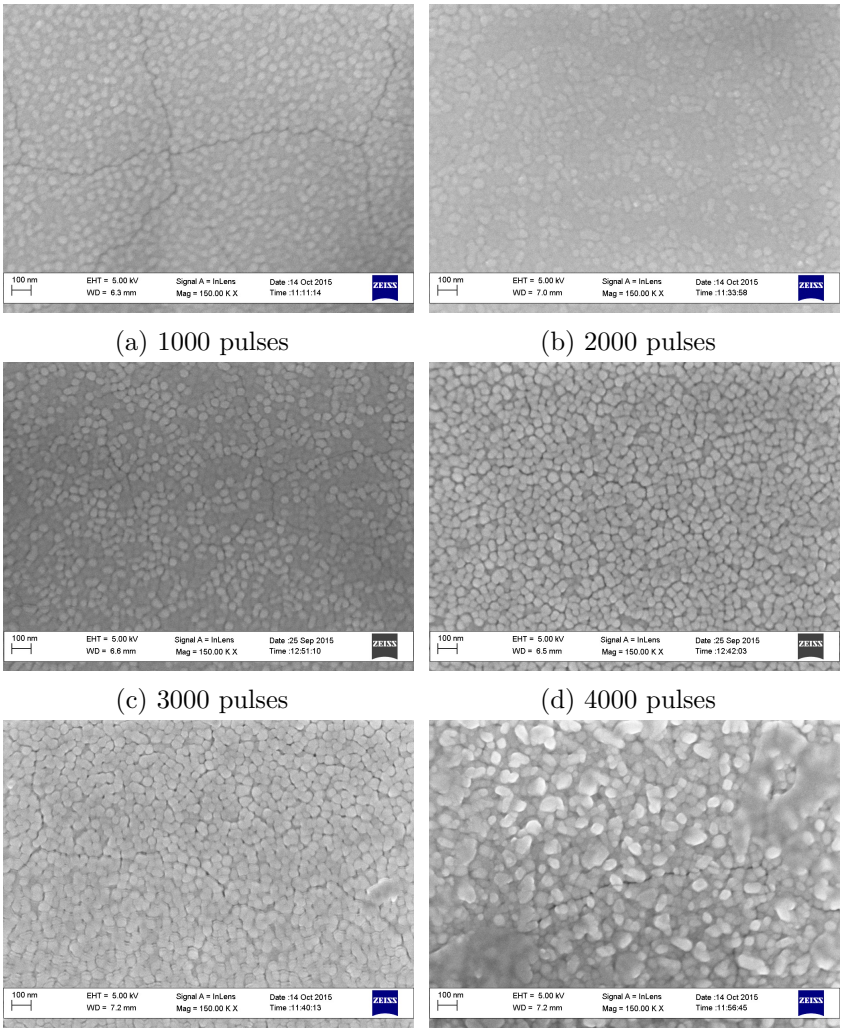
(c) 2000 pulses (d) 2500 pulses

Figure 9.20: SE images of the PCO films of sample set 2, where a different number of laser pulses were used in the deposition of the CGO buffer layer (as specified for each image). PCO grain size can be seen to increase substantially with the increase in CGO buffer layer thickness and subsequently also the PCO/CGO lattice mismatch, and film morphology can also be seen to evolve into less regularly shaped grains with a larger grain size distribution.

where only one reflection was observed [7, 8, 227, 27, 29], a number of orientations are present. In sample set 2, the PCO peaks remain fairly constant, while the CGO(200) reflection increases in intensity, and the opposite was observed for sample set 3 reflecting the increase in CGO buffer layer thicknesses and PCO film thicknesses of the two sample sets respectively.

The (020) and (040) reflections correspond to the structural configuration that has been previously reported for LCO and LSC (though a different space group notation was used) [7, 8, 227, 27, 29]. This is the arrangement that would result in minimal lattice strain. It was expected that the tetragonal PCO lattice would stack directly upon the cubic CGO with its (longest) b-cell parameter aligned to the out-of-plane normal as depicted in the schematic Fig 6.1 in Chapter 6. This should result in an in-plane lattice mismatch between PCO[100]/CGO[100] of 0.8%.

A PCO peak was also observed at $\sim$33.5° 2θ, which may correspond to either the(200), (121), or (002) reflection. This peak has been assigned to the PCO(002) reflection, as if it were assigned to the PCO(200), it would suggest an out-of-plane tension in the PCO film that increased with PCO film thickness (whereas the lattice mismatch between CGO and PCO predicts an out-of-plane compression should occur due to the lattice mismatch and when the PCO(002) assignment is used, PCO strain relaxation was indeed observed).



(a) 1000 pulses (b) 2000 pulses

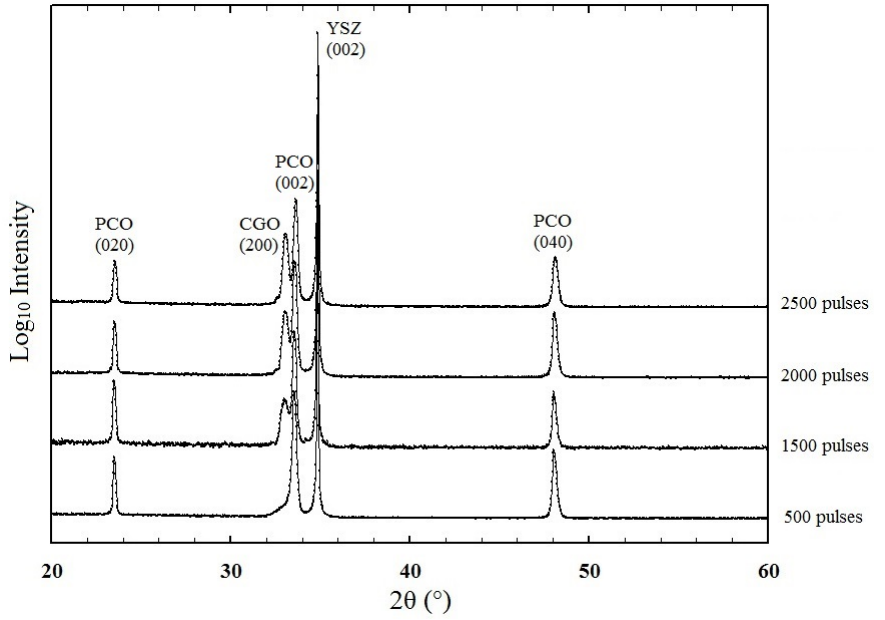
(c) 3000 pulses (d) 4000 pulses

(e) 5000 pulses (f) 6000 pulses

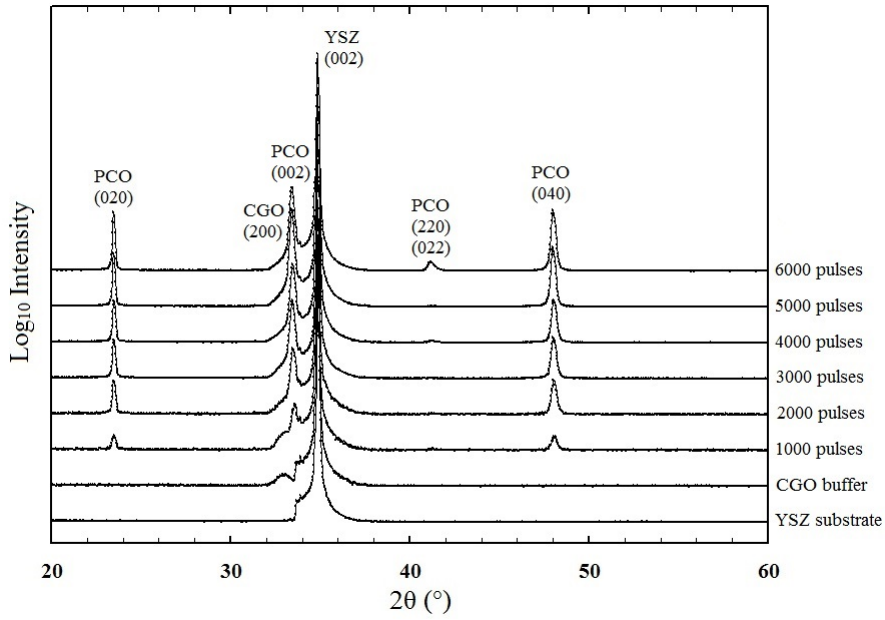
Figure 9.21: SE images of the PCO films of sample set 3, where a different number of laser pulses were used in the deposition of the PCO film (as specified for each image). Increasing PCO film thickness and thus decreasing the lattice strain in the PCO film, increased the average PCO film grain size.

Additionally it is of the same family of planes as the (020) diffracting plane. A likely arrangement given this orientation is that the PCO lattice stacks directly upon the CGO lattice but with a 45° rotation of the CGO lattice about the axis normal to the film surface. In-plane characterization is necessary to confirm the relation of these oriented PCO cells to each other in the film.

However, for PCO films of varying thicknesses deposited on CGO buffer layers of nominally identical thicknesses (sample set 3), another family of planes was observed. For PCO films deposited using 4000 and 6000 pulses an additional trace peak was detected at ∼41.2° 2θ (it should be noted that a $\log_{10}$ scale is used in Fig 9.22, underplaying the difference in high intensity reflections). This corresponds to the PCO(022) or PCO(220) reflection using the *Pnma* space group. This suggests that other PCO orientations may be present,



(a) Sample set 2



(b) Sample set 3

Figure 9.22: Out-of-plane XRD patterns of the PCO films of: (a) sample set 2, for which 1000 pulses were used for the deposition of the PCO film, but a range of pulses used for the deposition of the CGO buffer layer (as specified in the figure); and (b) sample set 3, for which a range of pulses were used for the depositin of the PCO film (as specified in the figure). PCO films of both sample sets appears highly textured. Only one family of diffraction planes was found of the PCO films of sample set 2. An additional orientation was found for the PCO films of sample set 3, corresponding to either the (220) or (022) diffraction planes.

below the detection limit. Increasing the PCO film thickness further may reveal all other orientations.

Sample	Peak intensity ratios of PCO reflections			
	PCO(020) ~23.4° 2θ	PCO(002) ~33.5° 2θ	PCO(220) ~41.2° 2θ	PCO(040) ~48.0° 2θ
Reference [6]	0.30	1	0.41	0.59
PCO target	0.33	1	0.52	0.63
PCO film (sample set 2)	0.14 - 0.23	1	0	0.19 - 0.27
PCO film (sample set 3)	0.18 - 0.27	1	0 - 0.06	0.34 - 0.50

Table 9.6: Peak intensities of the (020), (220), and (040) reflections of PCO, relative to the PCO(002) reflection. Two reference PCO patterns were used: from literature and from this work. The reflections at ~41.2° 2θ was assigned to the PCO(220) reflection. Despite the similar position of the PCO(220) and PCO(022) reflections, the 2θ position of PCO(220) was found to correspond best to that observed of the out-of-plane patterns. In any case, the peak intensities of the PCO(022) and PCO(220) reflections differ by no more than 7.0% of each other, using the PCO reference pattern [6] (or 8.6% using the PCO target diffraction pattern).

To investigate the texture of the PCO films, the peak areas of the detected reflections, relative to the highest intensity PCO(002) reflection at ~33.5° 2θ, were compared to published data of PCO [6] see Table 9.6. Thus, it can be seen that, from the peaks that were detected, there was some texture in the deposited PCO films with a preference for orientation corresponding to a 2θ position of ~23.4° 2θ and ~48.0° 2θ. Based on the lattice mismatch, this is likely to be the (0k0) orientation. It is also clear now that the (220) or (022) orientation, at ~41.2° 2θ, is suppressed. There are therefore grounds to believe that the films are textured, and that the peak assignments made on this assumption are valid.

There were no apparent trends in the relative peak intensities detected with increasing lattice mismatch (sample set 2) or with increasing PCO thickness (sample set 3). The changes in the strain state of the PCO film with CGO buffer layer thicknesses or PCO film thicknesses appear not to affect the relative growth of the different orientations present, despite having a clear effect on the morphology (and roughness, for sample set 3) of the PCO film.

Lastly, rocking curve data were collected for the PCO(020), PCO(040) and PCO(002) reflections from sample set 2 and 3. Unlike what was found for the CGO(200) rocking curves obtained from sample set 1, a good fit could be obtained using a Pseudo-Voigt model, see Fig 9.23. As would be expected, FWHM values for the PCO(0k0) reflections are comparable within the same film. For both sample sets, FWHM values were smaller for the PCO(002) reflection than the PCO(0k0) reflection, ranging between 1.10° to 1.18° in sample set 2, and between 1.13° to 1.35° in sample set 3, see Table 9.8 for FHWM values. This may be due to the smaller lattice mismatch for the (0k0) orientation, which may reduce the need to introduce dislocations to relieve the strain in the lattice, and also reduce surface curvature and mosaicity. No FWHM values could be found in the literature for LCO or LSC films on CGO/YSZ.

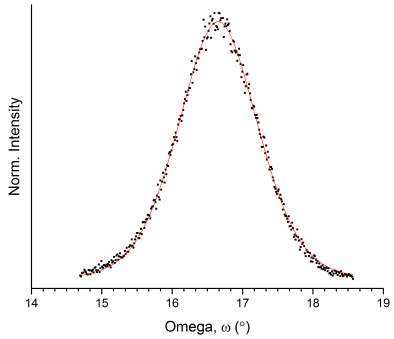


Figure 9.23: An example PCO(002) rocking curve of a PCO film of sample set 3, deposited using 5000 pulses with a Pseudo-Voigt fit (in red).

PCO films of sample set 2

No. CGO pulses	FWHM (°)		
	PCO(020)	PCO(040)	PCO(002)
1500	1.60	1.44	1.18
2000	1.41	1.39	1.13
2500	1.56	1.39	1.10

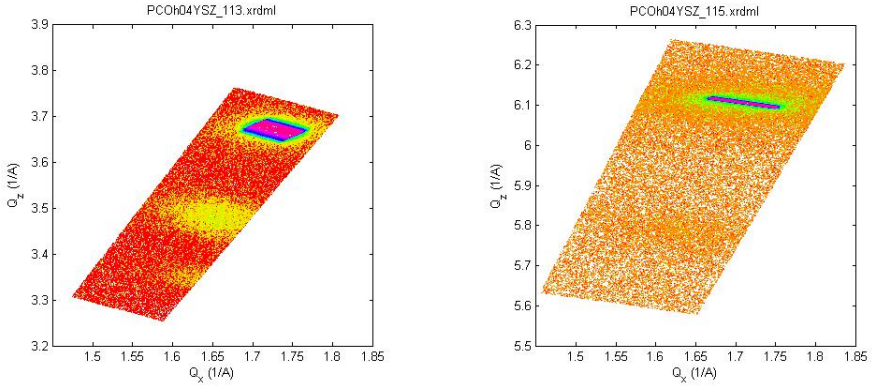
PCO films of sample set 3

No. PCO pulses	FWHM (°)		
	PCO(020)	PCO(040)	PCO(002)
2000	1.80	1.66	1.27
4000	1.40	1.37	1.13
5000	1.59	1.47	1.35

Table 9.7: FWHM of PCO rocking curves from sample sets 1 and 2, fitted using a Pseudo-Voigt profile.

RSM maps of the PCO(002) reflection, of the PCO113 film deposited using 3000 pulses, were obtained using asymmetric scans for in-plane analysis, see Fig 9.24. Both CGO(200) and PCO(002) reflections may be seen for the RSM of the (113) pole. For the (115) pole, the CGO(200) reflection was barely discernible, and the PCO(002) reflection out of the scan range (and unlikely to have been detected due to low intensities in any case). The PCO film was significantly strained with a large amount of mosaicity. Due to the diffuse nature and low intensity of the PCO reflection, it was not possible to calculate in-plane lattice parameters.

From the structural and morphological analysis of the PCO films of sample sets 2 and 3, it is clear that flat, (mostly) columnar grains have been deposited. Increasing the CGO buffer layer and increasing the PCO film both result in a larger grain size, though FWHM values of the films remain comparable. The films are polycrystalline, with the (0k0), (002) and traces of the (220) reflections detected, but appear to be highly textured with a preference for the (0k0) orientation, in accordance with minimizing lattice mismatch.

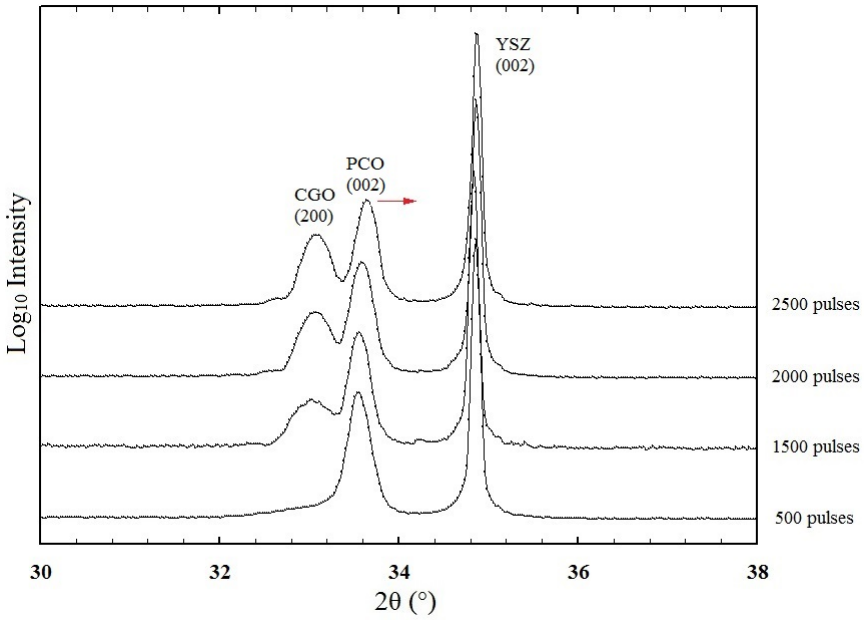


(a) Asymmetric 113 scan (b) Asymmetric 115 scan

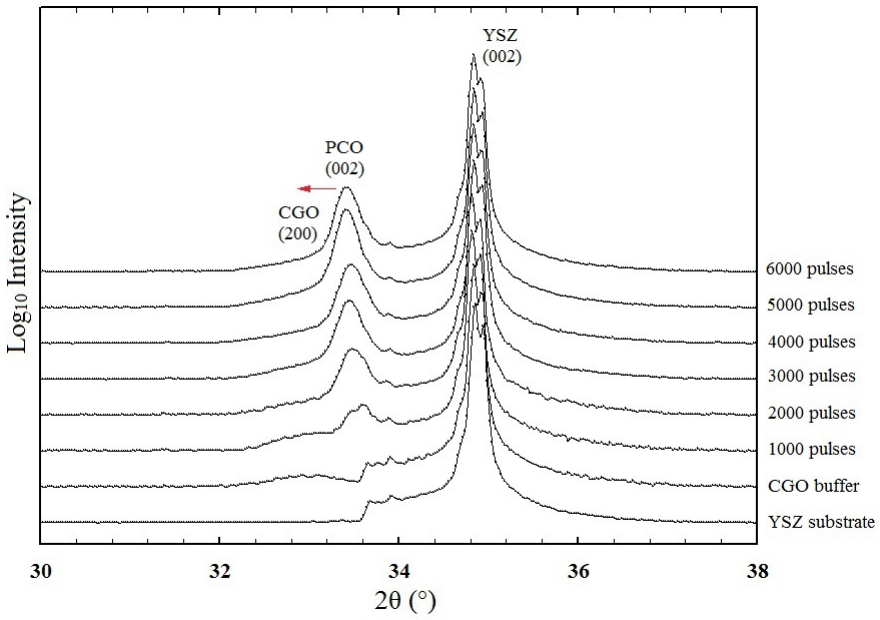
Figure 9.24: RSM of the PCO(002) reflection of PCO/CGO(200)/YSZ(002) deposited using 3000 pulses, of sample set 3. An in-plane relationship between PCO, the CGO buffer layer and YSZ substrate may be seen in the asymmetric 113 scan. The PCO film is highly strained, the PCO reflection is just within the boundaries of the scan. While the CGO(200) reflection may be seen in the asymmetric 115 scan, the PCO reflection was beyond the boundary of the scan, and likely to have been of too low an intensity to be detected.

A clear lattice strain has been observed in the PCO film from out-of-plane and in-plane XRD measurements. The extent of the lattice strain was found to vary as CGO/PCO lattice mismatched increased, or as PCO film thickness increased, as evinced by the continual shifts in 2θ position of the PCO(002) reflection, see Fig 9.25. Thus, though the deposited PCO films were not epitaxial, they must exhibit varying degrees of strain. This strain can be attributed to mechanical strain arising from lattice mismatch with the CGO buffer layer or the orientation relationships within the film, or chemical strain due to oxygen non-stoichiometry. Any contributions of chemical strain that arise from the fabrication process should be the same in all the films as they were all subject to the same deposition conditions. Further work would involve obtaining reliable in-plane lattice parameters, or to investigating the in-plane orientation relationships between PCO/CGO/YSZ within the PCO film, which was not covered in this work.

In the XRD patterns of sample set 2, PCO films of 72 nm nominal thickness are deposited upon CGO buffer layers between 4.8 and 24.1 nm thick. It was expected that the CGO(200) film on the YSZ(002) would experience in-plane lattice compression and out-of-plane lattice tension. Instead, an out-of-plane compression was measured in the CGO buffer layer. Following convention, increasing the CGO buffer layer thickness was thought to result in a relaxation of the CGO lattice, and subsequently a decrease in the out-of-plane lattice compression. The strain relaxation profile within the CGO buffer layer was obtained from the average strain measured, and the CGO out-of-plane compressive lattice strain at the CGO/PCO interface was found to vary between -0.21% to -0.01%. The CGO in-plane lattice parameter must also decrease in conjunction, from its larger tensile strained value to its bulk value.



(a) Sample set 2



(b) Sample set 3

Figure 9.25: Out-of-plane XRD patterns of the PCO films of: (a) sample set 2, for which 1000 pulses were used for the deposition of the PCO film, but a range of pulses used for the deposition of the CGO buffer layer (as specified in the figure); and (b) sample set 3, for which a range of pulses were used for the depositin of the PCO film (as specified in the figure). In sample set 2, as CGO film thickness increases and CGO/PCO lattice mismatch increases, the PCO(002) reflections can be seen to shift to larger 2θ values, while in sample set 3, as PCO film thickness increases and the PCO film relaxes, the PCO(002) reflection can be seen to shift to smaller 2θ values.

The lattice parameter of CGO is larger than PCO. The mismatch between the CGO buffer layer and the PCO film was originally expected to create a tensile in-plane strain

in the PCO of 1.51% and 0.83% between PCO[100]/CGO[100] and PCO[001]/CGO[100] respectively corresponding to the (0k0) reflection, and 1.28% between PCO[010]/CGO[110] for the (200) reflection. Thus an out-of-plane compression should be detected in the PCO film. As the CGO film thickness increases and its in-plane lattice parameter decrease, the PCO film would experience a decrease in in-plane tension that should be reflected in a decrease in its out-of-plane compression. According to this trend, a shift to smaller 2θ values, towards bulk values, should be seen in all CGO and PCO out-of-plane Bragg reflections.

However, from Fig 9.25a, although the PCO film was found to be in compressive out-of-plane strain, the PCO(002) reflection clearly moved to larger 2θ values as CGO buffer layer thickness increased, see also Fig 9.26. Thus, the out-of-plane PCO lattice parameter is actually decreasing, suggesting an increase in the in-plane tensile strain. Consequently, in light of the previous uncertainty regarding the trend in CGO strain as CGO buffer layer thickness increases, there are two possible interpretations for the CGO strain results. If the CGO buffer layer is really experiencing an out-of-plane compressive strain, then it must not strain relaxing as the CGO buffer layer thickness increases, rather it became increasingly strained. However, no published works could be found on mechanisms contrary to strain relaxation in lattice mismatched films. Thus, it is more plausible that the reference CGO cell parameters, if though it was obtained from the CGO target used during PLD deposition, is not transferable between target and film. Changes in oxygen stoichiometry and Gd- concentration have been reported during the deposition of CGO films by PLD [316, 319]. In future work, a more appropriate reference CGO cell parameter should be obtained by depositing a thick CGO film and measuring its cell parameters from the film.

Thus, it is proposed that the CGO reference cell parameters used to calculate the strain in the CGO buffer layer is too large; a compressive out-of-plane strain was calculated instead of a tensile out-of-plane strain. That being the case, it becomes clear that the out-of-plane strain measurement of the thinnest CGO buffer layer (4.9 nm thick, deposited using 500 pulses) is anomalous. As earlier discussed, there was difficulty in fitting a profile to the CGO(200) reflection for this film due to its low intensity and thus there was caution in assigning undue weight to it. Discounting this data point, the CGO buffer layer can be seen to relax as it gets thicker. This is supported by Fig 9.27, where the out-of-plane strain of the CGO and PCO films of both (0k0) and (002) reflections are calculated and plotted against CGO film thickness, and can be seen to correlate well with the exception of the thinnest CGO buffer layer in which a $\sim$-0.45% out-of-plane strain was erroneously measured. Decreasing the compressive out-of-plane CGO strain would decrease the CGO in-plane lattice parameters, which would decrease the in-plane lattice tension of the PCO film, and subsequently also decrease the compressive out-of-plane PCO strain, as is seen.

The strain measured from the PCO(002) reflection was consistently larger than from the PCO(0k0). This may be due to the inappropriate assignment of this reflection, or it may be that lattice strain was preferentially accommodated in the PCO(002) orientation. The trend in the out-of-plane strain with CGO film thickness appears to be the same in

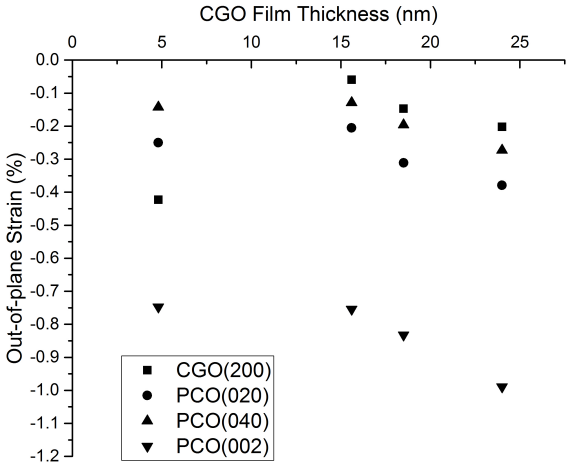


Figure 9.26: Out-of-plane strain in sample set 2, calculated from the CGO(200), PCO(020), PCO(040) and PCO(002) reflections. The differently oriented PCO grains all showed a similar trend. As CGO buffer layer thickness increased, the out-of-plane compressive strain in the PCO film also increased. The lattice strain of the (002) oriented grains of the PCO film appeared to be more highly strained than the (0k0) oriented PCO grains.

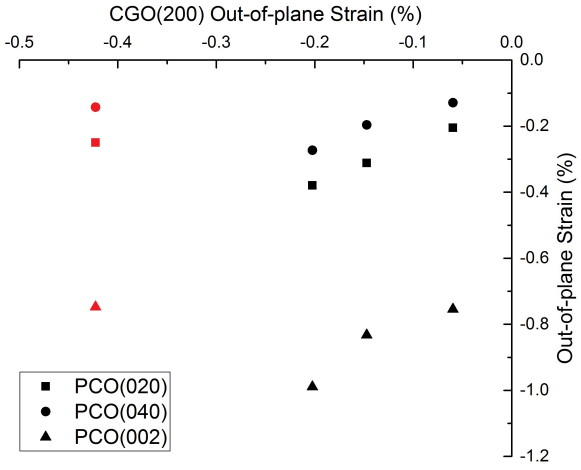


Figure 9.27: Out-of-plane strain in the PCO films of sample set 2 as a function of the out-of-plane strain in the CGO buffer layer. The strain in the PCO film on top of a CGO buffer layer with a CGO(200) out-of-plane strain of ∼-4.2% appears anomalous.

both reflections. It is unclear why there is a 0.1% difference in strain between the values calculated from the (020) and (040) reflections.

Earlier, it was seen that even within sample set 2, the PCO film thickness was not constant but varied between 58.0 nm and 89.5 nm and so relaxation effects are likely to also be present in sample set 2 (as is affirmed in sample set 3). Discounting the first data point for the 4.8 nm CGO buffer layer, see Fig 9.15a, the PCO film was at its thinnest when the CGO buffer layer was at its thickest. Thus any relaxation effects would magnify any strains present. It is a possibility that the amount of strain produced in the PCO films is less than portrayed. Removing the relaxation effects would decrease the gradient of the trend line.

It should be noted that having ascertained that the measured strain in the thinnest CGO buffer layer is anomalous and that the CGO reference cell parameters may not be appropriate, the CGO strain relaxation parameters, ϵ_0 and α, fitted earlier are also invalid.

In sample set 3, PCO films between 46.0 nm and 167.0 nm thick were deposited on CGO buffer layers ∼4.8 nm thick. Besides the additional reflection at 41.2° 2θ seen in two of the PCO films of sample set 3, sample set 2 and sample set 3 share similar diffraction patterns and thus a compressive out-of-plane strain was also expected in the PCO films of sample set 3, and has been measured: the PCO reflections have been shifted to larger 2θ values, see Fig 9.25b. As PCO layer thickness increases, the positions of its Bragg peaks shift back to bulk values. The strain in those films, calculated from the position of the Bragg peaks, is depicted in Fig 9.28. The PCO film relaxes as its thickness increase. A range of out-of-plane compressive strains in the PCO film have been obtained: between -0.17% to -0.01% from the (0k0) reflection; and between -0.60% to -0.37% from the (002) reflection. As was seen in sample set 2, a slight discrepancy exists between the lattice strain calculated from the PCO(020) and PCO(040) reflections, and also the PCO(002) reflection that appear to share a similar trend with PCO film thickness. It should be noted that in literature, no changes in unit cell dimensions were found of LCO films of different thicknesses [419]. This is not true for these PCO films.

To date, there has been no reported work on the strain relaxation of PCO113 films fabricated by PLD on CGO(200)/YSZ(002). Instead, a comparison has been made with out-of-plane strain measured in LSC20 (020) epitaxial films deposited on a ∼5 nm thick CGO(200) buffer layer on YSZ(002), see Fig 9.28 [7, 8]. This is a near identical system to what is investigated here. The LSC film prepared by La'O et al. is of a similar roughness, R_{rms} between 3 nm and 6 nm, while that by Crumlin et al. of a much lower roughness, R_{rms} of 0.5 nm. The LSC(020) films thicker than 45 nm experienced a similar strain to that calculated from PCO(0k0). Below a thickness of 45 nm, the LSC films have a much larger strain than the PCO films.

As was performed with the CGO films of varying thicknesses, the measured average lattice strains from the PCO(002) and PCO(0k0) reflections of sample set 3 were fitted separately against film thickness using Eqn. (9.4) in order to obtain ϵ_0 and α values for the two

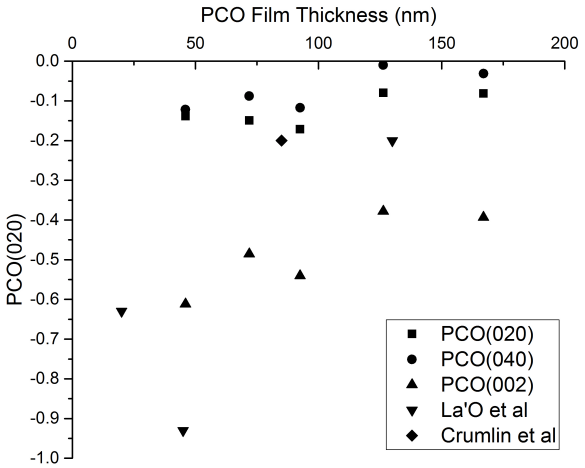


Figure 9.28: Out-of-plane strain in the PCO films of sample set 3 as a function of average PCO film thickness as measured using a Dektak 150 surface profilometer. The PCO lattice strain in the two differently oriented films can both be seen to relax as PCO film thickness increases. Reported out-of-plane lattice strain of LSC on a CGO buffer layer of similar thickness (∼5 nm), by La'O et al. and Crumlin et al. [7, 8] have also been included in the figure.

Sample	ϵ_0	α (nm^{-1})
PCO(002)	-0.74	0.01
PCO(0k0)	-0.22	0.02
LSC(020)	-1.00	0.03

Table 9.8: ϵ_0 and α obtained from fitting the measured out-of-plane strain in (002) and (0k0) oriented PCO films, and (020) oriented LSC films reported in literature [7, 8] to (9.4).

orientations. This should better indicate if the different orientations of the PCO film see a different lattice relaxation with increasing film thickness. Furthermore, in determining the relaxation length of the PCO film, it would allow the volume fraction of strained PCO films to be calculated. This would be of use in Chapter 11, where the effects of lattice strain on the transport properties of these films should be proportional to the actual PCO region experiencing the strain. Out-of-plane strain values obtained by La'O and Crumlin et al. in LSC films deposited on CGO/YSZ were also used to calculate ϵ_0 and α values as a comparison. These are presented in Table 9.8.

There is a large variation in ϵ_0 calculated for the two different PCO orientations. This may be attributed to the different CGO/PCO in-plane lattice relationships and thus the different out-of-plane lattice strain induced, or different bonding energies between planes. There is a possibility that the PCO(002) reflection was also incorrectly assigned, as in-plane analysis is required to confirm its designation. However, α values, describing the rate by which the film relaxes are similar, suggesting the same relaxation mechanism is at

work in PCO and LSC, also regardless of orientation. This would mean that the differently strained PCO orientations require different thicknesses before they are fully relaxed. Based on these values, the film thickness required for the PCO(0k0) and PCO(002) oriented grains to relax to 99.99% of its bulk value is 380 nm and 927 nm respectively. However this analysis assumes that the strain relaxation of the different PCO orientations are independent of each other, which may or may not be the case, and thus care should be taken not to give it undue significance.

Therefore, a range of in-plane compressive strains have been obtained in the PCO films of sample set 2 and 3. While this range overlaps between the two films, the mechanisms at work giving rise to these ranges are very different. In sample set 3, the variation in lattice strain can be attributed to strain relaxation of the PCO lattice. However, in sample set 2, increasing the CGO buffer layer thickness did not result in a reduction of lattice strain but increased it. As a result, compressive out-of-plane strains induced in the PCO film increased as CGO buffer layer thickness increased. Thus, though a similar strain may be measured in the PCO films of both sample sets, the mechanism(s) giving rise to the overall strain is not the same. Therefore, comparisons of transport properties between the films should be made with caution, bearing in mind the different factors that affect their strain state.

9.4 Conclusion and Further Work

Epitaxial CGO(200) and textured PCO thin films were successfully deposited by PLD upon YSZ(002) substrates. Three sample sets were investigated. In sample set 1, CGO films of increasing thicknesses were deposited on YSZ(002). In sample set 2, PCO films of constant thicknesses were deposited upon CGO(200) buffer layers of varying thicknesses, on YSZ(002). In sample set 3, PCO films of increasing thicknesses were deposited upon CGO buffer layers of constant thicknesses, on YSZ(002).

Increasing CGO(200) buffer film thickness in sample set 1 and 2 increased surface roughness but decreased the mosaicity of the film. However, within the CGO film thickness range investigated, the CGO(200) films were of comparable roughness to the Si(004) and YSZ(002) substrates earlier profiled. Thus the roughness of the CGO(200) film surface should not affect the deposition of PCO on top of it. A compressive out-of-plane strain was measured between -0.12% and -0.44%, and between -0.06% and -0.42% were measured for the CGO(200) films of sample set 1 and 2 respectively. It is unclear why these strains are compressive, as the lattice mismatch between CGO(200) and YSZ(002) would predict and an out-of-plane tensile strain, which has been reported in literature. It is proposed that there was a change in CGO composition during the PLD process resulting in a decrease in the CGO cell parameters and that an out-of-plane strain is actually present that decreases as the CGO buffer layer thickness increases and relaxes, though further work is required to verify this. Nevertheless, it is clear that on varying the thickness of the CGO buffer

layer, a range of out-of-plane strains has be obtained in the CGO buffer layer, and thus a range of lattice mismatch between CGO and PCO.

The average film thickness of PCO films of sample set 2, deposited under nominally identical conditions was ∼75.4 nm. PCO film thicknesses of sample set 3 ranged between 34.6 nm and 167.0 nm. The films were imaged using AFM and SEM. While there were some discrepancies, PCO grain size was found to increase with increasing PCO film thickness and CGO/PCO lattice mismatch. R_{rms} roughness also increased with PCO film thickness, R_{rms} values are comparable to similarly strain LSC films on CGO/YSZ [7]. From out-of-plane XRD patterns, the PCO films were found to be polycrystalline. A comparison of relative peak intensities suggested it was textured with two preferred orientations: (0k0) and what was presumed to be (002) (though further in-plane characterization is required to ascertain this). Traces of the (220) or (022) orientations were also found in two PCO films from sample set 3. No other orientations were detected. Rocking curves of were taken of the PCO(0k0) and PCO(002) reflections. A smaller FWHM was obtained for the PCO(002) reflection, at an average of ∼1.20°.

In sample set 2, PCO reflections saw a corresponding increase in 2θ position as CGO buffer layer increased. As the (suspected to be) out-of-plane tensile strained CGO buffer layer thickness increased and it relaxed, the lattice mismatch between CGO/PCO would have increased. The PCO film experienced a larger in-plane tensile strain; hence an increase in the out-of-plane compressive strain and subsequently the shift to larger 2θ values as was seen. A range of strains in the PCO films of sample set 2 was attained. In sample set 3, PCO reflections saw a decrease in 2θ position to bulk values as PCO film thickness increased. This decrease in lattice strain has been attributed to strain relaxation of the PCO lattice. An attempt was made to fit the measured strains to a strain relaxation model. Similar values of α, describing the rate of strain relaxation, were obtained from the measured strain of PCO(002) and PCO(0k0) orientations.

Thus, a range of strained textured PCO films have been fabricated by PLD. They exhibit a similar surface morphology, consisting of columnar grains of a low roughness. Possible CGO/PCO lattice relationships have been suggested though further in-plane structural characterization is required to ascertain the structure of the films, and the out-of-plane strains of these films have been calculated. The characterization of these films was necessary in order to determine the effect of lattice strain on the transport properties of PCO, if any.

Chapter 10

The Effect of Cation Non-stoichiometry on the Structure and Chemo-mechanical Expansion of $Pr_{1-x}CoO_{3-\delta}$

The objective of this work was to study the effects of chemical and mechanical strain on the charge transport properties of $PrCoO_{3-\delta}$. Two different systems were investigated: lattice mismatched (cation) stoichiometric $PrCoO_{3-\delta}$ films that were mechanically strained; and cation non-stoichiometric $Pr_{1-x}CoO_{3-\delta}$ bulk samples, which undergo chemical strain.

In the previous chapters, mechanically strained $PrCoO_{3-\delta}$ films have been fabricated by PLD on a CGO(200)/YSZ(002) substrates and characterized. Ranges of measured out-of-plane average lattice strains were obtained by varying the lattice mismatch between the $PrCoO_{3-\delta}$ film and the CGO buffer layer, and by varying the $PrCoO_{3-\delta}$ film thicknesses. Thus the samples for the first system have been prepared and characterized.

In this chapter the second system was addressed: the effects of chemical strain, arising from A-site deficiency, x, on the structure of $Pr_{1-x}CoO_{3-\delta}$ at room temperature and its thermo-mechanical behavior were examined. A range of A-site deficient PCO powders were synthesized and sintered into bars. These bars were morphologically, chemically and structurally characterized. SE images were obtained of polished surfaces of the samples. The chemical compositions of the samples were determined using EDX and XPS. Rietveld refinements of room temperature XRD patterns of the samples were performed. Additionally HT-XRD coupled with TGA results, up to 700°C, were analysed to observed the stability of PCO and the effect of cation non-stoichiometry on it. Unless otherwise stated, the use of $Pr_{1-x}CoO_{3-\delta}$, PCO, 'non-stoichiometry' in this chapter refers explicitly to cation non-stoichiometry or A-site deficiency, x, (and not oxygen non-stoichiometry, δ). The terms non-stoichiometric PCO and A-site deficient PCO have been used interchangeably.

10.1 Literature Review

Chemical strain arises from the dilation of a crystal lattice as a result of a change in composition, such as a change in oxygen stoichiometry due to the creation of a defect population in response to changes in temperature or oxygen partial pressure. This may cause undue stress within the device, leading to mechanical failure. However, the expansion of the lattice may also potentially facilitate (or obstruct) electronic or ionic transport across the lattice, and thus affect the performance of the oxide, hence its relevance in enhancing the ORR in IT-SOFC cathode materials.

In order to understand the effect of A-site deficiency on the chemical strain and thermo-chemical expansion (and later the transport properties in the next chapter) of PCO, it is necessary to first examine its defect chemistry. This identifies the defect species present, which are responsible for the chemical expansion. Thus a defect system is first proposed for the specific case of A-site deficient PCO. This is followed by a review of the chemical expansion in the similar LCO system. Thermo-chemical expansion is also considered. Lastly, current literature on A-site deficient perovskites is examined for the effects of defect chemistry on crystal structure and properties. While there has been no reported work on A-site deficient PCO, work has been done on the similar LSCF and LSM systems, and also A-site doped PCO.

10.1.1 Chemical Expansion of Perovskites

In Chapter 3, a brief introduction on chemical expansion was provided, with emphasis on the more easily-modeled fluorite structure. Difficulties in extending this modeling to the perovskite structure lay in its deviation from the assumptions underlying the Shannon assumptions for ionic radii. Nevertheless, two key mechanisms have been identified as the source of chemical expansion on the formation of an oxygen vacancy in the lattice: the increase in the (B-site) cation ionic radius expanding the lattice as it is reduced from its 4+ oxidation state to 3+, and the contraction in lattice as an oxygen anion is removed and neighboring oxide ions move towards the vacancy (this effect offsets the expansion as nearest cations, no longer screened by the oxygen anion, repel from each other). Thus the first is a dimensional mechanism, while the second results from a change in the Colombic interaction within the unit cell. While there have been many reports of chemical expansion in various perovskite systems, notably lanthanum chromites [423, 172, 424, 425], focus here will be directed at chemical expansion in LCO and Sr-doped variants, LSC.

One of the earlier works on chemical expansion of LSC was performed by Chen et al. where the chemical expansivity of LSC was determined from dilatometry studies and found comparable to that of other perovskite structures [426]. An expansion hysteresis, not due to changes in oxygen stoichiometry, was also observed on cycling ρO_2 levels, which has also been found of $LaMnO_3$ [427]. It is unclear if this hysteresis is due to cation ordering

following changes in their oxidation state, or if the range of oxygen hypo-stoichiometry exceeds the stability limit resulting in phase changes or segregation.

In 2008, following similar work on lanthanum chromate where the dominating mechanism for chemical expansion was the change in B-site cation radius [424] (and later $LaMmO_3$ [428]) Zuev et al. investigated chemical expansion of undoped LCO. A good fit between the measured chemical expansion and that calculated from a chemical expansion modeled proposed in earlier work on the LCO system [429, 430] was found. The chemical expansion of LCO was largely attributed to the dominating effect of the change in the Co cation radius- the dimensional mechanism. Additionally, as the chemical expansion model by Zuev et al. assumed an effective ionic radii of Shannon [9], the good correlation between predicted and experimental results suggest that the electronic defects are localized in undoped LCO.

No such work has been performed on the PCO system. Nevertheless, as it shares a similar defect chemistry, the same mechanisms for chemical expansion are expected. It is likely that in PCO, the dominating contribution to chemical expansion is also the change in cobalt ionic radii (as was also found through atomistic modeling of the fluorite system).

10.1.2 Thermo-Chemical Expansion of Perovskites

Perovskite (also fluorite) oxides typically exhibit a deficiency in oxygen stoichiometry, which varies according to oxygen partial pressure and temperature. High oxygen partial pressures result in an uptake of oxygen and oxidation of B-site cations resulting in a contraction in the lattice, whereas at low oxygen partial pressures the creation of oxygen vacancies as oxygen is expelled and the reduction of B-site cations see an expansion of the lattice expansion [431, 22, 432](see Chapter 2. However, in addition to chemical expansion or contraction, in the case where temperature is varied, there is the additional effect of thermal expansion. Thermo-chemical expansion therefore is a superposition of the effects of thermal expansion and chemical expansion. This has been observed on one occasion by Kostogloudis et at [162] for the PCO system, but has been extensively found of the doped LCO system [433, 434, 435, 426, 22, 436, 437, 438, 439, 440]. Thermo-chemical expansion was found to be the primary cause for lattice expansion at temperatures above 600°C.

In a key work by Bishop et al., thermo-chemical expansion has been modeled and validated with experimental results [431]. Thermal and chemical expansion were assumed to be independent of each other, and therm-mechanical expansion the sum of their contributions:

$$\epsilon_{T+C} = \epsilon_T + \epsilon_C \tag{10.1}$$

The chemical expansion contribution, ϵ_C, was derived from defect formation as a function of temperature, T [431]:

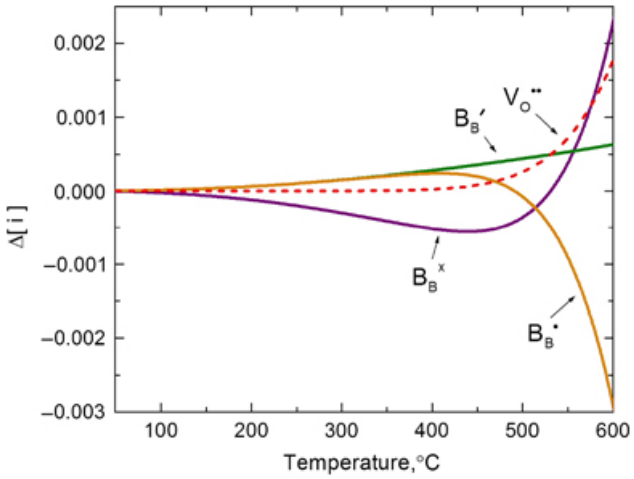


Figure 10.1: Dependence of the change in species concentration, $\Delta[i]$, of lattice (trivalent) B-site cations, ${B_B}^X$, oxidized (quadrivalent) B-site cations, ${B_B}^{\cdot}$, lattice neutral oxygen anions, ${O_O}^X$ and oxygen vacancies, ${V_O}^{\cdot\cdot}$, determined using defect equilibria calculations from [50]. Room temperature was taken as a reference for zero change in concentration. At high temperatures, above ∼600°C, chemical expansion is dominated by the formation of ${B_B}^X$ from ${B_B}^{\cdot}$.

$$\epsilon_C = \frac{\Delta l}{l_0}\Big|_T = \alpha_C \Delta\delta \tag{10.2}$$

Where l_0 is the initial sample length, α_C is the chemical expansion coefficient, and $\Delta\delta$ is the change in oxygen stoichiometry.

For the LSCF system investigated, the chemical expansion, as a function of temperature, was attributed to oxygen vacancy formation and the reduction of the B-site cation. The defect chemistry of LSCF is well established: charge disproportionation of the B-site cations at low temperatures but oxygen reduction and the formation of oxygen vacancies above ∼600°C [50, 431], see Fig 10.1. Subsequently, a relation between oxygen vacancy formation and temperature could be proposed for the chemical expansion contribution. The model for chemical expansion, in conjunction with the model for thermal expansion, based on the Morse potential for the interaction of between atoms, was found to fit experimental data well [441, 442, 431], see Fig 10.2. This fit only assumes defects related to the creation of oxygen vacancies are the only defects responsible for chemical expansion. The dominating effect of oxygen vacancy formation on thermo-chemical expansion is further supported by the narrow range of α_c values for a variety of perovksite oxides [431].

There are two works of interest on the thermo-chemical expansion of LSC; The first was in 2006, by Mastin at al who investigated the effect of Sr-doping on the high temperature crystal structure of LSC, and subsequently also its thermo-chemical expansion [443]. By using Rietveld refinement of HT-XRD data, Mastin at al attempted to measure the evolution of oxygen position with temperature, which trends were validated by similar findings in neutron diffraction studies of other perovskites [444, 445, 446]. The octahedral angle

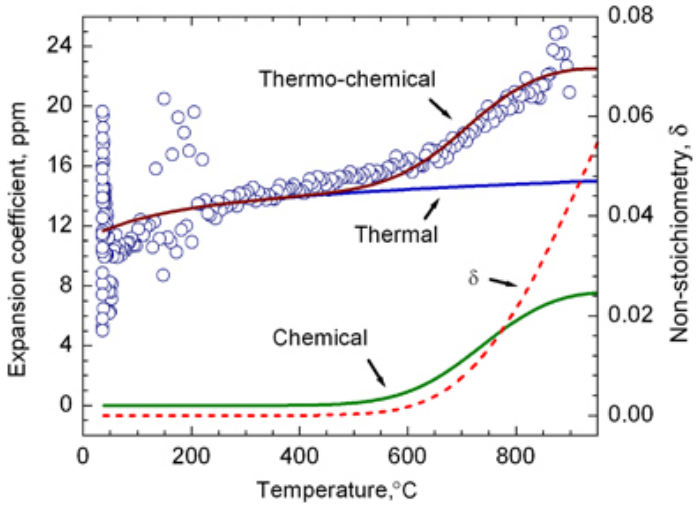


Figure 10.2: The predicted thermo-chemical expansion coefficient fitted to experimentally determined data in air. The concentration of oxygen vacancies, δ is also shown for comparison with the effective chemical expansion coefficient [51].

of rotation, ϕ, was calculated using $tan\phi = 2u\sqrt{3}$, where u can be calculated from the oxygen position ($x = \frac{1}{2} + u$) [444]. From this the octahedral strain, η, was also calculated: $\eta = ccos\phi/a\sqrt{6}$. On every occasion, the substitution of Sr-dopants resulted in a decrease in octahedral rotation and strain. As temperature increased, thermo-chemical expansion was initially linear, when only thermal effects contributed to the expansion, but became non-linear on the onset of chemical contributions [426, 432]. The effect of thermo-chemical expansion was to decrease octahedral rotation and subsequently also octahedral strain. An increasing Sr-content served to accelerate the decrease in octahedral strain with temperature.

In another similar work using HT-XRD structural characterization of LSC in pure O_2 and N_2 atmospheres, anisotropic expansion was also reported [438, 439]. Chemical strain was more pronounced in the c-axis than the a-axis of the rhombohedral $R\bar{3}c$ LSC structure. Additionally, the second order ferroelastic to paraelastic phase transition of LCO was investigated and also found to be strongly dependent on dopant concentrations and oxygen partial pressure. The substitution of Sr into the lattice or a reducing atmosphere, and the subsequent introduction of oxygen vacancies brings the LSC structure closer to a cubic structure and moves the Goldschmidt tolerance factor, t, towards unity. This lowers the transition temperature. The anisotropic chemical expansion and the depression of the transition temperature with oxygen partial pressure and Sr concentration both suggests a strong dependence of the octahedral tilt angle of oxygen vacancy concentrations.

Defect populations within a material have a strong effect of its structure. This was also seen in LSM [447]. LSM is oxygen hyperstoichiometric. This is effectively accommodated within its structure as cation vacancies. For LSM, it is the cation vacancies that affect octahedral tilt, and an opposite chemical expansion anisotropy was observed. In LSC, the oxygen vacancy concentration resulted in preferential expansion of the c-axis, while in

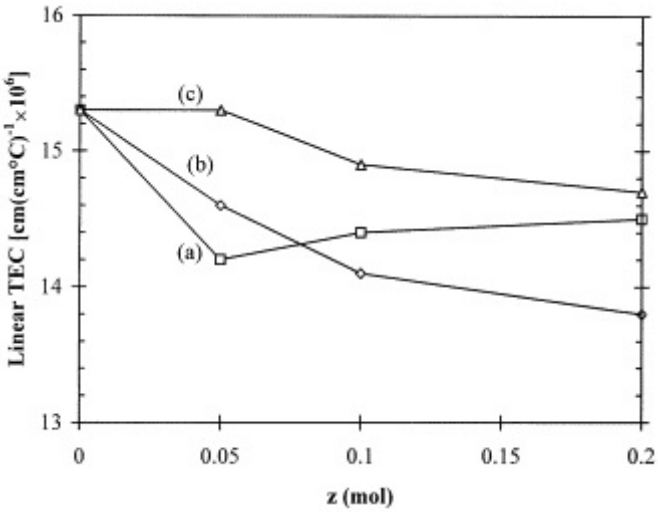


Figure 10.3: Linear thermal expansion coefficient at 700°C for (a)$La_{0.6-z}Sr_{0.4}Co_{0.2}Fe_{0.8}O_{3-\delta}$, (b)$La_{0.6}Sr_{0.4-z}Co_{0.2}Fe_{0.8}O_{3-\delta}$ and (c)$(La_{0.6}Sr_{0.4})_{1-z}Co_{0.2}Fe_{0.8}O_{3-\delta}$ as a function of A-site deficiency, z [52].

LSM, the cation vacancy concentration resulted in preferential expansion of the a-axis.

10.1.3 Current Literature on Cation Non-stoichiometric Perovskites

No published work on A-site deficient PCO or LCO could be found. However, the effect of A-site deficiency on the crystal structure and thermal behavior in doped Fe-doped $LaCoO_3$ (LSCF) and the $LaMnO_3$ system have been studied and summarized below. Its' defect chemistry having relevance to this work, the study of A-site doping on the structure (and conductivity) of PCO is also reviewed.

A-site deficient LSCF materials, $La_{1-x}Sr_xCo_{1-y}Fe_yO_{3-\delta}$, have been synthesized by Waller et al. to study the effect of the dopant on the LSCF structure and electrode performance [72]. $La_{0.6}Sr_{0.4-x}Co_{0.2}F_{0.8}O_{3-\delta}$ was found to be able to accommodate high levels of cation deficiency on the A-site, as much as x=0.30. Upward of a Sr deficiency of x = 0.25 a shift in the symmetry of the perovskite from rhombohedral to cubic was observed, and an increase in the lattice parameters and theoretical unit cell volume [72].

This was followed up in the work of Kostogloudis et al. where different types of A-site deficiency of the same system were investigated: a deficiency of La, Sr, and a La-Sr mix [52]. The same increase in cell parameter and decrease in symmetry was found with increasing A-site deficiency. This effect was increasingly marked in the A-site deficient LSCF in the order of Sr-deficiency, La-Sr mixed deficiency, and La-deficiency. Increasing A-site deficiency, in all three systems investigated, also lowered the TEC, Fig 10.3. From those results, it appeared that the charge compensation mechanism for the loss of an A-site cation is the formation of oxygen vacancies, and not the oxidation of the B^{3+} cations to B^{4+}.

Mineshige et al. also introduced Sr-deficiencies into LSCF, to increase oxygen vacancies with the intention of improving oxide ion conductivity [83]. By evaluating the mean valence of B-site cations using iodometry, and the weight loss during decomposition, it was confirmed that the Sr-deficiency was compensated through the creation of oxygen vacancies. Additionally, through consideration of the standard deviation for rhombohedral lattice parameters against A-site deficiency, it appears that the A-site deficiency causes a tilting of the BO_6 octahedron. However, in the most recent work by Hansen et al. of the LSCF system, a single phase perovskite could only be obtained in the near stoichiometic sample where $x = 0.01$ [448]. By varying A-site deficiency it could be seen that at large A-site deficiencies, a two-phase system of (two) cubic perovskites was found to form.

A review of A-site deficiency of LSCF was the closest alternative for PCO as they both have rare earth lanthanides sharing the same B-site cation. However, LSCF is A and B-site doped. The A-site deficiencies quoted here have either been Sr- La- or a mixture of Sr- and La-deficiencies, and the type of A-site deficiencies can be seen to be of consequence to its properties. Also, unlike La, Pr can exist in two oxidation states. Nevertheless, based on literature and assuming a trivalent Pr, possible consequences to Pr-deficiency are: the formation of oxygen vacancies, an expansion of cell parameters, a lowering of TEC, and a tilting of the BO_6 octahedron.

For LSCF, the B-site dopants appeared not to play a role in the affect of A-site deficiencies. The LSM system is now considered, which does not have B-site dopants (as in the case for PCO). This was the only system for which A-site deficiency in an undoped sample was predominantly investigated. However it should be noted that a different B-site cation is involved, and thus its defect chemistry and subsequent transport properties may be of limited relevance to colbaltate perovskites.

Initial work on A-site deficient LMO and its Sr-doped variants was first performed by Otoshi et al. [449]. Single phase $(LS)_{1-x}M$ could only be synthesized for A-site deficiency where x is between 0.11 and 0.03. At greater A-site deficiencies, Mn_2O_3 secondary phases were observed, and at lower A-site deficiencies, La_2O_3 secondary phases were observed despite still being A-site deficient. Thermogravimetric analysis showed oxygen desorption of the LSM samples from 750°C and above and a corresponding change in cell parameters. In this high-temperature phase, a linear relation of an approximate gradient of 0.5 was found between increasing Sr content and decreasing oxygen desorption. This was proposed to be due to the change in valence state of the Mn^{3+} to Mn^{4+}, which depends on the holes generated by Sr-doping, hence the 2:1 relationship between the number of doped Sr atoms and the number of desorbed oxygen atoms. Whereas, at temperatures below this transition no oxygen desorption was detected regardless of Sr content as the number of Mn^{4+} atoms remains constant. Of $La_{1-x}MnO_3$ samples, it was also seen that increasing A-site deficiency lowered the temperature for oxygen desorption, but had no effect on the quantity of oxygen released.

Subsequently, Berenov et al. investigated A-site deficient LMO for the effect of its high oxygen vacancy concentration on oxide ion conductivity [450]. This is further reviewed

in Chapter 11. Nevertheless, of interest is the extent of A-site deficiency that may be accommodated in LMO, found: even at a La-deficiency of $x = 0.1$, secondary Mn_2O_3 impurity oxides were detected. As has been reported previously of LMO [451], Berenov et al. saw that A-site deficiency, and the increased concentration of La vacancies, improved the sinterability of the ceramic. It shifted the sintering curve to lower temperatures and also increased the rate of sintering with temperature. Unlike with LSCF, most research on A-site deficient LMO has concentrated on its defect chemistry and subsequent transport properties, rather than the structural effects of its defect species. As mentioned earlier, the use of Mn as the B-site cation means it is of limited relevance to the colbatate system. However, this review does emphasize the range of potential defect chemistry that may be present given that, like Mn ions, Co ions may also exist in three different oxidation states. It is of crucial importance to establish the PCO defect chemistry.

Work on compositional effects on PCO typically examine the effect of Sr dopants, instead of A-site deficiency, on the crystal structure and properties. The first of these studies was performed by Kostogloudis et al. and investigated the structure, and thermal and electrical properties of undoped and Sr-doped PCO [162], PSC, where x varied between 0 and 0.5. PSC powders (and its doped variants) were synthesized using pyrolysis, calcined at 1100°C, milled and sintered at 1300°C. The resulting bars were used for thermal expansion and electrical conductivity measurements between room temperature and 800°C. Separate powders, with average crystallite sizes between 272 to 314 Å, were synthesized for XRD characterization. These underwent slow cooling in order to attain equilibrium oxygen content.

Dilatometry of PCO indicated a mostly linear thermal expansion, however at higher temperatures the gradient of this slope decreased. As Sr content increased to $x = 0.15$, the thermal expansion was linear, even at high temperatures. A change in the TEC was not observed. However as Sr content further increased, there was an increase in the TEC at high temperatures. The onset temperature for this change decreased with increasing Sr content. This was attributed to the defect chemistry of the system. The effect of doping with Sr and substituting Sr^{2+} for Pr^{3+}, was initially offset by a change in the oxidation state of Co^{3+} to Co^{4+}. However, as Sr content increases past a critical concentration, oxygen vacancies are formed instead, the concentration of which increases with Sr content. The increase in temperature served to increase the formation of tetravalent cobalt in PCO, but at higher Sr doping, instead increases the creation of oxygen vacancies instead of the tetravalent cobalt. As Co^{4+} has a smaller ionic radius, its creation at high temperatures resulted in a decrease in the thermal expansion. Conversely, increasing the oxygen vacancy expands the lattice, resulting in an increase in the thermal expansion.

Following that, Kim et al. also studied PSC, though with an even larger range of Sr-dopants, where x varied between 0 and 0.7 [452]. The focus of this was the high temperature structure and performance of PSC as a cathode material. The PSC lattice parameter was obtained between room temperature and 800°C. A cubic lattice was used for the characterization of PCO, whereas a monoclinic lattice was used for PSC. Increasing Sr-content

expanded the lattice. The thermal expansion of PSC was also measured. Undoped PCO had a linear thermal expansion up until ∼350°C, when there was a change in the gradient to lower TEC values. However, the thermal expansion curves of the Sr-doped PCO were significantly different. Linear thermal expansion occurred until ∼350°C, but increased at an increasing rate at high temperatures until ∼850°C, after which there was a sharp discontinuity thought to be related to a phase transformation at this temperature range [453]. Increasing Sr-content only affected the thermal expansion after ∼350°C, where it increased the rate of increase in thermal expansion.

The same defect chemistry as proposed by Kostogloudis et al., based on LCO and the substitution of Sr into the LCO lattice [454], was used for the interpretation of these results by Kim et al. Based on this, the increase in TEC with Sr-dopants was the result of three effects. Firstly, the substitution of Sr^{2+} is accompanied by the creation of oxygen vacancies, the presence of which causes an increase in the TEC as was observed. Secondly, as temperature increases, there is a change in the Co^{4+} charge state (effective ionic radius of 0.53 Å) to Co^{3+} (effective ionic radius of 0.545 Å) [9]. The increase in ionic radius between these oxidation states serve to increase the TEC more. Thirdly, the increase in ionic radius of Co^{3+} also reduces the Co-O bond strength of within the BO_6 octahedron [162] further increasing the TEC.

Even though the defect chemistry involves the substitution of Sr onto a Pr site, this may potentially be extended to an A-site deficient PCO system (having first been adopted from the LSC system and validated for the PSC system). This is contrary to what was seen of B-site cations (in LSM), a variation of which was found to greatly affect defect chemistry. Additionally, it has been of use to note the effects of defect species on the crystal structure, as well as its high temperature properties. These effects are also in accordance to what was found of the LSCF system. Therefore, the effects of A-site deficiency of similar lanthanide perovskite systems of different extents of A- and B-site doping, LSCF and LSM, have been examined. The crystal structure and high temperature properties of the crystal structure are intrinsically linked to the defect species present. Regardless of the particular perovskite systems reviewed, the effect of defect species on crystal structure is not specific, and can be applied across various systems. Notably, despite the dual valency of Pr, no changes in its oxidation state have been observed. Furthermore, the creation of oxygen vacancies is the expected charge compensating defect species. Based on this review, a defect system for A-site deficient PCO may now be proposed.

10.1.4 Defect Chemistry of $Pr_{1-x}CoO_{3-\delta}$

If both Pr and Co are originally trivalent, there are a number of possible situations that may arise upon the removal of Pr from the PCO lattice. Firstly, either a Pr vacancy or a Co interstitial is created. In perovskites, due to its close packed nature and thus the small free space between the ionic radii of atoms within the unit cell, the formation of an A-site vacancy is more favourable than a metal interstitial. Based on the LSC system, in

Cation	Coordination Number	Ionic Radius (Å)
Pr^{3+}	12	1.30
Co^{3+}	6	0.545
Co^{4+}	6	0.53

Table 10.1: The ionic radii for Pr and Co at different oxidations states and coordination number, as appropriate for the persovskite structure. It was not possible to obtain the ionic radii for Pr^{4+}. Nevertheless, it is expected to be smaller than Pr^{3+}, due to its more positive charge and thus less electrons. This can be seen in the 8-fold coordinated Pr^{3+} and Pr^{4+}, which have an ionic radii of 1.126 Åand 0.96 Årespectively [9].

order to charge compensate for the creation of a negatively charged defect species (the Pr vacancy), the oxidation state of the Co^{3+} is thought to increase to its tetravalent state. It should be noted that Pr may exist in either the 3+ or 4+ oxidation state. Thus, charge compensation could also be achieved by an increase in the oxidation state of Pr^{3+} to Pr^{4+}. However there has been no evidence to suggest that this occurs and neither has it been proposed in literature. Also, an increase in the Pr oxidation state would see a subsequent decrease in ionic radii [9] and lattice parameters. The ionic radii of Pr and Co cations are provided in Table 10.1. The removal of Pr and change in Co oxidation state is described in the defect equation below, using Kröger-Vink notation.

$$PrCoO_3 \rightarrow xPr_{Pr}{}^{X}{}_{(1-x)}V_{Pr}{}^{'''}{}_{(x)}Co_{Co}{}^{X}{}_{(1-3x)}Co_{Co}{}^{\cdot}{}_{(3x)}O_{O}{}^{X}{}_{(3)}$$

At high temperatures or low oxygen partial pressures, the oxidation state of Co^{4+} reverts back to Co^{3+}. This is charge compensated by the formation of oxygen vacancies. A larger A-site deficiency, and hence the larger the concentration of Co^{4+}, results in a potentially larger oxygen non-stoichiometry. The defect equation with the formation of oxygen vacancies now becomes:

If at high temperatures or low ρO_2:

$$2Co^{4+} \rightarrow Co^{3+} + V_O^{\cdot\cdot}$$

Then:

$$PrCoO_3 \rightarrow Pr_{Pr}{}^{X}{}_{(1-x)}V_{Pr}{}^{'''}{}_{(x)}Co_{Co}{}^{X}{}_{(1-3x+2\delta)}Co_{Co}{}^{\cdot}{}_{(3x-2\delta)}O_{O}{}^{X}{}_{(3-\delta)}\delta V_O^{\cdot\cdot} + \tfrac{\delta}{2}O_2$$

In addition to the creation of Co^{4+} by the introduction of A-site vacancies, Co^{4+} is also produced by the disproportionation of Co^{3+}, as described in the reaction below. This was first observed in $LaCoO_3$, where the colbalt ions were mostly found to exist in a low-spin Co^{3+} state at low temperatures [455, 456]. However at high temperatures, these ions had transformed into a high-spin Co^{3+} state. Disproportionation was the proposed mechanism for this. It involves the transfer of an e_g electron between a high-spin Co^{3+} ion

to its low spin counterpart, ($t_{2g}{}^4e_g{}^2$ and $t_{2g}{}^6e_g{}^0$ respectively), forming a low-spin Co^{2+} and high-spin Co^{4+} pair. It is a thermally activated process; as temperature increases (up to a certain temperature), so does the formation of disproportionate pairs. This transition in the electron state was found to be true of other rare earth cobaltites and is expected in the PCO system [455, 456]. The occurrence of disproportionation increases Co^{4+} concentration and subsequently also the formation of oxygen vacancies:

At T > 200K, charge disproportionation:

$$2Co^{3+} \rightarrow Co^{2+} + Co^{4+}$$

For this work, it was assumed that the defect concentration was sufficiently low, even at $x = 0.9$, that defect interaction and the potential formation of defect complexes and the ordering of these defects creating microdomains does not occur. On the other hand, in earlier work on PSC, it has been suggested that in undoped or lightly Sr-doped PCO, as temperature increases, the change in oxidation state of Co^{3+} to Co^{4+} dominates and does not result in the formation of oxygen vacancies. A critical Sr content is required for the formation of oxygen vacancies at high temperatures [162]. However, although each substitution of Sr on a Pr site results in the change in oxidation state of one Co^{3+} ion, the removal of Pr from a Pr site results in the change in oxidation state of three Co^{3+} ions. Although the range of A-site deficiency in this study may be small, it does create the equivalent defect population as acceptor(2+) concentrations of $x = 0.3$. Thus, oxygen vacancy formation is expected. Lastly, as mentioned at the start, it should be noted that the defect chemistry proposed is originally from the LSC system. Charge compensation may also occur through hole formation, however this cannot be assessed without variable oxygen partial pressure measurements, which are beyond the scope of this work but is necessary further work to verify the defect chemistry present.

10.2 Experimental Method

Non-stoichiometric $Pr_{1-x}CO_{3-\delta}$ powders were prepared using the Pechini sol-gel process where $x = 0$, 0.025, 0.050, 0.075, 0.100 following the method outlined in Chapter 6. For each batch, powder and bar samples were produced. The powder samples were used for room temperature and HT-XRD and TGA measurements, and the bar samples for all else.

The same method was used to make the bar samples, as for the PLD targets in Chapter 6, except that a bar-die was used to uniaxially press the green bodies prior to the isotatic press. The sintered bars also underwent an additional heat treatment at 1200°C for 12 h to ensure a high density was achieved. For each sample, density values above 95% were measured using the Archimedes method. The powder samples had exactly the same heat treatment as the bar samples, except they were not pressed but reground after each heat treatment. For the non-stoichiometric bar samples of a lower porosity, the additional heat treatment at 1200°C was omitted.

SE images were acquired of the dense and less dense bar samples using a Jeol JSM 6400 scanning electron microscope (SEM). It was fitted with an Oxford Instruments INCA energy dispersive analytical system with which EDX analysis and quantification of the detected elements were performed. Prior to its use, samples were ground and, for the dense samples, polished using the same procedure as for the CGO polycrystalline substrates of Chapter 6. Care had to be taken in the polishing of the more porous PCO samples, as these were extremely soft. The polishing served to improve the confidence in the EDX measurements.

EDX maps were obtained using an accelerating voltage of 20 kV and a 10A condenser lens. Reference measurements against a Co standard were also taken in order to optimize quantification of the elements using the INCA software. This was to account for any changes in temperature that may result in a shift of the EDX peaks, and thus enable accurate matching of profiles. A high process time of '5' (as specified in [274]) was used in all measurements to minimize noise in the spectra with a corresponding deadtime between 27% and 38%. Details of how the quantitative analysis by the INCA software may be found in the INCA Energy Operator Manual [274]. For the quantitative analysis used here, a fixed list of elements (Pr, Co and O peaks) was employed. All other trace peaks identified were omited. Additionally, the concentration of the oxygen, of which there is typically low sensitivity in EDX measurements, was calculated based on the stoichiometry of Pr and Co. This is the 'element by stoichiometry' processing option, often used for oxides. This assumes oxygen stoichiometry in PCO for the oxygen concentration quantification. PCO can be oxygen deficient. However, the objective of this is to obtain the Pr:Co cation ratio- there is less concern in the amount of oxygen detected.

XPS data were obtained at room temperature using a High-Throughput Thermo Scientific Kα^+ XPS spectrometer equipped with a MXR3 Al Kα monochromated X-ray source (hν = 1486.6 eV). X-ray gun power was set to 72 W (6 mA and 12 kV). With these X-ray settings, the intensity of the Ag $3d_{5/2}$ photoemission peak for an atomically clean Ag sample, recorded at 20 eV pass energy (PE), was 5×106 counts s^{-1} and the full width at half maximum (FWHM) was 0.58 eV. Binding energy calibration was made using Au $4f_{7/2}$ (84.01 eV), Ag $3d_{5/2}$ (368.20 eV) and Cu $2p_{3/2}$ (932.55 eV). Charge compensation was achieved using the FG03 flood gun using a combination of low energy electrons and the ion flood source. Survey scans were acquired using 200 eV pass energy, 1 eV step size and 100 milliseconds (50 ms x 2 scans) dwell times. The spectra were acquired using 20 eV pass energy, 0.1 eV step size and 1 second (50 ms × 20 scans = 1000 ms) dwell times. Pellets of the PCO113 samples were held onto the sample holder using metal pins and analyzed at an electron take-off angle normal to the surface with respect to the analyzer. Pressure during the measurement of XP spectra was $\leq 1\times10^{-8}$ mbar. All XPS measurements were performed by Dr. I. Villar-Garcia of Imperial College.

Thermo Avantage software was used to analyze the data. Shirley or two point linear background subtractions were employed depending on background shape. All background fits are included in the figures. Thermo scientific sensitivity factors were used for quantifica-

tion analysis. The XP spectra were charge corrected by referencing the fitted contribution of C-C graphitic like carbon in the C 1s signal to 285 eV.

Two different X-ray diffractometers were used: the Bruker D2 for all room temperature XRD measurements, and the Panalytical X'pert Multi-Purpose Diffractometer, MPD, equipped with a Buehler high temperature stage, for the high-temperature measurements. With the HT-XRD, XRD patterns were obtained between 35°C and 800°C. This encompasses the operating temperatures of an IT-SOFC and the temperatures experienced during the deposition process. The sample stage, a Pt foil, was placed on top of a heating element and heated at a rate of 10 °C/min. Upon reaching each set temperature, the temperature of the stage was held for 5 min in order for the sample to stabilize to a constant temperature. The temperature of the sample stage was calibrated by first performing a blank run and determining the lattice expansion of the Pt, as measured using XRD, to its actual temperature. A thin film of finely ground PCO powder was distributed over the Pt foil using acetone to minimize differences in temperature between the sample and sample holder. The HT-XRD patterns were not normalized or processed in any way.

Le Bail refinement was performed on these high temperature data to obtain lattice parameters of the PCO using the orthorhombic *Pnma* space group. Trace peaks from the Pt holder were detected, more noticeably in some samples than others. These were found to notably alter the Le Bail fit and the calculated lattice parameters. Therefore, a 2 phase refinement was performed, with $Fm\bar{3}m$ Pt being the second phase. At high temperatures, LSC is seen to revert to its lower symmetry rhombohedral $R\bar{3}c$ spacegroup. A similar transition to the ideal cubic $Pm\bar{3}m$ space group of PCO was expected. However, it was not possible to fit the high temperature XRD patterns of PCO to this space group; the low temperature *Pnma* spacegroup was used for all Le Bail fits.

Room temperature XRD runs on the Bruker were made between 20 to 80° 2θ, with a step size of 0.018° 2θ, and a time per step of 2 s. For the Rietveld refinements of these patterns, Pr and Co occupancies were initially set based on nominal Pr:Co ratios and then repeated using the Pr:Co ratios measured during XPS with little difference to the final refined outcome. Atomic positions and B-iso values of Pr and Co from the ICSD database were used as a starting point and also refined. No refinements of O parameters were made due to the insensitivity of X-rays to O. Similarly, O occupancies were not varied to maintain charge neutrality in the nonstoichiometric samples but fixed at 2 and 4, for O1 and O2 respectively, as if a stoichiometric sample.

Thermal analysis measurements were performed from room temperature to 700°C. A constant heating rate of 10 °C/min, and a purge gas (air) at a flow rate of 50 ml/min, and a protective gas (air) at a flow rate of 15 ml/min was used in all experiments. Powder samples were ground and loaded into a Pt crucible, Pt being unreactive with the samples. Only results after 100°C have been presented to ensure that a constant heating rate had been achieved and also to remove the fluctuation of microscale at the start of the experiment. TGA results have been normalized to the mass of the sample at 100°C. A calibration run was performed using the same Pt crucible under identical conditions of

heating rate and purge and protective air flow. TGA and DSC results have been corrected according to that calibration run and may be found in Appendix A.3.

10.3 Results and Discussion

10.3.1 Room Temperature Characterization of $Pr_{1-x}CoO_{3-\delta}$

SEM images and EDX maps were taken of non-stoichiometric PCO bars fabricated using two heat treatments (one was additionally held at 1200°C for 12 h). All samples produced with the same heat treatment, regardless of stoichiometry, had a similar porosity. On no occasion were segregates of a secondary phase detected. However, the difference in the porosity of the samples from the different heat treatment is significant, see Table 10.2. For the transport measurements of non-stoichiometric PCO in Chapter 11, the additional heat treatment was used to ensure dense samples.

Samples without the final sintering step at 1200°C were only partially sintered. Individual powder particles can be discerned and the sample is comprised of loosely connected particles. Archimedes density measurements of these samples gave density values between 94.4% and 97.5%, see Table 10.3. On the other hand, Archimedes density measurements of samples having an additional heat treatment at 1200°C in air of 6 h had lower density values, between 95.4% and 97.0%. Yet SE images of these heat treated samples 1200°C suggest they were fully sintered. No individual grains can be seen and the polishing was effective in removing surface features. However, pores of up to $\sim$2 μm can be also observed. These pores were likely to be closed pores, hence the reduction in the measured sample density. For the samples without the additional heat treatment, it was likely that the pores were mostly interconnected and water was able to displace most of the air trapped in the pores during the density measurement, hence the higher density measured.

EDX element maps indicated the a homogeneous distribution of the constituent elements, suggesting a single phase sample with no secondary deposits. Quantification of the ratio of the Pr and Co present can be found in Fig 10.4 of the dense samples. While there is error in the absolute values of the sample stoichiometries, a clear trend in the Pr:Co ratios can be seen, corresponding to their nominal stoichiometries. Regardless of their precise stoichiometry, there is certainty that a range of cation stoichiometries have been prepared.

Further chemical analysis was performed using XPS to identify the oxidation state of the Pr and Co cations, which would provide an indication of the oxygen nonstoichiometry. The emission spectra of the Co 2p and Pr 3d peaks, the most prominent of the Co and Pr peaks, are depicted in Table 10.4. There were no overlaps in the binding energy of constituent elements, which would otherwise have complicated the analysis.

A clear dual peak is seen for Co 2p and Pr 3d orbitals, arising from spin-orbital coupling, labeled in Table 10.4. The area ratio of the peak doublets are in agreement with what

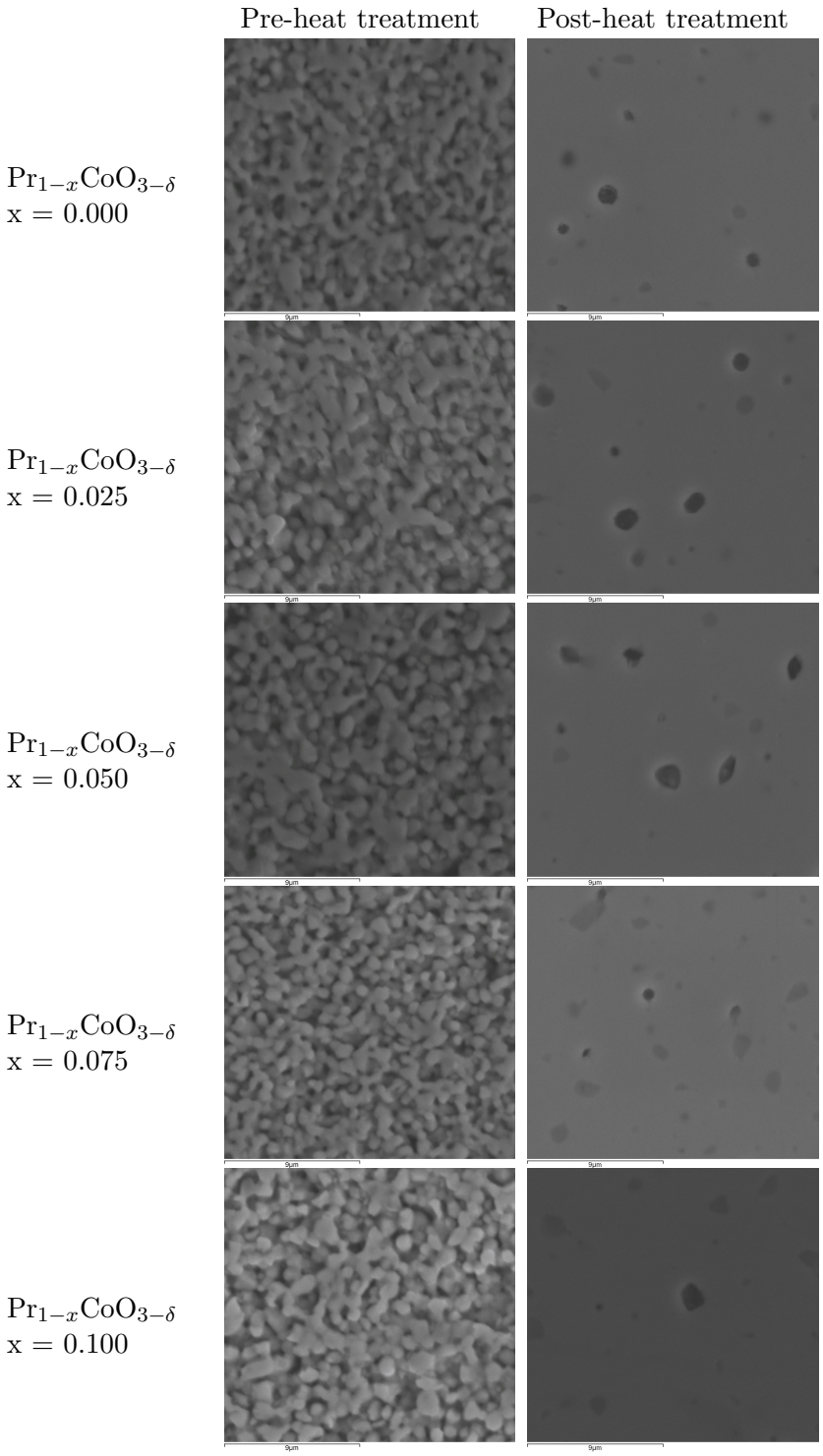


Table 10.2: SE images of the bar sample surface of PCO with a range of non-stoichiometry, pre- and post-heat treatment at 1200°C in air for 6 h. A greater extent of sintering may be seen in the non-stoichiometric bar samples post-heat treatment.

Nominal composition, $Pr_{1-x}CoO_{3-\delta}$ (x)	Density pre-heat treatment (%)	Density post-heat treatment (%)
0.000	96.8	95.5
0.025	97.5	95.4
0.050	94.4	95.5
0.075	97.4	96.5
0.100	95.7	97.0

Table 10.3: Measured densities of the non-stoichiometric PCO samples, $Pr_{1-x}CoO_{3-\delta}$, using the Archimedes method. On their own, these density measurements suggests a higher density was obtained in the non-stoichiometric PCO samples pre-heat treatment at 1200°C in air for 12 h. However, coupled with with the SE images of Table 10.2, the density of the non-stoichiometric PCO samples post-heat treatment was confirmed to be higher.

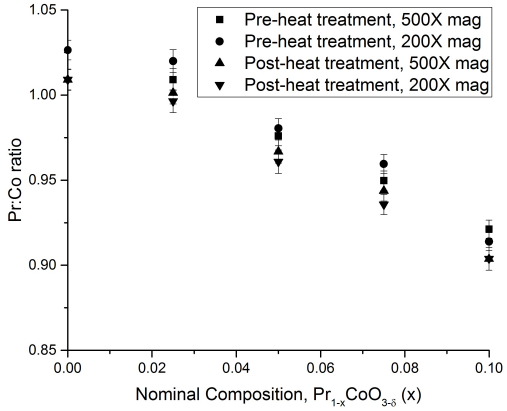


Figure 10.4: Pr:Co ratio as calculated from various EDX maps (at two magnifications: 200× and 500×) of the non-stoichiometric PCO samples pre- and post-heat treatment at 1200°C in air for 12 h.

would be expected: an area ratio of 1:2 and 2:3 between $p_{3/2}$ and $p_{1/2}$, and $d_{5/2}$ and $d_{3/2}$ respectively. The Pr $3d_{5/2}$ and Pr $3d_{3/2}$ binding energies were at 932.6±0.1 eV and 953.4±0.1 eV respectively. The Co $2p_{3/2}$ and Co $2p_{1/2}$ binding energies were at 780.0±0.1 eV and 794.5±0.5 eV respectively. These are in keeping with published values for the Pr^{3+} and Co^{3+} oxidation states, see Table 10.5 for the reported binding energy of various spectral lines. Unlike with Pr, the chemical shifts resulting from changes in oxidation state are very small between Co^{2+} and Co^{3+}, indicating there have a very similar effective charge [457].

As well as the binding energies, a visual comparison of the shapes of the Co 2p and Pr 3d peaks show them to be characteristic of Co and Pr elements of the oxide form, and also suggest that both Co and Pr exists predominantly in the 3+ oxidation state for all samples. It should be noted that CoO undergoes oxidization into Co_3O_4 at the sample surface, creating difficulties in obtaining the XPS spectra of pure CoO. Subsequently, CoO

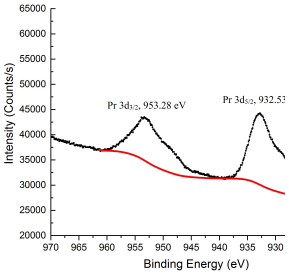
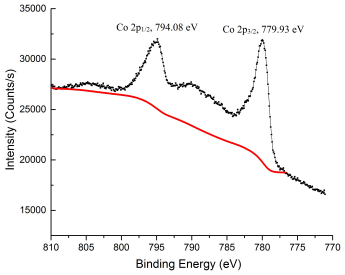
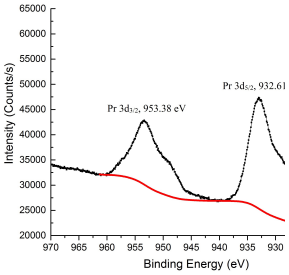
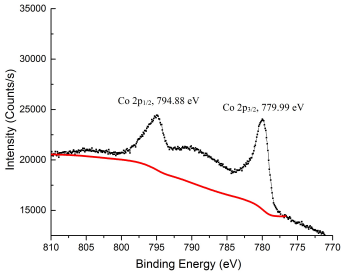
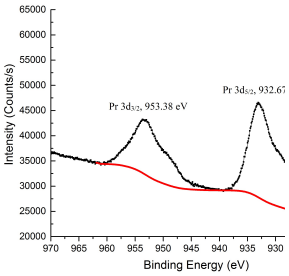
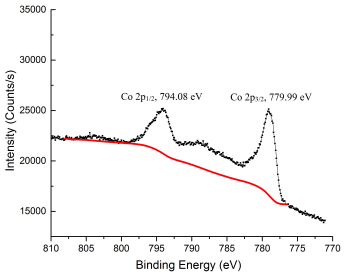
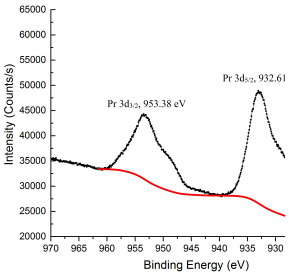
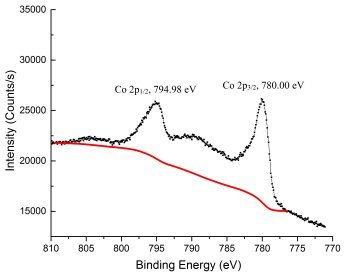
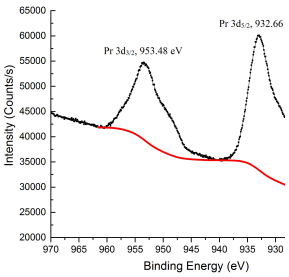
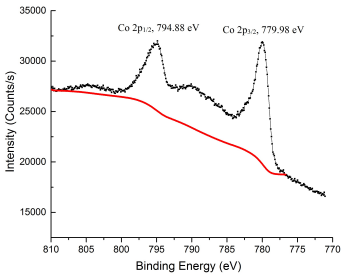
	Pr 3d	Co 2p
$Pr_{1-x}CoO_{3-\delta}$ x = 0.000		
$Pr_{1-x}CoO_{3-\delta}$ x = 0.025		
$Pr_{1-x}CoO_{3-\delta}$ x = 0.050		
$Pr_{1-x}CoO_{3-\delta}$ x = 0.075		
$Pr_{1-x}CoO_{3-\delta}$ x = 0.100		

Table 10.4: XPS spectra of the non-stoichiometric PCO bar samples, $Pr_{1-x}CoO_{3-\delta}$, at the Pr 3d and Co 2p edges. Background and the Pr $3d_{5/2}$, Pr $3d_{3/2}$, Co $2p_{3/2}$ and Co $2p_{1/2}$ binding energies were obtained Dr. I. Villar-Garcia of Imperial College using the Thermo Advantage software.

Element	Spectral line	Formula	Binding energy (eV)	Reference
Pr	$3d_{5/2}$	PrO_2	935.3	[458]
Pr	$3d_{5/2}$	Pr_2O_3	933.2	[458]
Pr	$3d_{5/2}$	Pr_2O_3	933.6	[459]
Co	$2p_{3/2}$	Co metal	778.0	[460]
Co	$2p_{3/2}$	CoO	780.0	[460]
Co	$2p_{3/2}$	Co_3O_4	779.9	[460]
Co	$2p_{3/2}$	CoO	780.5	[461]
Co	$2p_{3/2}$	Co_3O_4	779.6	[461]
Co	$2p_{3/2}$	CoO	778.1	[462]
Co	$2p_{3/2}$	Co_3O_4	779.6	[462]
Co	$2p_{3/2}$	CoO	780.0	[463]

Table 10.5: Reported binding energies of Pr $3d_{5/2}$ and Co $2p_{3/2}$ spectral lines in literature.

spectra have been reported for what is actually Co_3O_4 [464, 465]. The XPS spectra of the 2+ oxidation state of Co oxide may be differentiated from it's higher oxidation state by the shape of the Co $2p_{3/2}$ peak and the satellite peak at ∼803 eV.

The XPS measurements were taken under nominally identical conditions using the same equipment. Nevertheless, variations in the spectra may arise from the presence of contaminants on the sample. However, despite the cation non-stoichiometry, the shapes of the spectra are fairly consistent between samples. Given the low levels of A-site deficiency, and the effect of contaminants, it has not been possible to detect trends in the XPS spectra due to increasing A-site deficiency. Based on the proposed defect chemistry, the A-site deficiency should see a change in the Co^{3+} oxidation state to Co^{4+}. However, as the chemical shift to Co^{4+} is also very small, it is not possible to say if Co^{4+} is or is not present from the XPS spectra obtained, nor can any trends be clearly detected.

It was not possible to examine the oxygen nonstoichiometry by correlating the atomic% of oxygen detected to the atomic% of metal cations, with their respective oxidation states factored in, due to the presence of organic contaminants (traces of what may have been Na 1s, Ca 2p, N 1s peaks, and distinct C 1s peaks were detected) on the sample surface that were likely to be in an oxidised state. These contaminants were likely to have been introduced in the handling of the PCO samples. The effect of the Pr deficiency on oxygen non-stoichiometry shall be considered using TGA.

An objective of the XPS measurement was to verify the trend in Pr deficiency of the PCO samples. Due to the difficulties in differentiating between extrinsic background scattering events and the intrinsic signal, quantification of the sample composition should not be used as absolute values. However, comparisons of the relative peak areas of Pr to Co of the different samples should be indicative of the cation non-stoichiometries. The ratios of the areas of the most prominent Co and Pr peaks with the background subtracted (see Table 10.4), belonging to Co 2p and Pr 3d orbitals respectively, were calculated and can

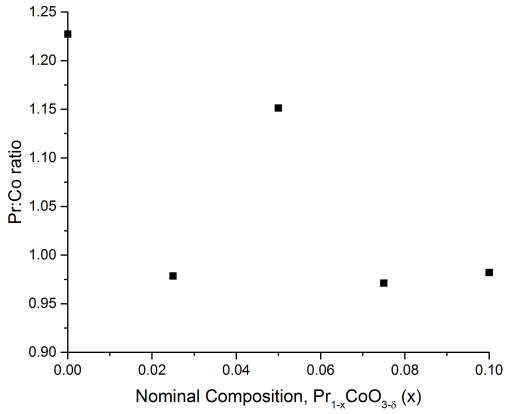


Figure 10.5: Pr:Co ratio as calculated from XPS measurements of the non-stoichiometric PCO samples, $Pr_{1-x}CoO_{3-\delta}$, showing a correlation with the nominal composition of the non-stoichiometric PCO samples, unlike the EDX compositional measurements in Fig 10.4.

be seen in Fig 10.5.

There does not appear to be a correlation between the nominal Pr:Co ratio and that measured using XPS, though not as clearly as seen of the EDX measurements. However, it has been noted that though experimental conditions for XPS have been kept identical, there was significant surface compositional variation especially in the extent of large amount of C contamination, see Fig 10.6. While physical conditions were consistent, chemical conditions were not. The presence of different contaminants would affect the scattering of the emitted electrons and the probability of their escaping the sample surface. Thus the different concentration of C would affect background levels. The variations in C concentration further stress that comparison of peak areas should not be made between samples. The variation in C concentration also appears to mirror the Pr:Co relative peak areas, suggesting it has also affected the measured peak areas and thus even comparisons of the relative peak areas between samples should only be made with caution. There is less confidence in these XPS results, but together with the EDX results, there is confidence that a range of PCO sample stoichiometries have been obtained, of the same trend as the nominal composition.

XRD patterns were obtained of the PCO samples at room temperature. The normalized patterns are presented in Fig 10.7. Despite the changes in stoichiometry, all samples are single phase PCO, within the detection limit of the Bruker. Besides a shift in 2θ position, reflecting the expansion of the PCO lattice with cation non-stoichiometry, the XRD patterns are near identical. Unlike what was seen in A-site LSCF, no increase in symmetry was observed with increasing A-site deficiency [72, 448, 52]; the peaks at $\sim 40^\circ$ 2θ, $\sim 58^\circ$ 2θ and $\sim 68^\circ$ 2θ remain split and unaffected by PCO stoichiometry. However, it should be noted that there is a slight difference in peak shape and background intensities for samples where $x = 0.000$ and $x = 0.100$, compared to the other samples. This is more apparent at 2θ values above 50° 2θ. This difference was attributed to use of two different

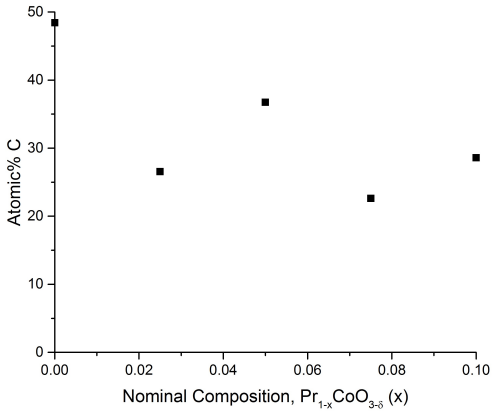


Figure 10.6: Atomic% C, as measured using XPS, as a function of the PCO nominal composition, $Pr_{1-x}CoO_{3-\delta}$.

Bruker 2D Phaser diffractometers; XRD patterns of samples where x = 0.000 and x = 0.100 were collected from one diffractometer, and the rest from the other.

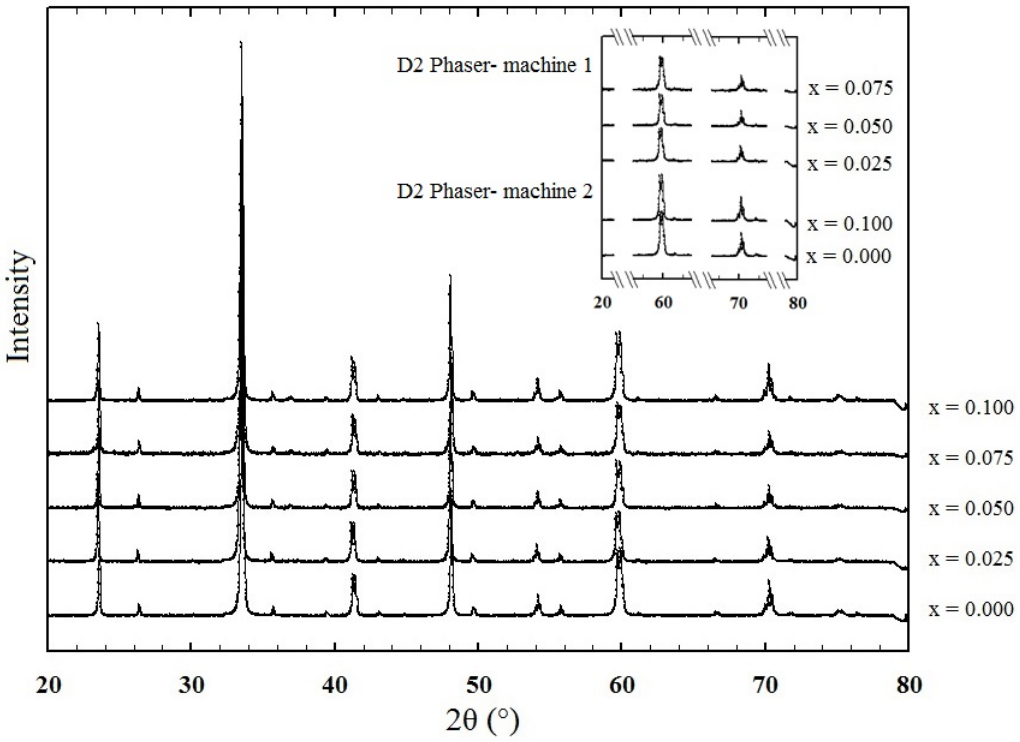


Figure 10.7: XRD powder diffraction pattern of non-stoichiometric PCO samples, $Pr_{1-x}CoO_{3-\delta}$, obtained using two D2 Phaser diffractometers. Inset shows the slight difference in peak shape between the non-stoichiometric PCO samples resulting from the use of the two diffractometers.

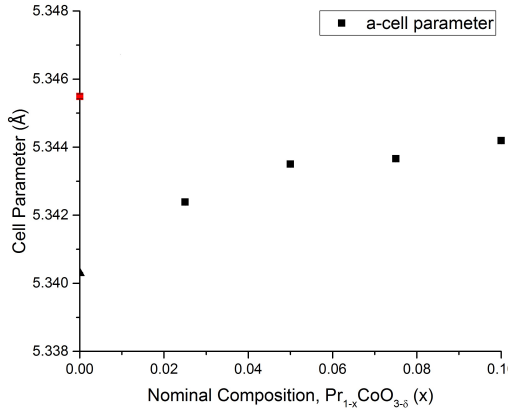
Rietveld refinements were performed on XRD patterns of the non-stoichiometric PCO powders at room temperature. The pattern fits and refinement output may be found in

Appendix A.4. All reflections were fitted according to the *Pnma* space group. There were no unmatched peaks or indications of any impurities within the XRD detection limits. All samples, regardless of composition, are single phase PCO. Cell parameters of the nonstoichiometric PCO, from the Rietveld refinement, are presented in Fig 10.8. As the Pr deficiency increased, the PCO unit cell underwent expansion along all three axes. This was observed by Kostogloudis et al. in doped PSC [162]. In PSC, the lattice expansion was associated with the larger ionic radii of Sr^{2+}, and the reducion of Co^{4+} to Co^{3+} (offsetting the lattice contraction with the formation of oxygen vacancies). Whereas, in A-site deficient LSCF (spacegroup *Pbnm*), while b lattice parameters increased with A-site deficiency, there was no clear trend in the expansion or contraction of the a- and c-lattice parameters. Overall cell volume increased with A-site deficiency in LSCF [52]. No explanation was provided for the lattice expansion of LSCF

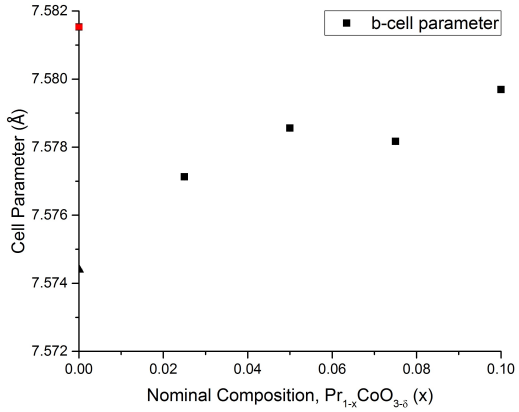
Following the defect chemistry outlined earlier, the removal of Pr from a lattice site would result in a change in the oxidation state of Co^{3+} to the smaller (ionic radii) Co^{4+}, which would increase the Co-O bond strength according to Pauling's second rule [466]. Similarly, though this is not anticipated, the A-site vacancy may be compensated by an increase in the oxidation state of Pr^{3+}, which would also result in a decrease in ionic radii and a subsequent contraction of the unit cell. As this measurement was performed at room temperature, it is unlikely to have a large concentration of O vacancies, the formation of which is a function of temperature (and oxygen partial pressure). Nevertheless, as was shown by Marrocchelli for the fluorite system, the creation of oxygen vacancies causes a contraction in the lattice [178, 176, 177]. However, as an increase in cell parameters is observed, it must be due to the formation of Pr vacancies, the effect of which must be large enough to offset the decrease in cell parameter with the change in Co oxidation state. The expansion of the lattice due to the Pr-deficiency, x, may be described using Vegard's law [467]. The Vegard's slope is 3.6-3.9 Å/x, and 4.7 Å/x, as calculated from the a-, c-, and b- cell parameters. The significantly steeper slope as calculated from the b-cell parameter is discussed later.

Within the detection limits of XRD and from the SEM images of the non-stoichiometric PCO, there was no indication to suggest the presence of a second phase; no cobalt oxide precipitates out. The symmetry of PCO should be maintained through the entire range of non-stoichiometry. Extending that found in the atomistic modeling of ceria, the removal of a Pr cation is likely to result in a repulsion of the surrounding oxide ions expanding the lattice, while the neighboring cations draw closer contracting the lattice. The net effect being the expansion of the lattice as observed here.

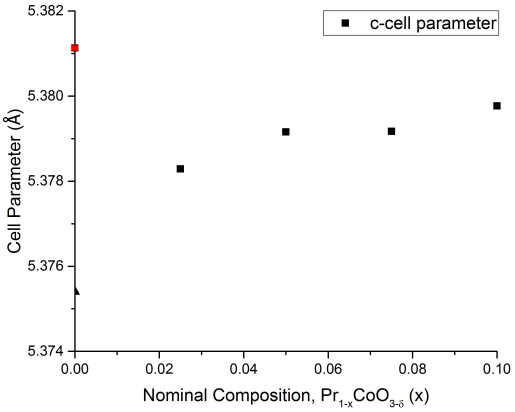
As the thermal expansion with Pr-deficiency remains somewhat linear for the entire range of Pr-deficiency examined, it is likely that the mechanism of chemical expansion is constant across the range and the only contributions to the chemical expansion is due to the change in oxidation state of the cobalt ions, and the creation of a Pr vacancy. It is not as seen in the case of LSC, where at high Sr-dopant concentrations, the creation of oxygen vacancies becomes more energetically favourable compared to the oxidation of Co resulting in a



(a) a-cell parameter



(b) b-cell parameter



(c) c-cell parameter

Figure 10.8: Lattice parameters of non-stoichiometric PCO samples, $Pr_{1-x}CoO_{3-\delta}$, calculated from Rietveld refinement of room-temperature powder XRD patterns obtained using a D2 Phaser diffractometer. Error bars have been included but are concealed by the data markers. A reference lattice parameter of stoichiometric PCO (traingle marker) has been included [6]. The lattice parameters of the stoichiometric PCO sample ($x = 0.000$) of this work was anomalous.

maximum concentration of Co^{4+} and thus a decrease in cell parameters as Sr concentration increases further [443, 82, 468]. Nevertheless, this effect may be present, but at larger Pr-deficiencies, beyond the range examined.

The stoichiometric sample has unusually large cell parameters, contrary to the trend that is seen. The cell parameters of *Pnma* PCO published in ICSD have been included in Fig 10.8(triangle marker) and follows the same trend in cell parameters of the nonstoichiometric samples. The stoichiometric sample is likely to be anomalous. Based on Vegard's law calculated from the other non-stoichiometric samples, it would have to have a composition of $Pr_{0.87\pm0.1}CoO_{3-\delta}$ to acquire such large cell parameters. This is improbable. Also, the EDX results suggest a near stoichiometric sample. The enlargement of its cell parameters is likely due to a different cause than the creation of vacancies. It is possible that this sample is Pr-rich. The excess Pr is unlikely to be accommodated as interstitials due to its large ionic radius. Instead, Co vacancies would have to be created, which would be a plausible explanation for the large expansion in the lattice. Additionally, it has been shown that even with a deficiency on the A-site in LSM, it is possible to form A_2O_3 oxides [449]. No Pr oxides can be observed within XRD detection limits, which may also suggest a preference of B-site vacancy formation. This (stoichiometric, $x = 0.000$) sample was omitted from all later discussion.

The expansion of the PCO lattice due to the Pr deficiency is stoichiometric expansion (as defined in Section 2.5.1, to arise from the creation of point defects) and a form of chemical strain. In Fig 10.9, this strain was calculated using the reference stoichiometric PCO parameters from ICSD. Here, it can more clearly be seen that the strain in all 3 cell parameters are of the same order, and are similarly affected by sample stoichiometry. However, there is a slight anisotropy with the expansion of the long b-axis being less than the other axes: as much as a quarter less than for the c-axis in the sample were $x = 0.075$. This anisotropy with the introduction of dopant species has been reported of other perovskite systems where the introduction of oxygen vacancies was found to affect the tilt of the CoO_6 octahedron, and thus effect a preferential expansion in a particular axis (the c-axis of the rhombohedral $R\bar{3}c$ structure) [443, 438, 439]. It is possible that a similar effect is being observed here, although it would then be expected that the anisotropy should increase with increasing Pr-deficiency, which is unclear in this current dataset. There are no indications in the room temperature XRD pattern of super structures.

With regards to oxide ion conductivity, there are two effects of interest with increasing A-site deficiency. First, it should be charge compensated by the creation of oxygen vacancies. Thus, Pr-deficiency should increase oxygen nonstoichiometry and consequently the probability of an available site for an oxide ion to hop onto. Second, there is the mechanochemical effect, which will be covered in detail in Chapter 11. Both these effects should be reflected in oxide ion conductivity measurements of the next chapter. The electronic transport of PCO arises from its CoO_6 octahedra and the overlap of the Co 3d and O 2p orbitals. Therefore, of interest are the variation in Co-O bond lengths and Co-O-Co bond angles of the nonstoichiometric samples.

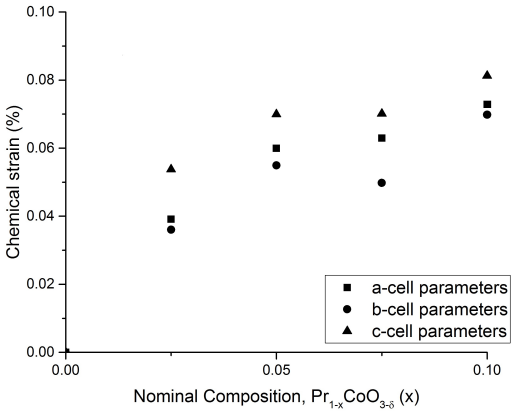
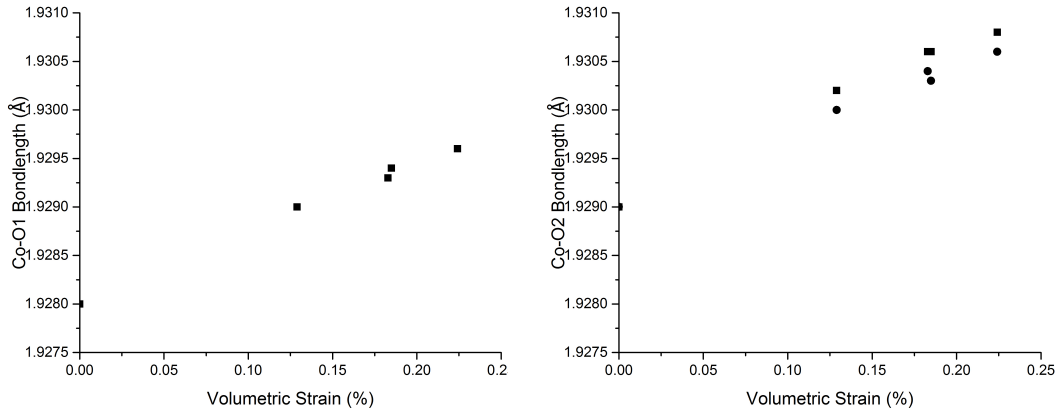


Figure 10.9: Chemical strain in each cell-parameter, as a result of the non-stoichiometry of the PCO samples, $Pr_{1-x}CoO_{3-\delta}$.



(a) Co-O1 bondlengths

(b) Co-O2 bondlengths

Figure 10.10: Co-O1 and Co-O2 bondlengths as a function of the volumetric chemical strain of non-stoichiometric PCO samples, $Pr_{1-x}CoO_{3-\delta}$.

The Co-O bond lengths were calculated from the Rietveld refinement of XRD patterns. As X-rays are less sensitive to lighter atoms such as O, it was not possible to refine the atomic positions of the O ions, and literature values were used. Based on the *Pnma* spacegroup, the Co positions were assigned to the origin. Thus the Co-O bond lengths calculated from this refinement are directly related to the volumetric strain of the lattice, as can be seen in Fig 10.10. Similarly for the Co-O-Co bond angles, which were also calculated and found to be mostly unchanged between samples, at 158.23° and 158.17° for Co-O1-Co and Co-O2-Co respectively, as would be expected given these refinement conditions. These bond lengths are only appropriate if the positions of the O atoms do not change between the nonstoichiometric samples. No trends could be found of the Pr-O1 or Pr-O2 bond lengths, either as a function of volumetric strain (or Co-O1 or Co-O2 bond length) or sample stoichiometry.

Similarly, it was not possible, using XRD, to accurately determine if they have been any distortions to the CoO_6 octahedra by calculating the octahedral angle or rotation, ϕ. This has been performed by Mastin et al. using HT-XRD measurements. However, this was only possible because, despite the poor sensitivity of X-rays to the oxygen atoms, Mastin el al was able to match the evolution of the LCO structure measured using HTXRD against neutron diffraction experiments and thus had reasonable confidence in XRD refinement of the oxygen positions. No such comparison (of neutron diffraction data) is available for the PCO system and subsequently the octahedral angle of rotation has not been calculated. Neutron diffraction is required for a full understanding of the structural changes of PCO of increasing Pr-deficiency, and the subsequent effect on its transport properties.

10.3.2 High Temperature Characterization of $Pr_{1-x}CoO_{3-\delta}$

XRD patterns were obtained of nonstoichiometric PCO powder samples between room temperature and 774°C, in air, using the Panalytical X'pert MPD. A comparison between the nonstoichiometric samples was made for the first room temperature data recorded, see Fig 10.11. However, as the same instrument was used for all the samples, the instrumental effect on the shape of the reflections seen between the different Bruker measurements was not seen here; all nonstoichiometric PCO samples have the same peak shapes.

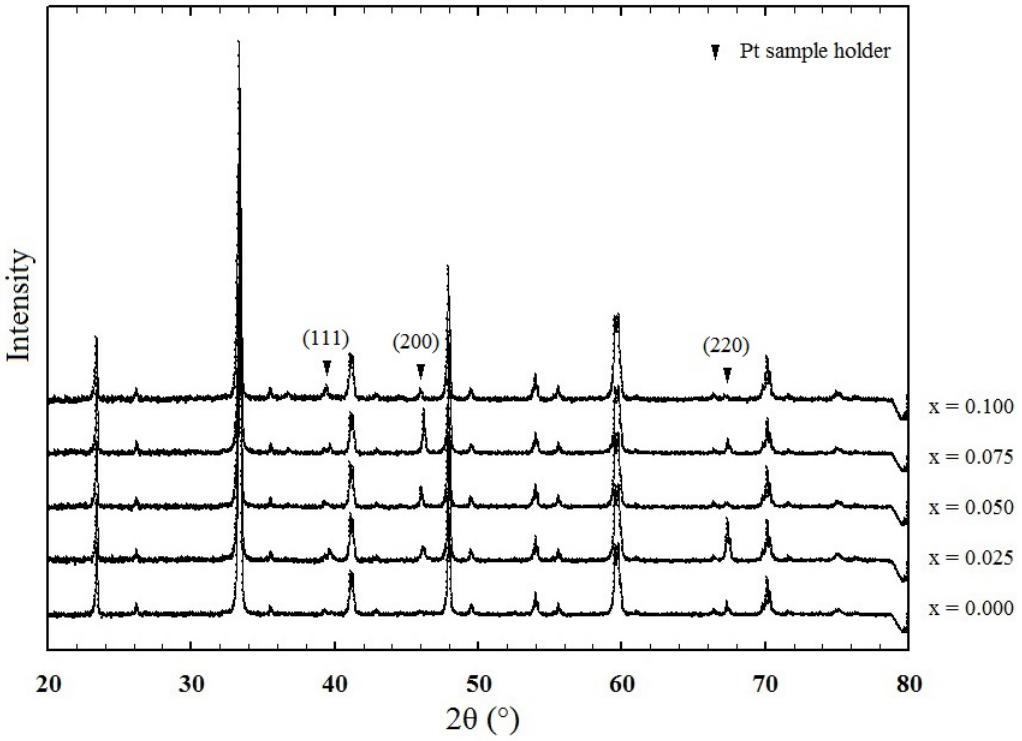


Figure 10.11: XRD powder diffraction pattern of non-stoichiometric PCO samples, $Pr_{1-x}CoO_{3-\delta}$, obtained using the Panalytical X'pert MPD. Trace reflections of the Pt sample holder were detected, the intensity of which depended on PCO sample coverage over the Pt film.

However, a slight difference in the relative intensities of the main PCO(200), PCO(121) and PCO(002) reflections around ∼33.5° 2θ and at ∼59.5° 2θ, was seen in the PCO sample where $x = 0.100$, compared to the others. It appears that the reflections of this sample were also broader. It was unclear if these differences were due to improper sample preparation, or if it was due to the large Pr-deficiency in this sample. This will be further investigated from its high temperature XRD patterns.

Lastly, compared to the XRD patterns obtained using the Bruker, these patterns have a few additional reflections around ∼39.6° 2θ, ∼46.2° 2θ, and ∼67.4° 2θ. These correspond to the (111), (200) and (220) reflections of the Pt $Fm\bar{3}m$ sample holder. As mentioned in the Experimental Section, only a thin layer of PCO powder was dispersed over the surface of a Pt film, which acted as the sample holder. Thus, trace signals from the Pt holder have been detected. There is a slight shift in the 2θ positions of the Pt reflections between samples. This is due to the variation in placement of the Pt holder below the sample surface; there was a variation in PCO powder layer thickness between the samples and therefore different height corrections are required for the different samples. The highest intensity reflection for Pt should be the (111) reflection at 39.27° 2θ . The different relative intensities of the Pt reflections detected suggests that the Pt film was textured.

The HT-XRD patterns of the PCO sample ($x = 0.025$), between 35°C and 774°C taken every ∼150°C are presented in Fig 10.12. The trends observed in this sample are representative of all the other samples, with the exception of the most cation-deficient sample ($x = 0.1$). The high temperature HT-XRD patterns of the all nonstoichiometric PCO samples are available in Appendix A.4. As temperature increases, there was a very slight decrease in FWHM, presumably due to the coarsening of the powder crystallite size. There is also a clear decrease in 2θ positions as the sample undergoes thermal, and potentially chemical expansion. A transformation is seen in this temperature range, as clear and gradual convergences of reflections around 2θ∼32° 2θ, ∼59° 2θ and ∼67° 2θ were observed. Corresponding increases in peak intensities were seen of all these reflections. However, this was not the case for all the PCO reflections. The reflections around θ∼22° 2θ, ∼47° 2θ, ∼54° 2θ and ∼69° 2θ did not see an increase in peak intensity, only a 2θ shift. Given the resolution of the instrument, it was not possible to identify the transformation temperature directly from the pattern. This transformation was more apparent when examining the change in lattice parameters with temperature.

The PCO sample with the largest A-site deficiency of $x = 0.100$, see Fig 10.13 shares the same trend as the other nonstoichiometric samples up until 308°C. In the other nonstoichiometric PCO samples two different behaviors were seen as temperature increased, as seen in the inset of Fig 10.12. For the PCO sample where $x = 0.100$, an additional feature is seen: a broadening of all the reflections. Thus, for the PCO reflections that stay at a constant peak intensity for the other PCO samples (such as at ∼22° 2θ), a decrease in peak intensity was observed for the sample where $x = 0.100$. Similarly for the PCO reflections that see an increase in peak intensity with temperature for the other PCO samples (such as at ∼34° 2θ), peak intensities also decrease after 308°C. As the same instrument and sample

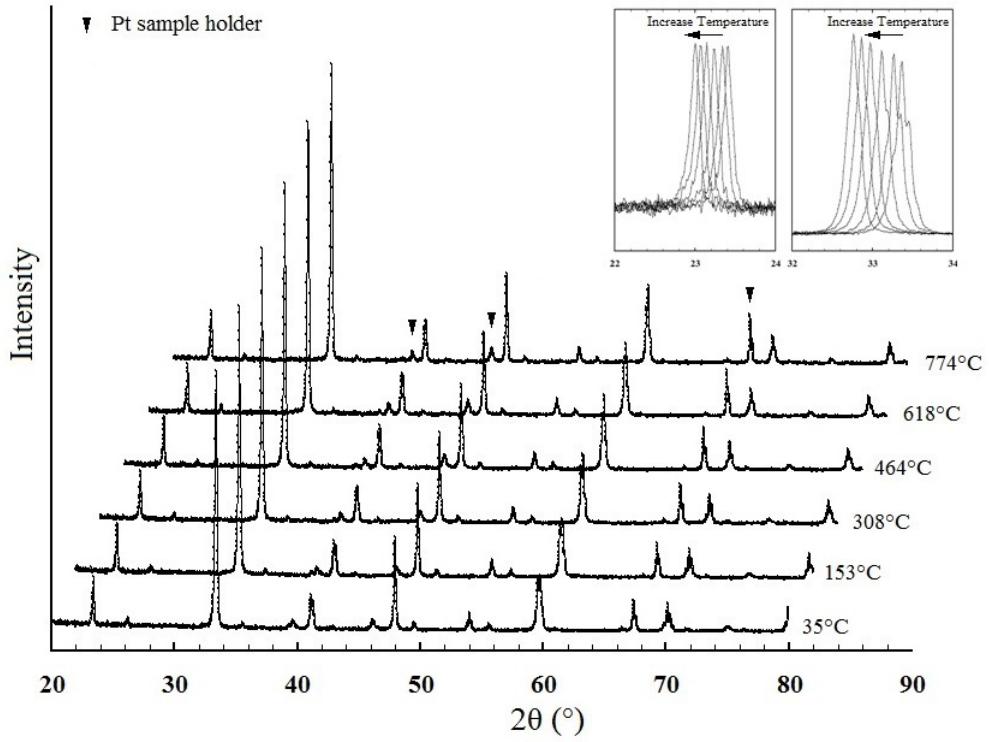


Figure 10.12: XRD powder diffraction pattern of non-stoichiometric PCO, $Pr_{1-x}CoO_{3-\delta}$, where $x = 0.025$, obtained using the Panalytical X'pert MPD. Trace reflections of the Pt sample holder were detected. Inset, the diffraction patterns at ∼22° 2θ and ∼34° 2θ superimposed on top of each other: as temperature increased the PCO reflection at ∼22° 2θ shifted to smaller 2θ values, whereas the PCO reflections at ∼34° 2θ shifted to smaller 2θ values, decreased in FWHM and increased in maximum peak intensity. A phase transformation may be observed between 308°C and 464°C.

setup was used in all the measurements, and broadening of the reflections between patterns must be due to specimen broadening, rather than instrumental. For this PCO sample, it sees either a decrease in crystallite size or microstrain broadening from temperature of 464°C, which was not observed for lower levels of A-site deficiency.

The increase in FWHM is unlikely to be due to a decrease in crystallite size. At lower temperatures, the crystallites were seen to progressively coarsen. Additionally, increasing A-site deficiency has been found to improve sinterability [450]. Thus, the PCO sample with the largest A-site deficiency is expected to exhibit the largest decrease in FWHM within the same temperature range. Microstrain broadening can arise from the presence of non-uniform lattice distortions, dislocations, stacking faults and antiphase domain boundaries (unlikely as all peaks broadened, not just the fundamental peaks), grain surface relaxation, and solid solution inhomogeneity. Without further characterisation with TEM, it was not possible to ascertain the cause of the peak broadening. However, that it was found in the most A-site deficient PCO sample suggests it may be due to solid solution inhomogeneity. This has been kept in consideration in later discussion of this sample.

A comparison was also made of room temperature XRD measurements taken at the start

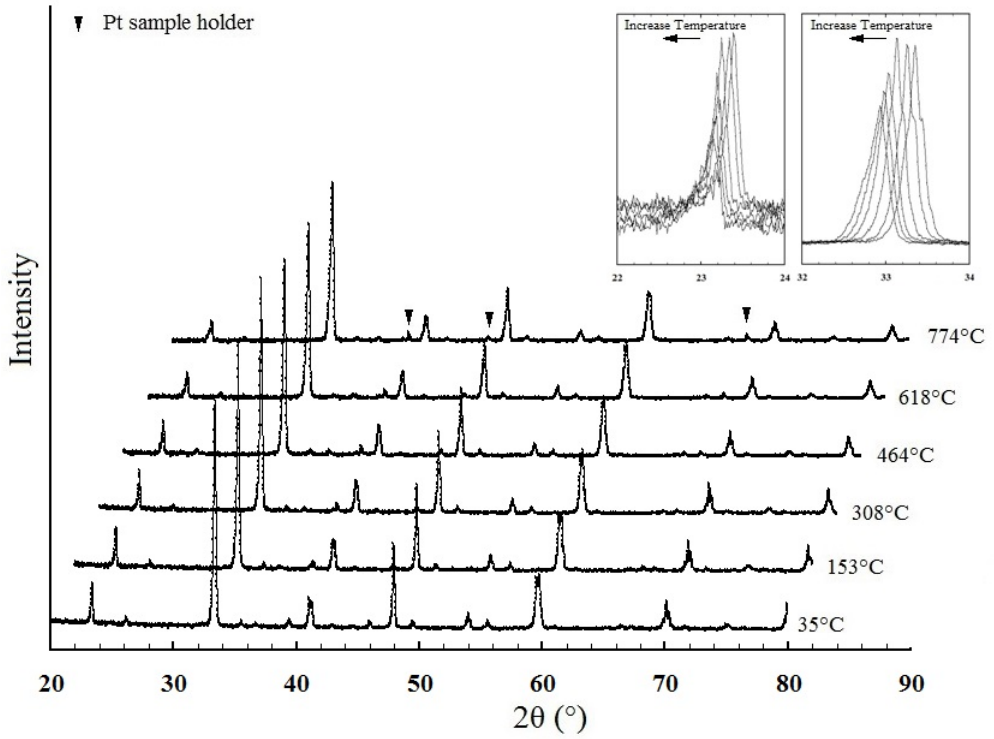


Figure 10.13: XRD powder diffraction pattern of non-stoichiometric PCO, $Pr_{1-x}CoO_{3-\delta}$, where $x = 0.100$, obtained using the Panalytical X'pert MPD. Trace reflections of the Pt sample holder were detected. Inset, the diffraction patterns at ∼22° 2θ and ∼34° 2θ superimposed on top of each other. At temperatures above 308°C, FWHM of all reflections broadened, accompanied by a decrease in peak intensity.

of the heating cycle, and at the end after slow cooling in air. The XRD patterns for a representative non-stoichiometric PCO sample (where $x = 0.025$) are depicted in Fig 10.14. For all samples the high temperature phase transformation was fully reversible on cooling. The XRD patterns pre- and post-heating were largely identical. A slight shift to larger 2θ values was observed. However, this may be attributed to slight changes to sample position during cooling as the sample and sample holder contracted. The slight decrease in FWHM on heating can more clearly be seen in the room temperature comparison, apart from the sample of A-site deficiency $x = 0.1$, where the broadening of the reflection from 464°C offset the decrease in FWHM.

A Le Bail refinement was performed on all HT-XRD patterns to obtain the lattice parameters of all non-stoichiometric PCO samples. These have been presented as the %change in volume and cell parameter as a function of temperature, the gradient of which is the (voulmetric or linear) expansion coefficient, EC, in Fig 10.15 and Fig 10.16. Thus it can be seen that a similar shape is observed in the linear EC of all cell parameters of all the samples and subsequently also in the volumetric EC: a linear expansion coefficient, followed by a phase transition, and a high temperature expansion coefficient that is arguably non-linear. There are four main points of discussion: first, the shape of the expansion coefficient curve (the occurrence of a phase transition, its linear behaviour at low temperatures

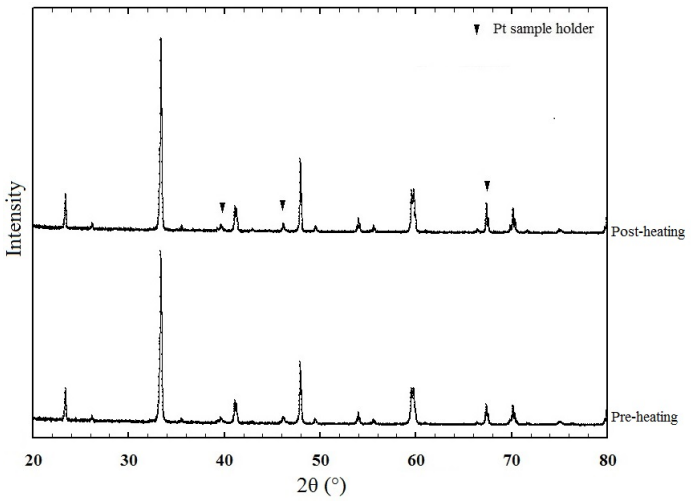


Figure 10.14: XRD powder diffraction pattern of non-stoichiometric PCO, $Pr_{1-x}CoO_{3-\delta}$, where $x = 0.025$, pre- and post- heating obtained using the Panalytical X'pert MPD. Trace reflections of the Pt sample holder were detected and labeled. The two diffraction patterns are virtually identical.

and non-linear behaviour at high temperature); second, the effect of Pr-deficiency on the low temperature linear expansion coefficient; third, the effect of Pr-deficiency on the high temperature non-linear expansion coefficient; and fourth, the effect of Pr-deficiency on the phase transition.

First, the shape of the lattice and volumetric expansion curves are considered. A phase transition is likely to have occurred, as evinced by the change in EC gradient. This is likely to be the second order ferrolastic to paraelastic phase transition [438, 439, 469]. This describes the non-linear stress-strain behaviour of the material and has been observed in lanthanum colbaltites [443, 438, 439]. At this transition temperature, it is now energetically favorable for ferroelastic domains to re-orientate to accommodate an applied stress. This reorientation of domains have been confirmed experimentally, and toughens the material as energy is directed into the transition [469]. Such a transition requires a shift from a low temperature low symmetry phase to a high temperature high symmetry phase, such as the ideal cubic $Pm\bar{3}m$ spacegroup for PCO. However, the change in spacegroup with the transition was not identified.

From Fig 10.16, it can also be seen that the TEC is initially linear with temperature, as would be expected from purely thermal expansion. However, it is non-linear at higher temperatures, above 600°C, as chemical expansion occurs. These results are similar to what has been previously reported of doped rare-earth colbaltites [443, 162]. The chemical expansion has been attributed to variations in oxygen non-stoichiometry. An upturn in the thermal expansion curve is typically found of doped lanthanum colbaltites as lattice oxygen is expelled and oxygen vacancies formed, expanding the lattice [443, 431]. However, consideration of the Sr-doped $PrCoO_3$ system indicates a flattening of the thermal expansion curve. This has been attributed to the thermally activated process of charge

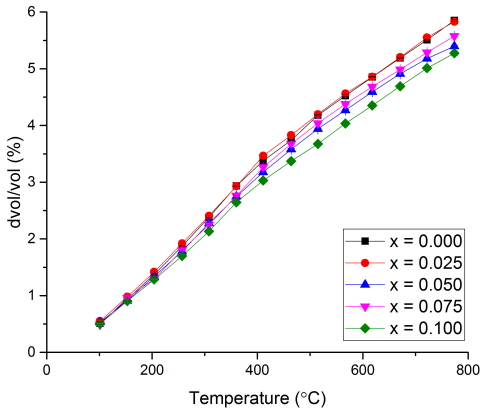
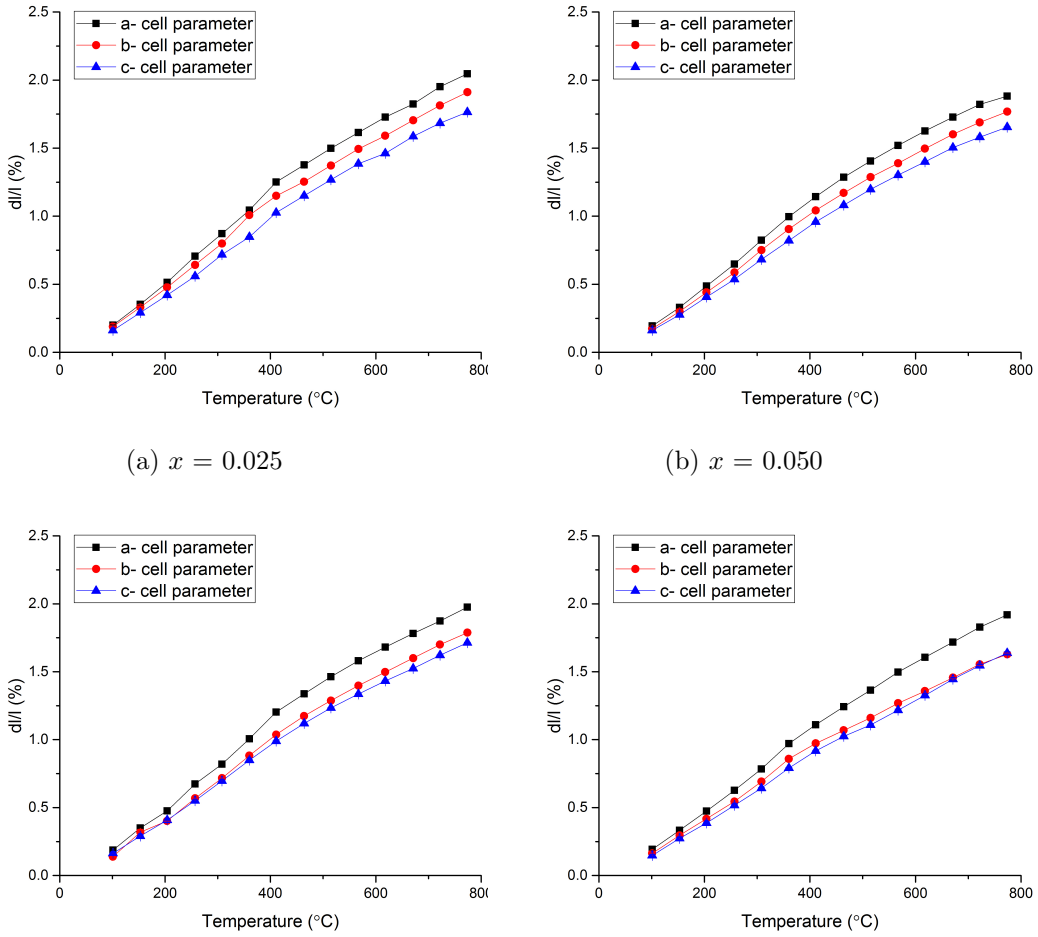


Figure 10.15: Volumetric strain (%) in the non-stoichiometric PCO, $Pr_{1-x}CoO_{3-\delta}$ as a function of temperature. Increasing A-site deficiency, x, increases the rate of lattice expansion with temperature. Error bars have been partially concealed by the data markers.

disproportionation of Co^{3+} into Co^{4+} and Co^{2+}, which results in a contraction of the lattice [162]. This could be the cause of the flattening of the thermal expansion curves obtained in this work. Contrary to its lanthanide variants, TGA measurements indicated mass gain starting around 400°C. PCO must be losing oxygen vacancies and gaining oxide ions at high temperatures, which would also contract its lattice. This also may be the cause for the flattening of the thermal expansion curve. However, it is not possible to pinpoint the exact mechanism for this chemical expansion, as it would require detailed information of the oxidation states of the cations, and also the oxygen non-stoichiometry of the sample, which may have structural effects (such as distortions of the BO_6 octahedra or the Jahn Teller effect) or defect ordering, all of which would affect the chemical expansion/contraction of the lattice. As oxygen uptake occurred, it would suggest the inherent presence of oxygen vacancies prior to heating, which may or may not have been affected by the Pr deficiency.

Second, the effect of A-site deficiency on the linear expansion coefficient at low temperatures is considered. At low temperature, before the onset of oxygen uptake, the lattice expansion is likely to comprise solely of thermal contributions. From earlier room temperature Rietveld refinements, increasing A-site deficiency was found to result in a larger unit cell. The expectation is that the increase in the atomic distances would decrease bonding strength and thus increase the TEC. Based on this, increasing A-site deficiency should increase the TEC and thus the EC over the entire temperature range. On the contrary, it can be seen that increasing A-site deficiency had the effect of decreasing the thermal expansion coefficient see Fig 10.17.

Mastin et al. found that increasing Sr content in LSC increased the symmetry of the system closer to that of a cubic structure [443]. Similarly from his refinement of XRD data, Chen et al. saw the Goldschmidt tolerance factor, t, tended to unity as Sr-doping increased with $La_{1-x}Sr_xCoO_{3-\delta}$ becoming cubic and the Co-O-Co bond angle increasing from 164.83° to



(a) $x = 0.025$ (b) $x = 0.050$

(c) $x = 0.075$ (d) $x = 0.100$

Figure 10.16: % change in a- b- and c-cell parameters of non-stoichiometric PCO samples, $Pr_{1-x}CoO_{3-\delta}$, as a function of temperature. Error bars have been partially concealed by the data markers. A phase transition may be observed in all the PCO samples, where the gradient of the % change in cell parameters, the thermal expansion coefficeint, TEC, changes.

180°, from an Sr content of $x = 0.6$ [438]. Such a change in symmetry would affect the bond strength within the crystal. Thus, a possibility is that the introduction of Pr and oxygen vacancies had a similar effect as introducing Sr-dopants and increased symmetry of the PCO system, with the potential effect of increasing overall bond strength within the crystal and thus decreasing its thermal expansion coefficient. While at room temperature, it could be seen that the creation of Pr vacancies resulted in an expansion of the lattice, it can also be seen in Fig 10.17 that the thermal expansion coefficient decreased as Pr vacancy increased.

Third, the effect of Pr-deficiency on the non-linear region of the thermal expansion curve is considered, focusing on the effect of Pr-deficiency on chemical expansion contributions. In his work with Sr-doped PCO, Kostoglodis et al. found that although increasing Sr-

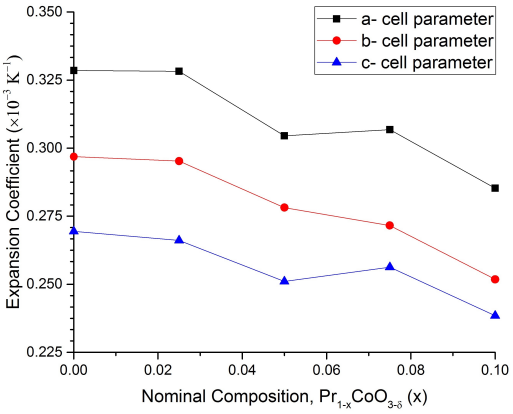


Figure 10.17: Thermal expansion coefficient as calculated from a-, b-, and c-cell parameters of non-stoichiometric PCO samples, $Pr_{1-x}CoO_{3-\delta}$, as a function of A-site deficiency, x.

doping in PCO decreased its thermal expansion coefficient, upon the onset of chemical expansion it resulted in an upturn in the thermo-chemical curve [162]. At higher Sr concentrations, vacancy formation became favorable and hence the lattice expansion. Thus, it was hypothesized that as higher Pr vacancy concentrations increased, an upturn in the EC would be observed confirming the formation of oxygen vacancies. However, the effect of increasing Pr-deficiency on chemical expansion is unclear. The thermo-chemical expansion curves obtained appear to follow the same gradient suggesting that the chemical expansion mechanism as a function of temperature in the samples were unaffected by the change in Pr-deficiency. It may also be argued that there was a slight down-turn in the thermo-chemical expansion curves with increasing Pr-deficiency. This would suggest that increasing Pr vacancies either increased oxygen uptake, or charge disproportionation. As raised earlier, given the limited information of the system, it is not possible to pinpoint the effect of increasing Pr vacancies on chemical expansion.

Nevertheless, what may clearly be observed is anisotropy in the chemical expansion of the PCO cell parameters. The rate of contraction of long b-axis as a result of chemical expansion increases as Pr deficiency increases. When $x = 0.025$, $b/\sqrt{2}$ is clearly larger than the c-cell parameter. By $x = 0.1$, $b/\sqrt{2}$ is of a comparable value to the c-cell parameter, see Fig 10.16. On the other hand, the ratio of a:c cell parameters remain largely unchanged with values of A-site deficiency, x. Thus, it appears that the chemical expansion of the b-cell parameter was especially sensitive to A-site deficiency and suggests a preferential ordering of defects along it.

This anisotropic chemical expansion has been reported for the LSC and LSCF system, as covered in the literature review [52, 438, 443]. Drawing parallels from the LSC system, it is possible that the CoO_6 octahedra of PCO is also sensitive to the presence of oxygen vacancies, which have been shown to affect its tilt angle and compression in LSC [443, 438, 439]. Distortions to the CoO_6 octahedra would affect Co-O-Co bond angle. A return to the ideal cubic structure would straighten it to 180°, increasing the O 2p and Co 3d orbital

overall and thus improving electronic conductivity. The anisotropic chemical expansion observed here may well affect the electronic properties of non-stoichiometric PCO, which will be investigated in the next chapter.

Fourth, the effect of Pr-deficiency on the ferroelastic to paraelastic phase transition is considered. Kostogloudis et al. reported a decrease in the transition temperature with increasing Sr-doping. This was attributed to preferable formation of oxygen vacancies at sufficiently high levels of Sr-doping. Mastin et al. also drew a correlation between Sr-doping to the transition temperature, proposing that the additional oxygen vacancies associated with the Sr-dopants lowered the symmetry of LSC closer to a cubic system thus shifting the transition temperature [443]. Unfortunately, for this work, it has not been able to extrapolate the transition temperature as the onset of chemical expansion occurs close to the transition temperature. To extrapolate the transition temperature, it is necessary just to use thermal expansion data and not a superposition of both thermal and chemical expansion. Nevertheless, based on all previous results and the parallels with the LSC system, it is expected that the increase in Pr-deficiency would result in a decrease of the ferroelastic to paraelastic phase transition of PCO, as oxygen vacancy concentration increases.

10.4 Conclusion and Further Work

A range of A-site deficient PCO powders, and bulk samples of two different densities, have been synthesized and imaged. Metal cation ratio was confirmed using EDX maps over two different sample areas and were found to contain consistently more Pr than expected from the nominal stoichiometry, suggesting that the nominally stoichiometric PCO sample was actually B-site deficient.

Room temperature XPS measurements were performed on the bulk samples. The Pr and Co ions existed predominantly in their 3+ oxidation state. Due to the small chemical shifts between the different Co oxidation states, it was not possible to confirm the presence of Co^{4+}, or whether the concentration of Co^{4+} present varies with A-site deficiency, as was proposed by the defect chemistry. It was not possible to determine oxygen stoichiometry as oxide-forming contaminants were detected. Similarly, quantification of the cation ratio proved unreliable. Further work would be to ascertain the cation ratio through the use of techniques such as inductively coupled plasma mass spectrometry, ICP-MS, or X-ray absorption near edge structure, XANES.

Rietveld refinement was performed on room temperature XRD patterns. Increasing A-site deficiency saw an isotropic expansion in unit cell parameters, attributed to the presence of Pr vacancies (that would have offset any contractions in the unit cell on increasing the oxidation state of Co^{3+} to Co^{4+}). Unit cell parameters of the nominally stoichiometric PCO sample were disproportionately large. This further enforces that the sample is actually B-site deficient, as suggested from the EDX measurements. Subsequently, this sample has

been discounted for the remainder of the study. Co-O bond lengths were found to increase with volumetric strain, while Co-O-Co bond angle remain mostly unchanged. However, it is unclear if this is because of the nature of the refinement, of if the presence of A-site vacancies do not affect octahedral tilting. This will be further investigated in the next chapter, when the electronic properties of the A-site deficient PCO will be measured, providing an indication of the octahedral tilt. Oxygen sensitive neutron diffraction of these samples would also shed light on the structural changes effected.

High temperature XRD was also performed on these samples, between 35°C and 774°C. As temperature increased, a slight coarsening of the PCO sample was detected. However, from 464°C, the FHWM of all reflections began to increase in the PCO sample with greatest A-site deficiency. TEM is required to identify the source of this broadening. Upon cooling back to room temperature, the XRD patterns of all PCO samples were largely identical to their post-heating form. On heating in air, all PCO samples exhibited low temperature linear thermal expansion and a second order ferroelastic to paraelastic phase transition. At higher temperatures, charge disproportionation of Co^{3+} occurred, decreasing the lattice parameters and marking the onset of chemical contraction. Thus the expansion coefficient comprised of both thermal and chemical contributions. The effect of increasing Pr-deficiency was seen to decrease the thermal expansion coefficient, but its effect on chemical expansion was unclear. Additionally there are also currently there are too many variables within the system that may contribute to chemical expansion to be able to identify the mechanism(s) by which it occurs. However, there is evidence for anisotropic uptake of oxygen, resulting in an increased contraction of the b-axis. It is expected that the increased oxygen vacancy concentration associated with increased Pr-deficiency would also decrease the transition temperature. It should be noted that the defect concentration present, or the effect of the defect concentration on the cell parameters, is much lower than has been reported in Sr-doped systems of equivalent defect chemistry.

Further work investigating the thermo-chemical expansion of PCO would require high temperature XPS to provide clear evidence of changes in Co oxidation state, as opposed to its inference. Also, high temperature neutron diffraction studies would clarify the relation between oxygen vacancies and the CoO_6 octahedra and thus the subsequent anisotropy in thermo-chemical expansion. While neutron diffraction data would be the ideal, there is also value in refining oxygen positions from the HT-XRD data obtained in this work, as done by Mastin et al. and Chen et al., to examine for octahedral distortions [443, 438]. Lastly, TGA measurements have been underutilized in this work. Further work should include the use of it to determine oxygen non-stoichiometry and its variation with temperature.

Chapter 11

The Effects of Chemical and Mechanical Strain on the Oxygen Tracer and Electrical Transport Measurements of $PrCoO_{3-\delta}$

In the previous chapters, strained PCO films, deposited on CGO/YSZ by PLD, and chemically strained sintered bars of non-stoichiometric PCO ($Pr_{1-x}CoO_{3-\delta}$) have been prepared and structurally characterized. For the PCO films, due to the lattice mismatch between PCO and CGO, a mechanical strain was induced. Increasing CGO buffer layer thickness had the effect of increasing PCO out-of-plane compressive lattice strain, while increasing PCO film thickness allowed the greater relaxation of the film and a reduction of the out-of-plane compressive lattice strain. For the nonstoichiometric PCO bars, the chemical strain was achieved by varying the PCO composition for A-site cation deficiency, x. Increasing A-site deficiency resulted in an expanded PCO lattice and should increase the material capability for charge compensation through the creation of oxygen vacancies.

In this chapter, the electrical and oxide ion transport properties of PCO thin film and nonstoichiometric PCO are measured, thus accomplishing the aim of this work to "investigate and compare the effect of various types of strain on the oxide ion and electrical transport of PCO," as outlined in Chapter 4. The effects of mechanical and chemical strain on the transport properties of PCO are discussed, drawing from the sample characterization of Chapter 9 and 10. It was not possible to correlate the transport properties of PCO to the CoO_6 octahedral distortion, which could not be measured with confidence in either the PCO thin films of nonstoichiometric bulk PCO, in this work.

11.1 Literature Review

As covered in Section 3.5, mechano-chemical coupling is the modification of the free energy 'landscape' of a system through the application of an internal or external stress. The application of a strain may potentially make certain reactions more or less thermodynamically favorable. Mechano-chemical coupling and its effect on oxygen transport is a key objective of this work. Thus the following review will briefly trace the discovery of this effect, before citing works on the mechano-chemical coupling effect on oxygen transport. While much work has focused on fluorite oxide electrolyte materials (namely ceria), there have been ingresses with respect to perovskite oxide cathode materials which are covered here.

All experimental validation of mechano-chemical coupling has come from strained films that are lattice-mismatched to their substrates. It is of interest to investigate if mechano-chemical coupling can be replicated from other sources of strain, such as chemical strain. A review of chemical strain in perovskites has been covered in Chapter 10. The source and effects of chemical strain has been reported and attempts made to model it [185, 184, 183, 182]; chemical strain has largely been viewed as a consequence of doping and the material defect chemistry. However, besides the contribution of its defect population to oxide ion conductivity, there should also be a mechano-chemical coupling effect as the lattice is chemically strained. There should be two effects. Yet, the mechano-chemical coupling effect in chemically strained perovskites has largely remained uninvestigated and no publications discussing this have been found. It is of interest, therefore, to compare the effects of mechanical and chemical strain in the thin film and bulk non-stoichiometric PCO respectively. Any enhancements in oxygen conductivity of the thin films should be a purely mechano-chemical coupling effect (if there are no changes in stoichiometry), while in the bulk non-stoichiometric samples it should arise from both a mechano-chemical coupling effect and variations in defect concentration.

11.1.1 Mechano-chemical Coupling in Perovskites

In Chapter 2.3 it was seen that the oxide ion conductivity of a material requires an oxygen reduction reaction at the surface and subsequent transport of the oxide ion away from the reaction site. It may be described by its surface exchange coefficient, k, and its diffusion coefficient through the bulk, D. The ORR involves the adsorption of an oxygen molecule onto a surface followed by its dissociation as it is incorporated into the lattice via an oxygen vacancy [470, 471, 472], and as such requires a high concentration of mobile oxygen vacancies at the surface to be accelerated [130]. Meanwhile the transport of the oxide ion occurs through a vacancy mechanism and improves with oxygen vacancy concentration. Thus both these properties are improved by the presence of oxygen vacancies; their role is crucial for good performance in an SOFC cathode. It is therefore of great interest that the application of strain has the potential to alter the energy landscape to make the formation

of oxygen vacancies and their transport more favorable (as well as affecting its electronic structure and reactivity [473]).

Early experimental work did indicate mechano-chemical coupling [474, 475, 476]; however, it was in a key study by Kushima et al. where the surface of LCO was modeled using DFT calculations that the dominant mechanism by which biaxial strain affected ionic conductivity was first identified [151]. Three processes, relating to each step of oxygen adsorption, dissociation and diffusion in the bulk, were examined separately for the effect of strain on them. Kushima et al. saw two different consequences to the application of lattice strain: elastic stretching of Co-O bonds and a LS to IS phase transition in spin state. The first response was elastoplastic in nature, while the second magnetoelastic. Another notable discovery was that if strained sufficiently, the adsorption mechanism of oxygen at the LCO surface changed from chemisorption to physisorption.

The application of a tensile strain and subsequent stretching of the Co-O bond (the elastoplastic response) decreased the overlap of the Co d-band/3d orbital and the O p-band/2p orbital. This lowered the formation energy of oxygen vacancies at the surface and in the bulk, $E_{vac}^{B,S}$. This additionally also decreased the oxygen adsorption energy, E_{ad} (the energy required for oxygen to adsorp onto the surface). Thus it improved both oxygen exchange at the surface and its transport through the bulk. However, at the same time, local relaxation occurred as Co-O bonds broke and reformed resulting in stronger Co-O bonds and subsequently an increase in the formation energy of oxygen vacancies in the bulk that effectively trap oxygens in the lattice, E_{vac}^{B}; and also increasing adsorption energy, E_{ad}, and inhibiting oxygen adsorption. This stress relaxation is detrimental to oxygen exchange and transport. The magnetoelastic response, like stress relaxation, increases the hybridization between the Co d-band/3d orbital and the O p-band/2p orbital and increases the formation energy of oxygen vacancies in the bulk. All three mechanisms and their effect on oxygen vacancy formation energies and oxygen adsorption energies are in competition with each other. Since then, the effect of strain has been seen to decrease the oxygen vacancy migration barrier of nine La-based perovskites systems [477].

The year following the publication by Kushima et al., the first direct experimental measurement of the mechano-chemical effect of perovskite oxide thin films was presented by Cai et al. on epitaxial LSC films, with a 1.4% tensile and -1.5% compressive strain, fabricated using PLD on single crystal $SrTiO_3$ and $LaAlO_3$ substrates respectively [252]. An indication of oxygen vacancy concentration was obtained through XPS measurements as this technique is sensitive to the concentration of reduced Co present (which can be correlated with oxygen vacancy concentration as the reduction of Co is necessary to maintain charge neutrality in the formation of an oxygen vacancy). Also a transition from a semiconducting state to a metallic-like state with an enhanced electronic density of states at the LSC surface was observed in both films, with the tensile strained LSC/$SrTiO_3$ film having the greater enhancement. These all suggest an increase in oxygen vacancy concentration with tensile strain, in agreement with the DFT calculations of Kushima et al. It should be noted that Sr-dopants have been introduced that were not included in the

DFT calculations. There appears to be a mechano-chemical effect on the transport of Sr too while both films exhibited Sr enrichment at the surface, it was greater for the tensile strained LSC/$SrTiO_3$ film. A similar work was later performed by Jalila et al. on the LSM system, with like results [478], and also by Han et al. on LCO where it was also seen that the enhanced mobility of oxygen transport at the surface was anisotropic [253].

Using these foundational works, Donner et al. proposed a physical mechanism by which the strain field changes the energy landscape and gives rise to mechano-chemical coupling [254]. Similar to Cai et al., Donner et al. fabricated epitaxial LSC films on a single crystal $SrTiO_3$ substrate. Enhancement of ionic conductivity due to mechano-chemical coupling was presumed to be present. XRD was used to investigate the evolution of the strained LSC structure with oxygen partial pressure and temperature. A reversible structural transformation was observed resulting in the ordering of La and Sr atoms, and oxygen vacancies. It was suggested that this ordering mechanism may in part contribute to the mechano-chemical effect. While DFT $ab-initio$ calculations do not predict that a strain field would significantly affect intrinsic ordering, it has been shown to facilitate the formation of oxygen vacancies and improve oxygen vacancy mobility, which in turn would allow the chemical ordering required for this ordered phase.

More recently in 2013, using the same LSC/$SrTiO_3$ and LSC/$LaAlO_3$ films in compressive and tensile strain of Cai et al., Kubicek et al. used the ^{18}O isotope exchange depth profile method to quantify the effect of lattice strain [255]. While Cai et al. showed an increase in the oxygen vacancy concentration with strain, Kubicek et al. measured the resulting enhancement in oxygen conductivity, which was four times in k^* and 10 times in D^* values in the tensile strained LSC films compared with those in compression, between 280°C to 475°C. This was true for other similarly fabricated LSC films with a different Sr content. However, it should be noted that the LSC films were only ∼20 nm thick, and thus at the geometrical limit of the isotope exchange method to measure k^* and D^*; some error is expected and there is not complete confidence that the enhancement is real.

The mechano-chemical effect on the enhancement of oxygen ion conductivity in LCO thin films was also studied by Hong et al. for its magnetoelastic nature. The LCO film was deposited on a CGO buffer layer over YSZ, and a variation in lattice strain was obtained through a range of film thicknesses. The effect of spin state transition on the hybridization of the Co-O bonds was investigated using Raman spectroscopy and revealed that a tensile strain weakened the Co-O bond strength, as was predicted by Kushima et al. of the mechano-chemical effect in thin films [151]. The exchange coefficient, k^* and oxygen hypo-stoichoimetry (as an indication of oxygen vacancy concentration and thus oxygen diffusion rates) were measured using yet another technique: electrochemical impedance spectroscopy, EIS. An enhancement in k and (indirectly) D was indeed observed.

The papers reviewed here all validate the calculations of Kushima et al. There is reasonable confidence that the enhancement in ionic conductivity of tensile strained thin films, if really present, is the result of the mechano-chemical effect as proposed by Kushima et al. In this present work, the effect of strain on oxygen transport is also investigated, but in the

PCO system. A similar outcome as in LCO is expected. However, in all the preceding work, lattice strain was achieved through deposition of a thin film on a lattice mismatched substrate, whereas strain can also be obtained through chemical means as has been done in this work. Therefore, besides testing for the effect of strain on oxygen transport, it is of interest to investigate if a chemical strain effects the same results as a mechanical strain. Certainly from the structural analysis of Chapter 10, a change in the Co-O bond length with A-site deficiency was observed. It is thus proposed that the mechano-chemical effect may also arise from chemical strain.

11.2 Experimental Methods

The same non-stoichiometric PCO bars, as described in Chapter 10, and the same PCO thin films, as discussed in Chapter 9 were used for the transport measurements. EDX elemental quantification was performed as described in Chapter 5 and 10.

Electrical conductivity measurements, 4-point DC for the PCO bars and Van der Pauw for the PCO thin films, were both performed using the instrumental setup as described in Chapter 5. Electrical conductivity of the samples was measured in static air as the insulated sample slowly cooled from 700°C to room temperature. Sample dimensions of the PCO bars were measured along each edge and an average value used in calculating the resistivity of the PCO bars. Conductivity values were also corrected for sample porosity, based on Archimedes density measurements presented in Chapter 10. The conductivity values of the PCO thin films were calculated using film thickness values based on average film growth rates of 25.8 nm/1000 pulses, as measured using the Dektak 150 surface profilemeter. The correction factor was allocated based on the average R_a/R_b values (where R_a and R_b are the resistance values measured using two different sample configurations, see Fig 5.11 of Section 5.10) of each film. Maximum and minimum R_a/R_b values were also calculated for each film; the correction factor, f, ranged between $f = 1$ to $f = 0.9711$ [287].

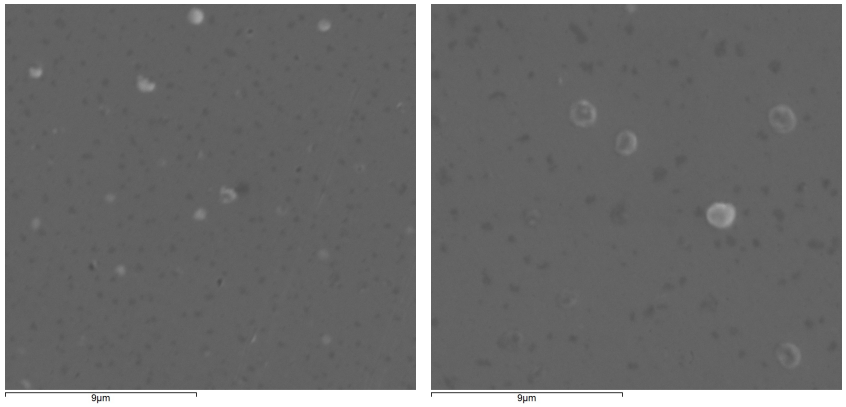
To test for the quality of the samples, measurements using a reverse current polarity should also be taken for each of the contact positions- eight different configurations in total using the van der Pauw method for thin films, and four using the linear DC setup for bar samples. Reversing current polarity should yield the same results. Additionally, for the van der Pauw method, given the symmetry of the sample, the reciprocity theorem requires that the sum of resistance measurements of both polarities for one contact configuration should be the same if the sample were rotated 180° (see Section 5.10). Deviations of greater than 5% may warrant investigations as to the sources of error. While, it was not possible to obtain conductivity measurements using all these configurations, there was also no reason to suspect poor quality films- AFM and SE images taken of the films in Chapter 9 suggest them to be flat with low surface roughness and no cracks.

IEDP was performed to obtain oxygen diffusivity values as described in Chapter 5. Ex-

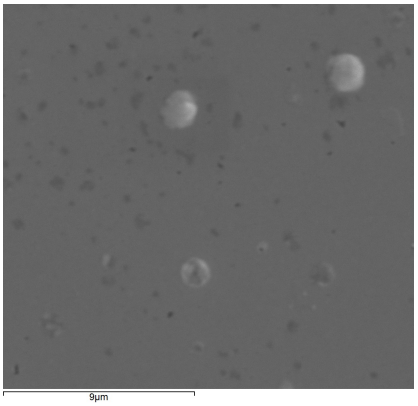
change annealing conditions are typically selected according to the diffusion length desired (within the measurement range of the SIMS depth profile). The diffusion length, x, that describes the decay of the concentration of diffusion species away from the exchange interface, can be related to the diffusion coefficient, D^*, and the exchange period, t, using the general rule: $x = \sqrt{\frac{t}{2D^*}}$. Thus an appropriate exchange time may be calculated. However, as there is little diffusivity data on the PCO system, the diffusivity of LCO was used instead as a starting point from which a range of exchange conditions were trialled. Subsequently, the exchanges of all PCO samples were performed at 400°C, for 15 min. 15 min was the minimum exchange time, given the actual time the exchange sample was at the exchange temperature and the time it took for the exchange sample to reach the exchange temperature, see Fig 11.3a.

An Au film was sputtered over the PCO film samples to prevent the ingress of ^{18}O via CGO/YSZ interfaces. The maximum peak to trough values of the thickest and roughest PCO films, deposited using 6000 pulses on Si, were not seen to exceed 50 nm. Consequently, Au film thicknesses between ∼60 nm and ∼120 nm were sputtered onto a Si substrate and annealed at 400°C as a trial. Au layers that are too thin and heated to too high a temperature have been known to blister, breaking the seal around the sample. Au films have been used before for this purpose under similar exchange conditions in literature. Burriel et al. successfully employed an 80 nm thick Au coat with a grain size of ∼1 nm to 2 nm to encapsulate a sample in the exchange experiment at 420°C [479]. SEM images of Au films 60nm, 80 nm, and 100 nm, are provided in Fig 11.1. The 60 nm thick Au coat was smooth and homogeneous with small Au blisters. However, as Au film thickness increased, so did the size of the blisters. Au films smaller than 60 nm were not investigated, as they were thought not to be sufficient thick to serve as a gas barrier during the exchange. Subsequently Au films 60 nm thick were used for the encapsulation of all PCO thin films.

The PCO films have been found to deposit at a rate of ∼25.8 nm/1000 pulses. PCO film thicknesses have been calculated according to this deposition rate for a given number of pulses, and correlated to the point at which the Cs^+ sputter beam reached the PCO/CGO interface in order to determine sputter rates of the PCO thin films. For the non-stoichoimetric PCO bar samples, it was necessary to measure the sputter crater depth using the Zygo NewView 200 interferometer. This was carried out by C. van den Bosch of Imperial College who ran 5 μm scans across the sample surface. The data was analyzed using the 'dapping' application in MetroPro64, version 9.1.1. Due to the curvature of the PCO bulk samples that resulted from grinding and polishing the soft PCO, a cylinder correction was made to the surface plane. Crater depths were measured by first defining the average height of the sample surface (the reference value where height = 0 nm) and crater floor (test value), by selecting areas of the sample that best represented this, based on the sample topography. An example is provided in Fig 11.2. This can also be found in Appendix A.5, for all non-stoichiometric PCO bar samples. Checks were made for a flat crater floor.



(a) With Au film, 60 nm (b) With Au film, 80 nm



(c) With Au film, 100 nm

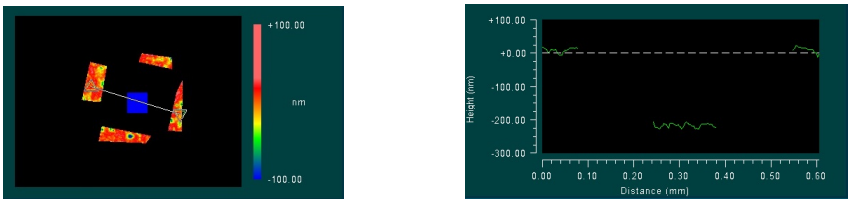
Figure 11.1: SE images of a trial (Si) surface encapsulated with Au films of various thicknesses that have been annealed at 400°C.

As covered in Chapter 5, the $^{18}O^-$ intensities were Poisson corrected using the ION-TOF SurfaceLab software. The fraction of $^{18}O^-$ during the exchange anneal was calculated from mass spectrometry measurements of the anneal atmosphere. Using Eqn. (2.5), the $^{18}O^-$ fraction corrected for the background isotope fraction and the isotope fraction during the exchange, $C'(x,t)$, was calculated and fitted to the Crank solution to Fick's 2nd law of diffusion, for diffusion in a semi-infinite medium using the TraceX Software developed by Dr. S. Cooper of Imperial College.

The effective exchange anneal time was determined from temperature profiles obtained during the exchange using the method of Killoran [10] and further developed by de Souza [11]. This required an oxide ion migration activation energy, E_A, value in PCO. As no published data on this could be found, the oxide migration energy of LCO was used instead. Molecular Dynamic studies by Cherry et al. predicted an activation energy of 0.61 eV for LCO [119], while measured activation energies ranged between 0.62 eV [480] and 0.78 eV [104]. Activation energies of 0.61 eV and 0.78 eV were both used to calculate the effective exchange times and temperatures of the samples, see Table 11.1, and show little sensitivity to activation energy values. At most, a 0.16 eV increase in the activation energy caused a 1 min decrease in exchange time.

	$E_A = 0.61$ eV [119]		$E_A = 0.78$ eV [104]	
Non-stoichiometric PCO, $Pr_{1-x}CoO_{3-\delta}$ (x)	Time (h)	Temperature (°C)	Time (h)	Temperature (°C)
$x = 0.000$	0.263	389	0.251	389
$x = 0.025$	0.248	388	0.237	388
$x = 0.050$	0.248	388	0.237	388
$x = 0.075$	0.263	389	0.251	389
$x = 0.100$	0.263	389	0.251	389
PCO film, sample set 2 CGO buffer (No. pulses)				
500	0.266	389	0.255	389
1500	0.266	389	0.255	389
2000	0.241	388	0.238	388
2500	0.238	389	0.227	389
PCO film, sample set 3 PCO film (No. pulses)				
1000	0.238	389	0.227	389
2000	0.288	389	0.276	389
3000	0.288	389	0.276	389
4000	0.288	389	0.276	389
5000	0.288	389	0.276	389
6000	0.241	388	0.238	388

Table 11.1: The effective exchange times and temperatures, calculated using two different activations energies: E_A of 0.61 eV and 0.78 eV, for all PCO samples (films and non-stoichiometric bar samples) using the method as proposed by Killoran [10, 11].



(a) Filled plot (b) Profile plot

Figure 11.2: Example ZYGO crater depth measurement of non-stoichiometric PCO ($x = 0.025$). In (a), the sample surface reference has been selected, and also the crater area. The profile taken across the plot is shown in (b).

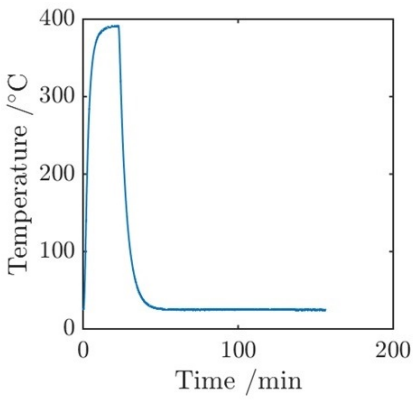
The sensitivity of exchange conditions with activation energy is depicted in Fig 11.3. Thus it can be seen that only within a small region of extremely low activation energies would the effective exchange conditions be sensitive to the activation energy. It has been found that the activation energy of oxide ion migration decreases as A-site cation radius decreases (see Chapter 2) [119]. Pr^{3+} has one of the smallest ionic radii of the R^{3+} series, smaller than La^{3+} [9], and as such should have a lower oxide ion migration energy. Therefore, a check was performed to calculate the effective exchange conditions using half of the lowest activation energy of LCO: $E_A = 0.3$ eV, to see if an activation energy this low would be in the sensitive region. This only resulted in an increase in the effective exchange time of 3 min and thus the use of the LCO activation energy value was deemed justifiable. Additionally, all samples were exchanged under nominally identical conditions: the furnace set to 400°C and an exchange time of 15 min that begun upon lift-down of the furnace, and ended upon lift-up of the furnace. All diffusion profiles in this chapter have been fitted using effective exchange conditions based on an oxide ion migration energy of 0.61 eV.

11.3 Results and Discussion

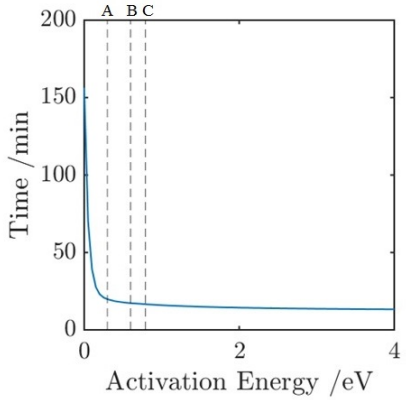
11.3.1 Time-of-Flight SIMS Depth Profiles

ToF SIMS depth profiles were obtained for all PCO samples. These have been used here to examine the composition of the samples. The ^{18}O diffusion profiles are discussed in the next section. Examples of the normalized profile of both thin film and bulk samples are presented in Fig 11.4 for the discussion of the profile features. Full profiles obtained from each sample may be found in Appendix A.6.

For the bulk PCO samples, except at the sample surface, the bulk sample composition appeared constant. The PrO^- signal was significantly lower than CoO^- due to its low sputter yield. At a depth up to ~25 nm below the sample surface, a peak then gradual increase in CoO^- intensity, and a slight depletion in PrO^- intensity was measured. This was also found of the strained thin film PCO samples. Additionally, the CoO^- signal



(a) Temperature profile of PCO during exchange



(b) Effective exchange time as a function of activation energy

Position	E_A (eV)	Time (h)	Temperature (°C)
A	0.30	0.333	389
B	0.61	0.288	389
C	0.78	0.276	389

(c) Calculated effective exchange times and temperatures for given activation energies.

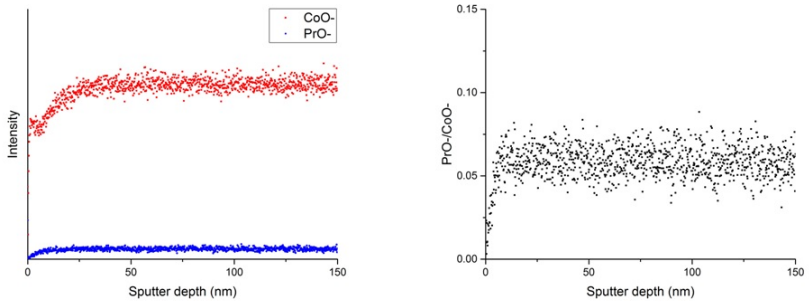
Figure 11.3: Example of the sensitivity of the calculated effective exchange time and temperature to the activation energy. Even if the activation energy of PCO were half that of LCO ($E_A = 0.61$ eV), the exchange time only decreased by ∼2.5 min, given the temperature profile of the PCO sample measured in (a).

was found to rise gradually with sputter depth before peaking again at the PCO/CGO interface.

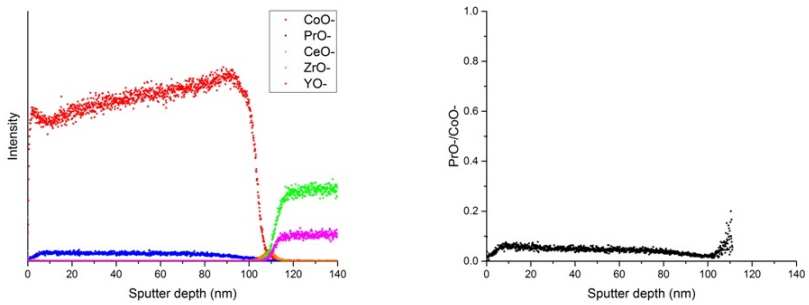
The shape of the CoO^- depth profile was consistent between all the SIMS depth profiles. Those three features- the peak in sputter yield at the surface and interface of the PCO film, and the rising sputter yield with increasing depth- may be features of the SIMS technique arising from the dynamic nature of ion sputtering away and damaging the sample surface. Sputter rates are sensitive to the lattice matrix. Lattice disorder at the PCO film interfaces may affect sputter rates resulting in higher yields and subsequently a peak in the CoO^- species detected. Similarly the different lattice strain in the PCO films may also affect sputter rates. Further work is required to confirm if these features are real or the product of the SIMS technique.

However, that these features are found only of the CoO^- species, and the other detected species (PrO^- and CeO^-) do not see these peaks in intensity and maintain a constant intensity with sputter depth, suggests that these features are real. Alternatively, it could also be that the signal of the other species are too low to see these features. Thus, while care should be taken not to read too much in to this, neither should these results be completely disregarded.

Interpreting the SIMS depth profile of the PCO thin films literally, it would seem that the PCO film is not of a homogeneous composition. From Fig 11.4, it could be argued that



(a) Non-stoichiometric PCO ($x = 0.025$)



(b) Depth profile into a PCO/CGO/YSZ film, where the CGO and PCO films were deposited using 1000 and 4000 pulses, respectively.

Figure 11.4: Example depth profile into (a) a non-stochiometric PCO bar sample and (b) a PCO film. The Pr:Co ratio was also calculated as a function of sputter depth to examine for variations in Pr^{O}:CoO^{-} cation ratio across the samples. Intensities of the measured species have been normalized. The GdO^{-} count was low and not included in the depth profile into the PCO film.

the PCO film is Pr deficient at its surface but is Pr excess at the PCO/CGO interface following a ∼20 nm region where Pr content is especially depressed. There may be Co oxide precipitates at the PCO film surface, but Pr oxides or RP Pr cobaltite oxide phases at the PCO/CGO interface, which may be the source of the Pr deficiency in its surrounding regions. Additionally, as the PCO film relaxes away from the PCO/CGO interface, its Pr content increases.

To further investigate this, SE images were taken of the sample surface of bulk PCO113 of a nominal stoichiometry where $x = 0$ (see Chapter 10 for sample details) immediately following ^{18}O exchange (before the SIMS profiling), see Fig 11.5 and Fig 11.6. In the pre-exchange images (see Fig 10.2), all sample surfaces were flat and clean, with no evidence of precipitates. However, it can now clearly be seen that the exchange process introduced surface precipitates up to ∼5 μm across that should be detected given the SIMS 100 μm by 100 μm analysis area within a 300 μm by 300 μm raster area. Composition analysis was performed using EDX over the area depicted in Fig 11.5. The element maps obtained suggested a homogeneous composition across the PCO film surface, likely due to the low magnification used. Quantification of the elements yielded a Pr:Co ratio of 1.026 ±0.017:1

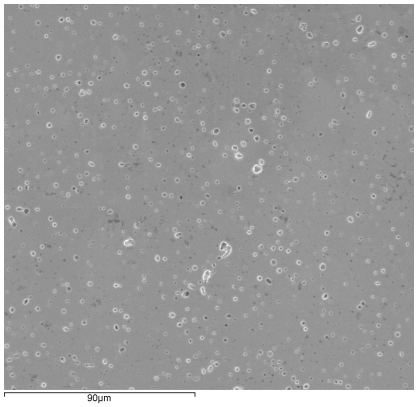
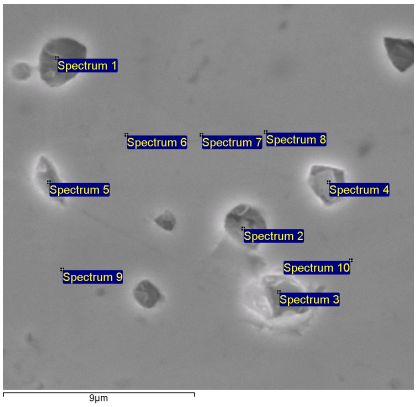


Figure 11.5: SE image of the surface of non-stoichiometric PCO ($x = 0.000$) bar sample post-exchange. Precipitates can clearly be observed where previously the sample surface was clean.

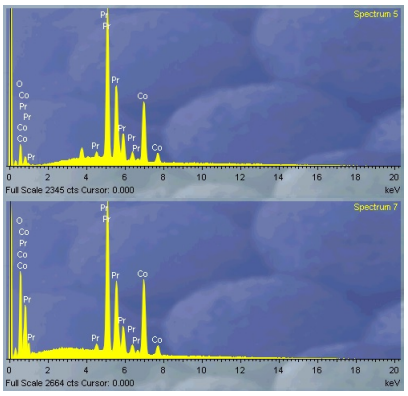
which is within error of the Pr:Co ratio of 1.009±0.006:1, earlier measured under nominally identical conditions in Chapter 10.

To identify the composition of the precipitates, point EDX measurements were also taken at a greater magnification, see Fig 11.6, where the first five measurements were of the precipitates, and the following five of the sample surface. Example EDX spectra are provided from both precipitate and bulk which shows that the intensity of the Pr spectra of the precipitate was much higher than the surrounding "bulk" material. The composition at each EDX measurement point is provided in Table 11.6c. While the surface composition was comparable to pre-exchange EDX measurements, the precipitates were clearly Pr rich, and were likely to be some form of Pr oxide or even PCO214. However, it was not possible to identify the composition of the precipitates, as there is concern that the penetration depth of the measurement may have exceeded the dimensions of the precipitate, and thus the composition measured includes the PCO sample. Thus it appears that the ^{18}O conditions have not been conducive to the stability of PCO113 and subsequently Pr oxides have precipitated on the PCO film surfaces. Other compositional analysis, such as cross-sectional TEM would be required to see if this is also the case at the PCO/CGO interface. Similarly, SE and EDX measurements are required of the other Pr-deficit bulk PCO samples, and the PCO thin film samples to ascertain if these precipitates are present on the surface of all the samples. There is a possibility that it is only present in this nominally stoichiometric bulk PCO sample examined, as this sample may actually have been Pr-excess.

There were no indications of these Pr-rich precipitates in the SIMS depth profiles. This may be because the sputter yields over the entire analysis area were summed to obtain a profile. Any points of high Pr content would be averaged out over the entire area, preventing detection of these precipitates. The presence of these precipitates was a concern regarding the accuracy of the SIMS depth profile: the depth profiles were on the order of nm, whereas the precipitates were on the um scale across the sample surface. However, Zygo measurements of the sputtered crater indicated a flat sample surface and crater base



(a) SE image



(b) EDX spectra

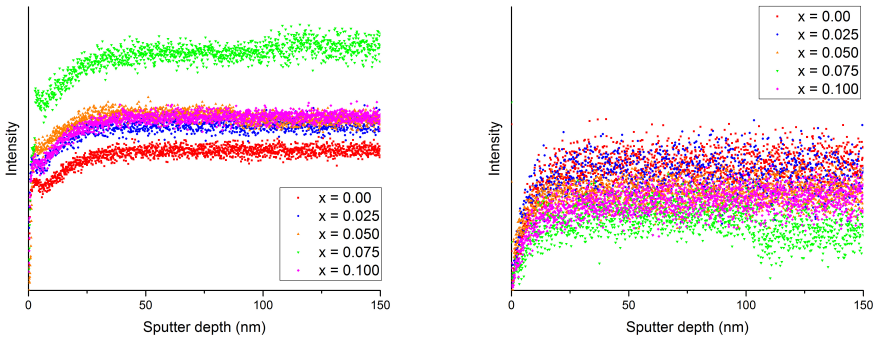
Spectrum	Pr:Co (atomic%)	error	Average Pr:Co atomic%)
1	1.33:1	0.04	
2	1.22:1	0.02	
3	1.39:1	0.03	1.27±0.03:1
4	1.21:1	0.03	
5	1.22:1	0.02	
6	1.02:1	0.02	
7	1.00:1	0.02	
8	1.02:1	0.02	1.03±0.02:1
9	1.06:1	0.02	
10	1.05:1	0.02	

(c) Measured Pr:Co atomic% from each EDX spectrum.

Figure 11.6: EDX measurements of the surface of non-stoichiometric PCO ($x = 0.00$) post-exchange. EDX spectra were obtained of the precipitates and PCO surface. The precipitates had a higher Pr:Co ratio, suggesting the formation of a Pr oxide.

on the nm order, restoring confidence in the SIMS profiles.

To further investigate sample composition, PrO^-:CoO^- ratios were calculated from the SIMS depth profiles of both the nonstoichiometric bulk and thin film PCO samples (from a depth of 50 nm past the sample surface, until the end of the depth profile). For the non-stoichiometric bulk PCO samples, it showed a clear correlation with PCO composition, see Fig 11.8. This is in support of EDX measurements and the refined lattice parameters of non-stoichiometric PCO, see Chapter 10. However, two trend lines may be drawn and it is arguable that the PCO sample where $x = 0.100$ had a higher Pr to Co content, or the PCO sample where $x = 0.075$ had a lower Pr to Co content, than would be expected given the trendline. However, the variation in Pr-deficiency between PCO samples was small, not exceeding $x = 0.100$. Assuming the sample where $x = 0.000$ had Pr-excess (PrO^-:CoO^- ~0.075), and the sample where $x = 0.025$ was nominally stoichiometric (PrO^-:CoO^- ~0.059), based on EDX measurements, the decrease in PrO^-:CoO^- ratio should not exceed 0.006 for the most Pr-deficient sample. So in consideration of the gradient of PrO^-:CoO^- ratio with Pr deficiency and also the anomalously high CoO^- profile intensity when $x = 0.075$, it does suggest that it was the PrO^-:CoO^- ratio, for the PCO sample



(a) CoO^- (b) PrO^-

Figure 11.7: Normalized intensities of CoO^- and PrO^- as a function of sputter depth of the non-stoichiometric PCO bar samples.

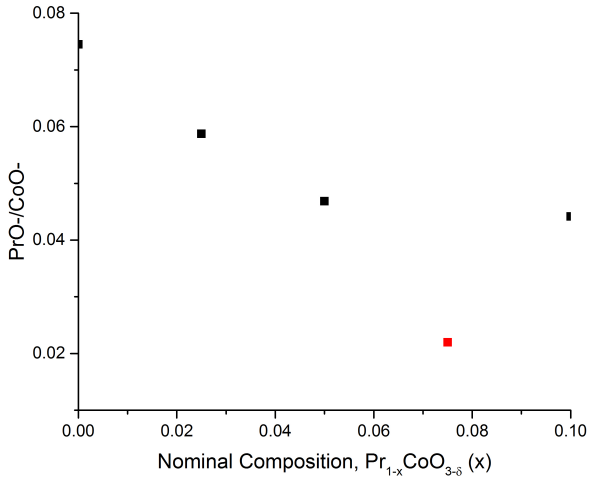
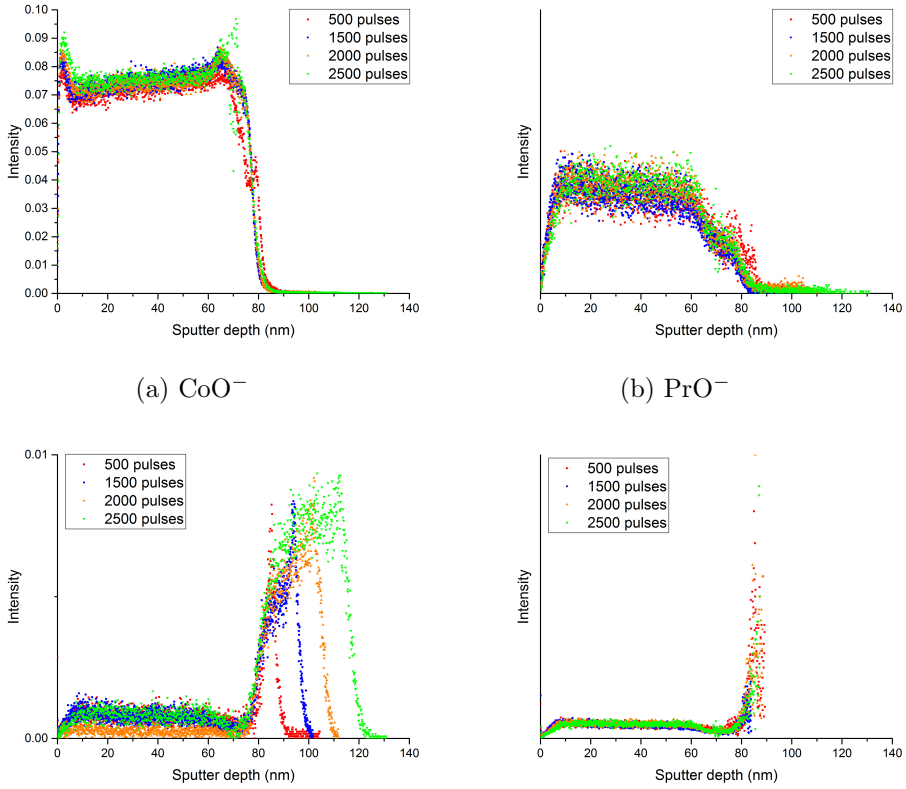


Figure 11.8: Average PrO^-:CoO^- ratios obtained across the depth of the non-stoichiometric PCO samples. The data point in red is thought to be anomalous.

where $x = 0.075$, that was disproportionately low (and not the PrO^-:CoO^- ratio when $x = 0.100$ being disproportionately large). It should also be noted that the PrO^-:CoO^- ratios from the SIMS depth profiles suggest a larger variation in PCO composition than expected from previous compositional analysis. The cause for this discrepancy was unclear.

A comparison of the depth profiles between PrO^-, CoO^- and CeO^- species of sample set 2, where CGO buffer layer thickness was varied (see Table 9.1) is provided in Fig 11.9. CeO^- profiles have also been included and the increase in CGO buffer layer thickness can clearly be seen. CoO^- and PrO^- species all have similar depth profiles features between the samples. The compositional variation at both PCO interfaces was much more pronounced in the PCO thin films than in the bulk. Between the differently strained PCO films, the compositional variation at the PCO surface remained roughly constant between films. However, as CGO film thickness increased, increasing the compressive out-



(a) CoO^- (b) PrO^-

(c) CeO^- (d) PrO^-:CoO^-

Figure 11.9: Normalized intensities of (a) CoO^-, (b) PrO^- and (c) CoO^-, also (d) PrO^-:CoO^- ratios, as a function of sputter depth of the PCO films of sample set 2 (where the CGO buffer layer thickness was varied).

of-plane strain in the PCO film, the CoO^- peak at the PCO/CGO interface can clearly be seen to increase. If this trend is real, compositional variations through the film are affected by the lattice strain distribution across the film.

In order to investigate the bulk composition of the PCO thin film, the average PrO^-:CoO^- ratio was calculated from a depth of 10 nm to 60 nm from the sample surface where PrO^- and CoO^- intensities are roughly constant, see Fig 11.10. Thus the regions where CoO^- intensities are enhanced and PrO^- intensities reduced as a result of the surface/interface precipitations were excluded. There may be a correlation between film composition and CGO buffer layer thickness, where increasing the CGO buffer layer thickness, increased the overall Pr content of the film.

This slight variation in film composition, if real, is thought not to be due to the formation of Pr-rich precipitates at the surface as seen on the SE image. Firstly, the regions in which compositions were affected by the precipitates were excluded. Secondly, even if not, it would predict an opposite effect to that observed: increasing film-substrate mismatch and increasing lattice strain would increase PrO precipitation at the PCO/CGO interface that, if it did affect the bulk composition of the film, would decrease the bulk PrO^-:CoO^-

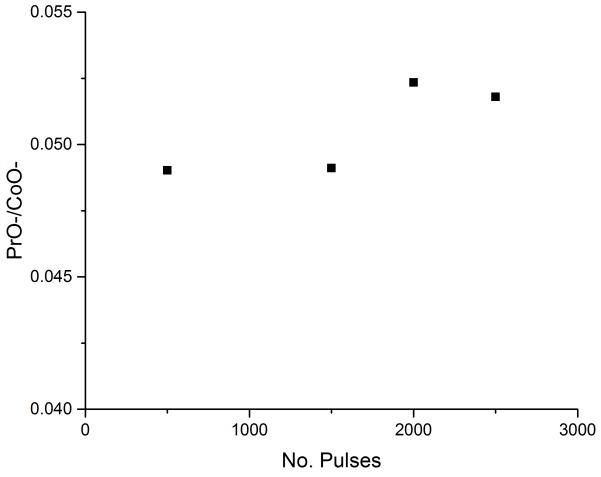
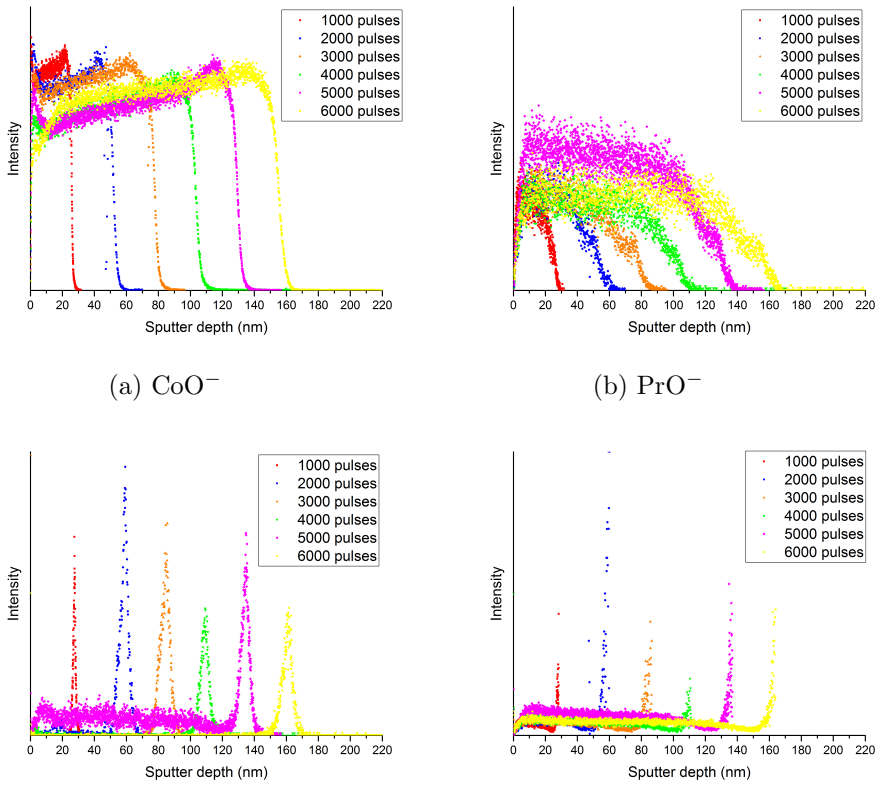


Figure 11.10: Average PrO^{-}:CoO^{-} ratios obtained across the depth of the PCO films of sample set 2, as a function of the number of laser pulses used in the deposition of the CGO buffer layer. There may be a trend of increasing PrO^{-}:CoO^{-} ratio with increasing CGO buffer layer thickness and subsequently with increasing PCO lattice strain.

ratio. The variation in film composition should also not arise from the film fabrication process as PLD involves stoichiometric transfer of the component elements, though Co volatisation has been known to occur at low laser fluences. It was not possible to ascertain the source of this compositional variation between the PCO thin films.

A comparison of these PrO^{-}:CoO^{-} ratios to that obtained from the non-stoichiometric bulk PCO samples suggests that the PCO thin films were slightly Pr deficient (if stoichiometric PCO is when the PrO^{-}:CoO^{-} ratio is ~ 0.059). If the PCO thin films are Pr-deficient, and the application of an out-of-plane compressive strain was the reason for the increased bulk PrO^{-}:CoO^{-} ratio, this implies that the out-of-plane compressive strain must have resulted in loss of Pr vacancies (the formation of Co interstitials being unlikely). The loss of the -ve charged Pr vacancies would have to be charge compensated, either through the creation of holes, the change in oxidation state of Pr^{3+} to Pr^{4+}, or the creation of oxygen vacancies. Any changes in hole concentration should be reflected in electrical conductivity measurements. If it is the latter, irrespective of any mechano-chemical coupling effects, the increase in oxygen vacancies due to the compressive out-of-plane strain would increase oxide ion conductivity.

Considering now mechano-chemical coupling, the out-of-plane compressive strain should also result in retarded oxygen transport in the direction of the depth profile. There are therefore two possible outcomes to an decrease in CGO buffer layer thickness observed in this work: an increase in Pr vacancy content in the bulk of the film that would inhibit oxygen transport, and a mechano-chemical coupling effect that would also inhibit out-of-plane oxygen transport. Though, as earlier mentioned, no explanation may yet be provided for the cause of the increase in PrO^{-}:CoO^{-} ratio, or if it is even related to the



(a) CoO^- (b) PrO^-

(c) CeO^- (d) PrO^-:CoO^-

Figure 11.11: Normalized intensities of (a) CoO^-, (b) PrO^- and (c) CoO^-, also (d) PrO^-:CoO^- ratios, as a function of sputter depth of the PCO films of sample set 3 (where the PCO film thickness was varied).

strain state of the PCO thin film.

A comparison of the depth profiles between PrO^-, CoO^- and CeO^- species of sample set 3, where PCO film thickness was varied (see Table 9.1) is provided in Fig 11.11. As with the thin films of sample set 2, there was a peak in CoO^- intensity within the first 10 nm of the film surface, a rising CeO^- intensity at increasing depths, and finally another peak in CeO^- prior to the PCO/CGO interface. The thicker the PCO film, the lower the intensity of this first peak and the lower the overall intensity of the CoO^- species.

There appeared to be no clear correlation between the thickness of the PCO film and the intensity of the CeO^- peak at the PCO/CGO interface, whereas in sample set 2, increasing the CGO buffer layer thickness and increasing the lattice mimatch between PCO and CGO increased the intensity of the CeO^- peak. This enforces the earlier suggestion that the compositional variation through the PCO film was the result of the lattice strain within the film. These PCO films of sample set 3 all experience the same lattice mismatch with the CGO buffer layer. Consequently, the CeO^- peak intensities at the PCO/CGO interface are all the same. As the PCO films relax, the CeO^- intensities all decline at a similar rate away from the PCO/CGO interface.

Sample set 2		Sample set 3	
No. pulses for CGO deposition	Out-of-plane lattice strain (%)	No. pulses for PCO deposition	Out-of-plane lattice strain (%)
500	-0.748	2000	-0.612
1500	-0.751	3000	-0.486
2000	-0.833	4000	-0.540
2500	-0.989	5000	-0.378
		6000	-0.393

Table 11.2: Measured out-of-plane lattice strain in the PCO films of sample set 2 and 3.

The PCO films of sample set 2 appeared to have a lower CoO^- peak at the PCO/CGO interface, relative to CoO^- intensities through the film, than seen for the PCO films in sample set 3. This suggests that the compressive strain experienced in these PCO films of varying thickness(sample set 3) is of a lower degree than the PCO films of sample set 2. A comparison of the out-of-plane strains in the two sample sets as measured from the PCO(002) reflection, see Table 11.2, supports this. The thinnest and most strained PCO113 film of sample set 3 was not as strained as the thinnest measured PCO film deposited on the thinnest CGO buffer layer of sample set 2. This further affirms that the intensities of the peaks in CoO^- at the PCO film interfaces were affected by lattice strain. Additionally, unlike in sample set 2, the CoO^- intensities at the PCO/CGO interface were similar across the films.

From Fig 11.11a, it does appear that the CoO^- intensities of the PCO films deposited using 4000 and 5000 pulses were lower than the trend would suggest. Also, the PrO^- intensity of the PCO film deposited using 5000 pulses seemed disproportionately large. From the PrO^-:CoO^- ratios, this film was inconsistent with other films, and was considered anomalous. It should also be noted that the CeO^- profile is much narrower in the PCO film deposited using 1000 pulses than the other films. Either the CGO buffer layer in this sample was exceptionally thin, or this film was thicker than would be predicted from the average deposition rate by which all thin film profiles have been scaled.

As was performed for sample set 2, the bulk film composition of sample set 3 was investigated. The average PrO^-:CoO^- ratio was calculated for this sample set from a depth of 10 nm from the sample surface to just before the second CoO^- peak, in Fig 11.12. A clearer trend between film composition and film thickness was found where increasing PCO film thickness increased the PrO^-:CoO^- ratio. This was contrary to expectations as the thicker PCO films would have experienced a lower out-of-plane lattice compression, which was correlated to a lower PrO^-:CoO^- ratio, based on that observed on sample set 2. Though there is a correlation, it is unlikely that the variation in film composition between the two sample sets is due to the film lattice strain. The cause for this compositional variation, if it does exist, is uncertain.

Thus from the compositional analysis of the thin films based on ToF-SIMS measurements, two different outcomes to the thin film core composition, if real, have been observed upon

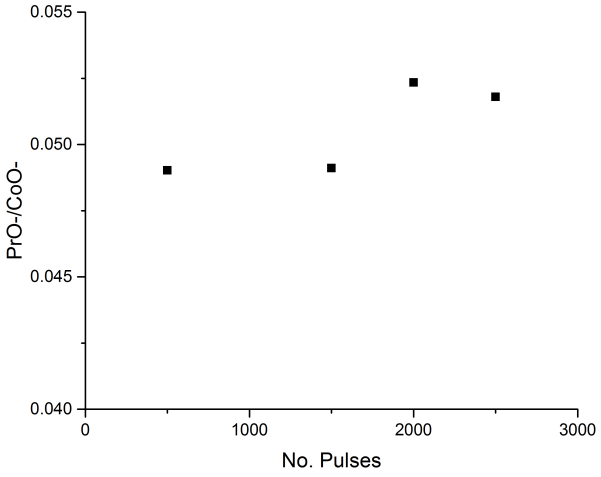


Figure 11.12: Average PrO^-:CoO^- ratios obtained across the depth of the PCO films of sample set 3, as a function of the number of laser pulses used in the deposition of the CGO buffer layer. There may be a trend of increasing PrO^-:CoO^- ratio withith increasing PCO film thickness and subsequently with decreasing PCO lattice strain (contrary to what was found of the PCO films of sample set 2).

the variation of PCO and CGO buffer layer, which appeared to be unrelated to the introduction of a lattice strain. Where PCO film thickness was maintained, the increase in CGO film thickness (and increase in compressive out-of-plane strain) resulted in an increase in the PrO^-:CoO^- ratio. On the other hand, where the CGO buffer layer thickness remained constant, the increase in PCO film thickness (and decrease in compressive out-of-plane strain) also resulted in an increase in the PrO^-:CoO^- ratio. The explanation for this phenomenon requires further investigation. The defect concentrations of the thin film samples are also expected to vary. Thus, any changes in oxygen transport cannot derive solely from the mechano-chemical effect, but must also arise from the changes in defect concentrations.

11.3.2 Oxygen Tracer Transport Measurements

It should be noted that previous EDX measurements of Chapter 10 suggested that the nominally stoichiometric sample was actually Pr-excess and had an enlarged cell parameter, and that the PCO sample where $x = 0.025$ was closer to stoichiometry. Nevertheless, ^{18}O isotope exchange measurements were performed on all PCO bulk samples of varying cation stoichiometry at an effective exchange temperature of ~388°C, the profiles of which are plotted in Fig 11.13.

All of the profiles were observed to be similar in shape, with the exception of the PCO sample with excess Pr ($x = 0.00$), which has a lower surface ^{18}O intensity than the other non-stoichoimetric PCO samples. This sample appears to have a lower surface exchange

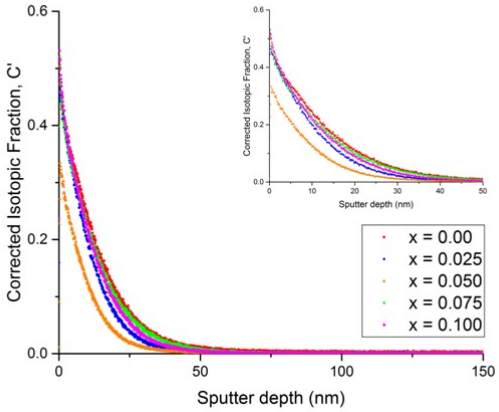
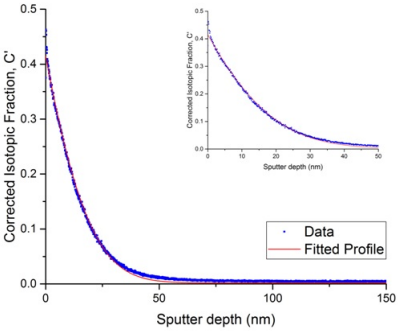


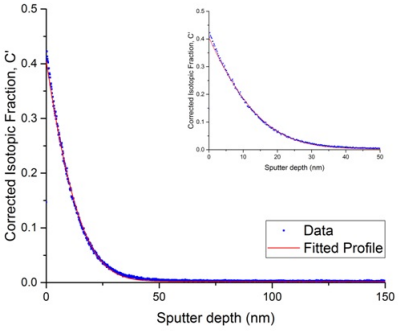
Figure 11.13: Corrected ^{18}O tracer profile, obtained at an effective exchange time and temperature of ∼15 min and ∼ 389°C, for the non-stoichiometric PCO bar samples. Inset, the diffusion profile at within the first 50 nm of the sample surface is expanded.

coefficient, relative to its diffusion coefficient, than the other non-stoichiometric samples. All things being constant, this must arise from its different defect chemistry. An excess of Pr would likely result in the formation of Co vacancies rather than Pr interstitials, which would also have to be charge compensated and oxygen vacancies created as with the case for Pr vacancies. Thus the difference in oxygen transport of the Pr-excess sample must be related to the creation of Co vacancies rather than the concentration of oxygen vacancies.

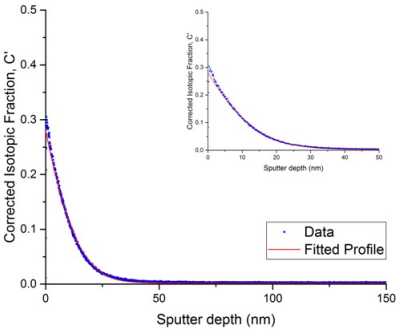
A good fit was obtained for all of the normalized tracer fraction profiles of all samples using Cranks solution for diffusion in a semi-infinite medium, as described in Chapter 2, see Fig 11.24. However, unlike the LSC films of Kubicek et al. where the normalized O fraction at the surface was lower than fitted in the first 1 to 1.5 nm of the film surface [255], the opposite is found here where the fits at the surface of the samples (sputter depth = 0), were consistently lower than the measured ^{18}O intensity for all the samples. As Pr oxide precipitates have been found on the PCO surface following the exchange procedure (despite the samples being Pr-deficient for the most part), it is possible that these precipitates were formed during the exchange and hence were ^{18}O rich and thus the source of the increased ^{18}O fraction at the sample surface. If this was the case, the samples where $x = 0.000$ and $x = 0.075$ should both have the greatest number of Pr oxide precipitates on their surface. This would not be unexpected of the PCO sample where $x = 0.000$ but is unclear why, if all things were constant, a large amount of precipitates would be found for the PCO sample where $x = 0.075$, which had the lowest PrO^-:CoO^- ratio of all the samples. Alternatively, there is a possibility that a fast oxygen transport path was present. These profiles are similar to that observed of Zhang et al. [57], which had a slight tailing function and subsequently had a higher ^{18}O concentration at the sample near-surface, than predicted by Crank's solution. More on this tailing function will be discussed later in this section when the ^{18}O profiles of PCO thin films (of sample set 2 and 3) are considered.



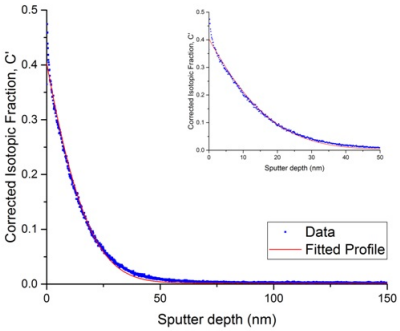
(a) $x = 0.000$



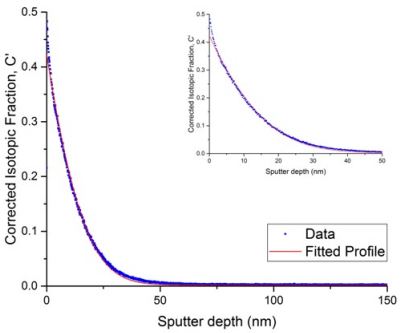
(b) $x = 0.025$



(c) $x = 0.050$



(d) $x = 0.075$



(e) $x = 0.100$

Figure 11.14: ^{18}O diffusion profiles in the non-stoichiometric PCO bar samples, $Pr_{1-x}CoO_{3-\delta}$, fitted to Crank's solution for diffusion in a semi-infinite medium. Inset, the near-surface profile: 0 to 50 nm. R^2 values of the fit vary between 0.9704 and 0.9966.

D^* and k^* values of PCO and Pr-deficient PCO have been calculated to be around 10^{-16} cm^2/s and 10^{-9} cm/s respectively, see Table 11.3. These are comparable to that of the traditional cathode material: Sr-doped LCO, in which D^* and k^* values have been measured to be $\sim 10^{-15}$ cm^2/s and 10^{-10} cm/s at $\sim 400°C$ [85], see Fig 11.15. Although its tracer diffusivity is up to 5 orders of magnitude lower than newer IT-SOFC materials such as $La_2NiO_{4\pm\delta}$, the use of PCO as a commercial IT-SOFC cathode does have its potential especially as improvements in oxide ion conductivity may be acquired through the use of

$Pr_{1-x}CoO_{3-\delta}$ (x)	Diffusion coefficient, D^* (cm^2/s)	Exchange coefficient, k^* (cm/s)	R^2
0.000	2.26×10^{-16}	10.1×10^{-10}	0.9966
0.025	1.55×10^{-16}	8.26×10^{-10}	0.9883
0.050	1.36×10^{-16}	4.48×10^{-10}	0.9704
0.075	2.06×10^{-16}	9.20×10^{-10}	0.9959
0.100	1.67×10^{-16}	8.97×10^{-10}	0.9930

Table 11.3: Table of the diffusion and exchange coefficients, D^* and k^*, obtained from the fits of the ^{18}O diffusion profiles in non-stoichiometric PCO at an effective exchange temperature of ~389°C, and the R^2 value of each fit.

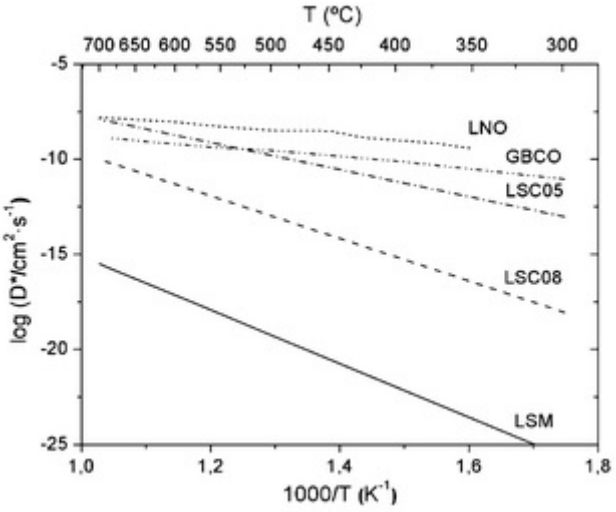
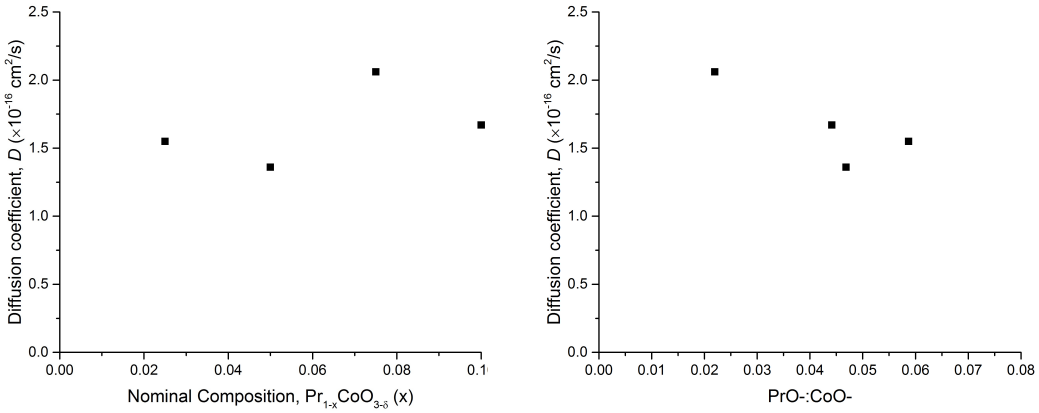


Figure 11.15: Arrhenius plot of measured oxygen tracer diffusivity for different oxides cathodes: $La_{0.8}Sr_{0.2}MnO_{3-\delta}$ [53], $La_{0.5}Sr_{0.5}CoO_{3-\delta}$ [53], $La_{0.8}Sr_{0.2}CoO_{3-\delta}$ [53], $GaBaCo_2O_{5+\delta}$ [54] and $La_2NiO_{4+\delta}$ [55], taken from [56].

dopants such as Sr, or by tailoring the strain state of PCO thin films. To date, no tracer diffusion or surface exchange coefficients have been published for PCO or doped PCO, although these results do provide the impetus for investigating Sr-doped PCO.

A plot of D^* and k^* against nominal PCO stoichiometry and the measured average PrO^-:CoO^- ratio is presented in Fig 11.16 and 11.17. The sample where $x = 0.000$ was omitted as it was determined to be Pr-excess and therefore has a different defect chemistry. Although the trend was not as apparent when compared against PCO nominal stoichiometry, one can be seen when D^* was compared against PrO^-:CoO^- ratio, which is the truer representation of trends in composition between PCO samples. A decrease in Pr content relative to Co resulted in an increase in D^*. This is in agreement with the defect chemistry earlier proposed in Chapter 10. A-site deficiency would result in the creation of Pr vacancies and also oxygen vacancies. The increase in oxygen vacancy contribution, and thus the increase in available lattice sites for oxide ions to migrate to, would increase oxygen transport. It has not been possible to identify a trend in the oxygen

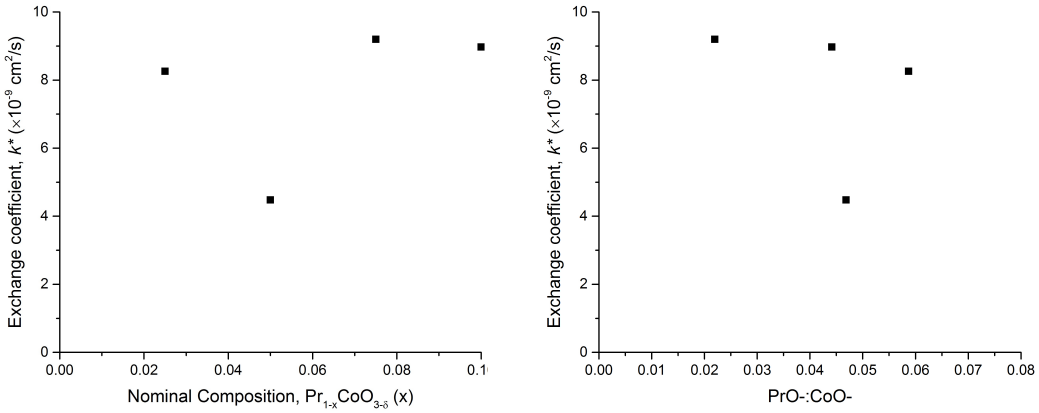


(a) D^* as a function of A-site deficiency, x (b) D^* as a function of PrO^-:CoO^- ratio

Figure 11.16: Diffusion coeffitients, D^*, obtained from ^{18}O diffusion profiles in the non-stoichiometric PCO bar samples at an effective exchange temperature of ∼389°C as a function a A-site deficiency, x, and PrO^-:CoO^- ratio. There appeared to be a trend between D^* and PrO^-:CoO^- ratio, which was not present with x.

surface exchange with PCO sample composition, even in consideration of varying degrees of Pr precipitation on the sample surface. Based on the trend observed, a decrease in the PrO^-:CoO^- ratio of 0.01 would result in an increase in oxygen diffusion coefficient by 0.16×10^{-16} cm^2/s. As was mentioned in the earlier section, the range of metal cation stoichiometries, as measured using the SIMS depth profile, was of a far larger range than based on EDX measurements and the synthesis of the PCO powders. While it has not been possible to obtain absolute values and to quantify the change in oxygen vacancy contribution to the change in oxygen diffusion the trend between the two can nevertheless be seen. No clear trends could be seen of k* as a function of either A-site deficiency, or PrO^-:CoO^- ratio (or lattice strain or cell volume).

The mechano-chemical effect found in thin films may also contribute to the changes in oxygen diffusion and surface exchange coefficient observed in these bulk PCO samples. In Chapter 10, decreasing Pr content resulted in an expansion of the lattice, by up to ∼ 0.08% in the b-cell parameter, attributed to the creation of Pr vacancies. Such an expansion of the lattice would result in the stretching of the Co-O bonds. As the mechano-chemical effect was attributed to the material response upon stretching of the Co-O bonds in DFT studies [151], there is reason to expect a mechano-chemical effect in these chemically strained films. The lengthening of the Co-O bonds would decrease the formation energy of oxygen at the surface and the oxygen adsorption energy for oxygen exchange at the surface, as well as reducing the migration energy barrier for oxygen diffusion. While an increase in oxygen diffusion coefficient has been measured, it was not possible to establish if this was purely due to the change in PCO defect concentration of if the mechano-chemical effect was present in chemically strained bulk PCO. To do that comparison needs to be made against the oxygen transport of similarly strained PCO thin films of sample set 3,



(a) k^* as a function of A-site deficiency, x (b) k^* as a function of PrO^-:CoO^- ratio

Figure 11.17: Exchange coefficient, k^*, obtained from ^{18}O diffusion profiles in the non-stoichiometric PCO bar samples as a function a A-site deficiency, x, and PrO^-:CoO^- ratio. No trends were apparent

which were of the same nominal chemical composition and PrO^-:CoO^- ratio and thus for which any transport must arise from the mechano-chemical effect.

However, it should be noted that the variations in the measured D^* values are not large. Error bars have not been included based on the goodness of fit of the diffusion profile to Cranks solution as they would have been misleading: R^2 values ranged between 0.970 and 0.997 suggesting only a small error. However, the experimental error arising from the anneal and exchange conditions, the history of the sample, sample preparation and handling would far exceed this error. As a rule of thumb, experimental error for such isotope exchange experiments is $\pm 20\%$. Nevertheless, even in consideration of this, there is still grounds that the trend in D^* with PrO^-:CoO^- ratio in Fig 11.16b is real.

The ^{18}O fraction against depth for PCO thin films of sample set 2, where CGO buffer layer thickness was varied thus varying the lattice mismatch between PCO and CGO, is presented in Fig 11.18. In the following paragraphs, the shape of the profile and trends will be discussed, prior to fitting it to Crank's solution.

The shape of the tracer profiles obtained for the PCO films were unlike that of a typical Crank profile: they had an extremely steep drop in tracer fraction past the sample surface, followed by an extremely long tail that does not reach the ^{18}O isotope background abundance fraction of 0.2%. This diffusion tail began at around 4 nm from the film surface for all samples. Such a profile shape (though not to this extent) would normally suggest a material with a high oxygen surface exchange, but low diffusion coefficient. The presence of this tail in the diffusion profile also suggests the presence of a fast diffusion, such as along grain boundaries [57, 57], and is discussed at the end of this section.

Given that: the tracer fraction was consistently underestimated at the surfaces of the bulk PCO samples that was attributed to the formation of ^{18}O rich Pr oxide precipitates; and

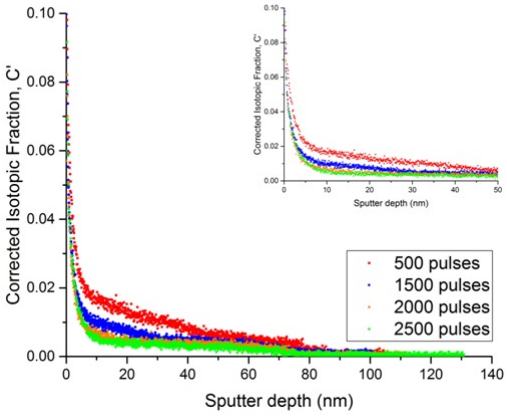


Figure 11.18: Corrected ^{18}O tracer profile, obtained at an effective exchange time and temperature of ∼15 min and ∼ 389°C, for strained PCO films of sample set 2 on a CGO buffer layer deposited using 500 to 2500 pulses. Inset, the diffusion profile at within the first 50 nm of the sample surface is expanded. The PCO/CGO interface was at a sputter depth of ∼77.4 nm.

the PrO^-:CoO^- ratio profile of the PCO thin films also suggested the formation of Pr oxide precipitates on the PCO film surfaces (and interfaces), this steep tracer fraction at the PCO film surface may be due to ^{18}O rich Pr oxide precipitates. In support of this, the depth around which the profile levels off was around 10 nm, which corresponded to the depth when CoO^- intensities and PrO^-:CoO^- ratios leveled off, see Fig 11.4b. It was possible also that the formation of the Pr oxide precipitates, resulting in depletion or Pr at the film surface and creation of Pr vacancies improving oxygen surface exchange. However, from what was seen earlier for the non-stoichiometric PCO samples, there was no obvious correlation between surface exchange and the extent of Pr oxide precipitates. For sample set 2, the CoO^- profiles suggest varying degrees of precipitation. Yet, it is not clear if the trend in the oxygen tracer fraction surface intensity with Pr precipitation is real.

The PCO/CGO interface for all films was set to be at a depth of ∼77.4 nm. At around this depth, it is arguable that another profile may be observed corresponding to the diffusion of ^{18}O into the CGO/YSZ substrate. This can more clearly be seen in the sample where the CGO buffer layer was at its thinnest (4.8 nm). Nevertheless, it is clear that around the interface, ^{18}O intensities dropped rapidly, see Fig 11.19 although it still does not attain background abundance of 0.02%. Isotope fractions were a magnitude lower at the PCO/CGO interface than measured in LSC/STO by Kubicek et al. [255], and such a profile (if it exists) cannot be fitted in any meaningful manner.

The ^{18}O surface intensities of the PCO films were almost identical, except for the PCO film deposited upon a 4.8 nm thick CGO buffer layer, which was significantly higher though it had the same profile shape as in the other PCO films. Visually, there appears to be a trend where higher isotopic fractions were obtained (and thus better oxygen transport) upon

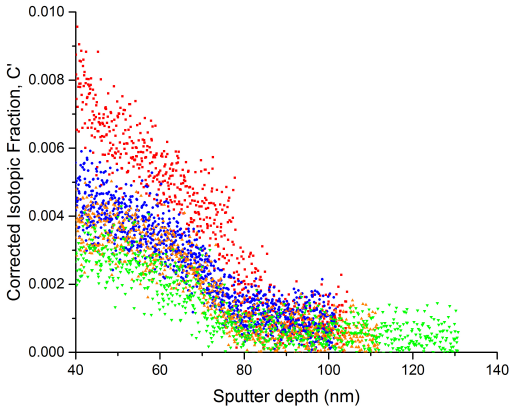


Figure 11.19: Corrected ^{18}O tracer profile, obtained at an effective exchange time and temperature of ∼15 min and ∼ 389°C, for strained PCO films of sample set 2 on a CGO buffer layer deposited using 500 to 2500 pulses. The profile at the PCO/CGO interface, a sputter depth of ∼77.4 nm, may be seen.

decreasing the thickness of the CGO buffer layer. As measured in Chapter 9, increasing CGO buffer layer increases the out-of-plane compressive strain of the PCO layer. This may be evidence of the mechano-chemical effect, which predicts a decrease of oxygen diffusion normal to the plane surface (in the direction of the depth profile). However, based on the PrO^-:CoO^- ratios calculated earlier in this section, there was cause to believe that the film composition was not constant between PCO films of sample set 2. A correlation was found between CGO buffer layer thickness and its composition. Increasing the CGO buffer layer thickness increased Pr content relative to Co, thus suggesting a decrease in the concentration of Pr vacancies and subsequently also a decrease in the concentration of oxygen vacancies. Thus, for the PCO films of sample set 2, there may have been a chemical contribution to its oxygen transport that would predict a decrease in oxygen transport with increasing CGO buffer layer thickness- the same outcome of the mechano-chemical effect. Similarly to the non-stoichiometric PCO bulk samples, it was not possible to confirm if the mechano-chemical effect really was present (and that the variation in oxygen transport was not solely due to its different composition), and if it was present, to distinguish the contributions of one phenomena from the other.

An attempt was made to fit these ^{18}O profiles obtained from the PCO films of sample set 2 to Cranks solution, see Fig 11.20. Only ^{18}O fractions up to a depth of 60 nm were used for the fit- the fit was made only from fractional ^{18}O values within the ∼77.4 nm thick PCO film. As can be seen, the fit was poor and unable to accommodate for the grain boundary diffusion tail (even if grain boundaries do not greatly affect the oxygen diffusion coefficient [481] though the initial fit close to the surface of the film was more reasonable. As was found for the PCO bulk samples, the measured isotope fraction was greater than the simulated value. The tracer D^* and k^* values obtained were comparable to bulk values. There appeared to be no apparent enhancement of the ORR in moving from bulk PCO to a textured PCO thin film. However, with such a poor fit and an R^2

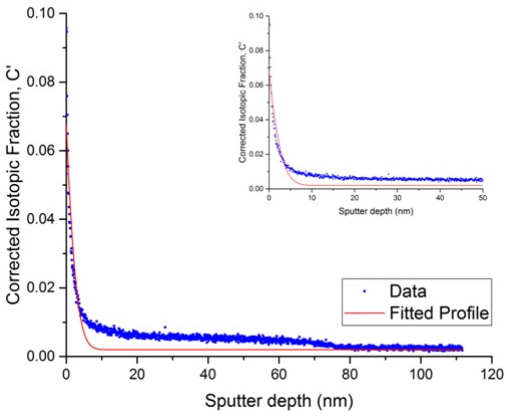


Figure 11.20: ^{18}O diffusion profiles in the strained PCO film (1000 pulses) on a CGO buffer layer (2000 pulses) of sample set 2, fitted to Crank's solution for diffusion in a semi-infinite medium. Inset, the near-surface profile: 0 to 50 nm. D^* and k^* values are 5.83×10^{-16} cm^2/s and 1.693×10^{-11} cm/s respectively were obtained, however the fit was poor with an R^2 value of 0.7447.

value of 0.7447, any D^* and k^* values would be questionable. While it has not been possible to quantify the change in D^* and k^* with lattice mismatch between the PCO and CGO, visual comparison of the profiles do still clearly indicate an improvement in oxygen transport as lattice mismatch decreased.

Normalized isotopic fraction profiles were also measured for the PCO thin films of sample set 3, see Fig 11.21. These films had a constant lattice mismatch with a 9.6 nm thick CGO buffer layer, but varied in thickness and thus experienced a range of lattice strains as strain relaxation occurred as a function of film thickness. The tracer profiles were similar to that of the PCO thin films of sample set 2. The profile was extremely steep close to the sample surface, before becoming very flat ∼4 nm into the film, with a long grain boundary diffusion tail. As seen earlier, ^{18}O levels do not reach background abundance (but rather levels out at a corrected fraction of $\sim 0.05\%$), even within the CGO/YSZ substrate. With the exception of the thinnest (25.8 nm) PCO, which had an extremely high tracer fraction at the film surface, tracer fractions at the film surfaces were of similar values.

The thickest (154.8 nm, deposited using 6000 pulses) PCO film had an exceptionally inhibited diffusion profile, and also a slightly different curvature to the other films. The cause for this is unclear. However, in all the other films, a clear trend may be seen where intensity of the ^{18}O diffusion tail increased with PCO film thickness. The measured lattice strain in the PCO films decreased with film thickness. This relaxation of lattice strain was likely through the creation of misfit dislocations that are present not just at the mismatched interface, but also throughout the strained film [482]. These dislocations may affect the oxygen diffusion in a similar way as the disordered grain boundaries, having a high concentration of lattice point defects that may facilitate the transport of oxygen and subsequently increase the ^{18}O diffusion tail.

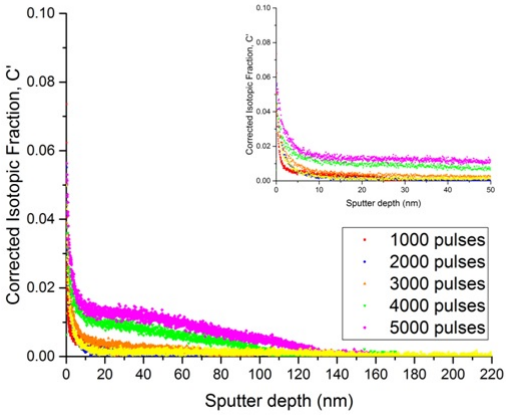
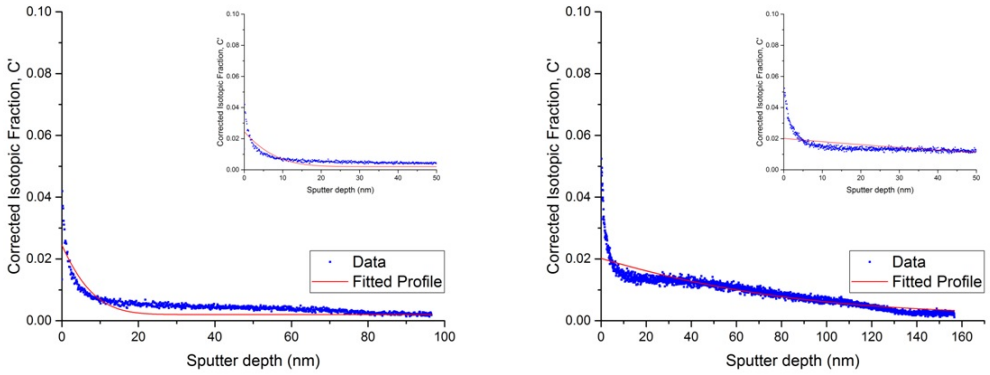


Figure 11.21: Corrected ^{18}O tracer profile, obtained at an effective exchange time and temperature of ∼16 min and ∼ 389°C, for strained PCO films of sample set 3, deposited using 1000 to 6000 pulses, on a CGO buffer layer of a constant thickness. Inset, the diffusion profile at within the first 50 nm of the sample surface is expanded.

Visually, it also appeared that oxygen transport improves with PCO film thickness. Increasing PCO film thickness allows the lattice to relax, relieving itself of the out-of-plane compressive strain induced by the lattice mismatched CGO buffer layer. For this situation of a decreasing out-of-plane compressive strain, the mechano-chemical effect would predict a decrease in the formation energy of oxygen vacancies and oxygen adsorption energy, and thus an increase in oxygen transport as does appear to be the case. Therefore, if the improvement in oxygen transport was real, it would support the presence of a mechano-chemical effect. Additionally, as mentioned earlier, the presence of grain boundaries do not appear to serve as fast transport pathways and thus the strain relaxation of the PCO film should not contribute to its oxide ion conductivity. However, it was also observed that the PrO^{-}:CoO^{-} ratio increased with PCO film thickness, with the likely effect of reducing Pr vacancy concentration and retarding oxygen transport in the thicker and less strained PCO films. That there appeared to be an increase in oxygen transport with PCO film thickness instead indicated that the mechano-chemical effect was present, and offset the effects of the compositional variation of the PCO films.

To confirm and quantify this combined effect on oxygen transport, D^* and k^* values need to be obtained from the profiles. Two example fits have been provided in Fig 11.22, one of a thinner PCO film with a smaller diffusion tail, and one of a thicker PCO film with a larger diffusion tail. In both cases, the fits were as poor as were found in sample set 2, if not worse depending on the intensity of the diffusion tail- the larger the grain boundary contribution, the worse the fit.

In an attempt to obtain a better fit, a fit of the plane sheet model by Crank was also attempted [105]. In a semi-infinite medium, the boundary conditions are such that the corrected (for the background isotope fraction and the isotope fraction during the exchange) ^{18}O tracer concentration, C', at the gas interface is the same as in the gas and



(a) PCO film ∼77.4 nm thick (3000 pulses) (b) PCO film ∼129 nm thick (5000 pulses)

Figure 11.22: ^{18}O diffusion profiles in two differently strained PCO films (∼77.4 nm and ∼129 nm thick) on a CGO buffer layer (deposited using 1000 pulses) of sample set 3, fitted to Crank's solution for diffusion in a semi-infinite medium. Inset, the near-surface profile: 0 to 50 nm. D^* and k^* values for the ∼77.4 nm thick PCO film are 4.95×10^{-16} cm^2/s and 1.57×10^{-11} cm/s respectively.D^* and k^* values for the ∼129 nm thick PCO film are 5.24×10^{-14} cm^2/s and 1.30×10^{-10} cm/s respectively. However, the fit was poor with R^2 value of 0.6649 and 0.7857 for the ∼77.4 nm and ∼129 nm thick PCO films respectively.

does eventually reach natural abundance. For the plane sheet model, there are instead two sources of the diffusing species at either interface of a sample (at $x = l$ and $x = -l$, where x is the thickness of thickness of the sample and $x = 2l$), both of which have an associated inward diffusion profile that is mirrored about the centre of the sample (at $x = 0$). However, a good fit could still not be obtained.

The use of composite profiles has been proposed to fit for oxygen diffusion profiles exhibiting a long tail in order to account for the standard lattice diffusion of oxygen and also the fast-path diffusion of oxygen (such as along grain boundaries). Thus an additional tailing term for grain boundary diffusion was derived by by Whipple [483] and Le Claire [484] of the form $Ae^{-Zx^{6/5}}$ for evenly distributed planar fast diffusion paths where the separation between the parallel paths of fast diffusion is large enough that their associated diffusion fields do not interact [485]. A schematic of this composite diffusion profile is illustrated in Fig 11.23. This model has been shown to be applicable even to polycrystals with randomly oriented grains [486] and has since been used to successfully fit diffusion profiles in multiple polycrystalline systems [487, 488, 57, 58, 489, 490, 491, 492].

Examples of diffusions profiles by Zhang et al. with a tailing function being fit with the standard Crank's solution may be seen in Fig 11.24. These diffusion profiles are not dissimilar to that obtained of the strained PCO films in this work, see Fig 11.22. It should be noted that there have been contrary findings on the role of grain boundaries for oxygen transport. On the one hand, (the traditional view) grain boundaries have been found to serve as fast transport paths and may even facilitate oxygen exchange [493], yet this has been disputed and grain boundaries have even been proposed to hinder oxygen transport

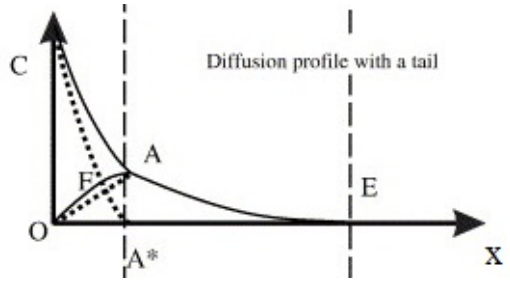
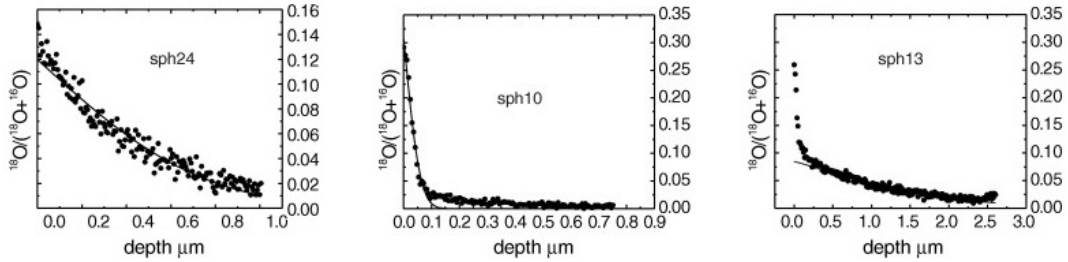


Figure 11.23: Schematic composition diffusion profile. The near-surface steep profile (curve CA) is due mainly to direct lattice diffusion from the surface along the X direction, while the shallow tail (curve AE) is due mainly to fast paths. The contribution of these fast paths to the composite diffusion profile may be described by the curve OFAE. Taken from [57].

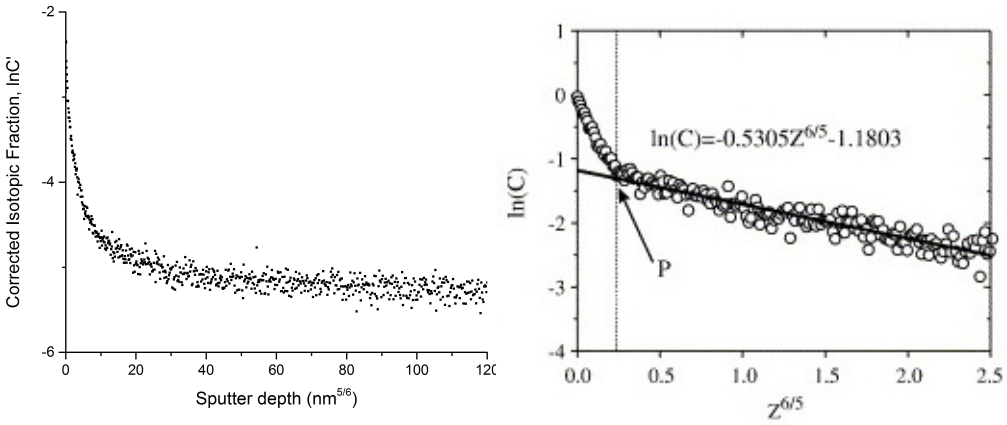


(a) Slight tail (b) Medium tail (c) Large tail

Figure 11.24: Composite diffusion profiles, fitted to Crank's solution for diffusion in a semi-infinite medium. In (A), there is a departure from Crank's solution due to fast transport paths but which does not result in a clear break and 'tail' section making identification difficult. In (b) and (c), different extents of a tailing function may be seen, similar to the profiles obtained of the PCO films in this work, resulting from the varying contributions of the fast transport paths to the profiles. Taken from [58].

[494].

Regardless, even if not due to grain boundaries, the diffusion profile of this work does appear to have a composite character. Subsequently, it was plotted as a graph of ln isotopic fraction against depth, $x^{6/5}$, to see Fig 11.25. It may be argued that two separate lines could be drawn to describe the fit and that this fit is better than that obtained using Crank's solution for purely lattice oxygen transport. Analysis of such composite profiles have been performed by applying the Whipple-Le Claire equation to the near-surface profile to obtain D^* and k^* values for lattice diffusion, [57, 490, 492]. In some cases, it has then also been applied to the tailed profiles [490, 492]. However, these separate fits over estimate oxygen diffusivites as contributions of one transport system to the other are ignored. Another method of analysis has been been proposed by Kuar and Gust, that does account for the overlap in profiles [495]. However it equires detailed knowledge of the fast transport diffusion of oxygen in order to determine its contribution of the diffusion profile, described by the curve OFAE in Fig 11.23, following which the remaining lattice diffusion of oxygen is fitted using the Whipple-Le Claire equation. As this is not typically



(a) (b)

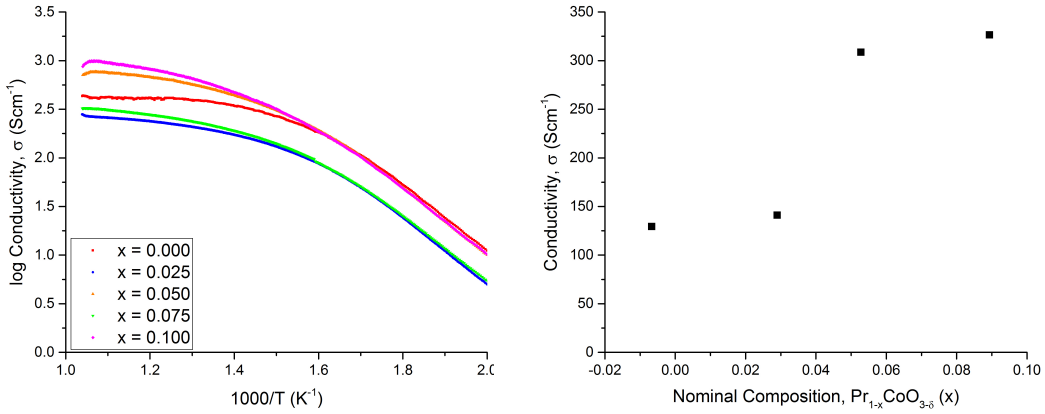
Figure 11.25: (a) Measured ^{18}O diffusion profiles in the strained PCO films on a CGO buffer layer (deposited using 1000 pulses) of sample set 2, plotted on a $ln(C')$ against $x^{6/5}$ axis to test for the presence of a tailing function and identify the break in the slope (point A in Fig 11.23). The transition arising from lattice diffusion contributions and fast diffusion paths contributions was less clear than in (b)- an example ^{18}O diffusion profile fit on the same axis by Zhang et al. [57], where the lattice and fast transport path contributions may clearly be fitted in the profile.

known, approximations have been made where the contributions by the fast transport path is described by OAE instead [58]. Either of such analysis lies outside the scope work but should be followed up in further work.

This inability to fit the oxygen profile and obtain meaningful values of D^* and k^* prevented comparison between the bulk and thin film sample sets where both changes in defect species and the mechano-chemical effect are thought to affect oxygen transport. Nevertheless, there is now a reasonable case to expect a mechano-chemical effect contributing to the oxygen transport of the chemically strained bulk PCO samples, and the thin film PCO samples with a range of lattice mismatches.

11.3.3 Electrical Transport Measurements

The conductivity measurements of bulk non-stoichiometric PCO and strained thin film PCO as a function of temperature were performed. Prior to the measurements, checks were made for the internal consistency and uniformity of the sample, as well as the quality of the ohmic contact. To ensure the latter, a current should be applied such that the power dissipation does not exceed 5 mW (or preferably 1 mW). Thus, as a rule of thumb, an applied current was applied where $I \leq (200R)^{-0.5}$ and there was confidence that a good ohmic contact had been obtained. SEM images taken about the cross-section of the non-stoichoimetric bar samples showed no indication of sample non-uniformity. For the thin film samples, PLD is a process capable of producing homogenous thin films,



(a) Conductivity as a function of temperature

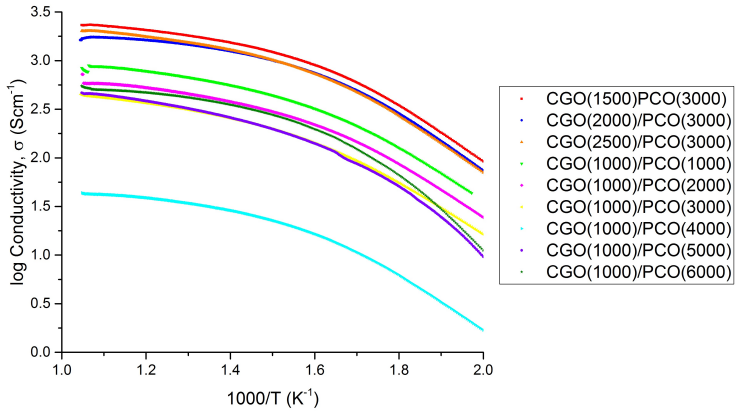
(b) Conductivity at 400°C

Figure 11.26: Conductivity measurements of non-stoichiometric PCO bar samples ($Pr_{1-x}CoO_{3-\delta}$ where x denotes A-site deficiency. Increasing x resulted in a decrease in electrical conductivity.

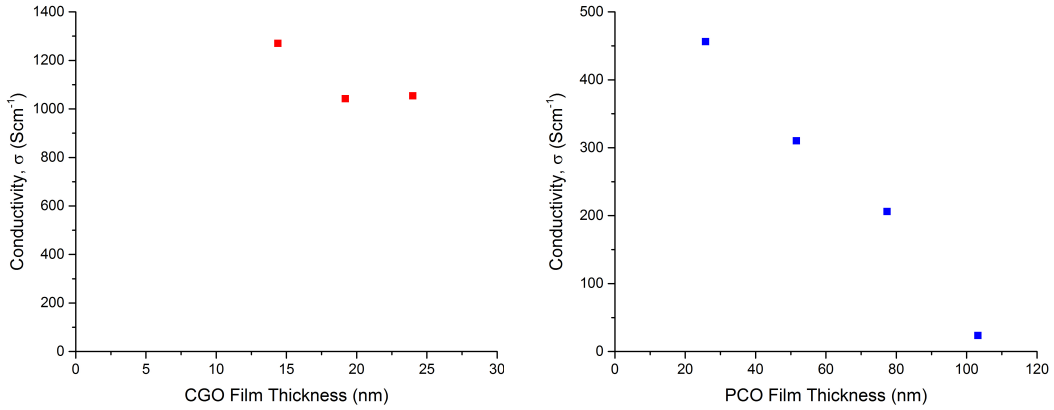
and AFM images of the film surface taken at various locations also suggest a uniform sample morphology. Thus there is no cause to suspect sample non-uniformity in the bulk non-stoichiometric PCO or PCO thin film samples.

The electrical conductivity measurements of the nonstoichiometric bulk PCO samples have been presented in Fig 11.26a, discounting that of the nominally stoichiometric PCO sample where $x = 0.00$ that was found to be Pr-excess according to EDX measurements. There appears to be an upward shift in conductivity with increasing Pr-deficiency. A deviation in the Pr site fraction of ~0.1 resulted in an increase in electrical conductivity by half an order of magnitude. As was pointed out by Ullmann, the deviation in cation stoichiometry has indeed resulted in large deviations in electrical conductivity [67]. This would have been expected from a purely chemical point of view, similar to that taken for A-site deficient LSCF by Mineshige et al. where an increase in Sr deficiency decreased conductivity as it was the introduction of Sr-dopants that resulted in the creation of electronic p-type carriers. In this case the removal of A-site Pr would create Pr vacancies, and subsequently also holes (see Chapter 10). This trend can be seen in Fig 11.26b of the electrical conductivity measured at 400°C against sample composition

In Fig 11.27a, it can be seen that while the majority of the conductivity measurements of the PCO thin films showed a similar dependence of electrical conductivity on temperature, a steeper curve was also observed at lower temperatures for the two thickest PCO films (of sample set 3) that exceeded 103 nm (deposited using 4000 pulses). The cause for this is unclear, though it may be possible there is a threshold PCO film thickness beyond which there is a change in the factors contributing to its electrical properties which also resulted in a different conductivity curve and an increase in electrical conductivity at 400°C for these two samples. Omitting the results of these two thickest films in sample set 3, a linear



(a) Conductivity as a function of temperature

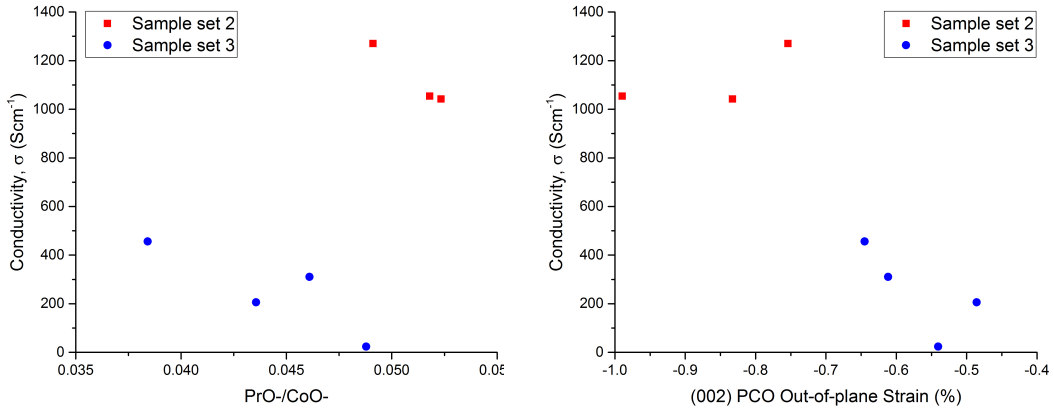


(b) Conductivity at 400°C, sample set 2 (c) Conductivity at 400°C, sample set 3

Figure 11.27: Conductivity measurements of strained PCO films of sample set 2 (where the CGO buffer layer was deposited using 500 to 2500 pulses, and the PCO film deposited using 3000 pulses) and sample set 3 (where the CGO buffer layer was deposited using 1000 pulses, and the PCO film was deposited using 1000 to 6000 pulses). The conductivity measurements of the two thickest PCO films of sample set 3 at 400°C in (c) have been omitted.

dependence of electrical conductivity on PCO film thickness may be seen where increasing film thickness decreased electrical conductivity, see Fig 11.27c. Increasing CGO buffer layer thickness in sample set 2 also resulted in a decrease in electrical conductivity, see Fig 11.27b.

Increasing PCO film thickness should decrease the in-plane tensile strain in the PCO film, while increasing CGO buffer layer thickness should increase the in-plane tensile strain in the PCO film- contrary effects. Thus to examine why the decrease in conductivity is seen as CGO film thickness increased in sample set 2, conductivity values were plotted as a function of two possible influences on electrical conductivity: PrO^{-}:CoO^{-} ratio and PCO lattice strain, see Fig 11.28.



(a) Conductivity at 400°C, as a function of PrO^{-}:CoO^{-} ratio

(b) Conductivity at 400°C, as a function of PCO out-of-plane lattice strain

Figure 11.28: Conductivity values at 400°C in the strained PCO films of sample sets 2 and 3.

In Fig 11.28a, it can be seen in both sample sets that there is a correlation between electrical conductivity and PrO^{-}:CoO^{-} ratio. On consideration of defect chemistry alone, increasing the Pr content would have decreased the negatively charged Pr vacancy concentration, and thus also decreased the need for a charge compensating species, resulting in a reduction in the concentration of electronic hole carriers. This was indeed reflected in the decrease in electrical conductivity measured as the PrO^{-}:CoO^{-} ratio increased.

The variation in electrical conductivity with composition was significantly different between the two sample sets of differently strained films. The PCO films of sample set 2 saw almost twice a decrease in electrical conductivity for the same change in composition as the PCO films of sample set 3. It should therefore be anticipated that in addition to compositional effects, strain effects must also be present. However, the effect of the PCO out-of-plane strain on electrical conductivity, see Fig 11.28b was difficult in confirm. In sample set 2, increasing PCO out-of-plane strain appeared to increase electrical conductivity- the opposite was seen of sample set 3. It may be that the different methods of inducing the lattice strain had different effects on the CoO_6 octahedral tilt hence these opposing behaviors. Or, it may be that the effect of out-of-plane strain on conductivity of the two sample sets may be combined, in which case increasing out-of-plane strain does clearly result in an increase in conductivity. This may then explain the difference in the effect of PrO^{-}:CoO^{-} ratio on conductivity between the two sample sets in Fig 11.28c. The difficulties in interpreting these results arise as the effects of strain and composition are not isolated. Further work is required, possibly using a different fabrication technique wherein strained films of identical compositions may be tested.

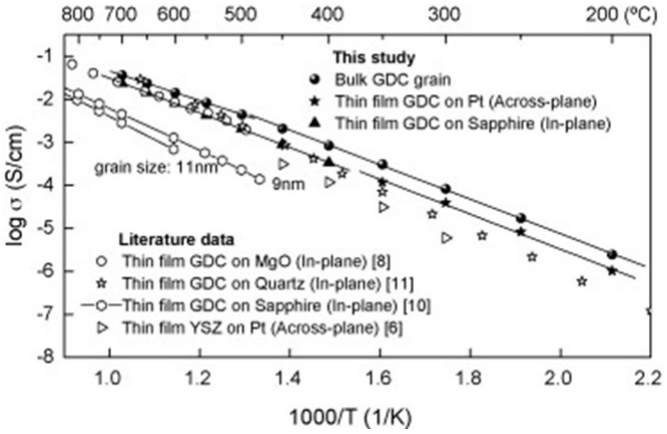
Additionally, to further investigate the effect of lattice strain on conductivity, it is necessary to characterize the nature of the CoO_6 distortion with the application of an out-of-plane compressive strain using the two different methods. In-plane XRD measurements would

be required to obtain in-plane lattice parameters from which to calculate the Goldschmidt tolerance factor and also the octahedral tilt. While RSMs have been obtained of a few of the PCO thin film samples, they were of insufficient quality to extract accurate lattice parameters. In order to pursue this further and identify the effect of lattice strain on the CoO_6 octahedral tilt, as has been performed by Vailionis et al. [496], further accurate in-plane structural analysis is required.

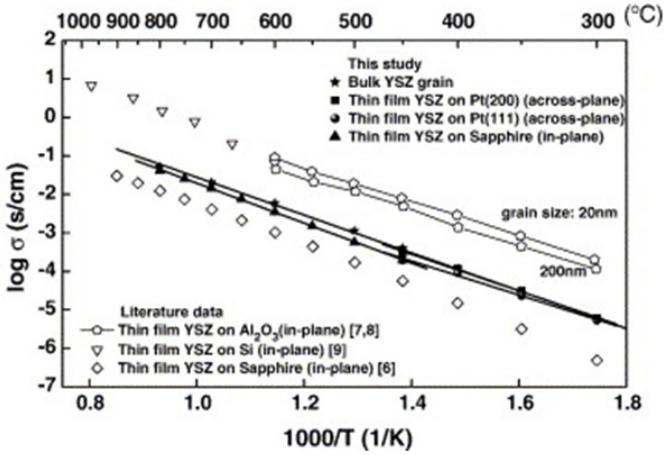
If a strain effect was present in the lattice strained PCO films, it may also be present in the chemically strained non-stoichiometric bulk PCO samples. The chemical expansion of PCO on decreasing Pr content resulted in lattice expansion of all three cell parameters. The effect of this chemical expansion on the CoO_6 octahedra responsible for electronic conductivity would not have been the same as for the directionally strained thin films, and parallels on the effect of lattice strain on conductivity may not be drawn. As with the thin films, further oxygen sensitive structural characterization is required to confirm any distortion of the CoO_6 octahedra to which the changes in electrical conductivity may be attributed.

It should be noted that a comparison of the measured electrical conductivities the two sample sets of strained PCO films suggested that the electrical conductivity of the PCO thin films of sample set 2 were enhanced, while the electrical conductivity of the PCO thin films of sample set 3 were inhibited, compared to bulk PCO. Yet, sample set 3 had: the lower range of PrO^-:CoO^- ratios, which should mean a higher concentration of electronic hole carriers; and smaller in-plane tensile strains, also thought to be associated with a poorer electrical conductivity (though this requires further structural characterization to confirm). At present, no explanation may be given to reconcile this discrepancy. The conductivities of the non-stoichiometric PCO samples may also have been inhibited by chemical expansion effects, a tensile strain having been measured in the non-stoichiometric samples).

A potential of error in the van der Pauw measurements of the PCO films is if there were substrate contributions to the electrical conductivity measured, short-circuiting the film. The electrical conductivity of the substrate should be several orders of magnitude lower than that of the thin film to minimize its contributions to the plane conductivity measurement. A comparison of published data on the electrical conductivity of thin film and bulk CGO shows that it was ~6 orders of magnitude lower than that of the values obtained here for bulk PCO [60, 313, 497, 498, 499], see Fig 11.29a. In the case that the CGO buffer layer did not act as a full blocking layer between the PCO and YSZ substrates, the electrical conductivities of YSZ have also been provided and can be seen to be of the same order as CGO [59, 500], see Fig 11.29b. Thus there is confidence that any contributions to the electrical conductivity measured of the PCO film, by the CGO buffer layer of YSZ substrate, would have been negligible and cannot be the cause for the discrepancy mentioned.



(a) CGO films, taken from [60]



(b) YSZ films, taken from [59]

Figure 11.29: Conductivity measurements of (a)CGO and (b)YSZ films on various substrates by [59, 60]- refer to these works for references in the the figures.

11.4 Conclusion and Further Work

Oxide ion and electrical conductivity measurements were performed on bulk PCO samples with a range of cation non-stoichiometry, and PCO thin films with a range of out-of plane compressive strains. The variation in out-of-plane compressive strain was achieved either by increasing CGO buffer layer thicknesses or increasing PCO film thickness. Compositional analysis of the samples was performed using the ToF SIMS measurements used to obtain an ^{18}O tracer diffusion profile. It revealed a compositional variation in the PCO thin films whereas the bulk PCO samples maintained a uniform composition past its surface. A correlation was found between the extent of compositional variation within the strained PCO thin films and the degree of lattice mismatch at the PCO/CGO interface. Additionally, SE images and EDX analysis indicated the presence of Pr-rich precipitates at the surface the nominally stoichiometric bulk PCO sample. These precipitates are likely to have been present on all the samples and are thought to have formed during the exchange process.

The ^{18}O fractional profiles were fitted using Cranks solution to obtain D^* and k^* values. An increase in the Pr deficiency of the PCO bulk samples resulted in an increase in D^*, and varied between 1.36×10^{-16} cm/s^2 and 2.06×10^{-16} cm/s^2 at 400°C, comparable to D^* values of other typical cathode materials. No clear trend was observed with respect to k^*. For all samples, surface ^{18}O fractions were underestimated by the fit. The increase in D^* with Pr-deficiency was attributed to the creation or Pr vacancies and subsequently O vacancies. Similarly, the electrical conductivity of PCO was found to increase with Pr vacancies, as a consequence of its defect chemistry.

There were two identified contributions to the oxide ion conductivity of the PCO thin film: the film composition and the mechano-chemical effect as determined by the strain state of the film. Where the CGO buffer thickness was increased, the increase in PrO^-:CoO^- ratio and increased out-of-plane compressive lattice strain both resulted in a decrease in oxide ion conductivity. Where the PCO film thickness was increased, the effect of increase in PrO^-:CoO^- ratio on inhibiting oxide ion conductivity was offset by the effect of the decrease in out-of-plane lattice strain promoting oxide ion conductivity resulting in an overall increase in oxide ion conductivity. The comparison of the two sample sets confirms the presence of the mechano-chemical effect. However, it was not possible to fit the ^{18}O diffusion profiles of the thin films to Cranks solution. There is evidence of the presence of a fast oxygen transport path. As such, further work is required to quantify oxide ion conductivity of the PCO thin films and confirm the trends described.

Due to compositional variations detected in the PCO films, changes to electrical conductivity have be the result of both strain and compositional effect. As a different gradient of electrical conductivity with respect to film composition was observed, it has been suggested that there may be a mechano-chemical effect on electrical conductivity and the application of an out-of-plane compressive strain may increase electrical conductivity. However, further work is required to identify the effect of lattice strain on the CoO_6 octahedral to explain this result.

Chapter 12

Conclusions

As outlined in Chapter 4, the objective of this work was to enhance the ORR in the $PrCoO_{3-\delta}$, PCO113, system. Two occasion have been identified where this has been accomplished: the pairing of a perovskite PCO113 to a Ruddlesden-Popper $Pr_2NiO_{4\pm\delta}$, PNO214, film as reported by Sase et al. for the $(La,Sr)CoO_3/(La,Sr)_2CoO_4$ system [32, 26], or the use of mechano-chemical coupling to "tailor the energy landscape" as has been proposed by Yildiz et al. [228]. With respect to mechano-chemical coupling, two forms of lattice strain have been investigated: mechanical strain in thin films resulting from lattice mismatch between PCO113 film and $Ce_{0.9}Gd_{0.1}O_2$/8mol%-YSZ, CGO/YSZ, substrate; and chemical strain in bulk samples resulting from cation non-stoichiometry ($Pr_{1-x}CoO_3$). To test for enhancement of the ORR oxide ion and electrical transport measurements were taken.

PLD was the thin film fabrication technique used. Much of the preliminary work involved the synthesis and characterization of dense, single phase PCO113, PNO214 and CGO (supplied) PLD targets to serve as a reference from which to calculate lattice strain. Space group assignments of *Pnma*, *Fmmm* and $Fm\bar{3}m$ were used for the three targets, respectively. CGO deposition conditions were obtained from literature [27, 29, 227, 310, 311]. A range of deposition substrate temperatures and oxygen partial pressures were used to optimize PLD conditions for PCO113 and PNO214.

PCO113 was deposited at substrate temperatures between 680°C to 780°C, and oxygen partial pressures between 10 mTorr and 500 mTorr. However, these deposition parameters did have an effect on film morphology: increasing substrate temperature resulted in the formation of an 'island' morphology, while decreasing oxygen partial pressure below 100 mTorr resulted in a porous film with irregularly shaped grains. Optimal deposition conditions were at a substrate temperature of 680°C and oxygen partial pressure of 300 mTorr. The PCO113 deposition rate under those conditions was ∼4.8 nm/1000 pulses. This is the first reported work of the deposition of PCO113 on Si(004) and CGO(200)/YSZ(002) substrates.

Using the same PLD conditions trialed for PCO113, single phase PNO214 could not be

deposited. The resulting film comprised of multiple phases, thought to include Pr_6O_{11} with any combination of $PrNiO_3$, PNO214 and $Pr_4Ni_3O_{10}$. Identification of these secondary phases was uncertain due to the textured nature of the deposited film and the similarities in the structure of the Pr oxides. There have been reports of the high temperature instability of PNO214 in air and its oxidative decomposition into Pr_6O_{11} and $Pr_4Ni_3O_{10}$ [47, 48]. Building on those works, isothermal measurements of PNO214 (which have not been reported before in literature) were performed at 800°C in air and showed the gradual formation of Pr_6O_{11} and $Pr_4Ni_3O_{10}$ suggesting this process to be kinetically limited. The fractions of Pr_6O_{11} and $Pr_4Ni_3O_{10}$ present were quantified using Rietveld refinements as a function of anneal time. The formation of $Pr_4Ni_3O_{10}$ appeared to facilitate the breakdown of PNO214. However, further work is required for oxygen sensitive structural characterization, such as high temperature neutron diffraction, to understand the gradual structural evolution of the PNO214 into Pr_6O_{11} and $Pr_4Ni_3O_{10}$. While this high temperature instability does not rule out PNO214 from application in IT-SOFCs, PLD does not appear to be a suitable technique for the fabrication of PNO214 films that are without stabilizing dopants such as Cu and Ga. Due to the inability to produce a PNO214 film, only the mechano-chemical effect could be investigated for its effect on the ORR.

In order to introduce a range of lattice strains into the PCO113 films, two methods were used. In the first method (sample set 2), PCO113 films ∼75.4 nm thick were deposited on CGO(200) buffer layers whose thicknesses varied between ∼6.2 and ∼24.1 nm. Contrary to expectations based on the relative cell parameters of CGO and YSZ, an out-of-plane compressive strain was measured (an out-of-plane tensile strain was expected). However, it later became clear that the CGO target stoichiometry must not have been maintained during the PLD process and should not be used in the calculation of the lattice strain in the deposited CGO film. Increasing CGO buffer layer thickness was found to increase the measured out-of-plane strain in the PCO113 film, from -0.75% to -0.99%. This is in keeping with the expectation that increasing the CGO buffer layer thickness would allow the CGO buffer layer to relax, increasing its in-plane lattice parameters and thus increasing the lattice mismatch between CGO and PCO.

For the second method (sample set 3), PCO113 films of thicknesses between ∼46.0 nm to ∼467.0 nm were deposited on CGO buffer layers ∼4.8 nm thick. Increasing PCO film thickness decreased PCO out-of-plane lattice strain from -0.61% to -0.39% (calculated from the PCO(002) reflection) as the lattice relaxed. The strain relaxation in the two PCO113 orientations detected, (002) and (0k0), was modelled and found to have similar rates of relaxation (α = 0.01 and 0.02 nm^{-1} respectively) comparable to that reported in literature of LSC films, though the initial lattice strain at the CGO/PCO interface of the two orientations were quite different (ϵ_0 = -0.74 and -0.22% respectively). Thus a range of PCO113 lattice strains in sample sets 2 and 3 were obtained. As with the PCO films of sample set 2, further work is required to examine the effect of lattice strain on the CoO_6 octahedral tilt, and whether these two different methods of achieving a lattice strain have the same effect on the CoO_6 octahedral tilt.

Lastly, to prepare chemically strained PCO113 samples, A-site deficient PCO113 ($Pr_{1-x}CO_{3-\delta}$) samples were synthesized. Rietveld refinements were performed on room temperature XRD patterns. The rate of lattice expansion with respect to A-site deficiency, x, may be described using Vegard's law and was found to be 3.3 - 3.9 Å/x for the a- and c-cell parameter, and 4.7 Å/x for the b-cell parameter. The expansion of the lattice with increasing A-site deficiency was attributed to the formation of Pr vacancies, which effect was sufficiently large to offset the decrease in lattice parameter associated to the increase in oxidation state of Co^{3+} to Co^{4+}. Due to the insensitivity of X-rays to oxygen, the effect of lattice expansion on the CoO_6 octahedral tilt could not be determined.

Additionally, HT-XRD measurements were performed on the A-site deficient PCO113 samples to check for instability and also to provide insights to the defect chemistry of PCO113, which needs to be accounted for in order to separate compositional effects from mechano-chemical effects in these samples. No secondary phases were detected for all A-site deficient PCO113 samples. The thermo-chemical effect was observed wherein there was a superposition of chemical expansion, on top of thermal expansion, as oxygen uptake occurred (the removal of oxygen vacancies causing a contraction in the lattice). Increasing A-site deficiency was found to decrease the thermal expansion coefficient while its effects the chemical expansion coefficient is not clear and no c. The presence of the thermo-chemical effect confirms that for the non-stoichiometric chemically strained PCO113 samples, there would be compositional contributions to the ORR, not just mechano-chemical. It was intended that a comparison be made between the transport properties of the lattice mismatched PCO113 films (purely mechano-chemical effect) and the chemically strained non-stoichiometric PCO113 samples (mechano-chemical and compositional effect).

However, ToF SIMS depth profiles of the PCO113 films indicated a slight variation in the overall cation stoichiometry between the films, despite the PLD technique being specifically chosen for its ability for stoichiometric transfer from target to film. It was unclear if these variations were real, more accurate compositional analysis is required to confirm the composition of the PCO113 films. The lack of this information created difficulty in interpreting trends in the transport measurements. Additionally, the ToF SIMS depth profiles also indicated a compositional variation within the films, depending on the extent of lattice strain experienced by the film. Further work is required the investigate the effect of strain on compositional gradation, and its effect on PCO113 performance. While the bulk non-stoichiometric PCO samples had a uniform composition at its core, SE images and EDX analysis revealed the formation of Pr-rich precipitates on the surface of the nominally stoichiometric PCO sample that were not present prior to the isotope exchange. Thus the effect of exchange conditions on the samples also warrants further investigation.

^{18}O diffusion profiles of the non-stoichiometric PCO113 samples were fitted using Crank's solution for diffusion in a semi-infinite plane. Increasing A-site deficiency increased D^*. No clear trend was found between x and k^*. There may have been a slight tailing function in the diffusion profiles of the non-stoichiometric PCO113 samples. For the strained PCO113 films, the extent of the tailing function increased with PCO113 lattice strain. It was not

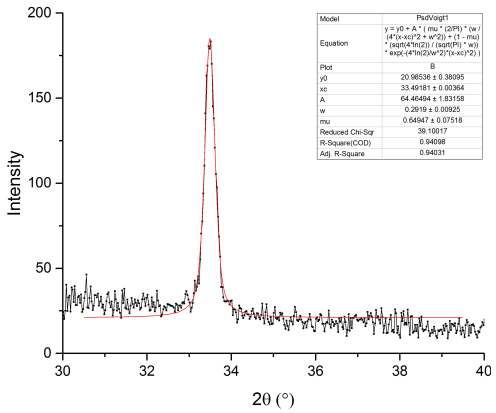
possible to obtain D^* and k^* values from these profiles. Further work would involve the fitting of a composite profile that would have a lattice contribution to the tracer diffusion as well as a fast transport path, in order to quantify the effect of out-of-plane strain on oxide ion transport. Based on a visual inspection of the diffusion profile and also a consideration of cation stoichiometry in the PCO113 films of both sample sets, it appeared that the introduction of a compressive out-of-plane strain in the PCO113 films inhibited oxide ion transport- there was evidence of a mechano-chemical effect. Thus, it is possible that there were strain effects also contributing to the oxide ion transport in the non-stoichiometric PCO113 sample. The lattice expansion upon increasing A-site deficiency may also have contributed to the increase in D^* measured.

Increasing A-site deficiency of the non-stoichiometric PCO113 samples was found to increase electrical conductivity, as would be expected given the defect chemistry of PCO113. Chemical strain effects on electrical conductivity could not be confirmed without an assessment of the CoO_6 ocatahedral tilt. The effect of chemical and lattice strain on the electrical conductivity of and PCO113 films was also open to interpretation. The PCO films of sample set 2 seemed to show a decrease in conductivity as PCO113 out-of-plane strain increased, while the PCO113 films of sample set 3 showed the opposite. Both sample sets did show an increase in conductivity with decreasing PrO^-:CoO^-, suggesting that compositional effects were present. It was not possible to arrive at firm conclusions without further work investigating the effect of lattice strain on the CoO_6 octahedral tilt.

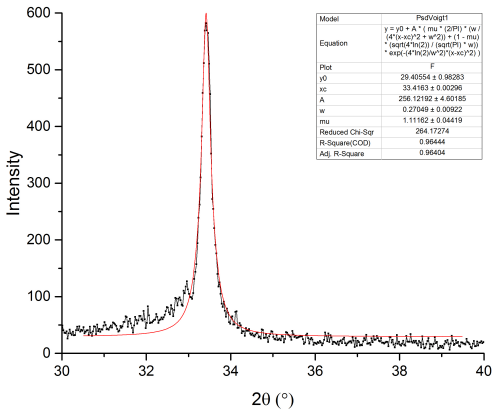
Lattice strain does clearly have an influence on the oxide ion and electrical conductivity of PCO113 and there is the potential to enhance cathode performance of PCO113 using lattice strain. However, even within the controlled nature of this work, there was difficulty in reliably and accurately depositing PCO113 films of progressing lattice strains and greater care was required in screening YSZ(002) substrates as well as the CGO(200) buffer layers prior to the deposition of PCO113. This was largely due to the laser ablation damage acquired by the targets. Despite efforts to minimize this by grinding away the damaged target surface between depositions, thicker films would allow an accumulation of ablation damage during the deposition. Thus, one of the major impediments of using lattice strain to enhance SOFC performance arises from the fabrication technique. Even if such strained components could be reliably produced, TEC mismatch between cell components are likely to affect the strain state of the electrolyte (or alternatively, TEC mismatch may be exploited to induce the lattice strain). Lastly, the effect of lattice strain on oxide ion conductivity measured in this work are not of the same order as reported by Sase et al. [32, 26]. While it may provide insights regarding the transport of oxygen through a strained landscape, it is unlikely to warrant the effort required to be applied in real SOFCs.

Appendix A

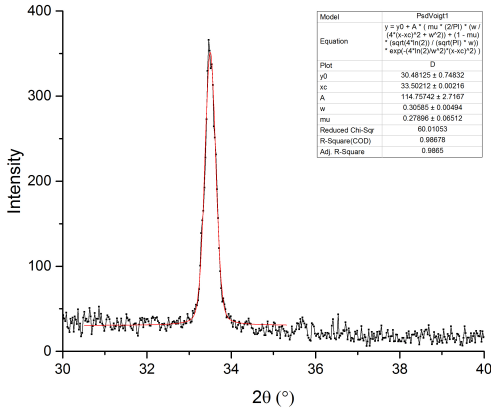
A.1 Pseudo-Voigt Fit of the Out-of-plane $PrCoO_3$ Reflections at $\sim$33.5° 2θ



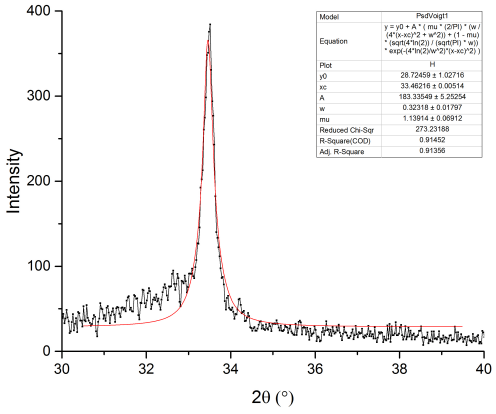
(a) 1000 pulses



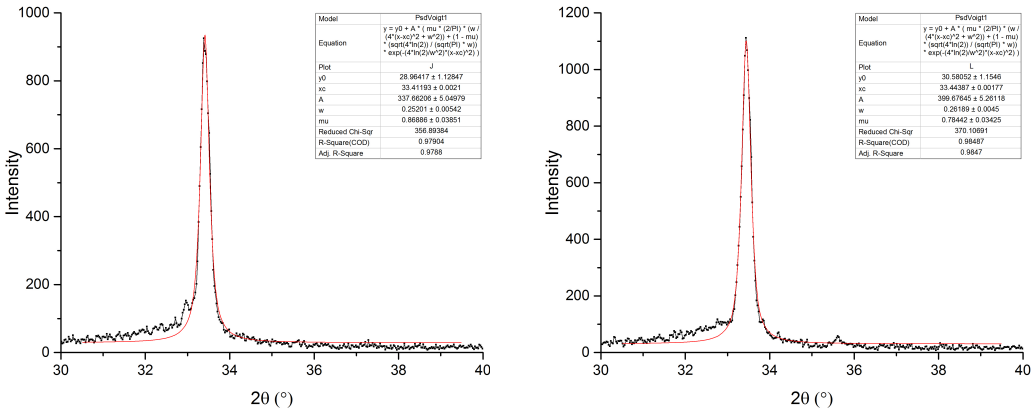
(b) 2000 pulses



(c) 3000 pulses



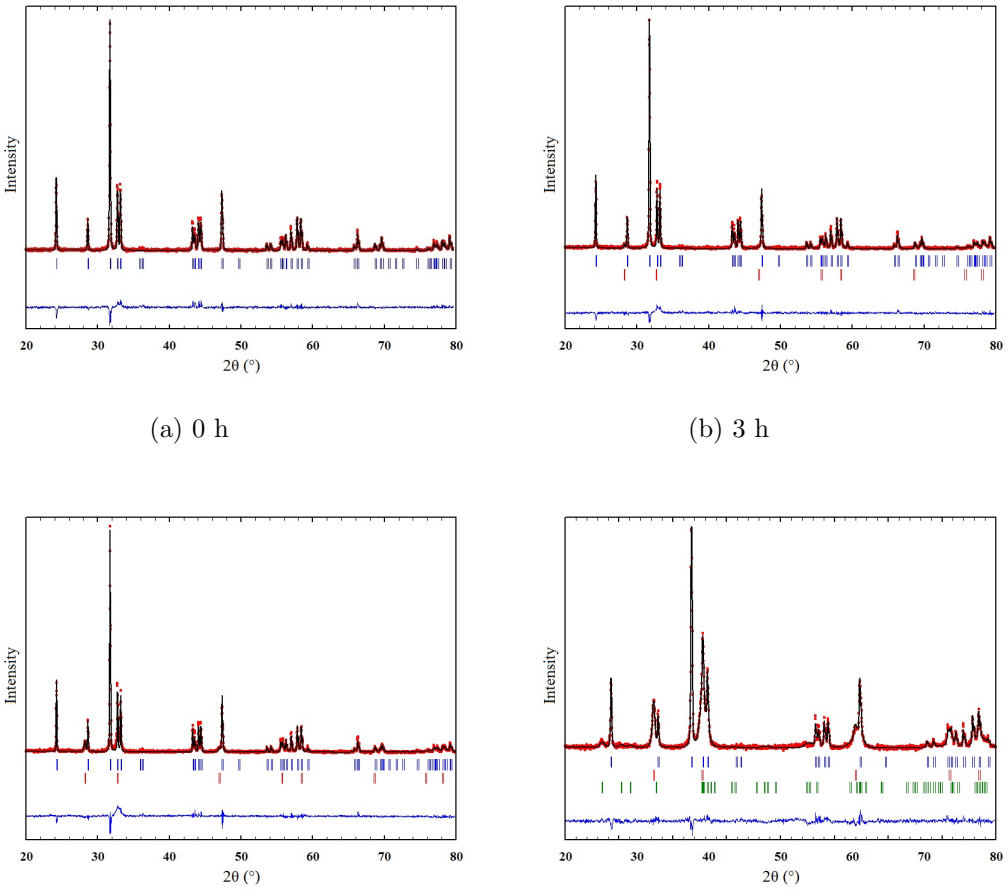
(d) 4000 pulses



(e) 5000 pulses (f) 6000 pulses

Figure A.1: Pseudo-Voigt fit of the out-of-plane XRD highest intensity $PrCoO_3$ reflection at ∼33.5° 2θ for $PrCoO_3$ films deposited on Si(004) single crystal substrates using a range of laser pulses between 1000 to 6000 pulses. The measured diffraction pattern is in black, and the pseudo-Voigt profile in red. The purple arrows indicate the range of data selected for the fit.

A.2 XRD Measurements and Rietveld Refinement of Pr_2NiO_4 following Isothermal Treatment



(a) 0 h

(b) 3 h

(c) 6 h

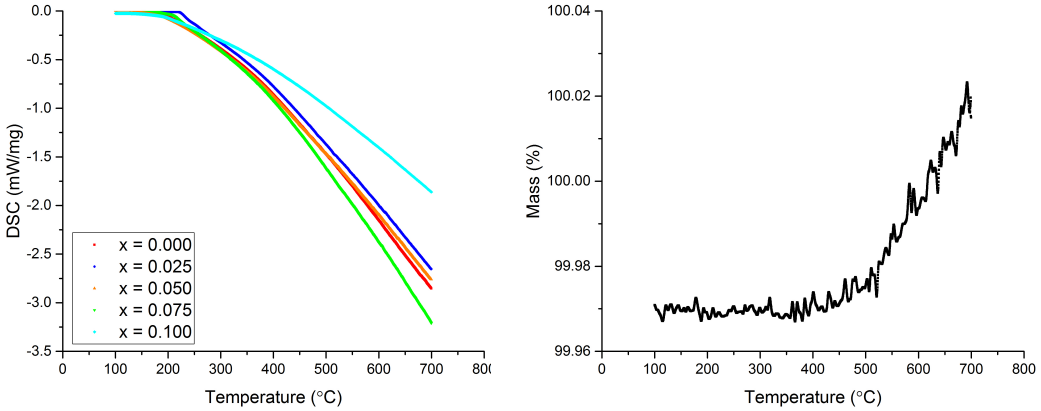
(d) 12 h

Figure A.2: XRD powder patterns of quenched Pr_2NiO_4 samples following an anneal at 800°C in air for up to 12 h. The measured data is in red, the Rietveld fit in black, and the difference between them in blue. The Bragg reflections of Pr_2NiO_4, Pr_6O_{11} and $Pr_4Ni_3O_{10}$ are marked in blue, red and green, respectively.

		0 h	3 h	6 h	12 h
Pr_2NiO_4,	a (Å)	5.4614(2)	5.4584(1)	5.4596(1)	5.4604(1)
$Fmmm$	b (Å)	5.3956(1)	5.3912(1)	5.3904(1)	5.3889(1)
	c (Å)	12.4617(3)	12.4547(2)	22.4579(2)	12.4625(3)
	Cell vol (Å^3)	367.22(17)	366.502(9)	366.63(11)	366.790(13)
	Fraction (%)	100.00(52)	99.67(49)	92.19(64)	51.54(33)
	R_{Bragg} (%)	9.11	9.27	11.7	4.79
Pr_6O11,	a = b = c (Å)	-	5.4741(8)	5.4719(5)	5.4729(2)
$Fm3m$	Cell vol (Å^3)	-	164.039(4)	163.837(25)	163.923(9)
	Fraction (%)	-	0.33(2)	7.81(24)	15.33(18)
	R_{Bragg} (%)	-	37.8	25.2	6.95
$Pr_4Ni_3O_{10}$,	a (Å)	-	-	-	5.3934(9)
$Fmmm$	b (Å)	-	-	-	5.4483(12)
	c (Å)	-	-	-	27.3483(50)
	Cell vol (Å^3)	-	-	-	803.637(265)
	Fraction (%)	-	-	-	33.13(34)
	R_{Bragg} (%)	-	-	-	9.66
R_{wp} (%)		16.0	17.2	22.1	17.8
R_{exp} (%)		13.12	12.95	13.17	17.01
χ^2		1.50	1.76	2.83	1.1

Table A.1: Refined parameters and reliability factors in Rietveld analysis of powder XRD sample held at 800°C in air for varying duration.

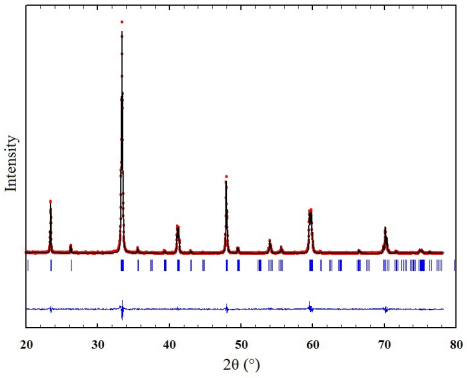
A.3 Thermal Analysis Data of $Pr_{1-x}CoO_{3-\delta}$



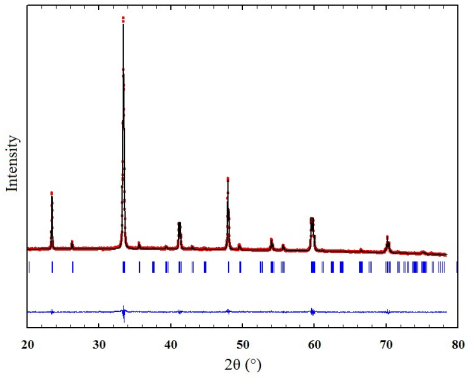
(a) DSC (b) TGA

Figure A.3: (a) DSC measurements of non-stoichiometric $Pr_{1-x}CoO_{3-\delta}$ samples, where x denotes A-site deficiency. (b) Example of a TGA measurement of an A-site deficient PCO where $x = 0.050$. An increase in mass can be seen past ∼400°C as oxygen is taken into the lattice.

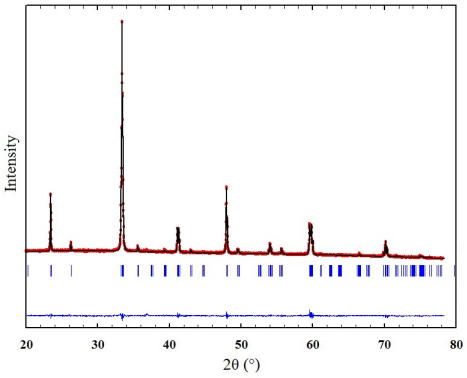
A.4 XRD Measurements and Rietveld Refinement of $Pr_{1-x}CoO_{3-\delta}$



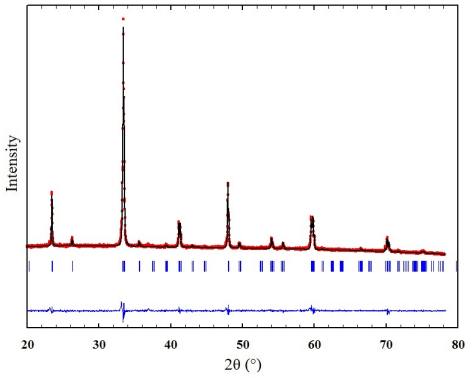
(a) $x = 0.000$



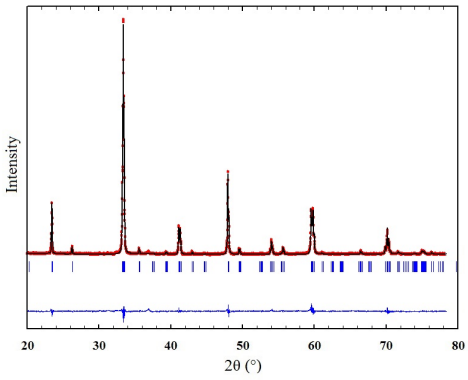
(b) $x = 0.025$



(c) $x = 0.050$



(d) $x = 0.075$

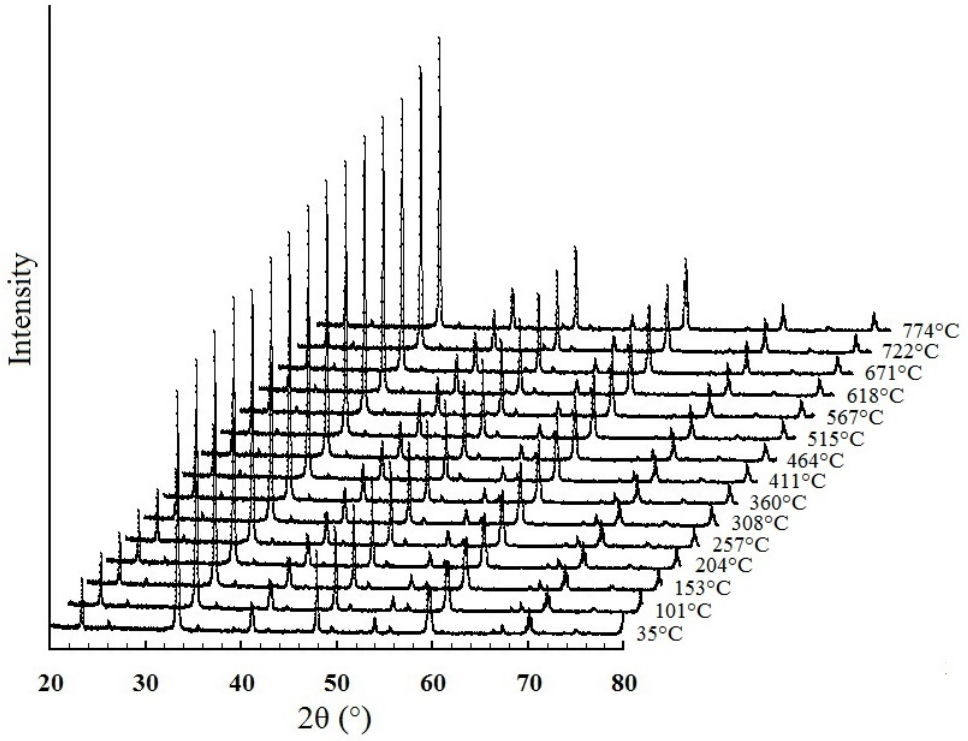


(e) $x = 0.100$

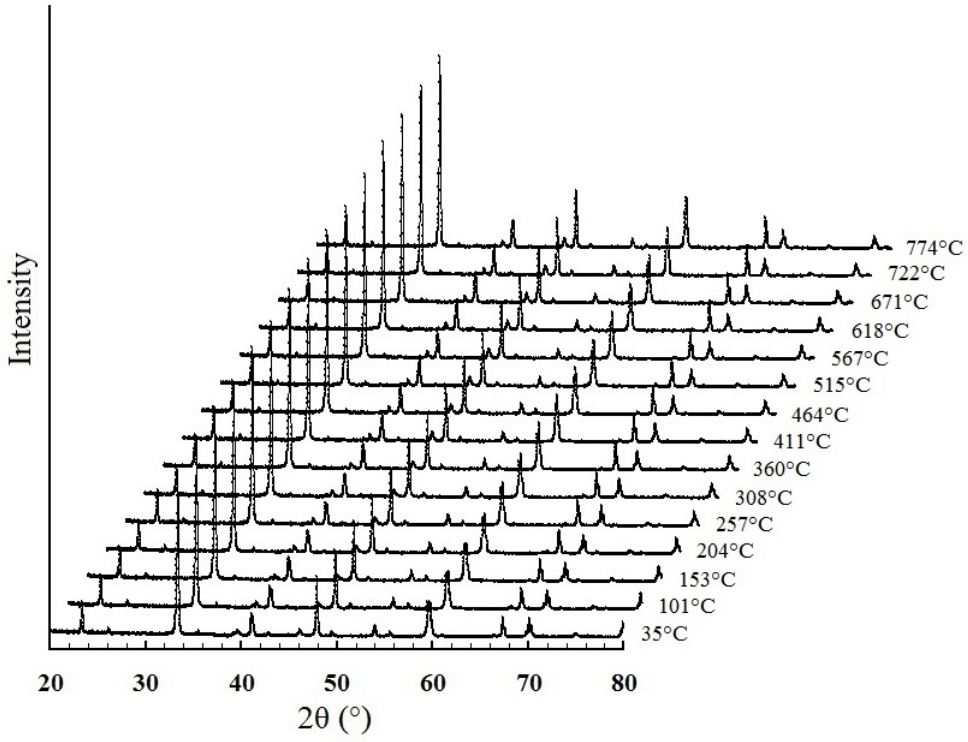
Figure A.4: XRD powder patterns of non-stoichiometric $Pr_{1-x}CoO_{3-\delta}$ samples, where x denotes A-site deficiency. The measured data is in red, the Rietveld fit in black, and the difference between them in blue. The Bragg reflections of $PrCoO_3$ is marked in blue.

	$x = 0.000$	$x = 0.025$	$x = 0.050$	$x = 0.075$	$x = 0.100$
a (Å)	5.3455(1)	5.3424(1)	5.3435(1)	5.3437(1)	5.3442(1)
b (Å)	7.5815(1)	7.5771(1)	7.5786(1)	7.5782(1)	7.5797(1)
c (Å)	5.3811(1)	5.3783(1)	5.3792(1)	5.3792(1)	5.3798(1)
Pr	4c	4c	4c	4c	4c
	(0.4714(2)	(0.4720(2)	(0.4713(2)	(0.4703(3)	(0.4710(2)
	0.25	0.25	0.25	0.25	0.25
	0.0041(6))	0.0021(9))	0.0035(8))	0.0037(13))	0.0021(8))
Co	4a(0 0 0)	4a(0 0 0)	4a(0 0 0)	4a(0 0 0)	4a(0 0 0)
Pr-O1	2.3565	2.3443	2.3525	2.3540	2.3453
	3.0373	3.0462	3.0394	3.0386	3.0473
	2.5193	2.5197	2.5176	2.5126	2.5152
	2.8817	2.8752	2.8805	2.8860	2.8814
Pr-O2	2.5905	2.5971	2.5913	2.5878	2.5952
	2.3859	2.3878	2.3867	2.3891	2.3915
	3.1358	3.1269	3.1331	3.1365	3.1307
	2.6734	2.6684	2.3708	2.6692	2.6672
Co-O1	1.9301	1.9290	1.9294	1.9293	1.9296
Co-O2	1.9313	1.9302	1.9306	1.9306	1.9308
	1.9311	1.9300	1.9303	1.9304	1.9308
Co-O1-Co angle (°)	158.231(3)	158.230(3)	158.231(2)	158.230(3)	158.231(3)
Co-O2-Co angle (°)	158.169(2)	158.169(2)	158.169(2)	158.170(2)	158.169(2)
R_{Bragg} (%)	3.65	4.90	5.03	6.52	4.88
R_{wp} (%)	9.77	8.37	8.79	13.3	10.9
R_{exp} (%)	7.27	6.44	7.04	8.69	7.91
χ^2	1.81	1.69	1.56	2.33	1.90

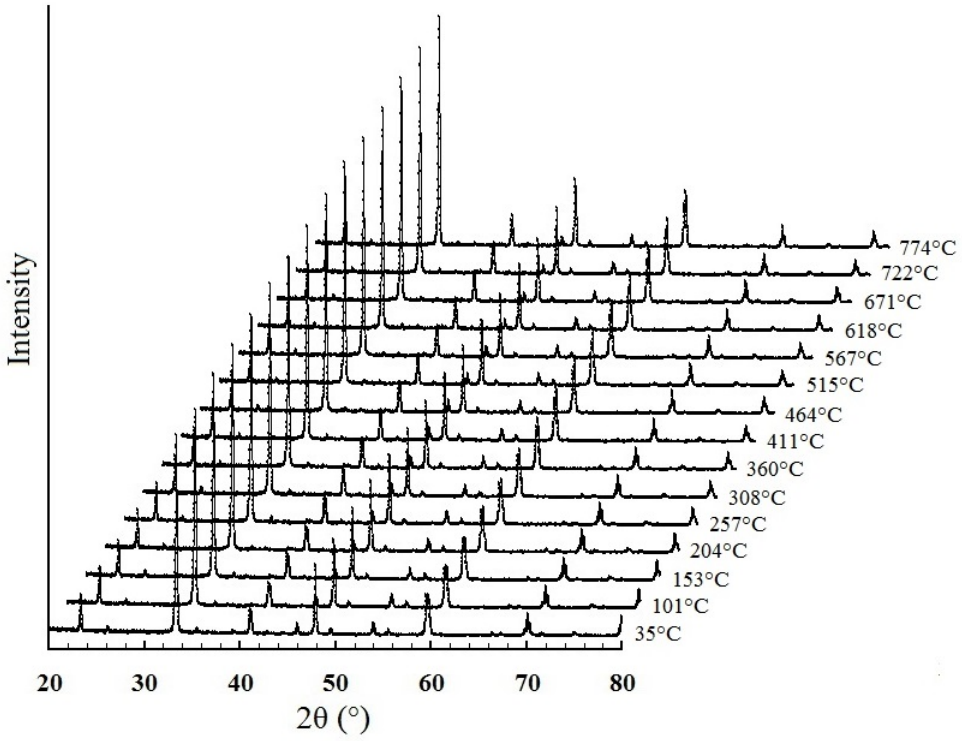
Table A.2: Refined parameters and reliability factors in Rietveld analysis of non-stoichiometric $Pr_{1-x}CoO_{3-\delta}$ samples, where x denotes A-site deficiency, using the *Pnma* spacegroup assignment. Oxygen positions were not refined but set to (0.5060, 0.25, 0.5675) and (0.2176, 0.0359, 0.2820) for O1 and O2, taken from [6].



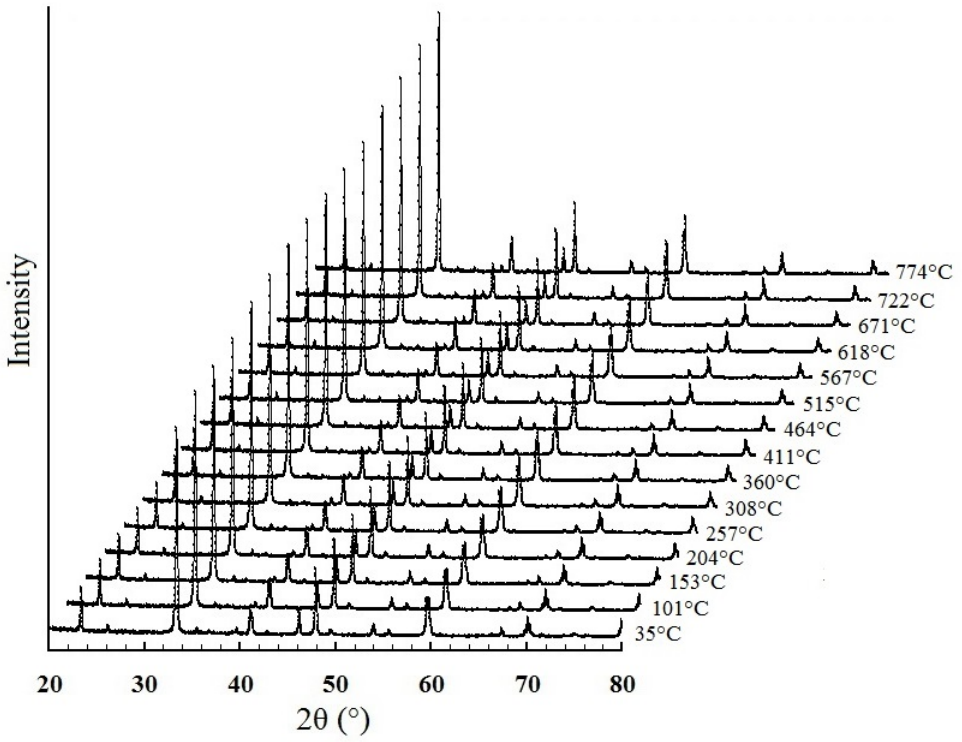
(a) $x = 0.000$



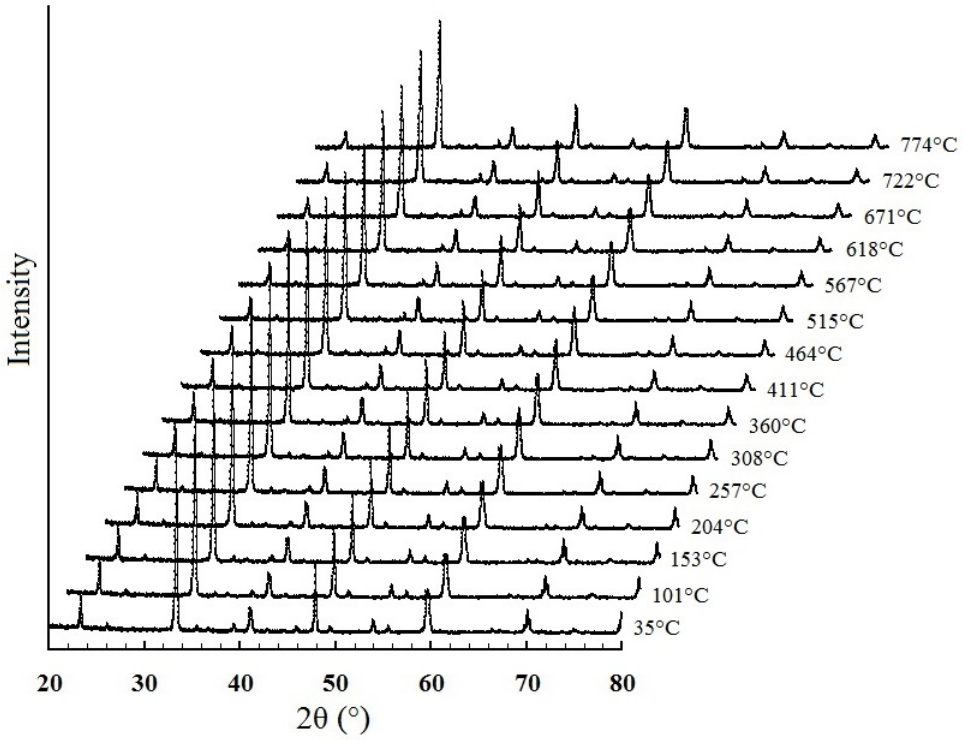
(b) $x = 0.025$



(c) $x = 0.050$



(d) $x = 0.075$



(e) $x = 0.100$

Figure A.5: In-situ HT-XRD powder patterns of non-stoichiometric $Pr_{1-x}CoO_{3-\delta}$ samples, where x denotes A-site deficiency, in air.

A.5 ZYGO Crater Depth Measurements of $Pr_{1-x}CoO_{3-\delta}$

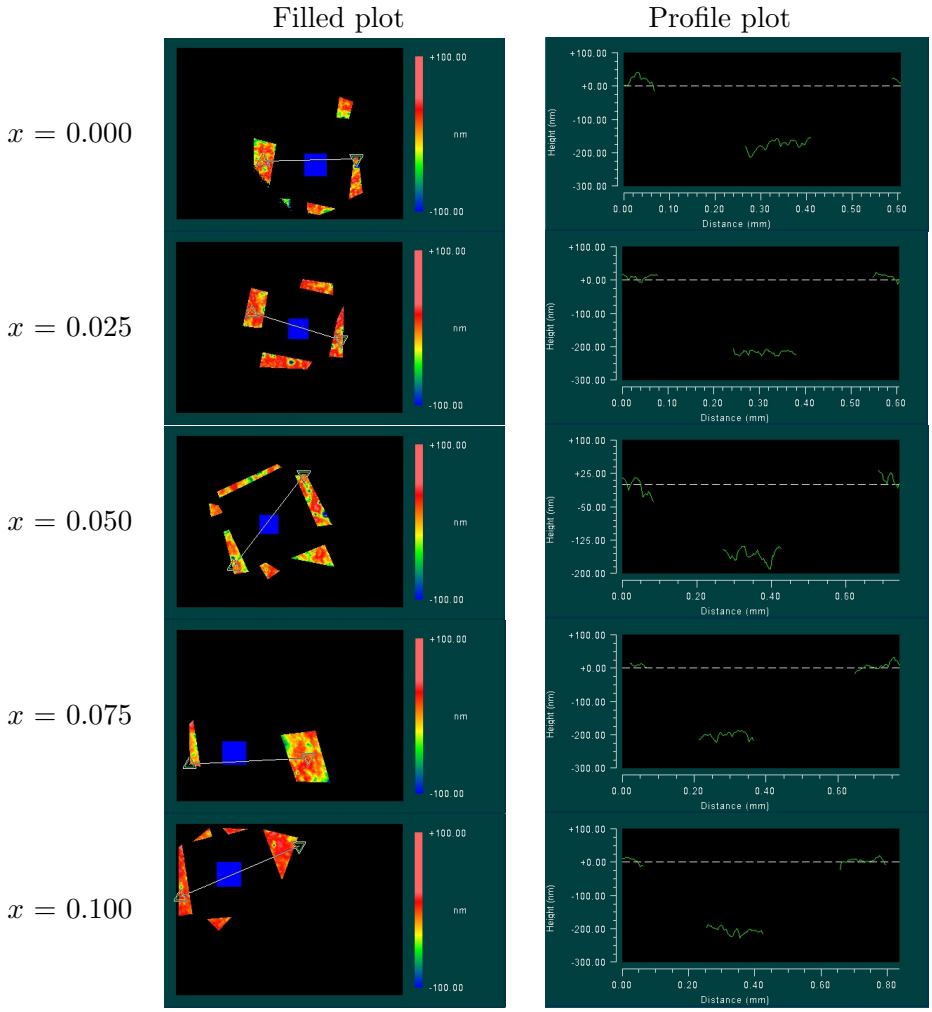
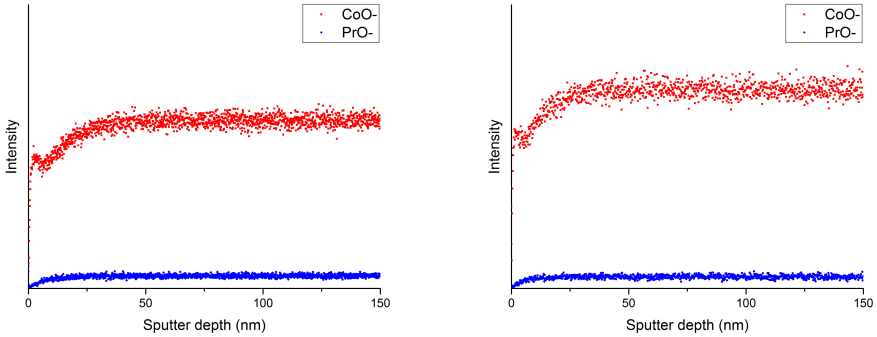


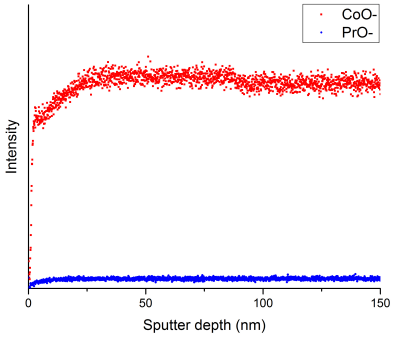
Table A.3: ZYGO crater depth measurement of non-stoichiometric $Pr_{1-x}CoO_{3-\delta}$ samples, where x denotes A-site deficiency.

A.6 ToF SIMS Profiles of $Pr_{1-x}CoO_{3-\delta}$ Bulk and Film Samples

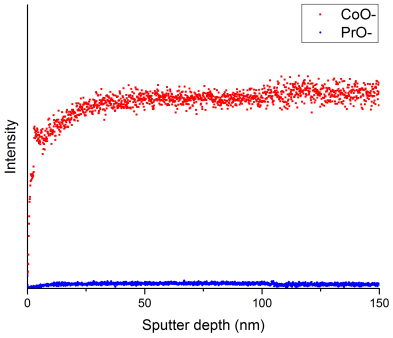


(a) x = 0.000

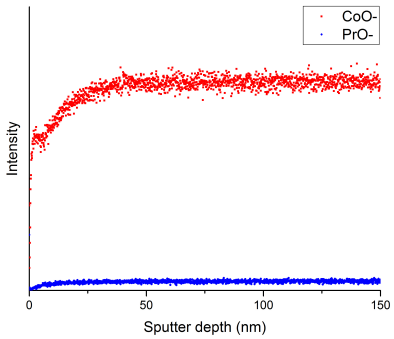
(b) x = 0.025



(c) x = 0.050

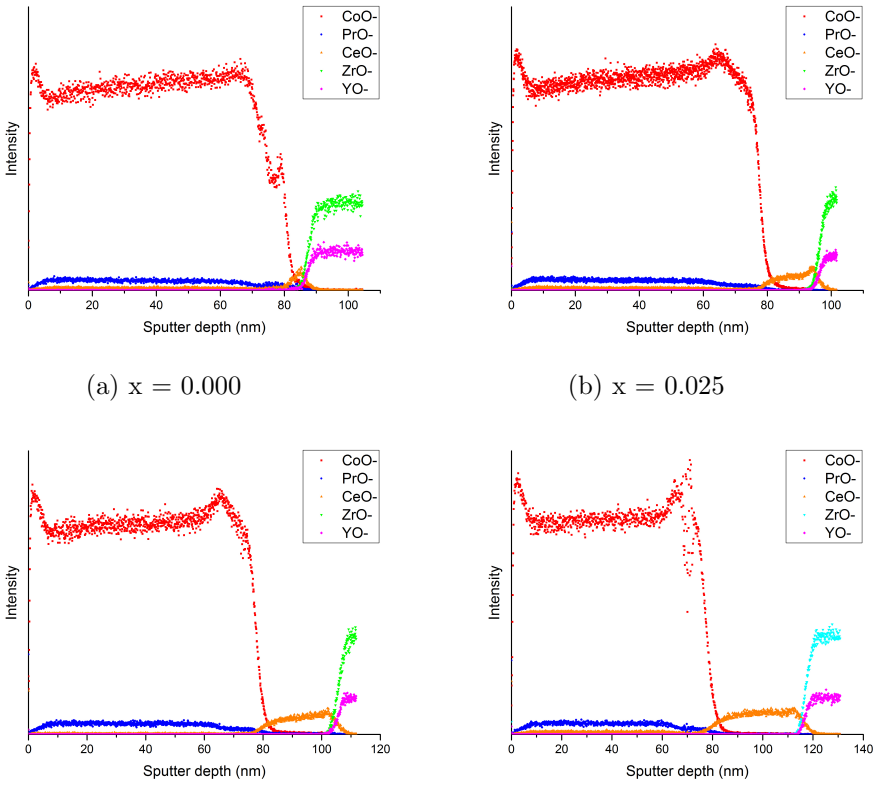


(d) x = 0.075



(e) x = 0.075

Figure A.6: SIMS depth profiles of non-stoichiometric $Pr_{1-x}CoO_{3-\delta}$ samples, where x denotes A-site deficiency. Normalized intensities detected are plotted against sputter depth.



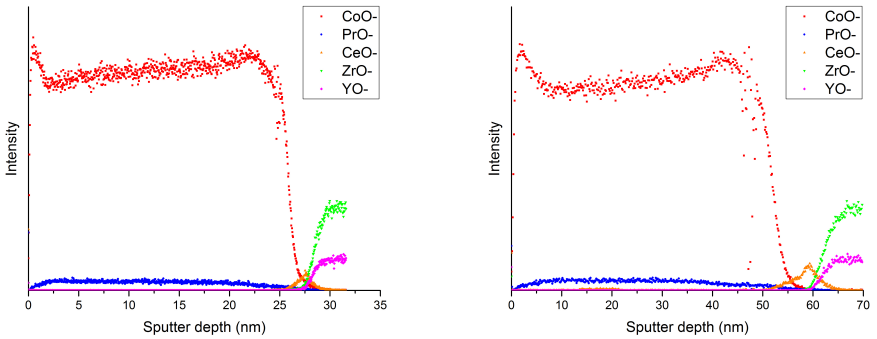
(a) x = 0.000

(b) x = 0.025

(c) x = 0.050

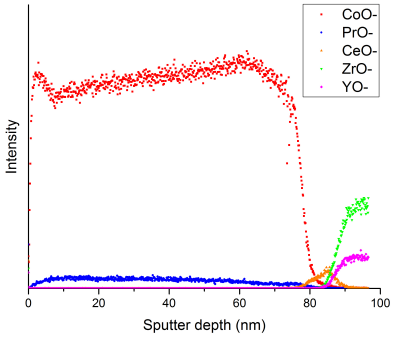
(d) x = 0.075

Figure A.7: SIMS depth profiles of PCO/CGO/YSZ films of sample set 2, where a range of pulses were used to deposit the $Ce_{0.8}Gd_0.2$ buffer layer. 3000 pulses used to deposit the $PrCoO_3$ film). Normalized intensities detected are plotted against sputter depth.

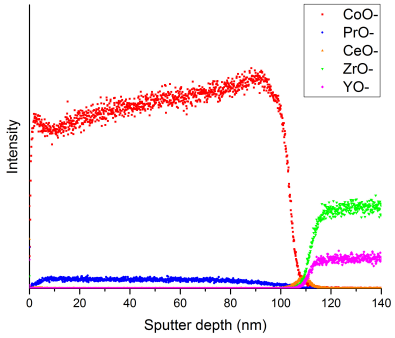


(a) 1000 pulses

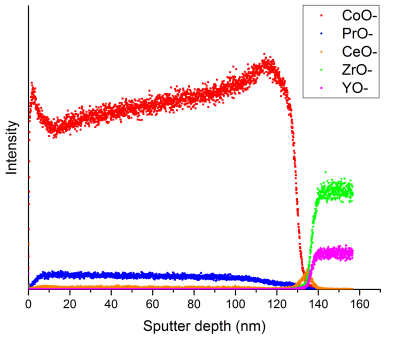
(b) 2000 pulses



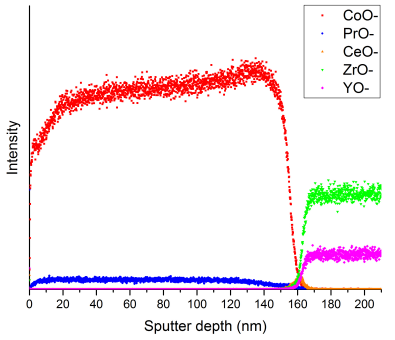
(c) 3000 pulses



(d) 4000 pulses



(e) 5000 pulses



(f) 6000 pulses

Figure A.8: SIMS depth profiles of PCO/CGO/YSZ films of sample set 3, where a range of pulses were used to deposit the $PrCoO_3$ film. 1000 pulses were used for the deposition of the $Ce_{0.8}Gd_0.2$ buffer layer. Normalized intensities detected are plotted against sputter depth.

Bibliography

[1] "EERE: Fuel Cell Technologies Office Home Page."

[2] a. Infortuna, a.S. Harvey, and L. Gauckler, "Microstructures of CGO and YSZ Thin Films by Pulsed Laser Deposition," *Advanced Functional Materials*, vol. 18, no. 1, pp. 127–135, 2008.

[3] K. Watanabe, H. Asakawa, G. Fujinawa, K. Ishikawa, and T. Nakamura, "Analysis of metal-semiconductor transition of $Ln_2NiO_{4+\delta}$ (La, Pr, Nd) by Rietveld refinement," *X-sen Bunseki no Shinpo*, vol. 29, pp. 137–152, 1998.

[4] B. Matović, J. Pantić, M. Prekajski, N. Stanković, D. Bučevac, T. Minović, and M. Čebela, "Synthesis and characterization of Pr_6O_{11} nanopowders," *Ceramics International*, vol. 39, no. 3, pp. 3151–3155, 2013.

[5] Z. Zhang and M. Greenblatt, "Synthesis, Structure, and Properties of $Ln_4Ni_3O_{10-\delta}$ (Ln = La, Pr, and Nd)," *Journal of Solid State Chemistry*, vol. 117, no. 2, pp. 236–246, 1995.

[6] H. Brinks, H. Fjellvåg, A. Kjekshus, and B. Hauback, "Structure and Magnetism of $Pr_{1-x}Sr_xCoO_{3-\delta}$," *Journal of Solid State Chemistry*, vol. 147, no. 2, pp. 464–477, 1999.

[7] G. J. la O', S.-J. Ahn, E. Crumlin, Y. Orikasa, M. D. Biegalski, H. M. Christen, and Y. Shao-Horn, "Catalytic activity enhancement for oxygen reduction on epitaxial perovskite thin films for solid-oxide fuel cells.," *Angewandte Chemie (International ed. in English)*, vol. 49, no. 31, pp. 5344–7, 2010.

[8] E. J. Crumlin, E. Mutoro, Z. Liu, M. E. Grass, M. D. Biegalski, Y.-L. Lee, D. Morgan, H. M. Christen, H. Bluhm, and Y. Shao-Horn, "Surface strontium enrichment on highly active perovskites for oxygen electrocatalysis in solid oxide fuel cells," *Energy & Environmental Science*, vol. 5, no. 3, p. 6081, 2012.

[9] R. D. Shannon, "Revised effective ionic radii and systematic studies of interatomic distances in halides and chalcogenides," *Acta Crystallographica Section A*, vol. 32, no. 5, pp. 751–767, 1976.

[10] D. Killoran, "The Effective Duration of a Linear Slow-Cool," *Journal of The Electrochemical Society*, vol. 109, no. 2, pp. 7–8, 1962.

[11] R. A. De Souza, J. A. Kilner, and J. F. Walker, "SIMS study of oxygen tracer diffusion and surface exchange in $La_{0.8}Sr_{0.2}MnO_{3+\delta}$," *Materials Letters*, vol. 43, no. 1, pp. 43–52, 2000.

[12] K. Huang and John B. Goodenough, *Solid oxide fuel cell technology Principles, performance and operations*. 2009.

[13] M. M. Mench, *Fuel Cell Engines*. John Wiley & Sons, 2008.

[14] "MIT Chemical Engineering Lecture Notes: Tafel Plot," 2013.

[15] R. P. O'Hayre, *Fuel cell fundamentals*. John Wiley & Sons, 2006.

[16] D. J. L. Brett, A. Atkinson, N. P. Brandon, S. J. Skinner, R. M. Ormerod, B. C. H. Steele, S. P. Jiang, S. H. Chan, B. C. H. Steele, M. Q. Minh, M. Yano, A. Tomita, M. Sano, T. Hibino, J. B. Goodenough, K. C. Wincewicz, J. S. Cooper, B. C. H. Steele, B. C. H. Steele, M. Mogensen, N. M. Sammes, G. A. Tompsett, V. V. Kharton, F. M. Figueiedo, L. Navarro, E. N. Naumovich, A. V. Kovalevsky, A. A. Yaremchenko, A. P. Viskup, A. Carneiro, F. M. B. Marques, J. R. Frade, S. Wang, H. Inaba, H. Tagawa, M. Dokiya, T. Hashimoto, M. Godickemeier, K. Sasaki, L. J. Gauckler, I. Riess, T. Ishihara, H. Matsuda, Y. Takata, H. Iwahara, H. Uchida, K. Ono, K. Ogaki, H. Iwahara, E. Kendrick, M. S. Islam, P. R. Slater, P. Lacorre, F. Goutenoire, O. Bohnke, R. Retoux, Y. Laligant, J. E. H. Sansom, J. R. Tolchard, M. S. Islam, D. Apperley, P. R. Slater, H. Yoshioka, S. Tanase, S. P. Jiang, S. H. Chan, N. P. Brandon, D. J. Brett, A. Atkinson, S. Barnett, R. J. Gorte, J. T. S. Irvine, A. J. Mcevoy, M. Mogensen, S. C. Singhal, J. Vohs, D. J. L. Brett, A. Atkinson, D. Cumming, E. Ramirez-Cabrera, R. Rudkin, N. P. Brandon, S. McIntosh, R. J. Gorte, S. Tao, J. T. S. Irvine, J. C. Ruiz-Morales, J. Canales-Vázquez, C. Savaniu, D. Marrero-López, W. Zhou, J. T. S. Irvine, J. M. Ralph, A. C. Schoeler, M. Krumpelt, S. J. Skinner, J. W. Fergus, J. W. Fergus, M. Gong, X. Liu, J. Trembly, C. Johnson, S. C. Singhal, D. J. L. Brett, P. Aguiar, N. P. Brandon, R. Bull, R. C. Galloway, G. W. Hayes, K. Lillie, C. Mellors, C. Smith, A. R. Tilley, D. J. L. Brett, P. Aguiar, N. P. Brandon, H. I. Onovwiona, V. I. Ugursal, A. D. Hawkes, P. Aguiar, C. A. Hernandez-Aramburo, M. A. Leach, N. P. Brandon, T. C. Green, and C. S. Adjiman, "Intermediate temperature solid oxide fuel cells," *Chemical Society Reviews*, vol. 37, no. 8, p. 1568, 2008.

[17] J. Richter, P. Holtappels, T. Graule, T. Nakamura, and L. J. Gauckler, "Materials design for perovskite SOFC cathodes," *Monatshefte für Chemie - Chemical Monthly*, vol. 140, no. 9, pp. 985–999, 2009.

[18] T. Ishihara, ed., *Perovskite Oxide for Solid Oxide Fuel Cells*. Fuel Cells and Hydrogen Energy, Boston, MA: Springer US, 2009.

[19] P. Garcia-Fernandez, J. Aramburu, M. Barriuso, and M. Moreno, "Key Role of Covalent Bonding in Octahedral Tilting in Perovskites," *The Journal of Physical Chemistry Letters*, vol. 1, no. 3, pp. 647–651, 2010.

[20] A. Tarancón, M. Burriel, J. Santiso, S. J. Skinner, and J. A. Kilner, "Advances in layered oxide cathodes for intermediate temperature solid oxide fuel cells," *Journal of Materials Chemistry*, vol. 20, no. 19, p. 3799, 2010.

[21] M. S. Islam, M. Cherry, and C. R. a. Catlow, "Oxygen Diffusion in $LaMnO_3$ and $LaCoO_3$ Perovskite-Type Oxides: A Molecular Dynamics Study," *Journal of Solid State Chemistry*, vol. 124, no. 2, pp. 230–237, 1996.

[22] S. B. Adler, "Factors Governing Oxygen Reduction in Solid Oxide Fuel Cell Cathodes," *Chemical Reviews*, vol. 104, no. 10, pp. 4791–4844, 2004.

[23] Y. Takeda, "Cathodic Polarization Phenomena of Perovskite Oxide Electrodes with Stabilized Zirconia," *Journal of The Electrochemical Society*, vol. 134, no. 11, p. 2656, 1987.

[24] J. Fleig, "On the width of the electrochemically active region in mixed conducting solid oxide fuel cell cathodes," *Journal of Power Sources*, vol. 105, no. 2, pp. 228–238, 2002.

[25] J. Fleig, "Solid Oxide Fuel Cell Cathodes: Polarization Mechanisms and Modeling of the Electrochemical Performance," *Annual Review of Materials Research*, vol. 33, no. 1, pp. 361–382, 2003.

[26] M. Sase, F. Hermes, K. Yashiro, K. Sato, J. Mizusaki, T. Kawada, N. Sakai, and H. Yokokawa, "Enhancement of Oxygen Surface Exchange at the Hetero-interface of (La,Sr)CoO_3/(La,Sr)$_2CoO_4$ with PLD-Layered Films," *Journal of The Electrochemical Society*, vol. 155, no. 8, p. B793, 2008.

[27] E. J. Crumlin, E. Mutoro, S.-J. Ahn, G. J. la O', D. N. Leonard, A. Borisevich, M. D. Biegalski, H. M. Christen, and Y. Shao-Horn, "Oxygen Reduction Kinetics Enhancement on a Heterostructured Oxide Surface for Solid Oxide Fuel Cells," *The Journal of Physical Chemistry Letters*, vol. 1, no. 21, pp. 3149–3155, 2010.

[28] R. De Souza, "Oxygen transport in $La_{1-x}Sr_xMn_{1-y}Co_yO_{3\pm\delta}$ perovskites Part I. Oxygen tracer diffusion," *Solid State Ionics*, vol. 106, no. 3-4, pp. 175–187, 1998.

[29] E. Mutoro, E. J. Crumlin, M. D. Biegalski, H. M. Christen, and Y. Shao-Horn, "Enhanced oxygen reduction activity on surface-decorated perovskite thin films for solid oxide fuel cells," *Energy & Environmental Science*, vol. 4, no. 9, p. 3689, 2011.

[30] G. J. la O', S.-J. Ahn, E. Crumlin, Y. Orikasa, M. D. Biegalski, H. M. Christen, and Y. Shao-Horn, "Catalytic activity enhancement for oxygen reduction on epitaxial perovskite thin films for solid-oxide fuel cells.," *Angewandte Chemie (International ed. in English)*, vol. 49, no. 31, pp. 5344–7, 2010.

[31] J. Hayd, H. Yokokawa, and E. Ivers-Tiffee, "Hetero-Interfaces at Nanoscaled (La,Sr)$CoO_{3-\delta}$ Thin-Film Cathodes Enhancing Oxygen Surface-Exchange Properties," *Journal of the Electrochemical Society*, vol. 160, no. 4, pp. F351–F359, 2013.

[32] M. Sase, "Enhancement of oxygen exchange at the hetero interface of (La,Sr)CoO_3/(La,Sr)$_2CoO_4$ in composite ceramics," *Solid State Ionics*, vol. 178, no. 35-36, pp. 1843–1852, 2008.

[33] S. Adler, "Mechanism and kinetics of oxygen reduction on porous $La_{1x}Sr_xCoO_{3\delta}$ electrodes," *Solid State Ionics*, vol. 111, no. 1-2, pp. 125–134, 1998.

[34] T. Kawada, "Oxygen isotope exchange with a dense $La_{0.6}Sr_{0.4}CoO_{3-\delta}$ electrode on a $Ce_{0.9}Ca_{0.1}O_{1.9}$ electrolyte," *Solid State Ionics*, vol. 121, no. 1-4, pp. 271–279, 1999.

[35] R. Ganeshananthan and A. V. Virkar, "Measurement of Transport Properties by Conductivity Relaxation on Dense $La_{0.6}Sr_{0.4}CoO_{3-\delta}$ With and Without Porous Surface Layers," *Journal of The Electrochemical Society*, vol. 153, no. 12, p. A2181, 2006.

[36] A. Egger, E. Bucher, and W. Sitte, "Oxygen Exchange Kinetics of the IT-SOFC Cathode Material $Nd_2NiO_{4+\delta}$ and Comparison with $La_{0.6}Sr_{0.4}CoO_{3-\delta}$," *Journal of The Electrochemical Society*, vol. 158, no. 5, p. B573, 2011.

[37] A. Berenov, A. Atkinson, J. Kilner, E. Bucher, and W. Sitte, "Oxygen tracer diffusion and surface exchange kinetics in $La_{0.6}Sr_{0.4}CoO_{3\delta}$," *Solid State Ionics*, vol. 181, no. 17-18, pp. 819–826, 2010.

[38] J. Hayd, L. Dieterle, U. Guntow, D. Gerthsen, and E. Ivers-Tiffée, "Nanoscaled $La_{0.6}Sr_{0.4}CoO_{3-\delta}$ as intermediate temperature solid oxide fuel cell cathode: Microstructure and electrochemical performance," *Journal of Power Sources*, vol. 196, no. 17, pp. 7263–7270, 2011.

[39] M. SOGAARD, P. HENDRIKSEN, M. MOGENSEN, F. POULSEN, and E. SKOU, "Oxygen nonstoichiometry and transport properties of strontium substituted lanthanum cobaltite," *Solid State Ionics*, vol. 177, no. 37-38, pp. 3285–3296, 2006.

[40] M. N. R. Ashfold, F. Claeyssens, G. M. Fuge, and S. J. Henley, "Pulsed laser ablation and deposition of thin films," *Chemical Society Reviews*, vol. 33, no. 1, p. 23, 2004.

[41] K. Oura, M. Katayama, A. V. Zotov, V. G. Lifshits, and A. A. Saranin, *Surface Science, An Introduction*. Springer Berlin Heidelberg, 2003.

[42] E. Meyer, "Atomic force microscopy," *Progress in Surface Science*, vol. 41, no. 1, pp. 3–49, 1992.

[43] S. Speakman, "MIT Material Science Lecture Notes: Introduction to HRXRD," 2013.

[44] R. A. De Souza, J. Zehnpfenning, M. Martin, and J. Maier, "Determining oxygen isotope profiles in oxides with Time-of-Flight SIMS," *Solid State Ionics*, vol. 176, no. 15-16, pp. 1465–1471, 2005.

[45] M. Yashima, M. Enoki, T. Wakita, R. Ali, Y. Matsushita, F. Izumi, and T. Ishihara, "Structural Disorder and Diffusional Pathway of Oxide Ions in a Doped Pr_2NiO_4 - Based Mixed Conductor," *Journal of the American Chemical Society*, vol. 130, no. 9, pp. 2762–2763, 2008.

[46] J. Hyodo, S. Ida, J. A. Kilner, and T. Ishihara, "Electronic and oxide ion conductivity in $Pr_2Ni_{0.71}Cu_{0.24}Ga_{0.05}O_4/Ce_{0.8}Sm_{0.2}O_2$ laminated film," *Solid State Ionics*, vol. 230, no. C, pp. 16–20, 2013.

[47] P. Odier, C. Allançon, and J. Bassat, "Oxygen Exchange in $Pr_2NiO_{4=\delta}$ at High Temperature and Direct Formation of $Pr_4Ni_3O_{10-x}$," *Journal of Solid State Chemistry*, vol. 153, no. 2, pp. 381–385, 2000.

[48] A. V. Kovalevsky, V. V. Kharton, A. A. Yaremchenko, Y. V. Pivak, E. V. Tsipis, S. O. Yakovlev, A. A. Markov, E. N. Naumovich, and J. R. Frade, "Oxygen permeability, stability and electrochemical behavior of $Pr_2NiO_{4+\delta}$ based materials," *Journal of Electroceramics*, vol. 18, no. 3-4, pp. 205–218, 2007.

[49] L. Chen, C. L. Chen, X. Chen, W. Donner, S. W. Liu, Y. Lin, D. X. Huang, and A. J. Jacobson, "Electrical properties of a highly oriented, textured thin film of the ionic conductor Gd:$CeO_{2-\delta}$ on (001) MgO," *Applied Physics Letters*, vol. 83, p. 4737, d 2003.

[50] S. R. Bishop, K. L. Duncan, and E. D. Wachsman, "Surface and Bulk Defect Equilibria in Strontium-Doped Lanthanum Cobalt Iron Oxide," *Journal of The Electrochemical Society*, vol. 156, no. 10, p. B1242, 2009.

[51] S. R. Bishop, K. L. Duncan, and E. D. Wachsman, "Surface and bulk oxygen nonstoichiometry and bulk chemical expansion in gadolinium-doped cerium oxide," *Acta Materialia*, vol. 57, no. 12, pp. 3596–3605, 2009.

[52] G. Kostogloudis and C. Ftikos, "Properties of A-site-deficient $La_{0.6}Sr_{0.4}Co_{0.2}Fe_{0.8}O_{3-\delta}$ -based perovskite oxides," *Solid State Ionics*, vol. 126, no. 1-2, pp. 143–151, 1999.

[53] F. Mauvy, J. Bassat, E. Boehm, P. Dordor, J. Grenier, and J. Loup, "Chemical oxygen diffusion coefficient measurement by conductivity relaxation- correlation between tracer diffusion coefficient and chemical diffusion coefficient," *Journal of the European Ceramic Society*, vol. 24, no. 6, pp. 1265–1269, 2004.

[54] A. Tarancón, S. Skinner, and R. Chater, "Layered perovskites as promising cathodes for intermediate temperature solid oxide fuel cells," *Journal of Materials*, 2007.

[55] J. B. Goodenough, "Oxide-Ion Electrolytes," *Annual Review of Materials Research*, vol. 33, no. 1, pp. 91–128, 2003.

[56] A. Chroneos, B. Yildiz, A. Tarancón, D. Parfitt, and J. A. Kilner, "Oxygen diffusion in solid oxide fuel cell cathode and electrolyte materials: mechanistic insights from atomistic simulations," *Energy & Environmental Science*, vol. 4, no. 8, p. 2774, 2011.

[57] X. Zhang, D. Cherniak, and E. Watson, "Oxygen diffusion in titanite: lattice diffusion and fast-path diffusion in single crystals," *Chemical Geology*, 2006.

[58] X. Zhang, E. Watson, and D. Cherniak, "Oxygen self-diffusion fast-paths in titanite single crystals and a general method for deconvolving self-diffusion profiles with tails," *Geochimica et cosmochimica acta*, 2007.

[59] J. H. Joo and G. M. Choi, "Electrical conductivity of YSZ film grown by pulsed laser deposition," *Solid State Ionics*, vol. 177, no. 11, pp. 1053–1057, 2006.

[60] J. H. Joo and G. M. Choi, "Electrical conductivity of thin film ceria grown by pulsed laser deposition," *Journal of the European Ceramic Society*, vol. 27, no. 13-15, pp. 4273–4277, 2007.

[61] E. Kendrick, M. S. Islam, and P. R. Slater, "Developing apatites for solid oxide fuel cells: insight into structural, transport and doping properties," *Journal of Materials Chemistry*, vol. 17, no. 30, p. 3104, 2007.

[62] P. Lacorre, F. Goutenoire, O. Bohnke, R. Retoux, and Y. Laligant, "Designing fast oxide-ion conductors based on $La_2Mo_2O_9$," *Nature*, vol. 404, no. 6780, pp. 856–8, 2000.

[63] J.-W. Moon, H.-J. Hwang, M. Awano, and K. Maeda, "Preparation of NiOYSZ tubular support with radially aligned pore channels," *Materials Letters*, vol. 57, no. 8, pp. 1428–1434, 2003.

[64] C. Sun, R. Hui, and J. Roller, "Cathode materials for solid oxide fuel cells: a review," *Journal of Solid State Electrochemistry*, 2010.

[65] S. P. Jiang, Y. J. Leng, S. H. Chan, and K. A. Khor, "Development of (La,Sr)MnO_3-Based Cathodes for Intermediate Temperature Solid Oxide Fuel Cells," *Electrochemical and Solid-State Letters*, vol. 6, no. 4, p. A67, 2003.

[66] S. M. Haile, "Fuel cell materials and components," *Acta Materialia*, vol. 51, no. 19, pp. 5981–6000, 2003.

[67] H. Ullmann, N. Trofimenko, F. Tietz, D. Stöver, and A. Ahmad-Khanlou, "Correlation between thermal expansion and oxide ion transport in mixed conducting perovskite-type oxides for SOFC cathodes," *Solid State Ionics*, vol. 138, no. 1, pp. 79–90, 2000.

[68] Y. Teraoka, H. Zhang, K. Okamoto, and N. Yamazoe, "Mixed ionic-electronic conductivity of $La_{1-x}Sr_xCo_{1-y}Fe_yO_{3-\delta}$ perovskite-type oxides," *Materials Research Bulletin*, vol. 23, no. 1, pp. 51–58, 1988.

[69] M. Petitjean, G. Caboche, E. Siebert, L. Dessemond, and L.-C. Dufour, "$(La_{0.8}Sr_{0.2})(Mn_{1-y}Fe_y)O_{3\pm\delta}$ oxides for ITSOFC cathode materials?," *Journal of the European Ceramic Society*, vol. 25, no. 12, pp. 2651–2654, 2005.

[70] L. Tai, "Structure and electrical properties of $La_{1-x}Sr_xCo_{1-y}Fe_yO_3$. Part 2. The system $La_{1-x}Sr_xCo_{0.2}Fe_{0.8}O_3$," *Solid State Ionics*, vol. 76, no. 3-4, pp. 273–283, 1995.

[71] H. Tu, "$Ln_{0.4}Sr_{0.6}Co_{0.8}Fe_{0.2}O_{3-\delta}$ (Ln = La, Pr, Nd, Sm, Gd) for the electrode in solid oxide fuel cells," *Solid State Ionics*, vol. 117, no. 3-4, pp. 277–281, 1999.

[72] D. Waller, "The effect of thermal treatment on the resistance of LSCF electrodes on gadolinia doped ceria electrolytes," *Solid State Ionics*, vol. 86-88, no. null, pp. 767–772, 1996.

[73] E. Maguire, "Cathode materials for intermediate temperature SOFCs," *Solid State Ionics*, vol. 127, no. 3-4, pp. 329–335, 2000.

[74] L. Tai, "Structure and electrical properties of $La_{1-x}Sr_xCo_{1-y}Fe_yO_3$. Part 1. The system $La_{0.8}Sr_{0.2}Co_{1-y}Fe_yO_3$," *Solid State Ionics*, vol. 76, no. 3-4, pp. 259–271, 1995.

[75] Y. Matsuzaki and I. Yasuda, "Dependence of SOFC Cathode Degradation by Chromium-Containing Alloy on Compositions of Electrodes and Electrolytes," *Journal of The Electrochemical Society*, vol. 148, no. 2, p. A126, 2001.

[76] J. M. Ralph, J. A. Kilner, and B. C. H. Steele, "Improving Gd-Doped Ceria Electrolytes for Low Temperature Solid Oxide Fuel Cells," *MRS Proceedings*, vol. 575, p. 309, 1999.

[77] C. Wagner and W. Schottky, "Theory of ordered mixed phases," *Z. Phys. Chem B*, vol. 11, no. 2/3, pp. 163–210, 1930.

[78] J. Frenkel, "Über die Wärmebewegung in festen und flüssigen Körpern," *Zeitschrift für Physik*, vol. 35, no. 8-9, pp. 652–669, 1926.

[79] F. Kröger and H. Vink, "Relations between the Concentrations of Imperfections in Crystalline Solids," *Solid State Physics*, vol. 3, pp. 307–435, 1956.

[80] K. Huang, H. Y. Lee, and J. B. Goodenough, "Sr- and Ni-Doped $LaCoO_3$ and $LaFeO_3$ Perovskites," *Journal of The Electrochemical Society*, vol. 145, no. 9, p. 3220, 1998.

[81] A. N. Petrov, V. A. Cherepanov, O. F. Kononchuk, and L. Y. Gavrilova, "Oxygen nonstoichiometry of $La_{1-x}Sr_xCoO_{3-\delta}$ ($0 < x \leq 0.6$)," *Journal of Solid State Chemistry*, vol. 87, no. 1, pp. 69–76, 1990.

[82] J. Mizusaki, Y. Mima, S. Yamauchi, K. Fueki, and H. Tagawa, "Nonstoichiometry of the perovskite-type oxides $La_{1-x}Sr_xCoO_{3-\delta}$," *Journal of Solid State Chemistry*, vol. 80, no. 1, pp. 102–111, 1989.

[83] A. Mineshige, J. Izutsu, M. Nakamura, K. Nigaki, J. Abe, M. Kobune, S. Fujii, and T. Yazawa, "Introduction of A-site deficiency into $La_{0.6}Sr_{0.4}Co_{0.2}Fe_{0.8}O_{3-\delta}$ and its effect on structure and conductivity," *Solid State Ionics*, vol. 176, no. 11-12, pp. 1145–1149, 2005.

[84] T. Ishigaki, S. Yamauchi, J. Mizusaki, K. Fueki, and H. Tamura, "Tracer diffusion coefficient of oxide ions in $LaCoO_3$ single crystal," *Journal of Solid State Chemistry*, vol. 54, no. 1, pp. 100–107, 1984.

[85] R. De Souza, "Oxygen transport in $La_{1-x}Sr_xMn_{1-y}Co_yO_{3\pm\delta}$ perovskites Part I. Oxygen tracer diffusion," *Solid State Ionics*, vol. 106, no. 3-4, pp. 175–187, 1998.

[86] R. H. van Doorn, I. C. Fullarton, R. A. de Souza, J. A. Kilner, H. J. Bouwmeester, and A. J. Burggraaf, "Surface oxygen exchange of $La_{0.3}Sr_{0.7}CoO_{3-\delta}$," *Solid State Ionics*, 1997.

[87] M. Kim, J. Boku, H. Haneda, J. Tanaka, T. Mitsuhashi, and S. Shirasaki, "Self-diffusion of Oxygen in $La_{1-x}Sr_xFeO_{3-\delta}$," *J. Mater. Sci. Lett*, vol. Vol. 9, 1990.

[88] O. Muller and R. Roy, *The major ternary structural families*. Springer-Verlag, 1974.

[89] A. S. Bhalla, R. Guo, and R. Roy, "The perovskite structure - a review of its role in ceramic science and technology," *Materials Research Innovations*, vol. 4, no. 1, pp. 3–26, 2000.

[90] R. S. Roth, "Classification of Perovskite and Other $AB0_3$," *Journal of Research of the National Bureau of Standards*, vol. 58, no. 2, pp. 75–88, 1957.

[91] N. Kimizuka and T. Katsura, "The standard free energy of formation of $YbFe_2O_4$, $Yb_2Fe_3O_7$, $YbFeO_3$, and $Yb_3Fe_5O_{12}$ at 1200°C," *Journal of Solid State Chemistry*, vol. 15, no. 2, pp. 151–157, 1975.

[92] N. Katsura, T., Kitayama, K., Sugihara, T., Kimizuka, "Thermochemical Properties of Lanthanoid-Iron-Perovskite at High Temperatures," *Bulletin of the Chemical Society of Japan*, vol. 48, pp. 1809–1811, 1975.

[93] C. Li, K. C. K. Soh, and P. Wu, "Formability of ABO_3 perovskites," *Journal of Alloys and Compounds*, vol. 372, no. 1-2, pp. 40–48, 2004.

[94] H. A. Jahn and E. Teller, "Stability of Polyatomic Molecules in Degenerate Electronic States. I. Orbital Degeneracy," *Proceedings of the Royal Society A: Mathematical, Physical and Engineering Sciences*, vol. 161, no. 905, pp. 220–235, 1937.

[95] Y. Tokura and N. Nagaosa, "Orbital physics in transition-metal oxides," *Science*, 2000.

[96] M. Johnsson and P. Lemmens, "Crystallography and chemistry of perovskites," *Handbook of magnetism and*, 2007.

[97] M. W. Lufaso and P. M. Woodward, "Jahn-Teller distortions, cation ordering and octahedral tilting in perovskites.," *Acta crystallographica. Section B, Structural science*, vol. 60, no. Pt 1, pp. 10–20, 2004.

[98] S. B. Wilkins, P. D. Spencer, P. D. Hatton, S. P. Collins, M. D. Roper, D. Prabhakaran, and A. T. Boothroyd, "Direct Observation of Orbital Ordering in $La_{0.5}Sr_{1.5}MnO_4$ Using Soft X-ray Diffraction," *Physical Review Letters*, vol. 91, no. 16, p. 167205, 2003.

[99] P. Odier, M. Leblanc, and J. Choisnet, "Structural characterization of an orthorhombic form of La_2NiO_4," *Materials Research Bulletin*, vol. 21, no. 7, pp. 787–796, 1986.

[100] K. Ishikawa, K. Metoki, and H. Miyamoto, "Orthorhombicorthorhombic phase transitions in $Nd_2NiO_{4+\delta}$ ($0.067 \ \delta \leq 0.224$)," *Journal of Solid State Chemistry*, vol. 182, no. 8, pp. 2096–2103, 2009.

[101] C. Allancon, J. Rordiguez-Carvajal, M. T. Fernandez-Diaz, P. Odier, J. M. Bassat, J. P. Loup, and J. L. Martinez, "Crystal structure of the high temperature phase of oxidised $Pr_2NiO_{4+\delta}$," *Zeitschrift für Physik. B, Condensed matter*, vol. 100, no. 1, pp. 85–90, 1996.

[102] V. Voronin, I. Berger, V. Cherepanov, L. Gavrilova, A. Petrov, A. Ancharov, B. Tolochko, and S. Nikitenko, "Neutron diffraction, synchrotron radiation and EXAFS spectroscopy study of crystal structure peculiarities of the lanthanum nickelates $La_{n+1}Ni_nO_y$ (n = 1,2,3)," *Nuclear Instruments and Methods in Physics Research Section A: Accelerators, Spectrometers, Detectors and Associated Equipment*, vol. 470, no. 1-2, pp. 202–209, 2001.

[103] P. G. Shewmon, *Diffusion in solids*. Minerals, Metals & Materials Society, 1989.

[104] T. Ishigaki, S. Yamauchi, K. Kishio, J. Mizusaki, and K. Fueki, "Diffusion of oxide ion vacancies in perovskite-type oxides," *Journal of Solid State Chemistry*, vol. 73, no. 1, pp. 179–187, 1988.

[105] J. Crank, *The Mathematics of Diffusion*. Oxford University Press, 2nd ed., 1975.

[106] R. De Souza and J. Kilner, "Oxygen transport in $La_{1-x}Sr_xMn_{1-y}Co_yO_{3\pm\delta}$ perovskites: Part II. Oxygen surface exchange," *Solid State Ionics*, vol. 126, no. 1, pp. 153–161, 1999.

[107] J. Kilner, "Surface exchange of oxygen in mixed conducting perovskite oxides," *Solid State Ionics*, vol. 86-88, no. null, pp. 703–709, 1996.

[108] J. A. Kilner, J. T. S. Irvine, W. Vielstich, H. A. Gasteiger, and H. Yokokawa, *Handbook of Fuel CellsAdvances in Electrocatalysis, Materials, Diagnostics and Durability*. John Wiley & Sons, 2009.

[109] H. He, X. Huang, and L. Chen, "The effects of dopant valence on the structure and electrical conductivity of $LaInO_3$," *Electrochimica Acta*, vol. 46, no. 18, pp. 2871–2877, 2001.

[110] J. E. ten Elshof, "Oxygen Exchange and Diffusion Coefficients of Strontium-Doped Lanthanum Ferrites by Electrical Conductivity Relaxation," *Journal of The Electrochemical Society*, vol. 144, no. 3, p. 1060, 1997.

[111] J. Lane, "Oxygen transport in $La_{0.6}Sr_{0.4}Co_{0.2}Fe_{0.8}O_{3-\delta}$," *Solid State Ionics*, vol. 121, no. 1-4, pp. 201–208, 1999.

[112] F. Figueiredo, "Electrochemical permeability of $La_{1-x}Sr_xCoO_{3-\delta}$ materials," *Solid State Ionics*, vol. 111, no. 3-4, pp. 273–281, 1998.

[113] R. Bredesen, F. Mertins, and T. Norby, "Measurements of surface exchange kinetics and chemical diffusion in dense oxygen selective membranes," *Catalysis Today*, vol. 56, no. 1-3, pp. 315–324, 2000.

[114] R. Vandoorn, I. Fullarton, R. DeSouza, J. Kilner, H. Bouwmeester, and A. Burggraaf, "Surface oxygen exchange of LaSrCoO," *Solid State Ionics*, vol. 96, no. 1-2, pp. 1–7, 1997.

[115] H. Bouwmeester, H. Kruidhof, and A. Bruggraaf, "Importance of the surface exchange kinetics as rate limiting step in oxygen permeation through mixed-conducting oxides," *Solid State Ionics*, vol. 72, no. null, pp. 185–194, 1994.

[116] J. A. Kilner, B. C. H. Steele, and L. Ilkov, "Oxygen self-diffusion studies using negative-ion secondary ion mass spectrometry (SIMS)," *Solid State Ionics*, vol. 12, no. C, pp. 89–97, 1984.

[117] S. Diethelm, "Simultaneous Determination of Chemical Diffusion and Surface Exchange Coefficients of Oxygen by the Potential Step Technique," *Journal of The Electrochemical Society*, vol. 146, no. 7, p. 2606, 1999.

[118] I. Yasuda, "Precise Determination of the Chemical Diffusion Coefficient of Calcium-Doped Lanthanum Chromites by Means of Electrical Conductivity Relaxation," *Journal of The Electrochemical Society*, vol. 141, no. 5, p. 1268, 1994.

[119] M. Cherry, M. Islam, and C. Catlow, "Oxygen Ion Migration in Perovskite-Type Oxides," *Journal of Solid State Chemistry*, vol. 118, no. 1, pp. 125–132, 1995.

[120] R. Cook and A. Sammells, "On the systematic selection of perovskite solid electrolytes for intermediate temperature fuel cells," *Solid State Ionics*, vol. 45, no. 3-4, pp. 311–321, 1991.

[121] A. Sammells, R. Cook, J. Wwhite, J. Osborne, and R. Macduff, "Rational selection of advanced solid electrolytes for intermediate temperature fuel cells," *Solid State Ionics*, vol. 52, no. 1-3, pp. 111–123, 1992.

[122] M. Mogensen, D. Lybye, N. Bonanos, P. Hendriksen, and F. Poulsen, "Factors controlling the oxide ion conductivity of fluorite and perovskite structured oxides," *Solid State Ionics*, vol. 174, no. 1-4, pp. 279–286, 2004.

[123] A. Bogicevic and C. Wolverton, "Nature and strength of defect interactions in cubic stabilized zirconia," *Physical Review B*, vol. 67, no. 2, p. 024106, 2003.

[124] H. Mehrer, *Diffusion in Solids*. Berlin Heidelberg: Springer, 2007.

[125] W. D. Kingery, H. K. Bowen, and D. R. Uhlmann, *Introduction to Ceramics*. New York: Wiley, 1976.

[126] Y.-m. Chiang, D. P. Birnie, and W. D. Kingery, *Physical ceramics*. J. Wiley, 1997.

[127] T. Ishigaki, S. Yamauchi, J. Mizusaki, K. Fueki, and H. Tamura, "Tracer diffusion coefficient of oxide ions in $LaCoO_3$ single crystal," *Journal of Solid State Chemistry*, vol. 54, no. 1, pp. 100–107, 1984.

[128] A. Bielanski and J. Haber, *Oxygen in catalysis*. M. Dekker, 1991.

[129] M. Misono and M. Nitadori, T., Ichiki, T., Misono, *Adsorption and Catalysis on Oxide Surfaces*. Amsterdam: Elsevier, 1985.

[130] M. M. Kuklja, E. A. Kotomin, R. Merkle, Y. A. Mastrikov, and J. Maier, "Combined theoretical and experimental analysis of processes determining cathode performance in solid oxide fuel cells," *Physical Chemistry Chemical Physics*, vol. 15, no. 15, p. 5443, 2013.

[131] C. L. Bull and P. F. McMillan, "Raman scattering study and electrical properties characterization of elpasolite perovskites $Ln_2(BB)O_6$ (Ln=La, Sm...Gd and B,B=Ni, Co, Mn)," *Journal of Solid State Chemistry*, vol. 177, no. 7, pp. 2323–2328, 2004.

[132] J. C. Boivin and G. Mairesse, "Recent Material Developments in Fast Oxide Ion Conductors," *Chemistry of Materials*, vol. 10, no. 10, pp. 2870–2888, 1998.

[133] E. J. Opila and H. L. Tuller, "Thermogravimetric Analysis and Defect Models of the Oxygen Nonstoichiometry in $La_{2-x}Sr_xCuO_{4-y}$," *Journal of the American Ceramic Society*, vol. 77, no. 10, pp. 2727–2737, 1994.

[134] M. S. D. Read, M. S. Islam, F. King, and F. E. Hancock, "Defect Chemistry of $La_2Ni_{1-x}M_xO_4$ (M = Mn, Fe, Co, Cu): Relevance to Catalytic Behavior," *The Journal of Physical Chemistry B*, vol. 103, no. 9, pp. 1558–1562, 1999.

[135] A. Cleave, J. Kilner, S. Skinner, S. Murphy, and R. Grimes, "Atomistic computer simulation of oxygen ion conduction mechanisms in La_2NiO_4," *Solid State Ionics*, vol. 179, no. 21-26, pp. 823–826, 2008.

[136] L. Minervini, R. W. Grimes, J. A. Kilner, and K. E. Sickafus, "Oxygen migration in $La_2NiO_{4+\delta}$," *Journal of Materials Chemistry*, vol. 10, no. 10, pp. 2349–2354, 2000.

[137] S. M. Aspera, M. Sakaue, T. D. K. Wungu, M. Alaydrus, T. P. T. Linh, H. Kasai, M. Nakanishi, and T. Ishihara, "Analysis of structural and electronic properties of Pr_2NiO_4 through first-principles calculations.," *Journal of physics. Condensed matter : an Institute of Physics journal*, vol. 24, no. 40, p. 405504, 2012.

[138] J. Jorgensen, B. Dabrowski, S. Pei, D. Richards, and D. Hinks, "Structure of the interstitial oxygen defect in $La_2NiO_{4+\delta}$," *Physical Review B*, vol. 40, no. 4, pp. 2187–2199, 1989.

[139] J. Bassat, "Anisotropic ionic transport properties in $La_2NiO_{4+\delta}$ single crystals," *Solid State Ionics*, vol. 167, no. 3-4, pp. 341–347, 2004.

[140] J. Claus, G. Borchardt, S. Weber, J.-M. Hiver, and S. Scherrer, "Combination of EBSP measurements and SIMS to study crystallographic orientation dependence of diffusivities in a polycrystalline material: oxygen tracer diffusion in $La_{2-x}Sr_xCuO_{4\pm\delta}$," *Materials Science and Engineering: B*, vol. 38, no. 3, pp. 251–257, 1996.

[141] C. Munnings, S. Skinner, G. Anow, P. Whitfield, and I. Davidson, "Oxygen transport in the LaNiCoO system," *Solid State Ionics*, vol. 176, no. 23-24, pp. 1895–1901, 2005.

[142] E. Boehm, J. Bassat, P. Dordor, F. Mauvy, J. Grenier, and P. Stevens, "Oxygen diffusion and transport properties in non-stoichiometric LnNiO oxides," *Solid State Ionics*, vol. 176, no. 37-38, pp. 2717–2725, 2005.

[143] T. Wagner and M. O'keeffe, "Bond lengths and valences in aluminates with the magnetoplumbite and β-alumina structures," *Journal of Solid State Chemistry*, vol. 73, no. 1, pp. 211–216, 1988.

[144] I. D. Brown, *The Chemical Bond in Inorganic Chemistry: The Bond Valence Model*. Oxford University Press, Incorporated, 2006.

[145] N. L. Allan and W. C. Mackrodt, "Oxygen ion migration in La_2CuO_4," *Philosophical Magazine A*, vol. 64, no. 5, pp. 1129–1132, 1991.

[146] G. Mazo, "The molecular dynamics study of oxygen mobility in $La_{2-x}Sr_xCuO_{4+\delta}$," *Solid State Ionics*, vol. 175, no. 1-4, pp. 371–374, 2004.

[147] A. K. Ivanov-Shits, G. N. Mazo, S. N. Savvin, S. N. Putilin, and A. S. Samokhin, "Prediction of transport properties of new functional materials based on lanthanum-strontium cuprates: Molecular mechanics calculations," *Russian Journal of Electrochemistry*, vol. 44, no. 12, pp. 1359–1365, 2009.

[148] S. Miyoshi, T. Furuno, O. Sangoanruang, H. Matsumoto, and T. Ishihara, "Mixed Conductivity and Oxygen Permeability of Doped Pr_2NiO_4- Based Oxides," *Journal of The Electrochemical Society*, vol. 154, no. 1, p. B57, 2007.

[149] J. L. Routbort, S. J. Rothman, B. K. Flandermeyer, L. J. Nowicki, and J. E. Baker, "Oxygen diffusion in $La_{2-x}Sr_xCuO_{4-y}$," *Journal of Materials Research*, vol. 3, no. 01, pp. 116–121, 2011.

[150] D. Parfitt, A. Chroneos, J. A. Kilner, and R. W. Grimes, "Molecular dynamics study of oxygen diffusion in $Pr_2NiO_{4+\delta}$," *Physical chemistry chemical physics : PCCP*, vol. 12, no. 25, pp. 6834–6, 2010.

[151] A. Kushima, S. Yip, and B. Yildiz, "Competing strain effects in reactivity of $LaCoO_3$ with oxygen," *Physical Review B*, vol. 82, no. 11, p. 115435, 2010.

[152] F. Hund, "No Title," *Zeits. f. Physik*, p. 657, 1926.

[153] F. Hund, "Zur Deutung der Molekelspektren," *Zeitschrift für Physik*, vol. 40, no. 10, pp. 742–764, 1927.

[154] R. S. Mulliken, "The Assignment of Quantum Numbers for Electrons in Molecules. I," *Physical Review*, vol. 32, no. 2, pp. 186–222, 1928.

[155] R. S. Mulliken, "Electronic structures of polyatomic molecules and valence," *Physical Review*, vol. 40, no. 1, pp. 55–62, 1932.

[156] M. Yashima, N. Sirikanda, and T. Ishihara, "Crystal Structure, Diffusion Path, and Oxygen Permeability of a Pr_2NiO_4-Based Mixed Conductor $(Pr_{0.9}La_{0.1})_2(Ni_{0.74}Cu_{0.21}Ga_{0.05})O_{4+\delta}$," *Journal of the American Chemical Society*, vol. 132, no. 7, pp. 2385–2392, 2010.

[157] A. Mineshige, M. Kobune, S. Fujii, Z. Ogumi, M. Inaba, T. Yao, and K. Kikuchi, "MetalInsulator Transition and Crystal Structure of $La_{1-x}Sr_xCoO_3$ as Functions of Sr-Content, Temperature, and Oxygen Partial Pressure," *Journal of Solid State Chemistry*, vol. 142, no. 2, pp. 374–381, 1999.

[158] H. W. Eng, P. W. Barnes, B. M. Auer, and P. M. Woodward, "Investigations of the electronic structure of d0 transition metal oxides belonging to the perovskite family," *Journal of Solid State Chemistry*, vol. 175, no. 1, pp. 94–109, 2003.

[159] M. Duczmal and L. Pawlak, "Magnetic properties and crystal field effects in $TlLnX_2$ compounds (X = S, Se, Te)," *Journal of Alloys and Compounds*, vol. 262-263, pp. 316–319, 1997.

[160] P. M. Raccah and J. B. Goodenough, "First-Order Localized-Electron to Collective-Electron Transition in $LaCoO_3$," *Physical Review*, vol. 155, no. 3, pp. 932–943, 1967.

[161] A. Mineshige, M. Inaba, T. Yao, Z. Ogumi, K. Kikuchi, and M. Kawase, "Crystal Structure and MetalInsulator Transition of $La_{1-x}Sr_xCoO_3$," *Journal of Solid State Chemistry*, vol. 121, no. 2, pp. 423–429, 1996.

[162] G. Kostogloudis, "Crystal structure, thermal and electrical properties of $Pr_{1-x}Sr_xCoO_{3-\delta}$ (x=0, 0.15, 0.3, 0.4, 0.5) perovskite oxides," *Solid State Ionics*, vol. 106, no. 3-4, pp. 207–218, 1998.

[163] J. Zaanen, G. A. Sawatzky, and J. W. Allen, "Band gaps and electronic structure of transition-metal compounds," *Physical Review Letters*, vol. 55, no. 4, pp. 418–421, 1985.

[164] A. M. Glazer and IUCr, "The classification of tilted octahedra in perovskites," *Acta Crystallographica Section B Structural Crystallography and Crystal Chemistry*, vol. 28, no. 11, pp. 3384–3392, 1972.

[165] K. Knight, "Structural phase transitions, oxygen vacancy ordering and protonation in doped $BaCeO_3$: results from time-of-flight neutron powder diffraction investigations," *Solid State Ionics*, vol. 145, no. 1, pp. 275–294, 2001.

[166] P. M. Woodward, "Octahedral Tilting in Perovskites. I. Geometrical Considerations," *Acta Crystallographica Section B Structural Science*, vol. 53, no. 1, pp. 32–43, 1997.

[167] A. N. Grundy, B. Hallstedt, and L. J. Gauckler, "Assessment of the LaSrMnO system," *Calphad*, vol. 28, no. 2, pp. 191–201, 2004.

[168] S. B. Adler, "Chemical Expansivity of Electrochemical Ceramics," *Journal of the American Ceramic Society*, vol. 84, no. 9, pp. 2117–2119, 2004.

[169] H. Ding, A. V. Virkar, M. Liu, and F. Liu, "Suppression of Sr surface segregation in $La_{1-x}Sr_xCo_{1-y}Fe_yO_{3-\delta}$: a first principles study," *Phys. Chem. Chem. Phys.*, vol. 15, no. 2, pp. 489–496, 2013.

[170] Y. Kimura, T. Kushi, S.-i. Hashimoto, K. Amezawa, and T. Kawada, "Influences of Temperature and Oxygen Partial Pressure on Mechanical Properties of $La_{0.6}Sr_{0.4}Co_{1-y}Fe_yO_{3-\delta}$," *Journal of the American Ceramic Society*, vol. 95, no. 8, pp. 2608–2613, 2012.

[171] D. Lee, A. Grimaud, E. J. Crumlin, K. Mezghani, M. A. Habib, Z. Feng, W. T. Hong, M. D. Biegalski, H. M. Christen, and Y. Shao-Horn, "Strain Influence on the Oxygen Electrocatalysis of the (100)-Oriented Epitaxial $La_2NiO_{4+\delta}$ Thin Films at Elevated Temperatures," *The Journal of Physical Chemistry C*, vol. 117, no. 37, pp. 18789–18795, 2013.

[172] P. H. Larsen, P. V. Hendriksen, and M. Mogensen, "Dimensional stability and defect chemistry of doped lanthanum chromites," *Journal of thermal analysis*, vol. 49, no. 3, pp. 1263–1275, 1997.

[173] S. Bishop, D. Marrocchelli, C. Chatzichristodoulou, N. Perry, M. Mogensen, H. Tuller, and E. Wachsman, "Chemical Expansion: Implications for Electrochemical Energy Storage and Conversion Devices," *Annual Review of Materials Research*, vol. 44, no. 1, pp. 205–239, 2014.

[174] D.-J. Kim, "Lattice Parameters, Ionic Conductivities, and Solubility Limits in Fluorite-Structure MO_2 Oxide [M = Hf^{4+}, Zr^{4+}, Ce^{4+}, Th^{4+}, U^{4+}] Solid Solutions," *Journal of the American Ceramic Society*, vol. 72, no. 8, pp. 1415–1421, 1989.

[175] J. Hong, S. J. Hong, and A. V. Virkar, "Lattice Parameters and Densities of Rare-Earth Oxide Doped Ceria Electrolytes," *Journal of the American Ceramic Society*, vol. 78, no. 2, pp. 433–439, 1995.

[176] D. Marrocchelli, S. R. Bishop, H. L. Tuller, G. W. Watson, and B. Yildiz, "Charge localization increases chemical expansion in cerium-based oxides," *Physical Chemistry Chemical Physics*, vol. 14, no. 35, p. 12070, 2012.

[177] D. Marrocchelli, S. R. Bishop, H. L. Tuller, and B. Yildiz, "Understanding chemical expansion in non-stoichiometric oxides: Ceria and zirconia case studies," *Advanced Functional Materials*, vol. 22, no. 9, pp. 1958–1965, 2012.

[178] D. Marrocchelli, S. R. Bishop, and J. Kilner, "Chemical expansion and its dependence on the host cation radius," *J. Mater. Chem. A*, vol. 1, no. 26, pp. 7673–7680, 2013.

[179] S. Omar and J. C. Nino, "Consistency in the chemical expansion of fluorites: A thermal revision of the doped ceria," *Acta Materialia*, vol. 61, no. 14, pp. 5406–5413, 2013.

[180] S. R. Bishop, K. L. Duncan, and E. D. Wachsman, "Defect equilibria and chemical expansion in non-stoichiometric undoped and gadolinium-doped cerium oxide," *Electrochimica Acta*, vol. 54, no. 5, pp. 1436–1443, 2009.

[181] H. Inaba, "Ceria-based solid electrolytes," *Solid State Ionics*, vol. 83, no. 1-2, pp. 1–16, 1996.

[182] L. Q. Jiang, J. K. Guo, H. B. Liu, M. Zhu, X. Zhou, P. Wu, and C. H. Li, "Prediction of lattice constant in cubic perovskites," *J. Phys. Chem. Soli.*, vol. 67, no. 7, p. 1531, 2006.

[183] R. L. Moreira and A. Dias, "Comment on "Prediction of lattice constant in cubic perovskites"," *Journal of Physics and Chemistry of Solids*, vol. 68, no. 8, pp. 1617–1622, 2007.

[184] R. Ubic and G. Subodh, "The prediction of lattice constants in orthorhombic perovskites," *Journal of Alloys and Compounds*, vol. 488, no. 1, pp. 374–379, 2009.

[185] A. S. Verma and V. K. Jindal, "Lattice constant of cubic perovskites," *Journal of Alloys and Compounds*, vol. 485, no. 1-2, pp. 514–518, 2009.

[186] D. Y. Wang, "Cathodic and Anodic Polarization Phenomena at Platinum Electrodes with Doped CeO_2 as Electrolyte," *Journal of The Electrochemical Society*, vol. 126, no. 7, p. 1155, 1979.

[187] M. Godickemeier, "Electrochemical Characteristics of Cathodes in Solid Oxide Fuel Cells Based on Ceria Electrolytes," *Journal of The Electrochemical Society*, vol. 144, no. 5, p. 1635, 1997.

[188] H. Hu, "Interfacial Polarization Characteristics of Pt-$BaCe_{0.8}Gd_{0.2}O_3$-Pt Cells at Intermediate Temperatures," *Journal of The Electrochemical Society*, vol. 144, no. 10, p. 3561, 1997.

[189] H. Okamoto, G. Kawamura, and T. Kudo, "Study of oxygen adsorption on platinum through observation of exchange current in a solid electrolyte concentration cell," *Electrochimica Acta*, vol. 28, no. 3, pp. 379–382, 1983.

[190] J. Bauerle, "Study of solid electrolyte polarization by a complex admittance method," *Journal of Physics and Chemistry of Solids*, vol. 30, no. 12, pp. 2657–2670, 1969.

[191] E. J. L. Schouler, "Electrocatalysis and Inductive Effects at the Gas, Pt/Stabilized Zirconia Interface," *Journal of The Electrochemical Society*, vol. 134, no. 5, p. 1045, 1987.

[192] J. Van Herle and A. McEvoy, "Oxygen diffusion through silver cathodes for solid oxide fuel cells," *Journal of Physics and Chemistry of Solids*, vol. 55, no. 4, pp. 339–347, 1994.

[193] M. J. Verkerk, "Oxygen Transfer on Substituted ZrO_2, Bi_2O_3, and CeO_2 Electrolytes with Platinum Electrodes," *Journal of The Electrochemical Society*, vol. 130, no. 1, p. 78, 1983.

[194] J. Mizusaki, "Electrode reaction at Pt, $O_{2(g)}$/stabilized zirconia interfaces. Part I: Theoretical consideration of reaction model," *Solid State Ionics*, vol. 22, no. 4, pp. 313–322, 1987.

[195] C. Schwandt, "Kinetics of Oxygen, Platinum/Stabilized Zirconia and Oxygen, Gold/Stabilized Zirconia Electrodes under Equilibrium Conditions," *Journal of The Electrochemical Society*, vol. 144, no. 11, p. 3728, 1997.

[196] T. Kenjo, "An Estimation of the Electrode-Electrolyte Contact Area by Linear Sweep Voltammetry in Pt/ZrO_2 Oxygen Electrodes," *Journal of The Electrochemical Society*, vol. 140, no. 8, p. 2151, 1993.

[197] K. Sasaki, "Pt-cermet cathode for reduced temperature SOFCs," *Solid State Ionics*, vol. 144, no. 3-4, pp. 223–232, 2001.

[198] A. Mitterdorfer, "Identification of the reaction mechanism of the Pt, $O_{2(g)}$/yttria-stabilized zirconia system Part II: Model implementation, parameter estimation, and validation," *Solid State Ionics*, vol. 117, no. 3-4, pp. 203–217, 1999.

[199] B. Luerßen, J. Janek, S. Günther, M. Kiskinova, and R. Imbihl, "Microspectroscopy at a moving reduction front in zirconia solid electrolyte," *Physical Chemistry Chemical Physics*, vol. 4, no. 12, pp. 2673–2679, 2002.

[200] O. Yamamoto, "Perovskite-type oxides as oxygen electrodes for high temperature oxide fuel cells," *Solid State Ionics*, vol. 22, no. 2-3, pp. 241–246, 1987.

[201] G. W. Coffey, L. R. Pederson, and P. C. Rieke, "Competition Between Bulk and Surface Pathways in Mixed Ionic Electronic Conducting Oxygen Electrodes," *Journal of The Electrochemical Society*, vol. 150, no. 8, p. A1139, 2003.

[202] A. Svensson, "A mathematical model of the porous SOFC cathode," *Solid State Ionics*, vol. 86-88, no. null, pp. 1211–1216, 1996.

[203] S. B. Adler, "Electrode Kinetics of Porous Mixed-Conducting Oxygen Electrodes," *Journal of The Electrochemical Society*, vol. 143, no. 11, p. 3554, 1996.

[204] A. Endo, "Cathodic reaction mechanism of dense $La_{0.6}Sr_{0.4}CoO_3$ and $La_{0.81}Sr_{0.09}MnO_3$ electrodes for solid oxide fuel cells," *Solid State Ionics*, vol. 135, no. 1-4, pp. 353–358, 2000.

[205] A. Ringuedé, "Oxygen reaction on strontium-doped lanthanum cobaltite dense electrodes at intermediate temperatures," *Solid State Ionics*, vol. 139, no. 3-4, pp. 167–177, 2001.

[206] Y. L. Yang, A. J. Jacobson, C. L. Chen, G. P. Luo, K. D. Ross, and C. W. Chu, "Oxygen exchange kinetics on a highly oriented $La_{0.5}Sr_{0.5}CoO_{3-\delta}$ thin film prepared by pulsed-laser deposition," *Applied Physics Letters*, vol. 79, no. 6, p. 776, 2001.

[207] C. A. Mims, "Oxygen Transport in Oxide Thin Film Structures Oriented $La_{0.5}Sr_{0.5}CoO_{3-\delta}$ on Single-Crystal Yttria-Stabilized Zirconia," *Electrochemical and Solid-State Letters*, vol. 3, no. 1, p. 59, 1999.

[208] H. Fukunaga, "Reaction model of dense $Sm_{0.5}Sr_{0.5}CoO_3$ as SOFC cathode," *Solid State Ionics*, vol. 132, pp. 279–285, jul 2000.

[209] Y. L. Yang, C. L. Chen, S. Y. Chen, C. W. Chu, and A. J. Jacobson, "Impedance Studies of Oxygen Exchange on Dense Thin Film Electrodes of $La_{0.5}Sr_{0.5}CoO_{3-\delta}$," *Journal of The Electrochemical Society*, vol. 147, no. 11, p. 4001, 2000.

[210] A. Esquirol, N. P. Brandon, J. A. Kilner, and M. Mogensen, "Electrochemical Characterization of $La_{0.6}Sr_{0.4}Co_{0.2}Fe_{0.8}O_3$ Cathodes for Intermediate-Temperature SOFCs," *Journal of The Electrochemical Society*, vol. 151, no. 11, p. A1847, 2004.

[211] S. Jiang, "A comparison of O_2 reduction reactions on porous (La,Sr)MnO_3 and (La,Sr)(Co,Fe)O_3 electrodes," *Solid State Ionics*, vol. 146, no. 1, pp. 1–22, 2002.

[212] M. Gong, R. S. Gemmen, D. S. Mebane, K. Gerdes, and X. Liu, "Simulation of Surface-Potential Driven ORR Kinetics on SOFC Cathode with Parallel Reaction Pathways," *Journal of the Electrochemical Society*, vol. 161, no. 3, pp. F344–F353, 2014.

[213] F. H. van Heuveln and H. J. M. Bouwmeester, "Electrode Properties of Sr-Doped $LaMnO_3$ on Yttria-Stabilized Zirconia," *Journal of The Electrochemical Society*, vol. 144, no. 1, p. 134, 1997.

[214] Y. Jiang, S. Wang, Y. Zhang, J. Yan, and W. Li, "Kinetic Study of the Formation of Oxygen Vacancy on Lanthanum Manganite Electrodes," *Journal of The Electrochemical Society*, vol. 145, no. 2, p. 373, 1998.

[215] V. Kharton, "Surface-limited oxygen transport and electrode properties of $La_2Ni_{0.8}Cu_{0.2}O_{4=\delta}$," *Solid State Ionics*, vol. 166, no. 3-4, pp. 327–337, 2004.

[216] V. Kharton, "Ionic transport in oxygen-hyperstoichiometric phases with K_2NiF_4-type structure," *Solid State Ionics*, vol. 143, no. 3-4, pp. 337–353, 2001.

[217] V. V. Kharton, "Ceramic Microstructure and Oxygen Permeability of $SrCo(Fe,M)O_{3-\delta}$ (M = Cu or Cr) Perovskite Membranes," *Journal of The Electrochemical Society*, vol. 145, no. 4, p. 1363, 1998.

[218] S. Skinner, "Oxygen diffusion and surface exchange in $La_{2-x}Sr_xNiO_{4+\delta}$," *Solid State Ionics*, vol. 135, no. 1-4, pp. 709–712, 2000.

[219] J. Lane, "Measuring oxygen diffusion and oxygen surface exchange by conductivity relaxation," *Solid State Ionics*, vol. 136-137, no. 1-2, pp. 997–1001, 2000.

[220] C. C. Kan, H. H. Kan, F. M. Van Assche, E. N. Armstrong, and E. D. Wachsman, "Investigating Oxygen Surface Exchange Kinetics of $La_{0.8}Sr_{0.2}MnO_{3-\delta}$ and $La_{0.6}Sr_{0.4}Co_{0.2}Fe_{0.8}O_{3-\delta}$ Using an Isotopic Tracer," *Journal of The Electrochemical Society*, vol. 155, no. 10, p. B985, 2008.

[221] Z. Shao and S. M. Haile, "A high-performance cathode for the next generation of solid-oxide fuel cells.," *Nature*, vol. 431, no. 7005, pp. 170–3, 2004.

[222] K. Yashiro, T. Nakamura, M. Sase, F. Hermes, K. Sato, T. Kawada, and J. Mizusaki, "Composite Cathode of Perovskite-Related Oxides, $(La,Sr)CoO_{3-\delta}/(La,Sr)_2CoO_{4-\delta}$, for Solid Oxide Fuel Cells," *Electrochemical and Solid-State Letters*, vol. 12, no. 9, p. B135, 2009.

[223] M. Sase, D. Ueno, K. Yashiro, A. Kaimai, T. Kawada, and J. Mizusaki, "Interfacial reaction and electrochemical properties of dense $(La,Sr)CoO_{3-\delta}$ cathode on YSZ (100)," *Journal of Physics and Chemistry of Solids*, vol. 66, no. 2-4, pp. 343–348, 2005.

[224] F. Morin, "The phase stability of $La_{0.5}Sr_{0.5}CoO_{3-\delta}$," *Solid State Ionics*, vol. 96, no. 3-4, pp. 129–139, 1997.

[225] V. A. Cherepanov, L. Y. Gavrilova, L. Y. Barkhatova, V. I. Voronin, M. V. Trifonova, and O. A. Bukhner, "Phase equilibria in the La-Me-Co-O (Me=Ca, Sr, Ba) systems," *Ionics*, vol. 4, no. 3-4, pp. 309–315, 1998.

[226] J. Crank, *The Mathematics of Diffusion*. Oxford University Press, 1979.

[227] E. J. Crumlin, S.-J. Ahn, D. Lee, E. Mutoro, M. D. Biegalski, H. M. Christen, and Y. Shao-Horn, "Oxygen Electrocatalysis on Epitaxial $La_{0.6}Sr_{0.4}CoO_{3-\delta}$ Perovskite Thin Films for Solid Oxide Fuel Cells," *Journal of the Electrochemical Society*, vol. 159, no. 7, pp. F219–F225, 2012.

[228] B. Yildiz, ""Stretching" the energy landscape of oxidesEffects on electrocatalysis and diffusion," *MRS Bulletin*, vol. 39, no. 02, pp. 147–156, 2014.

[229] M. Gsell, P. Jakob, and D. Menzel, "Effect of substrate strain on adsorption," *Science (New York, N.Y.)*, vol. 280, no. 5364, pp. 717–20, 1998.

[230] M. Mavrikakis, B. Hammer, and J. K. Nørskov, "Effect of Strain on the Reactivity of Metal Surfaces," *Physical Review Letters*, vol. 81, no. 13, pp. 2819–2822, 1998.

[231] M. Mavrikakis, P. Stoltze, and J. Nørskov, "Making gold less noble," *Catalysis Letters*, vol. 64, no. 2/4, pp. 101–106, 2000.

[232] B. Hammer and J. Nørskov, "Electronic factors determining the reactivity of metal surfaces," *Surface Science*, vol. 343, no. 3, pp. 211–220, 1995.

[233] Y. Xu and M. Mavrikakis, "Adsorption and dissociation of O_2 on Cu(111): thermochemistry, reaction barrier and the effect of strain," *Surface Science*, vol. 494, no. 2, pp. 131–144, 2001.

[234] Y. Xu and M. Mavrikakis, "Adsorption and Dissociation of O_2 on Gold Surfaces: Effect of Steps and Strain," *The Journal of Physical Chemistry B*, vol. 107, no. 35, pp. 9298–9307, 2003.

[235] J. Wintterlin, T. Zambelli, J. Trost, J. Greeley, and M. Mavrikakis, "Atomic-scale evidence for an enhanced catalytic reactivity of stretched surfaces," *Angewandte Chemie - International Edition*, vol. 42, no. 25, pp. 2850–2853, 2003.

[236] J. Greeley, W. P. Krekelberg, and M. Mavrikakis, "Strain-Induced Formation of Subsurface Species in Transition Metals," *Angewandte Chemie International Edition*, vol. 43, no. 33, pp. 4296–4300, 2004.

[237] L. Grabow, Y. Xu, and M. Mavrikakis, "Lattice strain effects on CO oxidation on Pt(111)," *Physical Chemistry Chemical Physics*, vol. 8, no. 29, p. 3369, 2006.

[238] P. Strasser, S. Koh, T. Anniyev, J. Greeley, K. More, C. Yu, Z. Liu, S. Kaya, D. Nordlund, H. Ogasawara, M. F. Toney, and A. Nilsson, "Lattice-strain control of the activity in dealloyed coreshell fuel cell catalysts," *Nature Chemistry*, vol. 2, no. 6, pp. 454–460, 2010.

[239] S. Akbulatov, Y. Tian, and R. Boulatov, "ForceReactivity Property of a Single Monomer Is Sufficient To Predict the Micromechanical Behavior of Its Polymer," *Journal of the American Chemical Society*, vol. 134, no. 18, pp. 7620–7623, 2012.

[240] S. L. Craig, "Mechanochemistry: A tour of force," *Nature*, vol. 487, no. 7406, pp. 176–177, 2012.

[241] Y. Kuru, D. Marrocchelli, S. R. Bishop, D. Chen, B. Yildiz, and H. L. Tuller, "Anomalous Chemical Expansion Behavior of $Pr_{0.2}Ce_{0.8}O_{2-\delta}$ Thin Films Grown by Pulsed Laser Deposition," *Journal of the Electrochemical Society*, vol. 159, no. 11, pp. F799–F803, 2012.

[242] A. D. Rata, A. Herklotz, K. Nenkov, L. Schultz, and K. Dörr, "Strain-Induced Insulator State and Giant Gauge Factor of $La_{0.7}Sr_{0.3}CoO_3$ Films," *Physical Review Letters*, vol. 100, no. 7, p. 076401, 2008.

[243] J. B. Goodenough and J.-S. Zhou, "Localized to Itinerant Electronic Transitions in Transition-Metal Oxides with the Perovskite Structure," *Chemistry of Materials*, vol. 10, no. 10, pp. 2980–2993, 1998.

[244] A. Herklotz, A. D. Rata, L. Schultz, and K. Dörr, "Reversible strain effect on the magnetization of $LaCoO_3$ films," *Physical Review B*, vol. 79, no. 9, p. 092409, 2009.

[245] D. Fuchs, E. Arac, C. Pinta, S. Schuppler, R. Schneider, and H. v. Löhneysen, "Tuning the magnetic properties of $LaCoO_3$ thin films by epitaxial strain," *Physical Review B*, vol. 77, no. 1, p. 014434, 2008.

[246] M. Kubicek, A. Limbeck, T. Fromling, H. Hutter, and J. Fleig, "Relationship between Cation Segregation and the Electrochemical Oxygen Reduction Kinetics of $La_{0.6}Sr_{0.4}CoO_{3-\delta}$ Thin Film Electrodes," *Journal of The Electrochemical Society*, vol. 158, no. 6, p. B727, 2011.

[247] W. C. Chueh and S. M. Haile, "Electrochemistry of Mixed Oxygen Ion and Electron Conducting Electrodes in Solid Electrolyte Cells," *Annual Review of Chemical and Biomolecular Engineering*, vol. 3, no. 1, pp. 313–341, 2012.

[248] J. Garcia-Barriocanal, A. Rivera-Calzada, M. Varela, Z. Sefrioui, E. Iborra, C. Leon, S. J. Pennycook, and J. Santamaria, "Colossal ionic conductivity at interfaces of epitaxial ZrO_2:Y_2O_3/$SrTiO_3$ heterostructures.," *Science (New York, N.Y.)*, vol. 321, no. 5889, pp. 676–80, 2008.

[249] A. Cavallaro, M. Burriel, J. Roqueta, A. Apostolidis, A. Bernardi, A. Tarancón, R. Srinivasan, S. N. Cook, H. L. Fraser, J. A. Kilner, D. W. McComb, and J. Santiso, "Electronic nature of the enhanced conductivity in YSZ-STO multilayers deposited by PLD," *Solid State Ionics*, vol. 181, no. 13, pp. 592–601, 2010.

[250] R. A. De Souza and A. H. H. Ramadan, "Ionic conduction in the $SrTiO_3$/YSZ/$SrTiO_3$ heterostructure," *Physical Chemistry Chemical Physics*, vol. 15, no. 13, p. 4505, 2013.

[251] J. L. Rupp, "Ionic diffusion as a matter of lattice-strain for electroceramic thin films," *Solid State Ionics*, vol. 207, pp. 1–13, 2012.

[252] Z. Cai, Y. Kuru, J. W. Han, Y. Chen, and B. Yildiz, "Surface Electronic Structure Transitions at High Temperature on Perovskite Oxides: The Case of Strained $La_{0.8}Sr_{0.2}CoO_3$ Thin Films," *Journal of the American Chemical Society*, vol. 133, no. 44, pp. 17696–17704, 2011.

[253] J. W. Han and B. Yildiz, "Enhanced one dimensional mobility of oxygen on strained $LaCoO_3$(001) surface," *Journal of Materials Chemistry*, vol. 21, no. 47, p. 18983, 2011.

[254] W. Donner, C. Chen, M. Liu, A. J. Jacobson, Y.-L. Lee, M. Gadre, and D. Morgan, "Epitaxial Strain-Induced Chemical Ordering in $La_{0.5}Sr_{0.5}CoO_{3-\delta}$ Films on $SrTiO_3$," *Chemistry of Materials*, vol. 23, no. 4, pp. 984–988, 2011.

[255] M. Kubicek, Z. Cai, W. Ma, B. Yildiz, H. Hutter, and J. Fleig, "Tensile lattice strain accelerates oxygen surface exchange and diffusion in $La_{1-x}Sr_xCoO_{3-\delta}$ thin films.," *ACS nano*, vol. 7, no. 4, pp. 3276–86, 2013.

[256] N. H. Behling, *Fuel cells current technology challenges and future research needs*. Elsevier, 2013.

[257] J. Di, M. Chen, C. Wang, J. Zheng, L. Fan, and B. Zhu, "Samarium doped ceria $(Li/Na)_2CO_3$ composite electrolyte and its electrochemical properties in low temperature solid oxide fuel cell," *Journal of Power Sources*, vol. 195, no. 15, pp. 4695–4699, 2010.

[258] R. Raza, X. Wang, Y. Ma, X. Liu, and B. Zhu, "Improved ceriacarbonate composite electrolytes," *International Journal of Hydrogen Energy*, vol. 35, no. 7, pp. 2684–2688, 2010.

[259] C. Xia, Y. Li, Y. Tian, Q. Liu, Y. Zhao, L. Jia, and Y. Li, "A high performance composite ionic conducting electrolyte for intermediate temperature fuel cell and evidence for ternary ionic conduction," *Journal of Power Sources*, vol. 188, no. 1, pp. 156–162, 2009.

[260] J. Huang, Z. Mao, Z. Liu, and C. Wang, "Development of novel low-temperature SOFCs with co-ionic conducting SDC-carbonate composite electrolytes," *Electrochemistry Communications*, vol. 9, no. 10, pp. 2601–2605, 2007.

[261] J. Huang, L. Yang, R. Gao, Z. Mao, and C. Wang, "A high-performance ceramic fuel cell with samarium doped ceriacarbonate composite electrolyte at low temperatures," *Electrochemistry Communications*, vol. 8, no. 5, pp. 785–789, 2006.

[262] B. Zhu, "Functional ceriasalt-composite materials for advanced ITSOFC applications," *Journal of Power Sources*, vol. 114, no. 1, pp. 1–9, 2003.

[263] B. Zhu, X. Yang, J. Xu, Z. Zhu, S. Ji, M. Sun, and J. Sun, "Innovative low temperature SOFCs and advanced materials," *Journal of Power Sources*, vol. 118, no. 1-2, pp. 47–53, 2003.

[264] T. T. Fister, D. D. Fong, J. A. Eastman, P. M. Baldo, M. J. Highland, P. H. Fuoss, K. R. Balasubramaniam, J. C. Meador, and P. A. Salvador, "In situ characterization of strontium surface segregation in epitaxial $La_{0.7}Sr_{0.3}MnO_3$ thin films as a function of oxygen partial pressure," *Applied Physics Letters*, vol. 93, p. 151904, oct 2008.

[265] D. Oh and D. Gostovic, "Mechanism of $La_{0.6}Sr_{0.4}Co_{0.2}Fe_{0.8}O_3$ cathode degradation," *Journal of Materials*, 2012.

[266] M. P. Pechini, "Method of Preparing Lead and Alkaline Earth Titanates and Niobate$ and Coating Method Using the Same To Form a Capacitor," 1967.

[267] L. A. Chick, L. R. Pederson, G. D. Maupin, J. L. Bates, L. E. Thomas, and G. J. Exarhos, "Glycine-nitrate combustion synthesis of oxide ceramic powders," *Materials Letters*, vol. 10, no. 1-2, pp. 6–12, 1990.

[268] R. Kelly and J. E. Rothenberg, "Laser sputtering," *Nuclear Instruments and Methods in Physics Research Section B: Beam Interactions with Materials and Atoms*, vol. 7-8, pp. 755–763, 1985.

[269] H.-U. Krebs, M. Weisheit, J. Faupel, E. Süske, T. Scharf, C. Fuhse, M. Störmer, K. Sturm, M. Seibt, H. Kijewski, D. Nelke, E. Panchenko, and M. Buback, *Pulsed Laser Deposition (PLD) – A Versatile Thin Film Technique*. Springer Berlin Heidelberg, jul 2003.

[270] B. Holzapfel, B. Roas, L. Schultz, P. Bauer, and G. Saemann-Ischenko, "Off-axis laser deposition of $YBa_2Cu_3O_{7-\delta}$ thin films," *Applied Physics Letters*, vol. 61, no. 26, p. 3178, 1992.

[271] I. Horcas, R. Fernandez, J. M. Gomez-Rodriguez, J. Colchero, J. Gomez-Herrero, and A. M. Baro, "WSXM: A software for scanning probe microscopy and a tool for nanotechnology," *Review of Scientific Instruments*, vol. 78, no. 1, p. 013705, 2007.

[272] K. C. A. Smith, C. W. Oatley, H. J. Zworykin V K, S. R. L, M. D, M. J. W. Holdgate H W, S. M, F. C, R. A, H. M. E. A, E. P, and H. S, "The scanning electron microscope and its fields of application," *British Journal of Applied Physics*, vol. 6, no. 11, pp. 391–399, 1955.

[273] C. Oatley, W. Nixon, and R. Pease, "Scanning Electron Microscopy," *Advances in Electronics and Electron Physics*, vol. 21, pp. 181–247, 1966.

[274] Oxford Instruments, *INCA Energy Operator Manual*, 2.1 ed., 2006.

[275] T. Degen, M. Sadki, E. Bron, U. König, and G. Nénert, "The HighScore suite," *Powder Diffraction*, vol. 29, no. December, pp. S13–S14, 2014.

[276] W. H. Bragg and W. L. Bragg, "The Reflection of X-rays by Crystals," *Proceedings of the Royal Society A: Mathematical, Physical and Engineering Sciences*, vol. 88, no. 605, pp. 428–438, 1913.

[277] A. Le Bail, H. Duroy, and J. Fourquet, "Ab-initio structure determination of $LiSbWO_6$ by X-ray powder diffraction," *Materials Research Bulletin*, vol. 23, no. 3, pp. 447–452, 1988.

[278] H. M. Rietveld, "A profile refinement method for nuclear and magnetic structures," *Journal of Applied Crystallography*, vol. 2, no. 2, pp. 65–71, 1969.

[279] J. Rodríguez-Carvajal, "FULLPROF: A Program for Rietveld Refinement and Pattern Matching Analysis," in *Abstracts of the Satellite Meeting on Powder Diffraction of the XV Congress of the IUCr,*, (Toulouse, France), p. p. 127, 1990.

[280] V. K. Pecharsky. and P. Y. Zavalij, *Fundamentals of powder diffraction and structural characterization of materials*, vol. 12. Boston, MA: Springer US, 2009.

[281] L. G. Parratt, "Surface Studies of Solids by Total Reflection of X-Rays," *Physical Review*, vol. 95, no. 2, pp. 359–369, 1954.

[282] T. C. Huang, R. Gilles, and G. Will, "Thin-film thickness and density determination from x-ray reflectivity data using a conventional power diffractometer," *Thin Solid Films*, vol. 230, no. 2, pp. 99–101, 1993.

[283] L. H. Van der Pauw, "A Method of Measuring Specific Resistivity and Hall Effect of Discs of Arbitrary Shape," *Phillips Res. Report*, vol. 1, p. 13, 1958.

[284] D. W. Koon, "Effect of contact size and placement, and of resistive inhomogeneities on van der Pauw measurements," *Review of Scientific Instruments*, vol. 60, no. 2, p. 271, 1989.

[285] R. Chwang, B. Smith, and C. Crowell, "Contact size effects on the van der Pauw method for resistivity and Hall coefficient measurement," *Solid-State Electronics*, vol. 17, no. 12, pp. 1217–1227, 1974.

[286] T. M. Baleshta and J. D. Keys, "Single Electrometer Method of Measuring Transport Properties of High-Resistivity Semiconductors," *American Journal of Physics*, vol. 36, no. 1, p. 23, 1968.

[287] A. Ramadan, R. Gould, and A. Ashour, "On the Van der Pauw method of resistivity measurements," *Thin Solid Films*, vol. 239, no. 2, pp. 272–275, 1994.

[288] J. C. Vickerman, *Surface Analysis The Principal Techniques*. Chichester, UK: John Wiley & Sons, Ltd, apr 2009.

[289] J. A. Alonso, M. J. Martinez-Lope, C. de la Calle, and V. Pomjakushin, "Preparation and structural study from neutron diffraction data of $RCoO_3$ (R = Pr, Tb, Dy, Ho, Er, Tm, Yb, Lu) perovskites," *Journal of Materials Chemistry*, vol. 16, no. 16, p. 1555, 2006.

[290] M. James, T. Tedesco, D. Cassidy, and R. Withers, "Oxygen vacancy ordering in strontium doped rare earth cobaltate perovskites $Ln_{1-x}Sr_xCoO_{3-\delta}$ (Ln=La, Pr and Nd; x > 0.60)," *Materials Research Bulletin*, vol. 40, no. 6, pp. 990–1000, 2005.

[291] L. Luo, H. Zhong, and X. Yang, "Oxidative performance and surface properties of Co-containing mixed oxides having the K_2MF_4 structure," *Journal of the Serbian Chemical Society*, vol. 69, no. 10, pp. 783–790, 2004.

[292] H. Zhong and X. Zeng, *Surface Properties and Catalytic Performance of $Pt/PrSrCoO_4$ Catalysts for NO Reduction by CO*. PhD thesis, Jinggangshan College, 2006.

[293] H. Zhong and X. Zeng, "Physicochemical properties and catalytic performance of $Pr_{2-x}Sr_xCoO_{4\pm y}$ mixed oxides for NO reduction by CO," *Kinetics and Catalysis*, vol. 47, no. 3, pp. 423–429, 2006.

[294] C. Allancon, A. Gontheirvassal, J. Bascat, J. Loup, and P. Odier, "Influence of oxygen on structural transitions in $Pr_2NiO_{4+\delta}$," *Solid State Ionics*, vol. 74, no. 3-4, pp. 239–248, 1994.

[295] R. Prakash, S. Kumar, C. G. Lee, and J. I. Song, "Low temperature Raman study of $PrCoO_3$ thin films on $LaAlO_3$ (100) substrates grown by pulsed laser deposition," *Journal of Central South University of Technology*, vol. 17, no. 6, pp. 1144–1147, 2010.

[296] R. Prakash, "Growth and study of $PrCoO_3$ thin films nanostructures deposited on various substrates," vol. 1, no. 1, pp. 1–4, 2013.

[297] V. V. Mehta, S. Bose, J. M. Iwata-Harms, E. Arenholz, C. Leighton, and Y. Suzuki, "Ferrimagnetism in $PrCoO_3$ epitaxial films," *Physical Review B*, vol. 87, no. 2, p. 020405, 2013.

[298] G. Brauer and H. Gradinger, "Über heterotype Mischphasen bei Seltenerdoxyden. I," *Zeitschrift für anorganische und allgemeine Chemie*, vol. 276, no. 5-6, pp. 209–226, 1954.

[299] S. H. Chung, Y. K, Kwon, Y. U, Byeon, "Synthesis structural and electrical characterizations of $Pr_{2-x}Ba_xNiO_{4+\delta}$," *Bulletin of the Korean Chemical Society*, vol. 16, no. 2, pp. 120–125, 1995.

[300] D. G. Lamas and N. E. Walsöe De Reca, "X-ray diffraction study of compositionally homogeneous, nanocrystalline yttria-doped zirconia powders," *Journal of Materials Science*, vol. 35, no. 22, pp. 5563–5567, 2000.

[301] D. L. D. L. Smith, *Thin-film deposition : principles and practice*. McGraw-Hill, 1995.

[302] R. Messier, "Revised structure zone model for thin film physical structure," *Journal of Vacuum Science & Technology A: Vacuum, Surfaces, and Films*, vol. 2, no. 2, p. 500, 1984.

[303] C. V. Thompson, "Structure Evolution During Processing of Polycrystalline Films," *Annual Review of Materials Science*, vol. 30, no. 1, pp. 159–190, 2000.

[304] I. Petrov, P. B. Barna, L. Hultman, and J. E. Greene, "Microstructural evolution during film growth," *Journal of Vacuum Science & Technology A: Vacuum, Surfaces, and Films*, vol. 21, no. 5, p. S117, 2003.

[305] M. Tillack, D. Blair, and S. Harilal, "The effect of ionization on cluster formation in laser ablation plumes," *Nanotechnology*, 2004.

[306] W. Marine, L. Patrone, B. Luk'yanchuk, and M. Sentis, "Strategy of nanocluster and nanostructure synthesis by conventional pulsed laser ablation," *Applied Surface Science*, vol. 154, pp. 345–352, 2000.

[307] A. Tsoga, A. Gupta, A. Naoumidis, and P. Nikolopoulos, "Gadolinia-doped ceria and yttria stabilized zirconia interfaces: regarding their application for SOFC technology," *Acta Materialia*, vol. 48, no. 18-19, pp. 4709–4714, 2000.

[308] M. SHIONO, K. KOBAYASHI, T. LANNGUYEN, K. HOSODA, T. KATO, K. OTA, and M. DOKIYA, "Effect of CeO_2 interlayer on ZrO_2 electrolyte/La(Sr)CoO_3 cathode for low-temperature SOFCs," *Solid State Ionics*, vol. 170, no. 1-2, pp. 1–7, 2004.

[309] T. Tsai and S. A. Barnett, "Increased solid-oxide fuel cell power density using interfacial ceria layers," *Solid State Ionics*, vol. 98, no. 3-4, pp. 191–196, 1997.

[310] D. Lee, Y.-L. Lee, W. T. Hong, M. D. Biegalski, D. Morgan, and Y. Shao-Horn, "Oxygen surface exchange kinetics and stability of $(La,Sr)_2CoO_{4\pm\delta}/La_{1-x}Sr_xMO_{3-\delta}$ (M = Co and Fe) hetero-interfaces at intermediate temperatures," *J. Mater. Chem. A*, vol. 3, no. 5, pp. 2144–2157, 2015.

[311] W. Ma, J. J. Kim, N. Tsvetkov, T. Daio, Y. Kuru, Z. Cai, Y. Chen, K. Sasaki, H. L. Tuller, and B. Yildiz, "Vertically aligned nanocomposite $La_{0.8}Sr_{0.2}CoO_3/(La_{0.5}Sr_{0.5})_2CoO_4$ cathodes electronic structure, surface chemistry and oxygen reduction kinetics," *J. Mater. Chem. A*, vol. 3, no. 1, pp. 207–219, 2015.

[312] K.-R. Lee, K. Ahn, Y.-C. Chung, J.-H. Lee, and H.-I. Yoo, "Lattice distortion effect on electrical properties of GDC thin films: Experimental evidence and computational simulation," *Solid State Ionics*, vol. 229, pp. 45–53, 2012.

[313] L. Chen, C. L. Chen, D. X. Huang, Y. Lin, X. Chen, and A. J. Jacobson, "High temperature electrical conductivity of epitaxial Gd-doped CeO2 thin films," *Solid State Ionics*, vol. 175, no. 1-4, pp. 103–106, 2004.

[314] T. Ishihara, K. Tominaga, J. Hyodo, and M. Matsuka, "Improved electrical conductivity in $Pr_2Ni(Cu,Ga)O_4$ film with nano thickness," *International Journal of Hydrogen Energy*, vol. 37, no. 9, pp. 8066–8072, 2012.

[315] J. Hyodo and T. Ishihara, "Electric Conductivity in Cu- and Ga-Doped Pr_2NiO_4 Nano Film Laminated with Sm-Doped CeO_2," *Meeting Abstracts*, vol. MA2012-02, no. 16, p. 1887, 2012.

[316] J. Schou, "Physical aspects of the pulsed laser deposition technique: The stoichiometric transfer of material from target to film," *Applied Surface Science*, vol. 255, no. 10, pp. 5191–5198, 2009.

[317] R. Eason and Wiley InterScience (Online service), *Pulsed laser deposition of thin films : applications-led growth of functional materials*. Wiley-Interscience, 2007.

[318] T. Venkatesan, X. D. Wu, A. Inam, and J. B. Wachtman, "Observation of two distinct components during pulsed laser deposition of high Tc superconducting films," *Applied Physics Letters*, vol. 52, no. 14, p. 1193, 1988.

[319] L. G. Coocia, G. C. Tyrrell, J. A. Kilner, D. Waller, R. J. Chater, and I. W. Boyd, "Pulsed laser deposition of novel materials for thin film solid oxide fuel cell applications: $Ce_{0.9}Gd_{0.1}O_{1.95}$, $La_{0.7}Sr_{0.3}CoO_y$ and $La_{0.7}Sr_{0.3}Co_{0.2}Fe_{0.8}O_y$," *Applied Surface Science*, vol. 96-98, pp. 795–801, 1996.

[320] H. Swanson, E. Tatge, and R. Fuyat, *Standard X-ray diffraction powder patterns*. National Bureau of Standards N1, 1953.

[321] C. R. Hubbard, H. E. Swanson, and F. A. Mauer, "A silicon powder diffraction standard reference material," *Journal of applied crystallography*, vol. 8, no. 1, pp. 45–48, 1975.

[322] H. Yokokawa, N. Sakai, T. Kawada, and M. Dokiya, "Thermodynamic stabilities of perovskite oxides for electrodes and other electrochemical materials," *Solid State Ionics*, vol. 52, no. 1-3, pp. 43–56, 1992.

[323] H.-S. Noh, J.-W. Son, H. Lee, H.-S. Song, H.-W. Lee, and J.-H. Lee, "Low Temperature Performance Improvement of SOFC with Thin Film Electrolyte and Electrodes Fabricated by Pulsed Laser Deposition," *Journal of The Electrochemical Society*, vol. 156, no. 12, p. B1484, 2009.

[324] J. Hwang, H. Lee, K. J. Yoon, H.-W. Lee, B.-K. Kim, J.-H. Lee, and J.-W. Son, "Study on the Electrode Reaction Mechanism of Pulsed-Laser Deposited Thin-Film $La_{1-x}Sr_xCoO_{3-\delta}$ (x = 0.2. 0.4) Cathodes," *Journal of the Electrochemical Society*, vol. 159, no. 10, pp. F639–F643, 2012.

[325] D.-H. Myung, J. Hwang, J. Hong, H.-W. Lee, B.-K. Kim, J.-H. Lee, and J.-W. Son, "Pulsed Laser Deposition of La0.6Sr0.4CoO3δ-Ce0.9Gd0.1O2δ Nano-Composite and Its Application to Gradient-Structured Thin-film Cathode of SOFC," *Journal of The Electrochemical Society*, vol. 158, no. 8, p. B1000, 2011.

[326] A. Evans, S. Karalic, J. Martynczuk, M. Prestat, R. Tolke, Z. Yang, and L. J. Gauckler, "$La_{0.6}Sr_{0.4}CoO_{3-\delta}$Thin Films Prepared by Pulsed Laser Deposition as Cathodes for Micro-Solid Oxide Fuel Cells," *ECS Transactions*, vol. 45, no. 1, pp. 333–336, 2012.

[327] J.-H. Park, W.-S. Hong, G. C. Kim, H. J. Chang, J.-H. Lee, K. J. Yoon, and J.-W. Son, "The Effect of Post-Annealing on the Properties of a Pulsed-Laser-Deposited $La_{0.6}Sr_{0.4}CoO_{3-\delta}$- $Ce_{0.9}Gd_{0.1}O_{2-\delta}$ Nano-Composite Cathode," *Journal of the Electrochemical Society*, vol. 160, no. 9, pp. F1027–F1032, 2013.

[328] A. D. Rata, A. Herklotz, L. Schultz, and K. Dörr, "Lattice structure and magnetization of $LaCoO_3$ thin films," *The European Physical Journal B*, vol. 76, no. 2, pp. 215–219, 2010.

[329] H.-S. Noh, J.-W. Son, H. Lee, J.-S. Park, H.-W. Lee, and J.-H. Lee, "Direct Applicability of $La_{0.6}Sr_{0.4}CoO_{3-\delta}$ Thin Film Cathode to Yttria Stabilised Zirconia Electrolytes at T $\leq$ 650°C," *Fuel Cells*, vol. 10, no. 6, pp. 1057–1065, 2010.

[330] C. Peters, A. Weber, and E. Ivers-Tiffee, "Nanoscaled $(La_{0.5}Sr_{0.5})CoO_{3-\delta}$ Thin Film Cathodes for SOFC Application at 500°C < T < 700°C," *Journal of The Electrochemical Society*, vol. 155, no. 7, p. B730, 2008.

[331] T. Nakamura, G. Petzow, and L. Gauckler, "Stability of the perovskite phase $LaBO_3$ (B = V, Cr, Mn, Fe, Co, Ni) in reducing atmosphere I. Experimental results," *Materials Research Bulletin*, vol. 14, no. 5, pp. 649–659, 1979.

[332] S. K. Sahu, S. Tanasescu, B. Scherrer, C. Marinescu, and A. Navrotsky, "Energetics of lanthanide cobalt perovskites: $LnCoO_{2-\delta}$ (Ln = La, Nd, Sm, Gd)," *J. Mater. Chem. A*, vol. 3, no. 38, pp. 19490–19496, 2015.

[333] D. Waller, "The effect of pulse duration and oxygen partial pressure on $La_{0.7}Sr_{0.3}CoO_{3-\delta}$ and $La_{0.7}Sr_{0.3}Co_{0.2}Fe_{0.8}O_{3-\delta}$ films prepared by laser ablation," *Solid State Ionics*, vol. 134, no. 1-2, pp. 119–125, 2000.

[334] J. Ovenstone, J. S. White, and S. T. Misture, "Phase transitions and phase decomposition of $La_{1-x}Sr_xCoO_{3-\delta}$ in low oxygen partial pressures," *Journal of Power Sources*, vol. 181, no. 1, pp. 56–61, 2008.

[335] M. J. Koponen, M. Suvanto, K. Kallinen, T.-J. Kinnunen, M. Härkönen, and T. A. Pakkanen, "Structural transformations in cubic structure of Mn/Co perovskites in reducing and oxidizing atmospheres," *Solid State Sciences*, vol. 8, no. 5, pp. 450–456, 2006.

[336] M. V. Kniga, I. I. Vygovskii, and E. E. Klementoviah, "Interaction of La_2O_3, Nb_2O_3, Pr_2O_3 rare earth oxides and cobalt oxide," *Russ. J. Inorg. Chem. (Engl. Transl)*, vol. 24, p. 652, 1979.

[337] S. Sasaki, K. Fujino, and Y. Takéuchi, "X-Ray Determination of Electron-Density Distributions in Oxides, MgO, MnO, CoO, and NiO, and Atomic Scattering Factors of their Constituent Atoms," *Proceedings of the Japan Academy. Ser. B: Physical and Biological Sciences*, vol. 55, no. 2, pp. 43–48, 1979.

[338] J. Picard, G. Baud, J. Besse, and R. Chevalier, "Croissance cristalline et étude structurale de Co_3O_4," *Journal of the Less Common Metals*, vol. 75, no. 1, pp. 99–104, 1980.

[339] T. Ishihara, K. Nakashima, S. Okada, M. Enoki, and H. Matsumoto, "Defect chemistry and oxygen permeation property of $Pr_2Ni_{0.75}Cu_{0.25}O_4$ oxide doped with Ga," *Solid State Ionics*, vol. 179, no. 27-32, pp. 1367–1371, 2008.

[340] M. Yashima, H. Yamada, S. Nuansaeng, and T. Ishihara, "Role of Ga^{3+} and Cu^{2+} in the High Interstitial Oxide-Ion Diffusivity of Pr_2NiO_4- Based Oxides: Design Concept of Interstitial Ion Conductors through the Higher-Valence d(10) Dopant and Jahn-Teller Effect," *Chemistry of Materials*, vol. 24, no. 21, pp. 4100–4113, 2012.

[341] T. Ishihara, H. Eto, and J. Yan, "Intermediate temperature solid oxide fuel cells using $LaGaO_3$ based oxide film deposited by PLD method," in *International Journal of Hydrogen Energy*, vol. 36, pp. 1862–1867, 2011.

[342] D. Telesca, B. O. Wells, and B. Sinkovic, "Structural reorientation of PLD grown La_2NiO_4 thin films," *Surface Science*, vol. 606, no. 9-10, pp. 865–871, 2012.

[343] L. Goux, M. Gervais, F. Gervais, C. Champeaux, and A. Catherinot, "Strongly oriented BST films on $La_{0.9}Sr_{1.1}NiO_4$ electrodes deposited on various substrates for integration of high capacitances on silicon," *Applied Surface Science*, vol. 252, no. 8, pp. 3085–3091, 2006.

[344] N. Hildenbrand, P. Nammensma, D. H. Blank, H. J. Bouwmeester, and B. A. Boukamp, "Influence of configuration and microstructure on performance of La2$NiO_{4+\delta}$ intermediate-temperature solid oxide fuel cells cathodes," *Journal of Power Sources*, vol. 238, pp. 442–453, 2013.

[345] K.-T. Wu, Y.-A. Soh, and S. J. Skinner, "Epitaxial growth of mixed conducting layered RuddlesdenPopper $La_{n+1}Ni_nO_{3n+1}$ (n = 1, 2 and 3) phases by pulsed laser deposition," *Materials Research Bulletin*, vol. 48, no. 10, pp. 3783–3789, 2013.

[346] K. Yashiro, Y. Kawamura, S. Nakakawaji, K. Sato, K. Amezawa, and J. Mizusaki, "Mechano-Electrochemical effect on Materials Property of Ion Conducting Oxides," *Meeting Abstracts*, vol. MA2012-02, no. 24, pp. 2296–2296, 2012.

[347] J. Hyodo, S. Ida, and T. Ishihara, "Oxide ionic conductivity in Pr_2(Ni,Cu,Ga)$O_{4+\delta}$/(Ce,Sm)$O_{2-\delta}$ laminated film estimated with the Hebb-Wagner method," *Solid State Ionics*, vol. 262, pp. 889–892, 2014.

[348] J. Hyodo, K. Tominaga, J.-E. Hong, S. Ida, and T. Ishihara, "Effects of Three-Dimensional Strain on Electric Conductivity in Au-Dispersed $Pr_{1.90}Ni_{0.71}Cu_{0.24}Ga_{0.05}O_{4+\delta}$," *Journal of Physical Chemistry C*, 2014.

[349] T. Ishihara, H. Matsuda, and Y. Takita, "Doped $LaGaO_3$ Perovskite Type Oxide as a New Oxide Ionic Conductor," *American Chemical Society*, 2002.

[350] C.-Y. Yeh, Z. W. Lu, S. Froyen, and A. Zunger, "Zinc-blendewurtzite polytypism in semiconductors," *Physical Review B*, vol. 46, no. 16, pp. 10086–10097, 1992.

[351] P. Lacorre, J. Torrance, J. Pannetier, A. Nazzal, P. Wang, and T. Huang, "Synthesis, crystal structure, and properties of metallic $PrNiO_3$: Comparison with metallic $NdNiO_3$ and semiconducting $SmNiO_3$," *Journal of Solid State Chemistry*, vol. 91, no. 2, pp. 225–237, 1991.

[352] H. Kroemer, "Heterostructure bipolar transistors and integrated circuits," *Proceedings of the IEEE*, vol. 70, no. 1, pp. 13–25, 1982.

[353] E. Kasper, H. J. Herzog, and H. Kibbel, "A one-dimensional SiGe superlattice grown by UHV epitaxy," *Applied Physics*, vol. 8, no. 3, pp. 199–205, 1975.

[354] E. Kasper and H.-J. Herzog, "Elastic strain and misfit dislocation density in $Si_{0.92}Ge_{0.08}$ films on silicon substrates," *Thin Solid Films*, vol. 44, no. 3, pp. 357–370, 1977.

[355] H. Nagai, "Structure of vapor-deposited $Ga_xIn_{1-x}As$ crystals," *Journal of Applied Physics*, vol. 45, no. 9, p. 3789, 1974.

[356] S. Jain, J. Willis, and R. Bullough, "A review of theoretical and experimental work on the structure of Ge_xSi_{1-x} strained layers and superlattices, with extensive bibliography," *Advances in Physics*, vol. 39, no. 2, pp. 127–190, 1990.

[357] S. Jain and W. Hayes, "Structure, properties and applications of Ge_xSi_{1-x} strained layers and superlattices," *Semiconductor Science and Technology*, 1991.

[358] T. Zheleva, K. Jagannadham, and J. Narayan, "Epitaxial growth in large-lattice-mismatch systems," *Journal of Applied Physics*, vol. 75, no. 2, p. 860, 1994.

[359] F. C. Frank and J. H. van der Merwe, "One-Dimensional Dislocations. II. Misfitting Monolayers and Oriented Overgrowth," *Proceedings of the Royal Society A: Mathematical, Physical and Engineering Sciences*, vol. 198, no. 1053, pp. 216–225, 1949.

[360] C. A. B. Ball, J. H. van der Merwe, and F. R. N. Nabarro, *Dislocations in solids*, vol. 123. 1983.

[361] J. van der Merwe, "Structure of epitaxial crystal interfaces," *Surface Science*, vol. 31, pp. 198–228, 1972.

[362] J. W. Matthews, "Defects associated with the accommodation of misfit between crystals," *Journal of Vacuum Science and Technology*, vol. 12, no. 1, p. 126, 1975.

[363] J. W. Matthews, ed., *Epitaxial growth (Part B)*. 1975.

[364] R. People and J. C. Bean, "Calculation of critical layer thickness versus lattice mismatch for Ge_xSi_{1-x}/Si strained-layer heterostructures," *Applied Physics Letters*, vol. 47, no. 3, p. 322, 1985.

[365] S. C. Jain, A. H. Harker, and R. A. Cowley, "Misfit strain and misfit dislocations in lattice mismatched epitaxial layers and other systems," *Philosophical Magazine A*, vol. 75, no. 6, pp. 1461–1515, 1997.

[366] J. Bean, "Silicon-based semiconductor heterostructures: column IV bandgap engineering," *Proceedings of the IEEE*, vol. 80, no. 4, pp. 571–587, 1992.

[367] S. Jain, T. Gosling, J. Willis, R. Bullough, and P. Balk, "Theoretical comparison of the stability characteristics of capped and uncapped Ge_xSi_{1-x} strained epilayers," *Solid-State Electronics*, vol. 35, no. 8, pp. 1073–1079, 1992.

[368] I. J. Fritz, "Role of experimental resolution in measurements of critical layer thickness for strained-layer epitaxy," *Applied Physics Letters*, vol. 51, no. 14, p. 1080, 1987.

[369] I. J. Fritz, P. L. Gourley, and L. R. Dawson, "Critical layer thickness in $In_{0.2}Ga_{0.8}As$/GaAs single strained quantum well structures," *Applied Physics Letters*, vol. 51, no. 13, p. 1004, 1987.

[370] D. Houghton, C. Gibbings, C. Tuppen, M. Lyons, and M. Halliwell, "The structural stability of uncapped versus buried $Si_{1-x}Ge_x$ strained layers through high temperature processing," *Thin Solid Films*, vol. 183, no. 1-2, pp. 171–182, 1989.

[371] D. C. Houghton, C. J. Gibbings, C. G. Tuppen, M. H. Lyons, and M. A. G. Halliwell, "Equilibrium critical thickness for $Si_{1-x}Ge_x$ strained layers on (100) Si," *Applied Physics Letters*, vol. 56, no. 5, p. 460, 1990.

[372] E. A. Fitzgerald, G. P. Watson, R. E. Proano, D. G. Ast, P. D. Kirchner, G. D. Pettit, and J. M. Woodall, "Nucleation mechanisms and the elimination of misfit dislocations at mismatched interfaces by reduction in growth area," *Journal of Applied Physics*, vol. 65, no. 6, p. 2220, 1989.

[373] R. Hull, J. C. Bean, and C. Buescher, "A phenomenological description of strain relaxation in Ge_xSi_{1-x}/Si(100) heterostructures," *Journal of Applied Physics*, vol. 66, no. 12, p. 5837, 1989.

[374] V. Higgs, P. Kightley, P. J. Goodhew, and P. D. Augustus, "Metal-induced dislocation nucleation for metastable SiGe/Si," *Applied Physics Letters*, vol. 59, no. 7, p. 829, 1991.

[375] T. J. Gosling, S. C. Jain, and A. H. Harker, "The kinetics of strain relaxation in lattice-mismatched semiconductor layers," *Physica Status Solidi (a)*, vol. 146, no. 2, pp. 713–734, 1994.

[376] C. G. Tuppen, C. J. Gibbings, M. Hockly, and S. G. Roberts, "Misfit dislocation multiplication processes in $Si_{1-x}Ge_x$ alloys for $x < 0.15$," *Applied Physics Letters*, vol. 56, no. 1, p. 54, 1990.

[377] F. K. LeGoues, J. A. Ott, K. Eberl, and S. S. Iyer, "In situ study of relaxation of SiGe thin films by the modified FrankRead mechanism," *Applied Physics Letters*, vol. 61, no. 2, p. 174, 1992.

[378] F. K. LeGoues, J. A. Ott, K. Eberl, and S. S. Iyer, "In situ study of relaxation of SiGe thin films by the modified FrankRead mechanism," *Applied Physics Letters*, vol. 61, no. 2, p. 174, 1992.

[379] H. J. Kim, S. H. Oh, and H. M. Jang, "Thermodynamic theory of stress distribution in epitaxial Pb(Zr,Ti)O_3 thin films," *Applied Physics Letters*, vol. 75, no. 20, p. 3195, 1999.

[380] M. Mogensen, N. M. Sammes, and G. A. Tompsett, "Physical, chemical and electrochemical properties of pure and doped ceria," *Solid State Ionics*, vol. 129, no. 1, pp. 63–94, 2000.

[381] N. Schichtel, C. Korte, D. Hesse, and J. Janek, "Elastic strain at interfaces and its influence on ionic conductivity in nanoscaled solid electrolyte thin filmstheoretical considerations and experimental studies," *Physical Chemistry Chemical*, 2009.

[382] J. Venables and G. Spiller, "Nucleation and growth of thin films," *Reports on Progress in*, 1984.

[383] G. Springholz, "Observation of large-scale surface undulations due to inhomogeneous dislocation strain fields in lattice-mismatched epitaxial layers," *Applied Physics Letters*, vol. 75, no. 20, p. 3099, 1999.

[384] M. Albrecht, S. Christiansen, J. Michler, W. Dorsch, H. P. Strunk, P. O. Hansson, and E. Bauser, "Surface ripples, crosshatch pattern, and dislocation formation: Cooperating mechanisms in lattice mismatch relaxation," *Applied Physics Letters*, vol. 67, no. 9, p. 1232, 1995.

[385] K. H. Chang, R. Gilbala, D. J. Srolovitz, P. K. Bhattacharya, and J. F. Mansfield, "Crosshatched surface morphology in strained III-V semiconductor films," *Journal of Applied Physics*, vol. 67, no. 9, p. 4093, 1990.

[386] J. W. P. Hsu, E. A. Fitzgerald, Y. H. Xie, P. J. Silverman, and M. J. Cardillo, "Surface morphology of related Ge_xSi_{1-x} films," *Applied Physics Letters*, vol. 61, no. 11, p. 1293, 1992.

[387] J. H. Li, G. Springholz, J. Stangl, H. Seyringer, V. Holy, F. Schäffler, and G. Bauer, "Strain relaxation and surface morphology of compositionally graded $Si/Si_{1-x}Ge_x$ buffers," *Journal of Vacuum Science & Technology B: Microelectronics and Nanometer Structures*, vol. 16, no. 3, p. 1610, 1998.

[388] M. A. Lutz, R. M. Feenstra, F. K. LeGoues, P. M. Mooney, and J. O. Chu, "Influence of misfit dislocations on the surface morphology of $Si_{1-x}Ge_x$ films," *Applied Physics Letters*, vol. 66, no. 6, p. 724, 1995.

[389] B. F. Lewis, "RHEED oscillation studies of MBE growth kinetics and lattice mismatch strain-induced effects during InGaAs growth on GaAs(100)," *Journal of Vacuum Science & Technology B: Microelectronics and Nanometer Structures*, vol. 2, no. 3, p. 419, 1984.

[390] K. Rodrigo, S. Heiroth, M. Döbeli, N. Pryds, S. Linderoth, J. Schou, and T. Lippert, "Factors controlling the microstructure of $Ce_{0.9}Gd_{0.1}O_{2-\delta}$ films in pulsed laser deposition process," *Journal of optoelectronics and advanced materials*, vol. 12, no. 3, pp. 511–517, 2009.

[391] A. Antonelli and J. Bernholc, "Pressure effects on self-diffusion in silicon," *Physical Review B*, vol. 40, no. 15, pp. 10643–10646, 1989.

[392] H. Hoshino, H. Yanagiya, and M. Shimoji, "Effect of hydrostatic pressure on the electrical conductivity of Ag_3SBr and $\beta - Ag_3SI$," $JournaloftheChemicalSociety, FaradayTransactions1 : PhysicalChemistryinCondensed$

[393] K. S. Kim and W.-K. Paik, "Effects of temperature and pressure on conductance of solid electrolyte, rubidium silver iodide," *Journal of Chemical & Engineering Data*, vol. 20, no. 4, pp. 356–359, 1975.

[394] B. Wang and A. N. Cormack, "Strain Modulation of Defect Structure in Gadolinia-Doped Ceria," *The Journal of Physical Chemistry C*, vol. 117, no. 1, pp. 146–151, 2013.

[395] H. Deguchi, H. Yoshida, T. Inagaki, and M. Horiuchi, "EXAFS study of doped ceria using multiple data set fit," *Solid State Ionics*, vol. 176, no. 23, pp. 1817–1825, 2005.

[396] H. Inaba, R. Sagawa, H. Hayashi, and K. Kawamura, "Molecular dynamics simulation of gadolinia-doped ceria," *Solid State Ionics*, vol. 122, no. 1, pp. 95–103, 1999.

[397] P. Li, I.-W. Chen, J. E. Penner-Hahn, and T.-Y. Tien, "X-ray Absorption Studies of Ceria with Trivalent Dopants," *Journal of the American Ceramic Society*, vol. 74, no. 5, pp. 958–967, 1991.

[398] S. Yamazaki, T. Matsui, T. Ohashi, and Y. Arita, "Defect structures in doped CeO_2 studied by using XAFS spectrometry," *Solid State Ionics*, vol. 136, pp. 913–920, 2000.

[399] L. Minervini, M. O. Zacate, and R. W. Grimes, "Defect cluster formation in M_2O_3-doped CeO_2," *Solid State Ionics*, vol. 116, no. 3, pp. 339–349, 1999.

[400] M. J. D. Rushton and A. Chroneos, "Impact of uniaxial strain and doping on oxygen diffusion in CeO_2," *Scientific reports*, vol. 4, p. 6068, 2014.

[401] M. Rushton, A. Chroneos, S. Skinner, J. Kilner, and R. Grimes, "Effect of strain on the oxygen diffusion in yttria and gadolinia co-doped ceria," *Solid State Ionics*, vol. 230, pp. 37–42, 2013.

[402] D. MORI, H. OKA, Y. SUZUKI, N. SONOYAMA, A. YAMADA, R. KANNO, Y. SUMIYA, N. IMANISHI, and Y. TAKEDA, "Synthesis, structure, and electrochemical properties of epitaxial perovskite $La_{0.8}Sr_{0.2}CoO_3$ film on YSZ substrate," *Solid State Ionics*, vol. 177, no. 5-6, pp. 535–540, 2006.

[403] F. Ye, T. Mori, D. R. Ou, A. N. Cormack, R. J. Lewis, and J. Drennan, "Simulation of ordering in large defect clusters in gadolinium-doped ceria," *Solid State Ionics*, vol. 179, no. 35, pp. 1962–1967, 2008.

[404] F. Ye, T. Mori, D. R. Ou, J. Zou, G. Auchterlonie, and J. Drennan, "Compositional and structural characteristics of nano-sized domains in gadolinium-doped ceria," *Solid State Ionics*, vol. 179, no. 21, pp. 827–831, 2008.

[405] B. Wang, R. J. Lewis, and A. N. Cormack, "Computer simulations of large-scale defect clustering and nanodomain structure in gadolinia-doped ceria," *Acta Materialia*, vol. 59, no. 5, pp. 2035–2045, 2011.

[406] K. Mohan Kant, V. Esposito, and N. Pryds, "Strain induced ionic conductivity enhancement in epitaxial $Ce_{0.9}Gd_{0.1}O_{2-\delta}$ thin films," *Applied Physics Letters*, vol. 100, no. 3, p. 033105, 2012.

[407] D. X. Huang, C. L. Chen, L. Chen, and A. J. Jacobson, "Strain relaxation by directionally aligned precipitate nanoparticles in the growth of single-crystalline Gd-doped ceria thin films," *Applied Physics Letters*, vol. 84, no. 5, p. 708, 2004.

[408] G. Chiodelli, L. Malavasi, V. Massarotti, P. Mustarelli, and E. Quartarone, "Synthesis and characterization of $Ce_{0.8}Gd_{0.2}O_{2-y}$ polycrystalline and thin film materials," *Solid State Ionics*, vol. 176, no. 17, pp. 1505–1512, 2005.

[409] Y.-L. Kuo, C. Lee, Y.-S. Chen, and H. Liang, "Gadolinia-doped ceria films deposited by RF reactive magnetron sputtering," *Solid State Ionics*, vol. 180, no. 26, pp. 1421–1428, 2009.

[410] S. Cho, J. Yoon, J.-H. Kim, X. Zhang, A. Manthiram, and H. Wang, "Microstructural and electrical properties of $Ce_{0.9}Gd_{0.1}O_{1.95}$ thin-film electrolyte in solid-oxide fuel cells," *Journal of Materials Research*, vol. 26, no. 07, pp. 854–859, 2011.

[411] Y. B. Kim, J. H. Shim, T. M. Gur, and F. B. Prinz, "Epitaxial and Polycrystalline Gadolinia-Doped Ceria Cathode Interlayers for Low Temperature Solid Oxide Fuel Cells," *Journal of The Electrochemical Society*, vol. 158, no. 11, p. B1453, 2011.

[412] J. W. Freeland, J. X. Ma, and J. Shi, "Ferromagnetic spin-correlations in strained $LaCoO_3$ thin films," *Applied Physics Letters*, vol. 93, no. 21, p. 212501, 2008.

[413] R. F. Klie, T. Yuan, M. Tanase, G. Yang, and Q. Ramasse, "Direct measurement of ferromagnetic ordering in biaxially strained $LaCoO_3$ thin films," *Applied Physics Letters*, vol. 96, no. 8, p. 082510, 2010.

[414] D. Fuchs, C. Pinta, T. Schwarz, P. Schweiss, P. Nagel, S. Schuppler, R. Schneider, M. Merz, G. Roth, and H. v. Löhneysen, "Ferromagnetic order in epitaxially strained $LaCoO_3$ thin films," *Physical Review B*, vol. 75, no. 14, p. 144402, 2007.

[415] Z. Cai, Y. Kuru, J. W. Han, Y. Chen, and B. Yildiz, "Surface electronic structure transitions at high temperature on perovskite oxides: the case of strained $La_{0.8}Sr_{0.2}CoO_3$ thin films.," *Journal of the American Chemical Society*, vol. 133, no. 44, pp. 17696–704, 2011.

[416] J. Januschewsky, M. Ahrens, A. Opitz, F. Kubel, and J. Fleig, "Optimized $La_{0.6}Sr_{0.4}CoO_{3-\delta}$ Thin-Film Electrodes with Extremely Fast Oxygen-Reduction Kinetics," *Advanced Functional Materials*, vol. 19, no. 19, pp. 3151–3156, 2009.

[417] Z. Cai, M. Kubicek, J. Fleig, and B. Yildiz, "Chemical Heterogeneities on $La_{0.6}Sr_{0.4}CoO_{3\delta}$ Thin FilmsCorrelations to Cathode Surface Activity and Stability," *Chemistry of Materials*, vol. 24, no. 6, pp. 1116–1127, 2012.

[418] N. Imanishi, T. Matsumura, Y. Sumiya, K. Yoshimura, A. Hirano, Y. Takeda, D. Mori, and R. Kanno, "Impedance spectroscopy of perovskite air electrodes for SOFC prepared by laser ablation method," *Solid State Ionics*, vol. 174, no. 1-4, pp. 245–252, 2004.

[419] W. T. Hong, M. Gadre, Y.-L. Lee, M. D. Biegalski, H. M. Christen, D. Morgan, and Y. Shao-Horn, "Tuning the Spin State in $LaCoO_3$ Thin Films for Enhanced High-Temperature Oxygen Electrocatalysis," *The Journal of Physical Chemistry Letters*, vol. 4, no. 15, pp. 2493–2499, 2013.

[420] H. M. Christen, E. D. Specht, S. S. Silliman, and K. S. Harshavardhan, "Ferroelectric and antiferroelectric coupling in superlattices of paraelectric perovskites at room temperature," *Physical Review B*, vol. 68, no. 2, p. 020101, 2003.

[421] D. P. Norton, C. Park, J. D. Budai, S. J. Pennycook, and C. Prouteau, "Plume-induced stress in pulsed-laser deposited CeO_2 films," *Applied Physics Letters*, vol. 74, no. 15, p. 2134, 1999.

[422] V. Kanchana, G. Vaitheeswaran, A. Svane, and A. Delin, "First-principles study of elastic properties of CeO_2 , ThO_2 and PoO_2," *Journal of Physics: Condensed Matter*, vol. 18, no. 42, pp. 9615–9624, 2006.

[423] T. R. Armstrong, J. W. Stevenson, L. R. Pederson, and P. E. Raney, "Dimensional Instability of Doped Lanthanum Chromite," *Journal of The Electrochemical Society*, vol. 143, no. 9, p. 2919, 1996.

[424] A. Zuev, L. Singheiser, and K. Hilpert, "Defect structure and isothermal expansion of A-site and B-site substituted lanthanum chromites," *Solid State Ionics*, vol. 147, no. 1-2, pp. 1–11, 2002.

[425] K. Hilpert, R. W. Steinbrech, F. Boroomand, E. Wessel, F. Meschke, A. Zuev, O. Teller, H. Nickel, and L. Singheiser, "Defect formation and mechanical stability of perovskites based on $LaCrO_3$ for solid oxide fuel cells (SOFC)," *Journal of the European Ceramic Society*, vol. 23, no. 16, pp. 3009–3020, 2003.

[426] X. Chen, J. Yu, and S. B. Adler, "Thermal and Chemical Expansion of Sr-Doped Lanthanum Cobalt Oxide ($La_{1-x}Sr_xCoO_{3-\delta}$)," *Chemistry of Materials*, vol. 17, no. 17, pp. 4537–4546, 2005.

[427] S. Miyoshi, J. O. Hong, K. Yashiro, A. Kaimai, Y. Nigara, K. Kawamura, T. Kawada, and J. Mizusaki, "Lattice expansion upon reduction of perovskite-type $LaMnO_3$ with oxygen-deficit nonstoichiometry," *Solid State Ionics*, vol. 161, no. 3-4, pp. 209–217, 2003.

[428] A. Y. Zuev and D. S. Tsvetkov, "Oxygen nonstoichiometry, defect structure and defect-induced expansion of undoped perovskite $LaMnO_{3-\delta}$," *Solid State Ionics*, vol. 181, no. 11-12, pp. 557–563, 2010.

[429] A. N. Petrov, V. A. Cherepanov, and A. Y. Zuev, "Thermodynamics, defect structure, and charge transfer in doped lanthanum cobaltites: An overview," vol. 10, no. 8, pp. 517–537, 2006.

[430] A. Y. Zuev, A. N. Petrov, A. I. Vylkov, and D. S. Tsvetkov, "Oxygen nonstoichiometry and defect structure of undoped and doped lanthanum cobaltites," in *Journal of Materials Science*, vol. 42, pp. 1901–1908, Kluwer Academic Publishers-Plenum Publishers, mar 2007.

[431] S. R. Bishop, K. L. Duncan, and E. D. Wachsman, "Thermo-Chemical Expansion in Strontium-Doped Lanthanum Cobalt Iron Oxide," *Journal of the American Ceramic Society*, vol. 93, no. 12, pp. 4115–4121, 2010.

[432] S. Y. Jeon, M. B. Choi, J. Y. Park, and S. J. Song, "Thermal and chemical expansion of mixed conducting $La_{0.1}Sr_{0.9}Co_{0.8}Fe_{0.2}O_{3-\delta}$," *Journal of Ceramic Processing Research*, vol. 12, no. 1, pp. 26–29, 2011.

[433] M.-B. Choi, D.-K. Lim, E. Wachsman, and S.-J. Song, "Oxygen nonstoichiometry and chemical expansion of mixed conducting $La_{0.1}Sr_{0.9}Co_{0.8}Fe_{0.2}O_{3-\delta}$," *Solid State Ionics*, vol. 221, pp. 22–27, 2012.

[434] S.-Y. Jeon, M.-B. Choi, J.-Y. Park, and S.-J. Song, "Thermal and chemical expansion of mixed conducting $La_{0.1}Sr0.9Co_{0.8}Fe_{0.2}O_{3-\delta}$," *Journal of Ceramic Processing Research*, vol. 12, no. 1, pp. 26–29, 2011.

[435] M. Kuhn, S. Hashimoto, K. Sato, K. Yashiro, and J. Mizusaki, "Oxygen nonstoichiometry, thermo-chemical stability and lattice expansion of $La_{0.6}Sr_{0.4}FeO_{3-\delta}$," *Solid State Ionics*, vol. 195, no. 1, pp. 7–15, 2011.

[436] S.-i. Hashimoto, Y. Fukuda, M. Kuhn, K. Sato, K. Yashiro, and J. Mizusaki, "Thermal and chemical lattice expansibility of $La_{0.6}Sr_{0.4}Co_{1-y}Fe_yO_{3-\delta}$ (y=0.2, 0.4, 0.6 and 0.8)," *Solid State Ionics*, vol. 186, no. 1, pp. 37–43, 2011.

[437] M. Kuhn, S. Hashimoto, K. Sato, K. Yashiro, and J. Mizusaki, "Thermo-chemical lattice expansion in $La_{0.6}Sr_{0.4}Co_{1-y}Fe_yO_{3-\delta}$," *Solid State Ionics*, vol. 241, pp. 12–16, 2013.

[438] X. Chen and T. Grande, "Anisotropic chemical expansion of $La_{1-x}Sr_xCoO_{3-\delta}$," *Chemistry of Materials*, vol. 25, no. 6, pp. 927–934, 2013.

[439] P. Materials, "Anisotropic and Nonlinear Thermal and Chemical Expansion of $La_{1-x}Sr_xFeO_{3-\delta}$ (x = 0.3, 0.4, 0.5) Perovskite Materials," *Chemistry of Materials*, no. 7491, 2013.

[440] M. Kuhn, Y. Fukuda, S. Hashimoto, K. Sato, K. Yashiro, and J. Mizusaki, "Oxygen Nonstoichiometry and Thermo-Chemical Stability of Perovskite-Type $La_{0.6}Sr_{0.4}Co_{1-y}Fe_yO_{3-\delta}$ (y = 0, 0.2, 0.4, 0.5, 0.6, 0.8, 1) Materials," *Journal of the Electrochemical Society*, vol. 160, no. 1, pp. F34–F42, 2012.

[441] A. R. Ruffa, "Empirical determination of thermal expansion in insulators with no experimental input," *Journal of Materials Science*, vol. 15, no. 9, pp. 2268–2274, 1980.

[442] H. Inaba and H. Tagawa, "Semi-empirical estimation of thermal expansion coefficients of Perovskite-type oxides," *Nippon seramikkusu kyokai gakujutsu ronbunshi*, 1998.

[443] J. Mastin, M. A. Einarsrud, and T. Grande, "Structural and thermal properties of $La_{1-x}Sr_xCoO_{3-\delta}$," *Chemistry of Materials*, vol. 18, no. 25, pp. 6047–6053, 2006.

[444] C. J. Howard and B. J. Kennedy, "The orthorhombic and rhombohedral phases of $LaGaO_3$ - a neutron powder diffraction study," *Journal Of Physics-Condensed Matter*, vol. 11, no. 16, pp. 3229–3236, 1999.

[445] P. Radaelli and S. Cheong, "Structural phenomena associated with the spin-state transition in $LaCoO_3$," *Physical Review B*, 2002.

[446] C. J. Howard, B. J. Kennedy, and B. C. Chakoumakos, "Neutron powder diffraction study of rhombohedral rare-earth aluminates and the rhombohedral to cubic phase transition," *Journal of Physics: Condensed Matter*, vol. 12, no. 4, pp. 349–365, 1999.

[447] T. Grande, J. R. Tolchard, and S. M. Selbach, "Anisotropic Thermal and Chemical Expansion in Sr-Substituted $LaMnO_{3+\delta}$: Implications for Chemical Strain Relaxation," *Chemistry of Materials*, vol. 24, no. 2, pp. 338–345, 2012.

[448] K. Hansen, "A-site deficient $(La_{0.6}Sr_{0.4})_{1s}Fe_{0.8}Co_{0.2}O_{3-\delta}$ perovskites as SOFC cathodes," *Solid State Ionics*, vol. 178, no. 23-24, pp. 1379–1384, 2007.

[449] S. Otoshi, "Changes in the Phases and Electrical Conduction Properties of $(La_{1-x}Sr_x)_{1-y}MnO_{3-\delta}$," *Journal of The Electrochemical Society*, vol. 138, no. 5, p. 1519, 1991.

[450] A. Berenov, "Oxygen tracer diffusion in undoped lanthanum manganites," *Solid State Ionics*, vol. 122, no. 1-4, pp. 41–49, 1999.

[451] J. W. Stevenson, P. F. Hallman, T. R. Armstrong, and L. A. Chick, "Sintering Behavior of Doped Lanthanum and Yttrium Manganite," *Journal of the American Ceramic Society*, vol. 78, no. 3, pp. 507–512, 1995.

[452] G. Kim, S. Wang, A. Jacobson, and C. Chen, "Measurement of oxygen transport kinetics in epitaxial $La_2NiO_{4+\delta}$ thin films by electrical conductivity relaxation," *Solid State Ionics*, vol. 177, no. 17, pp. 1461–1467, 2006.

[453] Z. Cheng, S. Zha, L. Aguilar, and M. Liu, "Chemical, electrical, and thermal properties of strontium doped lanthanum vanadate," *Solid State Ionics*, vol. 176, no. 23-24, pp. 1921–1928, 2005.

[454] Z. L. Wang and J. Zhang, "Tetragonal domain structure and magnetoresistance of $La_{1-x}Sr_xCoO_3$," *Physical Review B*, vol. 54, no. 2, pp. 1153–1158, 1996.

[455] V. G. Bhide, D. S. Rajoria, G. R. Rao, and C. N. R. Rao, "Mössbauer Studies of the High-Spin-Low-Spin Equilibria and the Localized-Collective Electron Transition in $LaCoO_3$," *Physical Review B*, vol. 6, no. 3, pp. 1021–1032, 1972.

[456] V. G. Bhide, D. S. Rajoria, Y. S. Reddy, G. R. Rao, G. V. S. Rao, and C. N. R. Rao, "Localized-to-Itinerant Electron Transitions in Rare-Earth Cobaltates," *Physical Review Letters*, vol. 28, no. 17, pp. 1133–1136, 1972.

[457] J. Haber and L. Ungier, "On chemical shifts of ESCA and Auger lines in cobalt oxides," *Journal of Electron Spectroscopy and Related Phenomena*, vol. 12, no. 3, pp. 305–312, 1977.

[458] D. Sarma and C. Rao, "XPES studies of oxides of second- and third-row transition metals including rare earths," *Journal of Electron Spectroscopy and Related Phenomena*, vol. 20, no. 1, pp. 25–45, 1980.

[459] Y. Uwamino, T. Ishizuka, and H. Yamatera, "X-ray photoelectron spectroscopy of rare-earth compounds," *Journal of Electron Spectroscopy and Related Phenomena*, vol. 34, no. 1, pp. 67–78, 1984.

[460] N. S. McIntyre and M. G. Cook, "X-ray photoelectron studies on some oxides and hydroxides of cobalt, nickel, and copper," *Analytical Chemistry*, vol. 47, no. 13, pp. 2208–2213, 1975.

[461] T. Chuang, C. Brundle, and D. Rice, "Interpretation of the x-ray photoemission spectra of cobalt oxides and cobalt oxide surfaces," *Surface Science*, vol. 59, no. 2, pp. 413–429, 1976.

[462] M. C. Biesinger, B. P. Payne, A. P. Grosvenor, L. W. Lau, A. R. Gerson, and R. S. Smart, "Resolving surface chemical states in XPS analysis of first row transition metals, oxides and hydroxides: Cr, Mn, Fe, Co and Ni," *Applied Surface Science*, vol. 257, no. 7, pp. 2717–2730, 2011.

[463] K. S. Kim, "X-ray-photoelectron spectroscopic studies of the electronic structure of CoO," *Physical Review B*, vol. 11, no. 6, pp. 2177–2185, 1975.

[464] D. Briggs, "Handbook of X-ray Photoelectron Spectroscopy," *Surface and Interface Analysis*, vol. 3, no. 4, pp. v–v, 1981.

[465] B. V. Crist, *Handbook of Monochromatic Xps Spectra, Vol. 2, Commercially Pure Binary Oxides,*. XPS International, LLC, 1999.

[466] L. Pauling, *The nature of the chemical bond and the structure of molecules and crystals: an introduction to modern structural chemistry*. 1960.

[467] L. Vegard, "Die Konstitution der Mischkristalle und die Raumfüllung der Atome," *Zeitschrift für Physik*, vol. 5, no. 1, pp. 17–26, 1921.

[468] R. H. E. Van Doorn and A. J. Burggraaf, "Structural aspects of the ionic conductivity of $La_{1-x}Sr_xCoO_{3-\delta}$," *Solid State Ionics*, vol. 128, no. 1-4, pp. 65–78, 2000.

[469] N. Orlovskaya, N. Browning, and A. Nicholls, "Ferroelasticity in mixed conducting $LaCoO_3$ based perovskites: A ferroelastic phase transition," *Acta Materialia*, vol. 51, no. 17, pp. 5063–5071, 2003.

[470] E. Kotomin, Y. Mastrikov, and E. Heifets, "Adsorption of atomic and molecular oxygen on the $LaMnO_3$ (001) surface: ab initio supercell calculations and thermodynamics," *Physical Chemistry*, 2008.

[471] Y.-L. Lee, J. Kleis, J. Rossmeisl, and D. Morgan, "Ab initio energetics of $LaBO_3$ (001) (B = Mn , Fe, Co, and Ni) for solid oxide fuel cell cathodes," *Physical Review B*, vol. 80, no. 22, p. 224101, 2009.

[472] M. Read, M. Islam, G. Watson, and F. King, "Defect chemistry and surface properties of $LaCoO_3$," *Journal of Materials*, 2000.

[473] U. Diebold, "The surface science of titanium dioxide," *Surface Science Reports*, vol. 48, no. 5, pp. 53–229, 2003.

[474] C. Castellarin-Cudia, S. Surnev, G. Schneider, R. Podlucky, M. Ramsey, and F. Netzer, "Strain-induced formation of arrays of catalytically active sites at the metaloxide interface," *Surface Science*, vol. 554, no. 2, pp. L120–L126, 2004.

[475] D. O. Klenov, W. Donner, B. Foran, and S. Stemmer, "Impact of stress on oxygen vacancy ordering in epitaxial $(La_{0.5}Sr_{0.5})CoO_{3-\delta}$ thin films," *Applied Physics Letters*, vol. 82, no. 20, p. 3427, 2003.

[476] D.-J. Shu, S.-T. Ge, M. Wang, and N.-B. Ming, "Interplay between External Strain and Oxygen Vacancies on a Rutile TiO_2 (110) Surface," *Physical Review Letters*, vol. 101, no. 11, p. 116102, 2008.

[477] T. Mayeshiba and D. Morgan, "Strain effects on oxygen migration in perovskites," *Phys. Chem. Chem. Phys.*, vol. 17, no. 4, pp. 2715–2721, 2015.

[478] H. Jalili, J. W. Han, Y. Kuru, Z. Cai, and B. Yildiz, "New Insights into the Strain Coupling to Surface Chemistry, Electronic Structure, and Reactivity of $La_{0.7}Sr_{0.3}MnO_3$," *The Journal of Physical Chemistry Letters*, vol. 2, no. 7, pp. 801–807, 2011.

[479] M. Burriel, G. Garcia, J. Santiso, J. A. Kilner, R. J. Chater, and S. J. Skinner, "Anisotropic oxygen diffusion properties in epitaxial thin films of $La_2NiO_{4+\delta}$," *J. Mater. Chem.*, vol. 18, no. 4, pp. 416–422, 2008.

[480] S. Carter, A. Selcuk, R. Chater, J. Kajda, J. Kilner, and B. Steele, "Oxygen transport in selected nonstoichiometric perovskite-structure oxides," *Solid State Ionics*, vol. 53-56, pp. 597–605, 1992.

[481] R. A. De Souza, M. J. Pietrowski, U. Anselmi-Tamburini, S. Kim, Z. A. Munir, and M. Martin, "Oxygen diffusion in nanocrystalline yttria-stabilized zirconia: the effect of grain boundaries," *Physical Chemistry Chemical Physics*, vol. 10, no. 15, p. 2067, 2008.

[482] Y. Huang, P. Y. Yu, M.-N. Charasse, Y. Lo, and S. Wang, "Raman study of an epitaxial GaAs layer on a Si [100] substrate," *Applied Physics Letters*, vol. 51, no. 3, p. 192, 1987.

[483] R. T. P. Whipple, "CXXXVIII. Concentration contours in grain boundary diffusion," *The London, Edinburgh, and Dublin Philosophical Magazine and Journal of Science*, 1954.

[484] A. L. Claire, "The analysis of grain boundary diffusion measurements," *British Journal of Applied Physics*, 1963.

[485] L. Harrison, "Influence of dislocations on diffusion kinetics in solids with particular reference to the alkali halides," *Transactions of the Faraday Society*, 1961.

[486] H. Levine and C. MacCallum, "Grain boundary and lattice diffusion in polycrystalline bodies," *Journal of Applied Physics*, 1960.

[487] J. Farver and R. Yund, "Oxygen grain boundary diffusion in natural and hot-pressed calcite aggregates," *Earth and Planetary Science Letters*, 1998.

[488] J. Farver and R. Yund, "Measurement of oxygen grain boundary diffusion in natural, fine-grained, quartz aggregates," *Geochimica et Cosmochimica Acta*, 1991.

[489] H. Yurimoto, M. Morioka, and H. Nagasawa, "Diffusion in single crystals of melilite: I. Oxygen," *Geochimica et Cosmochimica Acta*, 1989.

[490] D. Prot and C. Monty, "Self-diffusion in $\alpha Al_2O_3.II.Oxygendiffusionin`undoped'singlecrystals,''$ *Phi*

[491] D. Prot, M. Le Gall, B. Lesage, A. M. Huntz, and C. Monty, "Self-diffusion in $\alpha Al_2O.IV.Oxygengrain-boundaryself-diffusioninundopedandyttria-dopedaluminapolycrystals,''$ *Philosophical*, 1996.

[492] B. Amami, M. Addou, F. Millot, A. Sabioni, and C. Monty, "Self-diffusion in $\alpha - Fe_2O_3naturalsinglecrystals,''$ *Ionics*, 1999.

[493] E. Navickas, T. Huber, Y. Chen, and W. Hetaba, "Fast oxygen exchange and diffusion kinetics of grain boundaries in Sr-doped $LaMnO_3$ thin films," *Physical Chemistry*, 2015.

[494] R. D. Souza and M. Pietrowski, "Oxygen diffusion in nanocrystalline yttria-stabilized zirconia: the effect of grain boundaries," *Physical Chemistry*, 2008.

[495] I. Kaur, Y. Mishin, and W. Gust, *Fundamentals of grain and interphase boundary diffusion*. Ziegler Press, 1995.

[496] A. Vailionis, H. Boschker, W. Siemons, E. P. Houwman, D. H. A. Blank, G. Rijnders, and G. Koster, "Misfit strain accommodation in epitaxial ABO_3 perovskites: Lattice rotations and lattice modulations," *Physical Review B*, vol. 83, no. 6, p. 064101, 2011.

[497] C. Brahim, A. Ringuedé, E. Gourba, M. Cassir, A. Billard, and P. Briois, "Electrical properties of thin bilayered YSZ/GDC SOFC electrolyte elaborated by sputtering," *Journal of Power Sources*, vol. 156, no. 1, pp. 45–49, 2006.

[498] Y. Ji, J. Kilner, and M. Carolan, "Electrical conductivity and oxygen transfer in gadolinia-doped ceria (CGO)- $Co_3O_{4-\delta}$ composites," *Journal of the European Ceramic Society*, vol. 24, no. 14, pp. 3613–3616, 2004.

[499] J. L. Rupp and L. J. Gauckler, "Microstructures and electrical conductivity of nanocrystalline ceria-based thin films," *Solid State Ionics*, vol. 177, no. 26, pp. 2513–2518, 2006.

[500] I. Kosacki, T. Suzuki, V. Petrovsky, and H. U. Anderson, "Electrical conductivity of nanocrystalline ceria and zirconia thin films," *Solid State Ionics*, vol. 136, pp. 1225–1233, 2000.